Konstantinos Kontis *Editor*

Shock Wave Interactions

Selected Articles from the 22nd International Shock Interaction Symposium, University of Glasgow, United Kingdom, 4–8 July 2016

Springer

Shock Wave Interactions

Konstantinos Kontis
Editor

Shock Wave Interactions

Selected Articles from the 22nd International Shock Interaction Symposium, University of Glasgow, United Kingdom, 4–8 July 2016

Springer

Editor
Konstantinos Kontis
School of Engineering
University of Glasgow
Glasgow
UK

ISBN 978-3-319-73179-7 ISBN 978-3-319-73180-3 (eBook)
https://doi.org/10.1007/978-3-319-73180-3

Library of Congress Control Number: 2017962974

Printed on acid-free paper

This Springer imprint is published by the registered company Springer International Publishing AG part of Springer Nature
The registered company address is: Gewerbestrasse 11, 6330 Cham, Switzerland

Preface

This volume is a selection of peer-reviewed articles from the 22nd International Shock Interaction Symposium held at the University of Glasgow, Scotland, United Kingdom, 4–8 July 2016.

Founded in 1451, the University of Glasgow (UoG) has a tradition of excellence as the fourth oldest university in the English-speaking world. It is a member of the elite Russell Group of leading UK research universities and a founding member of Universitas21. UoG has fostered the talents of Nobel laureates, Scotland's first female medical graduates, and includes among its alumni, some of the world's most renowned innovators, from scientist Lord Kelvin, economist Adam Smith, engineer James Watt, to the pioneer of television John Logie Baird.

The University of Glasgow has been a home to aerospace research for over 80 years, and today our researchers are tackling the multidisciplinary challenges faced by the aerospace industry in the twenty-first century. The University has established major initiatives to deliver capability and technologies that contribute to the global aims of greener, faster and safer travel. The University is reinvigorated aerospace research by investing heavily, not only in new academic staff but also in new infrastructure and facilities expanding the existing aerodynamic testing, flight modelling and simulation capability. These investments include state-of-the-art flight simulators, and wind tunnels and testing facilities covering subsonic, transonic, supersonic and hypersonic flow regimes, unique in the UK.

The International Symposia on Shock Interaction merged as an heir to both the Mach Reflection and Shock Vortex Interaction Symposia. Started in 1981, these scientific biannual meetings provide an ideal platform to expose new developments and discuss recent challenges in the field of shock wave interaction phenomena. The goal of the symposia is to offer a forum for international interaction between young and established scientists in the field of shock and blast wave interaction phenomena. The conference welcomes contributions based on ongoing research and work in progress. After 2014 in Riga, Latvia, it was an honour for us to host the Symposium in Glasgow.

The scientific programme was complemented by a number of social events including a Civic reception hosted by Lord Provost in the Glasgow City Chambers and an excursion to Stirling Castle, Loch Lomond and Glengoyne distillery. The 22nd International Shock Interaction Symposium could not have been realised without the support of the University of Glasgow, the International Shock Wave Institute (ISWI) and the People Make Glasgow. The dedication, enthusiasm and team spirit of Dr. Sriram Rengarajan, Dr. A. Busse, Dr. H. Zare-Behtash, Dr. K. Ramesh, Dr. C. White, my research fellows and Ph.D. students should be acknowledged. I would like to express my gratitude to the members of the International Advisory Committee and Scientific Review Committee for their continuous support during the preparation and running of the conference.

Glasgow, UK

Professor Konstantinos Kontis
Chairman

Committee

International Advisory Committee

Takashi Abe
Nicholas Apazidis
Elangannan Arunan
Gabi Ben-Dor
Riccardo Bonazza
Martin Brouillette
Veronica Eliasson
Nikita Fomin
Sudhir Gai
Walter Garen
Michael Gedalin
Victor Golub
Abdellah Hadjadj
Klaus Hannemann
Ronald Hanson
Koichi Hayashi
David Mee
Richard Morgan
Ozer Igra
Jeff Jacobs
Gopalan Jagadeesh
In-Seuck Jeung
Zonglin Jiang
Georges Jourdan
Gennady Kanel
Valeriy Kedrinskiy
Harald Kleine
Konstantinos Kontis

Irina Krassovskaya
Assa Lifshitz
Meng-Sing Liou
Achim Loske
Frank K. Lu
Kazuo Maeno
Evgeny Zaretsky
David Zeituon
Christian Mundt
Charles Needham
Herbert Olivier
Marcello Onofri
K. P. J. Reddy
Oren Sadot
Yoshitaka Sakamura
Akihiro Sasoh
Friedrich Seiler
Beric Skews
Kazuyoshi Takayama
Evgeny Timofeev
Zbigniew Walenta
Chih-yung Wen
Ji Ming Yang
Hamid Hosseini
Lazhar Houas

Scientific Review Committee

Nicholas Apazidis
Gabi Ben-Dor
Victor Golub
Abdellah Hadjadj
Klaus Hannemann
S. Hamid R. Hosseini
Ozer Igra
Gopalan Jagadeesh
Valeriy Kedrinskiy
Friedrich Seiler
Susumu Kobayashi
Konstantinos Kontis
Kin Hong Lo
Frank K. Lu
Charles Needham

Herbert Olivier
Marcello Onofri
K. P. J. Reddy
Akihiro Sasoh
Beric Skews
Kazuyoshi Takayama
Evgeny Timofeev
Takahiro Ukai
Zbigniew Walenta
Craig White
Hossein Zare-Behtash
Irinia Znamenskaya
Harald Kleine

Local Organising Committee

Angela Busse
Sarah Fitzpatrick
Francesca Gnani
Konstantinos Kontis
Kin Hing Lo
Kiran Ramesh
Sriram Rengarajan
Andrew Russell
Shaun Skinner
Takahiro Ukai
Craig White
Hossein Zare-Behtash

Contents

Scale Effects on the Transition of Reflected Shock Waves

Kazuyoshi Takayama, Atsushi Abe and Mikhail Chernyshov

Abstract This is a summary of shock tube experiments performed at the Tohoku University from 1975 to 2005. Critical transition angles of reflected shock waves over concave and convex walls of radii from 20 to 300 mm were experimentally obtained and compared with the numerical simulation based on the Navier–Stokes equations. The experimental critical transition angles varied with the radii of curved walls and strongly affected by the presence of the boundary layer developing along curved walls. The effects of critical transition on shock wave dynamic, shock wave reflection from roughened wedges, double wedges, and shock focusing from curved walls were presented.

1 Introduction

This is a result of a collaboration started when the first author stayed in the Peter the Great Saint Petersburg Polytechnique University in 2015. He discussed with the third author and the second author to contribute to the project with his fine numerical simulations.

In steady flows, the pattern of oblique shock waves reflected from a solid wall is either a regular reflection RR or a Mach reflection MR, depending on the angle of their intersection with the wall. The reflection of a normal shock wave to a solid wall is MR, whereas a shock wave colliding head-on against a flat wall is RR. Hence, in changing the wall angle, the reflected shock wave transits from RR to MR or from MR to RR at an angle, which is defined as a critical transition angle θ_{crit} [1].

K. Takayama (✉)
Tohoku University, Sendai, Japan
e-mail: k.takayama@mac.com

A. Abe
Science & Engineering Analysis Department,
ITOCHU Techno-Solutions Corporation, Tokyo, Japan

M. Chernyshov
Peter the Great St. Petersburg Polytechnique University, St. Petersburg, Russia

K. Kontis (ed.), *Shock Wave Interactions*,
https://doi.org/10.1007/978-3-319-73180-3_1

The θ_{crit} typically represents the nonlinearity of the shock wave dynamics. The derivation of its analytical solution predicting the θ_{crit} is one of the important subjects of modern gas dynamics [1].

Patterns of reflected shock waves from straight wedges in shock tubes are self-similar, and hence, the flow is defined as pseudo-steady. The formulation of the oblique shock wave reflection in a steady flow and their analytical solutions of θ_{crit} are applied even to the pseudo-steady flow. In shock tube flows, the reflected shock wave patterns are either RR or MR depending on a wedge angle and Ms. In moderately strong shock waves, we renamed the MR as a single MR, SMR. In weak shock wave reflections from wedges of small inclination angles, distinct triple points are not formed. Hence, this reflection pattern was named as von Neumann MR. Some of irregular MR patterns were redefined as a transitional MR and a double MR.

In order to comprehensively resolve the MR phenomena, Prof. Dewy held, for the first time in 1981, Mach Reflection Symposium in Victoria. Later Ben-Dor summarized the state of art of reflected shock waves [2]. In those days, resources of super-computation were limited so that analytical studies were mostly to find analytical solutions. A long time before the advent of high-speed electronic imaging with better spatial resolution, shock tube experiments were directed to the high-speed visualization of time-frozen images.

In the third MRS held in 1982 held at Freiburg, we reported our preliminary results of the θ_{crit} over concave and convex walls of various radii in our 40 mm 80 mm shock tube [3, 4]. Referring our work Professor Reichenbach of the EMI Freiburg and Prof. Dewey of the University of Victoria also reported their results of θ_{crit} of curved walls of various radii and found that the θ_{crit} varied depending on the radii and deviated from analytical solutions. This trend contradicts the concept of self-similarity. We also found that in the shock wave reflection from wedges of roughened surface, θ_{crit} was decreased significantly from analytical predictions depending on the degree of surface roughness [5].

In 1994, when the MRS was held for second time in Victoria, Prof. Dewey presented his unreported experimental results. The reflection pattern from a wedge of slightly smaller wedge angle from θ_{crit} is RR near the leading edge and later MR appeared [6]. Audience argued but no one could explain such a strange transition. The first author at that time believed that experiments were erroneous.

Later in 1997, Henderson [6], for the first time, reported numerically the delayed transition in argon and proven that it was created by the displacement effect of the boundary layer developing along the wedge surface. To experimentally confirm the delayed transition, we performed a series of experiments in a 100 mm $\times$ 180 mm diaphragm-less shock tube and confirmed that the delayed transition occurred by the viscous effect [7]. At the same time, we solved numerically the Navier–Stokes equations with a fine mesh refinement and compared with the experiments. Then, we found that at low initial pressures, that is, the lower Reynolds number Re, the delayed transition distance L_d became longer [8]. This implies that if the reflection pattern was observed in a smaller shock tube at low initial pressures, it would be RR, whereas in a larger shock tube in the same initial condition, MR appears.

We understood that the deviation of θ_{crit} from analytical solutions and the dependence on radii on θ_{crit} [3] were created due to the boundary layer displacement effect. We decided to compare our previous data with the Navier–Stokes solvers and eventually confirmed the effects of Re on θ_{crit}. We visualized, by using double exposure holographic interferometry [9], a shock wave reflected from concave walls of various configurations. The transition of reflected shock wave contributed significantly to the focusing process and the geometry of concave walls.

Three MR patterns are defined depending on the motion of their triple point trajectories [1]. For the triple points moving away from the wall, the reflection pattern is named as direct MR, which is self-similar appearing in a pseudo-steady flow. In case the triple point is exactly parallel to the wall, this MR pattern is independent of the elapse of time and hence is named as the stationary MR. This MR is possible only in a steady flow. For the triple point moving toward the wall, the MR terminates soon or later. This pattern is called as the inverse MR and eventually transits to RR. Hence, this MR cannot be self-similar but belongs to a truly unsteady flow.

In the shock wave reflection over concave walls, all three MR patterns successively appear. When a shock wave reflected from a concave double wedge, a stationary MR can appear. However, in the shock tube flows, the consistent presence of a stationary MR violates the principle of shock tube flows. Hence, it exists only temporary and transits immediately to the inverse MR. Although Komuro numerically confirmed the presence of the stationary MR [10, 11], the boundary layer would discourage the consistent presence of the stationary MR.

2 Experiment

2.1 40 mm × 80 mm Shock Tube

Figure 1 shows a 40 mm × 80 mm shock tube test section having a 40 mm × 250 mm view field. We put a wedge model on a movable stage in the test section. The wedge angles were adjusted from outside by using a micrometer [3]. We tested a flat wedge, wedges of sawtooth surface roughness of 0.1, 0.2, 0.8, and 2.0 mm. Concave walls of 20, 50, 60, 160, and 300 mm radii and convex walls of 20, 40, 50, 56.5, 180 and 300 mm radii were placed directly on the shock tube bottom wall.

This is a conventional shock tube rupturing Mylar diaphragms where the degree of its reproducibility was not impressive. The scatter of Ms was about ±1.5% for Ms = 1.05–2.5 in air [3]. We used double exposure holographic interferometry and direct shadowgraphs for visualizing shock tube flows.

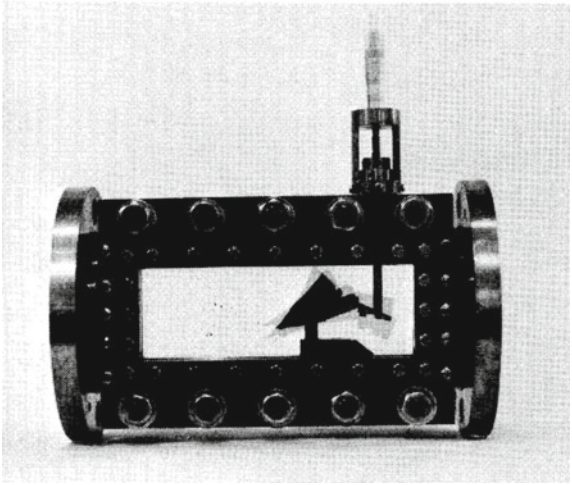

Fig. 1 A 40 mm × 80 mm shock tube

2.2 100 mm × 180 mm Shock Tube

In 1994, Prof. Glass donated his UTIAS hypervelocity shock tube to the Shock Wave Research Center of the Institute of Fluid Science, Tohoku University. Refurbishing it to a diaphragm-less operation, we improved the degree of its reproducibility in terms of the scatter of Ms ± 0.5% for Ms = 1.2–5.0 in air [12].

The test section had 100 mm × 300 mm view field, in which we install a flat wedge, 100 mm diameter convex and concave walls, and 80 mm base diameter cones of half-apex angles of 34.6°, 38.6°, 44.0°, 49.0°, and 50.5°. We measured L_d out of the triple points position on wedges of inclination angles of 34.6°, 38.6°, 44.0°, and 49.0° for Ms = 2.327 at the initial pressures at 14.1 kPa in air. The dependence of the initial pressure over a 49.0° wedge was measured for Ms = 2.327 at 1.41, 7.09, 2.82, and 14.1 kPa in air [8]. A large shock tube can accommodate a large wedge. At low initial pressures, or smaller *Re*, the transition occurs in the position away from the leading edge. This implies that in small shock tubes, the RR to MR transition might have not been observed.

2.3 Flow Visualization and Holographic Interferometry

We had visualized shock tube flows mostly by shadowgraph and schlieren method. In 1973, we introduced, for the first time, the first Q-switched ruby laser made in Japan as 25 ns short light source. The TEM_{00} of the laser had not necessarily a good coherency applicable to holography. Nevertheless, we struggled to use it for double exposure holographic interferometry. In 1980, introducing Apollo Holographic

Ruby Laser, we made holographic visualization of shock waves in gases as well as underwater shock waves [13].

The path of the object beam OB of our double exposure holographic interferometry was, in principle, the same as direct shadowgraph. The path length of the reference beam, RB, was exactly identical with OB. The RB was collimated and illuminated a 100 mm × 1,250 mm holographic sheet film. We had a stock of holofilms enough to perform holographic observations of shock wave phenomena until 2010.

We constructed image holograms. Then, OB and RB were superimposed simultaneously on a holofilm during the double exposures. The first exposure was conducted prior to the shock tube run and the second exposure was synchronized with the event. Sometimes the two exposures were synchronized in one shock tube run so that two events were superimposed on one holofilm. The phase change in the test section occurred during the double exposures produced fringe distribution.

Then, the holographic information stored on a holofilm were infinite fringe interferograms. However, if the RB was shifted horizontally or rotated during double exposures, the resulting interferograms had finite fringes consisting of fine parallel fringes. The event was modulated as deformation these fringes so that the density information should be extracted by analyzing the fringes.

Only phase changes occurring during the double exposures were recorded on the holofilm. Hence, in the double exposure holographic interferometry, any optical defects unvaried during the double exposures, in principle, would never contribute to the fringe formations. The inhomogeneity of optical components and test media did not cause fringes. The data stored on the holograms were transferred by means of the so-called reconstruction, in which the holograms were illuminated by a continuous laser beam and resulting images were recorded with a digital camera.

Bazhenova et al. [14] applied streak recording to visualize shock wave diffraction. We also collected time-resolved shock wave motion by using streak recording. We recorded the transition through images of wave interactions viewed through a narrow slit, say width of 0.5 mm, which was placed along the curved wall surfaces. The slit images were visualized in the direct shadowgraph and recorded in ImaCon High-Speed Camera (Type 675) in streak mode. To enhance the image resolution, the enlarged slit images were rotated: the concave wall image by 38° and the convex wall image by 40.5°. Then we could observe the transition at the center of the view field. Adjusting the streak speed to be 0.1–1.0 mm/μs depending on Ms, we correctly determine the transition by identifying subtle changes of wave trajectories along the curved walls [4].

3 Numerical Simulation

We solved numerically the Navier–Stokes equations applied to 100 mm × 180 mm shock tube flows. The scheme was VAS2D, two-dimensional vectorizable adoptive solver by Sun (1998) [15] using the Sutherlands formula for viscosity and thermal

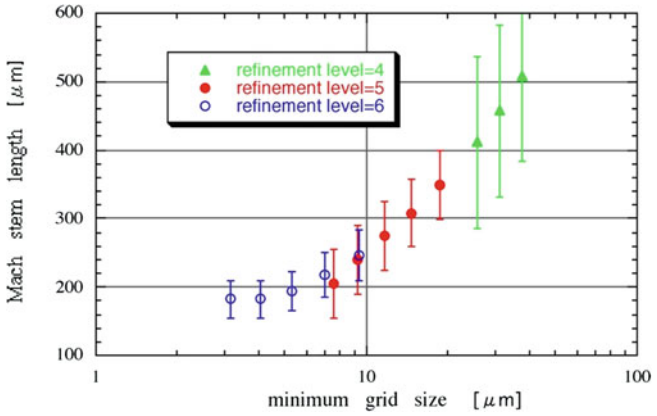

Fig. 2 Mach stem length in μm *versus* mesh size in μm. Effect of refinement levels [25]

conductivity. In order to resolve the boundary layer, we refined the mesh size near the wall. To test the sensitivity, we examined the effect of the mesh refinement level on the Mach stem length. The effect of the mesh size on the Mach stem length of shock wave Ms = 2.327 reflected from a 49.0° flat plate at 14.1 kPa in air is shown in Fig. 2. The Mach stem length converged at the refinement level 6 and then the mesh size converged to be about 3 μm.

To clarify the effect of the boundary layer on shock reflections over concave and convex walls in the 40 mm × 80 mm shock tube [3, 4], the Navier–Stokes equations were solved by Autodyne. We simulated 10 mm and 20 mm radii concave and convex walls for Ms = 1.4 at the initial pressure of 4 kPa and 40 kPa in air and $Re = 1.5 \times 10^4$ and 1.5×10^5, respectively. We applied the sixth level of mesh refinement on the walls.

4 Results and Discussions

4.1 Interferometric Observation Over Curved Walls in a 40 mm × 80 mm Shock Tube

Figure 3a, b show holographic interferograms of shock wave reflection over a 40 mm radius convex for Ms = 1.035 at 1600 hPa and 293.8 K in nitrogen: (a) delay time of 120 μs and (b) 140 μs, respectively. To produce weak shock waves, the test gas was pressurized up to 1,600 hPa. In Fig. 3a, the reflection pattern was RR and in Fig. 3b, it was MR. For weak shock wave, θ_{crit} can be small. Although we could identify the triple point, the slip line is hardly observable. It is noticed that unlike weak shock reflection over a flat wedge, the reflection pattern in Fig. 3b never belongs to the von Neumann Mach reflection.

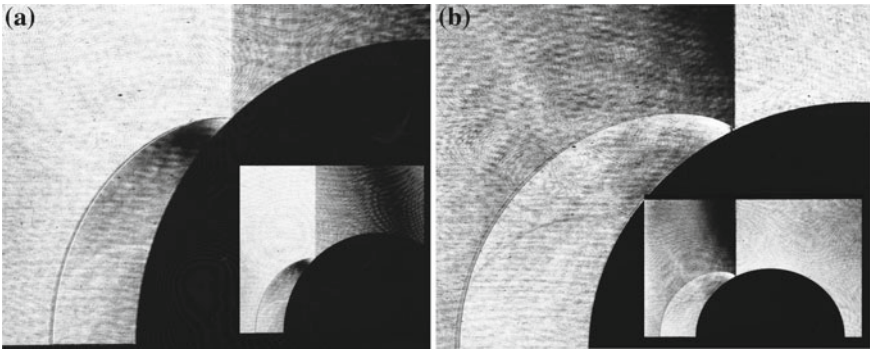

Fig. 3 Weak shock wave reflection over a 40 mm convex wall for Ms = 1.035 at 1600 hPa and 293.8 K in nitrogen: **a** #81101933, RR, delay time 120 μs; and **b** #81101937, MR, delay time 140 μs

In Fig. 4a, b, we can see the transition from RR to double MR over a 40 mm convex wall for Ms = 2.500 at 300 hPa: (a) delay time of 481 μs and initial temperature at 291.4 K, and (b) delay time of 500 μs and initial temperature at 291.7 K. When the RR terminated and the transition to the MR was initiated, a Mach stem developed at the reflection point at which the RR terminated. Across the slip line, the density changes discontinuously as clearly as shock waves.

Figure 5a–f show sequential interferograms of shock wave reflection over a 50 mm concave wall for Ms = 1.597 ± 0.02 at 300 hPa and 291.5 K in air: (a) delay time 50 μs, (b) 90 μs, (c) 160 μs, (d) 185 μs, and (e) 200 μs.

At the earlier stage of reflection over concave wall in Fig. 5a, unlike the reflection from a convex wall in Fig. 4b, the incident shock wave is reflected over a glancing incidence angle. The reflection pattern is so-called von Neumann MR [2].

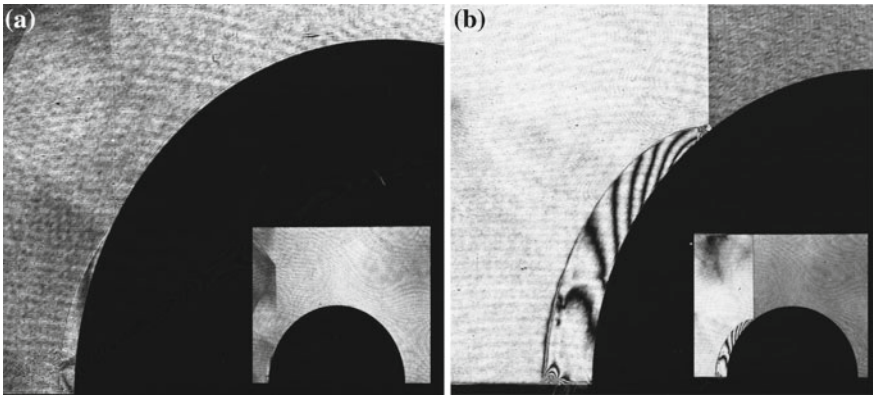

Fig. 4 Shock wave reflection over a 40 mm convex wall for Ms = 2.500 at 300 hPa in air: **a** #81102216, RR, delay time 481 μs; **b** #81102215, DMR, delay time 500 μs

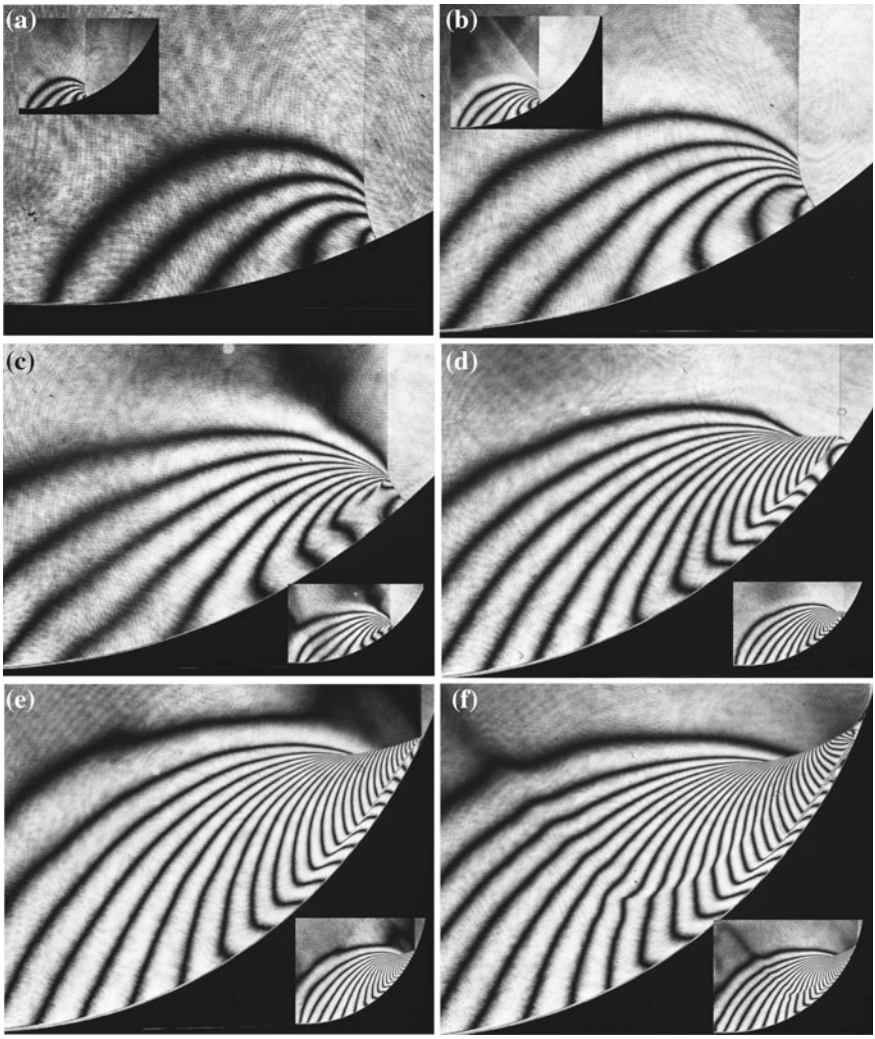

Fig. 5 Shock wave reflection over a 50 mm concave wall for Ms = 1.597 ± 0.02 at 400 hPa and 293.5 K in air: **a** #83101914, von Neumann MR, delay time 50 μs; **b** #83101912, von Neumann MR, delay time 90 μs; **c** #83101911, direct MR, delay time 110 μs; **d** # 83101908, stationary MR, delay time 160 μs; **e** #83101910, inverse MR,185 μs; and **f** #83101906, RR, delay time 200 μs

As a result, the incident shock is gradually curved and intersected perpendicularly to the concave wall.

Fringes increased continuously from the wall to the state behind the incident shock. The distinct triple point was not observed. The entropy increment is defined $\Delta s \propto (\Delta p)^3$ for $\Delta p \ll 1$. Hence, smaller pressure increment, the entropy increment is

nearly neglected $\Delta s \fallingdotseq 0$, which implies that the flow is almost isentropic [16]. Hence, the distinct triple point hardly exists in isentropic flows. When weak shock wave is reflected from a shallow wedge, the flow field is isentropic at such a small pressure increments behind a Mach stem. So a distinct triple point does not show up. The von Neumann MR appears in flow fields at which similar isentropic condition is valid.

In Fig. 5b, the inclination angle becomes steeper and the pressure increases behind the curved Mach stem. The fringe number behind the curved Mach stem is also increased. The fringes behind the Mach stem tend to merge near the trajectory of the shock–shock angle [17]. In Fig. 5c, we can see the merger of fringes toward the shock–shock angle and a distinct triple point forming the direct MR.

In Fig. 5d, the direct MR terminates and then the curved slip line is nearly parallel to the wall surface. This looks a stationary MR, which exists only temporary. This pattern transits to the inverse MR in Fig. 5e. In the inverse MR, the Mach stem finally hits the wall and is reflected. The MR vanishes forming into RR. However, as the slip line cannot disappear from the flow field, the second triple point appears behind the RR for maintaining the slip line.

RR on the wedges are divided into two types: shock waves reflected from a shallow wedge are curved and the flow behind it is subsonic, and those from a steep wedge are straight and the flow behind it is supersonic. The reflected shock wave in Fig. 5f is supersonic RR. Therefore, behind the supersonic RR, a normal shock wave is possible behind it.

Then, the triple point consists of three-shock confluence and the slip line. This is a flow mechanism which generates the double MR. The secondary shock wave behind the RR in Fig. 5f is created by the same flow mechanism as that of the double MR.

4.2 Streak Recording, Measurement of θ_{crit}

The error of estimating θ_{crit} from sequential images was about 5° to 8°. In streak photogrammetry, we can measure θ_{crit} relatively precisely by observing the change in wave trajectories. Figure 6 shows the streak image and its sketch for Ms = 1.30 over 40 mm convex wall using a slit of 0.7 mm in width.

Prior to the transition, the trajectories of incident shock wave I are combined with the reflected shock wave trajectory R because the slit width was 0.7 mm. At the transition point T, from RR to MR, the I turns into Mach stem trajectory MS. The trajectories I and MS merged at T but intersected discontinuously. Therefore, the T is readily identified. Repeating the tests, we could determine θ_{crit} from streak recordings in a wide range of Ms. However, for weaker shock waves, a distinct slip line is missing so that this method is not reliable.

Figure 7 shows the streak photograph and its sketch over a 50 mm concave wall for Ms = 1.40 and the slit width of 0.6 mm. Prior to the reflection, MR is von Neumann MR, only the trajectory of a Mach stem M was observable. At the

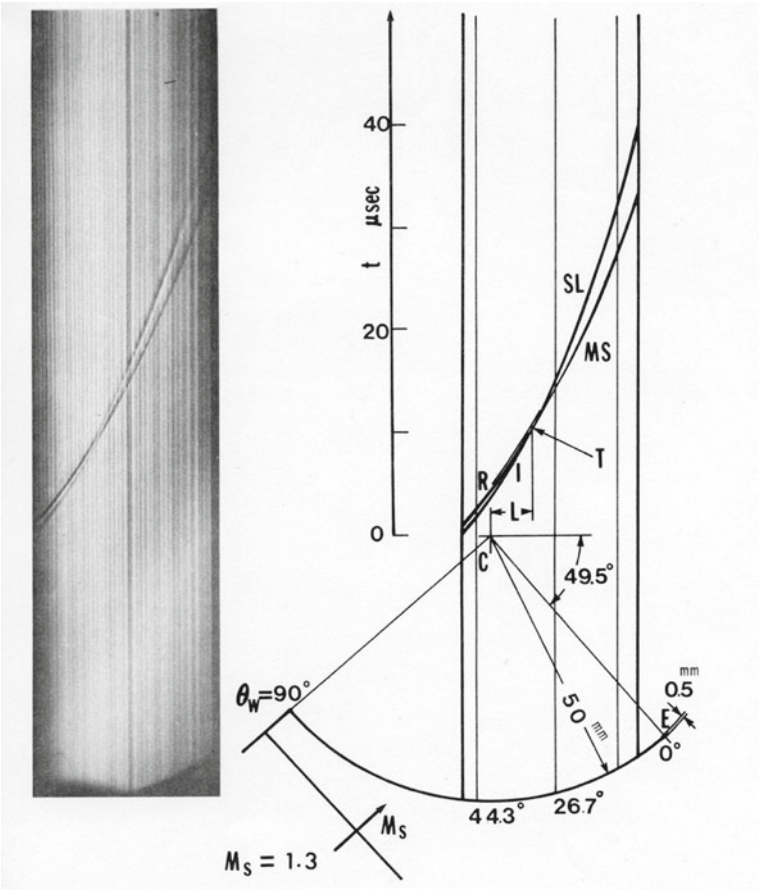

Fig. 6 Streak imaging of shock wave propagation over a 40 mm convex wall at Ms = 1.30 in air. I, incident shock trajectory; R, reflected shock trajectory; MS, Mach stem trajectory; T, transition point; M; and MS, Mach stem

transition T, RR appears and its resulting trajectories I and R also appear. MS is a normal shock wave holding the secondary triple point. The trajectory SL corresponds to a slip line emanating from the secondary triple point. Hence, the trajectories of M and I intersect discontinuously at T. In Figs. 6 and 7, we can readily determine the transition point, hence θ_{crit}.

4.3 Roughened Wedges

The shape of roughness is 90° triangular sawtooth. The heights of 0.1, 0.2, 0.8, and 2.0 mm were machined on brass plates and placed on the movable stage.

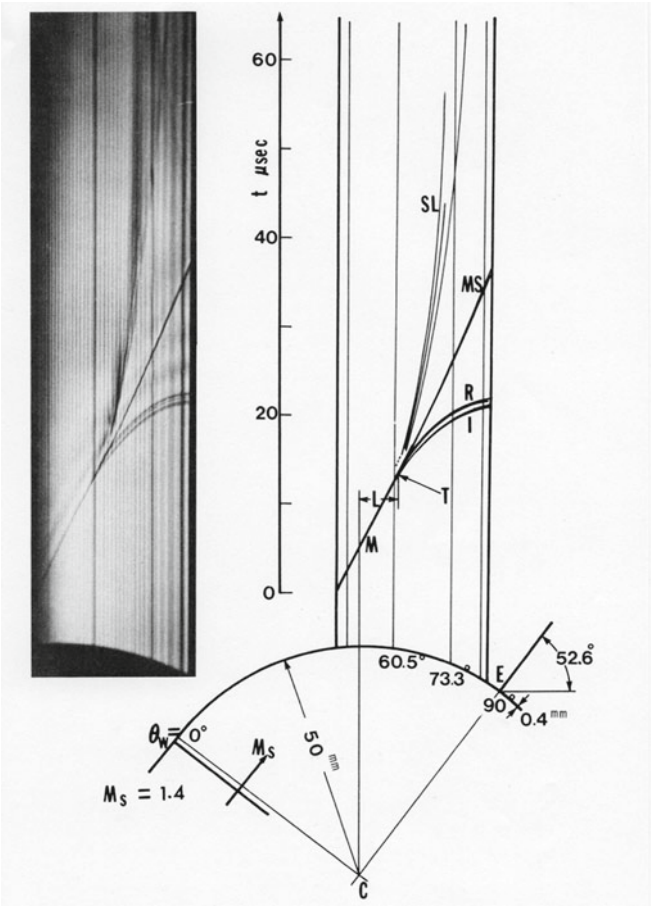

Fig. 7 Streak imaging shock propagation over a 50 mm concave wall at Ms = 1.40 in air. I, incident shock trajectory; R, reflected shock trajectory; MS, Mach stem trajectory; T, transition point; M, Mach stem; and MS, Mach stem

The incident shock wave interacts at every step with a sawtooth roughness and repeats the reflection and the diffraction producing then vortices. For a finer roughness of 0.1 mm and probably 0.2 mm, these vortices were imbedded in the boundary layer [5, 18].

However, in the coarser roughness of, say 2 mm, we can see the trains of vortices, which successively generate shock waves and expansion waves. By varying the inclination angles for shock waves of Ms = 1.04, corresponding $Re = 0.80 \times 10^5$; Ms = 1.12, $Re = 2.50 \times 10^5$; Ms = 1.25, $Re = 3.40 \times 10^5$; Ms = 1.44, $Re = 2.70 \times 10^5$; Ms = 1.86, $Re = 0.06 \times 10^5$; Ms = 3.77, $Re = 0.03 \times 10^5$, we collected the images of shock wave reflection and then determined the θ_{crit} with error of $\pm 2.0°$.

Figure 8a–h show shock wave reflections from roughened wedges: (a) and (b) 0.1 mm roughness for Ms = 1.92 ± 0.01 at 400 hPa, 286.1 K in air, (a) MR, $\theta_w = 40.5°$; (b) RR, $\theta_w = 50.5°$; (c) and (d) are direct shadow pictures of 0.2 mm roughness for Ms = 1.268 at 1013 hPa, 286.7 K in air, (c) MR, $\theta_w = 33.5°$; (d) RR, $\theta_w = 51.5°$: (e) and (f) are interferograms of 0.8 mm roughness for Ms = 1.886 at 400 hPa, 280.0 K in air, (e) MR, $\theta_w = 33.5°$; (f) RR, $\theta_w = 49.0°$: (g) and (h) are direct shadowgraphs of 2.0 mm roughness for Ms = 1.460 ± 0.01, at 500 hPa, 292.0 K; (g) MR, $\theta_w = 33.5°$; (h) RR, $\theta_w = 52.0°$.

In Fig. 8a, b, we can see that the vortices and the train of expansion waves effectively influence the region behind the Mach stem. The foot of the Mach stem is curved due to the local incident shock/sawtooth interaction. As the roughened wall attenuated reflected shock wave so that θ_{crit} was decreased. Figure 8b shows an RR. A red arrow shows a kink at which the curved reflected shock wave intersects with a straight reflected shock, which indicates the boundary between subsonic RR and supersonic RR. Similar trends are observed in Fig. 8c, d, and also in Fig. 8e, f.

Figure 8g shows a terminal stage of MR over a 33.5° wedge of a 2.0 mm roughness for Ms = 1.469. The evolution of vortices at the individual edges was clearly observed. The shock waves and expansion waves or wavelets emitted from the vortices intersect with each other. Their envelope formed the reflected wave.

The wavelets reached the triple point. In Fig. 8h, at a steeper wedge, the merger of the wavelets could not reach the triple point. The region of wavelet merger became slower than the incident shock. Hence, the area at which wavelets merged and reflected shock wave intersect slightly discontinuously forming a kink as marked with a red arrow. Kink points or areas are observed in Fig. 8b, d and f.

4.4 Results of a 40 mm × 80 mm Shock Tube Experiments

The experimental results of a 40 mm × 80 mm shock tube, θ_{crit} versus ξ inverse shock strength are shown in Fig. 10 [3, 4]. The symbols of convex and concave walls, a flat plate, and roughened wedges are shown in Fig. 9. Due to finite size of the shock tube, the initial angles of larger convex and concave walls are deviated from 90° and 0°, respectively.

In Fig. 10, the ordinate designates θ_{crit} in degree and the abscissa designates the inverse shock strength, that is, the inverse pressure ratio, $\xi = (\gamma+1)/\{2\gamma Ms^2 - (\gamma-1)\}$, where γ is the specific heats ratio. The solid lines correspond to the detachment criterion or two-shock solution [1], the mechanical equilibrium criterion, three-shock solution [2], and the approximate solution which was derived empirically [8].

In the derivation of self-similar solutions of the reflected shock wave transition over concave walls, for example [8] and many others, only shock wave propagation over a geometry of concave surface is taken into account. Neither the

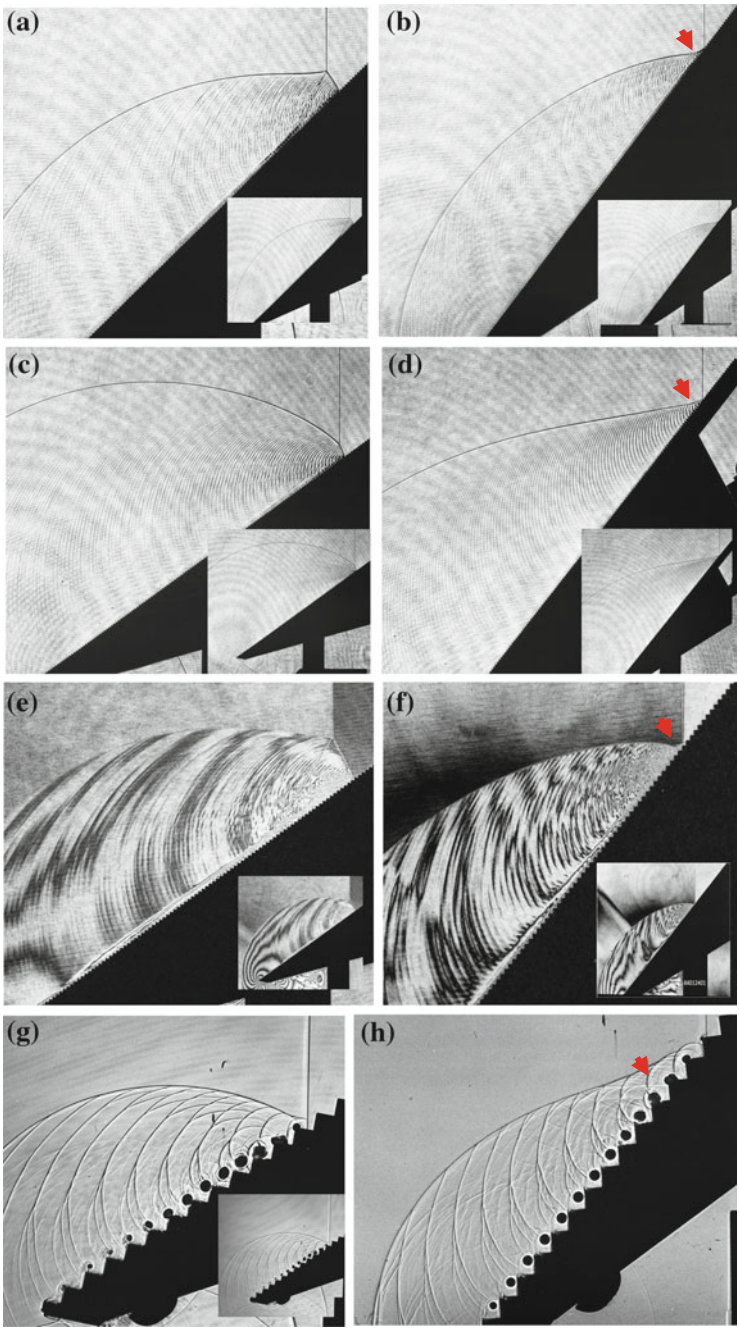
(a)
(b)
(c)
(d)
(e)
(f)
(g)
(h)

◀**Fig. 8** Shock reflection from roughened wedges: **a** #84012006, direct shadow; **b** # 84012003, direct shadow; **c** #84011718, direct shadow; **d** #84011713, direct shadow; **e** #84012406, interferogram; **f** #84012401, interferogram; **g** #80050810, direct shadow; **h** #80050801, direct shadow

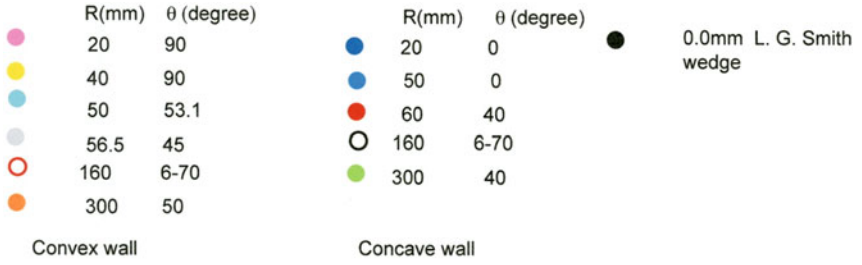

Fig. 9 Symbols appearing in Fig. 10

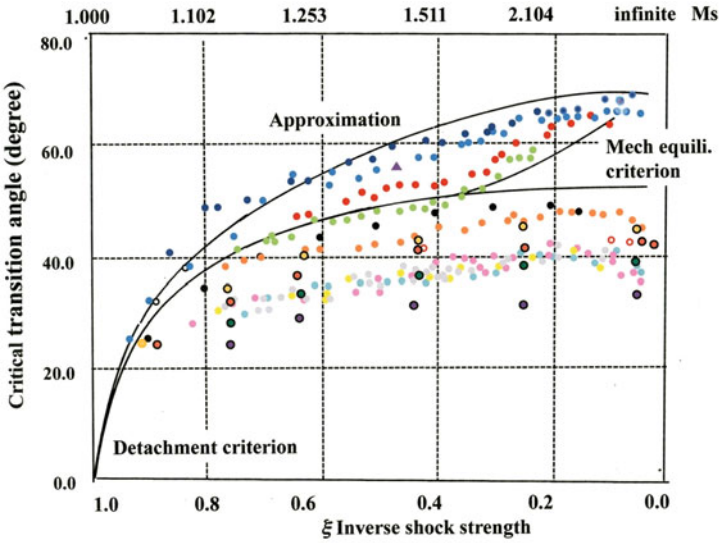

Fig. 10 θ_{crit} versus ξ inverse shock strength

abovementioned complex wave transformations from the direct MR, the inverse MR and to eventual RR nor the radius is not taken into account. The authors wonder that not depending on the numerical approach, someday a better inspiration may come out to solve this issue.

Colored data points show individual convex and concave walls of radii and initial angles as shown in Fig. 9. θ_{crit} over smooth flat wedges and roughened wedges [5, 18] are presented. As seen in Figs. 3 and 4, over convex walls in which

the wall angle varies from 90° to 0°, the transition occurs from RR to MR, whereas over concave walls in which the wall angle varies from 0° to 90°, the transition occurs from MR to RR. Analytical solutions of the critical transition angle are shown in solid lines, which are independent of the model radii. We once convinced that the self-similarity is a principle of shock tube flows and experimental results more or less agree well with the analytical solutions. However, in experiments, the transition from RR to MR takes place at much lower angles than the predictions and even the transition angles do vary depending on the model radii.

The critical transition angles θ_{crit} over a 20 mm radius convex wall shown in pink color circles are smaller than those of 50 mm radius convex wall shown in light blue color circles. It is noticed that the critical transition angles θ_{crit} over a 300 mm radius convex wall shown in orange color circles are distributed closer to the two-shock solution.

The θ_{crit} of roughened wedges as shown in Figs. 8 and flat wedges shown in black circles (Smith (1948) [19]) are compared. As defined in Fig. 9, black circles filled with yellow, red, green, and purple colors show sawtooth roughness of 0.1 mm, 0.2 mm, 0.8 mm, and 2.0 mm, respectively. With a coarser roughness, the θ_{crit} decreases significantly. In finer roughness, θ_{crit} is closer to that of a smooth wedge. On the contrary, in case of extremely course roughness, which is hard to imagine, θ_{crit} would be very small.

θ_{crit} over a 20 mm radius concave wall shown in dark blue circles are larger than those over a 50 mm radius concave wall shown in blue color circles and are far deviated from the three-shock solution. But these circles luckily agree well with the approximate self- similar solution [8]. θ_{crit} over a concave wall of a 50 mm radius and 40° initial angle shown in red color circles are larger than those over a concave wall of 300 mm radius and 40° initial angle as shown in light green color circles. The light green color circles agree fairly well with the three-shock solution.

The contribution of boundary layer is more significant for the curved wall of smaller radius. Analytical solutions and the solutions of the Euler solvers will agree ideally with results of imaginary large test models. In order to correctly compare the experiments, numerical simulations of the Navier–Stokes solvers would be meaningful.

Over the convex walls, the smaller radii are, θ_{crit} would be smaller. For larger radii, θ_{crit} would gradually approach the two-shock solution. Over the concave wall, the smaller radii are, θ_{crit} would be larger. For larger radii, θ_{crit} will approach the three-shock solution.

In an imaginary experiment, in case we may have such a bright technology to test shock wave reflections over a convex wall of very small radius and resolve experimentally the motion of miniature shock waves, θ_{crit} would be much smaller, presumably 0°. This situation would be analogous to the case of shock wave passing over the top corner of a forward facing step. Likewise, if a concave wall has an infinitesimally small radius, θ_{crit} would be closer to 90°. This situation would also be analogous to the shock impingement on the lower corner of the forward facing step.

4.5 Streak Display of Numerical Simulation

In Fig. 11, density variations of solving the Navier–Stokes equations for Ms = 1.4 in air are displayed in streak mode: (a) 10 mm radius convex wall at 400 hPa, $Re = 1.5 \times 10^5$ and; (b) 20 mm radius concave wall at 40 hPa, $Re = 1.5 \times 10^4$.

The ordinate designates the elapsed time in μs and the abscissa designates the wall inclination angle in degree displayed along the convex wall from 90° to 0° and displayed along the concave wall from 0° to 90°. The numerical density along a 0.05 mm wide slit placed along the edge of the curved walls is displayed. Dark blue color designates the ambient density and red color designates higher density behind the reflected shock wave.

As seen in Fig. 6, the incident shock I, reflected shock R, Mach stem MS, and the slip line SL are shown as discontinuous changes in color. The transition point T found from the intersection of I with MS and the extension of the SL trajectory. In Fig. 7, we can identify the transition point T from the intersection of MS with I and R. Likewise, we can identify the transition point T along the concave wall.

In Fig. 12, density variations of solving the Navier–Stokes equations for Ms = 1.4 in air are displayed in streak mode: (a) 10 mm radius concave wall at 400 hPa, $Re = 1.5 \times 10^5$ and; (b) 20 mm radius concave wall at 40 hPa, $Re = 1.5 \times 10^4$. The foot of MR propagates slightly faster than that of RR along

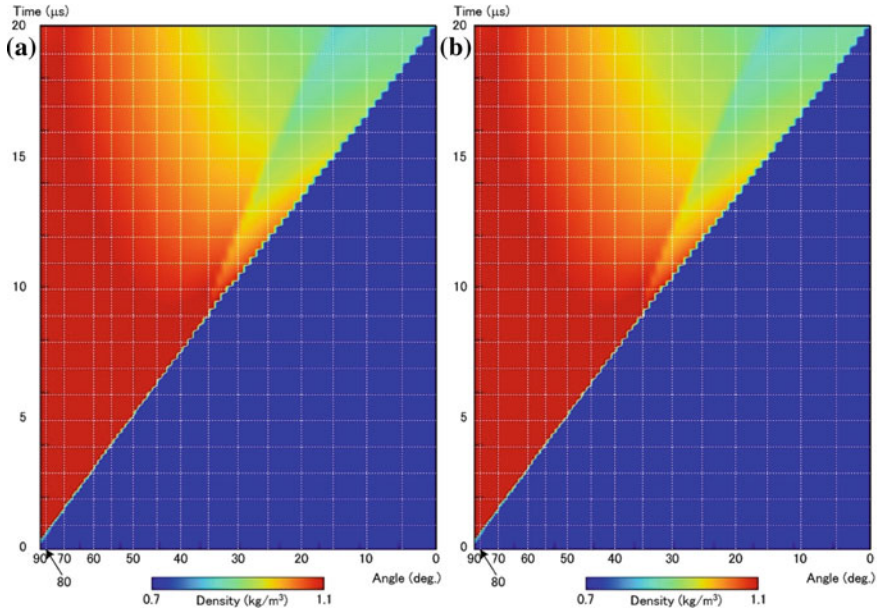

Fig. 11 The streak display of shock wave reflection along convex walls for Ms = 1.40 in air and with the slit width of 0.05 mm: **a** 10 mm radius at 400 kPa, $Re = 1.5 \times 10^5$: **b** 20 mm radius at 40 kPa, $Re = 1.5 \times 10^4$

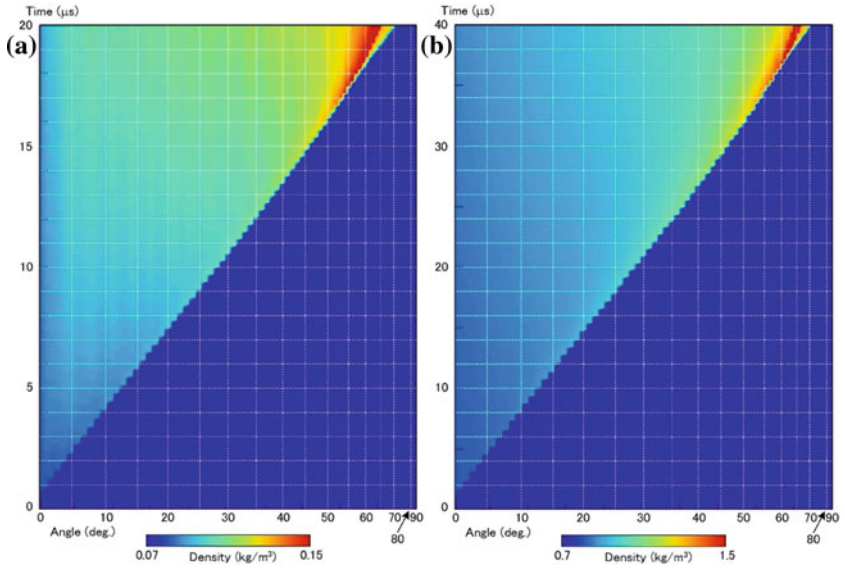

Fig. 12 The streak display of shock wave reflection along concave walls for Ms = 1.40 in air and with the slit width of 0.05 mm: **a** 10 mm radius at 400 kPa, $Re = 1.5 \times 10^5$; **b** 20 mm radius at 40 kPa, $Re = 1.5 \times 10^4$

the concave wall, and then the MR and RR trajectories intersect slightly discontinuously. We can estimate the transition point and then θ_{crit} with the error of a few degrees.

4.6 Delayed Transition Over Wedges in a 100 mm × 180 mm Shock Tube

Figure 13a, b show shock wave reflection for Ms = 2.32 in nitrogen over a *49°* wedge, which is close to the critical transition angle: (a) a double exposure holographic interferogram at 72 hPa and 296.0 K; (b) sequential numerical displays of solving the Navier–Stokes equations at 70.5 hPa. It is RR at the first exposure, whereas at the second exposure, it was transitional MR. Then, we confirmed the delayed transition occurring sometime during the double exposures.

In order to perform the CFD validation, we solved numerically the Navier–Stokes equations. In Fig. 13b, we plotted the numerical triple points in X-Y plane. We readily estimate the transition point in Fig. 13b, at which the RR terminates. This L_d is defined the point at which the RR terminates and MR is initiated. The experiments and numerical results agree well with each other, and hence, we intensively applied this numerical code for shock reflection over curved walls.

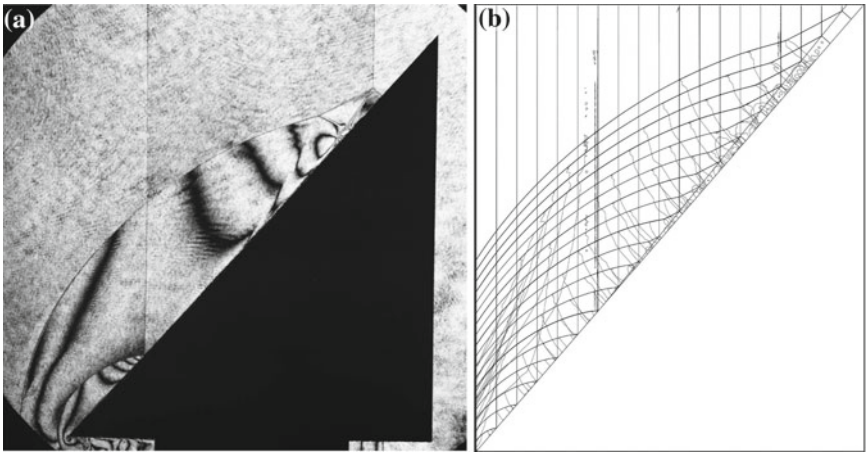

Fig. 13 Shock wave reflection over 49° wedge for Ms = 2,32 at 72 hPa in nitrogen: **a** #98091717 double exposure holographic interferogram and **b** sequential display of a Navier–Stokes solver

In Fig. 14, we summarized triple points for Ms = 2.33 over a 49.0° wedge in the X, Y coordinates at the initial pressures ranging from 1.41 to 14 kPa. The ordinate designates Y-axis in mm and abscissa designates X-axis in mm [8]. Within the scatter of experimental errors, the triple points increase monotonously.

The point at which the triple point trajectory intersects with the X-axis corresponds to the L_d. The L_d increases with the decrease in the initial pressure. The L_d is

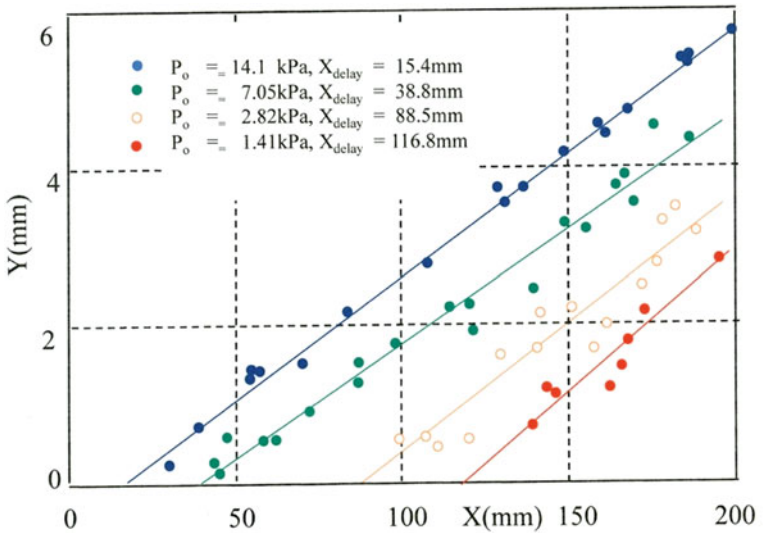

Fig. 14 The dependence of the L_d on the initial pressure for Ms = 2.33 over a 49° wedge

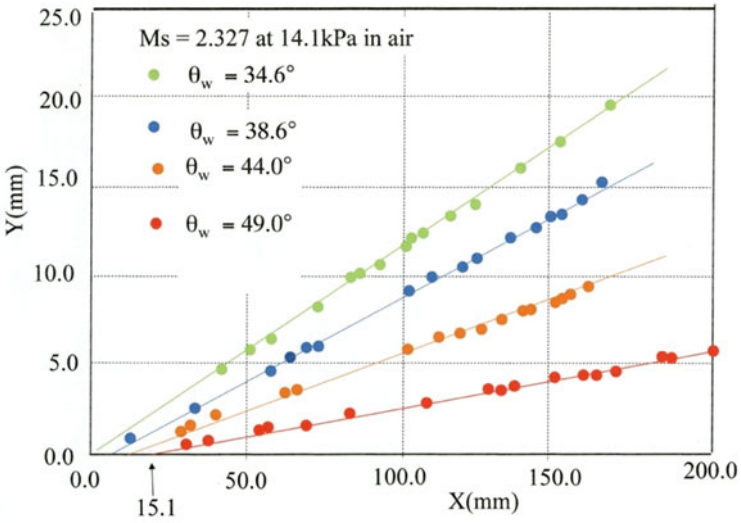

Fig. 15 The effect of the wedge angle on the delayed transition distance for Ms = 2.33 at the initial pressure of 14.1 kPa in air

about 116.8 mm at 1.41 hPa. MR would, presumably, never be reproduced experimentally in a smaller shock tube and at lower initial pressure. This would be one of the reasons why previous shock tube data scatter so widely. Hence, the discrepancies between experimental data and analytical solutions are caused by the size of shock tubes.

In the reflection over the wedge angles closer to the θ_{crit}, the L_d becomes unexpectedly long. When sequentially visualizing the shock reflection under the identical initial condition, we can experimentally determine the L_d. To prove the presence of L_d on the wedges of smaller wedge angles, we tested the triple point trajectory over the wedges of 34.6°, 38.6°, 44.0°, and 49.0° for Ms = 2.33 at the initial pressure of 14.1 kPa in air. Figure 15 shows the results: obviously over the 34.6° wedge, $L_d = 0$; on the wedges of larger angles, $L_d > 0$; and at $\theta_w = 49.0°$, $L_d = 15.1$ mm.

4.7 *Delayed Transition of Convex and Concave Walls in a 100 mm × 180 mm Shock Tube*

Figure 16a, b show the triple point trajectories over convex and concave walls of 50 mm radius for Ms = 2.33 at 1.41 kPa and 14.1 kPa in air: (a) convex wall and (b) concave wall. The ordinate designates Mach stem height in mm and abscissa designates the inclination angle of the curved walls in degree. In Fig. 16a, light blue and red circles show the initial pressure of 14.1 kPa and 1.41 kPa, respectively.

The critical transition angles are lower with the decrease in the initial pressure. The purple circle on the abscissa shows detachment criterion [1].

In Fig. 16b, light blue and red circles show initial pressure of 14.1 kPa and 1.41 kPa, respectively. The detachment criterion or the two-shock solution [1] and the mechanical equilibrium criterion, and the three-shock solution [2] are shown by arrows. Red arrows show experimental results. The lower the initial pressure is, the smaller the θ_{crit} becomes. Clearly, the Re decreases, θ_{crit} also decreases. It is still an open question that how θ_{crit} will be deviated from the analytical prediction at $Re \sim 10^6$ or 10^7.

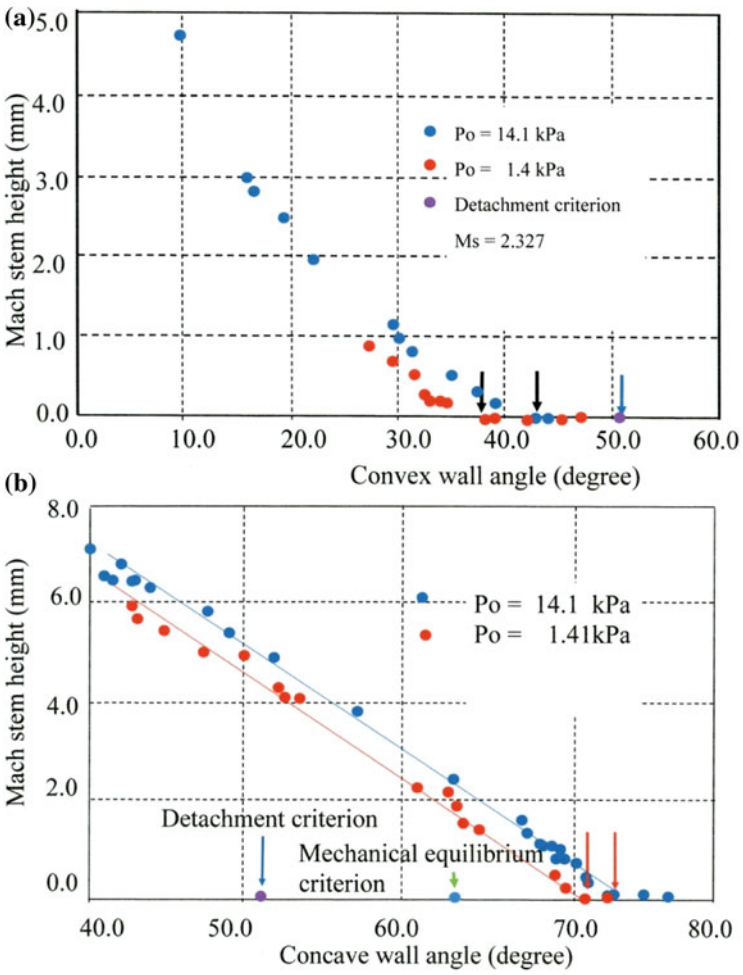

Fig. 16 The triple point trajectory for Ms = 2.33 at 1.41 and 14.1 kPa over **a** convex wall and **b** concave wall

4.8 Delayed Transition Over Cones in a 100 mm × 180 mm Shock Tube

We tested shock wave reflection over cones installed at first in a 40 mm × 80 mm shock tube [20] and later in 60 mm × 150 mm shock tube [21]. The presence of shock tube sidewalls sometimes affects flows over two-dimensional test models. However, flows over cones are free from the sidewall effect. Then, we decided to see the departure of shock wave reflection between wedges and cones.

We manufactured cones of half-apex angle at every 1° and measured the θ_{crit} for a wide range of ξ. Recently, we were interested in the delayed transition over a larger cone by using a 100 mm × 180 mm shock tube [22]. Figure 17 shows a double exposure interferogram of Ms = 2.33 shock reflected over a 49.0° half-apex angle cone. We readily found that the reflection pattern was RR at the first exposure whereas at the second exposure it was MR. In the present axial symmetry, unlike two-dimensional flow, the integrated density distribution across the axially symmetric flow field are different from 2D shock tube flows.

In Fig. 18, we summarized the triple point trajectories over cones of various half-apex angles for Ms = 2.30 at 14.1 kPa in air. The ordinate designates the radial distance Y in mm and the abscissa designates the distance along the cone, X-axis in mm. Filled circles show the triple points on the upper side of the one and open circles show those on the lower side of the cone. Over a cone of $\theta_w = 34.6°$ half-apex angle, similarly to the wedge, it was MR from the apex. However, with increasing the θ_w, like wedges as seen in Fig. 15, the delayed transition occurred.

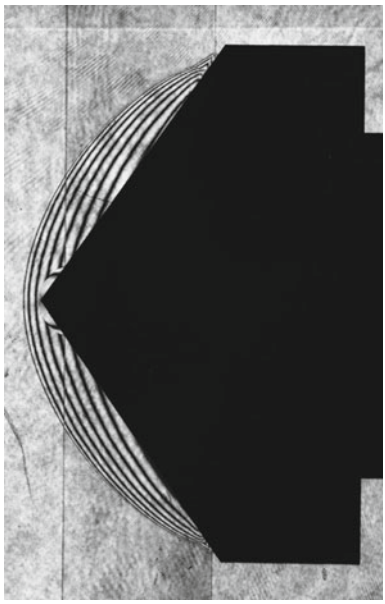

Fig. 17 The delayed transition over a 49.0° half-apex angle cone. #98121102 for Ms = 2.324 at 144 hPa and 292.9 K in air

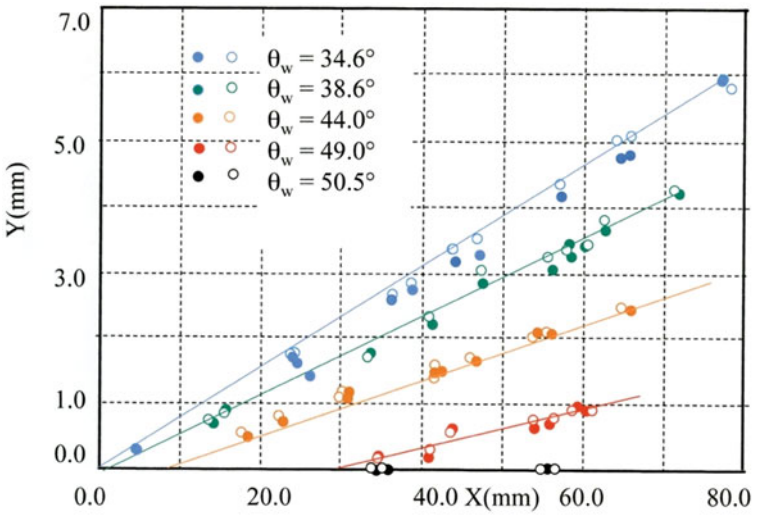

Fig. 18 The effect of half-apex angle θ_w on L_d for Ms = 2.30 at 14.1 kPa in air

At $\theta_w = 49.0°$ the L_d was about 30 mm. However, at $\theta_w = 50.5°$, RR started from the apex, in other words, L_d = infinite. The general trend is similar to the wedges. The L_d increases with θ_w approaching θ_{crit}.

Figure 19 summarizes the effect of initial pressures in kPa on L_d in mm at $\theta_w = 49.0°$. Red and green circles correspond to wedges and cones, respectively.

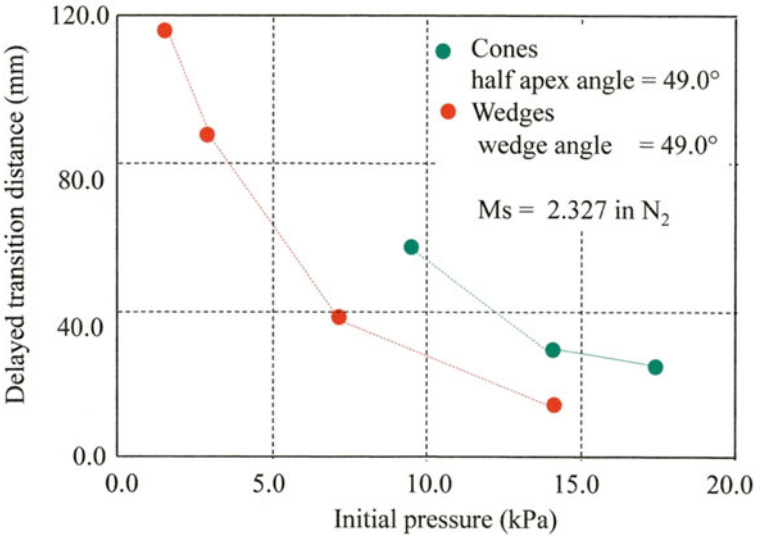

Fig. 19 The effect of the initial pressure on L_d. Comparison between wedges and cones

At lower initial pressures, the longer the L_d is. At identical initial pressures, the L_d over cones is about twice longer than that in wedges. However, in shock tube experiments, it is nearly impossible to test with very large base diameter cones and we have to trust numerical simulation for larger cones. From an engineering viewpoint, it is very interesting that the effect of the initial pressure, in other words, the effect of *Re* on the delayed transition is more significantly over cones than the wedges.

Figure 20a summarizes 40 mm × 80 mm and 100 mm × 180 mm shock tube experiments and numerical results displayed in a $\theta_{crit} - \xi$ diagram. Figure 20b shows symbols referred in Fig. 20a. Black diamonds show results of cones [21]. As seen in Fig. 11, orange and red color diamonds surrounded by thin red lines are numerical results of 10 mm and 20 mm convex walls, respectively. Open orange and red diamonds designate $Re = 1.5 \times 10^5$ and black diamonds filled with orange and red color designate $Re = 1.5 \times 10^4$.

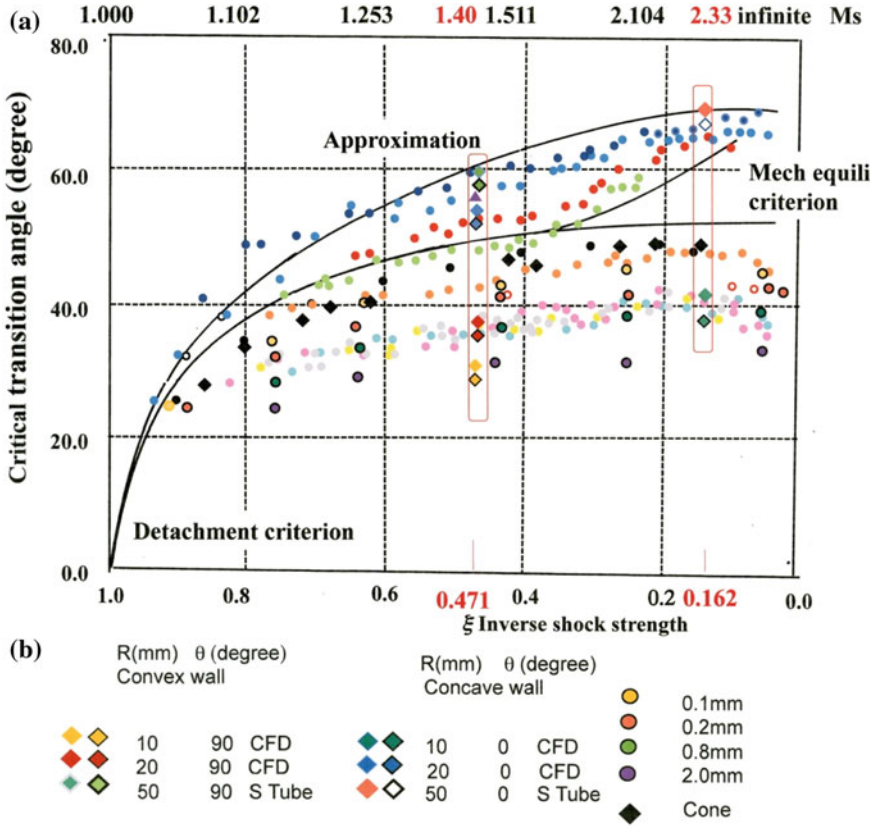

Fig. 20 **a** θ_{crit} - ξ diagram, summary of 40 mm × 80 mm and 100 mm × 180 mm shock tube experiments and numerical simulations, and **b** symbols

As seen in Fig. 12, green and blue diamonds surrounded by thin red lines correspond to numerical results of 10 mm and 20 mm concave walls, respectively. Open green and blue diamonds designate $Re = 1.5 \times 10^5$ and black diamonds filled with green and blue color designate $Re = 1.5 \times 10^4$. The similar trend as observed over convex walls exists even in the case of the concave walls:

A light green diamond and a black diamond filled with light green color show results of a 50 mm convex wall at 14.1 kPa and 1.41 kPa, respectively. A red diamond and an open diamond are results of a 50 mm concave wall at 14.1 kPa and 1.41 kPa, respectively.

The domain and boundary of data collected in the 100 mm × 180 mm shock tube laid in the same region as data collected in the 40 mm × 80 mm. θ_{crit} was a few degrees smaller if the *Re* is smaller ten times. It would worthwhile to request experimentalists to describe, in addition to Ms, the flow *Re* behind the shock wave.

4.9 Double Wedges

Superimposing two wedges in a staggered position, we can form a double wedge having a concave corner. Concave double wedges provide good test cases of double exposure holographic interferometry demonstrating MR. Selecting wedge angles, we produce three types of MR. We are interested in the presence of a stationary MR by solving the Euler equations based on the TVD method [11]. It is an open question whether or not a consistent stationary MR indeed exits in shock tube flows. Figure 21a shows shock wave reflection over a 27° and 52° double wedge installed in a 60 mm × 150 mm shock tube for Ms = 1.71 at 680 hPa and 294 K.

On the first wedge, MR appeared and on the second wedge, a stationary MR appeared. The slip line looked nearly parallel to the second wedge surface and apparently satisfied the definition of a stationary MR. However, the stationary MR can exist only in the steady flows, which implies hardly to exist consistently in the shock tube flows.

In Fig. 21a, we will readily find that the shape of the slip line is slightly broadening with the distance from the triple point. Hence, the image is slightly away from the definition of a stationary MR. In short, the stationary MR appears only in a very limited condition.

The shock wave reflection from the double wedge is self-similar. Hence, the length of the first wedge would be a scaling factor governing the pattern and the size of the reflected shock wave. In reality, for the shorter first wedge, the boundary layer would contribute decisively to the reflection pattern. In Fig. 21a, the length of the first wedge *L* was 52 mm. The stationary MR in Fig. 21a transited to an inverse MR. Figure 21b shows an inverse MR over a 30° and 55° wedge with $L = 25$ mm, for Ms = 1.83 at 600 hPa and 293 K in air. With a shorter *L,* the inverse MR in Fig. 21b would correspond to the far distance from the concave corner in Fig. 21a.

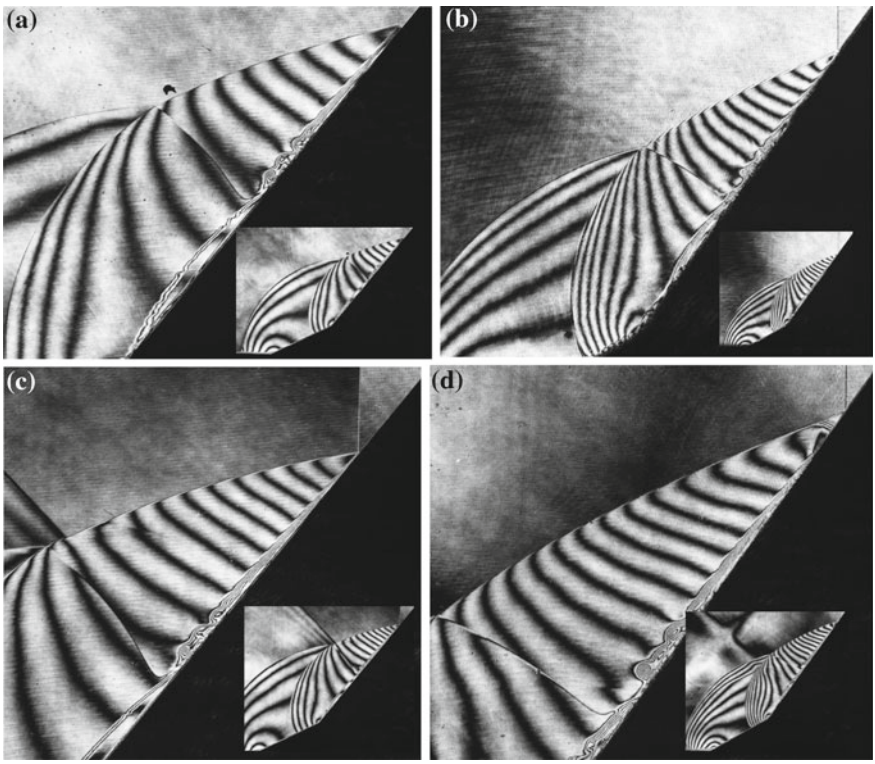

Fig. 21 Shock wave reflection over concave double wedges: **a** #87120806 Stationary MR, 27° and 52°, L = 52 mm, Ms = 1.71 at 680 hPa, 294 K in air; **b** #87120702 inverse MR, 30° and 55°, L = 25 mm, Ms = 1.83 at 600 hPa, 293 K; and **c** #87120803 Last stage of inverse MR, 27° and 52°, L = 52 mm, Ms = 1.639 at 680 hPa, 294.1 K; and **d** #87120718 RR, 30° and 55°, L = 50 mm, Ms = 1.785, at 700 hPa and 293.0 K

Solving the Euler equations, we found numerically a narrow region of MS and wedge angles in which the stationary MR existed consistently along the second wedge [11]. However, in Fig. 21a, b, the presence of the boundary layer on the wall and the interfacial diffusion gradually broadened slip line. In Fig. 21c, we can see the last stage of inverse MR for Ms = 1.639 27° and 52°, L = 52 mm, in which the Mach stem is nearly touching with the wall surface. In Fig 21d, the inverse MR terminated to RR, 30° and 55°, L = 50 mm Ms = 1.785. We can clearly see the second triple point just after the RR. We can clearly see the boundary layer developing on the wall surface, which would discourage the consistent presence of the stationary MR. Recently, Prof. Krasovskaya numerically confirmed this trend [23].

4.10 Shock Wave Focusing

In 1980, we observed the head-on collision of planar shock waves from a circular concave-shaped reflector. Then, we were interested in focusing on reflected shock waves. Then, the shock wave reflection along concave walls contributes to interpret the focusing of reflected shock waves from concaved reflectors.

Unlike a linear wave focusing, say light wave focusing from a concave mirror or acoustic wave focusing from a concave reflector, the focusing of a reflected shock wave from a concave reflector was a proper topic of nonlinear gas dynamics. Inspired by Stutevant et al. [24], we visualized, by using double exposure holographic interferometry, the focusing of planar weak shock waves from a circular reflector and realized that the topic was just a topic of shock wave reflection over a concave wall.

Figure 22a–d show a sequential display of shock wave reflection from a concave reflector for Ms = 1.431 at 1013 hPa and 297.8 K. The reflector has the depth of 75 mm and was a combination of 35 mm radius convex walls and a smoothly connected 40 mm radius circular end wall. In Fig. 22a, at the leading edge, the reflected shock wave transits to MR.

In Fig. 22b, the resulting Mach stem propagating along the concave wall formed the von Neumann MR. The triple point in Fig. 22a moved upward. While propagating along the steep wall, the von Neumann MR became SMR. In Fig. 22c, SMR took due course of evolution now became RR in Fig. 22c. The reflected wave emitted from the triple intersected at the center of the shock tube and reflected.

The reflection points along the concave wall and the triple points of MR are going to merge at the concave end wall. In Fig. 22d, we can see the secondary triple point behind the RR was reflected from the curved reflector. At the same time, the triple points impinged on the end wall. In enlarged images, we noticed the presence of the boundary layer developing along the reflector walk.

Figure 22e, f show a later stage and its enlargement. Whole wavelets and vortices reflected from the end wall and merged at the centerline. We can see an elongated vortex, which is a remnant of the entire interactions. The peak pressure should be a maximum at the point at which wavelets and vortices merged. However, unlike a focusing of the linear waves, nonlinear wave interactions in this funny configuration discouraged the peak pressure built up. The elongated vortex shape would explain that the peak pressure would have been diversified. In conclusion, every interaction of wavelets and vortices played a role to enhance higher peak pressures. Then, the shape of the efficient reflector would be designed.

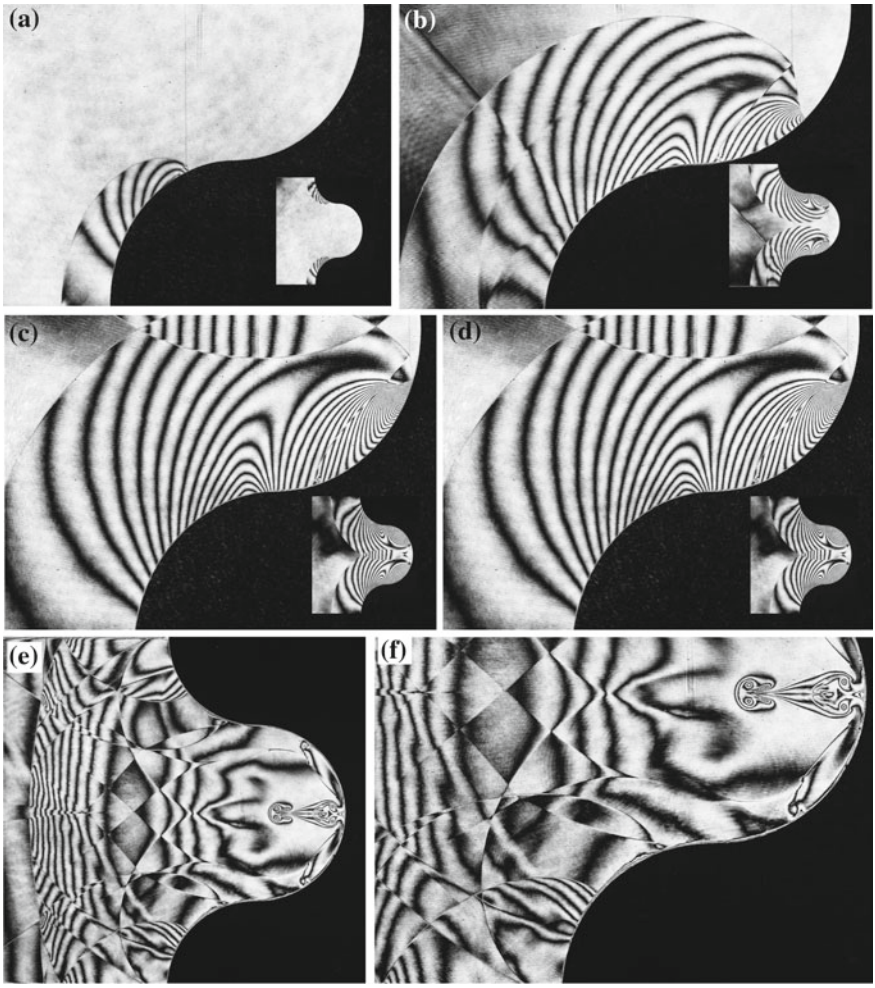

Fig. 22 Reflected shock focusing from a 75 mm concave reflector: **a** #86091902 delay time 190 μs, Ms = 1.436, 1013 hPa, 297.8 K; **b** #86091810, delay time 270 μs, Ms = 1.435 atm 297.9 K; **c** #86091806, delay time 290 μs, Ms = 1.416, 1013 hPa, 297.9 K; and **d** #86091903, delay time 305 μs, Ms = 1.431, 1013 hPa, 287.8 K; **e** #86091907, delay time 350 μs, Ms = 1.426, 1013 hPa, 287.8 K; and **f** enlargement of (**e**)

5 Concluding Remarks

We revisited previous data and compared them quantitatively with recent numerical results of solving the Navier–Stokes equations. This work was inspired by the discussions during the series of seminars conducted in the Peter the Great St. Petersburg Polytechnique University. We confirmed that the deviations of the critical transition angles over curved walls from analytical criterions are mostly

caused by the presence of boundary layer behind the transmitting shock and that such effects enhanced the deviation over smaller test models. Inspired by such basic studies, the authors wish to apply results of the basic studies to the mitigation of shock waves through wire grids.

When a shock wave propagates along a convex wall from 90° to 0°, the RR to MR transition occurs at a critical transition angle θ_{crit}. The two-shock solution can give the lower boundary of the termination of RR. Over convex walls of smaller radii, the θ_{crit} becomes smaller and even close to 0°. On the contrary, for a shock wave propagating along a concave wall from 0° to 90°, the MR to RR transition takes place at θ_{crit}. For stronger shock waves, the three-shock solution is a criterion of the transition and for moderate and for weak shock waves, the two-shock solution is a criterion of the transition. Hence, these criterions can be the upper boundary of the termination of MR. Over concave walls of very small radii, θ_{crit} becomes large and even tends to be 90° in extreme cases.

In shock tube flows, at a triple point, three shock waves merge and a slip line emanates Such a complex structure satisfies the gas dynamic conservation law. The slip line is a density jump at equal pressure, in short, entropy discontinuity. The conservation law requires such a complex wave structure in order to create an entropy discontinuity in flows. The entropy discontinuity is preserved but never vanishes.

Over convex walls, RR to MR transitions created a triple point emanating the entropy discontinuity. However, MR to RR transitions over concave walls are not simply its reverse process but the transition procedures are not straightforward.

At the MR to RR transitions, the RR does not hold any triple points so that the entire flow system is responsible the slip line. This is a gas dynamic procedure that a direct MR progressively transits to a stationary MR, an inverse MR and eventually RR. The secondary triple point behind the RR is a remnant of the triple point of the inverse MR.

Such a wave transformation agrees with the gas dynamic conservation law. Hence, the entropy discontinuity in the flow is always preserved. In the region surrounded by the three-shock solution and the two-shock solution, RR and MR coexist. Physically, this is the region adjusting complex shock transition procedure that only admits the transition from MR to RR. If we may have walls of any complicated geometries allowing MR to RR transition the resulting critical transition angle would lay in the region in which RR and MR coexist.

References

1. von Neumann, R., Friedrichs, K.O.: Supersonic Flow and Shock Waves. Wiley Int. Sci. (1948)
2. Ben-Dor, G.: Shock Wave Reflection Phenomena. Springer (1992)
3. Takayama, K., Sasaki, M.: Effect of radius of curvature and initial angle on the shock transition over concave or convex walls. Rep. Inst. High-Speed Mech. Tohoku Univ. **46**, 1–30 (1983)

4. Takayama, K., Honda, M., Onodera, O., Kawauchi, T.: Experimental study of shock reflection from curved walls. Mom Inst High Speed Mech. Tohoku Univ. **44**, 1–37 (1980) (in Japanese)
5. Takayama, K., Onodera, O., Gotoh, J.: Shock wave reflection over curved walls with surface roughness. Mem. Inst. High Speed Mech. Tohoku Univ. **48**, 1–21 (1980) (in Japanese)
6. Henderson, L.F., Crutchfield, W.Y., Virgona, R.J.: The effects of heat conductivity and viscosity of argon on shock wave diffracting over rigid ramps. JFM **331**, 1–49 (1997)
7. Henderson, L.F., Takayama, K., Crutchfield, W.Y., Itabashi, S.: The persistence of regular reflection during strong shock diffraction over rigid ramps. J. Fluid Mech. **431**, 273–296 (2001)
8. Itabashi, H.: The effect of viscosity and thermal conductivity on the transition of shock waves on wedges. Master thesis, Graduate School of Tohoku University, Faculty of Engineering (1998)
9. Takayama, K., Watanabe, W.: Shock reflection over a concave wall; double exposure holographic observation. Mom Inst. High Speed Mech. Tohoku Univ. **45**, 1–33 (1980) (in Japanese)
10. Komuro, R., Inoue, O., Takayama, K.: Study of shock wave reflection over double wedges. In: Proceedings of the JSSW, pp. 599–604 (1989)
11. Komuro, R.: Shock wave reflection over a double wedge. Master thesis, Graduate School of Tohoku University, Faculty of Engineering (1989)
12. Takayama, K., Igra, O.: Professor I.I. Glass A tribute and Memorial. Springer (2013)
13. Takayama, K.: Application of holographic interferometry to shock wave research. Proc. SPIE **398**, 174–180 (1983)
14. Bazhenova, T., et al.: Shock waves and real gases, NASA TIF **565** (1969)
15. Sun, M., Saito, T., Takayama, K., Tanno, H.: Unsteady drag on a sphere by shock wave loading. Shock Waves **14**, 3–9 (2005)
16. Liepmann, H., Roshko, A.: Element of Gasdynamcs. Wiley (1956)
17. Whitham, G.B.: A new approach of shock dynamics. Part 2 3D problems **5**, 369–375 (1959)
18. Takayama, K., Gotoh, J., Ben-Dor, G.: Influence of surface roughness on the shock transition in quasi-stationary and truly non-stationery flows. In: Proceedings of the 12th ISSW, pp. 326–334 (1981)
19. Smith, L.G.: Photographic investigation of plane shocks in air. OSRD Rep 6271, Off Sci Res Div., Washington DC (1948)
20. Takayama, K., Sekiguchi, H.: An experiment on shock eave diffraction by cone. Rep. Inst. High Speed Mech. Tohoku Univ. **36**, 36–53 (1977)
21. Yang, J., Sasoh, A., Takayama, K.: The Sock Reflection over a Cone, SW, vol. 6, pp. 267–273 (1996)
22. Kosugi, T., Mitobe, H., Takayama, K., Kitade, M.: Shock wave reflection over rigid wedges and cones. In: Proceedings of the 22nd ISSW, pp. 1279–1284 (1999)
23. Krasovskaya, I.: Private Communication (2015)
24. Sturtevant, B., Kulkarny, V.A.: The focusing of weak shock waves. J. Fluid Mech. **73**, 651–671 (1976)
25. Kitade, M.: Numerical and experimental study of delayed transition of Mach reflection over curved walls and cones. Master thesis, Graduate School of Tohoku University, Faculty of Engineering (2001)

Transition Effect on Shock Wave Boundary Layer Interaction on Compressor Blade

Ryszard Szwaba, Piotr Doerffer and Piotr Kaczynski

Abstract Intensive research on the laminar flow is carried out nowadays. The main objective is to keep the laminar boundary layer as long as possible for the drag or losses reduction, depending on the application. Nevertheless, in some applications, the laminar layer interaction with the shock wave may lead to a strong flow separation. The process of separation usually becomes unsteady and causes buffeting at airfoils and shock oscillations in the internal flows. Shock oscillation causes pulsation of pressure, and consequently a change of the blade load. The main objective of this research is to study the effect of transition on the flow structure of the shock wave boundary layer interaction. This paper focuses on the influence of boundary layer transition on the flow pattern in the blade passage of a compressor cascade. The main question is whether the induced transition upstream of the shock can improve the pressure unsteadiness and the flow downstream of the interaction. The results presented here concern experimental investigations and the used combination of various methods allowed gaining an insightful analysis of the application of transition control devices into a complex flow structure in a compressor cascade passage.

Keywords Laminar boundary layer · Transition · Compressor cascade

1 Introduction

A large part of drag or losses of aerodynamic devices in the flow is related to skin friction, decreasing the friction will significantly contribute to their reduction. One of the available solutions to achieve lower friction drag is to extend the laminar flow on the overflow surface. Therefore, intensive research concerning the laminar flow is carried out nowadays [1, 2]. The main objective is to keep the laminar boundary

R. Szwaba (✉) · P. Doerffer · P. Kaczynski
Experimental Aerodynamics Department, Institute of Fluid-Flow Machinery (IMP PAN), Gdansk, Poland
e-mail: ryszard.szwaba@imp.gda.pl

K. Kontis (ed.), *Shock Wave Interactions*,
https://doi.org/10.1007/978-3-319-73180-3_2

layer as long as possible for the drag or losses reduction, depending on the application. Nevertheless, in some applications, the laminar layer interaction with the shock wave may lead to a strong flow separation. The process of separation usually becomes unsteady and causes buffeting at airfoils and shock oscillations in the internal flows. Shock oscillation causes pulsation of pressure, and consequently a change of the blade load.

The main objective of the TFAST project (Transition Location Effect on Shock Wave Boundary Layer Interaction, EC 2012) was to study the effect of transition location on the structure of interaction. The main question is if the induced transition upstream of the shock can improve the pressure unsteadiness and the flow downstream of the interaction. One of the project flow cases was the shock wave boundary layer interaction (SWBLI) in a transonic compressor cascade. In order to investigate the flow structure on the suction side of the blade in a rectilinear test section of the transonic wind tunnel, a model of a turbine compressor passage was designed and assembled in a wind tunnel, Fig. 1. The model can reproduce the flow structure (dashed curve area), pressure distribution and boundary layer (BL) development similar to the obtained in a reference cascade profile.

This paper presents an experimental investigation concerning the influence of laminar and turbulent shock wave boundary layer interaction on the flow structure in a compressor passage. In some conditions of compressor work, the laminar shock waves boundary layer interaction induces separation and leads to strong unsteady effects [3, 4]. In these two contexts, it is proposed to use a tripping device to generate BL transition upstream of the shock for the interaction control. There are many methods that can be used to induce transition in the boundary layer, e.g. the air-jet vortex generators [5–7] or distributed roughness. In the present experiment, the simple spanwise step was used as the tripping device, just to demonstrate if there was any positive effect in changing the character of the interaction. The step location and height were investigated. The results are presented only for two chosen best flow cases.

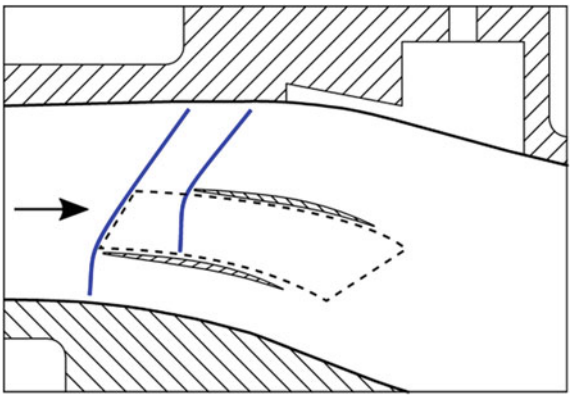

Fig. 1 Test section layout

2 Experimental Setup

An experimental programme was carried out in a transonic wind tunnel in the test sections shown in Fig. 2. The flow structure was investigated on the suction side (upper part) of the lower blade. The lower and upper profiles were located in a similar configuration as in the reference linear cascade (delivered by Rolls-Royce Deutschland) in order to keep a similar flow structure as in the reference passage. There was a nozzle with a uniform velocity region at its outlet upstream of the blade passage. The Mach number upstream of the blades was supersonic, $M = 1.22$ and the Reynolds number based on the blade chord was 1.4×10^6, which corresponded to the aircraft altitude condition. Both the blade cord c and the blade span were 100 mm. The turbulence level in the nozzle upstream of the passage was 0.8%.

A normal shock wave was generated upstream of each blade and interacted with the BL of the neighbouring blade on its suction side. The flow accelerated downstream of the blade leading edge up to $M = 1.42$ and the supersonic region was terminated by a normal shock wave. The interaction at such high Mach number induced a fully separated flow.

A complex suction system, partly visible also in Fig. 2, was used in the test section during the experiments to obtain a proper flow structure in the blade passage. There were two suction systems in the test section, one comprising two suction slots (short black arrows) in the side supports of the lower blade. These two slots were used for the proper AVDR (axial velocity density ratio) control in the measurement section. For the single passage compressor test section used in the experiment $AVDR = 1.2$, as assumed in design conditions. The mass flow rate through the two slots in the side supports was 428 L/min, i.e. 0.0084 kg/s. The second system included suction on the upper and lower limiting channel walls. In this system, it was possible to get unchoked flow beneath the lower and above the upper blade, and finally, the proper supersonic conditions upstream of the profiles were obtained. The upper wall suction was a perforated plate of perforation equal to

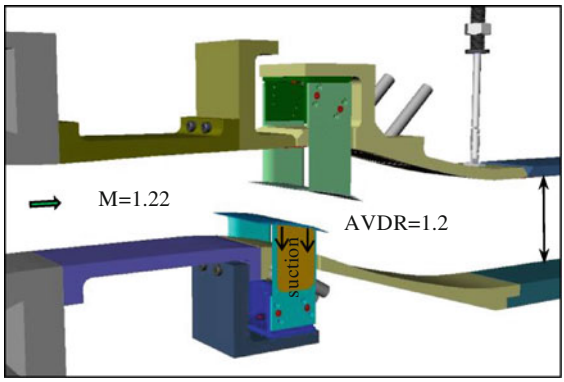

Fig. 2 Single passage compressor cascade model

5.2% and the holes were $d = 0.11$ mm in diameter. The additional suction slots on the lower wall were located both upstream and downstream of the blade supports. There were two vertical slots upstream of the blade supports and one slot downstream and between the supports in the spanwise direction. The mass flow in all suction slots and plates was considered as for choking (sonic velocity) conditions.

The boundary layer thickness, measured roughly, based on the schlieren picture upstream of the shock at $X/C = 0.3$ was about 0.4 mm. Without transition control, the laminar boundary layer reached the shock wave interaction zone. To force the transition, two locations of spanwise tripping step were chosen, one at the leading edge and the second at $X/C = 0.16$. The location of main shock wave in the blades passage was at $X/C = 0.48$. The width of the step was 5 mm and its height was 100 μm. To investigate some aspects of the BL transition effects on the SWBLI, the following measurements were carried out:

- static pressure distribution along the centre line of the blade;
- schlieren visualisation of the flow structure and the shock system topology;
- high-speed movie visualisation of normal shock wave oscillations;
- oil flow visualisation on the blade suction side to display the separation size and structure;
- PSP and TSP (pressure- and temperature-sensitive paints) on the blade wall;
- the flow velocity distribution across the blade wake by means of LDA (laser Doppler anemometry).

3 Results and Discussion

The normalised static pressure distributions on the blade profile versus normalised cord length (*X/C*) for different flow cases are shown in Fig. 3. The notation *P0* is the stagnation pressure at the inlet of the test section. The Ref-laminar notation means the clean flow without any tripping devices; for that case, in fact, a laminar interaction in the flow was obtained. The T-LE case is the flow with a 100 μm step height at the leading edge (LE) and the T-X/C = 0.16 case is the flow with the same tripping device located at 0.16 of the blade cord.

For the clean flow (red line, Fig. 3), one can observe upstream of the shock pressure jump a region where the flow slightly decelerates, the pressure gradient changes. This is a typical phenomenon for the laminar type of interaction [8, 9]. For both turbulent interactions, the flow accelerates till the shock pressure jump. In the schlieren visualisation for the laminar case (Fig. 4), an additional oblique shock wave appeared upstream of the interaction. Such phenomenon is not observed for turbulent interaction (Fig. 5). In fact, it shows that laminar interaction starts more upstream in relation to the turbulent one. The disturbance in the pressure distributions upstream of the shock (T-X/C = 0.16) observed in Fig. 3 is caused by the presence of a tripping step in the flow. In the flow with the step at the LE, a thicker boundary layer is received, which increases the λ-foot size (see Figs. 4 and 5), and

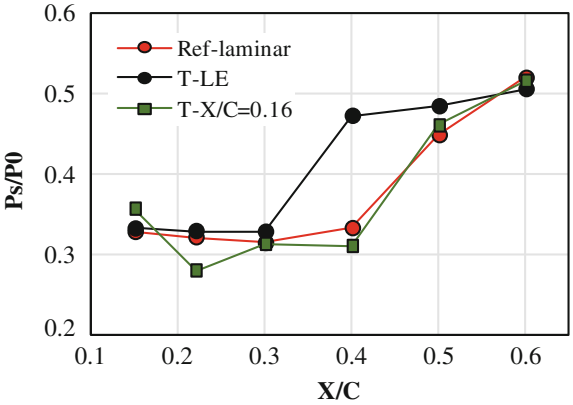

Fig. 3 Static pressure distribution along the blade

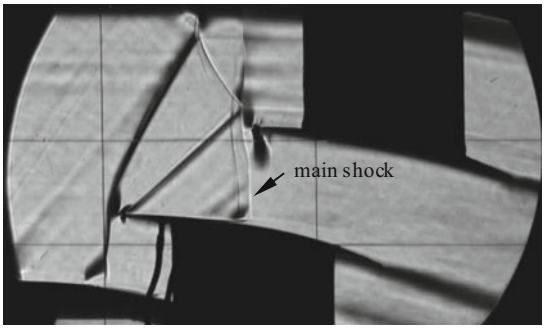

Fig. 4 Schlieren picture for laminar interaction

in consequence, the shock pressure jump appears more upstream. In the flow with the step at X/C = 0.16 a better pressure recovery downstream of the shock in relation to the laminar case is observed. A similar phenomenon cannot be observed for the T-LE flow case.

The schlieren picture in Fig. 5 shows that λ-foot increased in the flow with the step at LE because of the thicker boundary layer. In this case, the turbulent boundary layer at the weak longitudinal pressure gradient has favourable conditions for growth from the leading edge to the shock location. The transition tripped further downstream of the LE at *X/C* = 0.16 does not thicken the BL so much and λ-foot is comparable in size to that in the laminar interaction (the shock pressure jump in the same location, Fig. 3).

Oil visualisations for different flow cases are shown in Figs. 6, 7, 8 and 9. This is a view onto the blade suction side through a sidewall window. The flow is from left to right. A view of the whole blade for the laminar interaction is presented in Fig. 6, but the zoomed view for that flow case is shown also in Fig. 7. In these figures, one

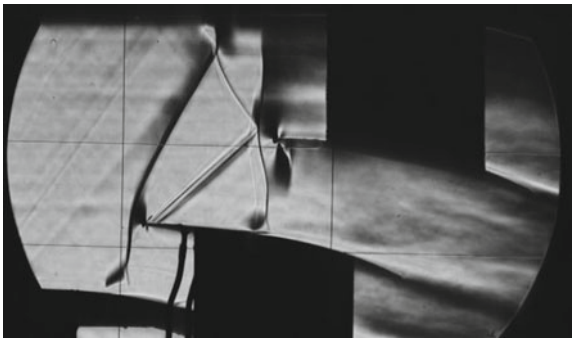

Fig. 5 Schlieren picture for turbulent interaction, step at the leading edge

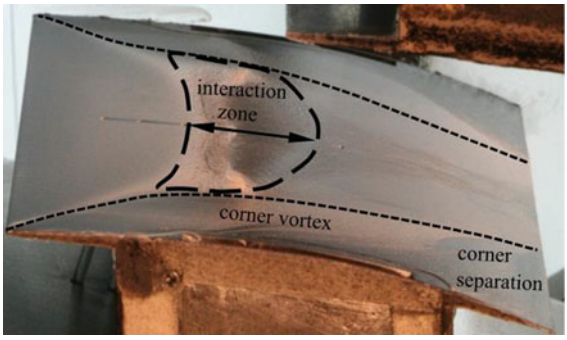

Fig. 6 Oil visualisation for laminar interaction

can observe that there is an area at the sidewalls formed as a result of the interaction between the corner and the main flow. This corner vortex starts to develop just downstream of the leading edge, widening considerably at the shock wave boundary layer interaction area (in the middle of the channel), then the corner interaction width growth slows down.

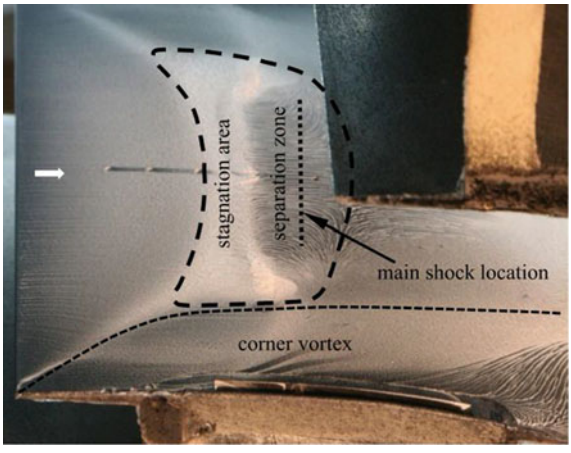

Fig. 7 Zoomed view of oil visualisation for laminar interaction

The main shock location in Fig. 7 is marked by a dotted line drawn transverse to the flow direction. The thicker oil layer upstream of the shock (dashed curve) was created due to reduced skin friction induced by the shock and means the onset of the interaction. Within the whole area of interaction (dashed closed curve), two subzones can be distinguished, namely, the stagnation and separation zone. There is a stagnation zone downstream of the interaction onset. The separation zone is displayed by the oil streaks downstream of the stagnation zone under the main shock wave, indicating a reverse flow area before reaching the dashed curve indicating reattachment. A significant distance between the onset of the interaction and the main shock wave location is an indication that we are dealing with the laminar type of the interaction. Generally, the size of the laminar interaction on the compressor blade at supersonic conditions is very large and occupies about a quarter of the blade cord.

Oil visualisations for the flow cases with different tripping strep locations are shown in Figs. 8 and 9. In Fig. 8, it can be observed that BL turbulisation significantly influences the corner flow, the beginning of the interaction is shifted further downstream, the oil thickening layer starts typically for turbulent interaction

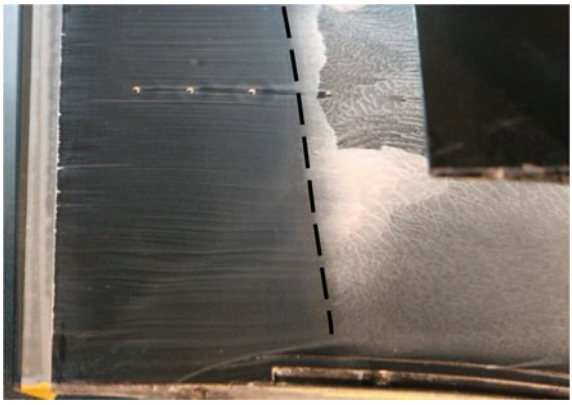

Fig. 8 Oil visualisation for turbulent interaction, step at the leading edge

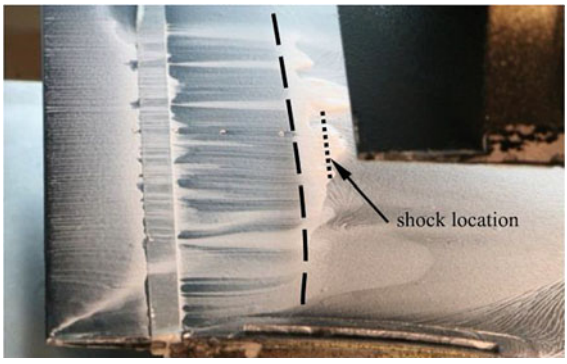

Fig. 9 Oil visualisation for turbulent interaction, step at X/C = 0.16

at the vicinity of the λ-foot front shock wave. The separation size is reduced in relation to the laminar interaction.

Oil visualisation for the flow with the next location of the tripping step is shown in Fig. 9. For this flow case, a turbulent type of interaction and the flow structure on the blade wall were also obtained. A typical turbulent interaction is displayed with an oil thickening layer starting in the vicinity of the λ-foot front shock, just upstream of the main shock location. The boundary layer turbulisation changes the flow in the corners also downstream of the tripping step.

The results of static pressure distribution on the whole surface of the lower blade obtained by means of PSP measurements are presented in Figs. 10 and 11. In these figures, one can observe a very well displayed pressure jump on the shock wave and the small flow acceleration (lower pressure region) downstream of the leading edge corners caused by the interaction of the main flow with the corner vortex. Probably this interaction creates a local vortex which locally increases the flow velocity, and what can be seen in the pressure distribution is the vortex downwash region. In Fig. 10 for the laminar interaction, one can also observe the spanwise pressure difference between the sidewall regions and the middle part of the channel. In the middle of the channel, the pressure is lower, which means higher flow velocity. The higher pressure region in the channel corners overlaps more or less the region of corner vortex influence from the oil visualisation (see Figs. 6 and 7). This spanwise pressure gradient is the reason why the shock wave is slightly bowed towards the downstream direction. For the flow in Fig. 11, as has been mentioned in the oil visualisation, the transition changes considerably the flow in the corners. The flow in the corners accelerates in relation to the clean flow, and finally, the lower pressure in the compared area is obtained.

The results of the temperature change on whole surface of the lower blade obtained by means of TSP measurements for the clean flow and with transition are presented in Figs. 12 and 13. Due to the fact that there was no exact calibration of the temperature paint, it is only the temperature change that is shown. The range of the temperature change is adequate to the difference between the air stagnation and

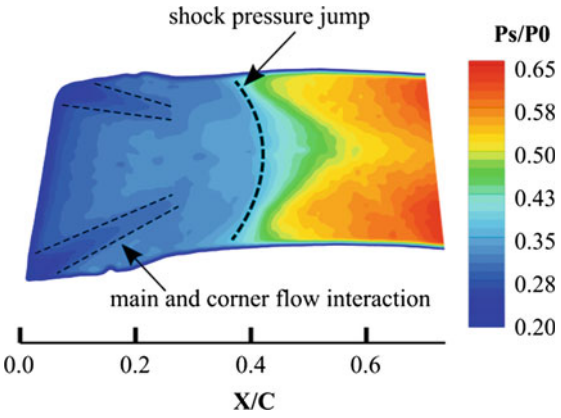

Fig. 10 Blade pressure distribution for laminar interaction

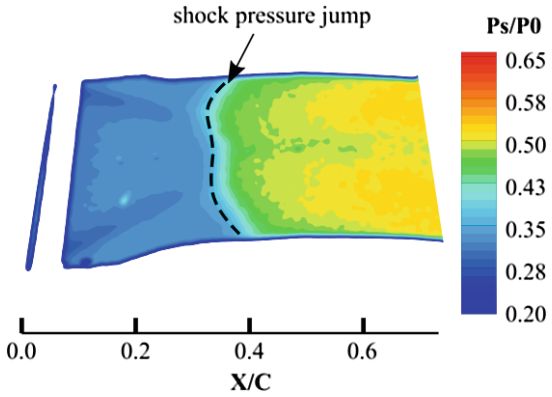

Fig. 11 Blade pressure distribution for the flow with the step at the leading edge

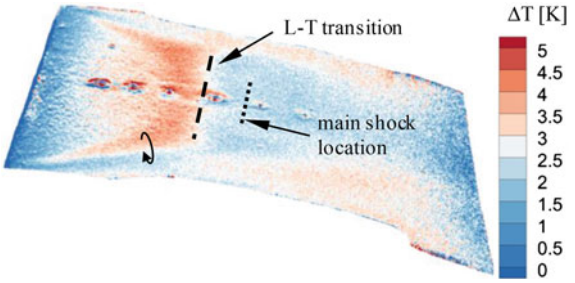

Fig. 12 Blade temperature change for laminar interaction

the blade temperature. The gas stagnation temperature was lower than the blade temperature.

In Fig. 12 for the clean flow, one can see a gradual temperature increase in the area downstream of the leading edge to the transition location. This is due to a gradual decrease in the shear stresses in the area upstream of the shock. The stresses are the highest just downstream of the LE. The laminar–turbulent transition in the boundary layer (sudden change of temperature) occurs approximately at the beginning of the separation zone (see Fig. 7) which corresponds to more or less the location of the front λ-foot shock wave. Upstream of the shock near the channel corners one can watch the temperature footprint of the vortex structure produced by the main and corner flow interaction. From one side in the vortex downwash region, there is a lower temperature (blue); on the other side in the upwash area (red), the temperature increases. In this way, one can also determine the sense of rotation of that vortex structure (Fig. 12). Application of a small tripping device (100 μm) at the leading edge (Fig. 13) causes BL transition downstream of the step and equalises the wall shear stresses (temperature) distribution in the spanwise direction, what can be also observed in oil visualisations (see Figs. 7 and 8).

In Fig. 12 downstream of the shock, one can also observe the spanwise temperature difference between the sidewalls and the channel centre regions. In the middle of the channel, the temperature is lower, which is caused by higher shear

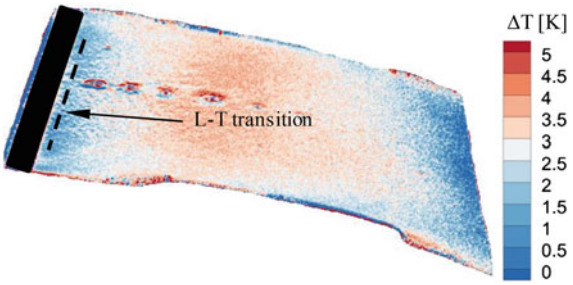

Fig. 13 Blade temperature change for the flow with transition

stresses (higher flow velocity). The region of higher temperature near the channel corners is a derivative of the vortex structure present in these areas which generally are characterised by higher pressure and lower velocity. The transition upstream of the interaction (Fig. 13) changes the flow at the corners and by the same token equalises the temperature distribution on the blade in the spanwise direction.

The location of the velocity traverse measurements downstream of the blades passage is shown in Fig. 14. One traverse was measured, 20 mm downstream of the passage crossing only the lower blade wake, W20. The traverse in the spanwise direction was located in the middle of the channel.

The results of velocity measurements in the wake of the lower blade are shown in Fig. 15. They are plotted as a function of distance Y along the traverse line versus the velocity magnitude. The beginning of the coordinate system (X, $Y = 0$, 0) was established on the blade trailing edge (blue point). According to this point, particular Y values of measurement points are related. The inclination angle of Y-axis regards to the vertical direction, as shown in Fig. 14, was 55.6°. The location of the point, being the result of the blade cord and measurement traverse crossing, is also marked in the figure as red small circles.

A comparison of the velocity profiles in the wake for the clean flow and for the two flows with transition is shown in Fig. 15. The integral parameters of the wake for these flow cases are also presented in Table 1. The parameters (thickness δ, displacement and momentum thickness δ^*, δ^{**}) for each flow cases were calculated only for the upper part of the wake.

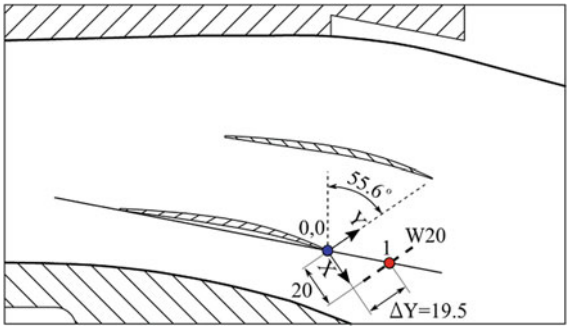

Fig. 14 Traverse location for velocity measurements

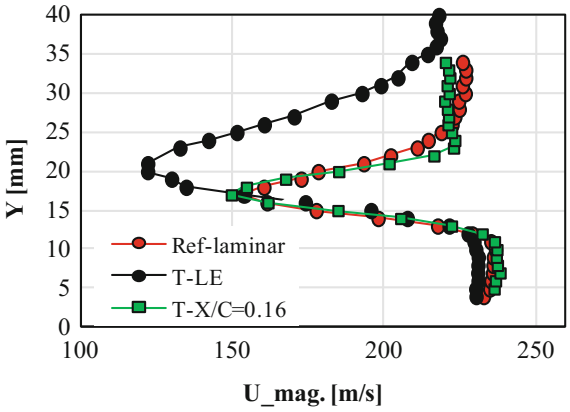

Fig. 15 Velocity profiles in the wake

Table 1 Wake integral parameters for all flow cases

	Ref-laminar	T-LE	T-X/C = 0.16
δ [mm]	9.2	21.0	5.7
δ* [mm]	1.31	4.15	1.02
δ** [mm]	1.03	2.90	0.77

The results of the velocity measurements and the parameters of the wake clearly show that too thick a boundary layer upstream of the interaction area (T-LE flow case) causes significant wake thickening. An adequate location of the tripping device (T-X/C = 0.16 flow case) reduces the wake thickness and other integral parameters even in relation to the flow with laminar interaction.

The flow unsteadiness in the blades passage was determined by means of shock oscillations measurements. The results were obtained from films based on the schlieren visualisation. The films were made using a fast CCD camera, and single frames were extracted. From each frame, only one line which crosses the main shock wave was analysed. The location of the line for the shock oscillations measurements is shown in Fig. 16. The distance from the blade wall to the measurement line was about 20 mm. The sampling frequency for all measurements was equal to 2 kHz. The results are shown in form of power spectrum plots of shock oscillations in Figs. 17 and 18. The unit of the power spectrum amplitude is [mm^2]. Additionally, the *RMS* from the shock oscillations signal and the shock amplitude for the measured flow cases are presented in Table 2.

Based on Fig. 17, one can notice that for the laminar interaction, it is difficult to distinguish any dominant frequencies (a similar distribution was also obtained for the flow case of T-X/C = 0.16). There are a lot of peaks in the range from 2 to 500 Hz. Approximately above 500 Hz, the power of the shock amplitude decreases significantly. A different result for the T-LE flow case was obtained, Fig. 18. In this case, one can distinguish one characteristic frequency of about 300 Hz in the shock oscillations. The high peaks at low frequencies for the laminar interaction are connected with the unsteadiness in the separation area [10, 11] the size of which is

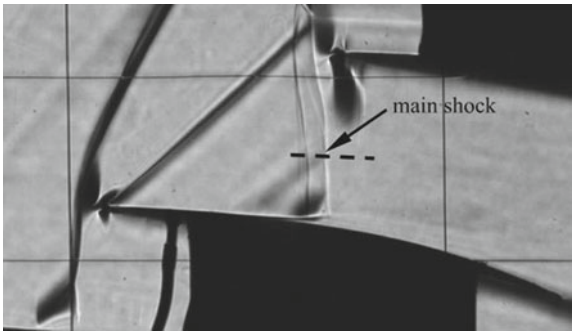

Fig. 16 Measurement location of shock oscillations

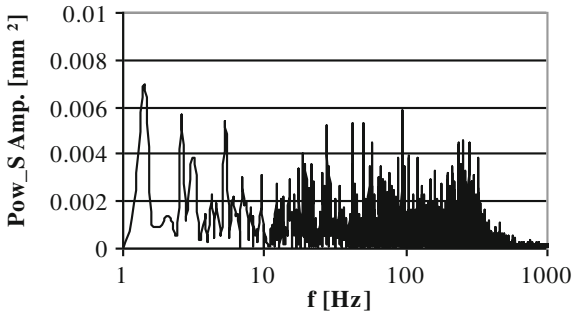

Fig. 17 Power spectrum of shock oscillations for laminar interaction

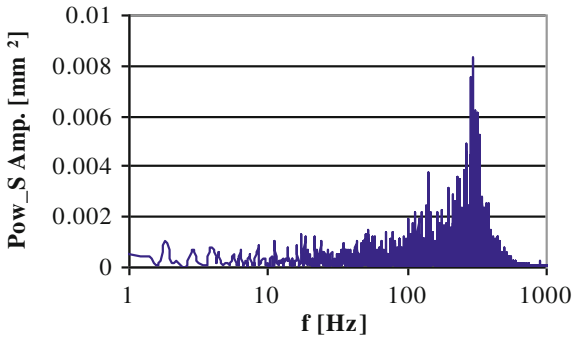

Fig. 18 Power spectrum of shock oscillations for the flow with the step at the leading edge

Table 2 RMS and amplitude of shock wave oscillations

	Ref-laminar	T-LE	T-X/C = 0.16
RMS [mm]	1.25	1.22	1.16
Amplitude [mm]	4.4	4.7	3.6

significant, and therefore, the low frequencies are dominating. In the case when the separation size is reduced, the low frequencies stop to play an important role and the higher frequencies start to dominate.

Based on Table 2 and Figs. 17 and 18, one can say that the effective values of shock oscillations (*RMS*) and shock amplitude are significant for both the laminar and turbulent interactions with the tripping at the leading edge. In those cases, the *RMS* is about 10% and the amplitude is about 20% higher in relation to the flow with the step at X/C = 0.16. The *RMS* of the shock oscillations is about 1.2% of the blade cord for the latter case. This flow case shows that transition induced at appropriate location can reduce the shock wave oscillation, both for the *RMS* and the amplitude.

4 Summary and Conclusions

The obtained results from the above-described experimental investigations show that induction of properly configured transition, upstream of the shock, has a positive influence on the shock wave boundary layer interaction region. Reduction of the separation size, losses in the wake and shock wave unsteadiness were observed in the flow in the case of the turbulent interaction. The following more detailed conclusions can be also drawn from the presented experimental results:

- The flow field contains characteristic features of the flow in the reference linear compressor cascade.
- In the reference flow (without transition control), the laminar shock wave boundary layer interaction is observed; such interaction starts with laminar separation upstream of the main shock wave location.
- The turbulent interaction starts just at the λ-foot beginning.
- The flow with transition started just downstream of the leading edge produces a thicker boundary layer in relation to the laminar one. It increases the λ-foot size and the shock wave pressure jump appears more upstream.
- Promising results for a properly configured transition control device were obtained:
  - the wake parameters (thickness, displacement and momentum thickness) are the lowest for the tripping step located at $X/C = 0.16$, probably the laminar zone upstream of the transition helps to diminish the viscous losses in the flow;
  - the unsteadiness in the flow with the tripping step at $X/C = 0.16$ in relation to the laminar interaction also decreases.

Generally, moderate treatment of the incoming boundary layer is required as overtripping can be easily induced; it appears in a rapid manner and causes deterioration of the downstream boundary layer. The too thick boundary layer upstream of the interaction leads to overtripping, i.e. losses in the wake increase. The flow at lateral walls should be also taken into account to gain a more general view of application of transition control devices.

Acknowledgements The research leading to these results received funding from the European Union Seventh Framework Programme (FP7/2007–2013) under Grant Agreement No. 265455 (TFAST) [12].

References

1. Joslin, R.D.: Aircraft laminar flow control. Annu. Rev. Fluid Mech. **30**, 1–29 (1998)
2. Messing, R., Kloker, M.J.: Investigation of suction for laminar flow control of free-dimensional boundary layers. J. Fluid Mech. **658**, 117–147 (2010)
3. Swoboda, M., Nitsche, W.: Shock boundary-layer interaction on transonic airfoils for laminar and turbulent flow. J. Aircr. **33**(1), 100–108 (1996)
4. Becker, B., Reyer, M., Swoboda, M.: Steady and Unsteady Numerical Investigation of Transitional Shock-Boundary-Layer-Interactions on a Fan Blade, German Aerospace Congress (2006)
5. Szwaba, R.: Comparison of the influence of different air-jet vortex generators on the separation region. Aerosp. Sci. Technol. **15**, 45–52 (2011)
6. Szwaba, R.: Influence of air-jet vortex generator diameter on separation region. J. Therm. Sci. **22**(4), 294–303 (2013)
7. Szwaba, R., Doerffer, P.: Separation control by air-jet vortex generators on turbine blades. In: 9th European Conference on Turbomachinery—Fluid Dynamics and Thermodynamics, vol. II, pp. 1199–1209 (2011)
8. Gomes, R.A., Niehuis, R.: Aerothermodynamics of a high-pressure turbine blade with very high loading and vortex generators. J. Turbomach. **134**(011020), 1–9 (2012)
9. Szwaba, R., Flaszynski, P., Szumski, J., Doerffer, P.: Influence of air cooling and air-jet vortex generator on flow structure in turbine passage. TASK Q. **19**(2), 153–166 (2015)
10. Dussauge, J.P., Dupont, P., Debiève, J.F.: Unsteadiness in shock wave boundary layer interactions with separation. Aerosp. Sci. Technol. **10**, 85–91 (2006)
11. Dussauge, J.P., Piponniau, S., Debiève, J.F., Dupont, P.: A simple model for low frequency unsteadiness in shock induced separation. J. Fluid Mech. **629**, 87–108 (2009)
12. http://www.tfast.eu (2012)

Shock Wave Reflection and Attenuation in the Combined Blast Inhibitors

M. V. Silnikov, M. V. Chernyshov, A. S. Kapralova, A. I. Mikhaylin, A. S. Pankov, V. N. Shishkin, A. I. Spivak and A. G. Tyapko

Abstract A robust blast-inhibiting bin is the most often used device for damage blast effects suppression. In particular, a top open cylindrical bin significantly reduces a fragmentation effect resulted from a detonation of an explosive device placed inside the bin. However, reduction of blast wave overpressure and impulse by such cylindrical bins is not sufficient (Gelfand et al, Shock Waves 20:317–321, 2010) [1]. A reasonable alternative to endless increase of height and thickness of robust blast-inhibiting bins is a development of destructible inhibitors having no solid elements in their structure and, therefore, excluding secondary fragmentation. So, the family of "Fountain" inhibitors (Vasil'ev et al, Izv Akad Nauk Energ 6:7–19, 2004) [2], (Silnikov and Mikhaylin, Acta Astronaut 97:30–37, 2014) [3] localizes and suppresses damaging blast effects due to multiphase working system. The present study is analyzing data obtained in testing of prototypes of new combined inhibitors. Their structure combines robust elements (bottoms, side surfaces) with elements responsible for blast loads reduction due to multiphase working system (top and low transverse embeddings) and fairings impeding wave propagation in undesirable directions.

M. V. Silnikov · M. V. Chernyshov (✉) · A. S. Kapralova · A. I. Mikhaylin
A. S. Pankov · V. N. Shishkin · A. G. Tyapko
Peter the Great Saint Petersburg Polytechnic University,
29 Polytechnicheskaya Str., 195251 Saint Petersburg, Russia
e-mail: mvcher@mail.ru

M. V. Silnikov · M. V. Chernyshov · A. I. Mikhaylin · A. S. Pankov
V. N. Shishkin · A. I. Spivak
Special Materials Corp., 28A Bolshoy Sampsonievsky Ave.,
194044 Saint Petersburg, Russia

K. Kontis (ed.), *Shock Wave Interactions*,
https://doi.org/10.1007/978-3-319-73180-3_3

1 Introduction

This study is dedicated to new ways and means of shock wave suppression and to new devices for this purpose and based on new technologies combining both geometrical and physical ways of shock wave mitigation.

The technologies of shock mitigation have a broad scope of applications—from communal services and house-building industry to special anti-terrorist equipment for security structures. These technologies can be also used even in the space industry, for example, to mitigate the influence of initial shock wave on rocket nozzle and to quench self-oscillating jet flow interaction with a launch complex. They can be used also to soften a destructing action of blast wave, because some modern devices of spaceship undocking are based on elastic HE composition (including, for example, such HE like PETN). Modern materials absorbing the blast energy and mitigating the shock wave can be used also for rocket nozzle protection from shock influence, as well as at launch complex subject to interaction with supersonic jet flows, sometimes in self-oscillating regimes.

Ways to protect biological and technical objects from shock wave damaging action can be conventionally divided into geometrical and physical. The geometrical methods of shock mitigation are characterized by special shape of solid structures designed to diminish a shock wave overpressure or to form a special direction of shock propagation. The physical methods of shock mitigation are based on specific features of some materials and structures, for example, the energy-absorbing features of multiphase media. The experimental data on blast-protecting devices which combine both geometrical and physical methods of shock suppression are presented in this study.

2 Objects of Study and Test Conditions

Among the numerous methods and devices to suppress the dangerous action of blast wave [4–6], application of multiphase relaxation media in destructible containers without hard elements has shown itself as one of the most effective ways, both in general [2, 3] and in extraordinary conditions, e.g., onboard an airplane [3], including the case of diminished ambient pressure [7]. But for some purposes (for example, garbage bins in cities), hard basis of blast-resistant and blast-protecting device seems to be necessary. It limits the application of the completely destructible containers and convinces us to combine the hard basis and elements of relaxation media.

Two series of field tests were applied to our objects of study that were the steel cans with open top and inserted elements of multiphase media (Figs. 1 and 2). The first series of field tests were provided with rather small TNT charges (0,2 kg) and four first types of blast-protecting device prototypes (Fig. 1a–d). The basic cylindrical blast-resistant bin (Fig. 1a) was made of steel tube; its diameter was equal to

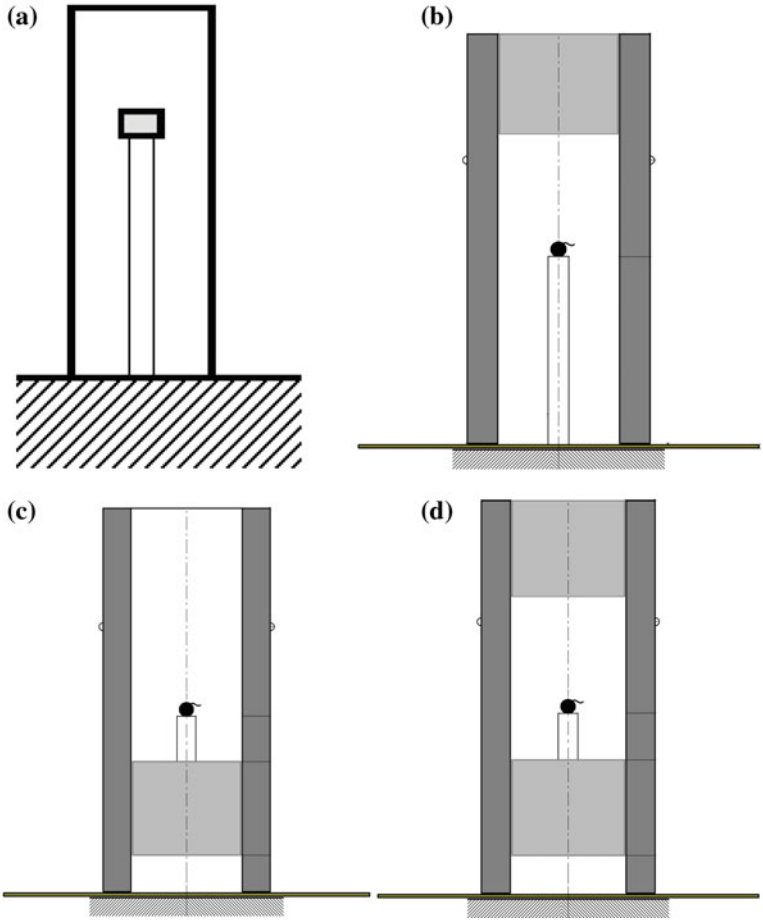

Fig. 1 First series of blast-protecting can prototypes tested at small HE charges

420 mm, its length to 1000 mm, and its wall thickness to 8 mm. This basic can has the weight of 82 kg and was welded with massive steel plate, which prevented its overturn at blast inside.

Because the CFD calculations have shown us the small efficiency of similar devices (see, for example [1]), three other prototypes of blast-protecting devices were elaborating (Fig. 1b–d) including the same steel basis and insertions (Fig. 2) made from the same multiphase media, which were successfully applied in "Fountain" blast inhibitors [2, 3, 7, 8]. The first modification of the basic device (Fig. 1b) can be characterized by upper insertion location, the second one (Fig. 1c) by its lower location at some small distance from can bottom, and the third one by both upper and lower locations of blast-inhibiting insertions.

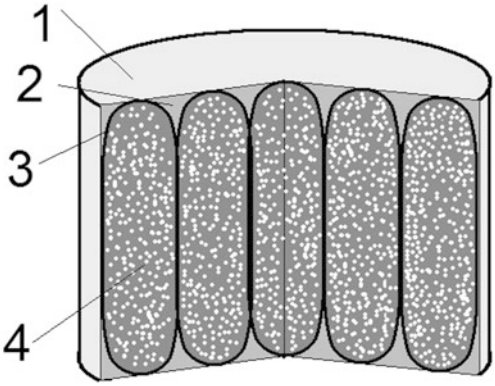

Fig. 2 Blast-protective insertion. 1—Covering, 2—polyurethane foam, 3—inhibiting elements fulfilled with multiphase media, and 4—multiphase media itself

Principles of blast mitigation with destructible blast inhibitors are based on the theory of shock interaction with solid and liquid foams. Theory of this interaction and shock mitigation was developed for the first time in studies [9, 10] and applied to the design of blast inhibitors by B. E. Gelfand and M. V. Silnikov in 1990s.

For larger TNT charges (Fig. 3) the element of steel (Steel 20 according to Russian State standards) tube (diameter—426 mm, length—1010 mm, wall thickness—12 mm, and weight—123,9 kg) welded with steel plate was used as the basic construction. The first modification of blast-protective device (Fig. 3b) included the inhibiting insertion (its length was equal to 220 mm, and its weight to 12 kg) at lower position, but at some distance (100 mm) from the can bottom. The multiphase insertion was thickened to 320 mm and was situated immediately at can bottom at the second modification (Fig. 3c). The building-up, which can be named as blast-protective flange (Fig. 4), was used at the third modification (Fig. 3d). Both flange and the multiphase insertion in its lower position were used at the fourth prototype (Fig. 3e). The bandage made of ballistic clothes accompanied the lower multiphase insertion in the fifth modification (Fig. 3f, the bandage is marked by two slanting St. Andrew's crosses).

Two rows of piezoelectric pressure transducers PD-7-1,5 (four transducers in each row) were situated at the angle of 90° one to another in all experiments (see Fig. 5). About 30 TNT charge blasts were performed in both series of experiments, so about 240 overpressure plots were achieved at the PC that registered the electric signal.

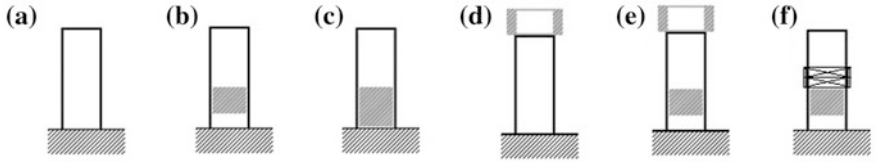

Fig. 3 Second series of blast-protecting bin prototypes tested at larger HE charges

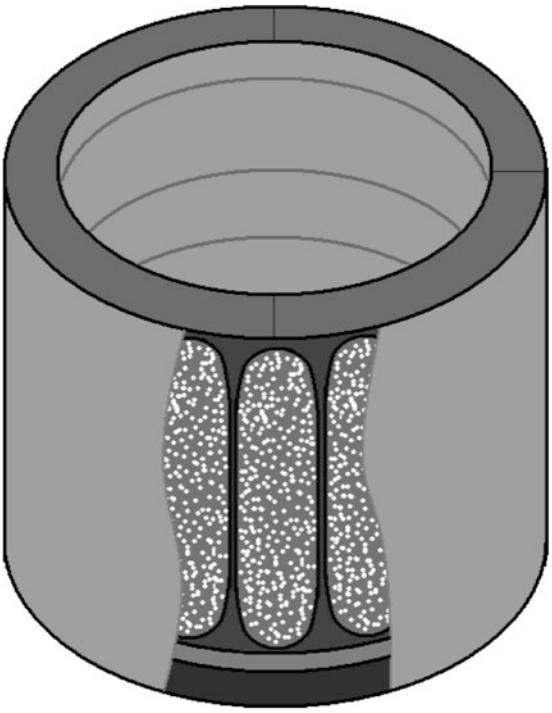

Fig. 4 Blast-protective flange construction

Fig. 5 Two rows, each composed of four pressure transducers and situated at the plane angle to each other, installed near the TNT charge at the field test [11]

After integrating, corresponding pressure impulse values were estimated at different distances (from 1,5 to 3 m) from the blast epicenter at each experiment.

Pressure transducers were amounted at the height equal to 1 m above ground level. Directions of rays (rows) along which they were installed corresponded to prevailing wind direction and normal line to the prevailing wind. It was shown in [11] as well as in numerous analogous experiments that this wind (up to 5 mps) does not influence sufficiently the results of measurements.

It was also proven at [11, 12] that the pressure transducers situated at the 0,5 m distance one after another do not interfere the measurements mutually. Protective elements made of steel beams (Fig. 6) also do not influence the experimental results, and studies [11, 12] are dedicated to this problem specially.

At the very end of experimental setup description, pressure transducers had successfully shown themselves in blast field tests during the last 12 years, including the experiments with blast-resistant and blast-protective devices. The height of pressure transducers was 1 m, the distance from the blast epicenter—from 1,5 to 3 m, the size of sensitive elements (white spheres at Fig. 6b)—about 5 mm. Open blasts (without any blast-protective cans) preceded the field tests of all outnumbered devices with corresponding TNT charge weights.

HE charges were situated in the geometrical centers of corresponding blast-protective devices. So the blast wave overpressures and pressure impulses registered in the field tests were compared not only with ground blast results but also with the blasts of the HE charges of the same weights heightened on the corresponding distance above the steel plate.

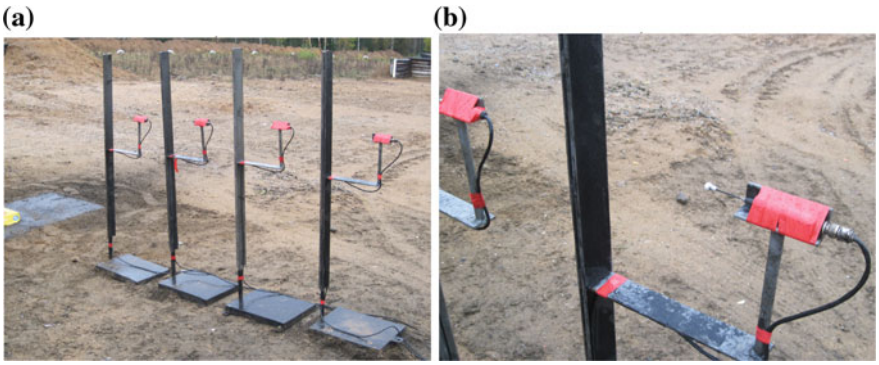

Fig. 6 **a** One row, composed of four pressure transducers mounted at steel plate and protected by vertical steel corner beam; **b** pressure transducers, its sensitive element (white one), and steel protecting beam ahead of it

3 Experimental Results

3.1 Small HE Charges

The results of the first series of field tests (with smaller TNT charges, which weights are equal to 0,2 kg here) are shown in Fig. 7. The reference results achieved for open blasts (curve 1) corresponds to well-known empirical formula and reference data [13–15] with the error not more than 10%. The experimental data for correspondingly heightened blasts (curve 2) can also be easily checked. The following conclusions about the blast wave pressure variation due to blast-resistant can application can be made:

1. The smallest efficiency of blast wave suppression corresponds to basic modification of the can (without any multiphase insertions). Overpressure was diminished in 1,2–1,5 times (see curve 3). Results for blast wave pressure impulse measurements and calculations (Table 2) are a little better but far from satisfactory.

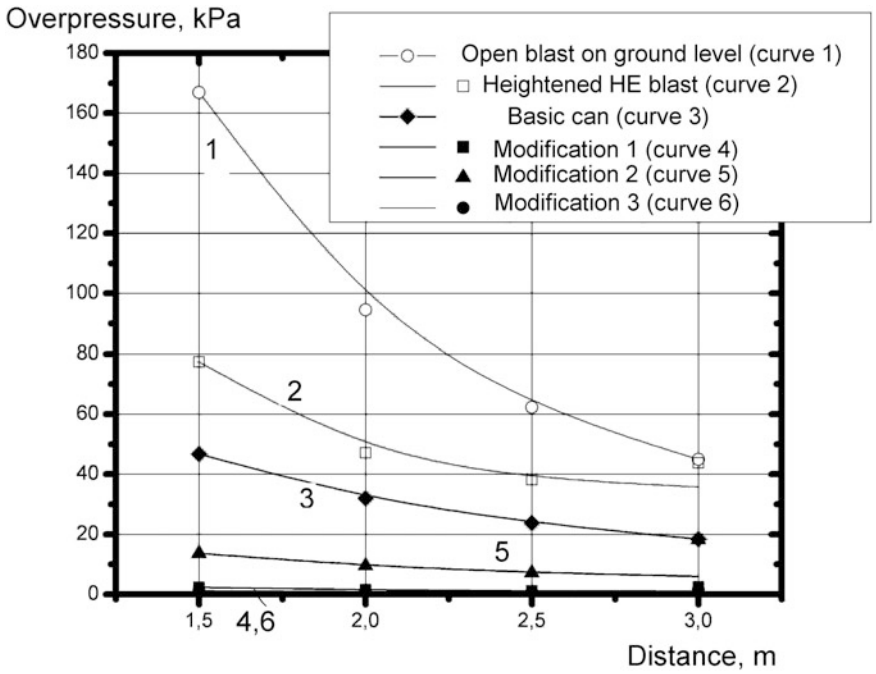

Fig. 7 Overpressure data for various blast-protective modification devices at 0,2 kg TNT charge explosion

This conclusion also corresponds to the numerical study [1] of solid cylindrical bins with open top which seems to be noneffective for blast wave mitigation even if their length is rather large.

2. At modification 1 (Fig. 1b), the blast wave overpressure diminishes in 19–33 times comparing with the open blast and in 8–20 times comparing with the initial prototype (i.e., exclusively due to multiphase insertion in its higher position). The results achieved allow us to say about the full suppression of blast energy of rather small HE charge (see curve 4 in Fig. 7).
3. The lower position of multiphase insertion (as in Fig. 1c) diminishes the blast wave overpressure in 3–5 times comparing with the open blast and in 2,5–4 times comparing with the blast inside the initial prototype (curve 5 in Fig. 7). The results achieved for the bin with multiphase insertion situated lower than the HE charge seem to be nontrivial and compel us to think about the role of blast waves reflected from can bottom, possibilities of its reduction, and its influence on blast wave amplitude at the distances important for blast-protecting devices.
4. The largest effect of blast wave overpressure diminishing (curve 6 in Fig. 7) was achieved in the third prototype (Fig. 1d) due to contemporary application of multiphase insertions in its upper and lower positions. The decrease of overpressure in 40–50 times means, in fact, the full suppression of mechanical action of HE blast.

Data achieved at blast overpressure and pressure impulse experiments with small HE charges are summarized in Tables 1 (overpressures) and 2 (pressure impulses). Pressure impulse decrease due to multiphase insertions seems to be enormous at the distance of 1,5–2,5 m and smaller but satisfactory at 3 m distance.

Table 1 Overpressure suppression factors at 0,2 kg TNT blast

Distance, m	Overpressure decrease rate			
	Basic can (Fig. 1a)	Modification 1 (Fig. 1b)	Modification 2 (Fig. 1c)	Modification 3 (Fig. 1d)
1,5	3,57	71,8	12,2	132
2	2,95	58,7	9,94	100
2,5	2,61	52,3	8,63	81,3
3	2,44	18,2	2,45	27,9

Table 2 Pressure impulse suppression factors at 0,2 kg TNT blast

Distance, m	Pressure impulse decrease rate			
	Basic can (Fig. 1a)	Modification 1 (Fig. 1b)	Modification 2 (Fig. 1c)	Modification 3 (Fig. 1d)
1,5	3,40	98,0	9,75	153
2	3,05	113	8,48	149
2,5	3,09	127	8,50	192
3	3,06	35,1	2,62	63,7

3.2 *Larger HE Charges*

Encouraged with the great success with small HE charge (see [16]), we decided to conduct field tests of the blast-protective bin prototypes using multiphase insertions in its lower position and special flanges at the top of the device as shown in Fig. 3. Blasts of HE charge weights of 0,5 and 0,8 kg were provided. Data on 0,5 kg TNT charge blast wave overpressure and impulse pressure reduction are summarized in Tables 3 and 4, correspondingly. Both multiphase media lower insertion and multiphase media flange increase the overpressure and pressure impulse suppression factors. But their influence is not so radical as for 0,2 kg TNT charges, maybe because the influence of shock wave reflected from the bottom of the bin is not so sufficient now. In fact, the rates of overpressure and pressure impulse decrease differ rather slightly between various prototypes of blast-protecting device. At least, it is a reason to think a little more about blast wave dynamics, including the influence of the shock reflected from the surface at the heightened blast on the general characteristics of blast wave at some distance from the blast epicenter.

The bandage made of ballistic clothes (Fig. 3f) increased the structural resistance of the object and allowed us to perform the field tests with 0,8 kg and, in general, with 1,0 kg TNT charge. The results achieved in these series of experiments are analogous to results achieved with 0,5 kg TNT charge.

Table 3 Overpressure suppression factors at 0,5 kg TNT blast

Distance, m	Overpressure decrease rate				
	Basic can (Fig. 3a)	Modification 1 (Fig. 3b)	Modification 2 (Fig. 3c)	Modification 3 (Fig. 3d)	Modification 4 (Fig. 3e)
1,5	3,64	3,92	4,00	5,90	6,11
2	4,54	4,92	5,40	5,96	6,66
2,5	3,07	3,26	3,37	3,71	3,82
3	2,81	3,23	3,31	3,57	3,59

Table 4 Pressure impulse suppression factors at 0,5 kg TNT blast

Distance, m	Pressure impulse decrease rate				
	Basic can (Fig. 3a)	Modification 1 (Fig. 3b)	Modification 2 (Fig. 3c)	Modification 3 (Fig. 3d)	Modification 4 (Fig. 3e)
1,5	3,25	3,62	3,51	4,69	4,29
2	4,05	4,17	4,51	5,25	5,17
2,5	2,59	2,64	2,41	3,45	3,27
3	3,15	2,99	2,73	3,46	3,54

4 Conclusions

Field tests of new cylindrical blast-inhibiting bin prototypes have revealed a significant reduction of shock blast wave parameters due to embeddings with the multiphase system located both on the top and on the bottom of a small charge (0,2–0,4 kg TNT). Reduction of blast effects parameters due to multiphase working system located inside a blast bin below a charge is rather a nontrivial result. While the use of the blast-inhibiting bin prototype of a basic modification (Fig. 1a) showed 2,5–3,5 times reduction of the blast overpressure and 3,0-3,4 times reduction of the impulse, the combined blast inhibitor showed 8,5–12,2 and 8,5–9,8 times reduction of those parameters, respectively.

The excellent results achieved with small HE charges were not confirmed by the field tests where the larger HE charges (0,5 kg and more) were used. The influence of the multiphase elements situated below the charge is much smaller at rather large HE charge weights. It seems that a deep penetration in shock wave reflection and interaction theory is necessary to explain a great difference between two examples described.

Acknowledgements The authors are grateful to Lieutenant-Colonel Yuri Frolenkov, Dr. Nikolay Vasilyev, Dr. Valery Dmitriev, Fedor Kompan, and other participants of the experiments.

References

1. Gelfand, B.E., Silnikov, M.V., Chernyshov, M.V.: On the efficiency of semi-closed blast inhibitors. Shock Waves **20**, 317–321 (2010)
2. Vasil'ev Yu, S., Gelfand, B.E., Silnikov, M.V.: Impulse-energy technologies assisted with mitigation systems. Izv. Akad. Nauk Energ. **6**, 7–19 (2004)
3. Silnikov, M.V., Mikhaylin, A.I.: Protection of flying vehicles against blast loads. Acta Astronaut. **97**, 30–37 (2014)
4. Igra, O., Falkovitz, J., Houas, L., Jourdan, G.: Review of methods to attenuate shock/blast waves. Prog. Aerosp. Sci. **58**, 1–35 (2013)
5. Ohtomo, F., Ohtani, K., Takayama, K.: Attenuation of shock waves propagating over arrayed baffles. Shock Waves **14**, 379–390 (2005)
6. Kitagawa, K., Yasuhara, M., Takayama, K.: Attenuation of shock waves propagating in polyurethane foams. Shock Waves **15**, 437–445 (2006)
7. Silnikov, M.V., Chernyshov, M.V., Mikhaylin, A.I.: Blast wave parameters at diminished ambient pressure. Acta Astronaut. **109**, 235–240 (2015)
8. Gelfand, B.E., Silnikov, M.V., Mikhaylin, A.I., Chernyshov, M.V.: Special devices "Fountain" for HE blast protection. In: IWSRIB 2009 CD Proceedings, Haifa, Israel (2009)
9. Gelfand, B.E., Gubanov, A.V., Timofeev, E.I.: Interaction of shock wave in air with a porous screen. Fluid Dyn. **18**(4), 561–566 (1983)
10. Gvozdeva, L.G., Faresov, YuM, Fokeev, V.P.: Interaction of air shock wave with porous compressible materials. J. Appl. Mech. Tech. Phys. **26**(3), 401–405 (1985)
11. Vasilyev, N.N., Danilov, N.A., Dmitriev, V.Y., Spivak, A.I., Shishkin, V.N.: Experimental checkup of protective elements influence on the registered parameters of air shock wave, Problems of Defense Engineering. Ser. 16. Technical Means of Counter-Terrorism, No. 1–2, 87–92 (2015)

12. Medvedev, S.P., Tyrnov, E.P., Khomik, S.V., Gelfand, B.E., Silnikov, M.V., Mikhaylin, A.I: Restoring of blast wave after interaction with detached obstacle. In: Proceedings of the 27th International Symposium on Shock Waves. St. Petersburg, Poster presentation 30138, p. 386 (2009)
13. Baker, W.E.: Explosions in Air. University Texas, Austin (1973)
14. Gelfand, B.E., Silnikov, M.V.: Barothermal Action of Blasts. Asterion, St. Petersburg (2006)
15. Gelfand, B.E., Silnikov, M.V.: Shock-wave Action of Blasts. Asterion, St. Petersburg (2007)
16. Takayama, K., Silnikov, M.V., Chernyshov, M.V.: Experimental study of blast mitigating devices based on combined construction. Acta Astronaut. **126**, 541–545 (2016)

Overexpanded Jet Flow Type of Symmetry Influence on the Differential Characteristics of Flowfield in the Compressed Layer

M. V. Silnikov and M. V. Chernyshov

Abstract The evolution of the incident shock in the plane overexpanded jet flow or in the axisymmetric one is analyzed theoretically at the whole range of governing flow parameters. Analytical results can be applied to avoid jet flow instability and self-oscillation effects at rocket launch, to improve launch safety and to suppress shock wave-induced noise harmful to environment and personnel.

1 Introduction

The rocket launch safety is dependent on overexpanded jet behavior and its interaction with the environment. Formation of longitudinal instability and self-oscillations contribute to generating shock wave noise. This paper presents results of theoretical analysis of the overexpanded supersonic jet flow. Some special features of this flow in the vicinity of the nozzle lip were studied, and theoretical relations describing them were derived analytically. Flow vorticity extreme values and its direction shift, as well as extreme and zero values of full and static pressure gradients, shock strength variation in the compressed layer just behind the incident shock were also described analytically.

A brief analysis of the outnumbered differential characteristics of the plane jet flow was partially presented in [1], and analysis of the incident shock geometrical curvature variation in axisymmetric jet contains in [2]. The present paper is the first attempt of full parametric and comparative analysis of the shock evolution in the vicinity of the plane nozzle edge and the axisymmetric one. So, shock curvature,

M. V. Silnikov · M. V. Chernyshov (✉)
Peter the Great Saint Petersburg Polytechnic University,
29 Politekhnicheskaya Str., 195251 Saint Petersburg, Russia
e-mail: mvcher@mail.ru

M. V. Silnikov · M. V. Chernyshov
Special Materials Corp., 28A Bolshoy Sampsonievsky Ave.,
194044 Saint Petersburg, Russia

K. Kontis (ed.), *Shock Wave Interactions*,
https://doi.org/10.1007/978-3-319-73180-3_4

its strength variation, vorticity of the flowfield downstream it, as well as static pressure variation are studied theoretically.

Research presented here becomes possible due to the differential conditions of dynamic compatibility [3] that connect not only flow parameters ("zero-order problem") but also their spatial derivatives ("first-order problem") at both sides of any strong or weak discontinuity, e.g., on the oblique or normal curved shock in nonuniform flow. The system of equations adopted here to connect the flow derivatives is certainly not alone (see, for example [4–6] and survey of these and other models in [7, 8]). But it seems to be most convenient because the basic parameters describing the shock are the most appropriate for application in supersonic aerodynamics (flow deflection angle β) and in gas jet problems (shock strength J that corresponds to jet incalculability).

The study performed in this paper is purely analytical and based on exact zero- and first-order relation at the stationary shock. The well-known method of characteristics, second-order accuracy, was used only to check the analytical results and to avoid any technical errors.

2 Jet Flow Layout and Governing Relations

2.1 Basic ("Zero-Order") Shock Relations

The incident shock AT (Fig. 1a–c) that falls from the nozzle edge A into the overexpanded jet of the inviscid perfect gas can be characterized [3, 9–11] by its strength $J = p_n/p_a$. Here, p_n is the ambient pressure, and p_a is the jet static pressure upstream the shock. The inverse ratio $n = p_a/p_n = 1/J$ is jet incalculability ($n < 1$ in an overexpanded jet flow, and $n = 1$ is correctly expanded one).

At any given flow Mach number M, shock strength belongs to the range $1 < J \le J_m$. The limit $J \to 1$ corresponds to shock degeneration into weak discontinuity, $J_m = (1+\varepsilon)M^2 - \varepsilon$ is the strength of the normal shock, $\varepsilon = (\gamma-1)/(\gamma+1)$, and γ is the ratio of the gas specific heats. At all examples of calculations shown at further, we accept that $\gamma = 1.4$, but the analytical relations are fit for all physically admissible values of γ.

The relation

$$J = (1+\varepsilon)M^2 \sin^2\sigma - \varepsilon \tag{1}$$

(σ is the angle of shock inclination to the streamlines before it) connects the shock strength with its shape.

Mach number M_2 of the flow behind the shock depends on its strength as follows [1, 2]:

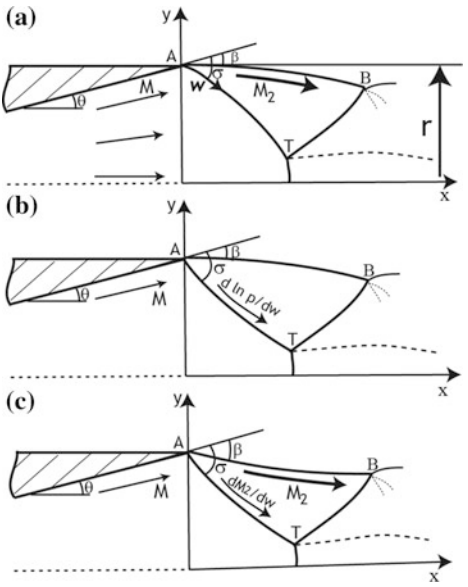

Fig. 1 Flow schematic of the initial segment of an overexpanded gas jet: **a** traditional "barrel" shape of both initial shock and jet boundary; **b** positive curvature of the incident shock; and **c** positive curvature of both initial shock and jet boundary

$$M_2 = \sqrt{\frac{(J+\varepsilon)M^2 - (1-\varepsilon)(J^2-1)}{J(1+\varepsilon J)}}. \tag{2}$$

Flow deflection angle β at the oblique shock depends on the shock strength and the Mach number upstream it:

$$\beta = \arctan\left[\sqrt{\frac{J_m - J}{J+\varepsilon}}\,\frac{(1-\varepsilon)(J-1)}{(1+\varepsilon)M^2 - (1-\varepsilon)(J-1)}\right]. \tag{3}$$

2.2 *Basic Nonuniformities of Ideal Gas Flow*

According to [3, 11–13], the gradients of the numerous parameters of plane or axisymmetric homenergic ideal inviscid gas flowfield can be determined by so-called basic nonuniformities N_i ($i = 1 \ldots 3$). These basic nonuniformities can be introduced into gas flow equations in natural (s, n) coordinates:

$$\frac{M^2-1}{\gamma M^2}N_1 + \frac{\partial\theta}{\partial n} + N_4 \sin\theta = 0, \quad \gamma M^2 N_2 = -\partial \ln p/\partial n, \quad \partial p_0/\partial s = 0\,. \tag{4}$$

The first value ($N_1 = \partial \ln p/\partial s$) characterizes flow non-isobaricity, the second one ($N_2 = \partial\theta/\partial s$) is the geometrical curvature of the streamlines, and the third one ($N_3 = \partial \ln p_0/\partial n$) can characterize the isoenergetic flow vorticity due to Crocco

relation. Here, p is flow static pressure, p_0 is the stagnation pressure, and θ is streamline inclination angle to the axis or plane of symmetry. For the jet flow problem considered here, flow angle θ coincides with nozzle throat half-angle.

2.3 *Differential ("First-Order") Conditions at the Curved Shock in Nonuniform Flow*

Basic nonuniformities of the flowfield on both sides of the shock are mutually dependent according to the differential conditions of the dynamic compatibility written in [3, 7] in the following manner:

$$\widetilde{N}_i = C_i \sum_{j=1}^{5} A_{ij} N_j. \tag{5}$$

Here, C_i and A_{ij} are corresponding influence coefficients (term from [14]), $\widetilde{N}_i$ ($i = 1 \ldots 3$) are flow nonuniformities downstream the shock (in the compressed layer of an overexpanded jet, for example), N_j ($j = 1 \ldots 3$) are the corresponding nonuniformities upstream the shock, $N_4 = \delta / y$ is symmetry factor ($\delta = 0$ in plane flow, $\delta = 1$ in axisymmetric one, and y is the distance from symmetry plane or axis), $N_5 \equiv K_\sigma$ is the geometrical curvature of the shock, and $\chi = \pm 1$ is direction of the shock incidence ($\chi = -1$ at the considered problem, as flow turns clockwise at the shock AT).

The differential conditions (5) were successfully applied earlier to the analysis of the differential characteristics of Prandtl–Meyer expansion of compression flowfield [12], overtaking [11] or counter [13] Prandtl–Meyer flow—oblique shock interaction.

2.4 *Special Shock Strengths. Crocco Point and Constant Pressure (Thomas) Point*

According to the correlation (2) between Mach numbers, the special ("critical") shock strength $J_*(M)$ corresponds to the critical flow velocity downstream the shock ($M_2 = 1$). The maximal flow deflection angle at the oblique shock at the fixed values of M and γ corresponds to the shock strength $J_l(M)$. This value corresponds to the condition $\partial\beta / \partial J = 0$ in (3); it traditionally divides "strong" and "weak" branches of the shock polars. Shock strength

$$J_\Gamma = M^2 - 1 \tag{6}$$

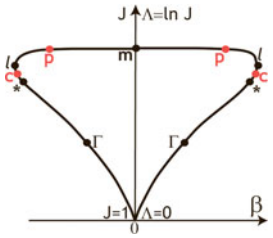

Fig. 2 Special shock strengths at typical shock polar ($M > \sqrt{2}$)

can be realized at $M > \sqrt{2}$. It corresponds to the maximum flow deflection angle among all shocks with the fixed values of J and γ and the different Mach numbers M upstream them (so-called envelope line of the shock polars family, Fig. 2). It is determined by the condition $\partial\beta/\partial M = 0$ applied to Eq. (3).

The condition $A_{15} = 0$ in the differential conditions (5) determines shock strength J_p which is the only one at any shock polar (Fig. 2). At this shock strength, shock geometrical curvature does not influence the local value of flowfield non-isobaricity downstream. Therefore, shock strength J_p corresponds to so-called constant pressure point [1, 3] (or Thomas point [14]). Local flow non-isobaricity behind the curved shock with the strength J_p formed in the uniform flow is always equal to zero. Shock strength J_p can be easily calculated:

$$J_p = \left[3(1+\varepsilon)M^2 - 2(1+3\varepsilon) + (1+\varepsilon)\sqrt{9M^4 + 16\varepsilon M^2 + 16(1-\varepsilon)}\right] \Big/ [2(3+\varepsilon)]. \tag{7}$$

The equation $A_{25} = 0$ in (5) determines the strength J_c of the shock whose curvature does not influence the curvature of the streamlines behind it. This shock strength corresponds to so-called Crocco point. The strength J_c is also the only value at any shock polar. Streamline curvature behind the curved shock, which occurs at the uniform flow downstream and corresponds to the Crocco point, is equivalent to zero. The simplest formula to determine the Crocco point is the inverse relation:

$$M = \sqrt{\frac{(1+3\varepsilon)J_c^3 + 4(1+\varepsilon)J_c^2 + (1-\varepsilon+4\varepsilon^2)J_c - 2(1-\varepsilon)}{(1+3\varepsilon)J_c^2 + (3+3\varepsilon+4\varepsilon^2)J_c + 2\varepsilon}}. \tag{8}$$

At given values of Mach number upstream and gas specific heats ratio, the outnumbered special strengths of the stationary shocks satisfy the inequality $1 < J_* < J_c < J_l < J_p < J_m$ (at $M < \sqrt{2}$), or $1 < J_\Gamma < J_* < J_c < J_l < J_p < J_m$ (at $M > \sqrt{2}$). The corresponding values of jet incalculability, which are inverse to the shock strengths, are shown in Fig. 3.

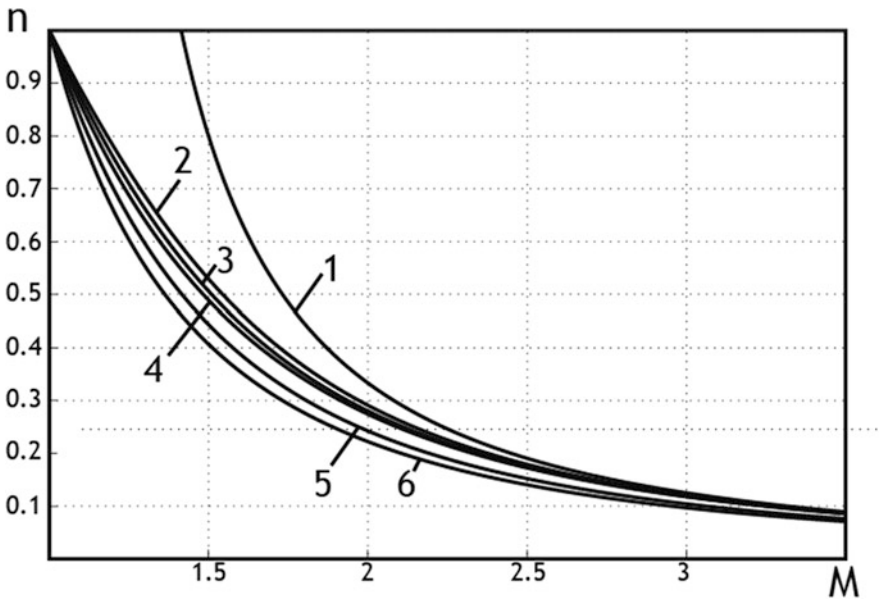

Fig. 3 Jet incalculabilities that correspond to the special values of incident shock strength

2.5 Application of the Differential Conditions at the Curved Shock in Nonuniform Stream to Jet Flow Analysis

The isobaricity condition ($\widetilde{N}_1 = 0$) at the jet boundary AB allows us to determine the geometrical curvature of the incident shock AT:

$$K_\sigma = -\sum_{j=1}^{4} A_{1j} N_j / A_{15}, \tag{9}$$

and, also, for example, the geometrical curvature of the jet boundary ($\widetilde{N}_2 \equiv K_\tau$):

$$K_\tau = C_2 \cdot \sum_{j=1}^{4} \left(A_{2j} A_{15} - A_{1j} A_{25}\right) N_j / A_{15}, \tag{10}$$

as well as the stagnation pressure variation:

$$\widetilde{N}_3 = C_3 \cdot \sum_{j=1}^{4} \left(A_{3j} A_{15} - A_{1j} A_{35}\right) N_j / A_{15}. \tag{11}$$

Taking into account the shock relations (1–3), we can calculate and analyze also the derivatives of shock strength (dJ/dw) and other flow parameters (such as static

pressure, entropy, and Mach number) in the direction w (see Fig. 1a) of incident shock, if only the corresponding jet flow parameters upstream the shock are known.

Well-applicable model of flow out of the conical nozzle or, in particular, the nozzle with the uniform stream at the exit section, is known as the model of the supersonic flow out of the cylindrical or conical source. The following relations for the nonuniformities at point A just before the shock are correct there:

$$N_1 = -[(1+\delta)\gamma M^2 \sin\theta]/[(M^2-1)r], \quad N_2 = N_3 = 0, \quad N_4 = \delta/r \tag{12}$$

Here, r is half-width (in plane case), or the radius (in axisymmetric one) of the nozzle exit section. When this model of flow before the shock is accepted in (5), the curvatures $\bar{K}_\sigma$ and $\bar{K}_\tau$, as well as other differential parameters of the shock and the flow downstream it, occur to be the function of four governing parameters (M, $J = 1/n$, γ and θ).

The analysis of the basic differential characteristics of overexpanded jet flowfield is to be conducted at further using the relations (5) and the model (12). It is provided at the whole theoretically possible range of the governing parameters ($M > 1$, $1 < J \le J_m$, $\gamma > 1$, $0 \le \theta \le 90°$). The key parameter of the problem (shock curvature K_σ) is analyzed and discussed in [2]. For text brevity, only variation of the shock strength (dJ/dw), full and static pressures behind the shock are discussed here. The real implementation of the symmetric supersonic non-separated jet flow in practice depends on the specific features of the technical devices and processes in each separate case.

3 Results and Discussion

3.1 *Flow Vorticity Rate (Stagnation Pressure Gradient) in the Vicinity of the Nozzle Lip*

According to Crocco relation between vorticity and entropy, the basic nonuniformity $\widetilde{N}_3 = \partial \ln p_0/\partial n$ presents vorticity rate in the compressed layer. Vorticity rate variation analysis is based on the relations (9) and (11) as well as on the analysis of incident shock curvature variation provided in [2].

3.1.1 Plane Jet

Dependence of the dimensionless vorticity rate $N_3^- = r\widetilde{N}_3/\sin\theta$ on jet incalculability is determined, in general, by flow Mach number. Stagnation pressure gradient $N_3^-(J)$ is negative and decreases monotonously in the whole range $(1; J_p)$ at $M < \sqrt{2}$ (Fig. 4a). Starting from the point $J = 1$ at $M = \sqrt{2}$, positive interval of the function $N_3^-(J)$ with the point of its maximum arises (Fig. 5b). Positive values of

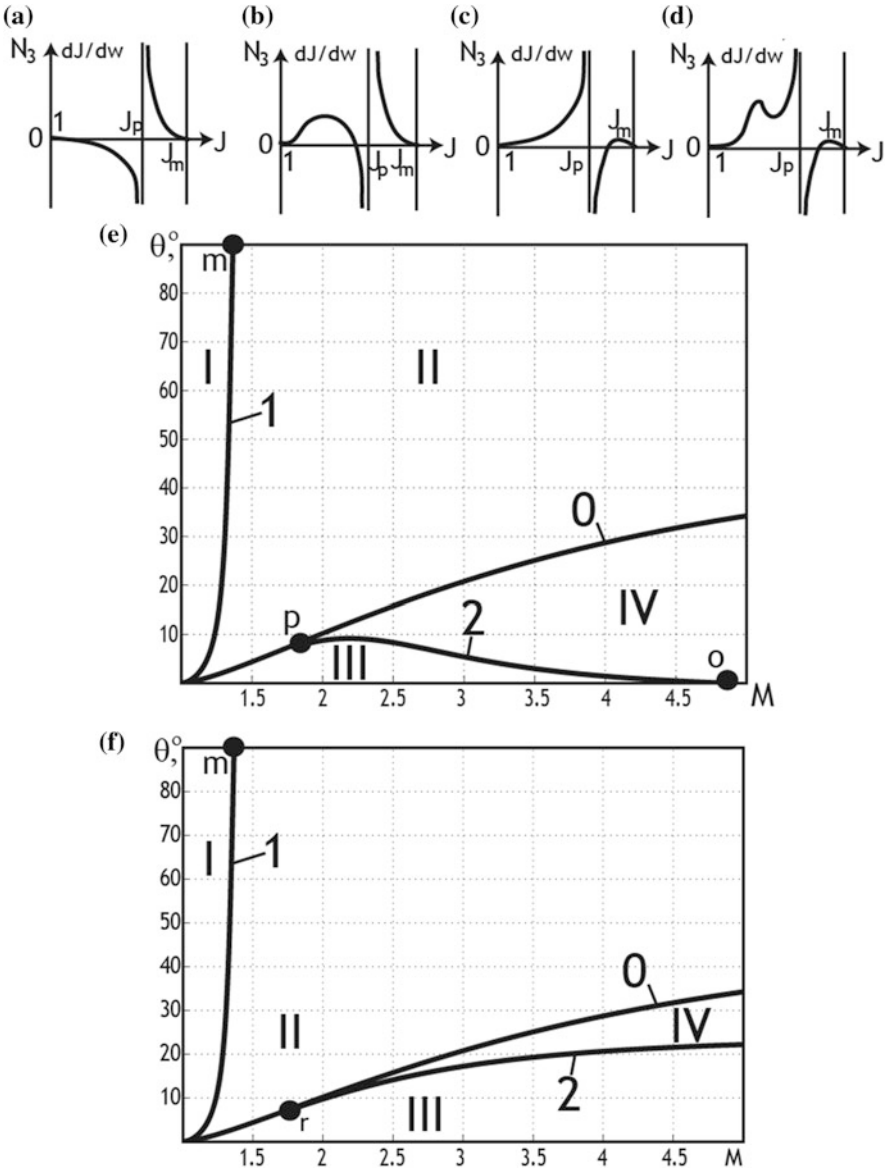

Fig. 4 Variation in flow vorticity rate (N_3) in the compressed layer and local variation in shock strength (dJ/dw): **a** plane jet, $M < \sqrt{2}$; axisymmetric one, zone I; **b** plane, $M > \sqrt{2}$; axisymmetric, zone II; **c** axisymmetric, zone III; **d** axisymmetric, zone IV; **e** zones of axisymmetric jet flow parameters with different variations in the function N_3; and **f** regions with different variations in the shock strength

$N_3^-(J)$ correspond to the traditionally considered strengthening of the shock that falls to symmetry plane or axis. Negative values of the function N_3^- are usually typical at small Mach numbers. Von Neumann paradox and absence of solutions for stationary Mach configurations are typical at those flow velocities. Therefore, local weakening of the incident shock ascertained here can be of interest for the problem of the subsequent incidence and reflection of the shock.

The right border of the interval of shock strengthening at $M > \sqrt{2}$ corresponds to the shock polars envelope line strength ($J_\Gamma = M^2 - 1$, see Eq. 6). Flow is always supersonic downstream such shocks.

Flow vorticity in the compressed layer of the axisymmetric jet is described using the dimensionless function $\bar{N}_3 = r\widetilde{N}_3$. As well as the dimensionless geometrical curvature of the shock, this vorticity rate function in axisymmetric flow behaves similar to the plane jet case at large nozzle angles and differs much from the plane case at small or zero nozzle throat angles.

3.1.2 Axisymmetric Jet

Dependence of plane flow vorticity rate on jet incalculability shown in Fig. 5a, b is typical for the regions I and II of the axisymmetric jet parameters (see Fig. 4e). Curve 1 in Fig. 4e corresponds to the appearance of the weak shocks strengthening near the nozzle lip. Unlike in the plane jet case, curve 1 corresponds to the relation

$$\tan\theta = -\frac{(1-\varepsilon)(M^2-1)^{3/2}}{(1+3\varepsilon)M^4 + 2(1-5\varepsilon)M^2 - 7(1-\varepsilon)}, \tag{13}$$

and it has no direct association with Mach number $M = \sqrt{2}$ and the envelope line (6) of shock polars family. Curve 1 ends at $\theta = 90°$ and at the following Mach number:

$$M_m = \sqrt{\frac{2\sqrt{2+\varepsilon+\varepsilon^2} - 1 + 5\varepsilon}{1+3\varepsilon}} = 1.365.$$

Change in the shock curvature infinite discontinuity direction that takes place at the curve 0 described by

$$\tan\theta = -\frac{(1-\varepsilon)\left((3+\varepsilon)J_p + 2 + 4\varepsilon\right)\left(J_p - 1\right)^{3/2}\sqrt{\left(1+\varepsilon J_p\right)\left(3J_p + 1 + 4\varepsilon\right)}}{\sqrt{J_p + \varepsilon}\left[(3+\varepsilon)(9\varepsilon - 1)J_p^3 + (28 + 34\varepsilon + 82\varepsilon^2 + 16\varepsilon^3)J_p^2 + cJ_p + d\right]} \tag{14}$$

leads to the corresponding change of the vorticity rate and other differential characteristics of the flowfield. The variation in flow vorticity rate in the regions III and

IV of axisymmetric jet parameters has no analogies in the plane jet flow. Zone III corresponds to the monotonous increase in the function $\bar{N}_3(J)$ in the whole interval $\left(1; J_p\right)$, see Fig. 4c. New points of local extrema (see Fig. 4d) which arise at the curve 2 (Fig. 4e) from the points of this function inflection exist in region IV of the axisymmetric flow parameters. Curve 2 starts at $M_n = 1.809$ and $\theta_n = 7.967°$; inflection point of the function $\bar{N}_3(J)$ strives to $J = J_p(M_n) = 3.338$ at these parameters.

Curve 2 finishes at $M_o = 4.849$ and $\theta_o = 0$; shock strength $J_o = 18.870$ determines the inflection point at these parameters of axisymmetric jet.

3.2 Incident Shock Strength Variation

The variation in shock strength J in the vicinity of the nozzle lip is characterized here using the dimensionless functions $W_J^- = r \cdot (dJ/dw)/\sin\theta$ in plane flow, and $\bar{W}_J = r \cdot (dJ/dw)$ in axisymmetric one. Here, w is the direction of shock incidence.

It is known that the relation I of stagnation pressures at both sides of the shock is monotonous function of the shock strength J:

$$I = \left(J\Omega^{\gamma}\right)^{-(1-\varepsilon)/2\varepsilon} \tag{15}$$

Here, $\Omega = (1+\varepsilon J)/(J+\varepsilon)$ is the ratio of the specific volumes according to Hugoniot adiabat.

The relation (12) that describes the flow upstream the shock, and formulas (1–3), (15) allow us to derive the mutual dependence between shock strength variation and vorticity rate function:

$$\frac{dJ}{dw} = \frac{2J(J+\varepsilon)(1+\varepsilon J)^2}{(1-\varepsilon)(J-1)^2\sqrt{(J_m-J)(J+\varepsilon)+(1+\varepsilon J)^2}} \cdot \widetilde{N}_3, \tag{16}$$

as well as between the analogous dimensionless functions.

3.2.1 Plane Jet

It is evident from (16) that positive, negative and zero values of the derivatives W_J^- and $\bar{W}_J$ are realized at the same flow parameters as the analogous values of vorticity functions N_3^- and $\bar{N}_3$ (in the plane flow and in the axisymmetric one, correspondingly). In particular, the variations in the function $W_J^-(J)$ at $M < \sqrt{2}$ and $M > \sqrt{2}$ are analogous to those depicted in Fig. 4a, b.

3.2.2 Axisymmetric Jet

Flow parameters zones with different shock strength variation in axisymmetric flow are shown in Fig. 4f. Shock strength variation at large throat angle corresponds much to the plane case:

(1) shock strength decrease at the whole interval $(1; J_p)$ (Fig. 4a) in zone I of the flow parameters;
(2) curve 1 that serves as border between regions I and II; and
(3) possibility of shock strength growth (Fig. 4b) in zone II.

The direction of the discontinuity of the function $\bar{W}_J(J)$ changes at the curve 0 (14) which is a border between large and small nozzle throat angles. At the regions III and IV (Fig. 4f) of small nozzle angles, function $\bar{W}_J(J)$ is positive at the whole interval $(1; J_p)$. It varies monotonously (in region III, see also Fig. 4c) or non-monotonously (in region IV, see also Fig. 4d) at this interval of incalculabilities. Border 3 of the zones III and IV in Fig. 4f starts at the point r ($M_r = 1.776$, $\theta_r = 7.582°$, $J_r = J_p(M_r) = 3.212$); it has horizontal asymptote at large Mach numbers.

Thus, incident shock strengthens in the vicinity of the nozzle lip at the small throat angle of the axisymmetric nozzle, and vorticity rate downstream it increases. In the event that nozzle throat angle is large enough, local decrease in shock strength and flow vorticity exists as a rule at small Mach numbers, and local increase in these parameters exists at moderate and large Mach numbers. The variation in these parameters at large throat angles of the axisymmetric nozzle generally repeats the case of plane flow, but their variation at small axisymmetric nozzle angles has no analogies in plane jet.

3.3 Static Pressure Variation in the Compressed Layer

Since the transversal gradient of the static pressure is also estimated as one of the parameters determining the development of Görtler vortices, it also seems to be the value deserving of parametrical analysis.

Two basic factors influence static pressure variation behind the shock that falls from the nozzle lip. They are pressure decrease before the shock and shock strength variation analyzed in Sect. 3.2. These factors act in the contrary directions if the incident shock strength increases ($dJ/dw > 0$). At the incident shock weakening ($dJ/dw < 0$), these factors are codirected, and they both lead to static pressure decrease after the shock along the trajectory of its incidence.

Static pressure variation downstream the shock is characterized by dimensionless derivatives $P_w^- = (r/\sin\theta) \cdot (d \ln p/dw)$ and $\bar{P}_w = r \cdot (d \ln p/dw)$ introduced for plane flow and axisymmetric one, correspondingly.

3.3.1 Plane Jet

The variations in the dimensionless pressure derivative $P_w^-(J)$ at the plane jet are shown in Fig. 5a–c. Monotonous decrease in the function $P_w^-(J)$ at the interval $(1; J_p)$ of practical importance (Fig. 5a) changes to local minimum presence (Fig. 5b) at Mach number

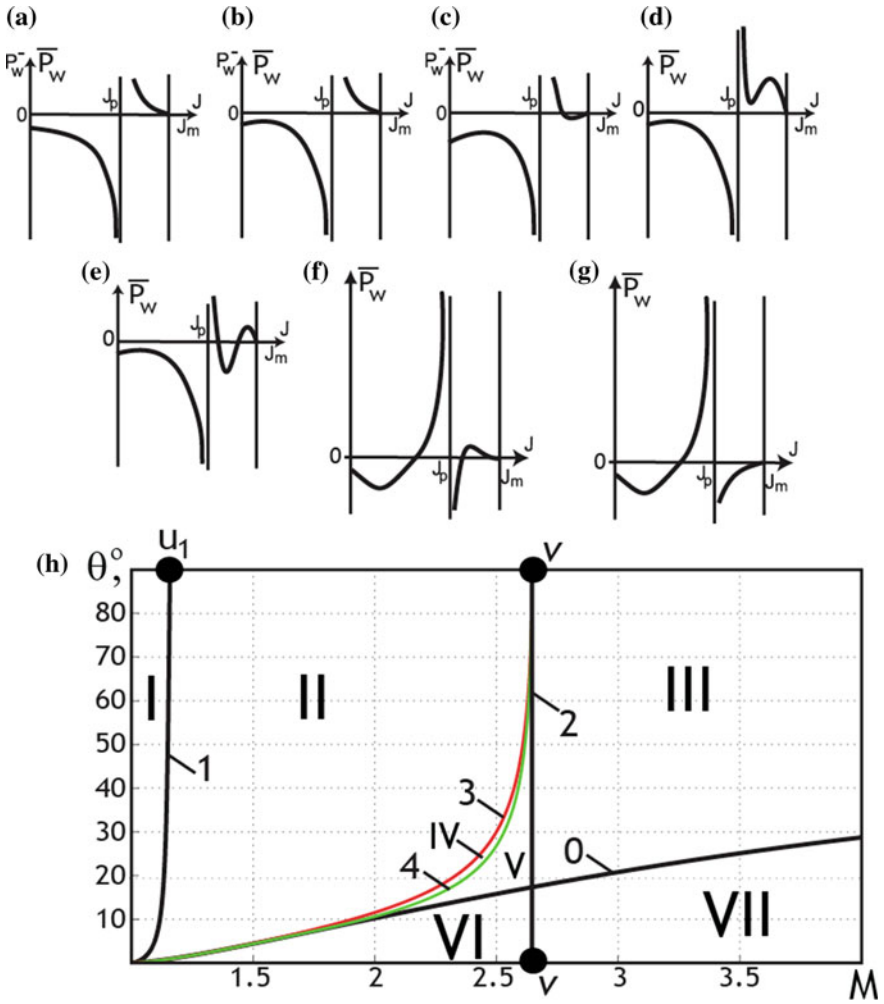

Fig. 5 Static pressure derivatives in the compressed layer behind the shock (functions $P_w^- = (r/\sin\theta)\cdot(d\ln p/dw)$ and $\bar{P}_w = r\cdot(d\ln p/dw)$ in plane jet and axisymmetric one, correspondingly): **a** plane jet, $M < M_u$; axisymmetric one, region I; **b** plane, $M_u < M < M_v$; axisymmetric, region II; **c** plane, $M > M_v$; axisymmetric, region III; **d** axisymmetric, region IV; **e** axisymmetric, region V; **f** axisymmetric, region VI; **g** axisymmetric, region VII; and **h** corresponding regions of the axisymmetric jet flow parameters

$$M_u = \sqrt{\frac{\sqrt{9-4\varepsilon+4\varepsilon^2}-3+6\varepsilon}{4\varepsilon}} = 1.166.$$

The only further change in the function plot is the appearance of the new local extreme (Fig. 5c) that arises at $M_v = \sqrt{(4-3\varepsilon)/(1-3\varepsilon)} = 2.646$ in the interval $(J_p; J_m)$ of a deep jet overexpansion.

The dimensional static pressure derivative behind the weak shock strives to the relation that is common for plane jet (at $\delta = 0$) and the axisymmetric one (at $\delta = 1$):

$$\lim_{J \to 1}\left(\frac{d\ln p}{dw}\right) = -\frac{(1+\delta)\gamma M \sin\theta}{r\sqrt{M^2-1}}.$$

This derivative is permanently equal to zero behind the normal shock (at $J \to J_m$) both for plane flow and axisymmetric one.

3.3.2 Axisymmetric Jet

Static pressure variation in the compressed layer of an axisymmetric jet is considered at the (M, θ)-plane of the flow parameters (Fig. 5h). Plot of the function $\bar{P}_w(J)$ at the regions I–III that correspond to large nozzle throat angles basically repeats the depicted one in Fig. 5a–c for various cases of the plane flow. The border 1 of the regions I and II where new maximum arises in the interval $(1; J_p)$ corresponds to the relation

$$\tan\theta = -\frac{(1-\varepsilon)(M^2-1)^{3/2}}{(1+3\varepsilon)M^4+2(2-5\varepsilon)M^2-7(1-\varepsilon)}.$$

It ends at Mach number

$$M_{u_1} = \sqrt{\frac{\sqrt{11-6\varepsilon+4\varepsilon^2}-2+5\varepsilon}{1+3\varepsilon}} = 1.158.$$

Instead of it, regions IV and V are present at the (M, θ)-plane that corresponds to two internal extrema of the function $\bar{P}_w(J)$ at the plot $(J_p; J_m)$, Fig. 5d, e. The vertical border 2 of the regions V and III, as well as VI and VII, with different variations in the function $\bar{P}_w(J)$ at the interval $(J_p; J_m)$ corresponds to the same Mach number $M_v = \sqrt{(4-3\varepsilon)/(1-3\varepsilon)} = 2.646$ as in the plane jet flow.

Values of the function $\bar{P}_w(J)$ are negative in the interval $(1; J_p)$ at all zones I–V situated above the curve 0 in Fig. 5h. It means that the static pressure just behind the incident shock decreases along its trajectory.

Change of the direction of the infinite discontinuity of the function $\bar{P}_w(J)$ at $J \to J_p$ occurs at the curve 0 determined by (14) and leads to the formation of the regions VI and VII. Values of the function $\bar{P}_w(J)$ are positive in the part of the interval $(1; J_p)$ at these regions. They are positive in this whole interval at $\theta = 0$. Consequently, at small axisymmetric nozzle throat angles the growth of the incident shock strength can exceed the flow expansion before the shock, and the static pressure behind the shock increases. There is no analogous increase in static pressure downstream the shocks of moderate strength in plane jet flow.

4 Conclusion

The dependencies of the geometrical curvature of the incident shocks, shock strength variation, and numerous differential characteristics of the flowfield in compressed layer on jet flow parameters are sufficiently different in plane and axisymmetric jets. The factor of axial symmetry is especially significant at small and moderate nozzle throat angles. It allows us to consider weakly or moderately overexpanded axisymmetric jets with characteristics that seem to be impossible in plane jet flows (for example, jets with positive curvature of its boundary or static pressure growth behind the incident shock).

Some considered features of the non-separated flow in the vicinity of the nozzle lip (for example, a possible change in incident shock convexity direction) are common for plane and axisymmetric jets. But their dependence on governing flow parameters is much more complex in axisymmetric jets. The parametric analysis allowed us to ascertain and to compare the conditions of incident shock and jet boundary convexity direction change, incident shock strength variation, and special features of some other flow parameters in the compressed layer depending on the type of symmetry of an overexpanded jet.

References

1. Uskov, V.N., Chernyshov, M.V.: Differential characteristics of the flow field in a plane overexpanded jet in the vicinity of the nozzle lip. J. Appl. Mech. Tech. Phys. **47**(3), 366–376 (2006)
2. Silnikov, M.V., Chernyshov, M.V., Uskov, V.N.: Two-dimensional over-expanded jet flow parameters in supersonic nozzle lip vicinity. Acta Astronaut. **97**, 38–41 (2014)
3. Adrianov, A.L., Starykh, A.L., Uskov, V.N.: Interference of Stationary Gasdynamic Discontinuities. Nauka, Novosibirsk (1995), in Russian
4. Brown, W.F.: The general consistence relations for shock waves. J. Math. Phys. **29**(4), 252–262 (1950)
5. Mölder, S., Timofeev, E., Emanuel, G.: Flow behind a concave hyperbolic shock. In: Kontis, K. (ed.) Proceedings of the 28th International Shock Waves Symposium, pp. 619–624. Springer, Berlin, London (2012)

6. Emanuel, G., Hekiri, H.: Vorticity and its rate of change just downstream of a curves shock. Shock Waves **17**(1–2), 85–94 (2007)
7. Uskov, V.N., Mostovykh, P.S.: The flow gradients in the vicinity of a shock wave for a thermodynamically imperfect gas. Shock Waves **26**(6) (2016)
8. Emanuel, G.: Shock Waves Dynamics: Derivatives and Related Topics. CRC Press, Boca Raton (2012)
9. Omel'chenko, A.V., Uskov, V.N.: Optimal shock-wave systems under constraints on the total flow turning angle. Fluid Dyn. **31**(4), 597–603 (1996)
10. Smirnov, N.N., Nikitin, V.F., Alyari Shurekhdeli, S.: Investigation of self-sustaining waves in metastable systems. J. Propul. Power **25**(3), 593–608 (2009)
11. Silnikov, M.V., Chernyshov, M.V., Uskov, V.N.: Analytical solutions for Prandtl-Meyer wave—oblique shock overtaking interaction. Acta Astronaut. **99**, 175–183 (2014)
12. Silnikov, M.V., Chernyshov, M.V.: The interaction of Prandtl-Meyer wave and quasi-one-dimensional flow region. Acta Astronaut. **109**, 248–253 (2015)
13. Meshkov, V.R., Omel'chenko, A.V., Uskov, V.N.: The interaction of shock wave with counter rarefaction wave. Vestnik Sankt-Peterburgskogo Universiteta. Ser. 1. Matematika Mekhanika Astronomiya. Issue 2, 101–109 (2002), (in Russian)
14. Mölder, S.: Curved shock theory. Shock Waves **26**(4), 337–353 (2016)

Shock Wave Interaction with a Solid Body Floating in the Air

M. Oshima, K. Nakayama and Y. Sakamura

Abstract A new shock tube system for the study of shock wave interaction with a solid body floating in the air has been developed. The system consists of a horizontally placed shock tube and a solid-body injecting device, which is mounted on the floor of the test section of the shock tube. A solid body initially placed on the shock tube floor was tossed into the air with the injecting device and then collided with a planar shock wave, which is generated by rapturing the diaphragm between the driver and the driven sections of the shock tube. By tuning the rapturing time of the diaphragm, we can make the shock wave interact with the solid body when it reaches the top of its trajectory almost at rest. In order to demonstrate the applicability of the present system, the shock-induced motion of a hexahedral solid body and the flow field around it were recorded using the shadowgraph technique coupled with a high-speed video camera. Representative results from the present experiments are reported in this paper.

1 Introduction

Shock-induced motion of a solid body in a gas flow has attracted significant interest because of its relevance for various engineering problems, including dispersion of inflammable dusts by shock waves [1], shock relaxation in dusty-gas flows [2], and risk assessment of flying debris generated during accidental explosions [3]. In order to obtain better understandings of these phenomena, several shock tube experiments have been conducted so far. Igra and Takayama [4], for example, studied the shock-induced motion of spherical solid particles initially placed on a shock tube floor

M. Oshima (✉) · K. Nakayama · Y. Sakamura
Department of Mechanical Systems Engineering, Toyama Prefectural University,
5180 Kurokawa , Imizu, Toyama 939-0398, Japan
e-mail: m-oshima@pu-toyama.ac.jp

K. Nakayama
e-mail: nak954@gmail.com

Y. Sakamura
e-mail: sakamura@pu-toyama.ac.jp

K. Kontis (ed.), *Shock Wave Interactions*,
https://doi.org/10.1007/978-3-319-73180-3_5

and measured the drag coefficients of the particles. Although the boundary layer developed along the shock tube wall was so thin that most of the tested particles were out of the boundary layer [4], it is possible that the friction between the floor and the particles might affect their initial motions. Jourdan et al. [5] conducted shock tube experiments with spherical particles suspended by a very thin wire (a spider's thread) from the shock tube ceiling to keep the particles away from the shock tube floor. Even though they successfully excluded the friction effect from the experiments, the wire stuck on the tested particles might alter the particles' motion. On the other hand, Suzuki et al. [6] performed another type of shock tube experiments, in which a solid particle was injected into the air just before the incident shock wave reached the particle, and thus succeeded in causing the interaction of a propagating shock wave with a solid body floating in the air without any supports. Since, however, the particle injecting device used in their work was developed only for the tested spherical particles, it could not apply to solid bodies of different geometry.

In the present work, we have developed a new shock tube system for the study of shock-induced motion of a solid body floating in the air. The present system is composed of a horizontally placed shock tube and a solid-body injecting device in the same way as Suzuki et al.'s system [6] was, but the injecting device has been newly developed in order to be able to inject various solid bodies. By using the present system, we examined shock wave interaction with a hexahedral solid body floating in the air. The motion of the solid body and the flow field around it were recorded using the shadowgraph technique coupled with a high-speed video camera to demonstrate the applicability of the present system.

2 Experimental Apparatus and Method

2.1 Shock Tube and Optical System

The experimental apparatus used in the present work is schematically shown in Fig. 1. Experiments were conducted in a horizontally placed shock tube consisting of a 1.46-m-long driver section of 120 mm inner diameter, a 4.6-m-long driven section of 30 mm × 100 mm rectangular cross section, and a dump tank. A plastic diaphragm set between the driver and the driven section is broken by a diaphragm rupturing device. A test section installed at the end of the driven section has a rectangular cross section of 30 mm × 100 mm and a pair of optical viewing windows of 99 mm × 204 mm. A solid-body injecting device is mounted on the floor of the test section at 3800 mm from the diaphragm location, and connected to the diaphragm rupturing device through a control unit. The Mach number of the shock wave generated was deduced from the signals from two pressure gauges mounted on the side walls of the driven section. The working gas was air. The gas in the test section was initially at atmospheric pressure and at room temperature, and the Mach number of the incident shock wave (M_s) was set to 1.3. In the present work, a hexahedral solid body (size: 30 mm × 9.0 mm × 14 mm, weight: 4.6 g, material: a mixture of polyvinyl chloride and rubber) was used.

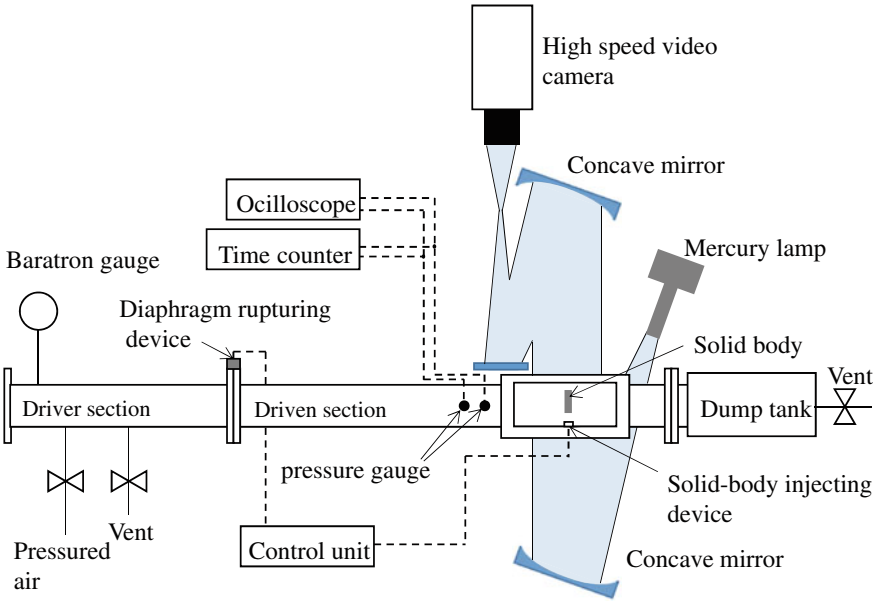

Fig. 1 Experimental apparatus

The shock-induced motion of a solid body and the flow field around it were visualized using the shadowgraph technique and recorded by a high-speed video camera (Photron, APX RS205K) with a camera lens (Nikon, Nikkor 200 mm, F4). The frame rate and the exposure time of the recording were set at 2,000 fps and 1/500,000 s, respectively. A mercury lamp (Ushio, UI-100) was used as the light source of the shadowgraph system. A concave mirror (focal length of 200 mm) was used to collimate the light from the mercury lamp, and the another one was used to focus the light passed through the flow field in the test section on the camera lens.

2.2 Solid-Body Injecting System

A schematic diagram of the solid-body injecting device coupled with the diaphragm rupturing device and a timing chart of the present system are shown in Figs. 2 and 3, respectively.

The solid-body injecting device is composed of a cylindrical rod, a spring, and a solenoid as illustrated in Fig. 2. The top of the rod is initially set to be flush with the shock tube floor by the solenoid, and a solid body is placed on the rod. A trigger signal from the control unit activates the solenoid and releases the spring-loaded rod to toss the solid body into the air. After tossing the solid body, the rod has to be quickly pulled back to the initial position by the solenoid again so as not to disturb

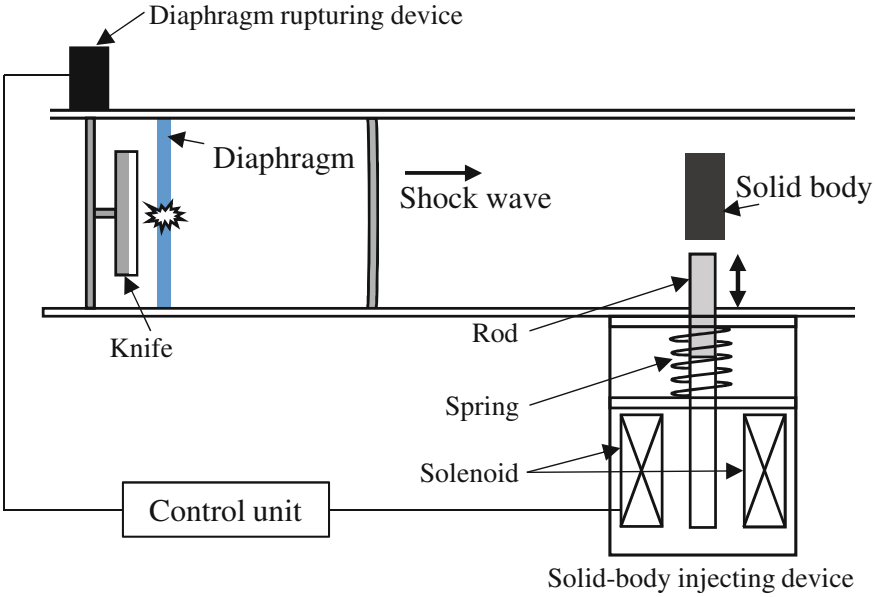

Fig. 2 Solid-body injecting system

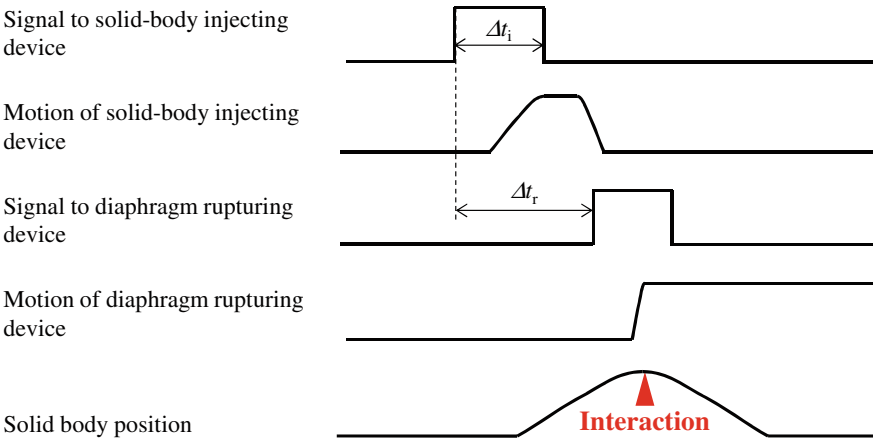

Fig. 3 Timing chart of the solid-body injecting system

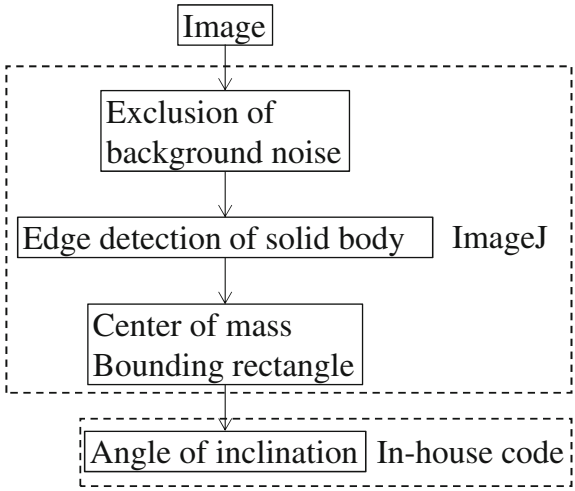

Fig. 4 Flowchart of the image analysis

the flow field in the test section. Hence, it is necessary to adjust the duration of the trigger signal sent to the injecting device (Δt_i in Fig. 3) to an appropriate value.

The diaphragm rupturing device consists of a spring-loaded plunger with a knife edge and a solenoid. By a trigger signal synchronized with the initiation of the injecting device mentioned above, the solenoid and the plunger are activated to break the diaphragm to generate a planar shock wave propagating in the driven and test sections. By tuning the delay time of the trigger signal after the initiation of the injecting device (Δt_r in Fig. 3), it is possible to make the shock wave interact with the solid body when it reaches just the top of its trajectory "almost" at rest.

2.3 *Image Analysis*

The location and orientation of the solid body were extracted from shadowgraph images using a public domain image processing software, ImageJ [7], combined with an in-house code. A flowchart of the extraction process is shown in Fig. 4. Shadowgraph images acquired by the high-speed video camera were initially processed using ImageJ to detect the center of mass and the width and height of the bounding rectangle of the solid body (X_1 and Y_1 in Fig. 5, respectively). The angle of inclination of the solid body, α in Fig. 5, is then calculated by

$$\alpha = \begin{cases} 90^\circ - \arccos\left(\frac{aX_1 - bY_1}{a^2 - b^2}\right) & \text{if } \beta < 90^\circ \\ -90^\circ + \arccos\left(\frac{aX_1 - bY_1}{a^2 - b^2}\right) & \text{if } \beta \geq 90^\circ \end{cases}$$

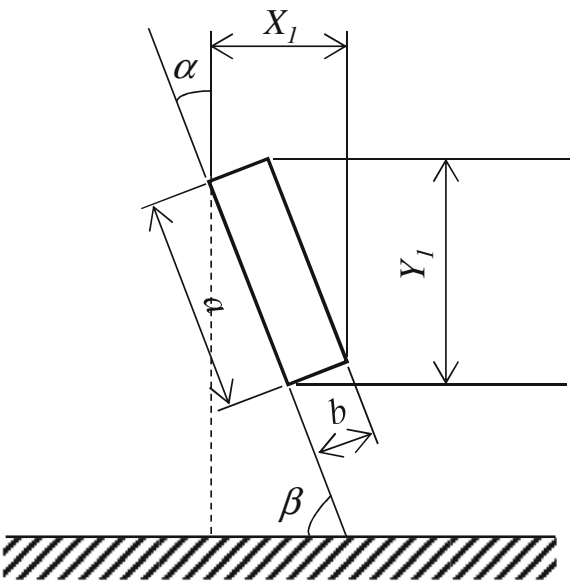

Fig. 5 Geometric parameters used to describe the orientation of a hexahedral solid body and to calculate the angle of inclination

3 Results and Discussion

3.1 Tuning of Operating Conditions

A set of preliminary experiments was conducted to determine the operating conditions of the present system: (1) the duration of the trigger signal sent to the solid-body injecting device (Δt_i in Fig. 3), and (2) the delay time of the trigger signal sent to the diaphragm rupturing device (Δt_r in Fig. 3). In the experiments, direct photographs of the solid body and the rod of the injecting device were taken using a high-speed video camera. Figure 6 shows a typical result obtained from the experiment with $\Delta t_i = 78$ ms. It was revealed from photographs such as shown in Fig. 6 that

1. The injected solid body reached the highest position about 130 ms after the initiation of the solid-body injecting device.
2. It took about 40 ms for the rod to be pulled back from the highest position to the initial position.
3. The duration of stay in the vicinity of the highest position was about 4 ms, which is much longer than the time during which an incident shock wave of $M_s = 1.3$ passes over the solid body (about 20 μs). Hence, we can practically regard the injected solid body as at rest during the interaction with the shock wave.

Based on these findings, we found that $\Delta t_i = 78$ ms and $\Delta t_r = 103$ ms were appropriate for the present purpose.

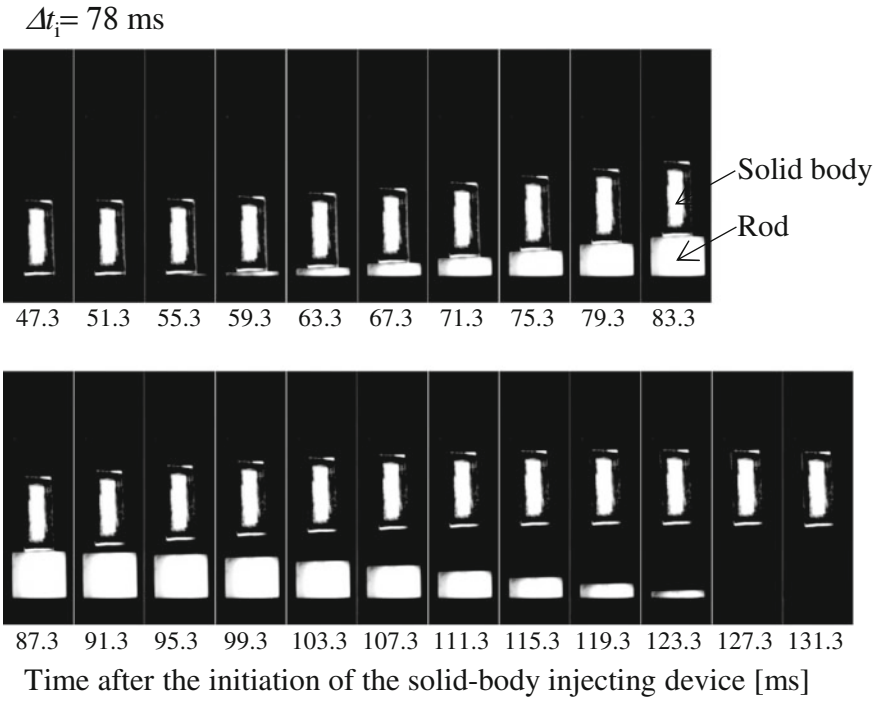

Fig. 6 Series of direct photographs of the solid body and the rod after the initiation of the solid-body injecting device (Δt_i = 78 ms)

3.2 Shadowgraph Images

Figure 7 shows a series of shadowgraph images taken at different times after shock passage, where the incident shock wave moves from left to right. It can be seen that the incident shock wave collides head-on with the front surface of the hexahedral body. The incident shock wave is reflected from the solid body and then diffracted (Fig. 7a and b). By the shock wave diffraction, a vortex ring is produced behind the solid body and the shadow of the vortex ring appears just behind the solid body in Fig. 7b. The vortex ring gradually deforms as shown in Fig. 7c–f, and eventually collapses on the lee side of the solid body. After the collapse of the vortex ring, a wake region is produced behind the solid body.

It is also found from the shadowgraphs that the solid body hardly moves until 1 ms after the shock passage. This fact supports our premise that the injected solid body can be regarded as at rest during the interaction with a propagating shock wave. Eventually, the solid body is accelerated and swept away by fluid dynamic forces.

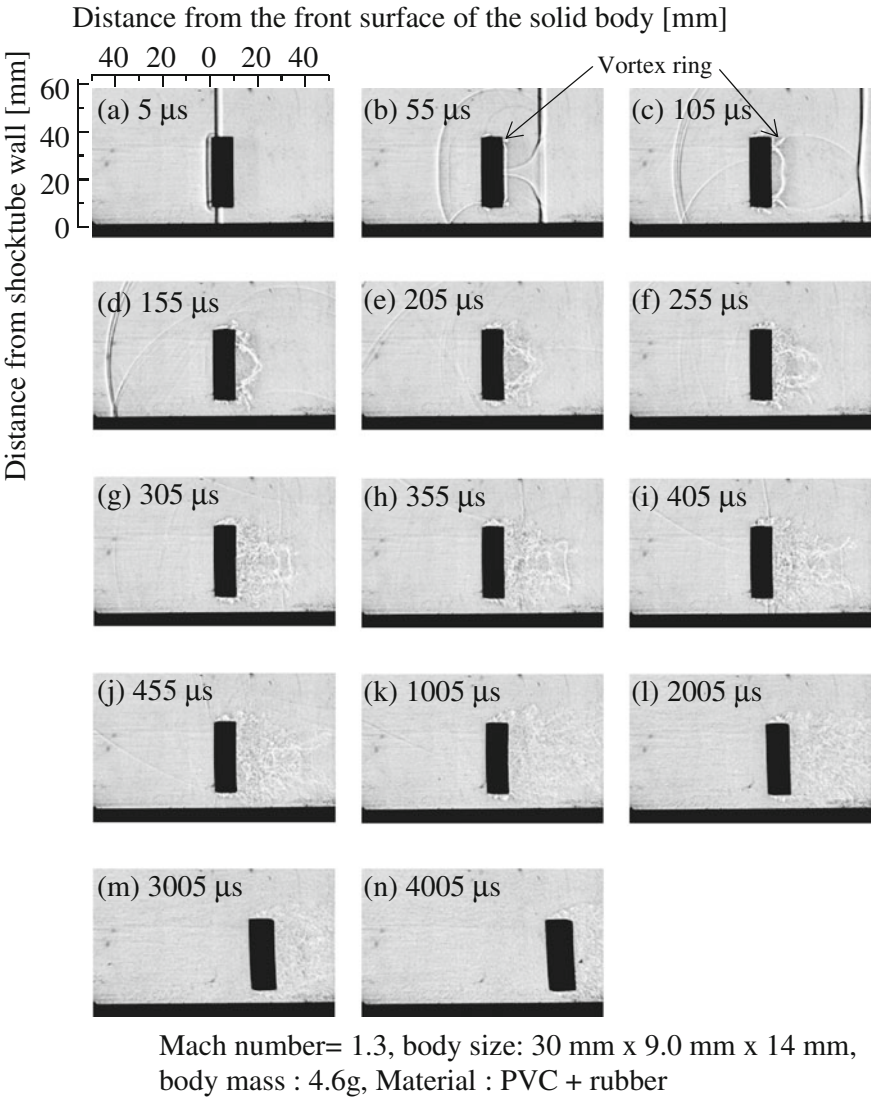

Fig. 7 Shadowgraph images taken at different times after shock passage. The incident shock wave moves from left to right.

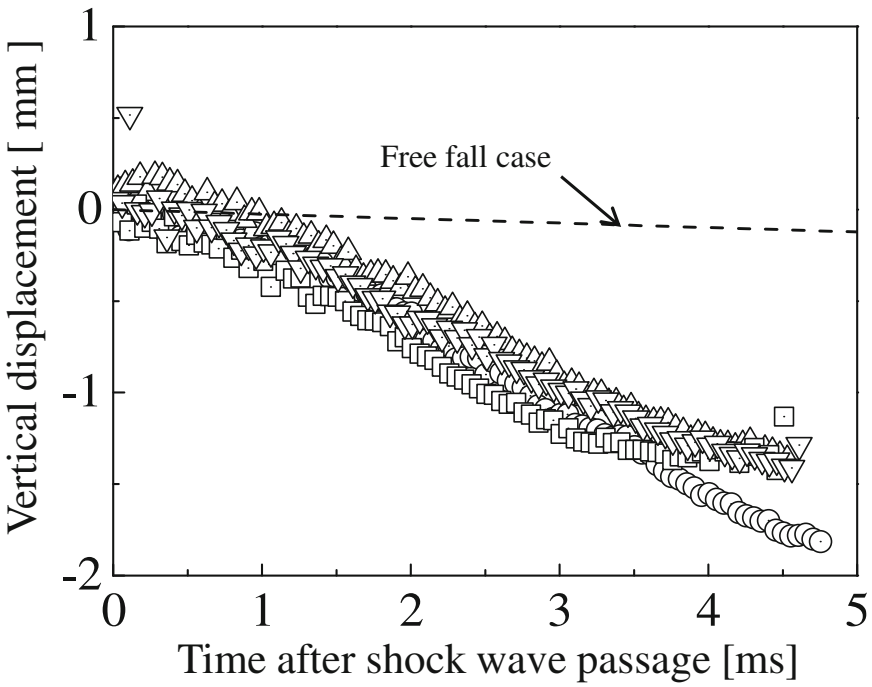

Fig. 8 Time histories of vertical displacement of the solid body

3.3 Results from Image Analysis

Representative results from the image analysis are depicted in Fig. 8. In this figure, time histories of vertical displacement of the solid body obtained from four different experiments are presented. As seen in Fig. 7, the solid body almost horizontally moved at a small angle of attack within ±4°. However, as clearly shown in Fig. 8, the solid body falls faster than the free-falling body. It is presumed that this is due to pressure decrease on the lower surface of the solid body caused by flow acceleration through a narrow channel between the solid body and the shock tube floor.

4 Conclusions

In the present work, a shock tube system for the study of shock wave interaction with a solid body floating in the air has been developed. By tuning the operating conditions, we have successfully made an incident shock wave with a Mach number of 1.3 interact with a solid body almost at rest without any support. The shock-induced motion of the solid body and the flow field around it were visualized using the

shadowgraph technique coupled with a high-speed video camera. Representative images obtained and results from the image analysis were presented.

References

1. Gerrard, J.H.: An experimental investigation of the initial stage of the dispersion of dust by shock waves. Br. J. Appl. Phys. **14**, 186–192 (1963)
2. Rudinger, G.: Some properties of shock relaxation in gas flows carrying small particles. Phys. Fluids **7**(5), 658–663 (1963)
3. Committee for the Prevention of Disasters: Methods for the Calculation of Physical Effects—Due to Release of Hazardous Materials (Liquids and Gases)—Yellow Book, 2nd edn., Gevaarlijkestoffen (2005)
4. Igra, O., Takayama, K.: Shock tube study of the drag coefficient of a sphere in a non-stationary flow. Proc. R. Soc. Lond. A **442**, 231–247 (1993). https://doi.org/10.1098/rspa.1993.0102
5. Jourdan, G., Houas, L., Igra, O., Estivalezes, J.L., Davals, C., Meshkov, E.E.: Drag coefficient of a sphere in a non-stationary flow: new results. Proc. R. Soc. A **463**, 3323–3345 (2007). https://doi.org/10.1098/rspa.2007.0058
6. Suzuki, T., Sakamura, Y., Igra, O., Adachi, T., Kobayashi, S., Kotani, A., Funawatashi, Y.: Shock tube study of particles's motion behind a planar shock wave. Meas. Sci. Technol. **16**, 2431–2436 (2005). https://doi.org/10.1088/0957-0233/16/12/005
7. Schneider, C.A., Rasband, W.S., Eliceiri, K.W.: NIH image to imageJ: 25 years of image analysis. Nat. Methods **9**, 671–675 (2012). https://doi.org/10.1038/nmeth.2089

Equation of State of Pure Water, Aqueous Solutions of Sodium Chloride, Gelatin Gel, and Glucose Syrup

Hiroaki Yamamoto, Kazuyoshi Takayama and Hiroaki Shimokawa

1 Introduction

For a medical application of shock waves, extracorporeal shock wave lithotripter (ESWL) has been established. It was demonstrated that the underwater shock focusing is one of most efficient methods to generate a controlled high pressure in a small region [1, 2]. However, the propagation of shock wave in the biological tissues has been approximated to the behavior in water because the acoustic impedances of organ and water are similar.

In order to develop a micromachined medical device which can generate focused shock waves in organs such as shock wave ablation catheter [3], it is important to predict shock wave behaviors in living body's soft tissues precisely [4, 5]. However, the shock wave propagation in liquid, especially for highly viscous fluid, is not so well understood as in gases.

Paper reports the result of preliminary tests on determining the equations of state (EOS) of pure water, aqueous solutions of sodium chloride, gelatin and starch syrup at the pressure range, which are primarily needed to perform numerical simulation uniquely predicting behaviors of shock waves used for medical treatment.

H. Yamamoto
Innovative Cardiovascular Medicine, Department of Cardiovascular Medicine, Graduate School of Medicine, Tohoku University, 2-1 Seiryo-Machi, Aoba-Ku, Sendai 980-8574, Japan

K. Takayama (✉) · H. Shimokawa
Tohoku University Hospital, 1-1 Seiryo-Machi, Aoba-Ku, Sendai 980-8574, Japan
e-mail: k.takayama@mac.com

K. Kontis (ed.), *Shock Wave Interactions*,
https://doi.org/10.1007/978-3-319-73180-3_6

2 Experimental Method

Underwater shock waves were generated at higher degree of reproducibility by explosion of 10 mg silver azide pellets (Showa kinzoku Kogyo Co. Ltd., Japan) [6], which were glued at on a tip of an optical fiber. Q-switched Nd: YAG laser (DSLT-ND-EOQ, $\lambda = 1064$ nm, nominal pulse duration 12 ns, 2 mJ/pulse, Sparkling Photon, inc., Japan) was used to ignite the pellet.

Figure 1 shows experimental setup. The test section is composed of a stainless steel chamber (100 mm in the inside diameter, 100 mm in depth) and an acryl window (140 mm × 140 mm × 25 mm) (Fig. 2). The chamber has the three pinholes to insert an optical fiber and two hydrophones. The shock wave motion at its earlier stage was visualized by high-speed shadowgraph. The shock wave overpressures were measured using PVDF Needle Hydrophone (Müller-Platte Needle Probe for −10 to 150 MPa, Dr. Müller Instruments, Germany). The signals were stored in the digital memory at 350 MHz of bandwidth and 2 GS/s of sampling rate (DS-5534, Iwatsu, Japan).

The test materials were purified water, NaCl aqueous solutions at 3, 10, and 20 wt.% gelatin gel, and commercial grades of hydrogenated glucose syrup (HS-20, Hayashibara Shoji, Inc., Japan). The purified water was deaerated by a vacuum drier (Type VO1-B, Shimizu Rikagaku Factory inc., Japan) prior to use. The required amount of NaCl powder (191-01665, Wako Pure Chemical Industries, Ltd, Japan) was measured corresponding to the concentrations of NaCl aqueous solutions, and then it was dissolved in the above-deaerated water at 313–323 K. Gelatin powder (077-3155, Wako Pure Chemical Industries, Ltd, Japan), which also was weighed by specified quantities, was completely dissolved in the deaerated water at 313–323 K. Then, pour the aqueous solutions of gelatin into the test chamber. Then, optical fiber with AgN3 10 mg pellet at one end was inserted into the

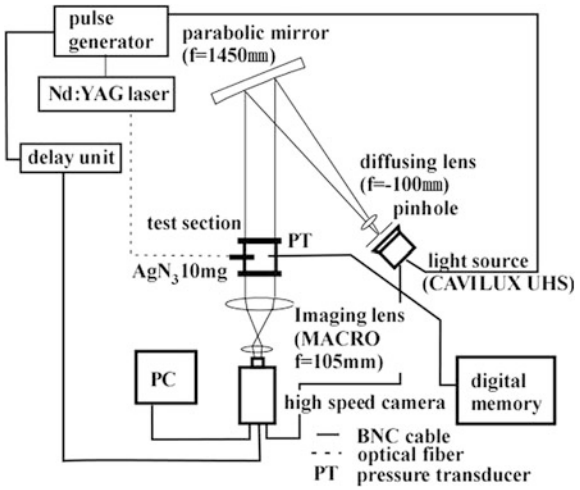

Fig. 1 Experimental setup

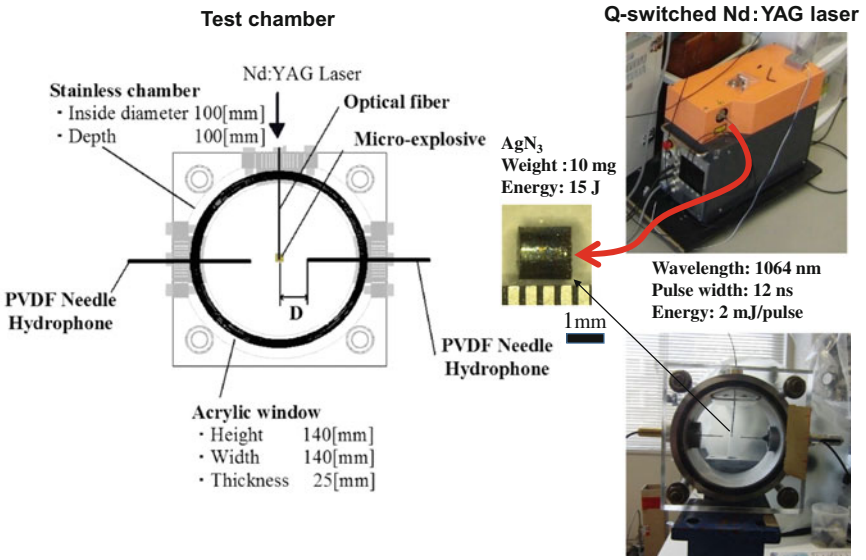

Fig. 2 Test chamber

chamber. After leaving it at 292 K for 20 h, gelatin gel was formed. The temperatures of all of these materials were maintained at 293 ± 0.3 K prior to experiment.

Because the AgN3 10 mg pellet is not water-resistant explosive, when the pellet is left as it is in a wet state for a long time, such as in gelatin gel, there is a possibility that the characteristics of ignition and detonation of the pellet will change. Therefore, to keep the inside of the pellet dry, the pellet was coated with a waterproof agent (Cyanoacrylate adhesive CN4, ALTECO, Japan).

Figure 3 shows the sequential images of explosion of the pellet without waterproofing after 20 h standing still in 10 wt.% gelatin gel. A laser irradiation was observed in the first frame. Although detonation began at 0.2 μs after laser irradiation, propagation of detonation continued until 3 μs. Because detonation velocity is lower than the shock wave velocity in water, weak shock waves were successively generated as detonation propagates from the fiber tip to the opposite end of the pellet.

On the other hand, the characteristics of ignition and detonation of the pellet with waterproofing are similar to that in air [7]. The pellet was also ignited after 20 h standing still in 10 wt.% gelatin gel. Figure 4 shows the sequential images of explosion. A flash of laser irradiation was observed in the second frame, ignition of the pellet occurred in between third and fourth frame, which means they are from 0.4 to 0.6 μs ignition delay. From these images, detonation velocity was estimated to be circa 4 km/s, which coincides approximately with nominal data [7].

Spherical shock wave was generated after 0.6 μs. Shock wave propagation through optical fiber formed a weak conical wave preceding a spherical wave, and shock wave fronts slightly bulge back the laser irradiation direction. Shock radius was defined in Fig. 5 as the average distances between SW front and center of the explosive were obtained from digital images.

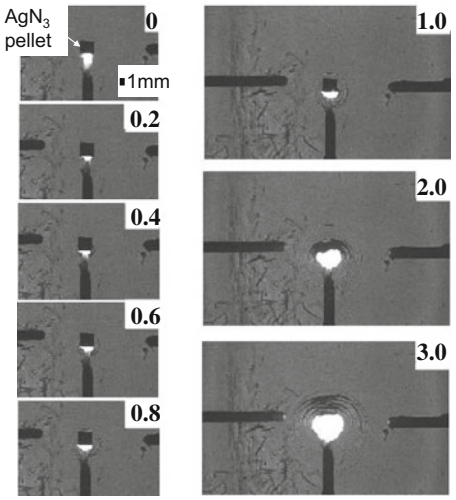

Fig. 3 Pressure histories in pure water, 3, 10, and 20 wt. % NaCl solution, 20 wt.% gelatin gel, and hydrogenated glucose syrup

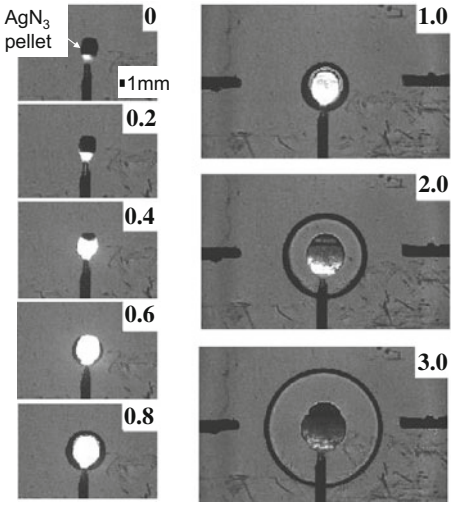

Fig. 4 Time-resolved shadowgram images of the explosion of a 10 mg AgN3 charge in the 3 wt.% NaCl aqueous solution

3 Result and Discussion

3.1 Shock Wave Velocities

Figure 6 shows pressure histories in the purified water, NaCl aqueous solutions at 3, 10, and 20 wt.% gelatin gel at 10, 20, and 30 wt.%, and commercial grades of hydrogenated glucose syrup at 293 K. In the every test medium, positive peak pressure with a steep rising edge attenuates to atmospheric pressure without following negative peak pressure.

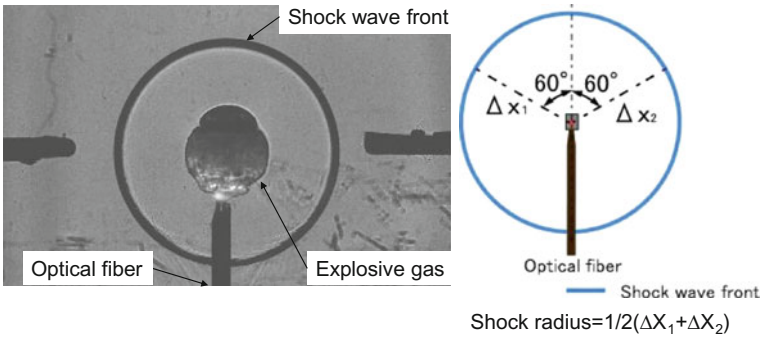

Fig. 5 Shock radii versus elapsed time after ignition

Figure 7 shows the relationship between the shock radius and the time after the ignition. Ordinate and abscissa designate shock radius in mm and time in microseconds. The data was analyzed in accordance with the method by Gojani et al. [4]. Shock wave velocities were found by the following procedure. Shock radii and times of arrival data were fitted by nonlinear least squares to an equation of the form proposed by Dewey [8, 9],

$$Rs = m_1(1 + m_4 t_s) + m_2 \ln(1 + m_4 t_s) + m_3 \sqrt{\ln(1 + m_4 t_s)}, \tag{1}$$

where m1, m2, and m3 are fitted coefficients; and Rs and ts are shock radius and time, respectively.

In Table 1, the fitted coefficients m1, m2, and m3 for the every test material are tabulated. The time derivative of Rs gives the shock velocity u_s.

$$u_s = m_1 m_4 + \frac{m_2 m_4}{1 + m_4 t_s} + \frac{m_3 m_4}{2(1 + m_4 t_s)\sqrt{\ln(1 + m_4 t_s)}} \tag{2}$$

3.2 Overpressure and Shock Speed

Assuming that relationship between shock velocity Us and particle velocity Up is written as

$$Us = C_0 + \beta Up, \tag{3}$$

then, based on momentum conservation law,

$$p = \rho_0 Us Up, \tag{4}$$

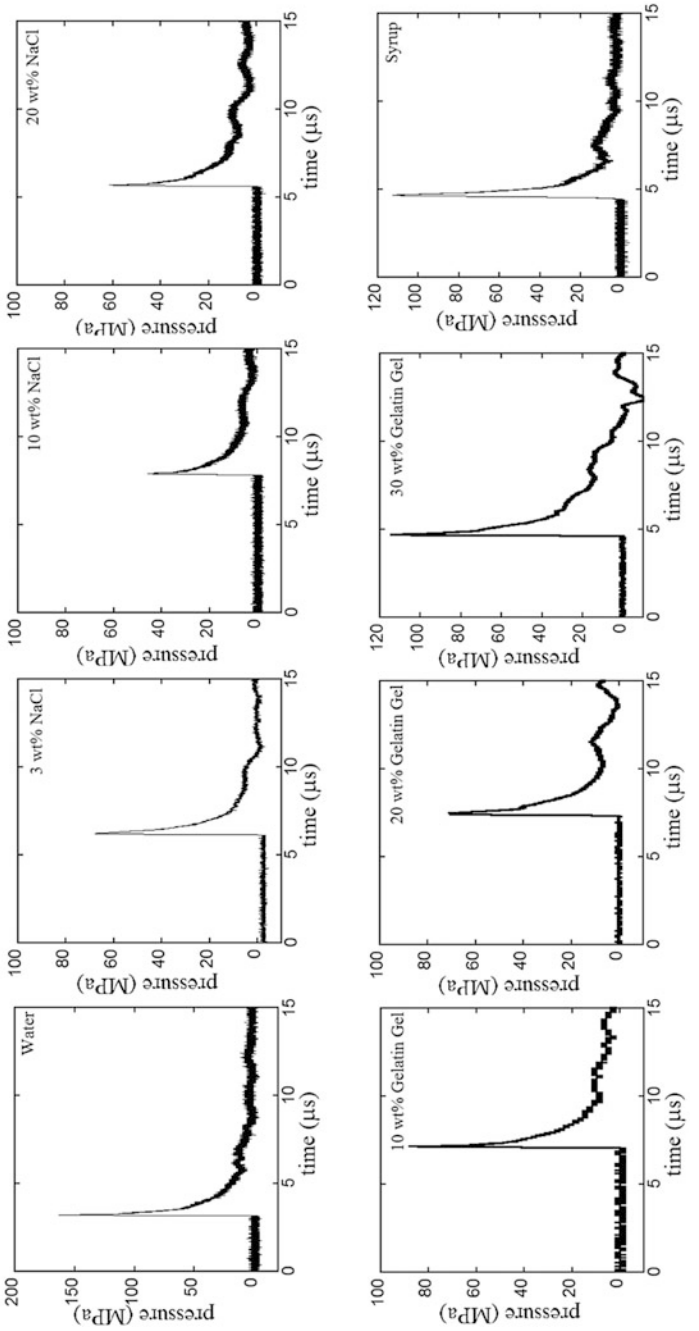

Fig. 6 Measured shock overpressure versus shock velocity

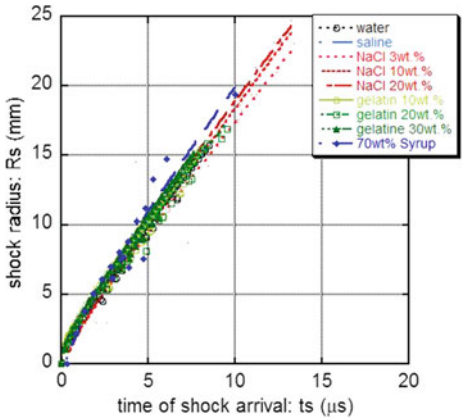

Fig. 7 Pressure–density ratio Hugoniot curves of pure water, 20 wt.% gelatin gel, hydrogenated glucose syrup and aqueous solutions of sodium chloride with 3, 10, and 20 wt.% at 293 K

Table 1 The coefficients determined by experiments. The date of density is taken from [13]

	density (kg/m^3)	β	B (MPa)	γ	m1	m2	m3	m4	sound speed (m/s)
water	998	2.40	244.67	8.77	1.1338	1.1464	-0.4909	1.2933	1.470
saline	1006	2.92	188.03	10.94	1.1022	1.2108	-0.3479	1.3009	1.434
NaCL 3Wt. %	1020	1.97	336.43	7.10	1.2137	0.7402	-0.5482	1.2672	1.538
NaCL 10Wt. %	1071	3.59	200.98	13.95	1.1628	1.4824	-1.8827	1.3984	1.626
NaCL 20Wt. %	1148	5.30	140.6	21.80	1.1516	1.9610	-2.3835	1.4342	1.652
gelatin 10Wt. %	1202	3.02	227.95	11.36	1.1071	1.2972	-0.6452	1.3286	1.471
gelatin 20Wt. %	1238	3.27	221.78	12.41	1.1146	1.3558	-0.7915	1.3411	1.495
gelatin 30Wt. %	1256	3.77	205.53	14.60	1.1240	1.3822	-0.7429	1.3795	1.551
syrup 70Wt. %	1370	6.47	149.43	27.09	1.0711	1.8761	-1.7024	1.6242	1.740

relationship between pressure p and shock speed Us is given by (3) and (4).

$$p = \rho_0 Us \frac{Us - C_0}{\beta}. \tag{5}$$

Relationship between density, particle velocity, and shock speed is given by mass conservation law as

$$\rho = \rho_0 \frac{Us - Up}{Us}. \tag{6}$$

Figure 8 shows the plot of overpressure and shock speed. β of the each medium is calculated based on the regression curve defined by (5).

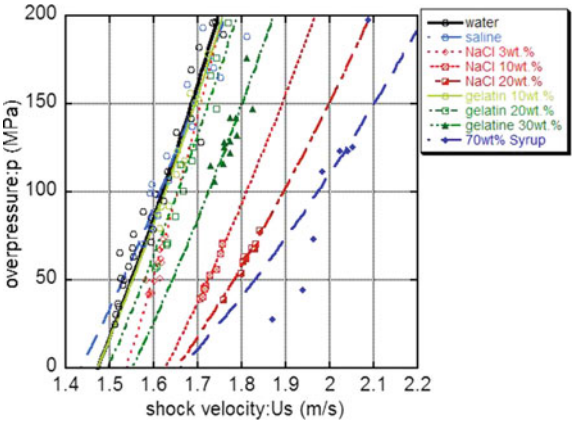

Fig. 8 The relationship between overpressure and shock velocity in purified water, NaCl aqueous solutions at 3, 10, and 20 wt. % gelatin gel at 10, 20, and 30 wt.% and commercial grades of hydrogenated glucose syrup at 293 K

3.3 Shock Hugoniot Curve

Combining (4) and (6) gives

$$p = \rho_0 Us^2 \left(1 - \frac{\rho}{\rho_0}\right). \tag{7}$$

Elimitating Us from (5) and (7),

$$p = \rho_0 \left(1 - \frac{\rho_0}{\rho}\right) \frac{C_0^2}{\left(1 - \beta + \beta \frac{\rho_0}{\rho}\right)^2}, \tag{8}$$

where C_0 is the sound speed of the medium.

Substituting C_0 and β which were calculated in Sects. 3.1 and 3.2, respectively, into (8), relationship between pressure and density is shown in Fig. 9. It is clear that

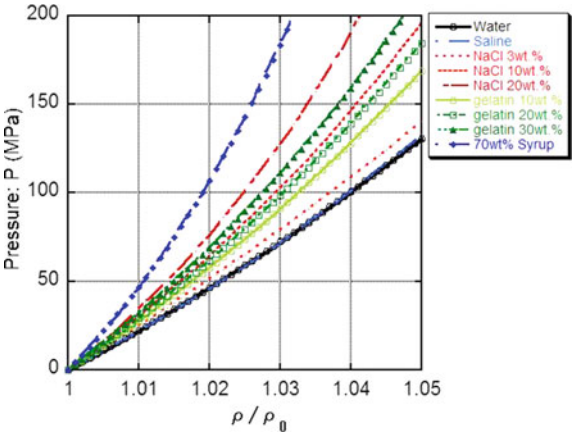

Fig. 9 The relationship between pressure and density in purified water, NaCl aqueous solutions at 3, 10, and 20 wt.% gelatin gel at 10, 20, and 30 wt.% and commercial grades of hydrogenated glucose syrup at 293 K

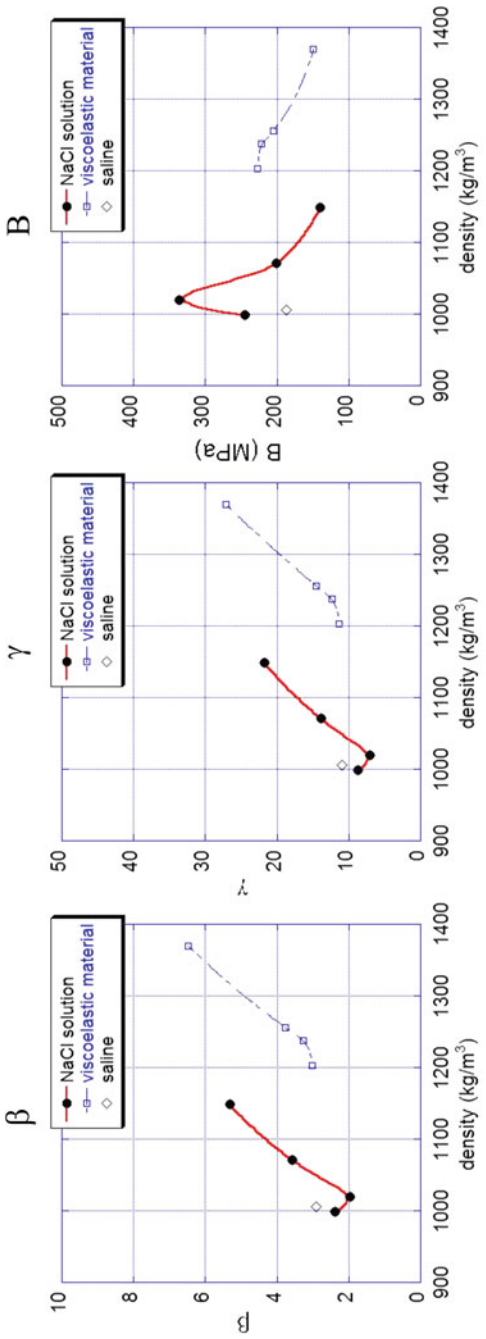

Fig. 10 Composition dependence for parameter β, γ, and B for NaCl + water, gelatin gel, and glucose syrup at 293 K

sodium chloride added to water tends to reduce compressibility of the solution. The Hugoniot curves of gelatin gel also indicate that addition of impurity to water tends to shift shock Hugoniot curves toward smaller density ratios.

The Tait-type EOS [10–12] which is useful for the medical application of shock waves with overpressure of less than 100 MPa can be expressed as

$$\frac{p+B}{p_0+B}=\left(\frac{\rho}{\rho_0}\right)^{\gamma}, \tag{9}$$

where B and γ are the constants of media.

B and γ of the each medium can be calculated based on the regression curve defined by (9). Coefficients of each medium are tabulated in Table 1. Data for density are taken from Lide [13].

Figure 10 shows composition dependence for parameters β, γ, and B. It is clear that β and γ increase or B decreases with increases in density. For sodium chloride aqueous solutions, it seemed that after β and γ reached minimum value at low density, they monotonically increase with the increase in the density. Conversely, B reached maximum in a low-density region and it decreases with the increase of the density. Similar behavior has been reported for water and alcohol mixtures [14]. When a small amount of alcohol is added, alcohol molecule forms hydrogen bonding with the surrounding water molecules in aqueous solutions and enhances the structure of total system rapidly. As the concentration of alcohol increases beyond a certain point, structure characteristics of the system decreases and it reduces compressibility of the solutions [15]. However, the sodium chloride aqueous solutions are electrolyte unlike aqueous mixtures with alcohol. It is considered that the effect of hydrogen bonding on compressibility of the sodium chloride aqueous solutions is relatively small. On the other hand, for gelatin gel and syrup, there is also composition dependence for parameters β, γ, and B, but without the maximum or minimum value.

4 Summary

In order to support numerical simulation aiming at medical application, time-resolved visualization and pressure measurement of underwater shock wave induced by small explosive were conducted.

The shock Hugoniot curves for pure water, 10, 20, and 30 wt.% gelatin gel, hydrogenated glucose syrup and aqueous solutions of sodium chloride with 3, 10, and 20 wt.% at 293 K were found experimentally.

Acknowledgements The authors wish to thank the staff of the Interdisciplinary Shock Wave Laboratory of the Institute of Fluid Science, Tohoku University. A part of this study was supported by JSPS KAKENHI Grant Number 25350518.

References

1. Takayama, K., Esashi, H., Sanada, N.: Propagation and focusing of spherical shock waves produced by underwater microexplosions. In: Archer, R.D., Milton, B.E. (eds.) Proceedings of the 14th International Symposium on Shock Tubes and Waves, pp. 553–562 (1983)
2. Takayama, K. (ed.): Shock Wave Handbook (in Japanese). Springer, Tokyo (1995)
3. Hasebe, Y., Yamamoto, H., Fukuda, K., Nishimiya, K., Hanawa, K., Shindo, T., Kondo, M., Nakano, M., Wakayama, Y., Takayama, K., Shimokawa, H.: Development of a novel shock wave catheter ablation system—the first feasibility study in pigs. PLoS ONE **10**(1), e0116017 (2015). https://doi.org/10.1371/journal.pone.0116017
4. Gojani, A.B., Ohtani, K., Takayama, K., Hosseini, S.H.R.: Shock Hugoniot and equations of states of water, castor oil, and aqueous solutions of sodium chloride, sucrose and gelatin. Shock Waves (2009). https://doi.org/10.1007/s00193-009-0195-9
5. Nagoya, H., Obara, T., Kuwahara, M., Takayama, K.: A study of shock wave propagation in human tissue. In: Proceedings of Sixth Japan Society of Medical Electronics and Biological Engineering Meeting, pp. 98–102 (1992)
6. Takayama, K., Esashi, H., Sanada, N.: Propagation and focusing of spherical shock waves produced by underwater microexplosions. In: Archer, R.D., Milton, B.E. (eds.) Proceedings of the 14th International Symposium on Shock Tubes and Waves, pp. 553–562 (1983)
7. Hamate, H., Kuwano, H.: Ignition and detonation characteristics of micro explosives. Proceedings of PowerMEMS 2008+microEMS2008, pp.9–12 (2008)
8. Dewey, J.M.: The properties of a blast wave obtained from an analysis of the particle trajectories. Proc. Roy. Soc. A **324**, 275–299 (1971)
9. Kleine, H., Dewey, J.M., Ohashi, K., Mizukaki, T., Takayama, K.: Studies of the YNT equivalence of silver azude charges. Shock Waves **13**, 123–138 (2003)
10. Tait, P.G.: Report on some of the physical properties of fresh water and of sea water. Phys. Chem. Chall. Exp. Part IV, 1–78 (1888)
11. Dymond, J.H., Malhotra, R.: The Tait equation: 100 years on. Int. J. Thermophys. **9**, 941–951 (1988)
12. Heuckroth, L.E., Glass, I.I.: Low-energy underwater explosions. Phys. Fluids **11**, 2095–2107 (1968)
13. Lide, D.R.: CRC Handbook of Chemistry and Physics. CRC Press, Florida (2000)
14. Moriyoshi, T., Uosaki, Y.: Compressive and dielectric properties of aqueous non-electrolyte mixtures. J. Soc. Mater. Sci. Jpn **33**(365), 127–133 (1984)
15. Tanaka, Y., Matsuda, Y., Fujiwara, H., Kubota, H., Makita, T.: Viscosity of (water + alcohol) mixtures under high pressure. Int. J. Thermophys. **8**(2), 147–163 (1987)

Forecasting Method of Shock-Standoff Distance for Forward-Facing Cavity

Wang Gang, MA Xiao-wei, Jiang Tao, Gong Hong-ming, KONG Rong-zong and YANG Yan-guang

Abstract Experiments are performed on a cylinder with a forward-facing cavity at the tip in the flow of $M_\infty = 10$ in FD-14A shock tunnel. The shock shape, shock-standoff distance, and oscillation characteristics are captured by the high-speed movie, and the dynamic pressure response is used to correlate with the acoustic characteristics of the cavity base through the transducer. By analyzing the amount of experimental and numerical results abroad, a forecasting method for shock-standoff distance is proposed. Combination of organ-pipe theory with experimental results of oscillation frequency validates the applicability and effectiveness of the method. Results of shock-standoff distance and oscillation frequency are also obtained for experiments in FD-14A shock tunnel. The forecasting results of oscillation frequency are in accordance with the experimental results. Furthermore, the oscillation amplitude and average velocity of the shock wave are analyzed for forward-facing nose cavity at $M_\infty = 10$.

Keywords Shock-standoff distance · Forward-facing cavity · Pressure oscillation

1 Introduction

Hypersonic vehicles such as hypervelocity projectiles, reentry vehicles, and hypersonic aircrafts are designed to withstand severe heat loads. Maximum aerodynamic heating and potential for material ablation are typically most critical at the nose tips and leading edges. A proposed passive heat transfer reduction mechanism is to locate a forward-facing cavity at the nose tip. There is strong evidence that the heat flux at the cavity base can be as little as 2 – 10 times less than the stagnation point heat flux of a convex hemispherical tip [1, 2].This fact can be used in the nose

W. Gang (✉) · M. Xiao-wei · J. Tao · G. Hong-ming · K. Rong-zong · Y. Yan-guang
China Aerodynamics Research and Development Center Hypervelocity Aerodynamic Institute, Mianyang 621000, China
e-mail: wgsxlong@mail.ustc.edu.cn

K. Kontis (ed.), *Shock Wave Interactions*,
https://doi.org/10.1007/978-3-319-73180-3_7

design by centrally locating a forward-looking sensor at the base of a forward-facing cavity. In doing so, the heat transfer to and temperature rise of the window material may be reduced enough for some applications to eliminate the need for active cooling [3–6].

Hartmann established that placing a forward-facing cavity in a nose can produce intense pressure oscillations at a discrete frequency when placed within a supersonic flow(i.e., the Hartmann whistle) [7]. Sambamurthi [8] showed numerically and experimentally that shock oscillation frequency and amplitude are related to the cavity depth. The frequency is inversely proportional and amplitude is directly proportional to the cavity base. Experiments by Marquart [9] indicated that the primary mode of pressure oscillation in the cavity is the classic organ-pipe frequency. Experiments and investigations by Engblom et al. [3] implied that freestream noise is the mechanism driving resonant pressure oscillations within relatively shallow cavities, while numerical simulations by them indicated that relatively deep cavities are unstable and would oscillate without freestream noise (self-sustain), and most of the energy of the oscillations for deep cavities is contained in the primary mode which had been indicated by Marquart.

However, most of the experimental and numerical researches aimed to examine the issue of unsteady phenomena and aerothermal characteristics. Only a few researches had concentrated on shock behaviors for the forward-facing cavity, but the prediction of shock behavior is significant for forecasting frequency of oscillation inside the cavity. Huebner [2], Sambamurthi [8], Marquart [9], Saravanan [10], and Engblom [11] measured shock-standoff distance using optical methods. Marquart [9] conducted the experiments to reveal that the average shock-standoff distance remained nearly unchanged while the cavity decreased for some cases, and the average standoff distance remained nearly unchanged with increasing angle of attack.

In the present study, the shock-standoff distance for different kinds of forward-facing cavities in supersonic and hypersonic flows are studied based on the experiments in FD-14A shock tunnel, as well as other experimental and numerical results.

2 Experimental Apparatus

2.1 Test Facility

The experiments were conducted in FD-14A shock tunnel in CARDC, as shown in Fig. 1. The FD-14A shock tunnel can produce flows using nitrogen as the main working fluid from Mach 6 to 16. The tunnel provides the capability to reach reservoir pressure levels of up to 69Mpa and it can achieve a total temperature of up to 4000 K. Runtimes were about 15 ms. A summary of the test conditions is presented in Table 1. The experiments were conducted at a freestream Mach

Fig. 1 FD-14A shock tunnel in CARDC

Table 1 Test conditions in FD-14A shock tunnel

M_∞	P_0(Mpa)	T_0(K)	$Re_{\infty L}$/(m)
6	2 ~ 12	800	$8.1 \times 10^6 \sim 6.7 \times 10^7$
9	3 ~ 69	800 ~ 3200	$1.0 \times 10^6 \sim 5.5 \times 10^7$
10	3 ~ 69	900 ~ 4000	$7.5 \times 10^5 \sim 4.5 \times 10^7$
12	3 ~ 50	1200 ~ 4000	$4.0 \times 10^5 \sim 9.0 \times 10^6$
14	5 ~ 40	1600 ~ 4000	$2.0 \times 10^5 \sim 4.0 \times 10^6$
16	5 ~ 40	1900 ~ 4000	$1.5 \times 10^5 \sim 1.0 \times 10^6$

number of 10 and a freestream Reynolds number of $7.4*10^6$/m. The pressure and the temperature are 11.66 Mpa and 1005 K, respectively.

2.2 Test Model and Data Acquisition

The model was a flat-head cylinder wedge, 300 mm in diameter, with a cavity at the tip. The cavity diameter was 80 mm and its depth was 200 mm (Fig. 2). A dynamic pressure transducer (model NS-2) with an effective frequency response of approximately 300 KHz and with a pressure range of 0–50 Kpa was used. The transducer is nominally 2 mm in diameter and was installed with its axes parallel to the model axis, and for the flat base with their face flush with the surface. The signals were amplified by DH3840Q Amplifiers and pass through DH5862A Electronic Filters with a cutoff frequency set at 300 kHz. Shock shape, shock-standoff distance, and oscillation amplitudes were obtained by high-speed

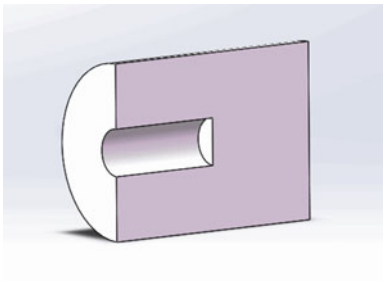

Fig. 2 Schematic drawing of forward-facing cavity in FD-14A shock tunnel

movies that were recorded at rates up to 5000 frames/s. A motion analyzer was used to determine the shock shape and to measure the time-dependent shock-standoff distance that yielded mean standoff distance and rms amplitude for runs in which the film was taken. The camera is with largest pixels of 1024*1024 and largest frame frequency.

3 Methodology

3.1 Forecast for Shock-Standoff Distance

Shock shape and shock-standoff distance mainly depend on two factors: Mach number and geometric shape. Some simple engineering correlations of blunt-body shock shapes and shock-standoff distance were given based on the experimental data [12], and the value of shock-standoff distance was correlated as

$$\frac{S}{R} = 0.143\exp(3.24/M_{\infty}^{2})\ \text{Sphere} - \text{cone} \tag{1}$$

$$\frac{S}{R} = 0.386\exp(4.67/M_{\infty}^{2})\ \text{cylinder wedge}, \tag{2}$$

where S is the shock-standoff distance, R is the radius of the nose, and M_{∞} is the Mach number of the incoming flow.

As the ratio of cavity diameter D and nose diameter D_n varies, the shock-standoff distance may change because the distance is mainly affected by the geometric shape. For sphere–cone, (A) the first half of the geometric shape remains as the original shape under the condition of relatively small D/D_n, the shock shape, and hence, shock-standoff distance are** similar to the one without a cavity. (B) As the value of D/D_n increases to a medium one, the central portion of the detached shock is nearly parallel to the frontline of the cavity, while other parts of the detached shock look like the shock shape of a sphere–cone without cavity. (C) Under the condition of relatively large value of D/D_n, Sambamurthi [8] found that the detached shock is almost parallel to the frontline of the cavity, and what is more, the shape of the whole detached shock is quite similar to the shape of the cylinder wedge's shock wave. Based on these phenomena and Eqs. (1) and (2), three forecasting equations for shock-standoff distance are proposed for three different cases as follows:

(1) For case A, as the shock shape is quite similar to a sphere–cone's shock shape without cavity, R in Eq. (1) is approximated by $\frac{1}{2}D_n$, so the shock-standoff distance is given by $S = \frac{1}{2}D_n * 0.143\exp(3.24/M_{\infty}^{2})$.
(2) For case B, as the central portion of the detached shock is nearly parallel to the frontline of the cavity, and hence, the shock shape is similar to the shock shape

of the cylinder wedge with a radius of $\frac{1}{2}D$. Therefore, R in Eq. (2) is approximated by $\frac{1}{2}D$, and accordingly, the shock-standoff distance for case B is approximated by $S = \frac{1}{2}D*0.386\exp(4.67/M_{\infty}^2)$.

(3) For case C, it is somewhat different from case B. As mentioned above in case B, the central portion of the detached shock is nearly parallel to the frontline of the cavity, but other parts of the shock still look like the shock shape of sphere–cone, accordingly. In contrast to case C, the geometric shape of sphere–cone, with relatively large cavity, is alike to a cylinder wedge. Hence, R in Eq. (2) is approximated by definition of the equivalent radius of $\frac{\sqrt{2}}{4}D_n$, and accordingly, the shock-standoff distance for case C is approximated by $S = \frac{\sqrt{2}}{2}*\frac{1}{2}D_n*0.386\exp(4.67/M_{\infty}^2)$.

3.2 Forecast for Oscillation Frequency

Experimental and numerical investigations have consistently found that all of the cavity configurations exhibit oscillatory flow due to resonance inside the cavity. Most of the energy of the oscillations is at the lowest distinctive frequency, which is considered as the primary resonance frequency. The primary resonance frequency can be calculated using simple linear theory, given the cavity depth and the speed of sound inside the cavity. In classic organ-pipe theory, the wavelength λ of the primary resonance is given as $\lambda = 4L$, where L is the cavity depth. Thus, the frequency f corresponding to this wavelength can be obtained knowing the speed of sound a. Assuming that the gas temperature inside the cavity is approximately the stagnation temperature T_0 of the flow, which leads to $a = \sqrt{\gamma R^* T_0}$ [13, 14]. Hence, $f = \frac{\sqrt{\gamma R T_0}}{4L}$, where γ is the ratio of specific heats and R^* is the specific gas constant.

However, some other scientists suppose that the sound wave oscillated between the base of the cavity and average position of the shock wave. Hence, the L in Eq. (5) should amended to be $L^* = L + S$ [3, 4, 14–16]. This issue would be discussed later.

4 Results and Discussion

4.1 Shock-Standoff Distance

Now, forecasting equations for case A, B, and C would be validated whether they are suitable for shock-standoff distance, according to experimental results.

Marquart [9], Sambamurthi [8], and Huebner [2] conducted experiments at a freestream Mach number of 10 on one geometric shape which differs in scales. The terms deep, medium, and shallow were used to make a distinction among different depths of cavity. The geometric shape is characterized for $D/D_n = 0.67$, as shown in

Fig. 3. Forecasting results based on Eqs. (3)–(5) are compared with experimental results in these three papers, shown in Fig. 4. Figure 4 presents the experimental data for three configurations. Each point in the figure shows the shock-standoff distance as a function of depth of cavity. "E1", "E2", and "E3" in the figure denotes forecasting results for case A, B, and C, respectively, hereinafter the same. Now that the depth varies for shallow cavity ($L = 62$ mm) and medium cavity ($L = 125$ mm), the shock-standoff distances almost remain the same for two cases as they are characterized by the same geometric shape of sphere–cone. For deep cavity ($L = 187.5$ mm), the geometric size of sphere–cone is larger than the other two cases; hence, the shock-standoff distance is larger than the other two cases. In general, forecasting results indicate that "E3" is able to predict shock-standoff distance accurately for a forward-facing cavity with varied geometric sizes of sphere–cone and varied cavity depth for $D/D_n = 0.67$, while forecasting results of "E1" and "E2" underestimate the shock-standoff distance for this case.

Saravanan [10] and Engblom [11] conducted experiments at a freestream Mach number of 5 and 8 on a forward-facing cavity for three models of $D/D_n = 0.17$, $D/D_n = 0.28$, and $D/D_n = 0.5$. Experimental results compared with the forecasting results are shown in Fig. 5. For the case of $D/D_n = 0.17$, "E1" predicts the

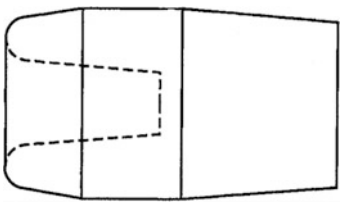

Fig. 3 Schematic drawing of a forward-facing cavity [9]

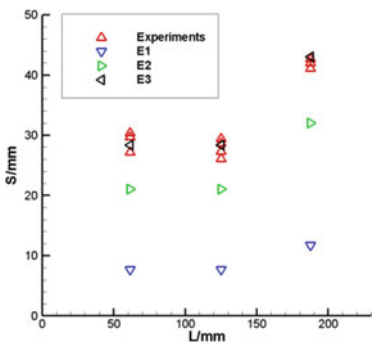

Fig. 4 Comparison of forecasting shock-standoff distance and experimental results($D/D_n = 0.67$)

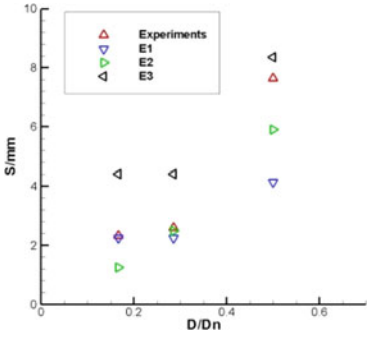

Fig. 5 Comparison of forecasting shock-standoff distance and experimental results ($D/D_n = 0.17 - 0.5$)

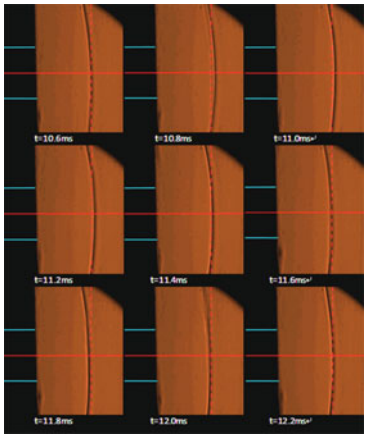

Fig. 6 Shock position in one period in FD-14A shock tunnel

experimental result accurately, while "E2" and "E3" fail to predict the standoff distance. For $D/D_n = 0.28$, "E1" and "E2" are able to predict shock-standoff distance, while the forecasting result of "E3" is somewhat larger than the experimental results. For $D/D_n = 0.5$, although the forecasting result of "E3" is a little larger than the experimental result, it is more accurate than the other two methods.

Shadow flow visualization of cylinder-wedge model in FD-14A shock tunnel is shown in Fig. 6. The results show that the shock-standoff distance to be an average of approximately 88 mm, with the oscillation frequency of 609 Hz. Applied with Eq. (2) for cylinder-wedge model, the calculation shows that the shock-standoff distance is approximately 63 mm, which deviates from the experimental results for about 28%.

In general, for the case of relatively small value of D/D_n, the existence of cavity weakly affects the shock shape and the shock-standoff distance. Therefore, "E1" is able to predict the shock-standoff distance. For medium value of D/D_n, the existence of cavity is quite similar to a cylinder wedge with a radius of $\frac{1}{2}D$, as shown in Fig. 5, the prediction of "E1" and "E2" is kind of accurate. For relatively large value of D/D_n, the forecasting result of "E3" is accurate to the experimental result, as shown in Fig. 4. Discussions would be continued in the following sections.

4.2 Oscillation Frequency

Controversy exists on the issue of how to define L in the forecasting equation $f = \frac{a}{4L}$ for oscillation frequency. The L may define as the depth of cavity, or the sum of the depth of cavity and shock-standoff distance. Based on plenty of experimental and numerical results abroad, the oscillation frequency is predicted using L and L^*, which can be calculated by "E1", "E2", and "E3", respectively. By comparing with the experimental results, two purposes would be achieved: On the one hand,

the controversy on the issue of "L" would be discussed; on the other hand, adaptability and effectiveness of the forecasting method for shock-standoff distance would be validated by this process.

Numerical simulations were performed at a freestream Mach number from 3 to 9 to study the oscillation frequency for forward-facing cavity by Engblom [11]. Comparisons using forecasting method of oscillation frequency with experimental results are shown in Fig. 7. "L" in Fig. 7 denotes the forecasting result by defining L as the depth of cavity. For the case of $L \in (2, 10)$ mm, $L/D = 0.75$, and $D/D_n \in (0.06, 0.25)$, the experimental results are just between the forecasting result of "E1" and "E2", which means that the forecasting results of shock-standoff distance are relatively accurate. For the case of $L > 12.7$ mm, $L/D \geq 1.4$, and $D/D_n = 0.5$, the effect of shock-standoff distance on oscillation frequency's prediction decreases as the cavity depth increases, as shown in Fig. 7, "E3" provides more accurate results of shock-standoff distance than the other two methods, and hence more accurate results of oscillation frequency.

Juliano [17] conducted experiments on forward-facing cavity with $D/D_n = 0.5$, and the result is shown in Fig. 8. The experimental results perfectly agree with the forecasting results based on "E3", while results by "L", "E1", and "E2" are larger than experimental results.

The numerical and experimental effort by Yuceil and Engblom [4, 15] were made on forward-facing cavity. For the case of $L/D \in (0.2, 1.2)$ and $D/D_n = 0.5$,

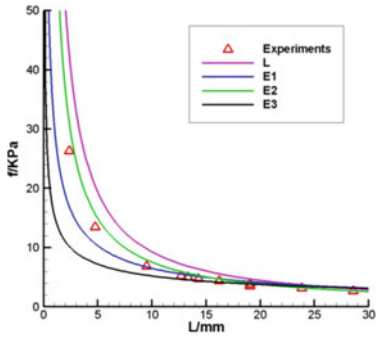

Fig. 7 Comparison of forecasting oscillation frequency and experimental results($D/D_n = 0.06 - 0.5$)

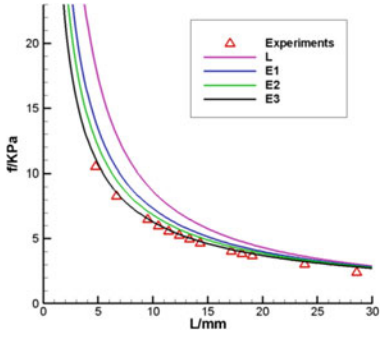

Fig. 8 Comparison of forecasting oscillation frequency and experimental results($D/D_n = 0.5$)

the result is shown in Fig. 9. As the cavity depth varies, "E3" predicts the oscillation frequency accurately. For the case of $L/D \in (0.3, 1.3)$ and $D/D_n = 0.25 - 0.5$, the result is shown in Fig. 10. The range of $L < 7$ mm corresponds to the geometric shape of $D/D_n = 0.25$, and in this case the forecasting results by "E3" close to but underestimate the experimental results a little. For the case of $L > 7$ mm and $D/D_n = 0.5$, the "E3" method predicts the experimental results accurately.

The experimental results were reported by Ladoon [1] and Segura [18] on forward-facing cavity of $D/D_n = 0.5$ and $L/D \in (0.5, 3.0)$. Based on the forecasting results of shock-standoff distance, the experimental results equal to the results predicted by "E3" method for most of the conditions. The results are shown in Fig. 11.

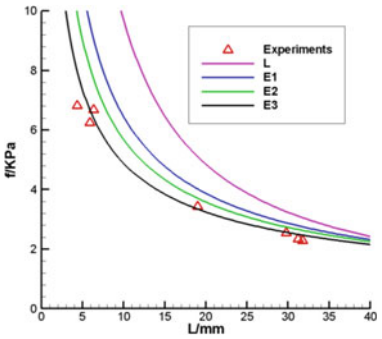

Fig. 9 Comparison of forecasting oscillation frequency and experimental results($D/D_n = 0.5$)

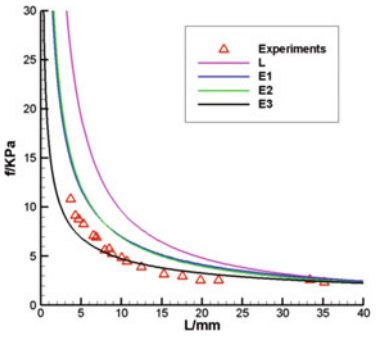

Fig. 10 Comparison of forecasting oscillation frequency and experimental results($D/D_n = 0.25 - 0.5$)

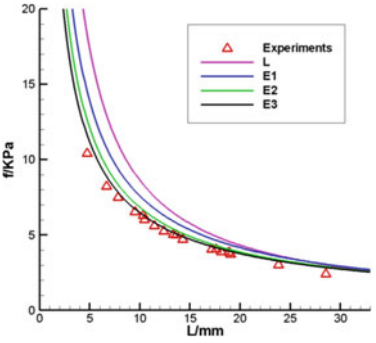

Fig. 11 Comparison of forecasting oscillation frequency and experimental results($D/D_n = 0.5$)

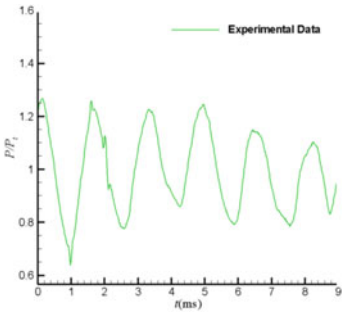

Fig. 12 Dynamic pressure signals at the cavity base for baseline in FD-14A shock tunnel

Figure 12 shows pressure signals measured at the base of the cavity in FD-14A. The pressure signals have been normalized by the total pressure behind the shock wave. The oscillation frequency is approximately 622 Hz based on the figure. According to organ-pipe theory, the oscillation frequency can be calculated to be 560 Hz. Furthermore, the result based on the forecasting equation for cylinder wedge is about 614 Hz. It is obvious that the forecasting result of cylinder wedge is close to the experimental results based on pressure signals, while the result obtained by high-speed movie may be a little lower than its true value.

To conclude the cases above, for the case of $D/D_n \leq 0.17$, "E1" is able to predict the shock-standoff distance accurately. For $D/D_n \in (0.17, 0.3)$, either "E1" or "E2" could forecast the shock-standoff distance though, the error may exist for some conditions. For the case of $D/D_n = 0.5$ and $D/D_n = 0.67$, "E3" provides satisfying results of shock-standoff distance. Limited by the amount of experimental and numerical results, the applicability of the forecasting method for shock-standoff distance should be validated further. However, the data that are collected and analyzed in the present paper cover the most of the published results of shock-standoff distance for forward-facing cavity.

The controversy exists on the issue of L in forecasting equation for oscillation frequency. Based on the results above, it is reasonable to believe that the sum of shock-standoff distance and cavity depth should be taken into account to predict the oscillation frequency. What is more, the estimation of shock-standoff distance takes an important part in forecasting the cavity oscillation frequency.

4.3 Oscillation Amplitude and Velocity

Marquart [9], Sambamurthi [8], and Huebner [2] conducted experimental research on oscillation amplitude in flow of $M_\infty = 10$. The model is characterized by $D/D_n = 0.67$. The normalized amplitude by D_n is plotted in Fig. 13. The average values of amplitudes are from 6 to 12%. It is also noted that the average values of shock velocities are from 2 to 4% of U in the upstream and downstream, respectively, shown in Fig. 14.

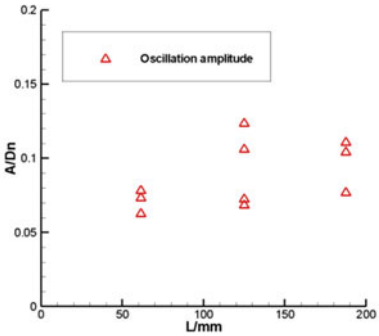

Fig. 13 Average of normalized upstream and downstream shock amplitudes [2, 8, 9]

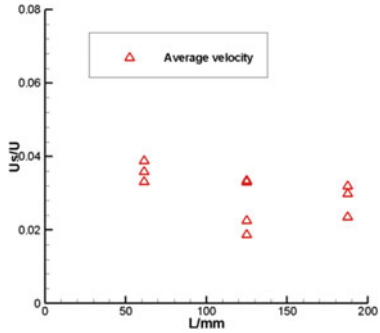

Fig. 14 Average of normalized upstream and downstream shock velocities [2, 8, 9]

5 Conclusions

A forecasting method has been developed for predicting shock-standoff distance of forward-facing cavity. Giving consideration on different shock shape for different geometric shapes, the forecasting method is divided into three cases to predict shock-standoff distance. Then, the adaptability and effectiveness of the method are validated based on plenty of experimental and numerical results as well as organ-pipe theory. What is more, the controversy on the forecasting equation of oscillation frequency is discussed and the authors take one side on this controversy.

Experiments have been conducted on a flat-head cylinder wedge with a forward-facing cavity at the tip of FD-14A shock tunnel. The forecasting results of shock-standoff distance are approximately equal to the experimental results. Furthermore, the specific distributions of shock amplitude and velocity are discussed.

References

1. Ladoon, D.W., Schneider, S.P., Schmisseur, J.D.: Physics of resonance in a supersonic forward-facing cavity. J. Spacecr. Rocket. **35**(5) (1998)

2. huebner, L.D., Utreja, L.R., Mach 10 bow-shock behavior of a forward-facing nose cavity. J. Spacecr. Rocket. **30**(3), 291–297 (1993)
3. Engblom, W.A., Goldstein, D.B., Ladoon, D.: Fluid dynamics of hypersonic forward-facing cavity flow. AIAA (1996)
4. Engblom, W.A., Yuceil, K.B., Goldstein, D.B.: Experimental and numerical study of hypersonic forward-facing cavity flow. J. Spacecr. Rocket. **33**(3), 353–359 (1996)
5. Yadav, R., Guven, U.: Aerothermodynamics of a hypersonic vehicles with a forward facing parabolic cavity at nose. J. Aerosp. Eng. **228**(10), 1863–1874 (2014)
6. Yadav, R., Guven, U.: Aerodynamic heating of a hypersonic projectile with forward-facing ellipsoid cavity at nose. J. Spacecr. Rocket. **52**(157–165) (2015)
7. Hartmann, J., Troll, B.: On a new method for the generation of sound waves. Phys. Rev. **20**, 719–727 (1922)
8. Sambamurthi, J.K., huebner, L.D., Utreja, L.R.: Hypersonic flow over a cone with nose cavity. In: AIAA 19th Fluid Dynamics, Plasma Dynamics and Lasers Conference, Hawaii. (1987)
9. Marquart, E.J., Grubb, J.P.: Bow shock dynamics of a forward-facing nose cavity. In: AIAA 11th Aerocoustics Conference, Sunnyvale. (1987)
10. Saravanan, S., Jagadeesh, G., Reddy, K.P.: Investigation of missile-shaped body with forward-facing cavity at Mach 8. J. Spacecr. Rocket. **46**(3) (2009)
11. Engblom, W.A., Goldstein, D.: Acoustic Analogy for Oscillations Induced by Supersonic Flow over a Forward-Facing Nose Cavity. In: 47th AIAA Aerospace Sciences Meeting Including The New Horizons Forum and Aerospace Exposition, Florida. (2009)
12. Billing, F.S.: Shock-wave shapes around spherical -and cylinderical-nosed bodies. J. Spacecr. Rocket. **4**(6), 822–833 (1967)
13. Wu, J.Z.Y.: An organ-pipe oscillation[R]. Imperial college of science and Technology London: 1984
14. Yuceil, K.B., Dolling, D.S.: Nose cavity effects on blunt body pressure and temperature at Mach 5. J. Thermophys. Heat Transf. **9**(4) (1995)
15. Yuceil, K.B., Dolling, D.S.: IR imaging and shock visualization of flow over a blunt body with a nose cavity. In: 34th Aerospace Sciences Meeting and Exhibit, Reno. (1996)
16. Engblom, W.A., Yuceil, B., Goldstein, D.B.: Hypersonic forward-facing cavity flow: an experimental and numerical study. In: 33rd Aerospace Sciences Meeting and Exhibit, Reno. (1995)
17. Juliano, T.J., Segura, R.: Starting issues and forward-facing cavity resonance in a hypersonic quite tunnel. In: 38th Fluid Dynamics Conference and exhibit, Seattle. (2008)
18. Segura, R: Oscillations in a Forward-Facing Cavity Measured Using Laser-Differential Interferometry in a Hypersonic Quiet Tunnel[D]], West Lafayette. Indiana: Purdue University, (2007)

Shock Interactions in Continuum and Rarefied Conditions Employing a Novel Gas-Kinetic Scheme

S. Colonia, R. Steijl and G. Barakos

Abstract Shock interactions can have a significant impact on heating rates and aerodynamic performance of hypersonic vehicles. The study presents different shock interactions in partially rarefied hypersonic flows predicted employing a recently developed gas-kinetic scheme for diatomic gases with rotational degrees of freedom. The new gas-kinetic schemes will be presented along with shock/wave boundary interactions as well as Edney Type IV shock–shock interactions. Various levels of rarefaction have been considered to highlight the effect of thermal relaxation between the translational and rotational modes. In addition, for the Edney test case, the imposed wall temperature on the shock-generating wedge and the cylinder surface has been varied, to evaluate the importance of the boundary layer thickness in the interaction region.

1 Introduction

The understanding of shock interactions is critical to the design of hypersonic vehicles since they can have a significant impact on both heating rates and aerodynamic performance affecting the requirements for vehicle control and thermal protection. The flow over deflected control surfaces may be dominated by shock wave/boundary layer interactions that can cause extensive separation, a laminar-to-turbulence transition and localised intense heating. A recent review of some of the key findings for shock wave/boundary layer interactions for laminar flows was presented in [1], where it was shown that mechanical and thermal loads over compression ramps depend strongly on ramp angle, wall temperature and geometric configuration. Furthermore,

S. Colonia (✉) · R. Steijl · G. Barakos
Aerospace Sciences Division, School of Engineering,
University of Glasgow, Glasgow, UK
e-mail: simone.colonia@glasgow.ac.uk

R. Steijl
e-mail: rene.steijl@glasgow.ac.uk

G. Barakos
e-mail: george.barakos@glasgow.ac.uk

K. Kontis (ed.), *Shock Wave Interactions*,
https://doi.org/10.1007/978-3-319-73180-3_8

the dependency of numerical predictions on grid resolution and the correctness of the employed physical and numerical modelling was addressed.

In the present work, shock interactions in partially rarefied hypersonic flows are considered. For the efficient simulation of such flows, a number of different approaches can be considered. One such approach involves hybrid techniques which couple Navier–Stokes methods with DSMC solvers or discrete-velocity methods (DVM) for kinetic Boltzmann equations. In these methods, the more expensive approach, DSMC or DVM, is employed only where needed and is coupled with a finite-volume scheme for the NS equations used where the flow is continuum. A hybrid technique couples two different simulation methods by means of information exchange between the parts of the flow domain. Recent works using these methods focused on rarefied high-Mach flow include [2, 3]. Early results for hybrid rarefied high-Mach simulations using the Multi-Physics Code (MΦC) used in the present work were reported in [4].

An alternative approach involves gas-kinetic schemes originally introduced as Navier–Stokes solvers, which more recently have been extended with a capability to resolve thermal non-equilibrium and flow rarefaction effects. In the present work, a recently developed gas-kinetic scheme for diatomic gas flows with rotational relaxation is employed in the analysis of flows with shock interactions. The strength of the gas-kinetic scheme lies in its capability to include the effect of collisions introducing a multi-scale effect which is missing in more commonly used Navier–Stokes schemes. Moreover, due to their nature, gas-kinetic schemes can predict flow fields with a certain degree of rarefaction enabling the computational analysis of shock interactions from the continuum to the rarefied regime without having to rely on different numerical methods. In gas-kinetic schemes, a finite-volume approach is used which reconstructs local kinetic problems around the cell interfaces in order to calculate the numerical fluxes. In contrast, more commonly used Roe or AUSM fluxes are based on approximations to a local continuum Riemann problem. In the present work, the local kinetic problem around the cell interfaces includes both convective and viscous contributions, while finite-volume methods employing more commonly used numerical flux methods, e.g. Roe or AUSM, for the convective fluxes typically employ a separate central difference-based discretisation of the viscous fluxes.

Among the gas-kinetic schemes available in the literature, a successful approach is represented by the BGK-NS method introduced by Xu [5], subsequently improved resulting in the Unified Gas-Kinetic Scheme (UGKS) by Xu and Huang [6] and extended to diatomic gas flows in [7]. The UGKS uses a finite-volume method where the numerical fluxes are based on the solution of the Shakhov model [8] for a monoatomic gas, or the Rykov model [9] for a diatomic gas with rotational non-equilibrium. Where the flow is under-resolved, by accounting for the pressure jump in the definition of the collision time, additional numerical viscosity is added resulting in a shock thickness of the order of the cell size. This allows the UGKS to simulate flows in both rarefied and continuum regimes. A further feature is the reconstruction and storage of the particle distribution functions around the cell faces, which are updated in time according to the considered kinetic model. It means that

the UGKS can deal with significant levels of flow rarefaction, but at a memory cost between that of Navier–Stokes gas-kinetic schemes and of discrete-velocity methods.

Recently, the authors developed a novel gas-kinetic scheme based on a Chapman–Enskog reconstruction of the kinetic problems around the cell interfaces which includes rotational relaxation consistent with the Rykov model, as published in [10]. The method does not store and update the particle distribution functions in state-space for each cell face, and it is therefore computationally more efficient than the UGKS, particularly in memory overhead. However, the Chapman–Enskog reconstruction limits the scheme to lower levels of rarefaction than the UGKS. Compared to earlier works of Xu and co-workers, the presented scheme is defined directly on the basis of kinetic models which involve a Prandtl number correction.

In the current work, an improved version of the gas-kinetic scheme presented by Colonia et al. [10] is used which involves a further efficiency improvement by replacing numerical evaluations of moments in state-space with analytically derived expressions. Furthermore, a modified GKS scheme is also considered in which equilibrium between the translational and rotational modes is assumed. Analysing the results of the different schemes will enable the assessment of the effect of thermal relaxation as well as the effect of changing Reynolds number which typically occurs when changing the Knudsen number for a fixed Mach number. The methods were designed for complex three-dimensional flow simulations, including flows around waverider geometries and moderate rarefaction levels, as shown in Fig. 1. For increasing Knudsen numbers, the translational temperature from the gas-kinetic scheme based on the Rykov model can be seen to deviate further from the results with the single-temperature gas-kinetic scheme, as could be expected. Considering the good computational efficiency of the gas-kinetic scheme derived from the Rykov model (RGKS), a major point of investigation is the determination of what level of flow rarefaction the results become inaccurate and a switch to more expensive

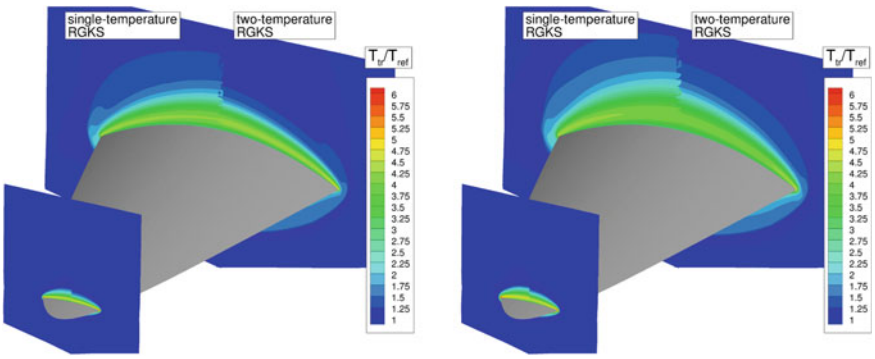

Fig. 1 Mach 8 flow around waverider with rounded leading edge. Translational temperature in two cross sections in RGKS simulations. RGKS model with rotational relaxation on right-hand side, single-temperature RGKS result on left-hand side. Two Knudsen numbers are shown, $Kn = 0.0005$ (left) and $Kn = 0.001$ (right) based on fuselage length

method such as DSMC or DVM would be needed. In the present work, the assessment of the schemes will first be considered for two-dimensional shock interaction test cases.

The new gas-kinetic schemes will be presented along with the application to hypersonic flows with shock/wave boundary interactions as well as hypersonic flow with Edney Type IV shock–shock interactions. Different levels of flow rarefaction are considered, highlighting the effect of thermal relaxation between the translational and rotational modes in the considered diatomic gases. Furthermore, the sensitivity of the shock interaction with respect the imposed wall temperature on the shock-generating wedge and the cylinder surface was considered, highlighting the importance of the boundary layer displacement thickness increase on the wedge.

2 Multi-physics Code

The methods used in the present work are built in the Multi-Physics Code (MΦC) under development at the University of Glasgow, described in [10, 11]. MΦC is a computational framework designed for simulations of complex flows, where different mathematical flow models are employed for different regions of the flow domain depending on the flow physics. For compressible flow applications, a cell-centred block-structured finite-volume method for the Navier–Stokes equations using the AUSM$^+$/up method for the convective fluxes forms the baseline model. For high-speed flows with thermodynamic non-equilibrium, the solver uses RGKS (gas-kinetic scheme based on the Rykov model), introduced in [10]. For more challenging flows at higher levels of flow rarefaction, discrete-velocity methods for the Shakhov and ES models are available for monoatomic gas flows, while the DVM uses the Rykov model or a poly-atomic ES model for diatomic gas flows. Considering the cost and memory requirement of the DVM, practical applications of high-speed flows involve hybrid simulations coupling of the DVM with the NS or RGKS solver. With improved gas-kinetic schemes as presented in [10], the extent to which the DVM needs to be used can be reduced in hybrid simulations and therefore achieve significant efficiency gains. In the present work, the emphasis is on simulations which use the RGKS in the entire computational domain.

3 Non-dimensional Rykov Model

A diatomic gas is considered at temperatures at which vibrational degrees of freedom are not significantly excited. Furthermore, we exclude extremely low temperatures, such that we can assume that rotational degrees of freedom can be considered fully excited. In this case, the particle distribution function $f(\mathbf{x}, \mathbf{c}, t, \zeta)$, which describes the state of the gas, will be a function not only of the spatial coordinate $\mathbf{x}$, the particle velocity $\mathbf{c}$ and the time t, but also of the rotational degrees of freedom ζ. The

Rykov model represents an extension of the Shakhov model where also rotational non-equilibrium is considered and has been proved to be a reliable kinetic approximation, up to the heat fluxes moments of the Boltzmann equation. Since the rotational degrees of freedom is considered fully excited, ζ is reduced by the model and a second distribution function is obtained. The non-dimensional distribution functions F_0 and F_1 are obtained from the dimensional distribution functions $\hat{F}_0$ and $\hat{F}_1$ as follows:

$$F_0 = \hat{F}_0 / \left(\rho_\infty (2RT_\infty)^{-3/2}\right) \; F_1 = \hat{F}_1 / \left(mRT_\infty \rho_\infty (2RT_\infty)^{-3/2}\right) \tag{1}$$

For the Rykov model written in terms of $F = mf$, we obtain

$$\begin{aligned}
&\frac{\partial F_0}{\partial t} + \mathbf{c}\frac{\partial F_0}{\partial \mathbf{x}} = \frac{F_0^{eq} - F_0}{\tau} \frac{\partial F_1}{\partial t} + \mathbf{c}\frac{\partial F_1}{\partial \mathbf{x}} = \frac{F_1^{eq} - F_1}{\tau} \\
&F_0^{eq} = \frac{1}{Z_r} F_0^r + \left(1 - \frac{1}{Z_r}\right) F_0^t F_1^{eq} = \frac{1}{Z_r} F_1^r + \left(1 - \frac{1}{Z_r}\right) F_1^t \\
&F_0^r = F_M(T)\Big[1 + \frac{8}{15}\omega_0 \frac{q_x^t}{p}\frac{c'_x}{T}\left(\frac{\mathbf{c}'^2}{T} - \frac{5}{2}\right)\Big] \\
&F_0^t = F_M(T_t)\Big[1 + \frac{8}{15}\frac{q_x^t}{p_t}\frac{c'_x}{T_t}\left(\frac{\mathbf{c}'^2}{T_t} - \frac{5}{2}\right)\Big] \\
&F_1^r = TF_M(T)\Big[1 + \frac{8}{15}\omega_0 \frac{q_x^t}{p}\frac{c'_x}{T}\left(\frac{\mathbf{c}'^2}{T} - \frac{5}{2}\right) + 4\omega_1(1-\delta)\frac{q_i^r c'_i}{pT}\Big] \\
&F_1^t = T_r F_M(T_t)\Big[1 + \frac{8}{15}\frac{q_x^t}{p_t}\frac{c'_x}{T_t}\left(\frac{\mathbf{c}'^2}{T_t} - \frac{5}{2}\right) + 4(1-\delta)\frac{q_i^r c'_i}{p_t T_r}\Big],
\end{aligned} \tag{2}$$

where the total collision time τ is expressed as μ_t/p_t with the viscosity determined from the translational temperature and F_M is the Maxwellian. In the present work, the values $\omega_0 = 0.5$ and $\omega_1 = 0.286$ and $\delta = 0.75$ are employed. Z_r is the collision number, representing the number of collisions between molecules required to force the rotational and translational motions towards equilibrium. In the recent literature, formulas for Z_r derived from data fitting, either from numerical or experimental results, have been employed. For the Rykov model, the collision number suggested by Rykov and co-workers is

$$\begin{aligned}
&Z_r^{Ryk.} = \frac{3}{4}\pi \frac{\psi(\tilde{T})}{\tilde{T}^{1/6}} \frac{9\tilde{T}}{\tilde{T} + 8} \frac{T_r}{T_t}\left[0.461 + 0.5581\left(\frac{T_r}{T_t}\right) + 0.0358\left(\frac{T_r}{T_t}\right)^2\right] \\
&\psi(\tilde{T}) = 0.767 + 0.233\tilde{T}^{-1/6}\exp\left(-1.17\left[\tilde{T} - 1\right]\right) \tilde{T} = T_t/T^*
\end{aligned} \tag{3}$$

$T* = 91.5\,\mathrm{K}$ is the characteristic temperature of the intermolecular potential for nitrogen. An alternative expression for $Z_r(T_t, T_r)$ derived from molecular dynamics simulations can be found in [12] as

$$Z_r^{Val.} = \left[a_1 \left(\frac{T_t}{1K}\right)^{1/4} + a_2 \left(\frac{T_t}{1K}\right)^{-1/4} - a_3 \left(\frac{T_t}{1K} - 1000\right)\right]\left[1 - b\left(1 - \frac{T_r}{T_t}\right)\right]$$

with $a_1 = 1.33868$, $a_2 = -6.19992$, $a_3 = -0.00107942$ and $0 < b \leq 1$. For the viscosity law, Rykov and co-workers suggest

$$\mu(T_t) = \mu(T^*)\frac{\tilde{T}^{2/3}}{\psi(\tilde{T})} \tag{4}$$

Alternatively, a simpler power law can be employed. In the present work, this power law was used exclusively, with an exponential factor of 0.72.

4 Gas-Kinetic Scheme Based on Rykov Model—RGKS

The present scheme is analytically defined on the basis of the Chapman–Enskog (CE) expansion of the non-dimensional Rykov model for diatomic gases. The derivatives of the equilibrium function and the time derivatives of the primitive variables are defined analytically employing the compatibility condition of the kinetic model for the latter. In previous works, e.g. [13], similar gas-kinetic schemes are defined using the CE solution of the BGK model with and without rotational non-equilibrium and a scaling of the energy numerical flux defined in [5] to correct the Prandtl number. Moreover, in those schemes, the required derivative is expressed in terms of Taylor series where the coefficient is calculated by means of properties of the employed BGK model. The proposed GKS, due to the use of CE expansion, is limited to near-continuum regions but is simpler than the UGKS methods presented in [6, 7]. For the present Rykov-based GKS solver, also this correction is defined fully analytically. Results for hypersonic partially rarefied flows with shocks using this correction were previously presented in [10], showing an improved agreement with experimental data for the obtained shock thickness and profiles.

From the non-dimensional reduced Rykov model (2), a system of equations for the vector of non-dimensional macroscopic variables $\mathbf{W_R} = (\rho, \rho\mathbf{c}, \frac{5}{2}\rho T + \rho c^2, \rho T_r)^T$ is obtained by taking moments $(1, \mathbf{c}, c^2, 0)^T$ and $(0, \mathbf{0}, 1, 1)^T$ and integrating over a time step Δt. The expressions for the numerical fluxes resulting from this step were previously described in detail in [10]. The moments involve integrations over the velocity space and in most general formulation published previously, numerical evaluation of these integrations was used. In the present work, analytical expressions for the velocity-space integrations were used, which further enhances the efficiency of the proposed gas-kinetic scheme. In the integration, upwinding in the velocity space is used. The full formulation is too long to be presented here. For illustration, the mass flux is presented here only. For the inviscid mass flux, we find

$$
\begin{aligned}
&F^{mass,inviscid} = \\
&\Big[\frac{\rho_l}{2}\Big(1+erf\big(\frac{u_{n,l}}{\sqrt{T_{t,l}}}\big)\Big)u_{n.l} + \frac{\rho_l}{2}\sqrt{\frac{T_{t,l}}{\pi}}\exp\big(-\frac{u_{n,l}^2}{T_{t,l}}\big)\Big]\Big(1-\frac{1}{Z_{r,l}}\Big) + \\
&\Big[\frac{\rho_l}{2}\Big(1+erf\big(\frac{u_{n,l}}{\sqrt{T_{eq,l}}}\big)\Big)u_{n.l} + \frac{\rho_l}{2}\sqrt{\frac{T_{eq,l}}{\pi}}\exp\big(-\frac{u_{n,l}^2}{T_{eq,l}}\big)\Big]\frac{1}{Z_{r,l}} + \\
&\Big[\frac{\rho_r}{2}\Big(1+erf\big(\frac{u_{n,r}}{\sqrt{T_{t,r}}}\big)\Big)u_{n.r} - \frac{\rho_r}{2}\sqrt{\frac{T_{t,r}}{\pi}}\exp\big(-\frac{u_{n,r}^2}{T_{t,r}}\big)\Big]\Big(1-\frac{1}{Z_{r,r}}\Big) + \\
&\Big[\frac{\rho_r}{2}\Big(1+erf\big(\frac{u_{n,r}}{\sqrt{T_{eq,r}}}\big)\Big)u_{n.r} - \frac{\rho_r}{2}\sqrt{\frac{T_{eq,r}}{\pi}}\exp\big(-\frac{u_{n,r}^2}{T_{eq,r}}\big)\Big]\frac{1}{Z_{r,r}}
\end{aligned}
\tag{5}
$$

The cell-face normal velocity component is u_n, while T_{eq} is the equilibrium temperature. The Prandtl number correction due to the Rykov model for the mass flux becomes

$$
\begin{aligned}
F^{mass,Pr,corr.} = \frac{8}{15}\Bigg[&\frac{\rho_l}{2}\sqrt{\frac{T_{t,l}}{\pi}}\exp\big(-\frac{u_{n,l}^2}{T_{t,l}}\big)\Big\{-\frac{q_{n,l}u_{n,l}}{2\rho_l T_{t,l}^2}\Big\}\Big(1-\frac{1}{Z_{r,l}}\Big) \\
&+\frac{\rho_l}{2}\sqrt{\frac{T_{eq,l}}{\pi}}\exp\big(-\frac{u_{n,l}^2}{T_{eq,l}}\big)\Big\{-\frac{q_{n,l}u_{n,l}}{2\rho_l T_{eq,l}^2}\Big\}\frac{\omega_0}{Z_{r,l}} \\
&-\frac{\rho_r}{2}\sqrt{\frac{T_{t,r}}{\pi}}\exp\big(-\frac{u_{n,r}^2}{T_{t,r}}\big)\Big\{-\frac{q_{n,r}u_{n,r}}{2\rho_r T_{t,r}^2}\Big\}\Big(1-\frac{1}{Z_{r,r}}\Big) \\
&-\frac{\rho_r}{2}\sqrt{\frac{T_{eq,r}}{\pi}}\exp\big(-\frac{u_{n,r}^2}{T_{eq,r}}\big)\Big\{-\frac{q_{n,r}u_{n,r}}{2\rho_r T_{eq,r}^2}\Big\}\frac{\omega_0}{Z_{r,r}}\Bigg]
\end{aligned}
\tag{6}
$$

where q_n is the heat flux associated with the translational motion normal to the cell interface. For the viscous fluxes, derived from the CE expansion around the local solution on the left-hand and right-hand side of the cell interface, we find

$$
\begin{aligned}
F^{mass,viscous} = \frac{\rho_l}{2}\sqrt{\frac{T_{t,l}}{\pi}}\exp\big(-\frac{u_{n,l}^2}{T_{t,l}}\big)\tau_l\Bigg[&-\frac{u_{n,l}}{T_{t,l}}\frac{\partial T_{t,l}}{\partial n} + \\
&\frac{T_{eq,l}-T_{t,l}}{2\tau_l Z_{r,l}T_{t,l}} + \Big(J_{11}^2-\frac{1}{3}\Big)\frac{\partial u_l}{\partial x} + \Big(J_{21}^2-\frac{1}{3}\Big)\frac{\partial v_l}{\partial y} \\
&+\Big(J_{31}^2-\frac{1}{3}\Big)\frac{\partial w_l}{\partial z} + J_{11}J_{21}\Big(\frac{\partial u_l}{\partial y}+\frac{\partial v_l}{\partial x}\Big) + \\
&J_{11}J_{31}\Big(\frac{\partial u_l}{\partial z}+\frac{\partial w_l}{\partial x}\Big) + J_{21}J_{31}\Big(\frac{\partial v_l}{\partial z}+\frac{\partial w_l}{\partial y}\Big)\Bigg]
\end{aligned}
\tag{7}
$$

$$-\frac{\rho_r}{2}\sqrt{\frac{T_{t,r}}{\pi}}\exp\left(-\frac{u_{n,r}^2}{T_{t,r}}\right)\tau_r\Bigg[-\frac{u_{n,r}}{T_{t,r}}\frac{\partial T_{t,r}}{\partial n}+\frac{T_{eq,r}-T_{t,r}}{2\tau_r Z_{r,r}T_{t,r}}+\left(J_{11}^2-\frac{1}{3}\right)\frac{\partial u_r}{\partial x}+\left(J_{21}^2-\frac{1}{3}\right)\frac{\partial v_r}{\partial y}+\left(J_{31}^2-\frac{1}{3}\right)\frac{\partial w_r}{\partial z}+J_{11}J_{21}\left(\frac{\partial u_r}{\partial y}+\frac{\partial v_r}{\partial x}\right)+J_{11}J_{31}\left(\frac{\partial u_r}{\partial z}+\frac{\partial w_r}{\partial x}\right)+J_{21}J_{31}\left(\frac{\partial v_r}{\partial z}+\frac{\partial w_r}{\partial y}\right)\Bigg]$$

where $J_{11},\ldots,J_{31}$ represent mesh transformation metrics in the general curvilinear mesh formulation used here. The source term is due to the rotational relaxation. The only non-zero contribution is for the last equation in the system, governing the rotational energy. For the rotational energy equation, the relaxation term has the following form for cell i and integration from time level n to $n+1$:

$$\frac{\rho(T|_i^{n+1}-T_r|_i^{n+1})}{Z_r\tau_i^{n+1}}+\frac{\rho(T|_i^{n}-T_r|_i^{n})}{Z_r\tau_i^{n}}, \tag{8}$$

where the trapezoidal rule was employed in the time integration. It is important to note that here the difference between the local equilibrium temperature $T|_i$ and the rotational temperature $T_r|_i$ in cell i is used, while many studies consider a relaxation term of the type introduced by Jeans–Teller involving translational and rotational temperatures. For a well-resolved flow, the exponential terms in the flux equations are small and represent numerical dissipation terms. Using the Rykov model as the basis for the flux formulation, it shows that the Prandtl number correction in Eq. (6) combines with the heat flux related terms in the viscous flux to consistently represent a Prandtl number correction for the part of the heat flux associated with the translational energy.

Based on the RGKS with rotational relaxation, a single-temperature version was also implemented in which it is assumed that the translational and rotational temperatures are in equilibrium, which significantly reduces the complexity of the scheme as can be seen from Eqs. (5), (6) and (7). For the Rykov kinetic model, the effective Prandtl number for continuum conditions can be derived from a Chapman–Enskog expansion. For the Rykov gas-kinetic scheme, the Prandtl can be similarly obtained in the limit of the translational and rotational temperatures approaching a common equilibrium temperature. The Prandtl number is defined as

$$\frac{1}{Pr}=\frac{5}{7}\left[\frac{3}{2+\frac{1-\omega_0}{Z_r}}+\frac{2/5}{\delta+\frac{(1-\delta)(1-\omega_1)}{Z_r}}\right] \tag{9}$$

which shows that for the values used in the present work, i.e. $\omega_0=0.5$, $\omega_1=0.286$ and $\delta=0.75$, the Prandtl number attains a value of 0.71 for $Z_r=5$. In the

single-temperature version of the gas-kinetic scheme, $Z_r = 5$ is used for the flow state at left-hand and right-hand side of the cell interface.

In the present work, solid wall boundary conditions are modelled using diffuse walls with full accommodation.

5 Shock Wave/Boundary Layer Interaction

The first test case considered is the laminar flow over a compression ramp with a sharp leading edge. The main point of interest here is the effect of the flow rarefaction on the shock wave/boundary layer interaction. The test case considered was conducted at Calspan-UB Research Center (CUBRC), with a free-stream Mach number of 14.1 and a Reynolds number of 236,200 per metre and a ramp angle of 15°. The free-stream temperature was 88.88 K and a wall temperature was 297.22 K. The viscous interaction parameter at the plate/ramp junction is large and for the ramp angle considered, the flow in the experiment stays attached. For larger ramp angles, a separation bubble is formed which is confined by separation and re-attachment shocks, as discussed in detail by Marini [1].

The Knudsen number for this test case is $\mathrm{Kn} = 8.85 \times 10^{-5}$ for a metre reference length as tested at CUBRC. In the present work, a more rarefied condition is also considered, obtained by scaling down the flow length scale by a factor of two while leaving the inflow conditions unchanged. This doubles Knudsen number and halves the Reynolds number. For this test case, a block-structured mesh with 68 blocks and a total of 10^6 cells in 2D was employed.

For the test conditions, the RGKS method with rotational relaxation as well as the version with a single-temperature assumption was used to simulate the flow over the compression ramp. Figure 2 shows the wall pressure (scaled with the free-stream pressure) for these two simulations, compared with the experimental data as well

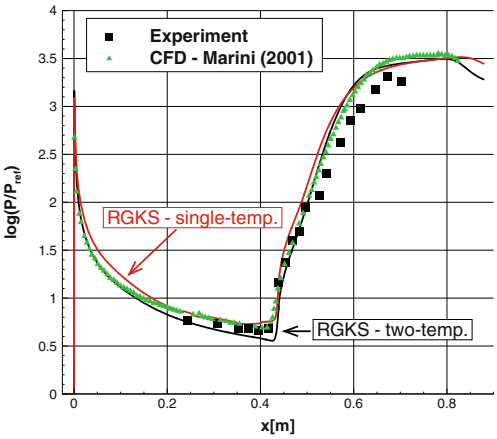

Fig. 2 Compression ramp (CUBRC) – $M_\infty = 14.1$, $Re_\infty/m = 236{,}200$ and $T_w/T_\infty = 3.344$. Comparison of wall pressure (scaled with free-stream pressure) for RGKS solver with experimental data as well as CFD results from Marini (2001)

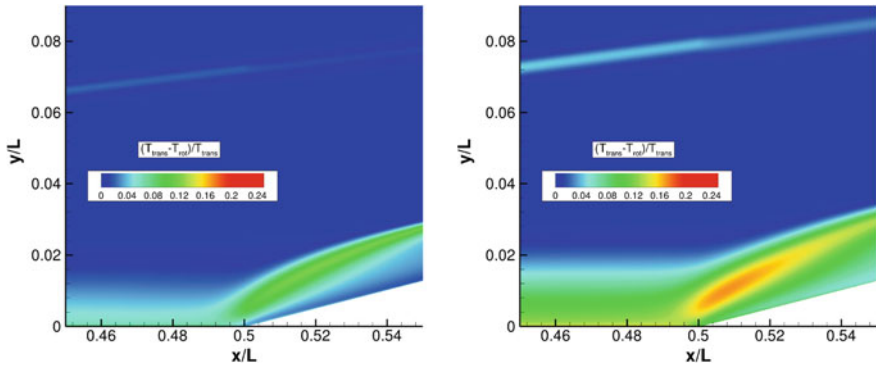

Fig. 3 Compression ramp (CUBRC) – $M_\infty = 14.1$ and $T_w/T_\infty = 3.344$. Difference in translational and rotational temperature for RGKS simulations at two Knudsen numbers. Flow at experimental test condition, $Kn = 8.85 \times 10^{-5}/\text{m}$ (left) and flow at double Knudsen number (right)

as CFD results from [1]. It can be seen that the proposed RGKS model (with rotational relaxation) generally produces results in better agreement with the experiments than the single-temperature version of the solver. Also, the agreement with the CFD results is generally better. From this comparison, it appears that despite the relatively small value of the Knudsen number involved in this test, the inclusion of rotational relaxation as well as a variable rotational collision number in the simulation leads to a more accurate representation of the flow for the gas-kinetic schemes.

The significant contribution from the rotational relaxation can also be seen in the top plot of Fig. 3, where the difference between the translational and rotational temperatures in the simulation at the Knudsen of the experiment is shown in the vicinity of the plate/ramp junction. The strongest deviation from thermal equilibrium can be observed in the shock wave/boundary layer interaction region on the ramp. However, a smaller but still significant relaxation takes places in the boundary layer leading up to the shock interaction. This may largely explain the difference in surface pressure between the full RGKS model and the single-temperature version in Fig. 2.

In the single-temperature version, a collision number $Z_r = 5$ was imposed to fix the Prandtl number to 0.711. For the RGKS results, the Z_r from the Valentini model as used in the simulations are shown in Fig. 4. In the boundary layers, the collision number is markedly different from 5, which would further explain differences in the boundary layer development and wall pressures between the RGKS model and its single-temperature version.

Figure 5 shows a comparison of the scaled pressure in the flow field at the conditions of the experiment for the RGKS with rotational relaxation and results from the single-temperature variant of the RGKS. The shock wave generated by the flat plate and its position can be seen to be different in both models due to the different boundary layer developments along the flat plate. The pressure in the interaction region is also significantly different with a stronger pressure rise along the ramp for the single-temperature model.

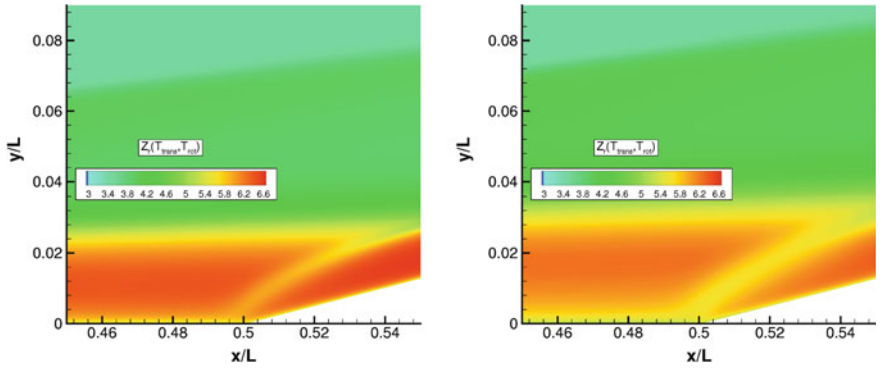

Fig. 4 Compression ramp (CUBRC) – $M_\infty = 14.1$ and $T_w/T_\infty = 3.344$. Rotational collision number for RGKS simulations. Flow at experimental test condition (left) and flow at double Knudsen number (right)

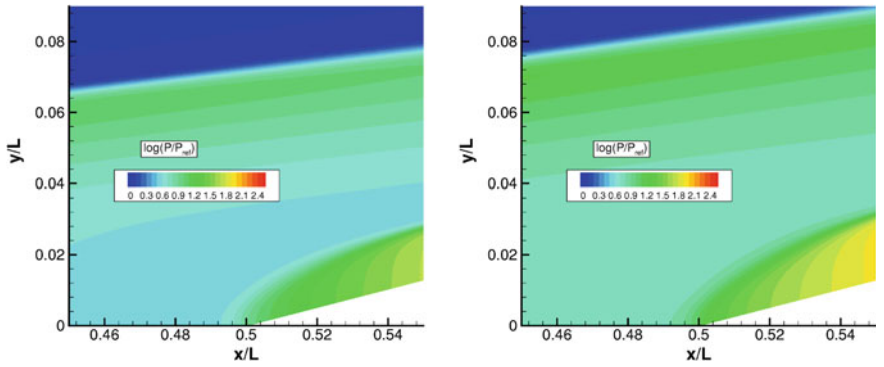

Fig. 5 Compression ramp (CUBRC) – $M_\infty = 14.1$ and $T_w/T_\infty = 3.344$. Logarithm of scaled pressure (free-stream pressure used as reference) in shock interaction region. RGKS results with rotational relaxation (top) and single-temperature RGKS result (bottom)

To assess the sensitivity of the wall pressure to the Knudsen number in this flow, Fig. 6 presents a comparison of three sets of results obtained using the RGKS model (with thermal relaxation). The different results are for different Knudsen numbers: the first result is at half the Knudsen number of the experiment, the second result was obtained for the Knudsen number of the experiment and the third result for a Knudsen number increased by two relative to the experiment. For reference, the experimental data is also shown in the figure. Since the Knudsen number changes were created by scaling the length scale of the flow, the Reynolds numbers will also be different for the simulation results. The increased Knudsen number simulation corresponds to the lowest Reynolds number. As could be expected, the wall pressure is already significantly different at the flat plate as a result of the different rate of growth of the boundary layer thickness, leading to a different in the shock wave/boundary layer interaction and the subsequent re-attachment.

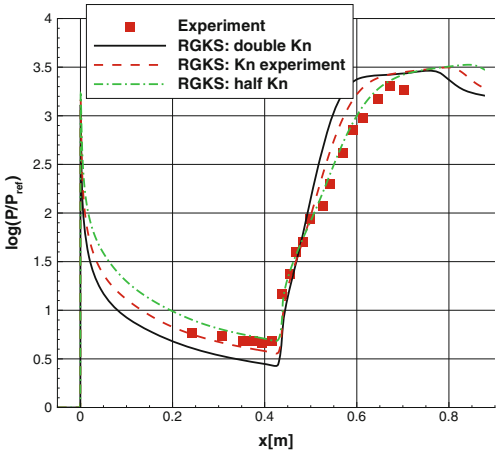

Fig. 6 Compression ramp (CUBRC) – $M_\infty = 14.1$ and $T_w/T_\infty = 3.344$. Comparison of wall pressure (scaled with free-stream pressure) for RGKS solver for different Knudsen numbers in simulation. For reference, experimental data (at $Re_\infty/m = 236{,}200$) also shown

From the results presented here, it follows that the strongest thermal relaxation effects result from the difference boundary layer development along the flat plate, which then creates an effect on the shock interaction. The boundary layer on the ramp is less affected by thermal relaxation effects, as a result on the increased density of the flow downstream of the shock and therefore locally small Knudsen number.

6 Edney Type IV Shock Interaction

The second test case considered is the Edney type IV interaction investigated experimentally at ONERA Chalais-Meudon as described by Pot et al. [14]. The tests were conducted in the R5Ch blowdown tunnel resulting in a free-stream Mach number of 9.95, free-stream temperature of 52.5 K and free-stream pressure of 5.9 Pa. The Reynolds number is 166,000/m, and the circular cylinder in the test had a radius of 0.008 m. A ramp at 20° angle was placed upstream of the cylinder to create an Edney type IV shock interaction. A complicating factor was the ramp extending for 0.050 m only followed by a flat plate giving rise to a Prandtl–Meyer expansion which in turn curves the oblique shock generated by the ramp before interacting with the bow shock of the cylinder. For this test case, a block-structured mesh with 76 blocks and a total of 10^6 cells in 2D was employed for the initial results obtained with the RGKS method. Three different Knudsen numbers were considered. The first simulation was conducted at the conditions in the ONERA experiment, while two further simulations involved a scaling down of the flow length scale by a factor of 2 and 4 while maintaining the free-stream conditions. For Knudsen number at experimental

conditions and two increased Knudsen numbers, Fig. 7 shows the difference in translational and rotational temperatures in the interaction region ahead of the cylinder. As can be expected, the rotational energy relaxation effect is more pronounced for the increased Knudsen number conditions. The plots show the extent of thermal non-equilibrium in the main features of the flow field, i.e. the strong bow shocks as well as the lambda shock, jet expansion and normal shock just before the jet impinges on the surface. Figure 8 compares the scaled wall pressure on the cylinder as computed with the RGKS method with the experiments from ONERA as well as the previous CFD result from [15]. It can be seen that the agreement of the present results with the experiment is satisfactory in terms of pressure peak and location, with a better agreement than the results from [15]. The convergence behaviour of the current steady-state simulations suggests some flow unsteadiness. This unsteadiness as well as the relatively large pressure tap used in the experiment could partially explain the discrepancy in pressure peak. The figure also shows the effect of the Knudsen number, an increase in Knudsen number (and the associated decrease in Reynolds number) reduces the peak pressure pressure value on the wall as well as moving its location. In addition to the dependency of the shock interaction on the Knudsen number, the sensitivity of the flow field with respect to the imposed wall temperatures was investigated. At the experimental conditions, the wall temperature on the shock-generating wedge as well as the cylinder surface was assumed to be 5.71 times the free-stream temperature. For the selected experimental setup, a strong type IV interaction was achieved. Here, the experimental setup in terms of geometry was maintained in the simulations. However, the imposed wall temperature was reduced in steps to 4.5, 3.5 and finally 2.5 times the free-stream temperature. For two different wall temperatures in the simulations, Fig. 9 shows Mach number contours in the vicinity of the shock interaction ahead on the cylinder. It can be see that an important effect is the slightly decreased oblique shock angle for reduced wall temperatures, which can be directly attributed to the reduced growth rate of the boundary layer on the shock-generating wedge, i.e. a reduced boundary layer displacement effect is present for lower wall temperatures. A second effect of the lower wall temperature is the reduced shock stand-off distance from the cylinder, although this effect is relatively small. Clearly, both effects combined lead to a significantly changed shock interaction with the type IV interaction pattern gradually disappearing for reduced wall temperatures. This can clearly be observed in the wall pressures on the cylinder surface shown in Fig. 10 for the different wall temperatures. Clearly, the reduced oblique shock angle moves the interaction region downwards, i.e. towards the negative angles, while the interaction loses strength with decreasing wall temperature. From these results, it would follow that for the reduced wall temperature conditions, the shock interaction intensity could be increased again by moving the shock-generating wedge slightly forward. The presented results clearly demonstrate the strong dependency of the shock interaction on both the levels of flow rarefaction and imposed wall temperatures. In both cases, a significant part of the sensitivity is the result of the changes in oblique shock location when the wedge-cylinder geometry is left unchanged.

The presented simulation results for the Edney type IV interaction case were obtained using the Rykov model for the rotational collisional model, as defined in

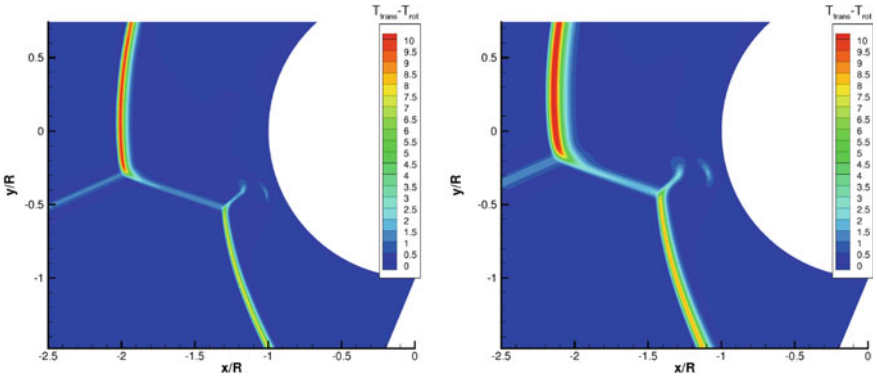

Fig. 7 Edney type IV interaction – $M_\infty = 9.95$ and $T_w/T_\infty = 5.71$. Difference in translational and rotational temperature for RGKS simulations at two Knudsen numbers. Flow at experimental test condition (left) and flow at double Knudsen number (right)

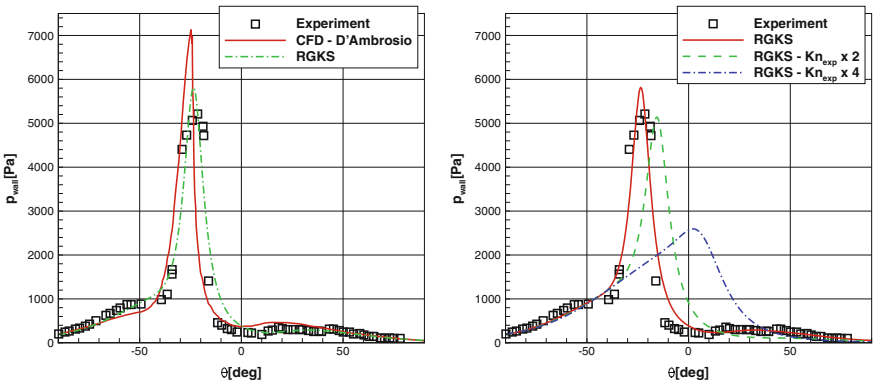

Fig. 8 Edney type IV interaction (experiment at ONERA) – $M_\infty = 9.95$ and $T_w/T_\infty = 5.71$. Comparison of wall pressure on cylinder (scaled with free-stream pressure) computed with RGKS solver compared with experiments and CFD result from D'Ambrosio (top). Comparison of Knudsen number effect on RGKS solution (bottom)

Eq. (3). The local value of the rotational collision number has a direct effect on the effective Prandtl number in the continuum limit, as can be seen from Eq. (9), as it is a function of translational and rotational temperatures. As discussed previously, a value of 5.0 would give a Prandtl number typically used in a CFD simulation (0.71). One important aspect of the RGKS solver is therefore its ability to model the gas dynamics at a range of conditions for which the constant Prandtl number assumption is no longer valid, using empirical models or molecular dynamics derived model for the rotational collision number.

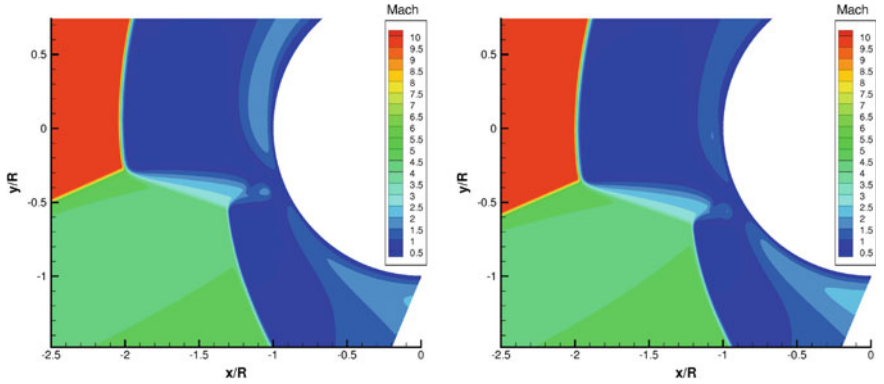

Fig. 9 Edney type IV interaction – $M_\infty = 9.95$ and model at experimental scale. Mach number contours from RGKS simulations. Different wall temperatures on wedge and cylinder. Flow at experimental test condition, i.e. $T_w/T_\infty = 5.71$ (left) and flow field for $T_w/T_\infty = 3.5$ (right)

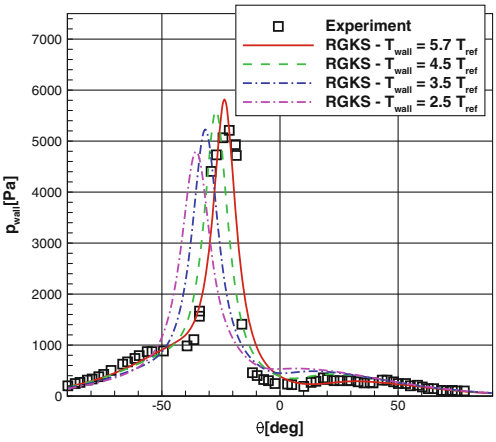

Fig. 10 Edney type IV interaction (experiment at ONERA) – $M_\infty = 9.95$. Comparison of wall pressure on cylinder (scaled with free-stream pressure) computed with RGKS solver for different wall temperatures imposed on wedge and cylinder compared with experiments (at $T_w/T_\infty = 5.71$). Knudsen number in RGKS solution matches that in experiment

7 Conclusions

The shock wave/boundary layer interaction on a compression ramp in laminar hypersonic flow was investigated using a gas-kinetic scheme derived from the Rykov kinetic model. The effect of flow rarefaction on the shock interaction region and the wall pressure distribution was analysed showing marked differences between the computational model results including rotational relaxation and a simplified approach assuming a single temperature. For the considered conditions, the Knudsen numbers were relatively low. However, in the boundary layer along the flat plate, the effect of thermal non-equilibrium was still significant. On the ramp, the boundary layer was less affected by thermal equilibrium effects. The thermal relaxation effect on the wall pressure on the ramp was mainly due to the altered interaction

pattern resulting from the different boundary layer developments along the flat plate when considering rotational relaxation. Furthermore, the Edney type IV interaction in a hypersonic flow was studied using the RGKS method. The sensitivity of the wall pressure peak and location with increasing Knudsen number was investigated as well as the extent of rotational relaxation in the interaction region. In future works, more detailed investigation of the hypersonic flows with Edney type IV interactions will be conducted. Furthermore, work on hybrid simulations using the gas-kinetic schemes presented here coupled with the DVM method for the Rykov kinetic model is also ongoing.

Acknowledgements The majority of the results presented were obtained using the EPSRC funded ARCHIE-WeSt High Performance Computer (https://www.archie-west.ac.uk). EPSRC grant no. EP/K000586/1.

References

1. Marini, M.: Analysis of hypersonic compression ramp laminar flows under sharp leading edge conditions. Aerosp. Sci. Technol. **5**, 257271 (2001)
2. Deschenes T., Boyd, I.: Extension of a modular particle-continuum method to vibrationally excited, hypersonic flows. AIAA J. **49**(9) (2011)
3. Degond, P., Dimarco, G., Mieussens, L.: A multiscale kinetic-fluid solver with dynamic localization of kinetic effects. J. Comput. Phys. **229**, 4907–4933 (2010)
4. Steijl, R., Barakos, G.: Computational fluid dynamics of partially rarefied flows with coupled kinetic Boltzmann/Navier-Stokes methods. In: ECCOMAS 2012, 10–14 Sept, Vienna, Austria (2012)
5. Xu, K.: A gas-kinetic BGK scheme for the Navier-Stokes equations and its connection with artificial dissipation and Godunov method. J. Comput. Phys. **171**, 289–335 (2001)
6. Xu, K., Huang, J.-C.: A unified gas-kinetic scheme for continuum and rarefied flows. J. Comput. Phys. **229**, 7747–7764 (2010)
7. Liu, S., Pubing, Y., Xu, K., Zhong, C.: Unified gas-kinetic scheme for diatomic molecular simulations in all flow regimes. J. Comput. Phys. **259**, 96–113 (2014)
8. Shakhov, E.: Generalization of the Krook kinetic relaxation equation. Mekhanika Zhidkosti i Gaza **3**(5), 142–145 (1968)
9. Rykov, V.: A model kinetic equation for a gas with rotational degrees of freedom. Fluid Dyn. **10**(6), 959–966 (1975)
10. Colonia, S., Steijl, R., Barakos, G.: Kinetic models and gas kinetic schemes for hybrid simulation of partially rarefied flows. AIAA J. **54**, 1264–1276 (2016)
11. Steijl, R., Barakos, G.: Coupled Navier-Stokes-molecular dynamics simulations using a multi-physics flow simulation framework. Int. J. Numer. Methods Fluids **62**, 1081–1106 (2010)
12. Valentini, P., Zhang, C., Schwartzentruber, T.: Molecular dynamics simulation of rotational relaxation in nitrogen: implications for rotational collision number models. Phys. Fluids **24**(106101), 1–23 (2012)
13. Xu, K., He, X., Cai, C.: Multiple temperature kinetic model and gas-kinetic method for hypersonic non-equilibrium flow computations. J. Comput. Phys. **227**, 6779–6794 (2008)
14. Pot, T., Chanetz, B., Lefebvre, M., Bouchardy, P.: Fundamental study of shock-shock interference in low density flow: flowfield measurements by DLCARS, ONERA TP 1998-140, July 1998
15. D'Ambrosio, D.: Numerical prediction of laminar shock/shock interactions in hypersonic flow. J. Spacecr. Rocket. **40**(2), 153–161 (2003)

Ballistic Range Experiment of Shock Stand-Off Distance for Spheres in Air with Flight Speeds Between 5.08 and 6.49 km/s

Liao Dongjun, Sen Liu, Hexiang Jian, Xie Aimin, Zonghao Wang and Jie Huang

Abstract To measure the shock stand-off distance for spheres with flight speeds above 5 km/s in air and provide experimental data for validation of theory and numerical methods, measurement of shock stand-off distance for hypersonic sphere has been conducted in the hypervelocity ballistic range of China Aerodynamic Research and Development Center. The measurement was made for spheres with diameters of 8, 10, 12 and 15 mm, flight speeds between 5.08 and 6.49 km/s, and ambient pressures between 1.5 and 6.3 kPa. The shock stand-off distance was measured using transient shadowgraph and schlieren. The measurement error was analyzed and found to be between about ±3% and ±8%. Under present test conditions, the flow near the stagnation point is speculated to be primarily nonequilibrium. The shock stand-off distance near stagnation point increases as the binary scaling parameter ρR increases. The data match well with previous investigations of similar conditions. Different values of ρR may have different influence on the state of the flow with different speed near the stagnation point.

1 Introduction

The distance between the detached shock and the model surface is known as the shock stand-off distance. During the hypersonic flight of space vehicles in the atmosphere, chemical reactions of different species occur in the shock layer due to the high temperature, which in turn changes the thickness of the shock layer. Thus, the shock stand-off distance to some extent indicates the degree of thermochemical nonequilibrium [1]. Spheres are commonly used models for theoretical, numerical and experimental research of the shock stand-off distance. Not being able to correctly predict the shock stand-off distance over a sphere means not being able to correctly describe the shock shape and pressure distribution over a flying object, which has an impact on the prediction of aerodynamic characteristics of a flying body in general [2].

L. Dongjun · S. Liu (✉) · H. Jian · X. Aimin · Z. Wang · J. Huang
China Aerodynamics Research and Development Center,
Hypervelocity Aerodynamics Institute, Mianyang 621000, People's Republic of China
e-mail: liusen@cardc.cn

K. Kontis (ed.), *Shock Wave Interactions*,
https://doi.org/10.1007/978-3-319-73180-3_9

The study on the shock stand-off distance over a sphere is fundamental and important for the high temperature real-gas effect research and hypersonic computational fluid dynamics validation, and therefore reliable experimental data is needed.

Many experiments have been carried out to obtain more accurate data of the shock stand-off distance. High-enthalpy pulse wind tunnel is one of the commonly used test facilities [3–6]. Belouaggadia et al. [7] measured the shock stand-off distance for spheres in air with the flight speeds between 2.5 and 4 km/s in the wind tunnel and compared experimental results with numerical results, showing that the two-temperature model underestimates the shock stand-off distance by about 10.

Ballistic range, on the other hand, is a facility in which a model is launched into quiescent gas at required speed and flies freely in the test section. With the initial test conditions being properly controlled, real flight speeds, Reynold numbers and high-enthalpy environment can be correctly simulated [8]. The experimental data measured in a ballistic range is free from the problem of the chemical reaction of the incoming flow and therefore is more reliable [9], making it an ideal facility for measurement of the shock stand-off distance over hypersonic spheres.

Such measurements have been conducted by Lobb [10] in 1960s but the accuracy was limited by the flowfield visualization technique at that time and oil vapor contamination in the test gas [11]. One of the more recent measurements was made by Nonaka et al. [11] in a ballistic range in the intermediate hypersonic regime. The shock stand-off distance was measured for hemispheres with the nose radius of 7, 14 and 15 mm, flight speeds between 2.44 and 3.85 km/s and ambient pressures between 5.6×10^2 and 2.0×10^4 Pa. Shadowgraph and schlieren were used to visualize the flowfield. The results show the distinct differences of shock stand-off distances among the frozen, nonequilibrium and equilibrium flows in the intermediate hypersonic regime (Fig. 1). The measured shock stand-off distance gradually approaches the equilibrium result toward the downstream. Nonaka's data is typical in theintermediate hypersonic regime and has been used as validation for several numerical calculations [12–14].

Liu et al. [15] measured the shock stand-off distance for spheres with the diameter of 12 mm, flight speeds between 5.10 and 5.57 km/s and ambient pressures between 1.3×10^3 and 11.2×10^4 Pa in a ballistic range. Shadowgraph and interferogram were used to visualize the flowfield. The results show that the flow near the stagnation point is nonequilibrium, while in the rest of the regime it is near equilibrium (Fig. 2) [16]. Related data were used to validate the accuracy of a nonequilibrium computational code [17].

The major limitations of ballistic range experiments are small model scales and limited flowfield measurement methods [18]. Previous ballistic range experimental data of the shock stand-off distance over spheres mainly focus on the intermediate hypersonic regime with flight speeds between 2.5 and 4 km/s. Data for higher flight speeds is relatively insufficient. To obtain clearer images of the detached shock and acquire reliable shock stand-off distance data for spheres with higher flight speeds, measurements of the shock stand-off distance for spheres with flight speeds above 5 km/s have been conducted in the hypervelocity ballistic range of China Aerodynamics Research and Development Center (CARDC).

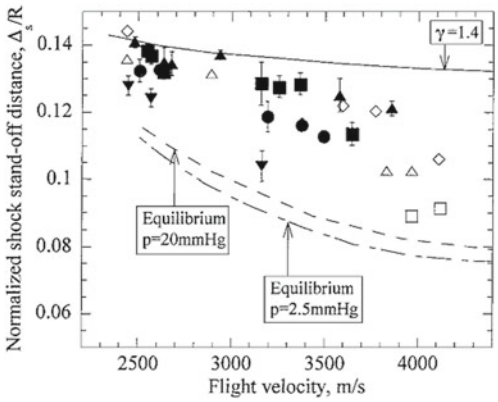

Fig. 1 Normalized shock standoff distance for sphere of Nonaka's experiment

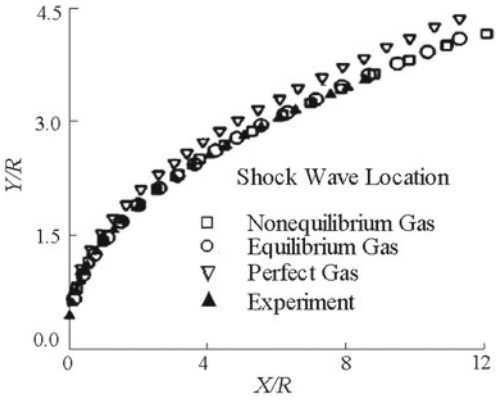

Fig. 2 Comparison of shock wave location of Liu Jun's experiment

2 Test Facilities and Methods

2.1 Ballistic Range Facilities

The experiment was conducted in the Aero-physics Range and the Hyper Velocity Impact Range [19] of CARDC, as shown schematically in Fig. 3. Models are covered with sabots and accelerated to required speeds by the 25 mm light gas gun of the Aero-physics Range and 16 mm light gas gun of the Hyper Velocity Impact Range. The speed measurement and control system is used to measure the flight speeds of models by the time they fly pass two laser beams and provide trigger signals for imaging system. The chamber system, which consists of detonation section and test section, provides space for sabot separation and shock stand-off distance measurement. The vacuum system provides required ambient pressure for experiment. Imaging system is used to visualize the flowfield and obtain images of detached shock over models. Figure 4 shows the photograph of the Aero-physics Range of CARDC.

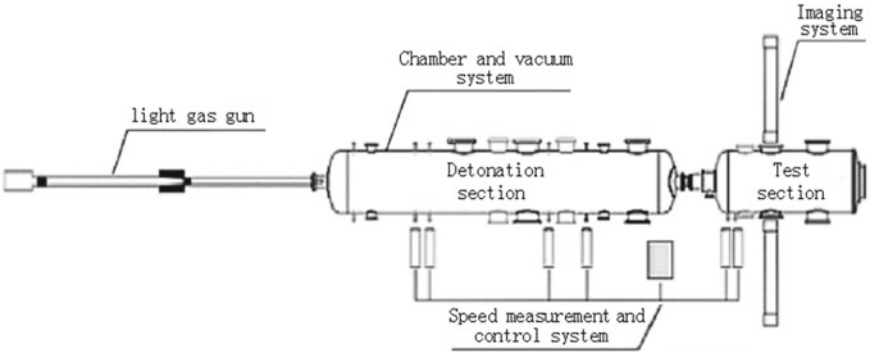

Fig. 3 Shematic of the ballistic range

Fig. 4 Aero-physics Range of CARDC

2.2 Imaging Methods

Transient shadowgraph and schlieren [20] were used for the imaging system in order to investigate the imaging quality of both methods under present test conditions. The light source is a YAG laser with a 10 ns pulse duration, which is capable for detached shock imaging of spheres with flight speeds above 5 km/s.

3 Test Models and Conditions

3.1 Test Models

Present models were spheres made of alumina and aluminum. The former benefit from smaller diameter error which can help to reduce the measurement error, and the latter can hold higher launch overload. Therefore the alumina spheres were used in Aero-physics Range with lower launch overload and the aluminum spheres were

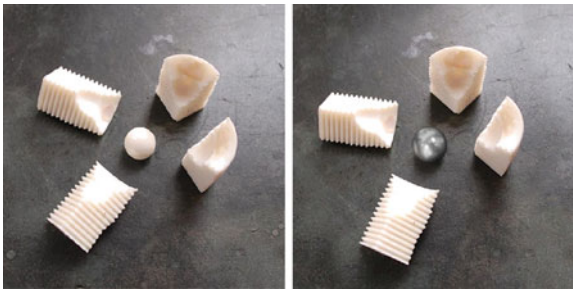

Fig. 5 Test models and sabots, Left: alumina sphere, Right: aluminum sphere

Table 1 Parameters of the test models

Sphere	Material	Diameter (mm)	Diameter error (mm)	Mass (g)
A	Alumina	8	$< \pm 0.01$	1.1
B	Alumina	10	$< \pm 0.01$	2.1
C	Alumina	12	$< \pm 0.01$	3.6
D	Alumina	15	$< \pm 0.01$	6.9
E	Aluminum	10	± 0.03	1.5

used in Hyper Velocity Impact Range with higher launch overload. The spheres were covered with separable sabots as shown in Fig. 5. Parameters of every kind of spheres are summarized in Table 1.

3.2 Test Conditions

Conditions of present experiment were chosen according to the binary scale parameter ρR similarity. ρR is an important parameter for nonequilibrium process which is involved with two-body reactions. The degree of thermochemical is characterized by the Damköhler number (Dm), which is in proportional to the product of freestream density ρ and model radius R. Meanwhile in hypersonic similarity experiment flow and real flow are supposed to have same Reynolds number (Re), which is also proportional to the product of ρ and R. This finally makes ρR identical. Therefore in ballistic range experiments Dm and Re of different flight conditions can be reproduced by changing ρR with different ambient pressure and model radius [11]. For present experiment, values of ρR of 1.3×10^{-4}, 2.0×10^{-4} and 3.0×10^{-4} kg/m^2 were chosen. Ambient pressures were calculated by the following formula:

$$P_0 = \rho R_{air} T_\infty \tag{1}$$

where P_0 is the ambient pressure of the test section. ρ is the required test gas density determined by chosen ρR . R_{air} is the gas constant of air. T_∞ is the temperature of the test section, which was about 296 K. For chosen ρR, ambient pressures of test section were calculated to be between 1.5 and 6.3 kPa. The flight speeds were chosen to be between 5.1 and 6.5 km/s. In order to compare with Nonaka's data, one test with flight speed between 2.5 and 4 km/s and $\rho R = 2.0 \times 10^{-4}$ kg/m^2 was also planned.

4 Measurement Methods and Error Analysis

Shock stand-off distance for spheres of present experiment was measured based on the shadowgraph and the schlieren of flowfield as schematically shown in Fig. 6. Number of pixels of the sphere diameter is measured along vertical axis of symmetry (VL) as Px_1. Number of pixels of the distance between outer edge of the shock layer and sphere nose is is measured along horizontal axis of symmetry (HL) as Px_2. Then the shock stand-off distance (Δ) can be related to the sphere diameter (D) as follows:

$$\frac{D}{Px_1} = \frac{\Delta}{Px_2} \tag{2}$$

Therefore we have:

$$\Delta = \frac{Px_2}{Px_1} D \tag{3}$$

According to propagation of error, the measurement error of shock stand-off distance is:

$$E = \left| -\frac{Px_2}{Px_1^2} D \right| \Delta Px_1 + \left| \frac{1}{Px_1} D \right| \Delta Px_2 + \left| \frac{Px_2}{Px_1} \Delta D \right| \tag{4}$$

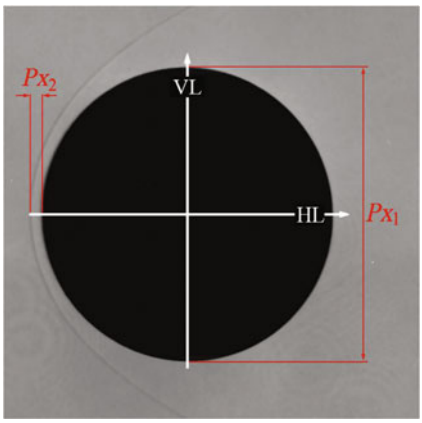

Fig. 6 Schematic of measurement method of shock stand-off distance for spheres

where ΔD is the error of sphere diameter, ΔPx_1 and ΔPx_2 are error of measured Px_1 and Px_2 respectively. For further analysis, Δ and E are normalized by sphere radius as Δ/R and E/R.

5 Results and Discussions

Results of shock stand-off distances of present experiment are summarized in Table 2. In total 14 results with flight speed between 5.08 and 6.49 km/s and 1 comparison result with flight speed of about 2.69 km/s were obtained. The errors of measured shock stand-off distances with flight speed above 5 km/s are basically between ±3% and ±8%.

Figure 7 compares the shadowgraph of test 5-07 of present experiment and test 5-4071 of Liu Jun's experiment with similar test conditions [17]. Shock layer imaged by present experiment is obviously clearer than that of previous investigation. The definition of the sphere and background is also improved, which will help to reduce the error caused by manual measurement.

Figures 8 and 9 show the shadowgraph of test 5-07 and the schlieren of test 5-09 with similar test conditions, respectively. It has been shown that both shadowgraph and schlieren are capable to clearly visualize the detached shock over spheres

Table 2 Shock stand-off distances and test conditions

ρR (kg/m^2)	Test number	Sphere	Diameter (D, mm)	Flight speed (V, km/s)	Ambient pressure (P_0, kPa)	Normalized shock stand-off distance Δ/R	Error E/R (±%)
1.3E-04	5-01	D	15	5.080	1.500	0.0735	4.56
	5-02	D	15	5.260	1.500	0.0737	2.97
2.0E-04	5-04	D	15	5.158	2.300	0.0747	2.93
	5-05	C	12	5.294	2.030	0.0816	7.80
	5-12	D	15	6.047	1.790	0.0699	7.12
	9-03	E	10	5.210	3.390	0.0765	6.31
	9-06	E	10	5.760	3.370	0.0687	6.00
	9-07	E	10	5.880	3.450	0.0671	5.63
3.0E-04	5-06	C	12	6.433	4.165	0.0753	8.35
	5-07	C	12	6.490	4.160	0.0772	8.17
	5-08	C	12	5.877	4.167	0.0833	7.60
	5-09	C	12	6.001	4.166	0.0794	8.08
	5-10	B	10	6.266	4.985	0.0771	3.48
	5-13	A	8	5.715	6.310	0.0876	3.90
	5-21	C	12	2.691	4.200	0.1331	9.19

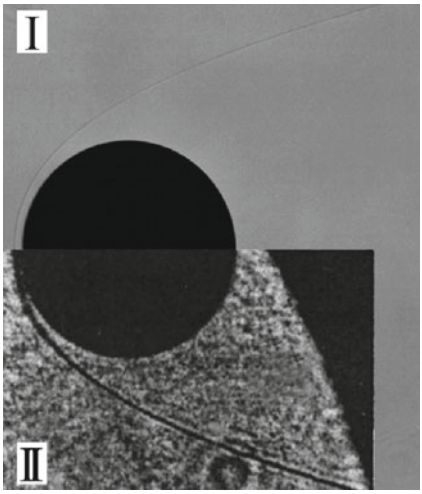

Fig. 7 Comparison of shadowgraph between test 5-07 and Liu Jun's test 5-4071, (I) test 5-07, $D = 12$ mm, $P_0 = 4.160$ kPa, $V = 6.490$ km/s, $\rho R = 3.0 \times 10^{-4}$ kg/m^2, (II) Liu Jun's test 5-4071, $D = 12$ mm, $P_0 = 4.013$ kPa, $V = 5.570$ km/s, $\rho R = 2.9 \times 10^{-4}$ kg/m^2

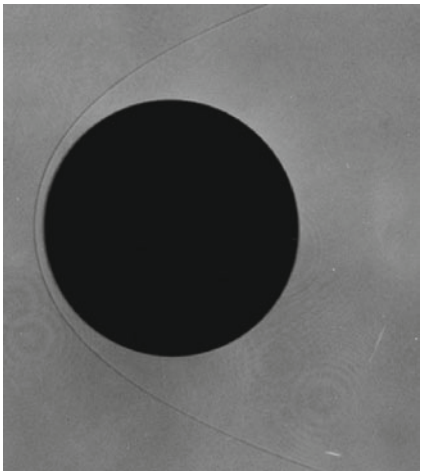

Fig. 8 Shadowgraph of test 5-07, $D = 12$ mm, $P_0 = 4.160$ kPa, $V = 6.490$ km/s, $\rho R = 3.0 \times 10^{-4}$ kg/m^2

under present test conditions. The edge of shock layer in the shadowgraph is thinner than that in the schlieren. This should be caused by the stronger diffraction effect of schlieren. Thinner edge of shock layer can help to accurately locate the location of detached shock. Therefore shadowgraph makes it easier to measure the shock stand-off distances under present test conditions.

Figure 10 shows the relationship between normalized shock stand-off distances and flight speeds as well as ρR of present experiment, Nonaka's experiment [11] and Liu Jun's experiment [17]. The curves of ideal gas, equilibrium and nonequilibrium model are from Zander's calculation [21] with $\rho R = 5.0 \times 10^{-5}$ kg/m^2. Although not the exact flow, Zander's calculation can serve as an indication of flow states. As shown in Fig. 10, present data are basically located between frozen flow and

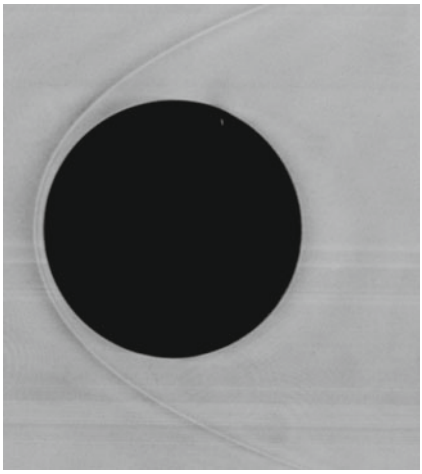

Fig. 9 Schlieren of test 5-09, $D = 12$ mm, $P_0 = 4.166$ kPa, $V = 6.001$ km/s, $\rho R = 3.0 \times 10^{-4}$ kg/m^2

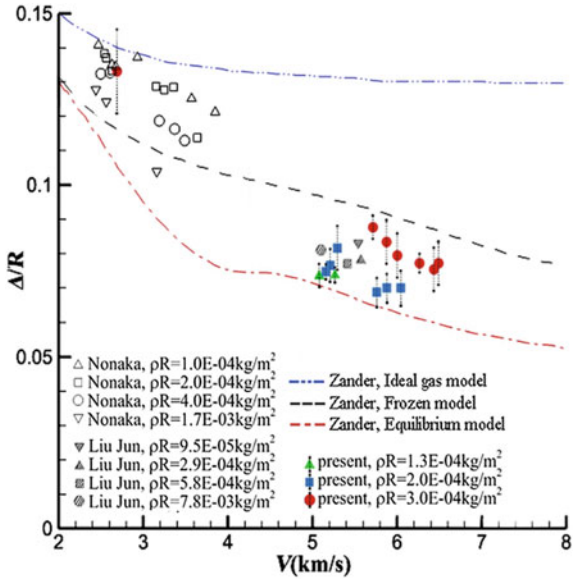

Fig. 10 Normalized shock stand-off distance dependence of flight speed

equilibrium flow, namely in the nonequilibrium regime. This indicates that flow near stagnation point may be primarily nonequilibrium under present conditions. Also present data gradually increase as ρR increases, indicating the degree of chemical reactions in the flow gradually decreases as ρR increases.

Present data match well with Nonaka's and Liu Jun's results with similar conditions. However the Nonaka's results with flight speeds between 2.5 and 4 km/s shows that normalized shock stand-off distance decreases as ρR increases, which is opposite to present experiment. It is speculated that different ρR may have different

influence on the state of the flow with different speed near the stagnation point. This phenomena may need to be studied with more data with flight speeds between 4 and 5 km/s.

6 Conclusions

Measurement of shock stand-off distance for hypersonic sphere was conducted in the Aero-physics Range and the Hyper Velocity Impact Range of CARDC with flight speeds between 5.08 and 6.49 km/s and ambient pressures between 1.5 and 6.3 kPa. Data of Normalized shock stand-off distances with $\rho R = 1.3 \times 10^{-4}$, 2.0×10^{-4} and 3.0×10^{-4} kg/m^2 were presented. Conclusions for present test conditions are drawn as follow:

1. Shock stand-off distance is easier to measure in the shadowgraph. The measurement errors of shock stand-off distances are basically between $\pm 3\%$ and $\pm 8\%$.
2. The flow near the stagnation point is speculated to be primarily nonequilibrium. Shock stand-off distance near the stagnation point gradually increases as ρR increases, indicating the degree of chemical reactions in the flow gradually decreases as ρR increases.
3. The data match well with previous investigations [11, 17] of similar conditions, but the trend of shock stand-off distance changes with ρR is opposite to that of Nonaka's results [11] with lower flight speeds between 2.5 and 4 km/s. It is speculated that different ρR may have different influence on the state of the flow with different speed near the stagnation point.

References

1. Liao, D., Liu, S., Jian, H., et al.: Review of research on shock standoff distance for hypersonic sphere. J. Exp. Fuid Mech. **29**(6), 1–7 (2015)
2. Park, C.: The limits of two-temperature model. AIAA. **911** (2010)
3. Spurk, J.H.: Experimental and numerical nonequilibrium studies. AIAA J. **8**(6), 1039–1045 (1970)
4. Hornung, H.G.: Non-equilibrium dissociating nitrogen flow over spheres and circular cylinders. J. Fluid Mech. **64**(4), 725–736 (1974)
5. Miller III, C.G.: Shock shapes on blunt bodies in hypersonic-hypervelocity helium, air, and CO_2 flows, and calibration results in Langley 6-inch expansion tube. NASA TN D-7800 (1975)
6. Hornung, H.G., Wen, C.Y.: Nonequilibrium dissociating flow over spheres. AIAA. **0091** (1995)
7. Belouaggadia, N., Hashimoto, T., Nonaka, S., et al.: Shock detachment distance on blunt bodies in nonequilibrium flow. AIAA J. **45**(6), 1424–1429 (2007)
8. Liu, S., Wang, Z., Xie, A., et al.: Ballistic range experiments of hypersonic boundary layer transition on a cone-cylinder-flare configuration. J. Exp. Fluid Dyn. **27**(6), 26–31 (2013)
9. Nonaka, S., Hashimoto, T., Furudate, M., et al.: Measurement of density distribution over a hemisphere in ballistic range. J. Thermophys. Heat Transf. **25**(3), 464–468 (2011)

10. Lobb, R.K.: Experimental Measurement of Shock Detachment Distance on Sphere Fired in Air at Hypervelocities, pp. 519–527. Pergamon Press, The High Temperature Aspects of Hypersonic Flow, New York (1964)
11. Nonaka, S., Mizuno, H., Takayama, K., et al.: Measurement of shock standoff distance for sphere in ballistic range. J. Thermophys. Heat Transf. **14**(2), 225–229 (2000)
12. Furudate, M., Nonaka, S., Sawada, K.: Behavior of two-temperature kinetic model in intermediate hypersonic. J. Thermophys. Heat Transf. **13**(4), 424–430 (1999)
13. Furudare, M., Suzuki, T., Sawada, K.: Calculation of intermediate hypersonic flow using multitemperature model. AIAA. **0343** (2000)
14. Furudare, M., Suzuki, T., Sawada, K.: Vibration-dissociation coupling effects on shock standoff distances. AIAA. **2499** (2000)
15. Liu, J., Shi, A., Yang, G.: Measurement of non-equilibrium shock stand-off distance for sphere in ballistic range. In: 11th National Conference on Shock and Shock Tube (2004)
16. Liu, J., Le, J., Yang, H.: Numerical simulation of hypersonic flowfield around sphere model and experimental verification. J. Exp. Meas. Fluid Mech. **16**(1), 67–79 (2002)
17. Liu, J.: Experimental and numerical research on thermo-chemical nonequilibrium flow with radiation phenomenon. Ph.D. thesis, National University of Defense Technology (2004)
18. Jiang, W.: Designation of Hypersonic Testing Facility. National Defence of Industry Press, Beijing (2001)
19. Liu, S., Huang, J., Li, Y., et al.: Recent advancement of hypervelocity impact tests at HAI. J. Manned Spacecraft. **17**(6), 17–23 (2011)
20. Liu, S., Xie, A., Huang, J., et al.: Laser shadowgraph for the visualization of hypervelocity impact debris cloud. J. Exp. Fluid Dyn. **19**(2), 35–39 (2005)
21. Zander, F., Gollan, R.J., Jacobs, P.A., et al.: Hypervelocity shock standoff on spheres in air. Shock Wave **14**, 171–178 (2014)

Oblique Shock Reflection over a Membrane

S. Kobayashi, H. Hemmi, T. Adachi and T. Koita

1 Introduction

Oblique shock reflection phenomena have long been studied both theoretically and experimentally. In ordinary situations, incident shock is considered to be reflected off some solid hard material. In this case, the deformation of the reflection surface is negligible even if the pressure rise is high, and the boundary condition can be easily assigned.

In regular reflection, the flow at the boundary is parallel to the boundary surface. This condition is realized, when the reflecting wedge angle θ_w is large. As the reflecting wedge angle decreases, this condition cannot be fulfilled, and a new reflection configuration called Mach reflection forms.

In inviscid flow theory, the reflection configuration depends on three parameters, i.e., the incident shock Mach number M_i, the reflecting wedge angle θ_w, and the specific heat ratio κ of the fluid. When the same fluid is used ($\kappa = \text{const.}$), and the incident shock number is assigned, regular reflection occurs for $\theta_w > \theta_{wtr}$ and Mach reflection occurs for $\theta_w < \theta_{wtr}$. The dividing wedge angle θ_{wtr} is called the transition wedge angle. In reality, the fluid has transport properties (viscosity and thermal conductivity), so the inviscid theory is not valid. When the reflecting wedge angle θ_w is slightly smaller than the transition wedge angle θ_{wtr}, a so-called dynamic transition occurs, in which the reflection is regular at an early stage, but later transitions to Mach reflection.

S. Kobayashi (✉) · H. Hemmi · T. Adachi
Department of System Engineering, Graduate School of Engineering,
Saitama Institute of Technology, Saitama 369-0293, Japan
e-mail: kobayasi@sit.ac.jp

T. Koita
Department of Mechanical Engineering, Saitama Institute of Technology,
Saitama 369-0293, Japan

K. Kontis (ed.), *Shock Wave Interactions*,
https://doi.org/10.1007/978-3-319-73180-3_10

For a reflecting surface of soft material, the surface may deform under high pressure. This will relax the boundary condition behind the reflected shock, and the transition wedge angle will decrease.

The authors conducted a series of experiments on oblique shock reflection over soft material to investigate the effect of acoustic impedance [1] of reflecting surface material. The results show that, for a reflecting wedge angle well below the transition wedge angle, the transition was delayed (i.e., the transition from regular to Mach reflection occurred near the wedge tip). The distance from the wedge tip to where the transition occurs *(take-off distance)* obviously depends on Young's modulus K of the reflecting surface material. Since the transition delay can be explained by the deformation of the reflecting surface, it was concluded that Young's modulus is more relevant than the acoustic impedance I. The relationship between Young's modulus and acoustic impedance is given by the following formula:

$$I = \sqrt{\rho K},$$

where ρ is the density of the material.

In this paper, we used a sheet of membrane (a Mylar film, which is more easily deformable than soft solid materials; thickness 50 μm) as the reflecting surface and investigated its effect on oblique shock reflection.

2 Experiment

The working gas was air, and the driven section was set to room temperature and atmospheric pressure for each experiment run. The incident shock Mach number M_i was 1.30 ± 0.005, and the reflecting wedge angle θ_w was about 43°, which is well below the transition wedge angle of 46.6° for $M_i = 1.30$ according to the detachment criterion.

Figure 1a shows an attachment devised for the present experiment to fix a membrane. A sheet of membrane was pulled tight and fixed by double-sided tape at the front, the base, and the rear of the attachment. However, the tension was not measured. Before the experiment, the shadowgraph image of the membrane was straight, but it loosened after being shocked. The membrane tension is thus low.

The leading edge is taken as the origin (Fig. 1b). The abscissa ξ is taken along the membrane, and the ordinate η is defined perpendicular to the abscissa. The locations of the reflection point and the triple point (ξ, η) can be converted to (x, y), where x is the abscissa taken in the shock propagation direction and y extends upward normal to the x-axis.

Shadowgraphy was employed to visualize the reflection configuration. The light source was a xenon flash lamp with a 180 ns pulse width. The flash lamp was triggered by the output of the pressure gauge nearest to the test section via a digital delay circuit.

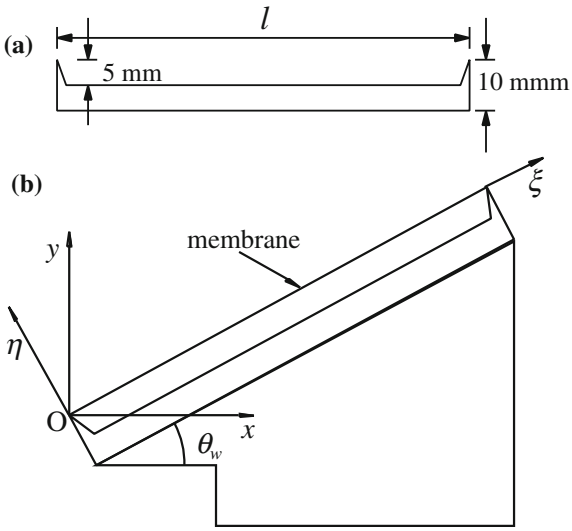

Fig. 1 **a** Attachment for membrane, **b** Model used in the present experiment and the coordinate system

Figure 2a shows a shadowgraph before the experiment; the membrane surface is almost straight. Figure 2b shows the membrane after a 1-day experiment (after 15 shots). The membrane is curved especially near the tip. This means that the membrane suffered plastic deformation, and the membrane tension became very low. After a series of experiments (about 150 shots), the membrane elongates only a little bit (Fig. 2c).

3 Results and Discussions

3.1 Visualized Wave Configuration

Figure 3 presents the development of the wave configuration. Since the reflecting wedge angle is below the transition wedge angle, the reflection should be Mach type when the reflecting surface is a hard solid. In reality, even with a brass wedge, the dynamic transition occurs at around $\xi = 20$ mm. In the present membrane case, surprisingly enough, similar behavior can be observed. This will be considered later. Moreover, a slightly curved transmitted wave can be observed but was unobservable in the previous experiment using soft materials.

In Fig. 3a, the reflection is regular. The transmitted wave, which is visualized less clearly than the incident shock, is almost linear just under the membrane but curved near the bottom of the attachment. The diffracted wave is invisible because of insufficient light. The curved transmitted wave is more apparent in Fig. 3b. The air behind the reflected shock intrudes under the membrane through the gap between the

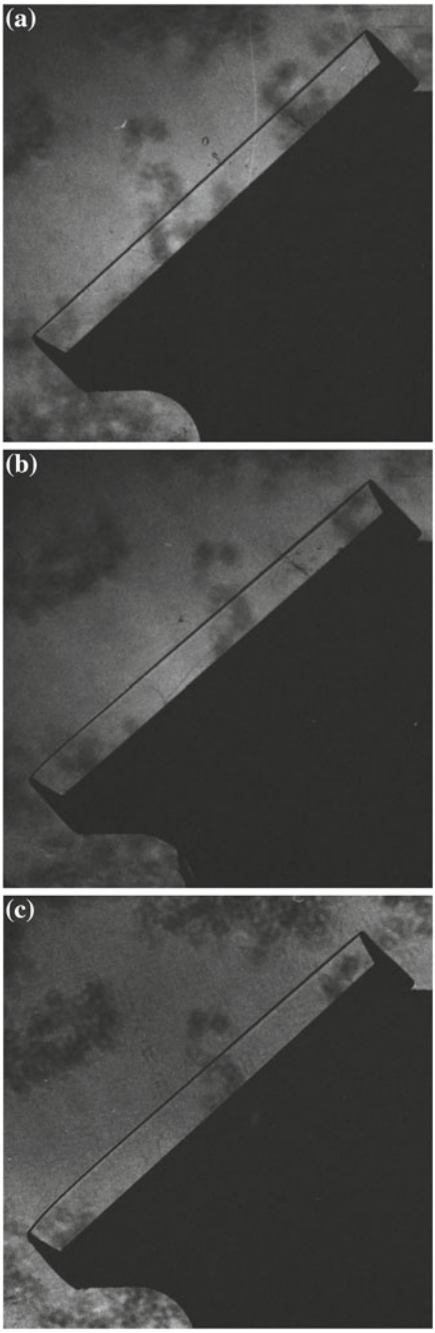

Fig. 2 Wedge model with a sheet of membrane. **a** Before experiment, **b** After 1-day experiment, **c** After about 150 shots

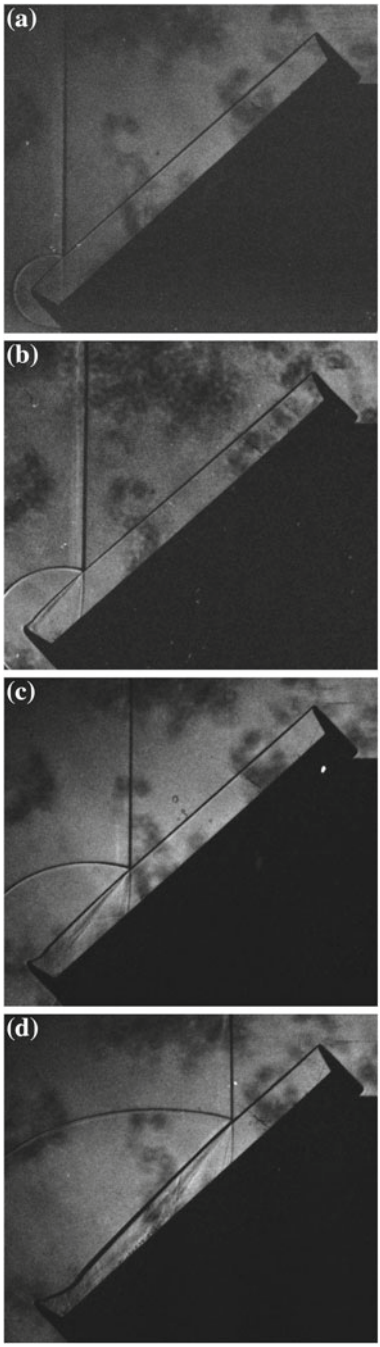

Fig. 3 Oblique shock reflection over a membrane ($M_i = 1.30$, $\theta_w = 42.72°$).
a $x = 5.06$ mm.
b $x = 9.04$ mm.
c $x = 15.82$ mm.
d $x = 30.65$ mm

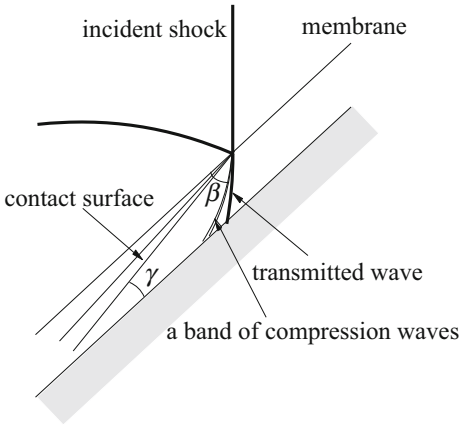

Fig. 4 Sketch of wave fronts and others

observation window and the membrane. It is visualized as a contact surface. A curved wave is observable just behind the transmitted wave. This is considered to be a band of compression waves generated by the contact surface. In Fig. 3c, d similar structure develops but the transition to MR takes place between Fig. 3c, d. A reflection of the transmitted wave from the bottom is visualized weakly. The membrane deformation is marked in Fig. 3d but it will not affect the reflection far ahead.

For clarity, we present a schematic diagram in Fig. 4. The symbol β represents the angle made by the membrane and the visualized precursory compression wave. Assuming steady wave propagation, from geometrical considerations, we have the following relation of the propagation Mach number M_c of the compression wave:

$$M_c = M_i \sin\beta / \cos\theta_w.$$

Actually, we measured the angle from the bottom of the attachment instead of from the membrane, as the membrane deforms. The measured value of β was about 36°, and thus $M_c = 1.045$. In a similar way, we measured angle γ between the contact surface and the bottom. The value of γ ranges from 6° to 12°, which means the Mach number of the moving contact surface is 0.19–0.37.

3.2 Behavior of Triple Point

We measured the location of the reflection and triple points, defined by the intersection of the high-pressure side of the incident shock front and the low-pressure side of the reflected shock front. However, due to the displacement of membrane and visualized wave-front thickness, the measured results have only a weak coherence. We therefore restricted measurement to Mach reflection data and measured the

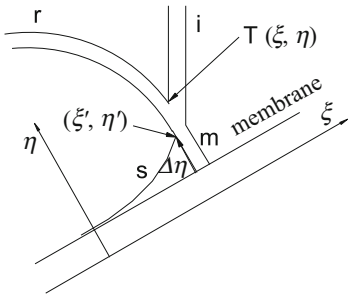

Fig. 5 Definition of measured values

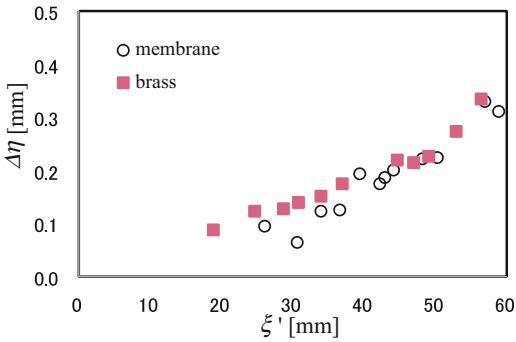

Fig. 6 Location of the slipstream root

coordinate (ξ', η') of the root of the slipstream. Furthermore, by deleting the displacement in the η-direction from η', we estimated $\Delta\eta$ in Fig. 5.

Figure 6 compares the location of the slipstream root for membrane and brass. In this figure, the development of the Mach stem is evident. In both cases (membrane and brass), the locations where the transition to MR occurs do not differ much. This is a curious result considering our previous result for soft materials. By observation, the membrane is convex upward, and thus the effective reflecting wedge angle slightly decreases, which facilitates transition to MR. In contrast, the inclination angle of the membrane increases slightly, which works to prevent the transition. We consider that the two effects cancel each other and no remarkable difference is observed.

3.3 Angle Between the Incident and Reflected Shocks

Figure 7 compares the angle between the incident and reflected shocks with that over a brass wedge. The angle decreases as the incident shock proceeds and we cannot observe any difference.

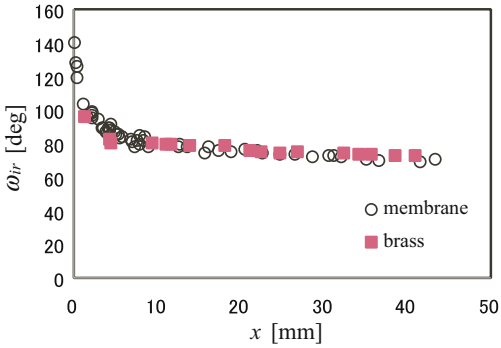

Fig. 7 Variation of the angle made by incident and reflected shocks

3.4 Behavior of the Transmitted Shock

Figure 8 presents a schematic diagram for estimating the propagating Mach number M_t of the transmitted wave at the bottom of the attachment and compares waves at two different times (time interval Δt). Let U_s, u, and v be the speeds of the incident shock, the reflection point (regular reflection is assumed), and the transmitted wave at the bottom. The symbol α stands for the angle of the tangent to the transmitted wave at the bottom. Furthermore, we assume that speed v is constant. From geometry, we easily have

$$v = u \sin \alpha,$$

and

$$U_s = u \cos \theta_w.$$

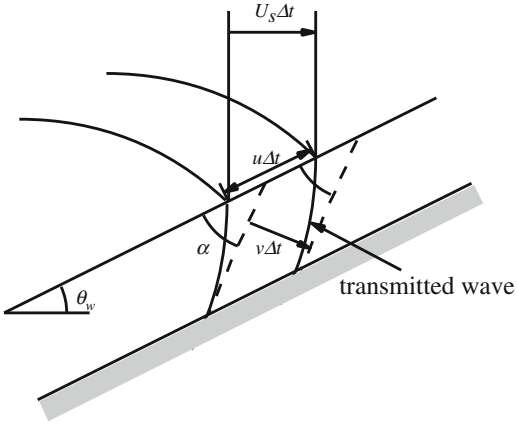

Fig. 8 Propagation of transmitted wave

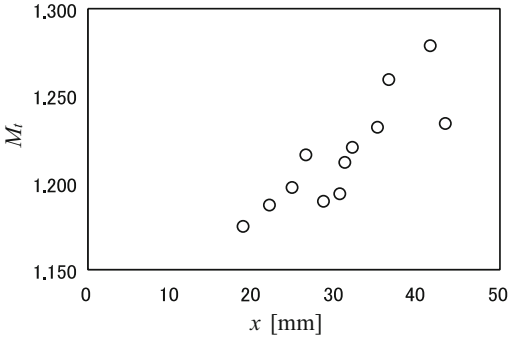

Fig. 9 Variation of transmitted shock Mach number

We then have

$$v = U_s \sin\alpha / \cos\theta_w,$$

or, dividing by the sound speed a ahead of the incident shock,

$$M_t = M_i \sin\alpha / \cos\theta_w.$$

Although reflection is assumed regular, since the triple-point trajectory angle χ is as small as 0.44°, the error due to this assumption is small. Figure 9 shows the variation of propagating Mach number M_t. As the incident shock proceeds, the value of M_t increases toward the incident shock Mach number M_i. As mentioned before, the contact surface generates compression waves, and they might overtake the precursory transmitted wave at the bottom of the attachment, and thus M_t is considered to increase.

If no air intrudes under the membrane, generation of compression waves will be suppressed, so this is not an intrinsic phenomenon. Since the transmitted wave just under the membrane lies on the extension of the incident shock, the effect of membrane over the transmitted wave is considered to be minute.

4 Conclusion

We performed oblique shock reflection experiments using a shock tube in our institute. The reflected shock characteristics unexpectedly turned out to be similar to ordinary oblique reflection. The interesting result was the transmitted wave through the membrane. Our future research will investigate the transmitted wave characteristics through various materials.

Reference

1. Kobayashi, S., Adachi, T.: The effect of acoustic impedance of reflecting surface on oblique shock reflection. In: Proceedings 30th International Symposium on Shock Wave

Formation of Shock Wave Reflection Configurations in Unsteady Flows

I. V. Krassovskaya and M. K. Berezkina

In spite of the fact that the process of shock wave reflection has been the subject of considerable research effort over the last few decades [1–12], the question of the transition between the so-called regular and irregular reflection types is still of particular interest. The analytical approach to describing regular (**RR**) and Mach (**MR**) reflection pattern was initiated by von Neumann [13]. He developed the local theory of two- and three-shock configurations that are valid in the vicinity of the intersection point of shock waves. Von Neumann's theory has been successfully applied to shock wave reflection in steady flows. As for the reflection in pseudo-steady flows, this case is more adequately described by a model proposed by Cabannes [14] for the reflection of a shock wave off an immobile wedge. The main assumption of the theory is that the Mach stem is rectilinear along all its length and perpendicular to the wedge surface. The Cabannes's theory of pseudo-steady Mach reflection is valid in the finite flow domain. Both theories are mathematically equivalent to each other, and the formal difference is that the given and unknown variables swap places. In the case of the pseudo-steady straight wedge reflection, the given parameters are the Mach number M_s of an incident shock wave (or the ratio of densities at the shock front), the wedge angle β and the gas specific heat ratio γ. Note that in the absence of experimental data one can describe the pseudo-steady reflection process using exclusively Cabannes's theory, since without experimental data, only two initial parameters, the incident shock Mach number and the wedge angle, are known.

Figure 1 shows the main boundaries and existence domains for regular and Mach reflection patterns in the (β, ζ)–plane for $\gamma = 1.29$. Here, β is an angle of a reflecting

I. V. Krassovskaya (✉) · M. K. Berezkina
Ioffe Institute, St. Petersburg 194021, Russia
e-mail: i.kras@mail.ioffe.ru

K. Kontis (ed.), *Shock Wave Interactions*,
https://doi.org/10.1007/978-3-319-73180-3_11

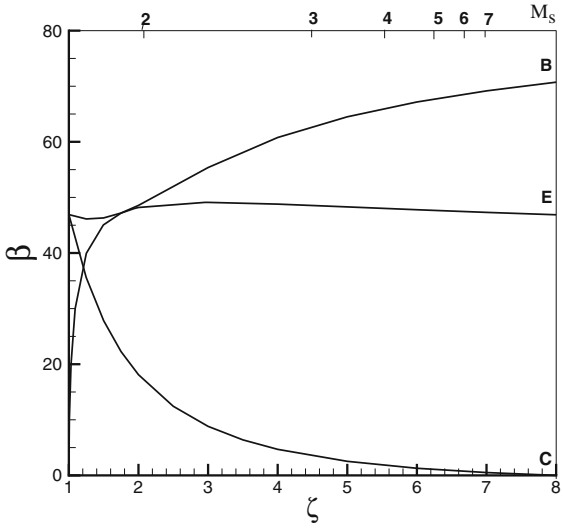

Fig. 1 Boundaries and domains of different reflection patterns of shock wave reflections in the (β, ζ)–plane for $\gamma = 1.29$

wedge, and ζ is the densities ratio across an incident shock wave. The value ζ is related to a Mach number of an incident shock wave M_s through

$$M_s^2 = (n-1)\zeta/(n-\zeta),$$

where $n = (\gamma+1)/(\gamma-1)$ is the limiting value of the density ratio across the shock front. For the purpose of convenience, M_s is plotted on the upper abscissa.

Line **E** is predicted by the two-shock theory. It is the boundary between the domains of regular reflection (above **E**) and irregular reflection (below **E**). The three-shock theory of pseudo-steady reflection predicts two (**B** and **C**) boundaries. **B** is the boundary of the stationary Mach configurations and **C** is the boundary of two merging shock waves resulting in one shock wave. The domain of the Mach reflection patterns lies between lines **B** and **C**. Both **RR** and **MR** configurations are possible in the dual-solution domain situated between **B** and **E**. It should be emphasized that all aforementioned curves are the boundaries of the existence domains of the different reflection patterns. But these lines are commonly accepted as transition lines (**E** corresponds to detachment criterion, and **B** corresponds to mechanical-equilibrium criterion) between a regular and a Mach reflection patterns. This point of view needs to be interpreted correctly. On a straight wall, it is not impossible to realize the transition from one reflection pattern to the other in the course of one continuous process. Each pseudo-steady reflection process has to start from the moment when a shock wave makes contact with the independent reflecting wall. Therefore, the **RR↔MR** transition in the case of pseudo-steady flows cannot be considered a continuous process in which one pattern changes into the other.

When a planar shock wave propagates toward a multifaceted or a smooth curvilinear surface, it interacts with and adapts to a changing wall angle. The process

is inherently unsteady and not self-similar. The most thoroughly investigated case is that of cylindrical obstacles. The cases of concave and convex cylindrical obstacles have been investigated in a number of studies: Ben-Dor [1], Ben-Dor et al. [2], Syshchikova et al. [3], Takayama and Sasaki [4], Bazhenova et al. [5], Ben-Dor et al. [6], Berezkina and Krassovskaya [7], Skews and Kleine [8], Glazer et al. [9], Geva et al. [10], Gruber and Skews [11], and Kleine et al. [12]. In the case reflection off a concave cylindrical surface with the initial angle equal to zero, the sequence of events is the following: von Neumann reflection (**vNR**), Mach reflection (**MR**), inverse Mach reflection (**InMR**), and transitioned regular reflection (**TRR**). It has been found that the angle at which the transition from irregular to regular reflection pattern was obtained that was greater than the known transition values, predicted by two-shock and three-shock theories (detachment and mechanical-equilibrium criteria).

In the case of a convex cylindrical reflecting wall, the reflection is initially regular. It may then transit into **MR** pattern when the incident shock wave encounters decreasing wall angles. At present, there are two points of view on the parameters of **RR→MR** transition. The first is that on a cylindrical surface, the regular reflection patterns appear to be maintained longer compared with the straight wedge case [1–10]. In other words, a visible Mach stem (if one defines the transition as the location of the first occurrence of a visible Mach stem) is arrived at wall angles lower than that found in the pseudo-steady case for a straight surface with the same Mach number.

This finding is at variance with recent numerical results [12]. Their data show that the transition occurs at the same wall angle as for the straight wedge.

The intention of the study presented here is to elucidate the mechanism of formation of the reflection pattern in fully unsteady flow and to consider whether the comparison between the transition parameters obtained in unsteady reflection process and the transition parameters predicted by the pseudo-steady two- and three-shock theories is appropriate. To elucidate the mechanism of formation of the reflection patterns, we performed numerical simulation of a shock wave reflection over multifaceted concave and convex wedges. A polyhedron inscribed in a cylinder can be successfully used because the cylindrical surface is the limit of a polyhedron with $i \to \infty$ (where i is the number of facets of the polyhedron). Computations were performed for $M_s = 2.5$, $\gamma = 1.29$ and for 1/4 of tetraicosagon (24 facets) as the reflecting surface. The numerical density contours for different instances for the case of concave and convex walls are presented in Fig. 2 and Fig. 3, respectively. The data give a clear indication of how the initial incident shock wave "receives the information about the reflecting surface" and how the reflection configurations are formed. The single incident shock wave interacts with the reflecting surface at $t = 0$. At this moment the initial reflection configuration arises. After that, shock wave configurations rather than the incident shock wave as such propagate toward and interact with the reflecting surface. In essence, the shock reflection in a fully unsteady flow can be interpreted as continuous transition from one pattern to other. In the case of concave reflecting surface, the initial configuration is irregular **vNR** pattern (Fig. 2a). The Mach stem interacts with the second facet. Further, pictures of flow field (Fig. 2b–f) illustrate

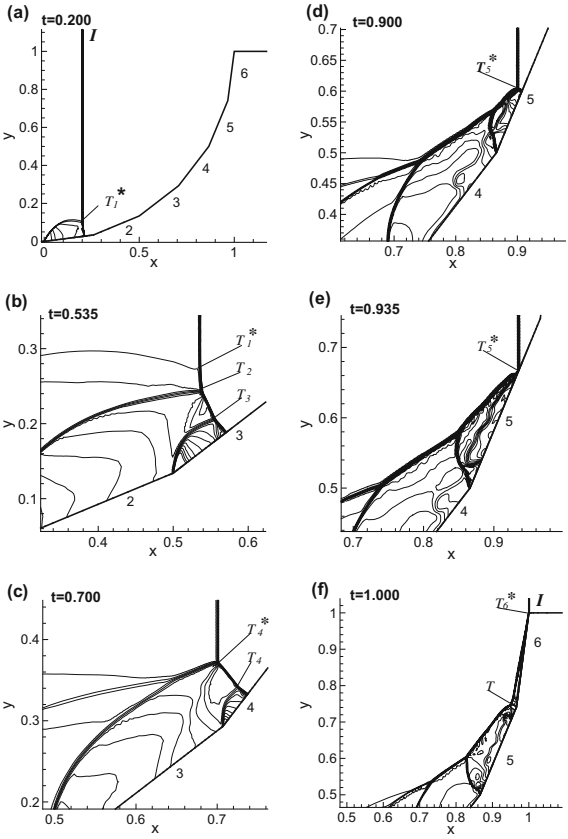

Fig. 2 Numerical simulation of $M_s = 2.5$ shock wave reflecting off the concave tetraicosagon ramp (sequential shock wave patterns)

very clearly how the reflection patterns are formed. Two processes are responsible for the formation of the shock wave configurations. These are successive collisions of the triple points leading to the formation of new three-shock patterns, and the reflections of newly formed Mach stem from the succeeding facets of the polyhedron. In the case of the convex reflecting surface where the initial configuration is a **RR**, the reflection point (common point for incident and reflected shocks) moves along the first, second, and third facets of the surface forming **RR** configurations (Fig. 3). In other words, both the incident and reflected waves make contact and interact with the reflecting surface simultaneously. Note that the parameters of these **RR** patterns are different from the parameters of the patterns described by two-shock theory. The **MR** configuration arises and develops on the fourth facet. The reflection process on the fourth facet is presented in Fig. 4. As one can see, the Mach stem of the **MR** is not perpendicular to the surface, and the angle between the Mach stem and the surface changes over time. This reflection process on the plane surface is unsteady and not self-similar. In the next moments, the formed Mach stem diffracts over the succeeding facets of the polyhedron, and the successive collisions of the triple point

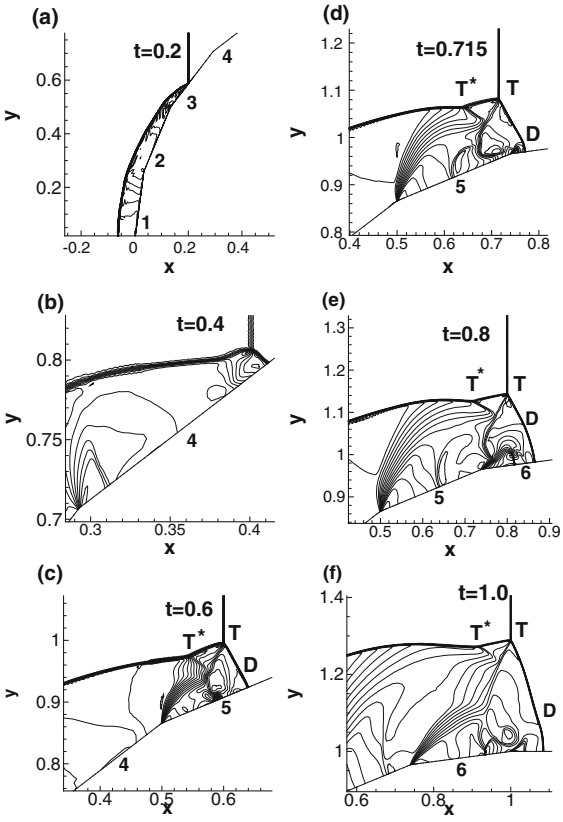

Fig. 3 Numerical simulation of $M_s = 2.5$ shock wave reflecting off the convex tetraicosagon ramp (sequential shock wave patterns)

and diffraction point lead to the formation of new three-shock reflection patterns. The model of a polyhedron inscribed in a cylinder as the reflecting surface provided better understanding of the mechanism of formation of shock wave configurations in unsteady flows. It is shown that reflection patterns formed in unsteady flows are not determined by the incident shock Mach number M_s, the angle of the wedge, and the specific heat ratio, but result from complex subprocesses and cannot be described with the use of the two- and three-shock theories. The evolution of the reflection patterns is determined by the curvature of the reflecting surface.

The numerical results of the shock wave reflection from the concave cylindrical arc are shown in Figs. 5 and 6 for $M_s = 2.5$ and $M_s = 1.2$, respectively.

Since a smooth cylindrical surface is the limit of a polyhedron where the number of facets tends to infinity, it is clear that the foot of a shock wave moving along a smooth surface will generate continuous perturbations. These perturbations will be continuously passed on to the incident wave causing formation of reflection patterns. Apparently, the reflection patterns will have curved reflected waves and Mach stems, and a gradient flow field behind them. The characteristics of the unsteady reflection patterns are different from the ideal patterns described by Cabannes's theory.

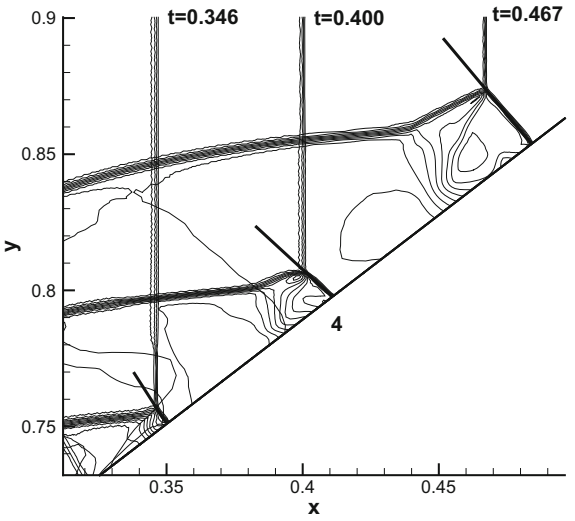

Fig. 4 The reflection patterns on the fourth facet of the convex tetraicosagon ramp

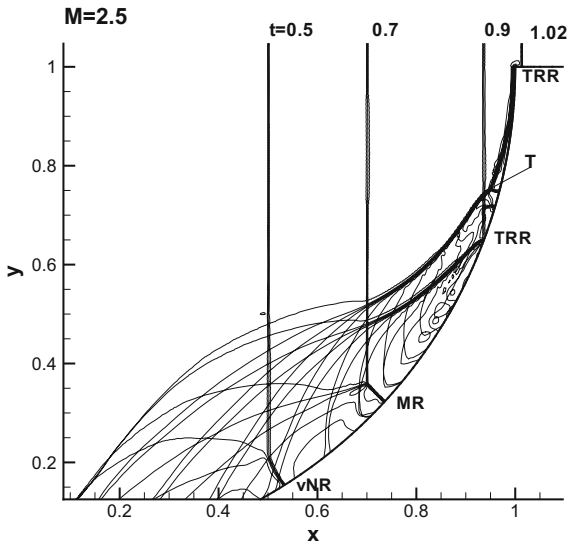

Fig. 5 Numerical simulation of $M_s = 2.5$ shock wave reflecting off the concave cylindrical surface (sequential shock wave patterns)

Comparison of the data obtained for $M_s = 2.5$ with the data for $M_s = 1.2$ shows that the sequence of events depends on the initial shock Mach number. For $M_s = 2.5$, the **TRR** structure arises after termination of a Mach reflection pattern (Fig. 5). In the case of weak incident shock (Fig. 6), the termination of a **MR** leads to the formation of a **RR** pattern. The interaction of the reflected wave of a **RR** pattern and the old reflected wave of a **MR** configuration results in a **TRR** structure. Because the unsteady reflection patters are the results of complex subprocesses, the **MR→RR**

transition angles have to depend on the shape of the reflecting wall and differ from transition angles calculated for pseudo-steady shock reflection.

The reflection process over a convex cylindrical arc is shown in Figs. 7 and 8 for $M_s = 2.5$ and $M_s = 1.2$, respectively. The initial reflection pattern is a **RR**. In this case, the reflection point follows the shape of the smooth reflecting surface. Having regard to the fact that the reflection point belongs to both the incident and the

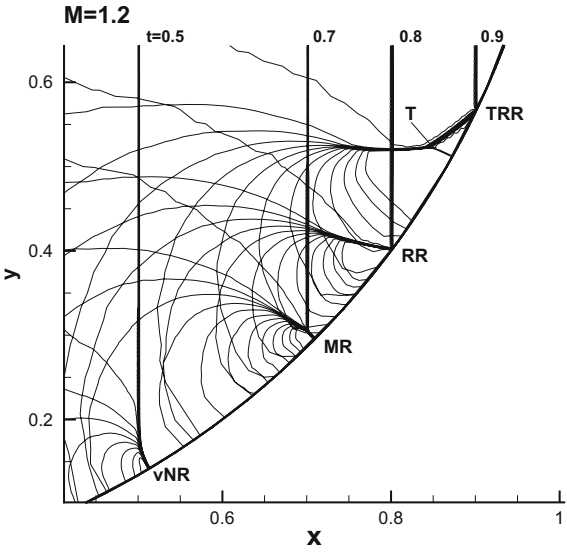

Fig. 6 Numerical simulation of $M_s = 1.2$ shock wave reflecting off the concave cylindrical surface (sequential shock wave patterns)

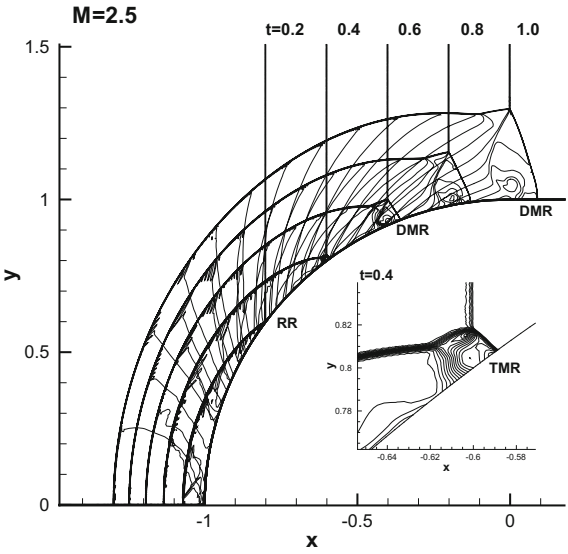

Fig. 7 Numerical simulation of $M_s = 2.5$ shock wave reflecting off the convex cylindrical surface (sequential shock wave patterns)

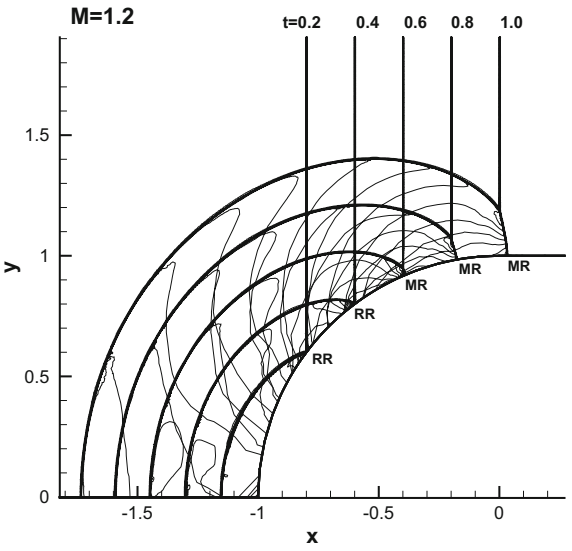

Fig. 8 Numerical simulation of $M_s = 1.2$ shock wave reflecting off the convex cylindrical surface (sequential shock wave patterns)

reflected waves, it is reasonably suggested that both shock waves play a role in the reflection process and interact with the reflecting surface simultaneously. It may be suggested that the Mach reflection pattern is formed when the reflected wave of the **RR** is of primary importance compared with the incident shock wave. After the transition from a two-shock to the three-shock configuration, the foot of Mach stem follows the shape of the surface and generates the continuous perturbations. The triple point accumulates the perturbations, and new **MR** configurations are formed. The incident shock wave with $M_s = 1.2$ has subsonic flow behind its front. The pressure pulse of rarefaction comes to the triple point of a **MR**. In this case, the single Mach reflection configurations are formed (Fig. 6). The incident shock wave with $M_s = 2.5$ has supersonic flow behind its front. In this case, the pressure pulse of compression comes to the triple point. As a result, the double Mach reflection patterns are formed.

It has been found that reflection configurations arising in unsteady reflection cannot be interpreted with the help of two-shock and three-shock theories. Unsteady shock reflection is a process much more complicated than a sequence of ideal shock wave patterns corresponding to the local values of an incident shock and a wall angle. It can be assumed that the **RR→MR** transition will occur at different parameters in the case of reflection of the same incident shock off different reflecting walls.

Acknowledgements This work has been partially supported by RFBR grant 15-01-04635.

References

1. Ben-Dor, G.: Shock Wave Reflection Phenomena, 2nd edn. Springer (2007)
2. Ben-Dor, G., Igra, O., Elperin, T.: Handbook of Shock Waves, vol. 2. Academic Press (2001)
3. Syshchikova, M.P., Semenov, A.N., Berezkina, M.K.: Shock wave reflection by a curved concave surface. Sov. Tech. Phys. Lett. **2**, 61–66 (1976)
4. Takayama, K., Sasaki, M.: Effects of radius of curvature and initial angle on the shock transition over concave and convex walls. Technical Report 46. Institute of High Speed Mechanics, Tohoku University, Sendai, Japan (1983)
5. Bazhenova, T.V., Gvozdeva, L.G., Nettleton, M.A.: Unsteady interactions of shock Waves. Prog. Aerosp. Sci. **21**, 249–331 (1984)
6. Ben-Dor, G., Takayama, K., Kawauchi, T.: The transition from regular to Mach reflection and from Mach to regular reflection in truly nonstationary flows. J. Fluid Mech. **100**, 147–160 (1980)
7. Berezkina, M.K., Krassovskaya, I.V.: Interaction of a planar shock wave with a cylindrical concave wedge. In: 20th International Shock Interaction Symposium, Stockholm (2012)
8. Skews B.W., Kleine H.: Shock wave interaction with convex circular cylindrical surfaces. J. Fluid Mech. **654**, 195–205 (2010)
9. Glazer, E., Sadot, O., Hadjadj, A., Chaudhuri, A.: Velocity scaling of a shock wave reflected off a circular cylinder. Phys. Rev. E **83**, 066317 (2011)
10. Geva, M., Ram, O., Sadot, O.: The non-stationary hysteresis phenomenon in shock wave reflections. J. Fluid Mech. **732**(R1), 1–11 (2013)
11. Gruber, S., Skews, B.: Weak shock wave reflection from concave surfaces. Exp. Fluids **54**, 1–14 (2013)
12. Kleine, H., Timofeev, E., Hakkaki-Fard, A., Skews, B.: The influence of Reynolds number on the triple point trajectories at shock reflection off cylindrical surfaces. J. Fluid Mech. **740**, 47–60 (2014)
13. von Neumann J.: Collected Works, Taub, A.H. (ed.), vol. 1. Pergamon, Oxford, UK (1961–1963)
14. Cabannes, H.: Lois de la reflection des ondes de choc dans les ecoulements plans non stationares. ONERA, no. 80 (1955)

Experimental and Numerical Visualisation of Supersonic Flow over the British Isles

Craig White and Konstantinos Kontis

Abstract Colour schlieren experimental results for Mach 5 flow over an arbitrary geometry that generates complex shock structures and shock interactions are presented. The experiment is rebuilt using the *rhoCentralFoam* solver to solve the compressible Navier–Stokes equations and a numerical analogue, the density gradients (i.e. pseudo-schlieren), is compared to the experimental result, showing very good qualitative agreement. The numerical results give data that can be post-processed to visualise the shock waves by taking advantage of changes in pressure, entropy, velocity, etc. across a shock, in addition to the gradients of density. It is shown that, at least for the geometry and Mach number studied here, the divergence of the velocity field produces the best numerical shock detection method.

1 Introduction

Schlieren imaging is a well-known technique that can be used to visualise shock waves in supersonic and hypersonic flows. It relates the refractive index of light passing through a transparent medium, such as air, to the density of the medium. It is a useful technique for gaining experimental knowledge of the location of shock waves and their interaction with other shock waves, solid boundaries or boundary layers. However, the data that can be acquired using schlieren techniques are qualitative and must be complemented with data from quantitative techniques, such as pressure transducers on the model surface. Numerical data from computational fluid dynamics (CFD) packages can also be used to gain more knowledge about a compressible flow but is important that these results are validated against experimental data. Since a numerical result can give information about many fields throughout the domain, it is possible to visualise discontinuities in various manners; authors have suggested using gradients of density (pseudo-schlieren), gradients of pressure, divergence of velocity, and gradients of entropy [1].

C. White (✉) · K. Kontis
Aerospace Sciences Division, School of Engineering, University of Glasgow, Glasgow G12 8QQ, UK
e-mail: Craig.White.2@glasgow.ac.uk

K. Kontis (ed.), *Shock Wave Interactions*,
https://doi.org/10.1007/978-3-319-73180-3_12

The purpose of the current work is to compare experimental and numerical techniques for visualising shock wave discontinuities over an arbitrary geometry in high resolution. It is possible that properties other than gradients of density, that can only be investigated numerically, will reveal extra data, allowing a deeper understanding of the flow field to be achieved. The choice of flow property is not a trivial decision, but Samtaney et al. [1] have made some recommendations that will be tested in the current work. The arbitrary geometry chosen is a scale model of the British Isles, which is subjected to a Mach 5 flow, generating a complicated flow field that has many shock waves and interactions. The aim of the work is to compare different qualitative methods for visualising shock waves both experimentally and numerically over a complex, arbitrary geometry, and not to provide quantitative values.

2 Experimental Method

The supersonic wind tunnel is an intermediate blowdown (pressure-vacuum) type which uses dry air as working fluid and is shown schematically in Fig. 1. Air from a high-pressure airline is dried and stored in a pressure vessel at a pressure over 15 bar. After passing through a pneumatically operated quick acting ball valve, the gas enters the electric resistive heater section. The gas temperature is raised from ambient to a temperature that is sufficient to avoid liquefaction on its expansion through the nozzle and that of a maximum enthalpy flow condition of 700 K. On leaving the heater, air enters the settling chamber which is downstream of the flow straightener matrix. Immediately downstream of the settling chamber a contoured axisymmetric Mach 5 nozzle is situated. The stagnation pressure can range from 5 to 8 bar and thereby unit Reynolds numbers, Re/m, of between $4 - 16 \times 10^6$ m^{-1} can be achieved [2–4]. The tunnel working section is an enclosed free jet design with dimensions 325 mm × 325 mm × 900 mm (height × width × length) having two circular quartz windows of 195 mm diameter. The variations in Mach number and unit Reynolds number were found to be 0.4% and 3.7%, respectively [5]. The useful running time is found to be 7.5 s. Stagnation pressure p_0 and stagnation temperature T_0 measurements are done using a Pitot probe attached to an absolute pressure transducer, Kulite XTE-190M (6.89 bar range), and a K-type thermocouple probe at the settling chamber. Analogue signals from the sensors are acquired by a high-speed Data Acquisition (DAQ) card, National Instruments (NI) PCI-6251, after they are conditioned by an SXCI-1000 unit. The existing system has the capability of collecting data at a frequency up to 333 kHz at 16-bit digitisation.

Conventional black and white schlieren systems utilising a slit as source and horizontal or vertical knife edge have the ability to show refractive index gradients which deflect the light rays normal to the knife edge, making the system a one-dimensional tool [7, 8]. This presents a disadvantage when studying complicated flows, e.g. where shock waves and boundary layers deflect light rays in the same direction [9, 10]. Using two-dimensional colour schlieren systems, where a coloured wheel is placed at the knife edge location, allows for the detection of flow features that would be

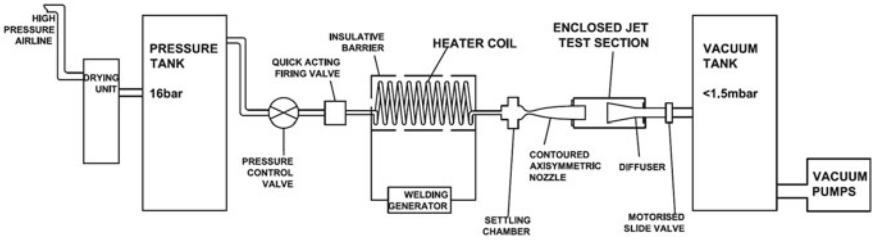

Fig. 1 Supersonic wind tunnel schematic layout [5]

more difficult to identify using one-dimensional schlieren. In the present case, colour schlieren is utilised to study the generated flow field.

Toeplers z-type schlieren technique, adopted for flow visualisation, consists of a continuous light source of Palflash 501 (Pulse Photonics) with a focusing lens and a 1-mm-wide slit, two 203.2 mm parabolic mirrors with 1828.8 mm focal length, a knife edge, a set of Hoya 49 mm close-up lenses, and a digital Canon SLR camera, EOS-450D, 12 MP. A parallel beam of light is passed through the test section windows before focusing on the knife edge plane that is placed perpendicular to flow direction and the focused beam is shone on the CMOS sensor of the camera [11, 12]. The camera is set to continuous recording mode at 3.5 fps with full resolution; the shutter speed is adjusted to maximum value of 1/4000 s with an ISO speed of 400 to provide enough detail and appropriate brightness. The digital resolution is approximately 34 pixels per mm. In addition, a high-speed Photon SA-1

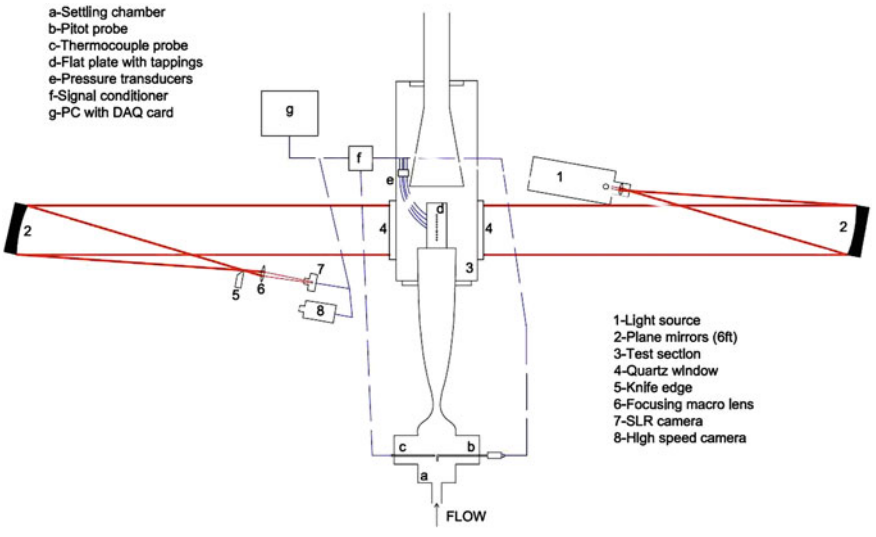

Fig. 2 Schematic setup of schlieren visualisation with data acquisition architecture [6]

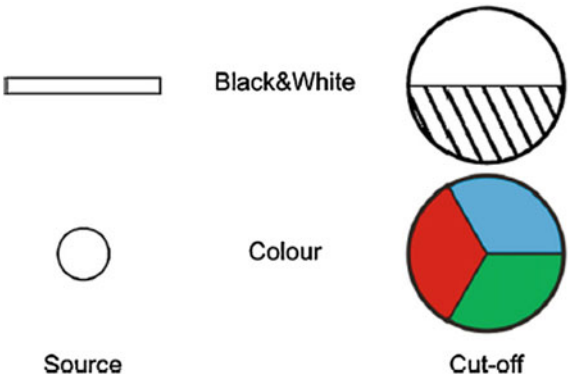

Fig. 3 Schlieren arrangements for black and white and colour [12]

High Speed Video system is utilised to record time-resolved schlieren images up to 675,000 fps at various pixel resolutions and shutter speeds. The optimum frame rate is based on a compromise between adequate temporal resolution and pixel resolution. The shutter speed is set to 1 μs to resolve flow features with sharpness. The digital resolution is approximately 10 pixels per mm. The layout of the optical setup and the data acquisition architecture with measurement chain is shown in Fig. 2. Colour images are acquired when the slit at the source is replaced with a circular pinhole and a three-colour (red, blue, and green) wheel placed at the knife edge location, see Fig. 3. The model used for this study is a miniature British Isles (with minor topological details omitted) shape stainless steel plate with north-to-south maxima of 4 cm and connected to a λ-shape support.

3 Numerical Method

A computer-aided design (CAD) geometry of the British Isles was created using image editing and 3D modelling software, starting from a high-resolution drawing of the British Isles. The CAD geometry was modified to closer resemble the experimental model, for example, the Western Isles were deleted from the northwest of Scotland. The CAD model was finally scaled to have a height of 4 cm and a depth to match the experimental model and is shown in Fig. 4. This 3D model was then used to create a fine, structured mesh using OpenFOAM's *snappyHexMesh* tool. The final mesh had dimensions of 0.044 m × 0.048 m × 0.01 m and contained 6.3 million cells.

The high-speed compressible flow solver, *rhoCentralFoam* [13], implemented within the C++ framework of OpenFOAM [14] was used to perform the numerical simulation in this work. *rhoCentralFoam* uses finite volume discretisation and solves the compressible Navier–Stokes equations using semi-discrete, non-staggered

Fig. 4 Screenshot of the CAD model used to generate the numerical mesh

second-order central schemes on a polyhedral mesh. The inlet boundary conditions were static pressure $p_\infty = 1228.52$ Pa, velocity $U_\infty = 792.5$ m/s, and static temperature $T_\infty = 61$ K, corresponding to a Mach number of 5 at the nozzle exit. The thermodynamic properties for dry air used in the simulation were specific gas constant $R = 287$ J/(kg K) and ratio of specific heats $\gamma = 1.4$. The viscosity was modelled using Sutherlands Law:

$$\mu = A_s \frac{T^{1.5}}{T + T_s}, \tag{1}$$

with the Sutherland coefficient $A_s = 1.458 \times 10^{-6}$ Pa/K$^{0.5}$, and Sutherland temperature $T_s = 110.4$ K. The time step was modified throughout the simulation to maintain a maximum Courant–Friedrichs–Lewy (CFL) number of 0.1. The solver is transient and a first-order time scheme was used. The Mach 5 flow enters the domain from the inlet boundary in the form of a normal shock wave, similar to the real flow in the wind tunnel, and the flow develops over the model as the simulation proceeds in time.

4 Results

The numerical results presented are from a physical time of 226 μs, enough time for the Mach 5 flow to traverse the entire numerical domain. This required 42.3 h of compute time on 6 cores of a desktop PC equipped with an i7 processor. The experimental result was obtained using the colour schlieren system described in Sect. 2. Figure 5 compares the experimental schlieren with a pseudo-schlieren calculated from the gradients of the numerical density field. Very similar discontinuities in the flow are found by both the experimental and numerical methods. The experimental data obtained shows the capability to obtain high-resolution (10 pixels per millimetre) colour schlieren results that allow the complex flow field generated by hypersonic flow over an arbitrary geometry to be visualised.

As discussed previously, it is possible to view shock waves and discontinuities from various properties generated by the numerical solution. The results from several properties suggested for this purpose in the literature have been calculated in post-processing and are displayed below, with the aim of comparing the shock wave structures observed from different fields. Gradients of the pressure field are shown in Fig. 6. Compared to the results for gradients of density, the same main features can be observed. The shock waves are not captured with the same intensity as when the gradients of density are used, so the more oblique regions of the shock waves are not captured. It should also be noted that pressure gradients will not allow contact discontinuities to be visualised as there are no pressure gradients across such a discontinuity [1].

Fig. 5 Qualitative contours of density gradient. Left: results from *rhoCentralFoam*. Right: Experimental colour schlieren results

Fig. 6 Qualitative numerical gradients of pressure.

Figure 7 shows the gradients of the entropy field calculated from *rhoCentralFoam*. There is an entropy jump across a shock wave [15]; therefore, gradients of the entropy field can be used to visualise strong shock waves and other discontinuities in the domain. The change in entropy from the freestream value Δs can be calculated as

$$\Delta s = c_p \ln \frac{T}{T_\infty} - R \ln \frac{p}{p_\infty}, \tag{2}$$

where c_p is the specific heat at constant pressure, R is the specific gas constant, T is the static temperature, and p is the static pressure. The subscript ∞ denotes freestream properties. Figure 7 shows the result of the gradients in entropy from *rhoCentralFoam*, where the main shock waves in the flow are captured well compared to Figs. 5 and 6, oblique regions of the shock waves are not captured with the same intensity as they are when using the gradients of density. There is some noise in the wake regions in this field; Samtaney et al. [1] applied smoothing and noise suppression in their method to help reduce this.

Fig. 7 Qualitative numerical gradients of entropy

Figure 8 shows the divergence of the velocity field $\nabla \cdot U$. Again, the main shock wave features are captured well compared to Fig. 5, but similar to the result from the gradients of entropy above, some noise in the wake regions can be seen when displaying this property. This method captures shock waves well, but similar to pressure gradients, it has to be kept in mind that it cannot visualise contact discontinuities because there is no change of velocity across such a discontinuity.

5 Conclusions

Qualitative visualisation of shock waves in a gas is possible using schlieren techniques that rely on the refractive index of a gas changing with its density. However, such discontinuities have other influences on a gas, bringing about large changes in pressure, velocity, and entropy, across a shock wave, for example. Although it may not be possible to visualise these effects experimentally, numerical results do give an opportunity to investigate these properties, although it is important to validate the numerical results against experimental schlieren images. As such, the two approaches are complementary.

Fig. 8 Qualitative numerical velocity divergence

Experimental colour schlieren has been performed over an arbitrary geometry to demonstrate the capability to generate high-resolution experimental flow visualisation results over such a geometry. The experiment has been rebuilt numerically using the *rhoCentralFoam* solver, with the aim of making qualitative comparisons using different flow properties to visualise the shock waves.

It is has been shown that plotting gradients of pressure allow the main shock waves to be visualised but oblique regions are not captured with the same intensity. Plotting gradients of entropy also successfully allow the shock waves to be visualised but with some noise; similar to gradients of entropy, the oblique portions of the shock waves are not particularly well resolved. However, the best alternative to the gradients of density, at least for this specific case with strong shock waves and shock interactions, is to plot the divergence of the velocity field. It is clear that the shock waves are well captured compared to the gradients of density.

References

1. Samtaney, R., Morris, R.D., Cheeseman, P., Sunelyansky, V., Maluf, D., Wolf, D.: Visualization, extraction and quantification of discontinuities in compressible flows. In: International Conference on Computer Vision and Pattern Recognition (2000)
2. Erdem, E., Kontis, K.: Numerical and experimental investigation of transverse injection flows. Shock Waves **20**(2), 103–118 (2010)
3. Kontis, K., Lada, C., Zare-Behtash, H.: Effect of dimples on glancing shock wave turbulent boundary layer interactions. Shock Waves **17**(5), 323–335 (2008)
4. Saad, M.R., Zare-Behtash, H., Che-Idris, A., Kontis, K.: Micro-ramps for hypersonic flow control. Micromachines **3**(2), 364–378 (2010)
5. Erdem, E., Kontis, K., Yang, L.: Steady energy deposition at mach 5 for drag reduction. Shock Waves **23**(4), 285–298 (2012)
6. Ukai, T., Zare-Behtash, H., Lo, K.H., Kontis, K., Obayashi, S.: Effects of dual jets distance on mixing characteristics and flow path within a cavity in supersonic crossflow. Int. J. Heat Fluid Flow **50**, 254–262 (2014)
7. Kontis, K., Stollery, J.L.: Control effectiveness of a jet-slender body combination at hypersonic speeds. J. Spacecr. Rockets **34**(6), 762–768 (1997)
8. Mariani, R., Kontis, K.: Experimental studies on coaxial vortex loops. Phys. Fluids **22**(12), 126102 (2010)
9. Zare-Behtash, H., Lo, K.H., Kontis, K., Ukai, T., Obayashi, S.: Transverse jet-cavity interactions with the influence of an impinging shock. Int. J. Heat Fluid Flow **53**, 146–155 (2015)
10. Gongora-Orozco, N., Zare-Behtash, H., Kontis, K.: Global unsteady pressure-sensitive paint measurements of a moving shock wave using thin-layer chromatography. Measurement **43**(1), 152–155 (2010)
11. Zare-Behtash, H., Gongora-Orozco, N., Kontis, K.: Effect of primary jet geometry on ejector performance: a cold-flow investigation. Int. J. Heat Fluid Flow **32**(3), 596–607 (2011)
12. Yang, L., Erdem, E., Zare-Behtash, H., Kontis, K., Saravanan, S.: Pressure-sensitive paint on a truncated cone in hypersonic flow at incidences. Int. J. Heat Fluid Flow **37**, 9–21 (2012)
13. Greenshields, C.J., Weller, H.G., Gasparini, L., Reese, J.M.: Implementation of semi-discrete, non-staggered central schemes in a colocated, polyhedral, finite volume framework, for high-speed viscous flows. Int. J. Numer Methods Fluids **63**(1), 1–21 (2010)
14. OpenFOAM Foundation (2015). http://www.openfoam.org
15. Anderson, J.A.: Modern Compressible Flow: With Historical Perspective. McGraw-Hill Education (2002)

The Diffraction of a Two-Dimensional Curved Shock Wave Using Geometric Shock Dynamics

Bright B. Ndebele and Beric W. Skews

Abstract The diffraction of a cylindrical shock wave segment around convex sharp corners is considered. This investigation is approached from a numerical and analytical perspective. The numerical investigation was carried out using ANSYS Fluent while Whitham's theory of geometric shock dynamics was used as a basis for the analytical approach. A model based on Whitham's theory was developed, wherein the cylindrical shock profile is viewed as being composed of connected plane shocks with varying orientation. As the length of these plane shocks approaches zero, their combined shape approximates the cylindrical shock's profile. Upon diffraction, disturbance waves propagate along this sequence of plane shocks; the theory of sound was used to model the propagation of these disturbances (taking into account the variation of shock orientation). Using this method, the inflection point (the point where the disturbed and undisturbed portions of the shock meet) was calculated. The results from the calculation were compared to those from ANSYS Fluent and they showed good correlation. A further attempt was made at modelling an elliptical shock, which produced unexpected results. In plane and cylindrical shocks, the disturbed region grows weaker; yet, it grows stronger in elliptical shock producing another wave between the reflected shock and the wall.

1 Introduction

In this paper, the diffraction of curved shock waves around convex corners is presented. To a certain extent, this work can be viewed as an extension of the work of Skews [5], where the diffraction of a plane shock wave around convex corners was investigated (Fig. 1a) using the theory of sound.

B. B. Ndebele (✉) · B. W. Skews
Flow Research Unit, School of Mechanical, Industrial, and Aeronautical Engineering, University of the Witwatersrand, Johannesburg, WITS 2050, South Africa
e-mail: brightndebele@hotmail.com

B. W. Skews
e-mail: Beric.Skews@wits.ac.za

K. Kontis (ed.), *Shock Wave Interactions*,
https://doi.org/10.1007/978-3-319-73180-3_13

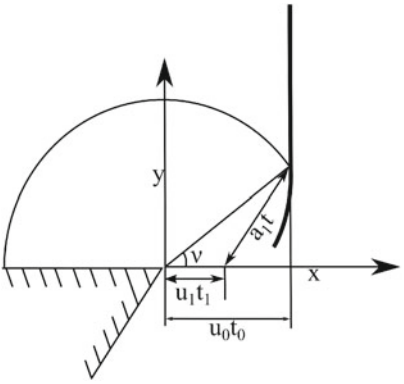

(a) An illustration of the diffraction of a plane shockwave

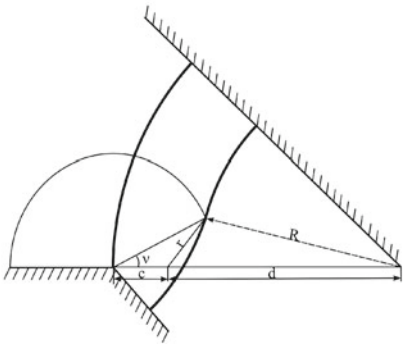

(b) An illustration of the diffraction of a curved shockwave

Fig. 1 Illustrations of plane and curved shock diffraction showing the point of inflection and sound wave behind the shock

In that work, it was shown that Whitham's theory of Geometric Shock Dynamics (GSD) [6] was adequate for predicting the profiles of strong shocks although its accuracy decreased as the shock weakens. The inaccuracies inherent in Whitham's theory when considering weak shocks were attributed to it ignoring post-shock conditions (the free propagation assumption). In light of that, Milton [4] accounted for the post-shock conditions, while Itoh et al. [3] generalised the resulting expression for both strong and weak shocks.

Upon encountering a convex corner, the curvature and shape of the shock change. The angle made by the line joining the point where shock curvature begins to change to the corner with the x-axis is the angle ν. On the shape of the diffracted plane shock, it was shown that the shape was self-similar in time, wherein the angle ν is independent of time. Moreover, the angle ν was shown to be independent of the wall angle (Fig. 1).

Here, it is shown that qualitatively, a curved shock behaves just as a plane shock does albeit with quantitative differences. While the flow behind a plane shock is uniform, the same cannot be said for a curved shock. As the curved shock propagates in its channel, it converges on itself and accelerates. Therefore, unlike a plane shock, the speed of sound and of the perturbed gas behind the shock are always changing.

For this investigation, ANSYS Fluent v 15.0 solver was used for the CFD simulations and MATLAB 8.0.0.783 was used for solving the generalised equations of geometric shock dynamics.

2 Diffraction Model

Diffraction occurs when a shock wave encounters a convex corner (Fig. 1). Expansion waves propagating along the shock cause the shock's shape and Mach number to change. In addition, a reflected wave travelling at the local speed of sound is generated behind the shock.

To calculate shock Mach number, the area Mach number relationship can be used which when combined with GSD allows for the calculation of the shock's profile.

2.1 Geometric Shock Dynamics

The shock Mach number can be related to the cross-sectional area of the channel through which it propagates. Chester [1], Chisnell [2] and Whitham [6] independently showed that by ignoring post-shock conditions, Eq. 1 can be used to calculate the shock's speed. The expression was subsequently revised by Milton [4] and Itoh et al. [3] (Accounting for reflected waves behind the shock) resulting in a correction factor $(\eta(A, M_s)/M_s)$ added to the right-hand side of Eq. 1:

$$-\frac{1}{A}\frac{dA}{dM_s} = \frac{2M_s}{(M_s^2 - 1)K(M_s)} \tag{1}$$

$$\frac{\partial}{\partial \alpha}\left(\frac{1}{M}\frac{\partial A}{\partial \alpha}\right) + \frac{\partial}{\partial \beta}\left(\frac{1}{A}\frac{\partial M}{\partial \beta}\right) = 0 \tag{2}$$

In addition to the relationship between area and Mach number, Whitham [6] derived a geometric relation (Eq. 2) for a shock on a curvilinear coordinate system (Fig. 2). In order to account for the change in shape of a shock's profile, Whitham introduced the concept of a disturbance propagating along the shock. The disturbance propagates at a Mach number $c(M)$ which depends on the shock's Mach number. Introducing this concept allows the reduction of Eq. 2 into conservative form (Eqs. 3 and 4):

$$\theta + \int \frac{dM}{Ac} = \text{constant along } \frac{dy}{dx} = \tan(\theta + \nu) \tag{3}$$

$$\theta - \int \frac{dM}{Ac} = \text{constant along } \frac{dy}{dx} = \tan(\theta - \nu) \tag{4}$$

In Eqs. 3 and 4, the line along which the invariant $(\theta \pm \int \frac{dM}{Ac})$ is constant represents the characteristic which is the locus followed by disturbances in the laboratory frame of reference. Equations 3 and 4 represent upward and downward moving disturbances

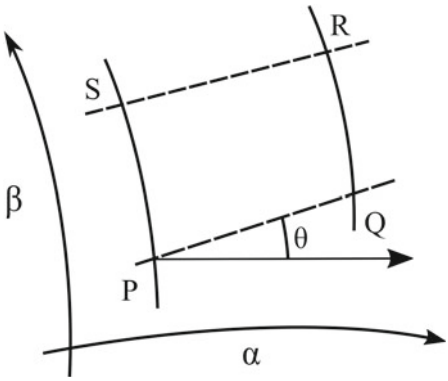

Fig. 2 Curvilinear coordinate system for the derivation of GSD where $\overline{PQ} = M\delta\alpha$, $\overline{SP} = A\delta\beta$, $\overline{SR} = \left(M + \frac{\partial M}{\partial \beta}\delta\beta\right)\delta\alpha$ and $\overline{RQ} = \left(A + \frac{\partial A}{\partial \alpha}\delta\alpha\right)\delta\beta$

on the shock front. θ is the shock's orientation relative to the x-axis, M is the shock's Mach number, A is the channel's cross-sectional area, and c is the Mach number of the disturbance. In the characteristic equation, ν is the angle made by the line joining the disturbance to the corner with the line parallel to the wall at the corner.

3 Diffraction Around a Convex Sharp Corner

In general, when a shock encounters a convex corner, a sequence of disturbances of decreasing strength propagate along the shock front causing it to bend. Consider a case of simple waves wherein the disturbances originate from one end of the shock. In the following section, a plane shock is considered then with that insight generalised to cylindrical shocks. Furthermore, only the first disturbance that propagates along the shock is considered. Since we consider a simple wave, then we may neglect one of Eqs. 3 or 4.

3.1 Plane Shock

Assuming an upward moving disturbance, we neglect Eq. 4. When the shock is incident at the corner, its orientation and Mach number are θ_0 and M_0, respectively. Taking these as the initial conditions of the shock, we can find the constant of the invariant and hence re-write Eq. 3 as

$$\theta + \int_1^M \frac{dM}{Ac} = \theta_0 + \int_1^{M_0} \frac{dM}{Ac} \tag{5}$$

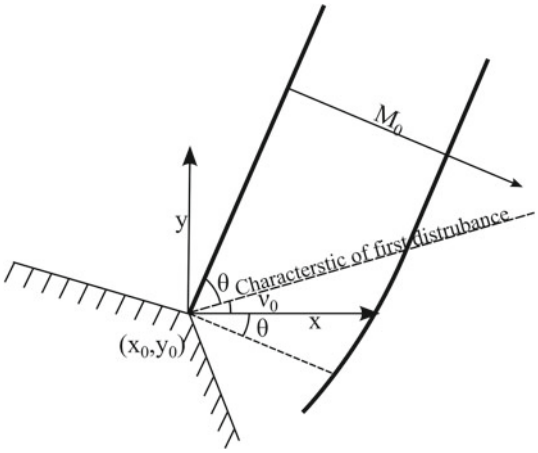

Fig. 3 Diffraction of a plane shock with orientation θ with respect to the x-axis

Since the Mach number of an undisturbed plane shock is constant, it follows from Eq. 5 that $\theta = \theta_0$. Furthermore, since the Mach number of the plane shock is constant, it follows that ν, a function of the shock's Mach number, is also constant (say ν_0).

From the above argument and Eq. 3, the locus of the first disturbance is then given by the straight line (Eq. 10), which is also the characteristic of the first disturbance (Fig. 3):

$$y = \tan(\theta_0 + \nu_0)(x - x_0) + y_0 \tag{6}$$

3.1.1 Theory of Sound

Using the theory of sound [5], the locus of the first disturbance was calculated. A schematic of the concept is shown in Fig. 1a. Using the theory, it was shown that ν can reliably be calculated from Eq. 7 instead of 9 which is based on Whitham's theory:

$$\tan(\nu) = \sqrt{\left(\frac{(M^2-1)((\lambda-1)M^2+2)}{(\lambda+1)M^4}\right)} \tag{7}$$

$$\tan(\nu) = \sqrt{\frac{(M^2-1)((\lambda-1)M^2+2)}{((\lambda+1)M^2))}}\frac{1}{M} \tag{8}$$

$$\tan(\nu) = \sqrt{\frac{1}{2}\frac{(M^2-1)K(M)}{(\lambda+1)M^2}} \tag{9}$$

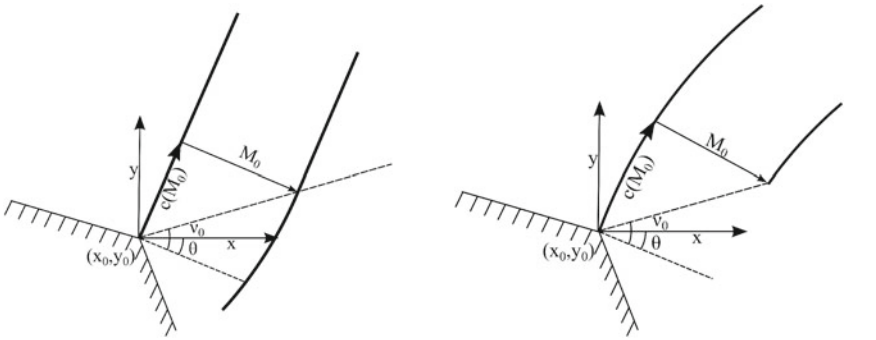

(a) Disturbance travelling along a plane shock (b) Disturbance travelling along a curved shock

Fig. 4 Diffraction of a plane shock with orientation θ_0

Equation 8 is a rearrangement of 7; the numerator is the Mach number ($c(M)$) of the disturbance along with the shock according to the theory of sound while the denominator is the Mach number of the shock. Thus, $\tan(\nu)$ is the ratio of the distance travelled along the shock to the distance travelled by the shock (Fig. 4a). In an attempt to extend the theory of sound to curved shocks, it might be tempting to consider the intersection of a sound wave with the curved shock but in Sect. 3.3, we show a different way for extension. Figure 4b shows the concept applied to a curved shock.

3.2 Cylindrical Shock

The orientation of a cylindrical shock varies along the shock (Fig. 5), while the Mach number of the undisturbed part of the shock varies with time. As a consequence, the locus of the first disturbance is not expected to be linear. As with a plane shock, taking the initial conditions at the wall when the shock had orientation θ_i and Mach number M_i (at position $i = 0$), the invariant reduces to Eq. 5. Since the shock's Mach number is not constant as the shock propagates, Eq. 5 can be rearranged to give the change in shock orientation when the shock Mach number changes from M_i to M_{i+1}. This is then used to calculate the orientation of the point on the shock occupied by the moving disturbance.

$$\theta_{i+1} = \theta_i + \int_{M_{i+1}}^{M_i} \frac{dM}{Ac} \tag{10}$$

From Eq. 3, the characteristic corresponding to Eq. 10 is

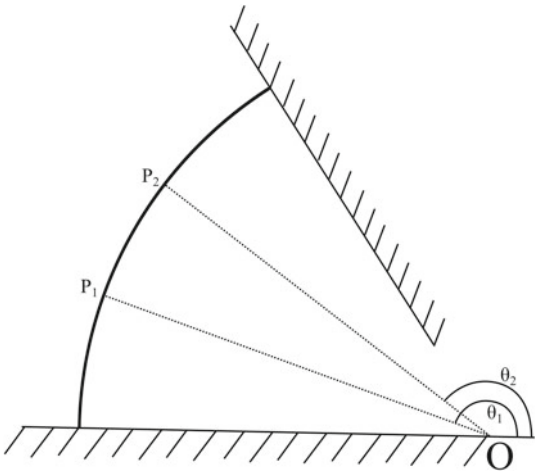

Fig. 5 An illustration of the variation of shock orientation along a cylindrical shock wave segment profile

$$\frac{dy}{dx} = \tan(\theta + \nu)$$
$$y_{i+1} = y_i + (x_{i+1} - x_i)\tan(\theta_{i+1} + \nu_{i+1}) \tag{11}$$

While Eq. 11 is linear between i and $i+1$, it will not be linear for all i since the gradient $\tan(\theta_{i+1}+\nu_{i+1})$ is variable. Therefore, the characteristic of the first disturbance which is also its locus will not be a straight line.

3.3 A Physical Interpretation

When a shock is incident on a corner, Whitham [6] showed that disturbance signals ($c(M_s)$) propagate along the shock causing the shock to change shape. For the case of a diffracting shock, the corner sends a sequence of disturbances that is decreasing in strength ($c_1 > c_2 > c_3 > \cdots$). An assumption made in this paper is that, other than initiating the disturbance signals and acting as a boundary constraint (i.e. The shock is always perpendicular to the wall), the wall has no other impact on the shock's diffraction.

Before we consider the diffraction of a curved shock we recall Eq. 7, derived by Skews [5]. In comparison with experimental data, Eq. 7 was found to predict the inflection point (ν_0) of a diffraction shock well (see Fig. 1a).

For a cylindrical shock, Eq. 7 will not directly apply. However, with reference to Fig. 6 it can be used. Key to this argument is that the curvature of the shock is not communicated to all points that make up the shockwave. When the cylindrical shock is incident on the corner (A) (Fig. 6), the system can be treated as a plane shock, tangential to the curved shock at point A moving at the curved shock's speed (M_0) at A. With that view, Eq. 7 can be applied to calculate the inflection point (ν_0).

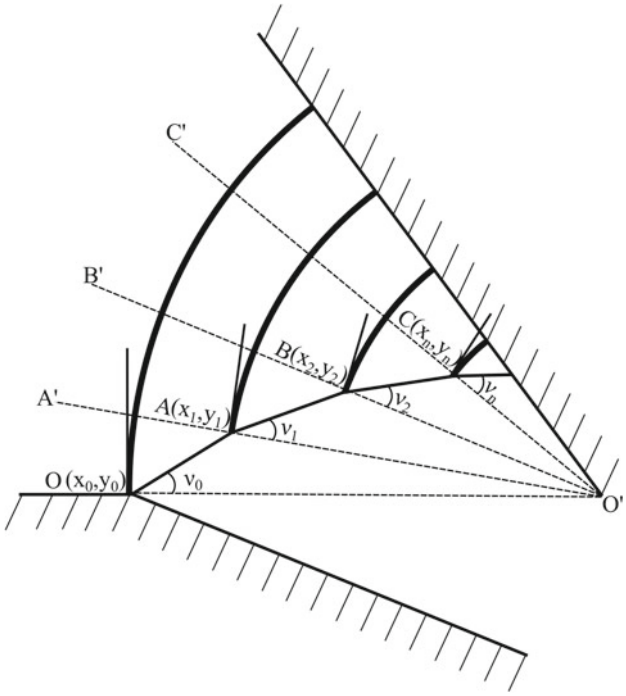

Fig. 6 An illustration of the new model

After a time Δt when the shock has propagated a distance Δx, the inflection point will be propagated to point B.

According to Skews [5], point B represents the first disturbance that was generated by the corner. Alluding to the assumption made above that the wall serves no other purpose than as a signal generator and boundary condition, point B can be treated as a virtual corner. This is so because

- There is a signal $c(M_s)$ which, relative to point C, D, … was generated at points B.
- The direction of propagation of point B is perpendicular to the shock at B (A virtual wall). This can be compared with Whitham's [6] assumption that in the ray shock network, the rays can be treated as the walls of stream tubes.

That being the case, the shock at point B can be treated as a planar shock tangential to the curved shock at B with the wall slightly inclined according to the virtual wall described above. Equation 7 can then be applied to find the new inflection point ν_1 measured with respect to the virtual wall. Note that because the shock's speed is not constant then $\nu_1 \neq \nu_2 \neq \nu_3 \neq \cdots$. Corrolary, the locus of the inflection point will be curved. As Δt becomes infinitesimal, a smooth locus for the inflection point can be obtained.

The above method should similarly apply to any shock with a smooth profile. It is also easy to see how it generalises back to a plane shock.

4 CFD and GSD Simulation Profiles

As expected, the diffraction of a cylindrical shock is qualitatively similar to that of a plane shock with similar features being observed behind both plane and cylindrical shocks. Quantitative differences are to be expected considering that the flow behind a cylindrical shock is non-uniform unlike that of a plane shock. Figures 7 and 8 show a CFD simulation of a 165 mm radius shock diffracting around a 27.5° and a 45° corner.

4.1 Point of Inflection

Upon diffraction, the shock's curvature changes from convex to concave. The point where the shock changes from concave to convex is its inflection point. Using the method presented in Sect. 3.2 in conjunction with Geometric Shock Dynamics, points of inflection were calculated for cylindrical shocks with radii 50 mm, 100 mm and 200 mm at Mach numbers 1.2 and 1.5. The resulting loci were compared to those determined from CFD simulations.

In Figs. 9, 10, 11 and 12, the circular data points represent CFD data and the line is the locus calculated using the method presented here. For the cases considered, the fit was found to be good. For example, for the 200 mm shock, the model presented in

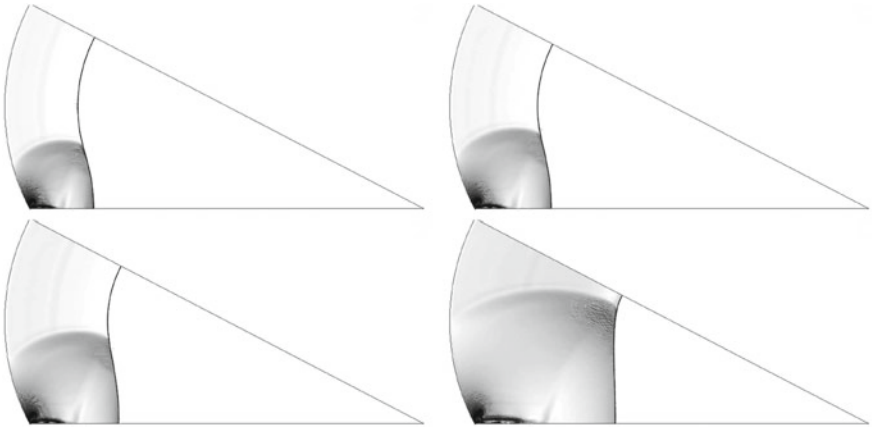

Fig. 7 Diffraction of a 165 mm radius cylindrical shock around a corner of 27.5°

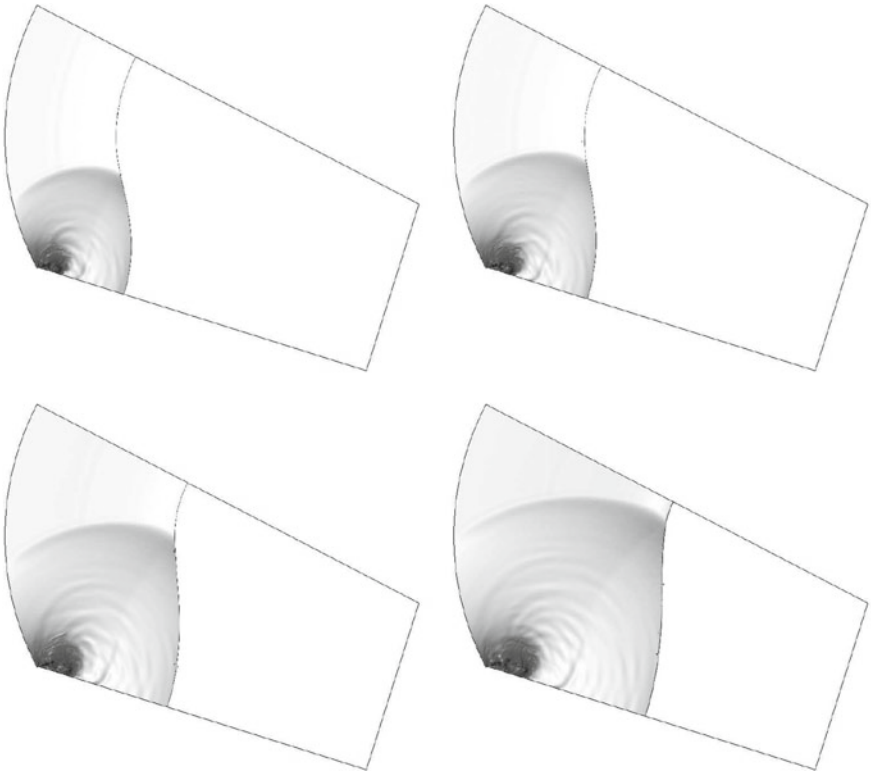

Fig. 8 Diffraction of a 165 mm radius cylindrical shock around a corner of 45°

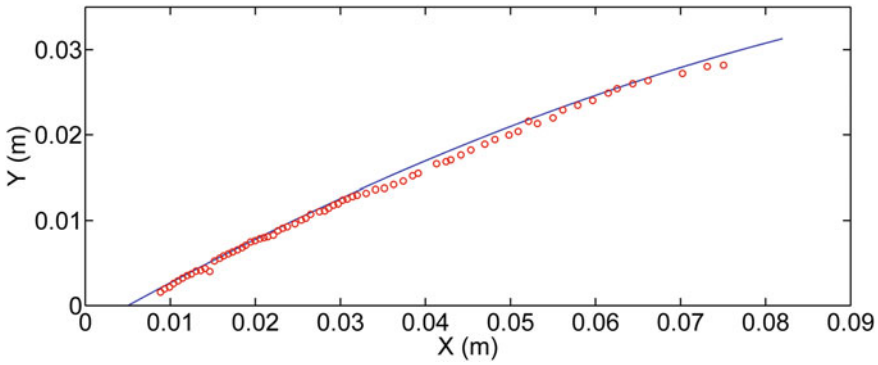

Fig. 9 The locus of the inflection on 200 mm shock at Mach 1.5

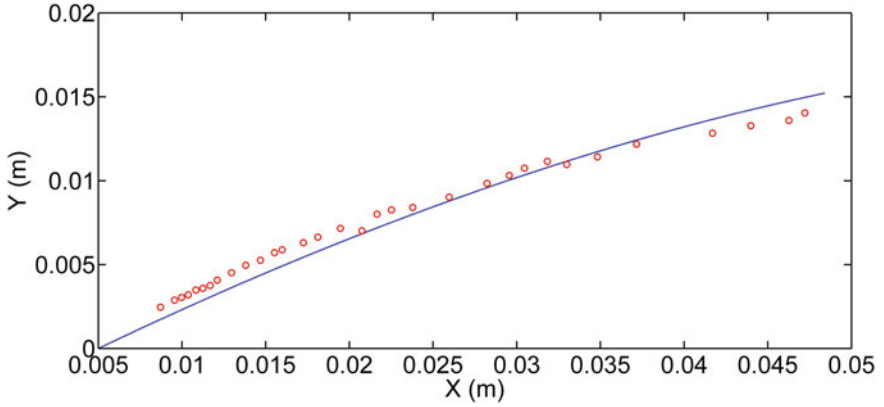

Fig. 10 The locus of the inflection on a 100 mm shock at Mach 1.2

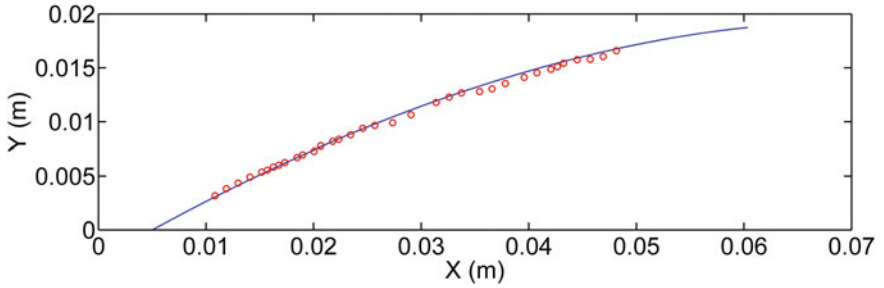

Fig. 11 The locus of the inflection on a 100 mm shock at Mach 1.5

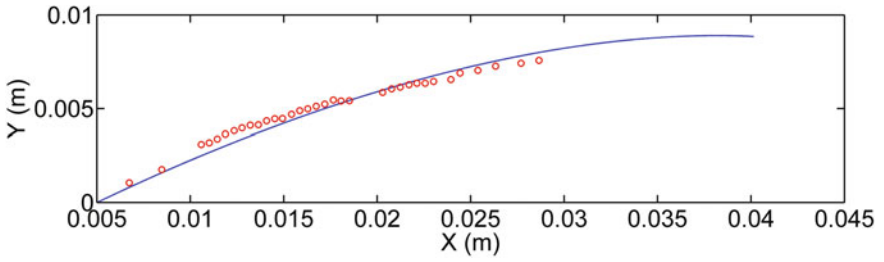

Fig. 12 The locus of the inflection on a 50 mm shock at Mach 1.5

Sect. 6 was satisfactory at 95% confidence level using a χ^2 goodness of fit statistic. From the figures it can be seen that, as the shock radius increases, the locus of the inflection point on the shock becomes more linear as expected.

In calculating ν, Eq. 7 was used. Whitham's Eq. 9 was found to be inadequate for weak plane shocks and for this reason might be inadequate for cylindrical shocks as well.

5 Conclusion

A method to calculate the locus of the first disturbance is presented which generalises from curved to plane shocks. While it was applied only to cylindrical shocks, it should apply equally well to other shock shapes with a smooth profile. This method does not give the shape of the diffracted section of the shock wave. However, by accounting for the other disturbances generated at the wall, it might be possible to calculate the shape shock since the same method is successful with plane shocks.

6 Future Work: Elliptical Shocks

While cylindrical shock diffraction patterns are qualitatively similar to those of plane shocks, elliptical shocks are slightly different. This difference could be accorded more to geometry than physics. In particular, the normals of a cylindrical shock converge onto a single point (the centre), those of an ellipse form a locus (an astroid) (Fig. 13). Therefore, the manner in which an elliptical shock converges on itself will be considerably different. Any two normals will intersect along the astroid and where they intersect marks the point of wave focusing. Thus, for an elliptic shock, focusing occurs continuously unlike a cylindrical shock which focuses only at the centre point. Figure 14 shows the simulation results of the diffraction of an elliptic shock around a 27.5° convex corner. The profile of the diffracted shock starts off as one would expect from plane and cylindrical shocks. At a time of 0.0004 s, a second reflection appears, attached to the diffracted shock. Using the concept of a disturbance on the shock's profile, as the part of the shock that has not yet diffracted propagates,

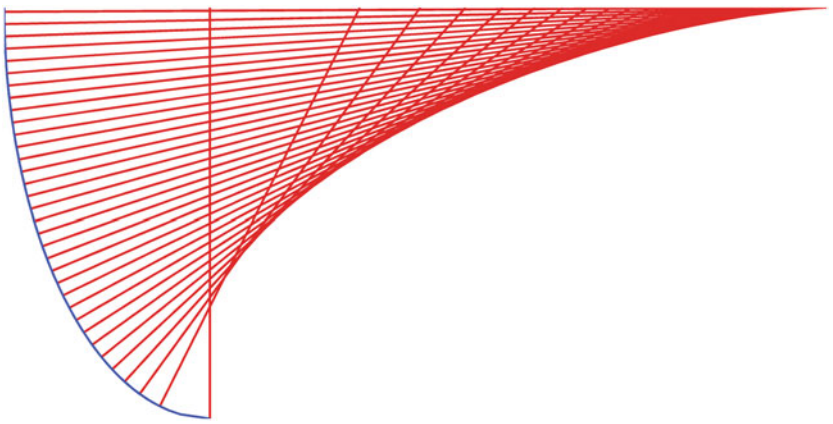

Fig. 13 An illustration of the convergence of an ellipse. Shown here are the normals of an elliptic profile and how any two normals always intersect at distinct points

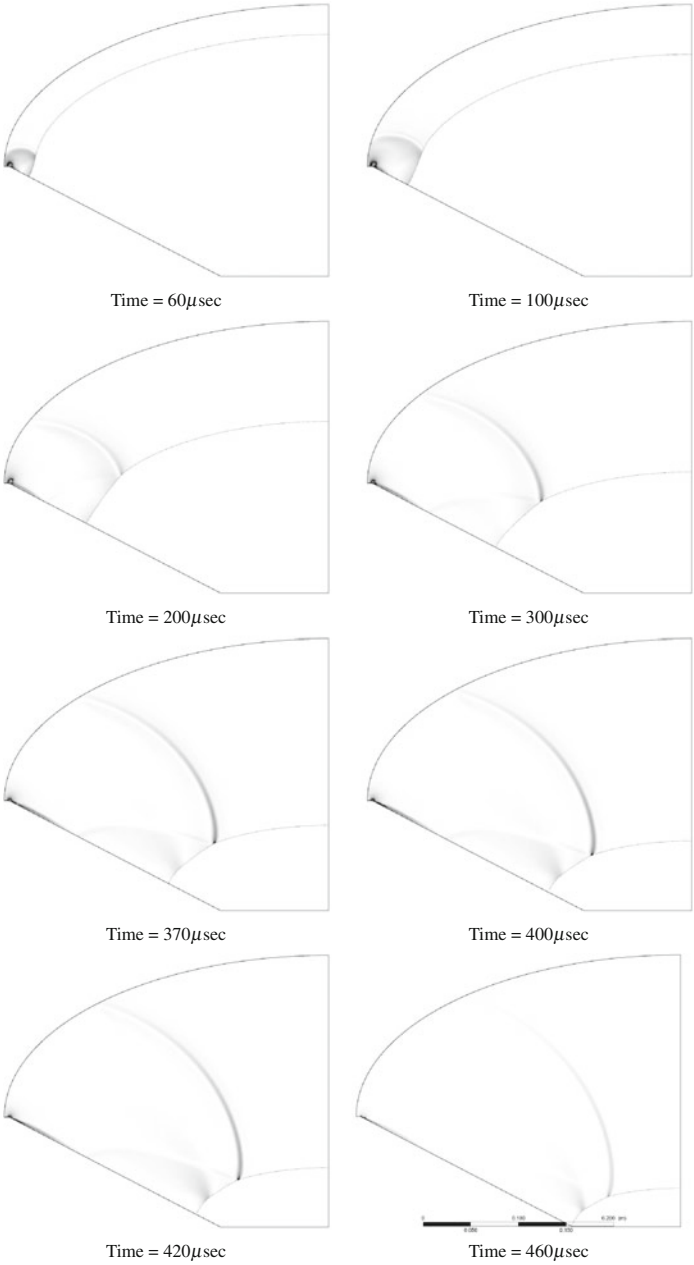

Fig. 14 Diffraction of an elliptic shock around a 27.5° convex corner

it gradually converges on itself causing disturbances to propagate towards the wall. Because the shock is converging, its increasing means that the sequence of disturbances sent towards the wall is of increasing strength. The point where they meet is the where the second reflection occurs.

References

1. Chester, W.: The quasi–cylindrical shock tube. Philos. Mag. **45**, 1293–1301
2. Chisnell, R.F.: The motion of shock waves in a channel with applications to cylindrical and spherical shock waves. J. Fluid Mech. **2**, 286–298
3. Itoh, S., Okazaki, N., Itava, M.: On the transition between regular and mach reflection in truly non-stationary flows. J. Fluid Mech. **108**, 384–400
4. Milton, B.E.: Mach reflection using ray shock theory. AIAA. **13**, 1531–1533
5. Skews, B.W.: The shape of a diffracting shock wave. J. Fluid Mech. **29**, 297–304
6. Whitham, G.B.: A new approach to problems of shock dynamics, Part 1: Two dimensional problems. J. Fluid Mech. **2**, 146–171

Viscous Correction and Shock Reflection in Stunted Busemann Intakes

H. Ogawa, B. Shoesmith, S. Mölder and E. Timofeev

Abstract Air intakes play a crucial role in hypersonic air-breathing propulsion by compressing incoming airflow to high pressure and temperature for combustion. Axisymmetric Busemann intakes can achieve highly efficient compression for scramjet engines in inviscid flow. In practice, however, viscous effects exert significant influence on the flowfield and performance of scramjet intakes, necessitating effective methods for viscous correction and intake shortening. The present study develops a robust correction methodology by coupling viscous flow simulations with a wall correction method based on local displacement thickness of the boundary layer, whose edge is detected based on the total enthalpy profile. This iterative correction process is applied to hypersonic stunted Busemann intakes and supersonic M-flow ring geometries. Flow features in the initial inviscid fields are successfully reproduced in the presence of viscosity for both applications, except for highly stunted Busemann intakes, where the mode transition to Mach reflection occurs at different shortening lengths.

H. Ogawa (✉)
School of Engineering, RMIT University, GPO Box 2476, Melbourne, VIC 3001, Australia
e-mail: hideaki.ogawa@rmit.edu.au

B. Shoesmith · E. Timofeev
Department of Mechanical Engineering, McGill University, 817 Sherbrooke Street West, Montreal, QC H3A 0C3, Canada
e-mail: ben.shoesmith@mail.mcgill.ca

E. Timofeev
e-mail: evgeny.timofeev@mcgill.ca

S. Mölder
Department of Aerospace Engineering, Ryerson University, 350 Victoria Street, Toronto, ON M5B 2K3, Canada
e-mail: smolder@ryerson.ca

K. Kontis (ed.), *Shock Wave Interactions*,
https://doi.org/10.1007/978-3-319-73180-3_14

1 Introduction

Scramjet engines are a promising hypersonic air-breathing propulsion technology to enable economical and flexible atmospheric cruise as well as access to space. The air intake of the scramjet plays a key role in scramjet operation by compressing the inflow to high pressure and temperature for combustion, while ensuring a high total pressure for thrust production. The theoretical axisymmetric Busemann intake is generally regarded as producing an efficient compression field and is often used as a basis for hypersonic intake studies [2, 7–10, 13]. The axisymmetric full Busemann intake for a Mach 8 freestream can achieve a total pressure recovery of 97% and uniform outflow in inviscid flow, with the 3% loss occurring over a downstream conical shock wave at the end of the initial isentropic compression [8]. However, boundary layer losses, on the long (and heavy) isentropic surface, of such intakes, can lead to as much as a 50% decrease in total pressure recovery [9]. The presence of the boundary layer also has a considerable effect in modifying the inviscid flow (Fig. 1). These two factors suggest that the 'inviscid' intake should be shortened and that the effect of such shortening on the inviscid core flow be compensated so as to retain as much as possible of its original performance. This chapter presents results of shortening the intake surface together with a method of calculating the boundary layer properties and their effects on the inviscid flow.

Intake stunting (axial contraction) has been suggested as a shortening method to improve the overall performance of the Busemann intake [9].[1] These studies noted that mode transition of the centreline shock reflection occurred from a configuration with an infinitesimally small Mach disk, resembling a regular reflection (which is prohibited theoretically at the axis, see [11]) to that with a distinct Mach disk (stem), as seen in Fig. 2. The intermediate transition process was characterised by highly unsteady, complex flow structures including a toroidal (ring) vortex, as shown in Fig. 3. The variations of the centreline pressure in the stunting process in inviscid flow indicated that the shock reflection features a reflected shock in two-shock regular reflection before mode transition and a three-shock Mach reflection after transition. Simulations for the reverse (stretching) process revealed possible existence of hysteresis during mode transition.

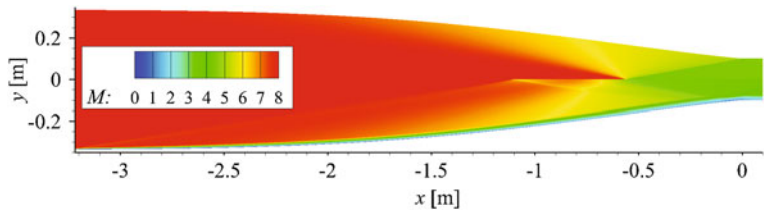

Fig. 1 Inviscid (top) and viscous (bottom) Busemann intake flowfields (Mach number) from [9]

[1]The word 'stunted' is used to designate lengthwise contracted intakes, in contrast to 'truncated' intakes that have been shortened by deleting some leading edge portion.

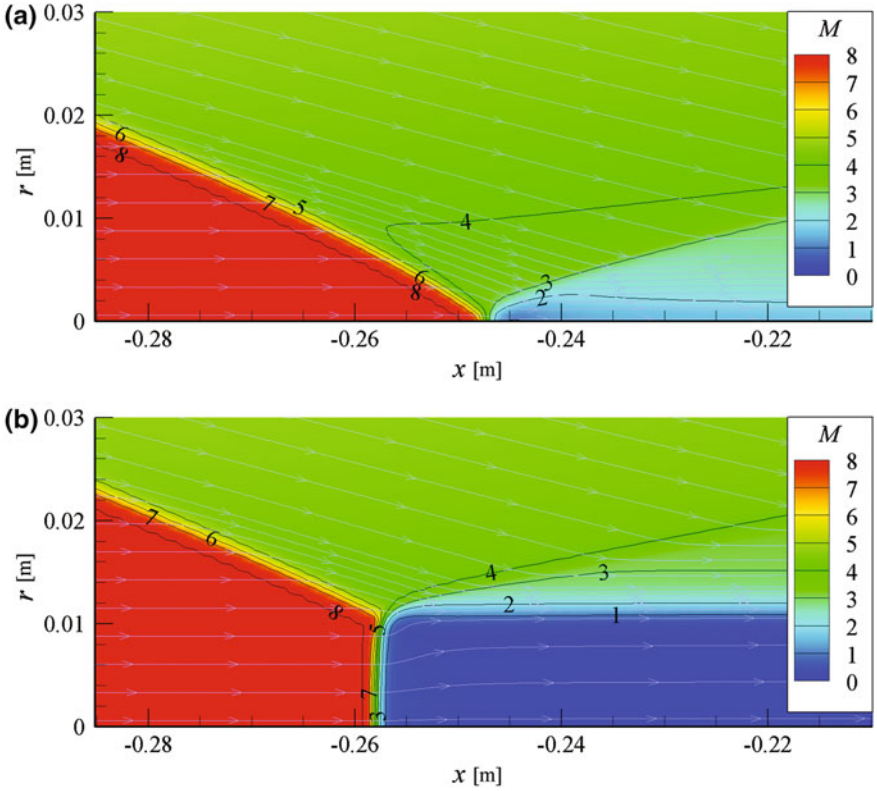

Fig. 2 Centreline shock reflection in stunted Busemann intakes before/after transition (Mach number). Left: apparent regular reflection, right: Mach reflection [10]

The importance of viscous correction methodologies have attracted considerable attention and research efforts. In particular, accurate calculation of the boundary layer displacement thickness plays a pivotal role in the development of such methods. Flock and Gülhan [2] and Walsh et al. [14] applied viscous correction to the

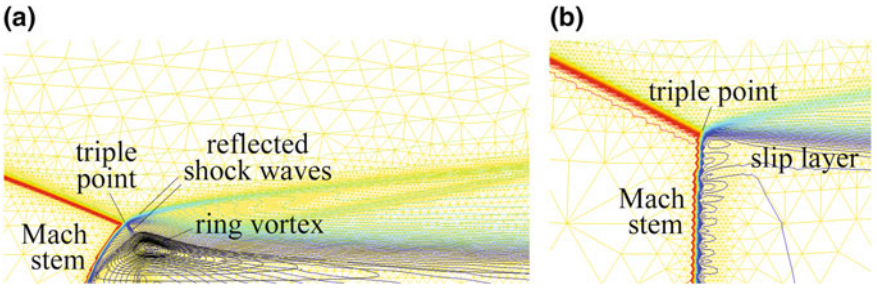

Fig. 3 Flow structure of centreline shock reflection in stunted Busemann intakes (Mach number and adaptive grid). Left: during mode transition, right: Mach reflection after transition [10]

full and truncated Busemann intakes by using the displacement thickness obtained through numerical integration of the boundary layer properties. They detected the boundary layer edge by examining the velocity profiles and pressure distributions, respectively. However, the complex interactions of the shock waves and boundary layers developed on the curved surface of the Busemann intakes pose a challenge to accurate detection of the boundary layer edge. Green and Hamilton [3] and Mcnally [4] employed detection approaches based on the distributions of total enthalpy and reported reasonable detection of the boundary layer edge in such complex flowfields. Viscous correction is typically applied only once to produce the final geometry. However, the importance of repeating the process with subsequent iterations was highlighted by Carter [1], who proposed the application of an updating procedure of the displacement thickness.

The present study describes a robust boundary-layer correction technique, incorporating an iterative method where the intake contour is updated progressively until convergence is achieved. The results are compared with those obtained from non-iterative results. In particular, viscous correction is applied to two intake configurations of interest, namely, stunted Busemann intakes and M-flow intake rings. The inviscid and viscous-corrected flowfields are compared for the validation of the correction method, and the resultant flowfields are examined, with a primary focus on the shock structures and flow attributes in the vicinity of the symmetry axis.

Experimental investigation is needed to verify the flowfields and shock structures in the stunted Busemann intakes due to significant impact on the intake performance as well as for purely scientific interest. An experimental study is currently underway to be conducted in a supersonic wind tunnel by employing the so-called M-flow intake rings, which are shaped to produce conical shocks of constant strengths to focus on the centreline, as described in the companion paper [12]. To preserve the inviscid flow and its pressure distribution, it is necessary to correct the surface shape of the wind tunnel models by the boundary layer displacement thickness.

2 Approaches

2.1 Conditions and Configurations

The Busemann intake captures a uniform hypersonic airflow at Mach 8 with a static pressure and temperature of 1,197 Pa and 226.5 K, respectively. The full intake length L_{full} is 3.215 m and the intake entrance radius is 0.335 m with a contraction ratio of 11.2. The compression ratio is 33.0 and 49.7 for the inviscid and viscous full Busemann intakes, respectively. Stunting to the length L is achieved by contracting the original (full) Busemann intake in the axial direction as follows: $x_{\text{stunted}} = (x_{\text{full}} - x_0) \times L/L_{\text{full}}$. For linear stunting, the resulting contour is independent from x_0 which can be conveniently chosen to be at the intake exit located at the trailing edge of the intake wall surface. In the present chapter, the origin is also

chosen to be the intake exit, i.e. $x_0 = x_{\text{exit}} = 0$. The outflow is forced to be fully supersonic by imposing a small divergence downstream of the intake exit. Stunting leads to changes in the compression ratio, while the intake entry and exit diameters and hence the contraction ratio and the mass flow rate remain constant. The Reynolds number based on the intake exit radius of 0.1 m is 3.01×10^5.

The M-flow intake rings are designed to generate conical axisymmetric focusing shock waves with internal cone angles of 80° and 100° [6]. They capture a uniform supersonic airflow at Mach 2 with a static pressure and temperature of 25,560 Pa and 166.7 K, respectively. The intake entrance radius is 0.03 m and the ring length (in the axial direction) is 0.0057 m and 0.0042 m for the internal shock cone angles of 80° and 100°, respectively. The Reynolds number based on the intake entrance radius is 7.32×10^5. Testing is contemplated at these conditions in the supersonic wind tunnel of the Institute of Fluid Science, Tohoku University.

2.2 Computational Fluid Dynamics

The intake flowfields are computed by utilising a commercial high-fidelity code CFD++ [5], which solves the Navier–Stokes equations implicitly with second-order spatial accuracy, assisted by multigrid convergence acceleration. The advanced wall-function technique is used for near-wall treatment and turbulence is modelled by the two-equation SST $k - \omega$ RANS model. The air is treated to be a calorically perfect gas with a specific heat ratio of 1.4. The intake surface is set to be adiabatic for viscous simulations.

The axisymmetric computational domains are represented by two-dimensional fully structured meshes. The domain for the stunted Busemann intakes is composed of 220,000 cells (1,101 nodes along the wall and 201 nodes in the wall–normal direction). The minimum cell thickness on the wall is 10^{-5} m for viscous computations, which provides a dimensionless wall distance value y^+ of 1.4. The flowfields for the M-flow intake geometries are represented by a domain comprising 2,040,000 cells, where 2,041 nodes are distributed along the wall (41 nodes allocated for a short section upstream of the wall, 201 nodes on the ring wall, and 301 nodes downstream of the wall), with 1,001 nodes assigned for the radial direction. The minimum cell thickness on the wall is 2×10^{-6} m for viscous computations, which results in a y^+ value of 2.1.

2.3 Boundary Layer Correction

Boundary layer profile data is obtained by extracting wall–normal data planes from CFD solutions. A total of 51 data planes is deemed sufficient to capture the distribution of the displacement thickness for both the Busemann and M-flow geometries. In both of these cases, there are wall normal gradients that extend well beyond the

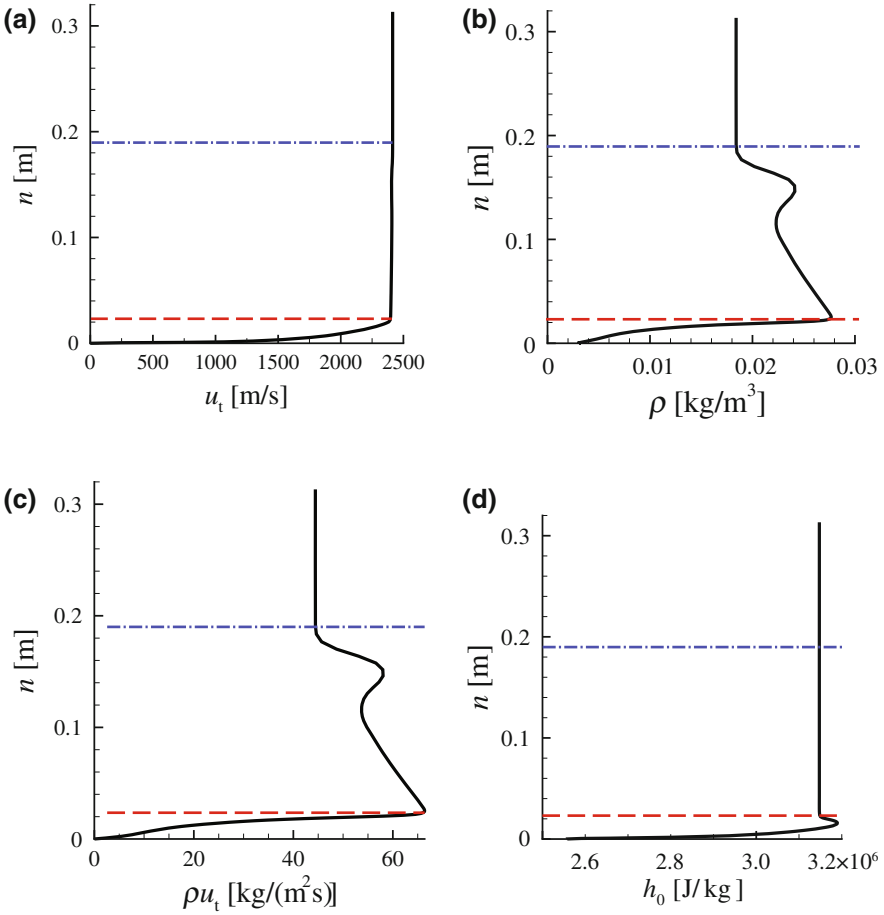

Fig. 4 Boundary layer profiles in full Busemann intake ($x = 2.016$ m): the dashed lines correspond to the boundary layer edge and the dash-dotted lines correspond to the boundary of undisturbed freestream

boundary layer edge (see Fig. 4). This is particularly true for the mass-flux tangential to the wall, and therefore the calculation of displacement thickness δ^* is highly dependent on the calculation of boundary layer thickness δ, which defines the limit of integration in the following equation:

$$\delta^* = \int_0^{\delta} \left(1 - \frac{\rho u}{\rho_e u_e}\right) \mathrm{d}n, \tag{1}$$

where n is the wall–normal coordinate and subscript e denotes the boundary-layer edge values.

An edge detection method based on profiles of total enthalpy is used. Since computations are performed with an adiabatic boundary condition, it is assumed that the

total enthalpy of the flow outside of the boundary layer is equal to the freestream value, which limits any total enthalpy gradients to the boundary layer region [3, 4]. The search for the boundary layer edge begins at the wall and the edge is found when the following conditions are satisfied simultaneously: (a) Total enthalpy is within 1% of the freestream value; (b) The gradient of total enthalpy with respect to the wall normal distance is zero. The final streamwise distribution of displacement thickness is then smoothed using a simple 3-point moving average, which results in a distribution sufficiently smooth for the CFD.

The wall correction process is performed in an iterative manner until convergence is achieved with respect to the mean-squared error given by

$$y_{\text{mse}} \equiv \frac{1}{N} \sum_{k=1}^{N} \sqrt{1 - \left(\frac{y_{\text{vis}} - \delta^*}{y_{\text{inv}}} \right)^2}, \tag{2}$$

where N is the number of data points (i.e. 51); δ^* is the boundary layer displacement thickness; and y_{inv} and y_{vis} are the distances of the point k ($1 \leq k \leq N$) on the intake wall from the symmetry axis in inviscid and viscous flows, respectively. The position of each node point k on the intake wall is updated for the next iterative step by

$$y_{\text{vis}}^{i+1} = \frac{y_{\text{inv}}}{y_{\text{vis}}^{i} - \delta^*} y_{\text{vis}}^{i} \tag{3}$$

until convergence is achieved by satisfying $y_{\text{mse}} \leq \epsilon$, which is set to be 10^{-7} in the present study.

Figure 5 shows the resulting distributions of (a) boundary layer thickness and (b) displacement thickness for the stunted Busemann intakes of various lengths ranging from 100 to 60% of the full Busemann intake length. Both plots indicate that the boundary layer grows along the intake wall from the leading edge at all stunting lengths in terms of both thicknesses, except the full Busemann intake ($L/L_{\text{full}} = 100\%$), where the thicknesses decline slightly upstream of the intake exit.

3 Results

3.1 Stunted Busemann Intakes

The viscous correction methodology has been applied to the stunted Busemann intakes. Figure 6 displays the progression of the mean-squared error defined by Eq. (2) for various intake lengths. Convergence, to 10^{-7}, is achieved in fewer iterations for highly stunted intakes and in more iterations, up to seven, for less stunted ones.

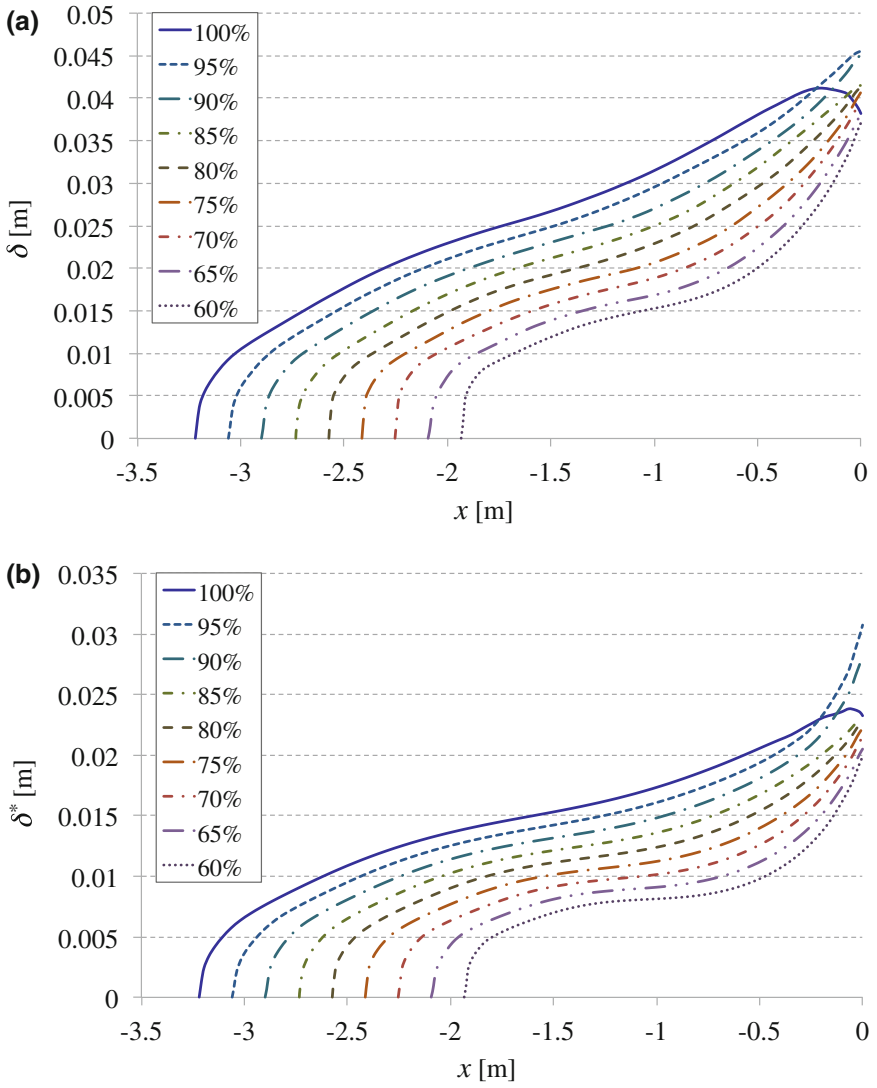

Fig. 5 Distributions of boundary layer thicknesses for stunted Busemann intakes of various length L/L_{full}

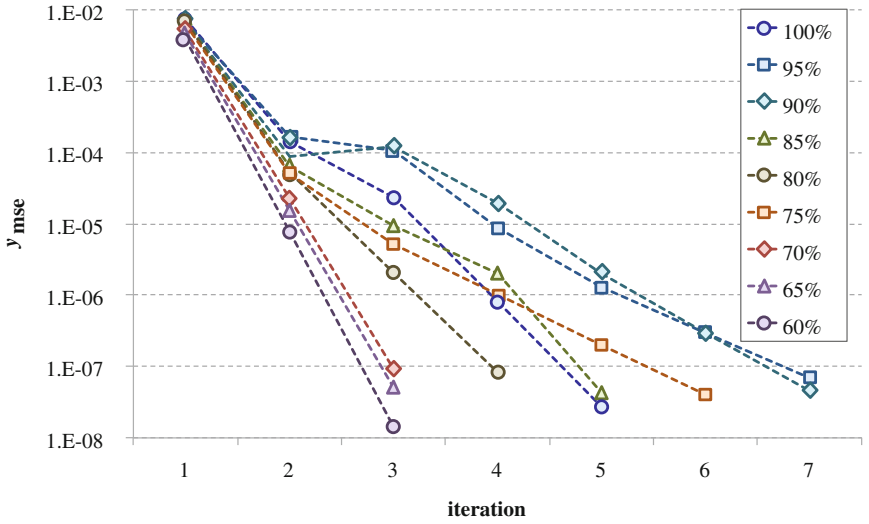

Fig. 6 Progression of viscous correction process with respect to the mean-squared error y_{mse} of intake surface geometries for stunted Busemann intakes of various length L/L_{full}

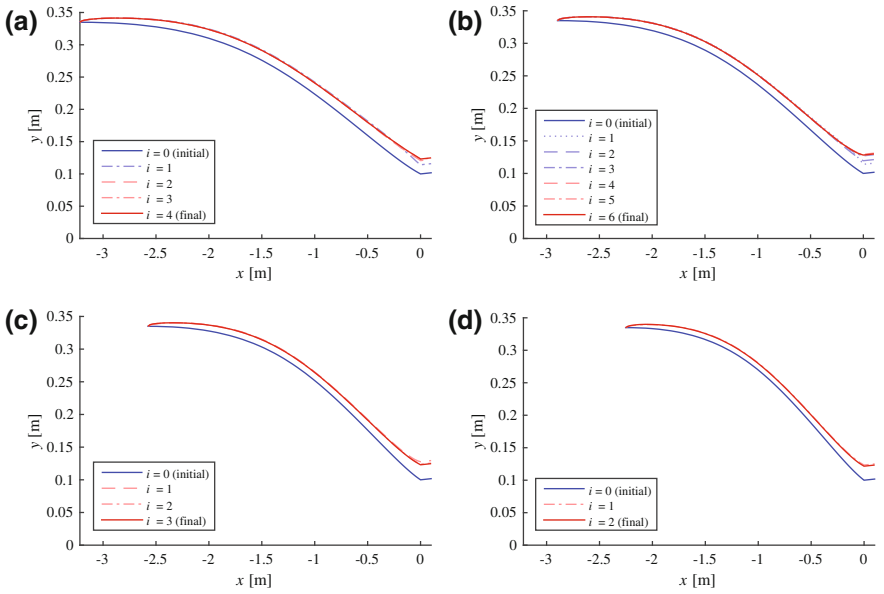

Fig. 7 Geometry progression (not to scale) in the viscous correction process starting with the inviscid geometry ($i = 0$)

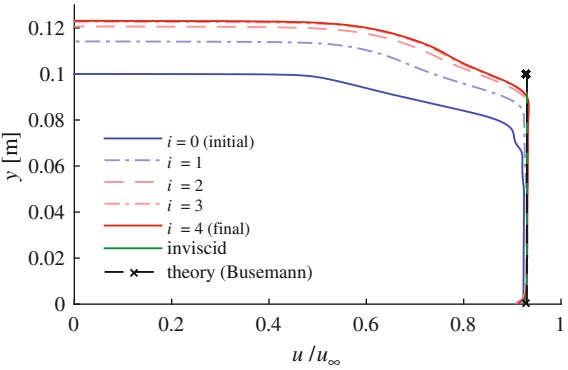

Fig. 8 Progression of velocity profiles at the exit of the full Busemann intake during the viscous correction iterative process from initial to final profile

Plotted in Fig. 7 is the progression of the intake contour shape iterations during the viscous correction process starting initially with the inviscid geometry till convergence at the final iteration step for the intake length ratios L/L_{full} of 100, 90, 80 and 70%. The intake contour is updated most significantly from the initial geometry at $i = 0$ to the next step $i = 1$ for all intake lengths, followed by rather minor modifications that occur mainly near the intake exit ($x \approx 0$ m) in the subsequent steps.

The velocity profiles (normalised by the freestream velocity) at the exit plane of the full Busemann intake at sequential iterative steps, $i = 1$ to 4, are shown in Fig. 8 in comparison with the inviscid profile. Note that the inviscid profile (green) is well duplicated by the final (solid red) profile, and that the inviscid and theoretical profiles are hardly discernible due to excellent agreement between them. A typical flat core flow is achieved in four iterations over almost entire original inviscid exit area. The effects of the boundary layer require opening the intake throat from a radius of 0.1–0.126 m, as indicated by the boundary layer velocity profiles in Fig. 8.

Figure 9 displays the viscous-corrected flowfields (bottom half of each sub-figure) in comparison with the inviscid flows (top half) for the Busemann intakes with the stunting length ratio L/L_{full} varied from 100% (full) to 60%. Reasonable similarity in flow structure is observed for the length ratios from full to ~75%. However, distinct difference appears for $L/L_{\text{full}} \leq 70\%$, where the boundary layer correction has postponed the onset of the Mach disk structure at the centreline. Distinct Mach reflection with a sizeable Mach disk occurs in the inviscid case, as seen also in the preceding studies (Figs. 2 and 3), whereas mode transition to Mach reflection is yet to take place for the viscous-corrected intakes until L/L_{full} is reduced to 60%. It appears that the severity of the centreline shock interaction is eased on the boundary layer corrected intakes, especially for the more significantly stunted intakes.

The flowfields in the vicinity of the centreline region are compared in Fig. 10. Reasonable agreement between the inviscid and viscous-corrected results can be seen for $L/L_{\text{full}} = 100, 90$ and 80%. However, the flowfields at $L/L_{\text{full}} = 70$ and 60% exhibit substantial difference in the flow structures with different types of shock reflection in inviscid and viscous flows despite virtually the same effective intake contour.

Figure 11 shows the distributions of centreline static pressure normalised by the freestream pressure at each iteration step, compared with that for the inviscid case for

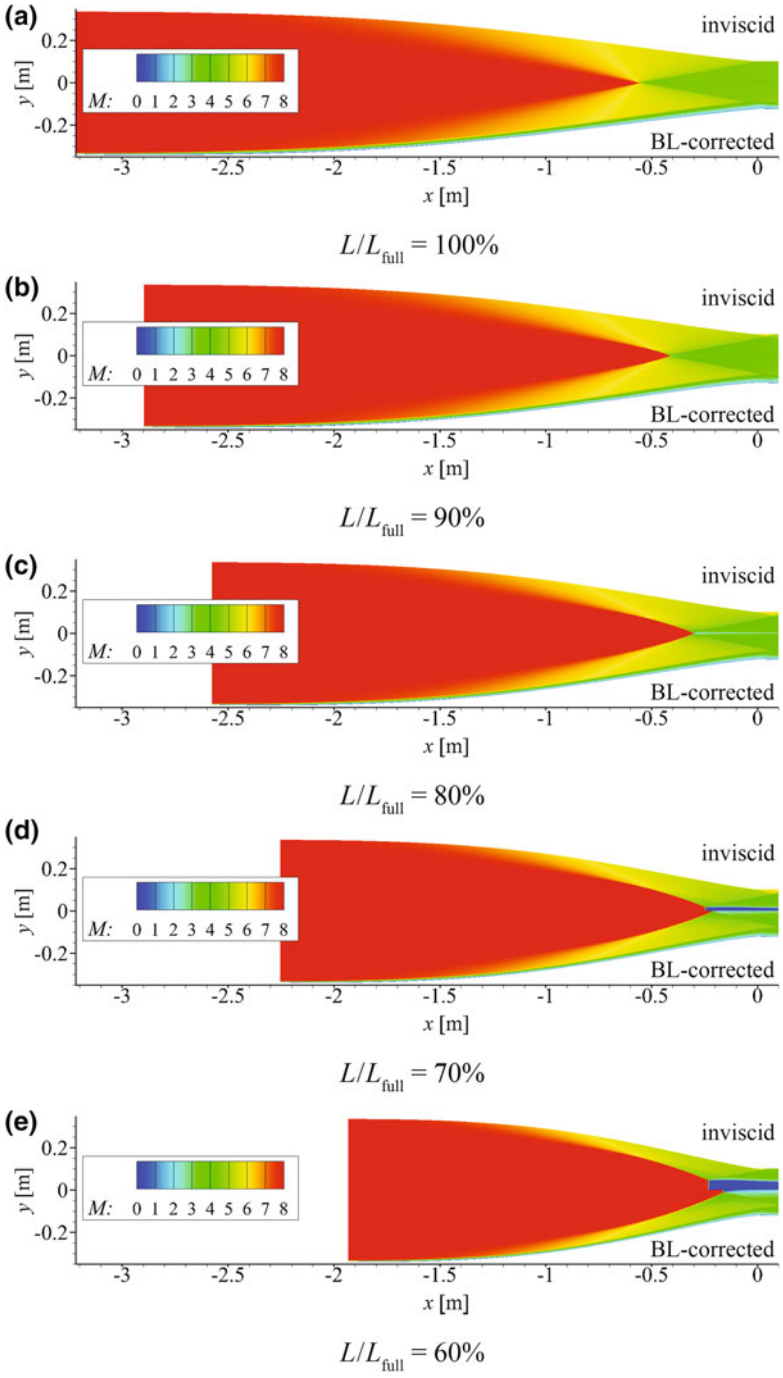

Fig. 9 Inviscid and viscous-corrected stunted Busemann intake flowfields (Mach number)

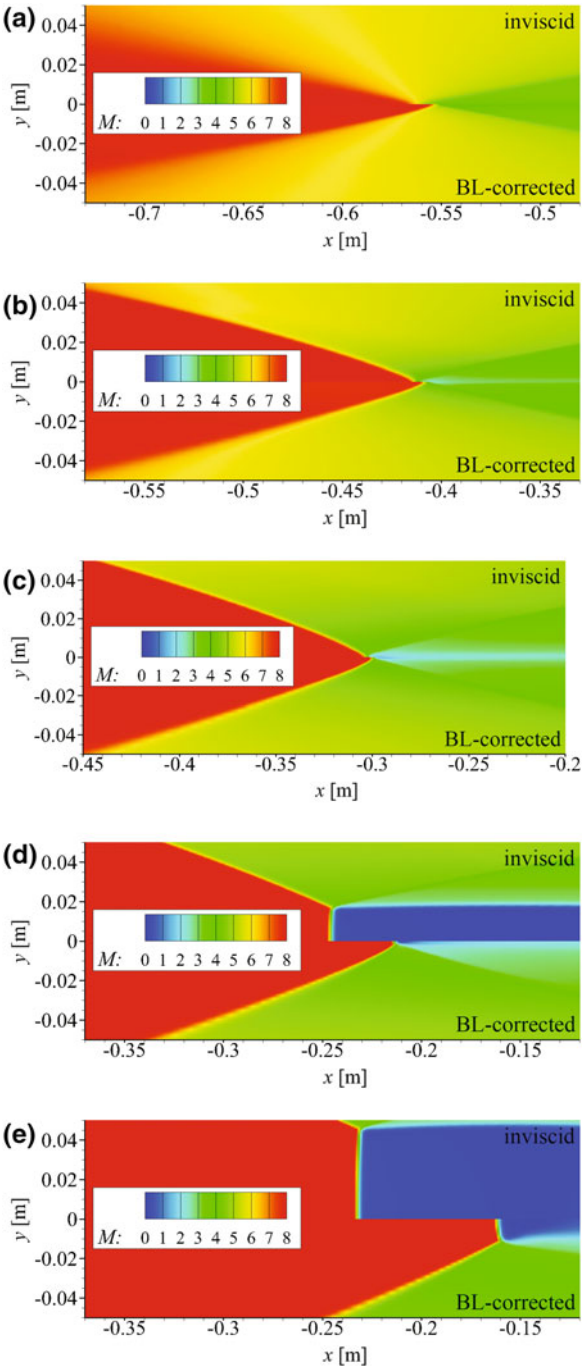

Fig. 10 Inviscid and viscous-corrected stunted Busemann intake flowfields (Mach number, close-up)

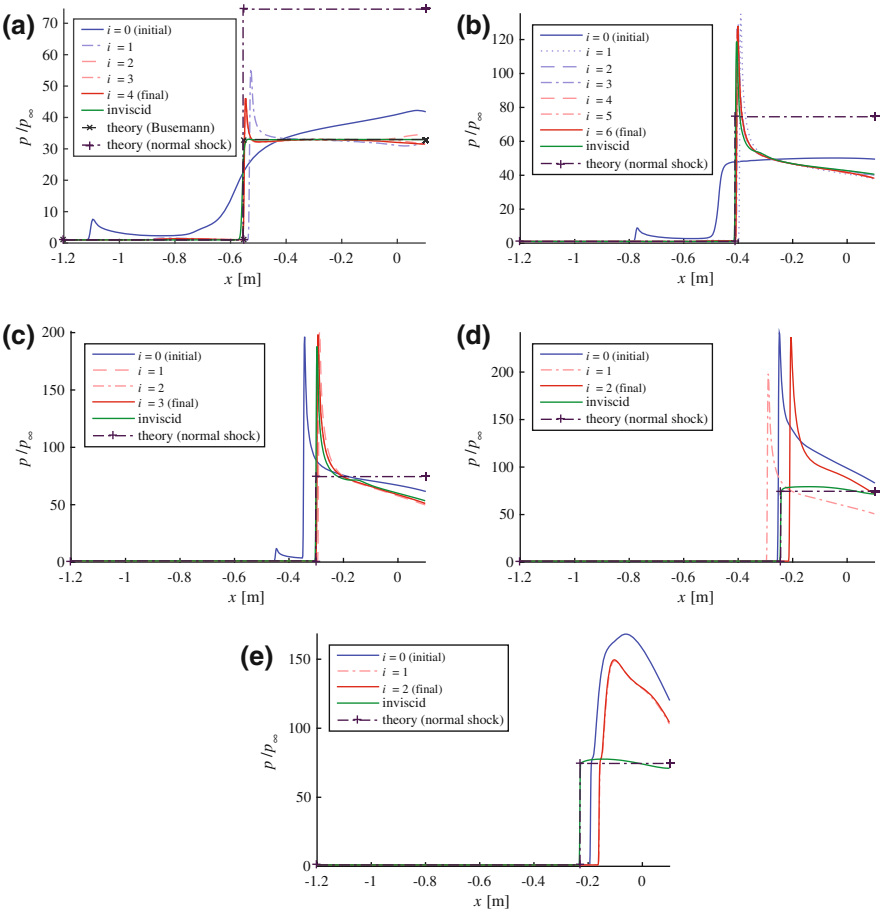

Fig. 11 Centreline pressure distributions in the viscous correction process compared with inviscid results

each intake length. The theoretical pressure jump across a normal shock is plotted for all intake lengths, and the inviscid pressure rise is also included for the full Busemann intake for comparison. The pressure distributions of the viscous flowfields calculated with the inviscid intake contours ($i = 0$) exhibit substantial discrepancy, compared with that for the inviscid case. The degree of change is the greatest at the first iteration (transition from $i = 0$ to $i = 1$) for all intake lengths. When compared to the inviscid pressure distributions, considerable deviation still exists after this initial adjustment at $i = 1$, where higher pressure is observed downstream of the initial peak due to the reflection of the compression waves coalesced at the centreline. This observation was also reported in [14].

The pressure distribution of the viscous-corrected Busemann intake is characterised by the presence of a little overshoot for the full Busemann intake in Fig. 11a. This is attributed to the coalescence of the compression waves that does not occur

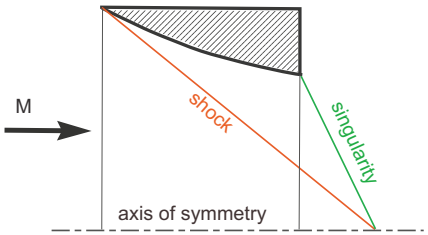

Fig. 12 Axisymmetric M-flow ring. Flow inside the three-sided region, bounded by the shock, the singularity and the inner surface, is axially and conically symmetric and irrotational and is governed by the Tailor–Mccoll equation. In reality, there is a Mach shock structure near the symmetry axis

precisely at the focal point due to slight deviations, unlike the inviscid case characterised by a step-like pressure rise across a conical shock wave. It is noteworthy that as a result of the viscous correction at $i = 4$, the centreline pressure downstream of the focal point settles at the theoretical value for the full Busemann intake, *i.e.* $p/p_\infty = 33.0$, along with the inviscid case. On the other hand, difference is evident in the pressure distributions for the stunted Busemann intakes at $L/L_{\text{full}} = 70$ and 60% in Figs. 11d and e, respectively, between the inviscid and viscous-corrected flowfields, resulting from the mode transition to Mach reflection (Figs. 9 and 10, the inviscid case), as also indicated by the pressure distributions for the inviscid flow, which are close to those from the normal shock theory.

3.2 M-Flow Intake Rings

M-flow is a conically and axially symmetric supersonic flow that occurs downstream of a conical, axisymmetric shock that has a downstream-pointing apex [6] (Fig. 12). Because of a high degree of flow convergence, such a shock cannot propagate all the way to the symmetry axis [11]. Instead, a Mach shock structure appears at the axis (Fig. 13a). However, the fact that such a shock has a constant strength over most of its surface results in irrotational and conical flow downstream of the shock. The annular ring, required to produce the conical shock and flow, becomes an attractive candidate for the leading edge shape of a truncated or stunted intake. It is then relevant to calculate the boundary layer development on the ring surfaces and the effect of the boundary layer on the internal flow, particularly at the centreline. Two rings were considered, one with an internal shock cone angle of 80° and the other with an angle of 100°. Figure 13a shows the overall shock structure inside the 100° ring. The top half view is for inviscid flow and the bottom half is for flow on the inviscid contour with a surface boundary layer. In both cases the incident, conical shock reverts to a Mach interaction structure at the centreline. The Mach disk is somewhat further forward for the contour with the boundary layer. Figure 13b is a close-up of the flow in the vicinity of the centreline.

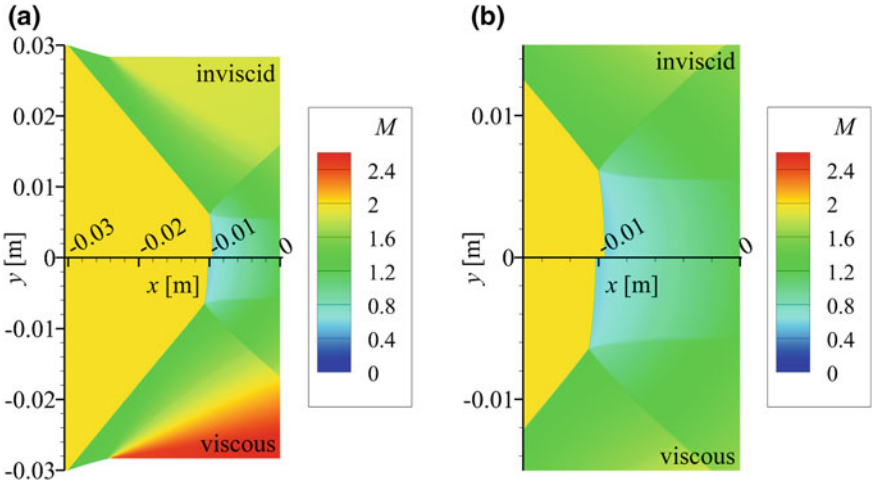

Fig. 13 Mach number contours of flow in M-flow ring that produces a conical shock with internal cone angle of 100° for flow without (top half) and with boundary layer (bottom half)

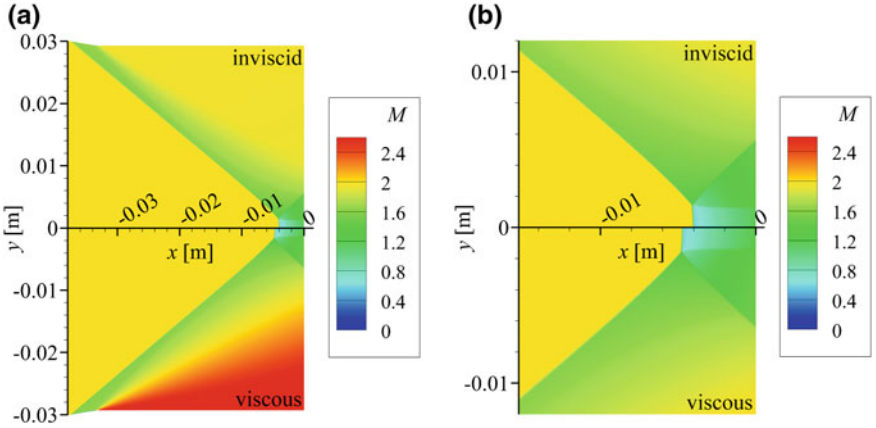

Fig. 14 Mach number contours of flow in M-flow ring that produces a conical shock with internal cone angle of 80° for flow without (top half) and with boundary layer (bottom half)

Figures 14a and b show the same boundary layer effect on the M-flow centreline for the 80° shock. The iterative boundary layer correction technique, described above for the Busemann intake, has been applied to both M-flow rings in Figs. 15 and 16. Figures 15a, b both show the flow for the inviscid flow, on the top half, and the flow in the boundary layer corrected ring in the lower half of the figures. Figure 16 shows similar results for the 100° shock. The similarity of the inviscid and the viscous-corrected flows indicates that the boundary layer correction method is successful.

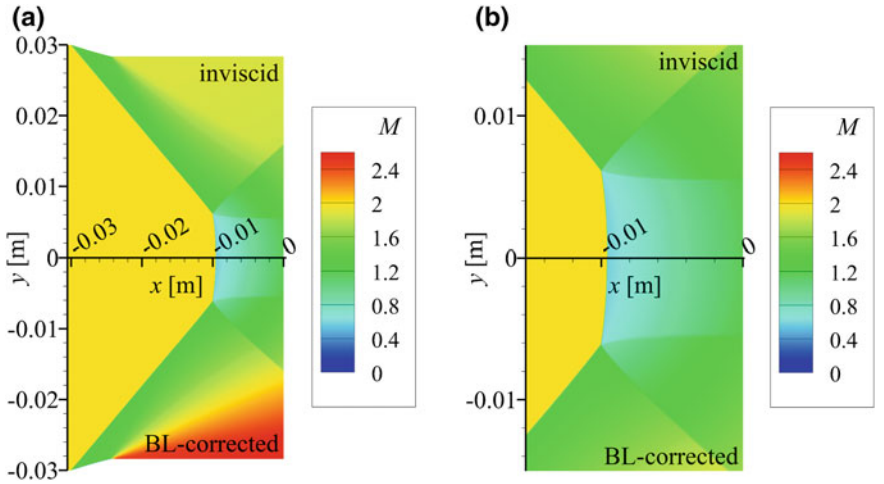

Fig. 15 Mach number contours of flow in M-flow ring that produces a conical shock with internal cone angle of 100° for flow on an inviscid contour (top half) and a boundary-layer corrected contour (bottom half)

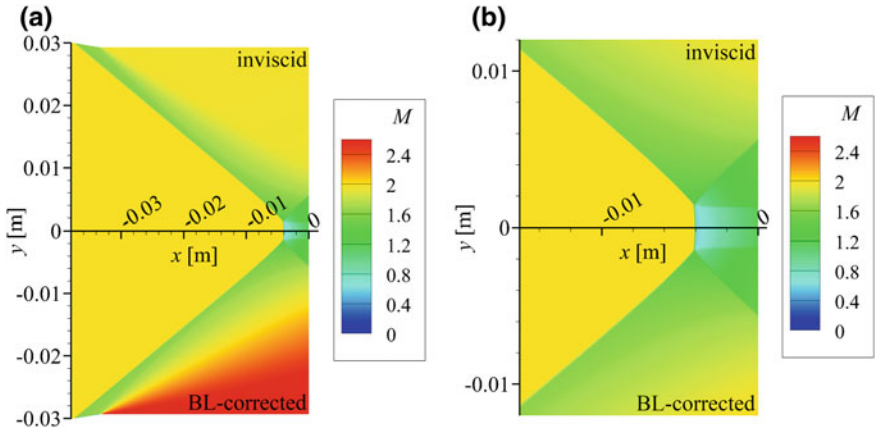

Fig. 16 Mach number contours of flow in M-flow ring that produces a conical shock with internal cone angle of 80° for flow on an inviscid contour (top half) and a boundary-layer corrected contour (bottom half)

4 Conclusions

An effective and robust viscous correction methodology has been developed by coupling viscous CFD computations with a wall correction method based on local boundary layer displacement thickness. One particularly important factor in achieving this is the use of an edge detection method based on the total enthalpy profile. This iterative process has been applied to two classes of high-speed air intakes,

namely, stunted (axially contracted) Busemann intakes for a hypersonic freestream at Mach 8 and M-flow intake ring geometries in a supersonic freestream at Mach 2.

For moderately stunted intakes, the viscous-corrected geometries have been shown to reproduce the inviscid flow conditions with a high degree of accuracy, validating the overall approach. Single application of viscous correction has been found to be inadequate for the full and stunted Busemann intakes, requiring an iterative process in order to achieve accurate reproduction of inviscid features in the presence of viscous effects. Boundary layer correction attenuated the severity of centreline shock reflection and delayed the onset of its mode transition to Mach reflection. For more highly stunted intake surfaces the boundary layer correction leads to centreline flows that exhibit a less severe centreline interaction than that of the inviscid flow.

Overall, an improvement has been achieved in the reproduction of the initial inviscid fields, which indicates that the methods outlined here can be usefully employed to improve the design of axisymmetric internal compression intakes for viscous flows.

Acknowledgements This study has been conducted in line with the General Collaborative Research Projects J14054 and J16090 and Multiple Collaborative Research Project J15R005 coordinated and funded by the Institute of Fluid Science, Tohoku University. The authors are grateful for their support, which inspired and enabled the present research. Hideaki Ogawa is thankful to the Australian Research Council for their financial support in the ARC DECRA (Discovery Early Career Research Awards) fellowship (DE120102277). Ben Shoesmith gratefully acknowledges the MEDA scholarship funded by the Faculty of Engineering, McGill University, and the FRQNT and NSERC funding agencies.

References

1. Carter, J.E.: A new boundary-layer interaction techniques for separated flows. NASA-TM-78690 (1978)
2. Flock, A.K., Gülhan, A.: Viscous effects and truncation effects in axisymmetric Busemann scramjet intakes. AIAA Paper 2015-0108 (2015)
3. Greene, F.A., Hamilton, H.H.: Development of a boundary layer properties interpolation tool in support of Orbiter return to flight. AIAA Paper 2006-2920 (2006)
4. Mcnally, W.D.: BLAYER—Compressible laminar and turbulent boundary layers in arbitrary pressure gradients. Computer Program, LEW-11097, NASA Lewis Research Center (1994)
5. Metacomp Technologies Inc: CFD++. Software Package, Ver. 15.1 (2015)
6. Mölder, S.: Internal, axisymmetric, conical flow. AIAA J **5**(7), 1252–1255 (1967)
7. Mölder, S., Romeskie, J.M.: Modular hypersonic inlets with conical flow. SP-30, Advisory Group for Aeronautical Research and Development, NATO (1968)
8. Mölder, S., Szpiro, E.J.: Busemann inlet for hypersonic speeds. J. Spacecraft Rockets **3**(8), 1303–1304 (1966)
9. Ogawa, H., Mölder, S., Boyce, R.R.: Effects of leading-edge truncation and stunting on drag and efficiency of Busemann intakes for aisymmetric scramjet engines. JSME J. Fluid Sci. Technol. **8**(2), 186–199 (2013)
10. Ogawa, H., Mölder, S., Timofeev, E.V.: Numerical investigation of Mach reflection hysteresis in stunted Busemann intakes for axisymmetric scramjet engines. In: Proceedings of the 10th International Conf on Fluid Dynamics, Tohoku University, Sendai, Japan, 25–27 Nov 2013 (2013)

11. Rylov, A.I.: On the impossibility of regular reflection of a steady-state shock wave from the axis of symmetry. Prikl Mat Mekh **54**, 200–203 (1990)
12. Shoesmith, B., Mölder, S., Timofeev, E., Ogawa, H.: Shock reflection in axisymmetric internal flows. In: Present ISIS22 Proceedings (2016)
13. Van Wie, D.M., Mölder, S.: Applications of Busemann inlet designs for flight at hypersonic speeds. AIAA Paper 92-1210 (1992)
14. Walsh, P.C., Tahir, R.B., Mölder, S.: Boundary-layer correction for the Busemann hypersonic air inlet. Can. Aeronaut. Space J. **49**(1), 11–17 (2003)

Experimental and Numerical Results from Shock Propagation Through Dust Columns in a Shock Tube

M. G. Omang, K. O. Hauge and J. Trulsen

Abstract This chapter presents experimental and numerical work in progress on shock propagation through dust columns in a shock tube environment. The shock tube consists of a short double driver chamber separated by membranes from the driven section. The shock tube is instrumented with pressure sensor and high-speed cameras. A specially designed window section allows Schlieren and shadow photography to be recorded simultaneously, in directions perpendicular to each other. The dust column is injected from below in the driven section, using a spark generator. The timing is such that the dust is in suspension before the shock arrives. The numerical method Regularized Smoothed Particle Hydrodynamics has been used to simulate shock–dust interaction problems, with a full multiphase description. Comparison with experimental data shows promising results for further studies on shock–dust interactions.

1 Introduction

This chapter presents the experimental and numerical work in progress on shock propagation through dust columns in a shock tube environment. A new laboratory is under development at Østøya, close to Horten, Norway, where the experimental work has been performed. The project has been aimed at redesigning the shock tube with a proper window section to allow both optical techniques and pressure sensors to be used.

The numerical work is performed with our in-house code, Regularized Smoothed Particle Hydrodynamics (RSPH), which has been demonstrated to simulate shock–dust interaction problems, with a full multiphase description Omang and Trulsen [6], presenting good results.

M. G. Omang (✉) · J. Trulsen
Institute of Theoretical Astrophysics, University of Oslo, 1029 Blindern, 0315 Oslo, Norway
e-mail: momang@astro.uio.no

M. G. Omang · K. O. Hauge
Norwegian Defence Estates Agency, Forsvarsbygg Futura, 405 Sentrum, 0103 Oslo, Norway
e-mail: knut.ove.hauge@forsvarsbygg.no

K. Kontis (ed.), *Shock Wave Interactions*,
https://doi.org/10.1007/978-3-319-73180-3_15

Development of numerical methods within this field is dependent on complete and relevant experimental data set, which unfortunately has been difficult to find in the literature, both for inert and reactive particles. Although the results presented here are preliminary, they demonstrate the potential of both the experimental facility and the numerical work, and have already given valuable knowledge for further developments of the experimental setup.

2 Numerical Method

RSPH is a Lagrangian particle interpolation method, where particles are used to simulate a continuous fluid flow. Each particle carries a set of properties, typically mass, pressure, density, velocity, and energy. In multiphase problems, additional properties are introduced, such as the void fraction, θ, describing how dilute the gas-particle distribution is. The smoothing length is the measure of the interaction zone for a given particle. Typically, particles within two smoothing lengths interact with each other in the simulations. A fundamental review on SPH is given in Monaghan [5].

In a multiphase SPH description, each phase has separate sets of particles and a separate set of equations of motion. In the case of nonreactive particles, the two phases are coupled through heat exchange, viscosity, and drag effects. In the present work, the Knudsen and Katz [4] Nusselt number for heat exchange, the dynamic viscosity coefficient from Chapman and Cowling [2], and the Ingebo [3] drag coefficient have been used.

RSPH has two extra functionalities different from regular SPH. First of all, it allows a stepwise variable resolution, in which the smoothing length is allowed to vary in steps of a factor 2. In production simulations, three or four levels of smoothing lengths are typically chosen.

A regularization process is also implemented, which allows the particle distribution to be redistributed at regular time intervals. The regularization is typically carried out every 40–50 time steps. To ensure conservation of mass, momentum, and energy, the particles inherit their properties from the old particle distribution. The regularization process is introduced to optimize the resolution and maintain numerical accuracy over time. A thorough description of RSPH could be found in Borve et al. [1].

3 Experimental Setup

The shock tube consists of a double driver chamber of lengths, $L_{D1} = 0.09$ and $L_{D2} = 0.03$ m, separated by Mylar Dupont membranes from the driven section of $L_{D3} = 8.6$ m. Initially, both driver chambers are pressurized. The first membrane will burst when the pressure in the second chamber is reduced, and the pressure difference between the two driver sections increases above the membrane threshold

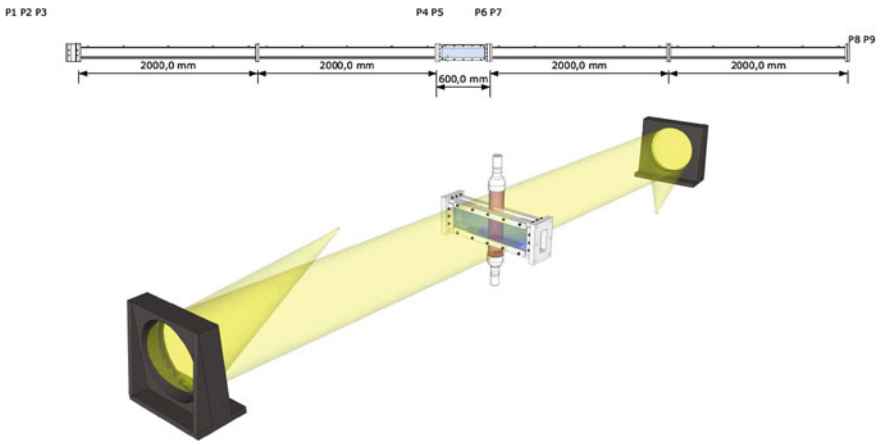

Fig. 1 Upper panel shows a sketch of the shock tube, with positions for pressure sensors P. The lower panel shows a sketch of the optical system. In both panels, the window section glass is illustrated in blue

Table 1 Pressure sensor positions

Test	P_1	P_2	P_3	P_4	P_5	P_6	P_7	P_8	P_9
x [m]	0.015	0.105	0.22	4.22	4.22	4.62	4.62	8.72	8.705
h [m]	0.084	0.084	0.10	0.10	0	0.10	0	0.054	0.10

level. A high degree of repeatability is observed with the use of the double driver chamber facility. The shock tube is illustrated in Fig. 1, with pressure sensor positions $P_{1,2,3,\ldots,9}$ included. The exact pressure sensor positions are given in Table 1. Preliminary tests to reduce the pressure in the driven section have also been investigated, as this technique could extend the experimental Mach number range as well as increase the temperature, which is important for shock ignition of reactive particles.

A specially designed window section allows Schlieren and shadow photography to be recorded simultaneously, in directions perpendicular to each other. The system is illustrated in the sketch of Fig. 1. A Z-type Schlieren system is set up, with parabolic mirrors of diameter 317.5 mm and effective focal length of 2540 mm used together with a Cree XM–L Led lamp. As illustrated in Fig. 1, the shadow photography technique is mounted in the vertical direction. The dust column is injected from below, at $x = 4.442$ m, using a spark generator. The dust consists of aluminum-coated barium titanate solid glass microspheres manufactured by Cospheric. The glass particles have a density of 4490 kg/m^3, and a mean diameter size of 40–50 μm. The timing is such that the dust is in suspension before the shock arrives. The image from the second parabolic mirror is focused on a knife-edge and captured with a Phantom Miro 310 high-speed camera using a Nikkor 70–200 mm 2.8 lens. A frame rate of 8680 frames per second is used.

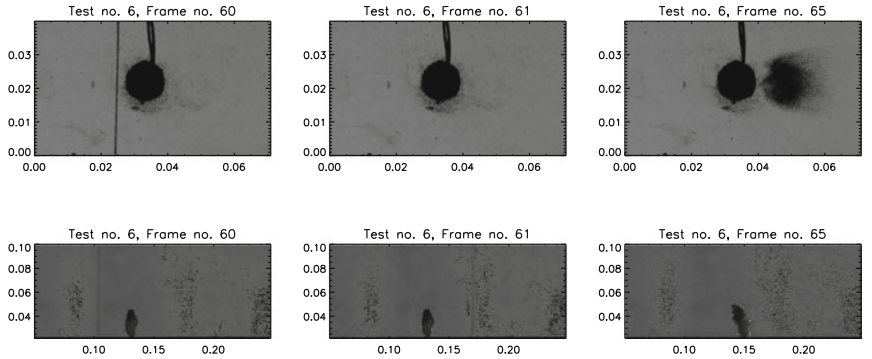

Fig. 2 High-speed video of a shock propagating through a dust column. The upper panel shows the shadow photography as observed from above. The lower panel shows the results from the Schlieren photography, as observed from the side

Test results of the high-speed video are illustrated in Fig. 2. The upper panel shows the video from the shadow photography as observed from above. In the first two frames, it is difficult to distinguish the dust, which has been injected from below, from the injection system, consisting of a black circular disk and cable. The left panel shows the situation right before the shock arrives at the dust cloud. The shock is observed as a black vertical line. In the next frame, the shock has passed through the cloud, and out of the picture, but the dust cloud has not moved significantly jet and is still difficult to observe. The last picture shows the same situation 4 frames, or 0.46 ms later. Here, the dust cloud clearly has moved to the right, relative to the initial position. The circular shape of the cloud is worth noticing.

In the lower panel of Fig. 2, the results from the Schlieren photography technique are presented, with a larger field of view. In the left panel, the dust column is observed prior to shock passage, with the shock visible to the left of the cloud. The next panel illustrates the situation right after shock passage. At this time, the dust column has not moved significantly yet, whereas in the right panel, we observe how the dust has been accelerated and moved to the right relative to the previous results. For these preliminary experimental results, the synchronization of the two high-speed cameras are within or less than one picture cycle time. For the experiment presented in Fig. 2, there is a synchronization difference of approximately one-third of a picture cycle time.

4 Results Presentation and Discussion

The initial conditions of the numerical simulations are determined from the pressure gauges in the two driver sections. In these preliminary test, the temperature is measured for the atmospheric conditions in the room, only. In Table 2, the densities given

Table 2 Initial conditions for the numerical simulations

Test no.	P_0 [kPa]	P_1 [kPa]	P_2 [kPa]	ρ_0 [m/kg^3]	ρ_1 [m/kg^3]	ρ_2 [m/kg^3]	ρ_d	θ_d	d_d [μm]
4	100.01	167.53	980.52	1.203	1.8	10.0	2702	0.0005	6
6	32.47	165.100	998.36	0.4134	1.8	10.0	4490	0.0005	40

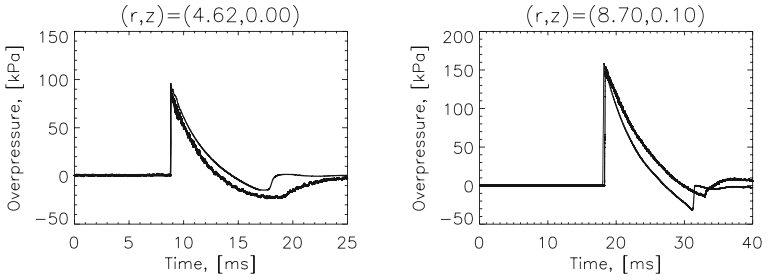

Fig. 3 Experimental and numerical pressure–time histories downstream of the window section for two different sensor positions

in the two driver sections are, therefore, based on assumptions relating the external and internal temperatures. The void fraction has so far been difficult to determine experimentally. Techniques to determine the void fraction are currently being evaluated. In Fig. 3, pressure sensor measurements downstream of the window section is plotted for both numerical and experimental results, the experimental results with the thicker line style. Results are presented for two different positions, $x = 4.62$ m and $x = 8.70$ m. As the figure illustrates, both time of arrival and pressure levels show good agreement with the experimental results.

Numerical simulations were also performed to study shock interaction with the dust cloud. Figure 4 shows a density contour plot of the dust cloud, plotted in x-y coordinates. In the results presented here, a dust particle diameter of 40 μm was chosen, as this choice was found to give the best agreement with the experimental data. The dust cloud position was determined manually from the high-speed Schlieren pictures and has been plotted on top with a black contour line. The plot illustrates the situation for two different time steps, $t = 6.4$ ms and $t = 7.1$ ms after membrane rupture.

In the current work, only one-size dust particles were assumed, described with a constant smoothing length. In the real experiments, the particles had a mean size of 40–50 μm, but particles of other sizes were also present in the distribution, although fewer. The specifications for the particles indicate a size range from 32 to 80 μm. Introducing particles of different sizes in the simulations, also implies introducing one phase for each particle size, this would be possible, but quite time-consuming. Although the results presented here were based on relatively low-resolution simulations, using 270 dust particles, and gas simulation particles starting at approximately

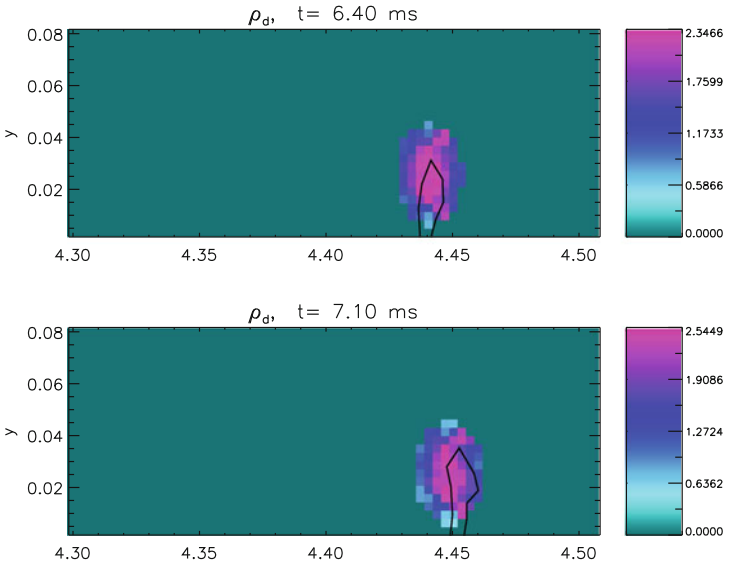

Fig. 4 Numerical simulations of the dust column at two different time steps, before and after shock interaction. The black contour line illustrates the position of the cloud captured manually from the Schlieren high-speed video

60000, and increasing to 400000 at the end, the results show good agreement and are promising for further studies on shock–dust interactions.

References

1. Børve, S., Omang, M., Trulsen, J.: Regularized smoothed particle hydrodynamics with improved multi-resolution handling. J. Comput. Phys. **208**(1), 345–367 (2005)
2. Chapman, S., Cowling, T.G.: The Mathematical Theory of Non-uniform Gases. Cambridge University Press (1961)
3. Ingebo, R.D.: Drag coefficients for droplets and solid spheres in clouds accelerating in air streams. Technical Report No. TN 3762, NACA Technical Note TN (1956)
4. Knudsen, J., Katz, D.: Fluid Mechanics And Heat Transfer. McGraw-Hill, New York (1958)
5. Monaghan, J.J.: Smoothed particle hydrodynamics. Rep. Prog. Phys. **68**(8), 1703–1759 (2005)
6. Omang, M., Trulsen, J.: Multi-phase shock simulations with Smoothed Particle Hydrodynamics (SPH). Shock Waves **24**(5), 521–536 (2014)

Triple-Point Singularity and the Neumann Paradox of Mach Reflection

A. Sakurai and S. Kobayashi

Abstract The singular nature of the flow near the triple point is investigated analytically based on a solution of the steady 2D Navier–Stokes equations system in polar coordinates, with special attention on the cause of the Neumann paradox. It gives a centered fan-like flow from the triple point in widening the slip flow region. Angles and curvatures of the reflected (R) and Mach stem (m) shock lines given in the solution are consistent with existing experiment data.

1 Introduction

We consider the flow field behind Mach reflection, especially its singular nature at its triple point in connection with the problem of the Neumann or triple-point paradox [1–4]. Neumann's three-shock theory [5, 6] based on nonviscous gas dynamics indicates two parallel uniform flows separated by a slip streamline, and it provides shock angles in excellent agreement with experiment data for strong Mach reflection. Rather paradoxically, no agreement at all is observed for weaker cases.

In these experiments and direct numerical simulations of the flow field, we observe uniform flows with a slip line for stronger cases, but this becomes blurred for weaker cases, where we can see a disturbance from the edge reaching to the triple point [7, 8], making the entire flow field nonuniform. Thus, it is necessary to find the details of the flow field, especially the singular nature near the triple point. To do so, we must use an analytical approach because of the singularity, for which a conventional numerical approach is inappropriate. The use of the Euler equations is useless in providing a solution for two uniform flows separated by a slip flow line, as given in Neumann's three-shock theory. Instead, we use the Navier–Stokes equations in polar coordinates.

A. Sakurai
Tokyo Denki University, Senju, Tokyo 120-8551, Japan

S. Kobayashi (✉)
Saitama Institute of Technology, Fukaya, Saitama 369-0293, Japan
e-mail: kobayasi@sit.ac.jp

K. Kontis (ed.), *Shock Wave Interactions*,
https://doi.org/10.1007/978-3-319-73180-3_16

The three-shock configuration appears in both steady (e.g., supersonic inlet flow) and unsteady (e.g., advancing plane shock wave over a sharp wedge surface) flows. The Neumann paradox phenomenon occurs in both cases. The feature of the flow, especially the singular nature at the triple point, is common to both; thus, in the present study, we focus mainly on steady flow.

2 Basic Equations for the Flow Field Behind Steady Mach Reflection

We consider the flow field in the angular region between the reflected shock wave (R) and the Mach stem (m) behind a steady Mach reflection (Fig. 1). We use the polar coordinate system (r, θ) $(0 < r < \infty, -\pi < \theta < \pi)$ with the basic line $\theta = 0$ at the x-axis for the direction of incoming flow with its origin at the triple point. Here, m is at $\theta = -\lambda$ and R is at $\theta = \omega'$, both angles at the triple point. Let $\mathbf{V} = (V_r, V_\theta)$ be the flow velocity, its r, θ components be the pressure of the flow field, and p, ρ be its density. They are all functions of the variables r, θ. We use the Navier–Stokes system of equations for steady 2D flow as

$$
\begin{aligned}
&\frac{V_\theta}{\rho}\frac{\partial \rho}{\partial \theta} + \frac{\partial V_\theta}{\partial \theta} + V_r + \frac{r}{\rho}\frac{\partial}{\partial r}\rho V_r = 0 \\
&\quad [\rho(\bar{D}V_r - V_\theta^2) + r\frac{\partial p}{\partial r}]r \\
&= \mu[\Delta V_r - V_r - 2\frac{\partial V_\theta}{\partial \theta} + \frac{r^2}{3}\frac{\partial}{\partial r}\frac{1}{r}(r\frac{\partial V_r}{\partial r}\frac{\partial V_\theta}{\partial \theta} + V_r)] \\
&\quad [\rho(\bar{D}V_\theta + V_r V_\theta) + \frac{\partial p}{\partial \theta}]r \\
&= \mu[\Delta V_\theta - V_\theta + 2\frac{\partial V_r}{\partial \theta} + \frac{1}{3}\frac{\partial}{\partial \theta}(r\frac{\partial V_r}{\partial r} + \frac{\partial V_\theta}{\partial \theta} + V_r)] \\
&\quad \rho(\bar{D}E + p\bar{D}\rho^{-1})r = \kappa\Delta T + \mu\Phi \\
\Phi &\equiv 2(r\frac{\partial V_r}{\partial r})^2 + 2(\frac{\partial V_\theta}{\partial \theta} + V_r)^2 \\
&\quad + (r\frac{\partial V_\theta}{\partial r} + \frac{\partial V_r}{\partial \theta} - V_\theta)^2 - \frac{2}{3}\frac{\partial}{\partial r}(r\frac{\partial V_r}{\partial r} + \frac{\partial V_\theta}{\partial \theta} + V_r)^2
\end{aligned}
\tag{1}
$$

where

$$
\bar{D} \equiv V_r r\frac{\partial}{\partial r} + V_\theta\frac{\partial}{\partial \theta}, \quad \Delta \equiv r\frac{\partial}{\partial r}r\frac{\partial}{\partial r} + \frac{\partial^2}{\partial \theta^2}.
$$

These are supplemented by the equations of a perfect gas, $E = c_v T$, $p = \rho RT$, where E is internal energy, T is temperature, R is gas constant, c is specific heat

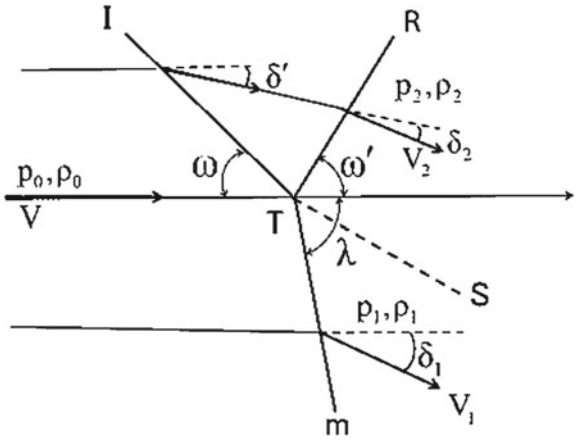

Fig. 1 Three-shock configuration

at constant volume, μ is the coefficient of the viscosity, and κ is heat conductivity, which are assumed to be constant.

This system is suitable for analyzing the flow field in the angular region between two shock lines (R and m) and is particularly useful for visualizing the singular nature of the flow field at the triple point by extending it to a line segment of ($r = 0,\ -\lambda < \theta < \omega'$) in this coordinate system.

Let $\theta = \theta_1(r),\ \theta = \theta_2(r)$ be the shapes of m and R; let $\mathbf{X} = (V_\theta, V_r, \rho, p)$; and let $\mathbf{X}_1 = (V_{\theta 1}, V_{r1}, \rho_1, p_1),\ \mathbf{X}_2 = (V_{\theta 2}, V_{r2}, \rho_2, p_2)$ be the shock wave values at the shock fronts $\theta = \theta_1(r),\ \theta = \theta_2(r)$, which express m and R. Thus, we have the boundary condition

$$\mathbf{X}(\theta_1) = \mathbf{X}_1, \mathbf{X}(\theta_2) = \mathbf{X}_2. \tag{2}$$

Furthermore, we keep in mind the fact that angular velocity component V_θ must be zero for some $\theta = \theta_0$, to be determined later, since the flow field is almost uniform and parallel. Furthermore, $\partial\rho/\partial\theta$ in Eq. (1) must be continuous so that

$$\begin{aligned} &(V_\theta)_{\theta=\theta_0} = 0, \\ &[(\partial V_\theta/\partial\theta) + V_r + (r/\rho)\cdot(\partial\rho V_r/\partial r)]_{\theta=\theta_0} = 0. \end{aligned} \tag{3}$$

3 Solution in Integral Form

We use the conditions of Eqs. (1)–(3) to determine the flow field, along with the shapes of shock front lines. We consider this in an integrated form of Eq. (1):

$$
\begin{aligned}
\frac{V_\theta}{\rho}\frac{\partial \rho}{\partial \theta} + \frac{\partial V_\theta}{\partial \theta} + V_r &= f_0 \\
3\frac{\partial^2 V_r}{\partial \theta^2} - 4V_r - 7\frac{\partial V_\theta}{\partial \theta} &= rf_1 \\
4\frac{\partial^2 V_\theta}{\partial \theta^2} - 3V_\theta + 7\frac{\partial V_r}{\partial \theta} &= rf_2 \\
\frac{\partial^2}{\partial \theta^2}\left(\frac{p}{\rho}\right) + \frac{\mu}{\kappa}[\Phi]_0 &= f_3,
\end{aligned}
\tag{4}
$$

where

$$
\begin{aligned}
f_0 &\equiv -\frac{r}{\rho}\frac{\partial}{\partial r}\rho V_r \\
f_1 &\equiv \frac{3}{\mu}[\rho(\bar{D}V_r - V_\theta^2) + r\frac{\partial p}{\partial r}] \\
&\quad + 4\frac{\partial}{\partial r}r\frac{\partial V_\theta}{\partial r} - \frac{\partial V_r}{\partial r} + \frac{\partial}{\partial r}(\frac{\partial V_\theta}{\partial \theta} + V_r) \\
f_2 &\equiv \frac{3}{\mu}[\rho(\bar{D}V_\theta + V_r V_\theta) + \frac{\partial p}{\partial \theta}] - 4\frac{\partial}{\partial r}r\frac{\partial V_r}{\partial r} - \frac{\partial^2 V_r}{\partial r \partial \theta} \\
f_3 &\equiv \frac{r}{R}\{\frac{1}{\kappa}(\rho\bar{D}E + p\bar{D}\rho^{-1}) - \frac{\partial}{\partial r}r\frac{\partial}{\partial r}\frac{p}{\rho}\} - \frac{\mu}{\kappa}\Phi + \frac{\mu}{\kappa}[\Phi]_0.
\end{aligned}
$$

We express Eq. (4) in integral form in the following way. First, we find the solution of the second and third equations of Eq. (4), which are simultaneous ordinary differential equations with f_1, f_2 terms assumed to be given functions of θ only including a fixed r as a parameter. We then use these solutions in the first and the fourth equations of Eq. (4) to have expressions for ρ and p:

$$
\begin{aligned}
\mathbf{V} = \begin{pmatrix} V_\theta \\ V_r \end{pmatrix} &= \begin{pmatrix} V_{\theta 0} + \tilde{V}_\theta \\ V_{r0} + \tilde{V}_r \end{pmatrix} \begin{pmatrix} V_{\theta 0} \\ V_{r0} \end{pmatrix} \\
&\equiv \begin{pmatrix} A + B\theta & C + D\theta \\ C + \frac{1}{7}B + D\theta & -\left(A + \frac{1}{7}D + B\theta\right) \end{pmatrix} \begin{pmatrix} \sin\theta \\ \cos\theta \end{pmatrix} \\
\begin{pmatrix} \tilde{V}_\theta \\ \tilde{V}_r \end{pmatrix} &\equiv \int_{\theta_0}^{\theta} \sin(\theta - \theta^*)\{\int_{\theta_0}^{\theta^*} \sin(\theta^* - \theta^{**}) \\
&\qquad \begin{pmatrix} 4\partial^2/\partial\theta^2 - 3 & 7(\partial/\partial\theta) \\ -7(\partial/\partial\theta) & 4\partial^2/\partial\theta^2 - 3 \end{pmatrix} \begin{pmatrix} f_1 \\ f_2 \end{pmatrix} (\theta^{**}) d\theta^{**}\} d\theta^* \\
\rho &= E\exp\{-\int_\theta^\theta d\theta^*\} \\
p &= \rho[F\theta + G + \int_\theta^\theta f_3(\theta^*)(\theta - \theta^*)d\theta^*],
\end{aligned}
\tag{5}
$$

where A, B, C, D, E, F, and G are integration constants including r as a parameter. Now we have ten conditions given in Eqs. (2), (3) to determine the ten unknowns

$A, B, C, D, E, F, G, \theta_0, \theta_1$, and θ_2 for the given parameter r. First, we use the condition of Eq. (3) for $\mathbf{V}$ in Eq. (5):

$$\frac{B}{A} = \frac{D}{C} \equiv k, \tan\theta_0 = -\frac{D}{B}, \frac{V'_{\theta 0} + V_{r0}}{V_{\theta 0}} = \frac{6}{7}\frac{1}{1+k\theta}$$

from which we have

$$\begin{aligned}
\rho &= \bar{E}(1+k\theta)^{-\frac{6}{7}}\Gamma(\theta) \\
\bar{E} &\equiv (1+k\theta_0)^{-\frac{6}{7}}; \\
\Gamma(\theta) &\equiv \exp\{-\int_{\theta}^{\theta} \frac{V'_{\theta 0} + V_{r0}}{V_{\theta 0}} - \frac{\partial V_\theta/\partial\theta + V_r - f_0}{V_\theta} d\theta^*\} \\
V_{\theta 0} &= (1+k\theta)(A\sin\theta + C\cos\theta) \\
V_{r0} &= (1+k\theta)(C\sin\theta - A\cos\theta) - (k/7)(A\sin\theta + C\cos\theta).
\end{aligned} \tag{6}$$

Now we use the boundary condition of Eq. (2) in Eq. (6):

$$\begin{aligned}
\rho_1 &= \bar{E}(1+k\theta_1)^{-\frac{6}{7}}\Gamma(\theta_1), \\
\rho_2 &= \bar{E}(1+k\theta_2)^{-\frac{6}{7}}\Gamma(\theta_2) \\
V_{\theta 1} &= (1+k\theta_1)(A\sin\theta_1 + C\cos\theta_1) + \tilde{V}_{\theta 1} \\
V_{\theta 2} &= (1+k\theta_2)(A\sin\theta_2 + C\cos\theta_2) + \tilde{V}_{\theta 2} \\
V_{r1} &= (1+k\theta_1)(C\sin\theta_1 - A\cos\theta_1) \\
&\quad - (k/7)(A\sin\theta_1 + C\cos\theta_1) + \tilde{V}_{r1} \\
V_{r2} &= (1+k\theta_2)(C\sin\theta_2 - A\cos\theta_2) \\
&\quad - (k/7)(A\sin\theta_2 + C\cos\theta_2) + \tilde{V}_{r2}.
\end{aligned} \tag{7}$$

These two equations are used to determine k and E:

$$\begin{aligned}
k &= (1-\tilde{S})(\tilde{S}\theta_1 - \theta_2)^{-1}, \\
\tilde{S} &\equiv \{\rho_2/\rho_1 \cdot [\Gamma(\theta_1)/\Gamma(\theta_2)]\}^{7/6} \\
\bar{E} &= [(\theta_1 - \theta_2)(Z_2\theta_1 - Z_1\theta_2)^{-1}]^{-7/6}, \\
Z_{1,2} &= [\rho_{1,2}/\Gamma(\theta_{1,2})]^{-6/7}.
\end{aligned} \tag{8}$$

Then, we eliminate A and C from the remaining four equations to have two equations to determine θ_1, θ_2,

$$\begin{aligned}
\Delta_1 &\equiv (r\tilde{V}_{\theta 1} - V_{\theta 1})[K_1K_2\cos\Theta + k/7.K_2\sin\Theta] \\
&\quad - (\tilde{V}_{\theta 2} - V_{\theta 2})K_1^2 + (r\tilde{V}_{r1} - V_{r1})K_1K_2\sin\Theta \\
&\equiv r\Delta_{10} + \Delta_{11} = 0
\end{aligned} \tag{9}$$

and

$$\begin{aligned}\Delta_2 \equiv & (r\tilde{V}_{\theta 1} - V_{\theta 1})K_2^2 - (r\tilde{V}_{\theta 2} - V_{\theta 2})\cdot \\ & \cdot [K_1 K_2 \cos\Theta - k/7.K_1 \sin\Theta] \\ & + (r\tilde{V}_{r2} - V_{r2})K_1 K_2 \sin\Theta \\ \equiv & \, r\Delta_{20} + \Delta_{22} = 0,\end{aligned} \tag{10}$$

where

$$K_{1,2} \equiv 1 + k\theta_{1,2},\ \Theta \equiv \theta_1 - \theta_2.$$

These values of $\theta_1(r)$, $\theta_2(r)$ provide the shapes of the R and m fronts, and $\theta_1(0)$, $\theta_2(0)$ are their values at the triple point, or λ, ω' (Fig. 1). Using these θ_1, θ_2, we can determine A and C from Eq. (7). The remaining F and G values are determined simply from unused conditions for p in Eq. (2): $p = p_1, p_2$ at $\theta = \theta_1, \theta_2$.

4 Solution for Weak Mach Reflection

Here, we focus the flow field in the angular region of the weak Mach reflection, which is observed to be almost uniform in the region. Now $f_i, i = 0, 1, 2, 3$ in the right-hand terms of Eq. (4) vanish to a uniform flow, since we can verify it directly applying a uniform flow formula: $u_r = U_{00}\cos(\theta - \theta_{00})$, $u_\theta = U_{00}\sin(\theta - \theta_{00})$ with constants p, ρ, U_{00}, and θ_{00}, to f_i. Therefore, we can assume that the magnitudes of f_i are small in general, and we can utilize $\mathbf{X} = (V_\theta, V_r, \rho, p)$ given in Eqs. (5), (6) as an approximate solution of the present flow when we use the appropriate approximate solution in $f_i, i = 0, 1, 2, 3$. Conveniently, we can assume uniform flow to have $f_i = 0$, and further improvement of this solution can be obtained using Eqs. (5), (6) again with use of this solution to f_i. However, later, this results in little change.

Since $\hat{f} = 0$, $K(\theta) = 1$, $\tilde{V}_\theta = \tilde{V}_r = 0$ for $f_i = 0$, from Eq. (6) we simply have

$$\begin{aligned}V_\theta = V_{\theta 0} &= (1 + k\theta)(A\sin\theta + C\cos\theta) \\ V_r = V_{r0} &= (1 + k\theta)(C\sin\theta - A\cos\theta) \\ &\quad - (k/7)(A\sin\theta + C\cos\theta) \\ \rho &= \bar{E}(1 + k\theta)^{-\frac{6}{7}}.\end{aligned} \tag{11}$$

It is noted here that the right-hand sides of Eq. (4) vanish when $r = 0$ as well as when $f_i = 0$. As a result, the reduced system of equations system for $r = 0$ is the same as the one given in the first-order term of the power series expansion in r of the original system of Eq. (4) [9], and its smooth solution given in there is the same except for the difference in notations with the one in Eq. (9). Furthermore, this provides two equations to determine angles λ and ω' for the given incident shock angle ω, which correspond to the conditions in Eq. (8) at $r = 0$: $(\Delta_1)_{r=0} = 0$, $(\Delta_2)_{r=0} = 0$.

The λ and ω values determined from these conditions for given incident shock angle ω and its strength are presented in Sakurai [9] in the form of λ versus ω and ω' versus ω graphs for various ξ values, which is the inverse of the pressure ratio at the incident shock. Thus, the value of ξ is larger for weaker cases, approaching one. Figure 2 presents one of the graphs given there and a ω' versus ω graph for $\xi = 0.9$, representing a weaker case, to compare experiment data with results using the three-shock theory. The angles using the present theory are reasonably consistent with experiment data, indicating the effect of the nonuniformity of the flow field due to singularity at the triple point.

The solution in Eq. (11) is illustrated in Fig. 3a for velocity $\mathbf{V}$ in real space and (b) for density ρ in the (r, θ) coordinates system. The flow spreads from the origin T as it widens at the slip streamline, which is the nature of singularity. We can see the details in (b), extending the point to a line segment of $(r = 0, -\lambda < \theta < \omega')$.

Although this is an approximate solution and valid only along the boundary of two shock fronts, we can assume that it approximates the flow inside the $r > 0$ region as well. The effect of the fan-like singularity at their intersecting point $r = 0$ spreads to the flow there in prevailing its essential feature inside the region of $r > 0$. In fact, numerical simulation provides density distribution along a circle of $r > 0$ similar to that for $r = 0$ as seen in Fig. 4. Figure 4a illustrates density distribution in the isovalue lines, and Fig. 4b plots density distributions along various circle lines of $r > 0$, which can be compared with the density distribution near $r = 0$ in Fig. 3b.

The small difference in density distribution between $r = 0$ and $r > 0$ is assumed to due to the nonuniformity of the flow field in $r > 0$ in connection with the slight deformation of shock lines. To consider its details, we improve the approximation, by substituting f_i in Eqs. (5)–(11). Since f_1, f_2 in Eq. (5) are functions of θ only for this case, this improved solution in Eq. (5) is in the form of an equation of first degree in r, with its coefficients being functions of θ only. So we may assume to the shapes $\theta_1(r), \theta_2(r)$ of the bounding shock waves R and m in linear in r as well:

$$\theta_1 = -\lambda + r\tilde{\theta}_1, \theta_2 = \omega' + r\tilde{\theta}_2,$$

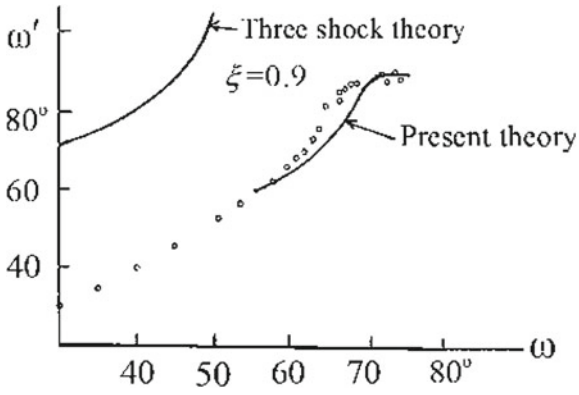

Fig. 2 ω' versus ω graph for $\xi = 0.9$ from the present theory compared with Harrison and Bleakney's data and three-shock theory results [9]

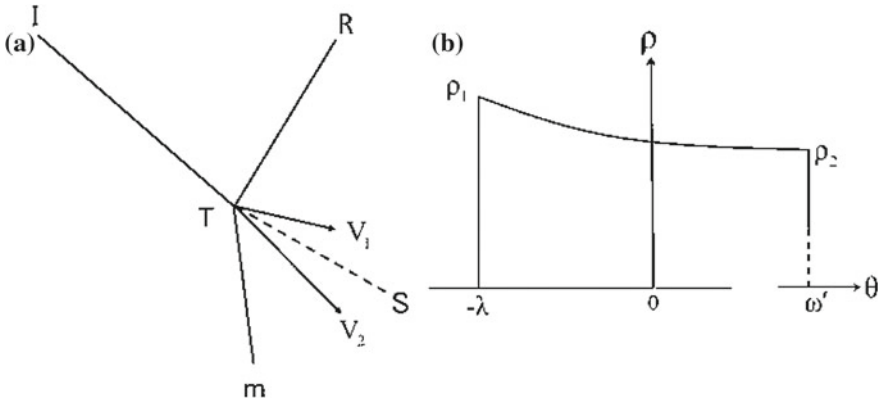

Fig. 3 **a** Velocity and **b** density

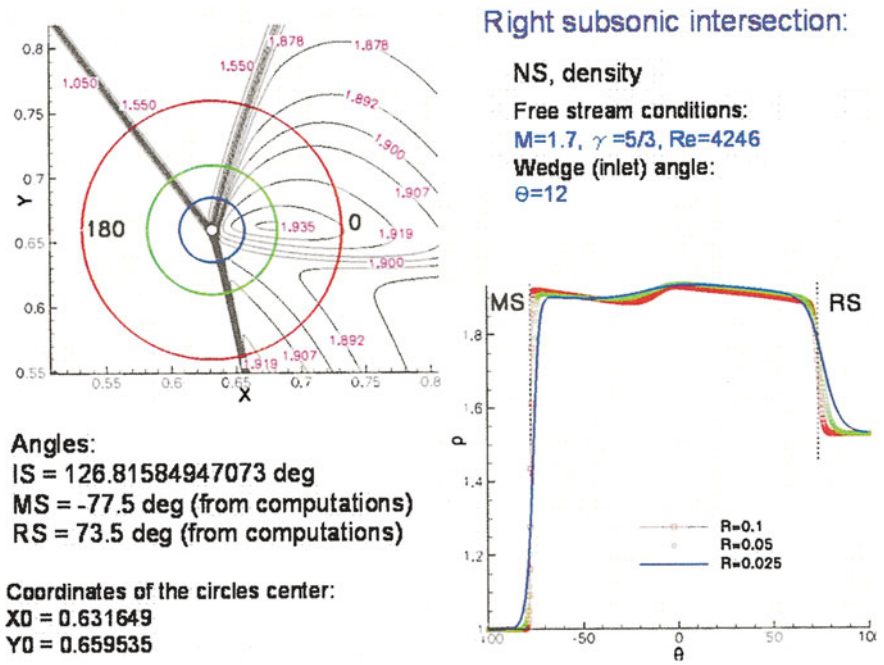

Fig. 4 **a** Density contour and **b** density distribution around the triple point [10]

where $\theta_1(0) = -\lambda, \theta_2(0) = \omega'$ and constants $\tilde{\theta_1}, \tilde{\theta_2}$ should be determined from Eqs. (9), (10):

$$(\Delta_1)_{r=0} + r(\Delta_{10} + \tilde{\theta}_1 \frac{\partial \Delta_{11}}{\partial \theta_1} + \tilde{\theta}_2 \frac{\partial \Delta_{11}}{\partial \theta_2})_{r=0} + \cdots = 0$$
$$(\Delta_2)_{r=0} + r(\Delta_{20} + \tilde{\theta}_1 \frac{\partial \Delta_{21}}{\partial \theta_1} + \tilde{\theta}_2 \frac{\partial \Delta_{21}}{\partial \theta_2})_{r=0} + \cdots = 0$$

Here, $(\Delta_1)_{r=0} = (\Delta_2)_{r=0} = 0$ determines $-\lambda, \omega'$, and we have the second terms for $\tilde{\theta_1}, \tilde{\theta_2}$:

$$\tilde{\theta}_1 = (-\Delta_{10}\frac{\partial\Delta_{21}}{\partial\theta_2} + \Delta_{20}\frac{\partial\Delta_{11}}{\partial\theta_2})_{r=0}.\Delta^{-1}$$
$$\tilde{\theta}_2 = (-\Delta_{20}\frac{\partial\Delta_{11}}{\partial\theta_1} + \Delta_{10}\frac{\partial\Delta_{21}}{\partial\theta_1})_{r=0}.\Delta^{-1}$$
$$\Delta \equiv (\frac{\partial\Delta_{11}}{\partial\theta_1}\frac{\partial\Delta_{21}}{\partial\theta_2} - \frac{\partial\Delta_{21}}{\partial\theta_1}\frac{\partial\Delta_{11}}{\partial\theta_2})_{r=0}.$$

We utilize here the fact that k is small and $[\Theta]_{r=0} = -\lambda - \omega' \approx -\pi$ for weak reflection in approximation:

$$\tilde{\theta}_1 = \tilde{\theta}_2 \approx (\acute{V}_{\theta 1} + \acute{V}_{\theta 2})(V'_{\theta 1} + V'_{\theta 2})^{-1}, \tag{12}$$

where

$$\acute{V}_{\theta 1}, \acute{V}_{\theta 2} \equiv (\acute{V}_{\theta 1})_{r=0}, (\acute{V}_{\theta 2})_{r=0}.$$

The term $V'_{\theta 1} + V'_{\theta 2}$ can be estimated simply from the shock conditions at R and m, while the term $\acute{V}_{\theta 1} + \acute{V}_{\theta 2}$ is somewhat involved, as we can see in Eq. (5). Nevertheless, these values can be simplified in approximation using again the fact that k is small and $[\Theta]_{r=0} = -\lambda - \omega' \approx -\pi$ for weak reflection:

$$\tilde{\theta}_1 = \tilde{\theta}_2 \approx L \cdot k,$$

where L is a number depending on the incoming shock strength ξ and angle ω. It is almost 2 for the extreme angle in weak reflection, and these shocks should bend slightly, since k is small. In fact, we observe this in Fig. 4a for numerical results and in Fig. 5a for an experimental picture [11], where these shocks deviate only slightly from straight lines, Also, we can see this kind of curve in an analytical solution [7] for very weak Mach reflection in a diffracting blast wave.

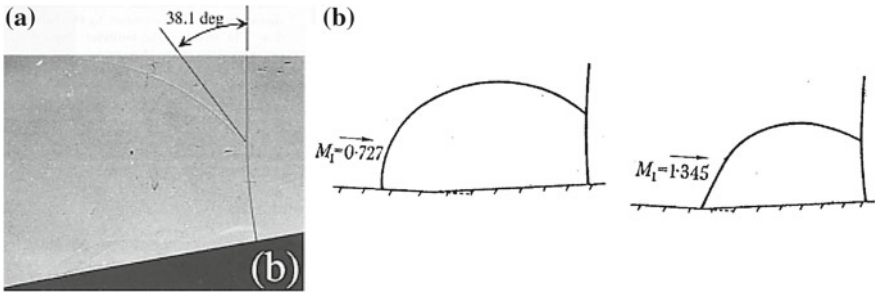

Fig. 5 **a** Visualized reflection configuration after [11], the incident shock Mach number $M_i = 1.30$ and the reflecting wedge angle $\theta_w = 10.75°$, **b** result by Lighthill [7]

5 Conclusion

A solution to the Navier–Stokes equations in a polar coordinate system is sought to satisfy the shock conditions at bounding reflected and Mach stem shock lines. The solution is singular at the triple point. Its nature is to provide a centered fan-like flow, which is in effect widening the slip flow line. The reflected and Mach stem shock angles and their curvatures at the triple point are determined using the solution, and they compare favorably with experiment data as well as numerical simulation.

References

1. Birkoff, G.: Hydrodynamics, A Study in Logic, Fact, and Similitude, 1st edn. Princeton Univ. Press, Princeton (1950)
2. Bleakney, W., Taub, A.H.: Interaction of shock waves. Rev. Modern Phys. **21**, 584–605 (1949)
3. Sternberg, J.: Triple-shock-wave Interactions. Phys. Fluids **2**(2), 172–206 (1959)
4. Tesdall, M., Sanders, R., Keyfitz, L.: Self-similar solutions for the triple point paradox in gas-dynamics. SIAM J. Appl. Math. **68**, 1360–1377 (2008)
5. von Neumann, J.: Collected Works, vol. 6. Pergamon Press, New York (1963)
6. Courant, R., Friedrichs, K.O.: Supersonic Flow and Shock Waves, pp. 332–333. Interscience, New York (1963)
7. Lighthill, M.J.: Diffraction of blast 1. Proc. Roy. Soc. London **A198**, 454 (1949)
8. Sakurai, A., Takahashi, S.: An analytical solution for weak Mach reflection and its application to the problem of the von Neumann paradox. J. Phys. Soc. Japan **74**, 1490–1495 (2005)
9. Sakurai, A.: On the problem of weak Mach reflection. J. Phys. Soc. Japan **19**, 1440–1450 (1964)
10. Sakurai, A., Tsukamoto, M., Khotyanovsky, D., Ivanov, M.: The flow field near the triple point in steady shock reflection. Shock Waves **21**, 267–272 (2011)
11. Adachi, T., Sakurai, A., Kobayashi, S.: Effect of boundary layer on Mach reflection over a wedge surface. Shock Waves **11**, 271–278 (2002)

Experimental Investigation of Mist Injection at the Stagnation Point of a Blunt Body in Hypersonic Flow

J. L. K. Sindhu, S. Mohammed Ibrahim and K. P. J. Reddy

1 Introduction

A spacecraft re-entering Earth's atmosphere at orbital speeds or higher is subjected to severe aerodynamic heating. Generally, large angle sphere-cone configurations are preferred as forebody to minimize aerodynamic heating. Though these configurations reduce heat transfer to some extent, they are not alone sufficient to withstand the harsh conditions existing during re-entry. Hence, a spacecraft requires a Thermal Protection System (TPS) to ensure its survival when travelling at hypersonic speeds. TPS commonly used on Earth, and other planetary entry spacecrafts are ablative cooling. Though ablative cooling has been successfully employed, it has certain drawbacks. Especially, when re-usability of the spacecraft is concerned, ablative cooling is very expensive. This drove us to explore an alternate TPS. Several techniques for TPS were explored by researchers around the globe.

Film cooling is one such technique, where a coolant gas is injected from the body surface into the shock layer, with the injected coolant modifying the boundary layer characteristics and minimizing the heat transfer rate. In this technique, coolant properties, specifically specific heat of coolant and pressure ratio of injection, play a significant role. Reported film cooling experiments were carried out using gaseous coolants like air, helium, carbon dioxide, and nitrogen by Sriram and Jagadeesh [1], Sahoo et al. [2], and Mohammed Ibrahim et al. [3]. In this back drop, an experimental work was started at Laboratory for Hypersonic and Shock wave research (LHSR), Indian Institute of Science, Bangalore to investigate the influence of coolants having high heat capacity. Water has a heat capacity of 4.2 KJ/Kg K and a high latent heat

J. L. K. Sindhu (✉) · S. Mohammed Ibrahim · K. P. J. Reddy
Laboratory for Hypersonics and Shock Wave Research, Department of Aerospace Engineering, Indian Institute of Science, Bangalore 560012, India
e-mail: sindhu@aero.iisc.ernet.in

K. Kontis (ed.), *Shock Wave Interactions*,
https://doi.org/10.1007/978-3-319-73180-3_17

of vaporization of 2442 J/Kg. Water's specific heat is more when compared to any gaseous coolant used in literature till date, and is thus expected to alter heat transfer rate to a significant value.

Previously, transpiration cooling studies involving liquid water injection through a heated surface made out of a porous material were carried out by Wang et al. [4, 5] and Van Foreest et al. [6]. However, direct liquid water injection is not a feasible option for film cooling studies. Atomizing liquid water into finer droplets (mist) not only facilitates easier injection but also increases the surface area available for heat absorption and evaporation. Thus, a test campaign has been set up at LHSR's Hypersonic shock tunnel (HST2) to study the effect of mist injection on heat transfer rate distribution over the model surface. It is believed that varying pressure of injection alters the heat transfer rate accordingly. To facilitate mist injection at different pressures, an in-house seeder has been used.

2 Experimentation

2.1 Experimental Facility

Experiments are carried out at flow enthalpy of 1.5 MJ/kg using Hypersonic Shock Tunnel HST-2. A schematic of HST-2 is shown in Fig. 1. HST-2 is a conventional shock tunnel facility, operated in diaphragm-less mode, consisting of driver and driven section separated using a direct acting solenoid valve ISTA KB-40. The driver side is filled with 40 bar of helium and driven with 0.3 bar of air (test gas). The fast opening of the valve results in the generation of shock wave which travels along the length of the driven section and after its reflection at the end of the driven section creates the reservoir condition for the nozzle. The nozzle and test section are initially maintained at vacuum level of 10^{-5} mbar using rotary-diffusion pump and are separated from the driven side using a thin paper diaphragm. The test gas expands to

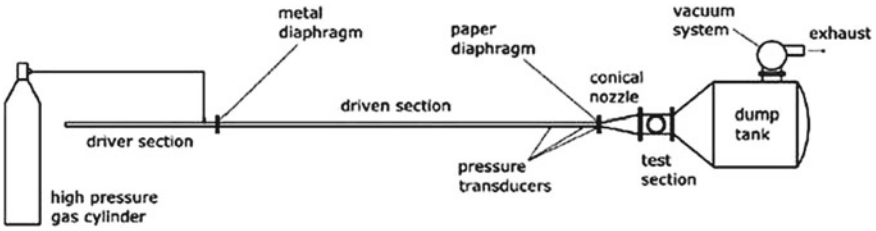

Fig. 1 Schematic of HST-2

Table 1 Flow conditions in nozzle reservoir and freestream

P_o (kPa)	1432.85
T_o (K)	1559.58
H_o (MJ/kg)	1.56
P_∞ (kPa)	0.118
T_∞ (K)	106.29
ρ_∞ (kg/m^3)	0.0038
V_∞ (m/s)	1708.7
M_∞	8.27
Re_∞ (million/m)	0.896

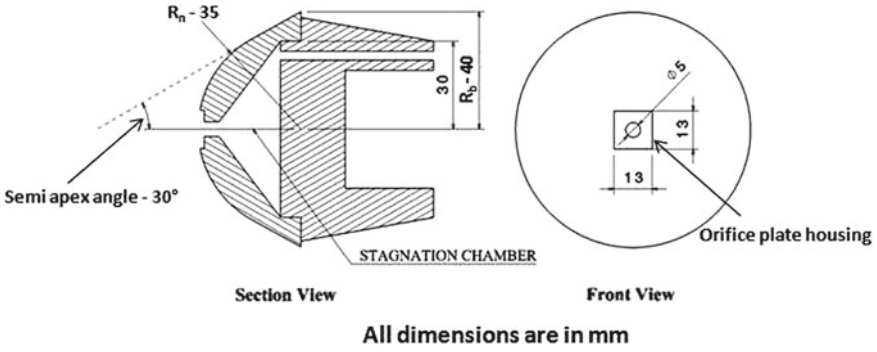

Fig. 2 Schematic of test model

hypersonic velocity in the nozzle and exits into the test section where the test model is mounted producing a steady flow test time of ~500 μs. The flow conditions generated for the present set of experiments are tabulated in Table 1.

2.2 Test Model

The test model used is a 60° apex angle blunt cone with a base diameter of 80 mm and nose radius of 35 mm. The nose portion of the model has a square slot of 13 mm × 13 mm area and thickness of 2 mm where the plate containing the 2 mm orifice, through which the mist is injected into the hypersonic mainstream, is housed. A schematic sketch and photograph of the model are shown in Figs. 2 and 3, respectively.

Platinum thin film sensors deposited on MACOR surface are flush mounted on the surface of the model to measure the convective heat transfer rates as shown in Fig. 3. A total of eight thin film sensors, four on each side of the stagnation point, are

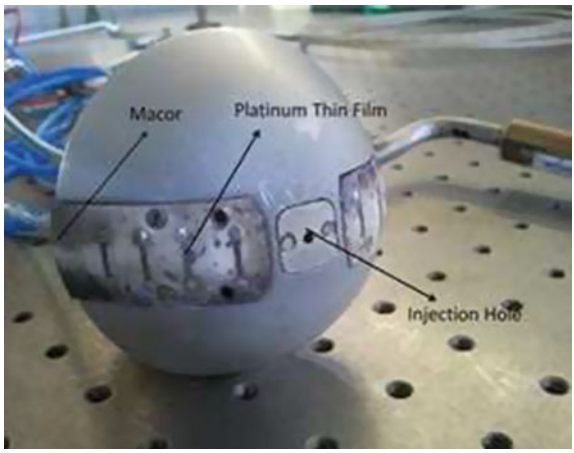

Fig. 3 Photograph of test model

used in the present investigation. Since the coolant is injected from the nose of the model, it is not possible to have thin film sensor at the stagnation point. However, the closest was at $s/R_b = 0.4$, in the nose region of the model and the remaining was in the conical region of the body.

2.3 Mist Generator

Mist particles are generated using an in-house seeder unit, schematic shown in Fig. 4, developed by Karthick et al. [7], which works on the principle of Laskin nozzle arrangement. The unit consists of a cylindrical strut immersed in the water with four nozzle holes (each of 1 mm diameter) drilled on its periphery. High-pressure gas supplied to the strut from an external cylinder disperses into water through the nozzle feed holes, producing a mixture of the supplied high-pressure gas and mist particles of size varying 0.8–1 μm. The outlet of seeder is directly connected to model, and thus the pressure of injection (P_i) can be controlled by varying the supply pressure (P_s) to the seeder.

The seeder used for mist generation is placed inside the dump tank and its outlet is connected directly to the 2 mm injection hole of the model via solenoid valve and flexible pipeline as shown in Fig. 5. The seeder is pressurized with nitrogen and the solenoid valve is opened (by supplying voltage) just before the arrival of test flow. The supply pressure (P_s) of nitrogen is equal to the chamber pressure of seeder, and thus by varying P_s the pressure of mist injection (P_i) can be varied.

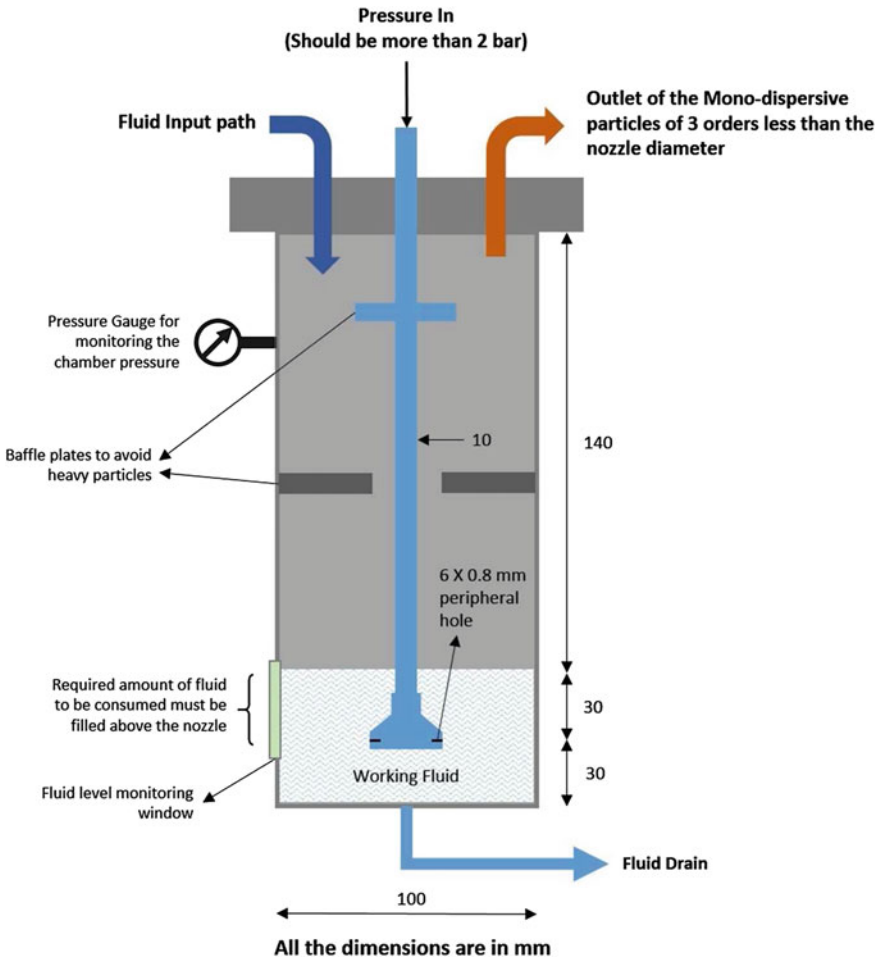

Fig. 4 Schematic of mist generator

3 Results and Discussion

The heat transfer rate distribution on the model surface in the absence and presence of mist injection is plotted in Fig. 6. The mist was injected at a chamber supply pressure of (P_s) of 4bar. An increase in heat transfer rate was observed with mist injection, the increase being higher in the nose region of the model, close to the point of injection. The integrated heat transfer signals, for the gauge located in the nose region, is shown in Fig. 7 for both cases, with and without mist injection.

The flowfield in the absence and presence of mist injection was visualized using Schlieren technique and shown in Fig. 8. In the presence of mist injection, the body shock was found to be disturbed. The increase in heat transfer rate due to mist

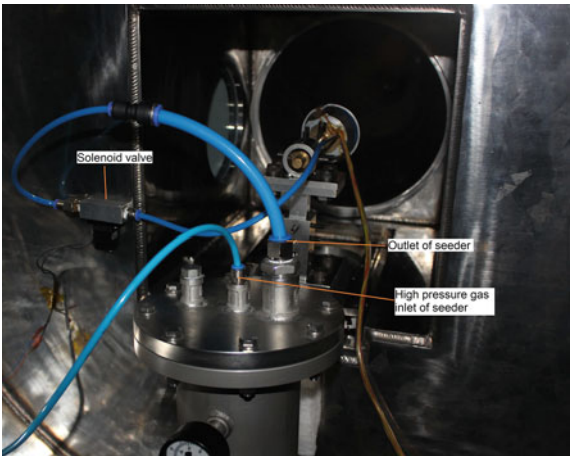

Fig. 5 Photograph of mist generator

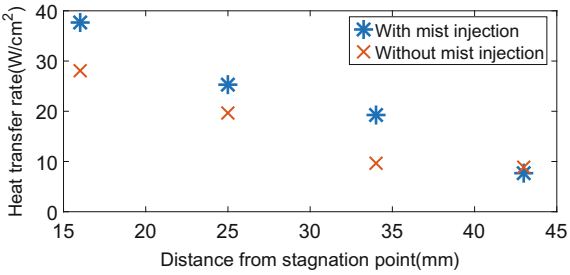

Fig. 6 Heat transfer rate distribution on the model surface for $P_s = 4$bar

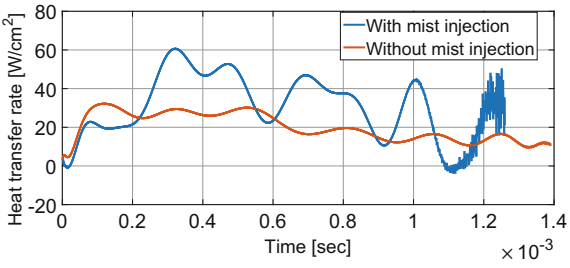

Fig. 7 Typical heat transfer rate signals for the gauge closest to nose region of model for the cases of with and without mist injection at $P_s = 4$bar

injection is caused by shock wave bifurcation and its reattachment near the nose region of the model as shown in Fig. 8 (left). The reattachment shock might cause the boundary layer to undergo transition to turbulence, resulting in a higher heat transfer rate downstream, in the conical region of the model.

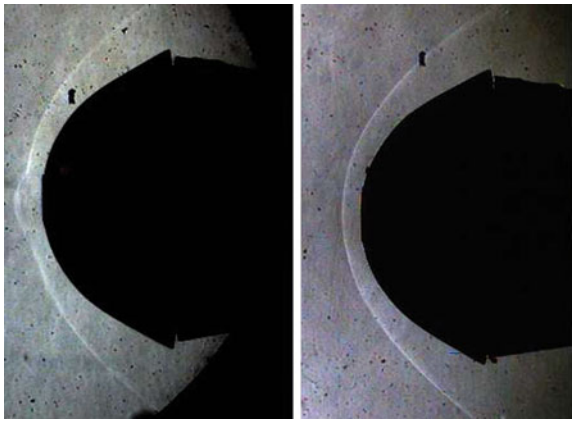

Fig. 8 Schlieren visualization of the flowfield with (left) and without (right) mist injection

4 Conclusion

Mist injection from the stagnation point of a blunt body model was carried out for a flow enthalpy condition of 1.5 MJ/Kg and at a supply pressure of 4bar. An increase in heat transfer rate over the surface of the model has been reported in this case. Further studies are planned at supply pressures higher and lower than 4bar in order to reach a conclusion about the mist behaviour in the flow field around the model.

References

1. Sriram, R., Jagadeesh, G.: Film cooling at hypersonic mach numbers using forward facing array of micro-jets. Int. J. Heat Mass Transf. **54**, 3654–3664 (2009)
2. Sahoo, N., Kulkarni, V., Saravanan, S., Jagadeesh, G., Reddy, K.P.J.: Film cooling effectiveness on a large angle blunt cone flying at hypersonic speed. Phys. Fluids **17**, 036102 (2005)
3. Mohammed Ibrahim, S., Sriram, R., Reddy, K.P.J.: Experimental investigation of heat flux mitigation during martian entry by coolant injection. J. Spacecr. Rockets **51**(4), 1363–1368 (2014)
4. Wang, J.H., Messner, J., Casey, M.V.: Performance investigation of film and transpiration cooling. In: Proceedings of the ASME Turbo Expo. Vienna, Austria, 14–17 June 2004
5. Wang, J.H., Messner, J., Stetter, H.: An experimental investigation on transpiration cooling part II: comparison of cooling methods and media. Int. J. Rotating Mach. **10**(5), 355–363 (2004)
6. Van Foreest, A., Sippel, M., Guelhan, A., Esser, B., Ambrosius, B.A.C., Sudmeijer, K.: Transpiration cooling using liquid water. J. Thermophys. Heat Transf. **23**(4), 693–702 (2009)
7. Karthick, S.K., Jagadeesh, G., Reddy, K.P.J.: Visualization of supersonic free and confined jet using planar laser mie scattering technique. J. Indian Inst. Sci. (2016)

Shock Wave Development Within Expansive Flows

Beric W. Skews and Randall T. Paton

Abstract The propagation of two-dimensional expansion waves over a corner has received very little attention in the past. It can be studied experimentally in a standard shock tube by placing the test section at the end of the high-pressure section rather than the conventional method with placement at the driven section. It is found that reflected compression and shock waves can form as the wave propagates over the corner. An attached flow separation bubble develops at the corner and for a strong enough wave can develop a region of supersonic flow above it, and, in some cases, a transonic shock wave. Furthermore, for a sufficiently strong expansion wave, the flow behind the trailing edge of the expansion wave becomes supersonic. It has also been shown that when an expansion wave reflects off a wedge, shock waves can also develop due to the induced velocity flowing down the surface of the wedge striking the corner. The development of shock waves can also occur if the expansion wave focuses on a cavity.

1 Introduction

Recent studies of expansion wave dynamics show the development of imbedded shock waves under certain conditions, as described below. The experimental generation of a one-dimensional expansion wave is to place a test section in the driver section of a shock tube. The basic properties of one-dimensional expansion waves can easily be derived from standard shock tube analysis and have been presented by Mahomed and Skews [1]. A shock tube wave diagram is shown in Fig. 1 in order

B. W. Skews (✉) · R. T. Paton
Flow Research Unit, School of Mechanical, Industrial, and Aeronautical Engineering, University of the Witwatersrand, Johannesburg
PO WITS 2050, South Africa
e-mail: Beric.Skews@wits.ac.za

R. T. Paton
e-mail: Randall.Paton@wits.ac.za

K. Kontis (ed.), *Shock Wave Interactions*,
https://doi.org/10.1007/978-3-319-73180-3_18

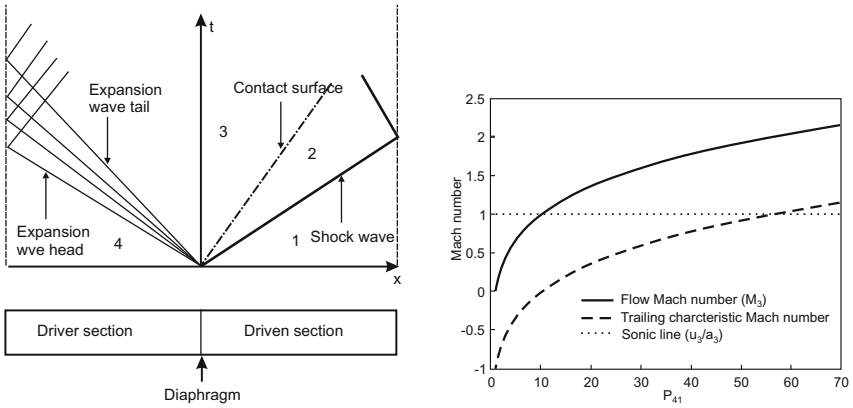

Fig. 1 Shock tube wave diagram, and properties across the expansion wave as a function of diaphragm pressure ratio

to define the flow regions. The head of the expansion wave travels to the left into region 4 and induces flow to the right. The flow in region 3 into which the tail of the expansion moves has the same pressure as that in region 2 behind the shock but is at a lower temperature having passed through the expansion wave. These regions are separated by the contact surface which are then at different Mach numbers even though the velocities are the same.

Relating to considerations of shock wave development, it is of interest to establish conditions for the development of supersonic areas of flow. In the one-dimensional flow case, region 2 becomes supersonic at a shock Mach number greater than 2.07 corresponding to diaphragm pressure ratios above 40. However, in region 3, between the tail of the expansion wave and the contact surface diaphragm pressure, ratios only above 10.4 are required. This is shown in Fig. 1. At this pressure ratio of 10.4, the tail of the expansion will be stationary because it is propagating at sonic velocity in an opposing sonic gas flow. For pressure ratios above this value, the tail of the wave will propagate to the right into the supersonic flow and will have an absolute Mach number as shown in the figure. Two-dimensional expansion wave dynamics is achieved by placing a test section at the end of the driven section in region 4. If further expansion is to occur such as for diffraction over a convex profile, supersonic regions will then occur at lower pressure ratios.

Two basic cases are considered here: reflection and diffraction over two-dimensional concave and convex corners, respectively. In all the examples given, the expansion is propagating to the left thereby inducing flow in the opposite direction.

2 Diffraction over a Convex Corner

The basic flow field for diffraction over a 90° corner is shown in Fig. 2 and has been analysed by [1]. A separation bubble, which remains attached to the corner, is generated as the flow develops. Since the head of the wave moves at sonic velocity, its diffracted portion is a circular arc. However, as the flow expands around the corner, reflected compression waves are generated back into the flow, in the opposite way as a shock wave emerging from a shock tube results in reflected expansions back into the tube in order to satisfy the exit pressure boundary condition.

In this diffraction case, two situations occur when shock waves can be generated [1]. One results from the convergence of the reflected compression waves into a shock wave. The formation of this wave depends on a number of factors: the pressure ratio across the shock tube diaphragm, P_{41}, which determines the strength of the expansion; the distance of the diaphragm from the corner, D, which determines the width of the wave at the corner when the leading edge arrives there; and the time after the start of diffraction, t. A typical result from numerical simulation is given in Fig. 2.

The effect of diaphragm pressure ratio and diaphragm position is illustrated in Fig. 3. The Further the diaphragm is away from the corner; the expansion wave will be wider when it reaches the corner for the same initial pressure ratio. This results in the reflected compression wave spreading out before a shock wave develops. On the other hand, a shock wave develops earlier when the pressure ratio is lower as shown in Fig. 4.

The steepening up of the compression is demonstrated in Fig. 5 by plotting the pressure distribution along a vertical line such as that shown as a red line in Fig. 4. The initial drop in pressure is because the line passes through part of the separation bubble and is due to the low pressure caused by the vortex. As the diaphragm is moved further and further away from the corner, the wave becomes more spread out and thus it takes more time to steepen up. Unfortunately, the domain in the

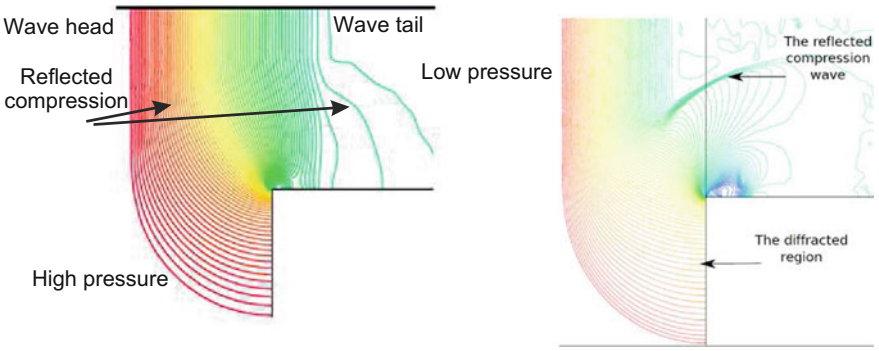

Fig. 2 Expansion diffraction over a corner, with and without shock wave development. Contours of pressure

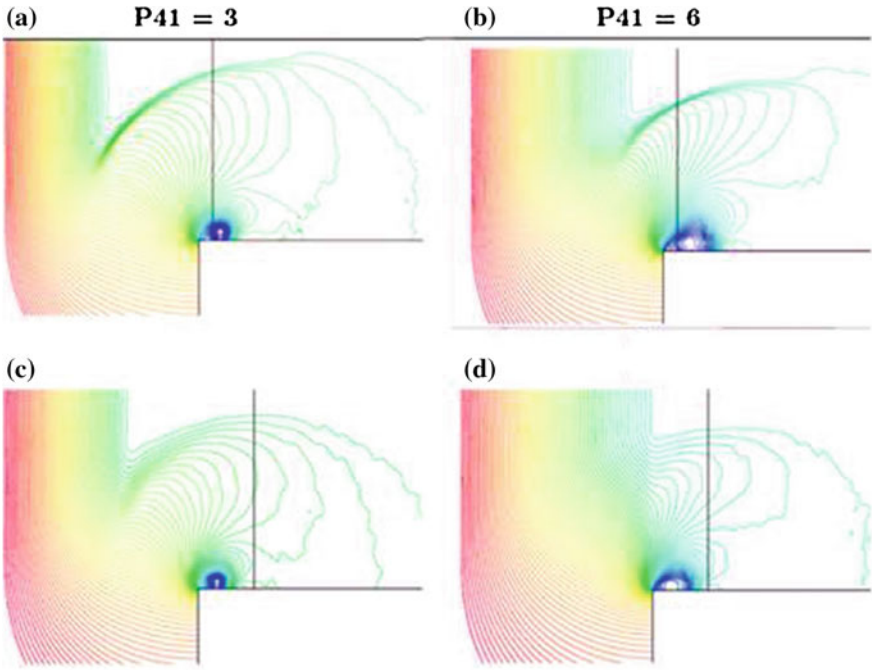

Fig. 3 Effect of pressure ratio and diaphragm position. Top row $D = 10$ mm, Bottom row $D = 40$ mm, $t = 400\,\mu$s

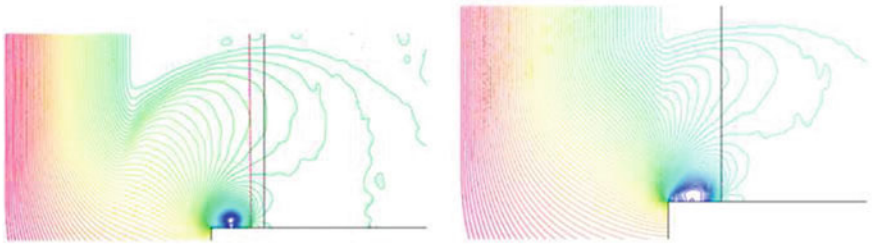

Fig. 4 Effect of pressure ratio. $P_{41} = 3$ and 6, $D = 40$ mm, $t = 450\,\mu$s

experiment was not large enough to capture these waves due to reflection from the boundaries of the test section.

For shock waves to develop within the overall flow, regions of supersonic flow need to develop. The influence of the separation bubble's curvature on the nearby flow field causes acceleration of the oncoming flow which leads to a reduction of pressure (including temperature and density), above the separation bubble. A shock was found to develop, through experiment and simulation, under certain conditions. Two areas of supersonic flow can occur: one as described above due to flow over

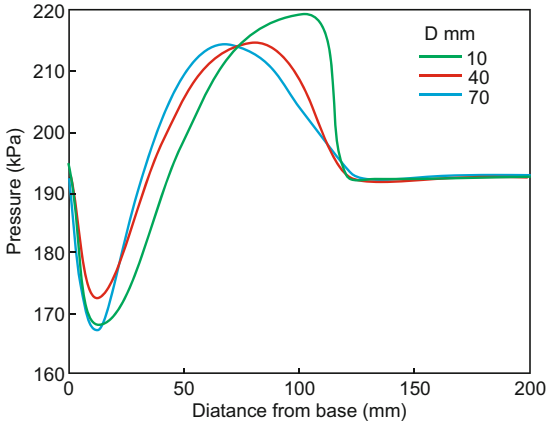

Fig. 5 Vertical pressure distribution 30 mm from the corner. $P_{41} = 3$, $D = 10, 40$ and 70 mm, $t = 400\,\mu$s

the bubble and one due to a sufficiently high diaphragm pressure ratio as described previously.

The development of a shock wave due to the flow over the separation bubble depends on the diaphragm pressure ratio, the position of the diaphragm, and the time from the start of diffraction. In the figures below, the supersonic patch is circumscribed by a red line. For $P_{41} = 3$, a patch only starts to appear at a time of $t = 300\,\mu$s with $D = 0$ mm and not at the same time for $D = 40$ mm although it does develop then at $t = 400\,\mu$s. Enlarged views in the vicinity of the bubble for $t = 600\,\mu$s are given in Fig. 6. No shocks are present above the bubble but interestingly there is a small patch within the bubble which may terminate in a shock. The flow within the bubble is complex as shown in the enlargement at the bottom of the figure.

As the patch grows, a shock will develop on the bubble surface as it does for a transonic airfoil, as shown in Fig. 7. The supersonic area continually increases as shown by the sonic line. No shock wave is evident at early times but as the separation bubble grows and the velocity over it increases, a transonic shock wave develops. It is not a normal shock as is evident by the fact that the flow immediately behind it is still supersonic. The obliqueness becomes more apparent at later times.

Some evidences of these waves are evident in the experiment, as shown in Fig. 8, but are not as well defined. Part of the reason for this is that the expansion wave generated does not have the plane front as assumed in the simulation but is curved under the influence of the initial pressure difference across it, so that when it bursts the flow is more complicated and non-uniform, including transverse effects, and the bubble has a more rounded profile. The surface of the bubble is also uneven due to vortices and turbulence.

The other area where supersonic flow can occur is for pressure ratios larger than 10.4, where the flow in region 3 becomes supersonic and the trailing characteristic of the expansion propagates in the same direction as the flow, since it is propagating

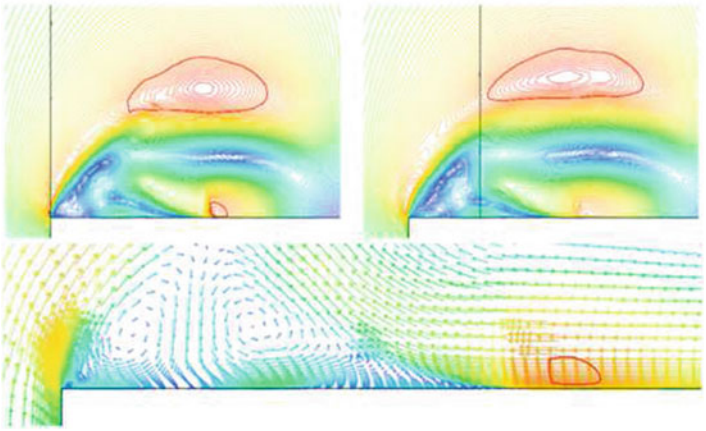

Fig. 6 Mach number contours for $P_{41} = 3$ and $D = 0$ and 40 mm, at a time of 600 μs. Enlargement shows a density contour plot adjacent to the surface

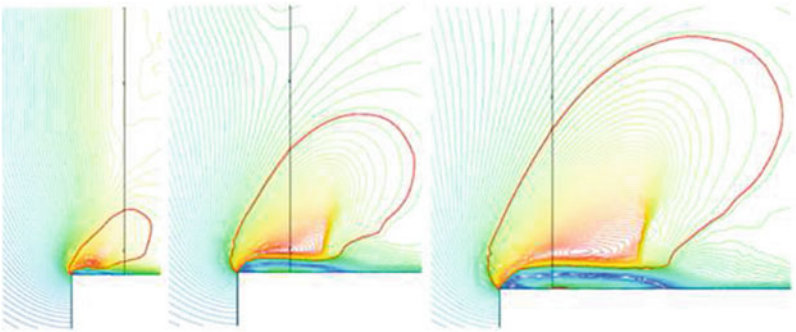

Fig. 7 Mach number contours for $P_{41} = 9$, $D = 10$ and times of 100, 200 and 300 μs

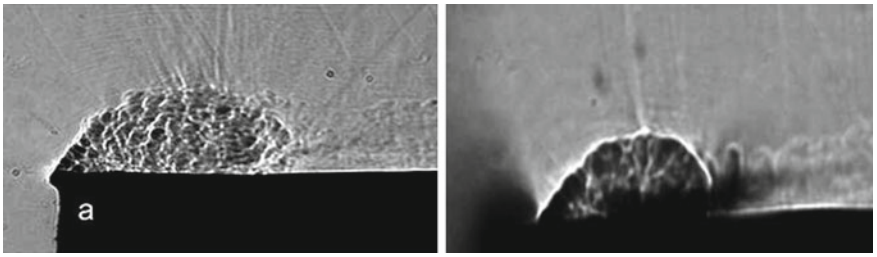

Fig. 8 Shadow and schlieren images of separation bubble showing shocks

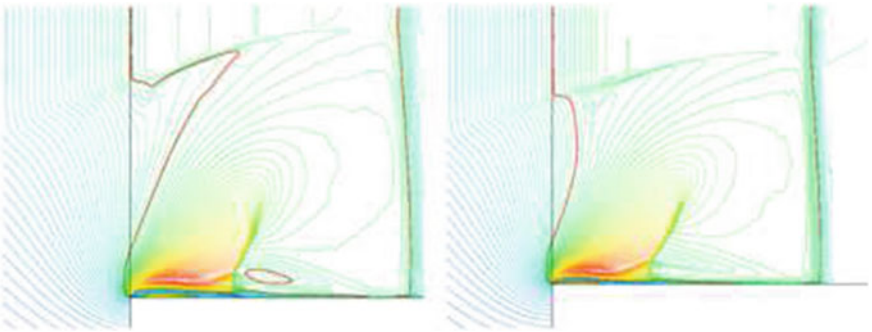

Fig. 9 Mach number contours for $D = 0$ and $P_{41} = 12$, (left) and 15 (right) at a time of 300 μs

at sonic velocity relative to this flow. Two cases are shown in Fig. 9. It will be noted that the sonic line is positioned in the contact surface since the flow on the other side, in region 2, will still be subsonic for the pressure ratios shown. The sonic line to the left of this supersonic region is at the position of the diaphragm in the region where the expansion wave is still undisturbed by the presence of corner. It then becomes distorted as it enters the flow generated by the reflected compression wave from the corner. It is also noted that the shock develops a lambda configuration and in the left-hand case a small region of subsonic flow appears.

3 Reflection Off a Concave Wedge

There has been very little work done for the case of a plane expansion wave, as generated in an ideal shock tube, encountering a plane wedge. As the wave moves up the wedge, the flow is induced downward back towards the corner at the wedge leading edge, and as could be expected for a strong enough wave, a shock wave will develop at the compressive corner, as indicated by the numerical simulation given in Fig. 10. C is the receding contact surface and D is the initial position of the diaphragm. The flow down the surface sees the corner as the entrance to a concave surface and an oblique shock may develop. The flow is clearly complex since the velocity along the surface is continually changing, both because of the properties of the wave propagation up the wall and the fact that the wave is continuously becoming wider. At the same time, the density and temperature are dropping. Thus, the position of the diaphragm and the initial wave pressure ratio will have an influence on the shock strength and its appearance.

Experimentation in the study of such flows is very demanding for a variety of reasons. Visualisation of an expansion wave is particularly difficult because the gas densities are low and the density gradients very shallow, so both shadowgraphy and schlieren require very high sensitivity. For this reason, in order to keep the wave

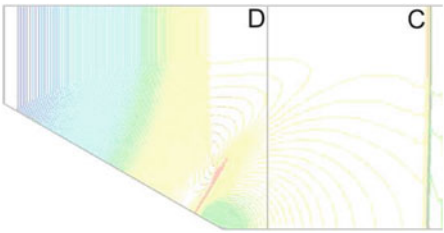

Fig. 10 Shock wave development on a plane wedge at late times

narrow, the diaphragm position needs to be very close to the test section. However, the diaphragm is initially curved under the pressure difference across it which results in an initially curved expansion wave. This is compounded by the finite opening time of the diaphragm, so if the opening starts at the centre and then propagates outwards, the shape of the issuing expansion wave will also be modified. Clearly, detailed studies will need to be undertaken to characterise these effects so that they can be incorporated in the numerical modelling.

Some experimental results are given in Fig. 11 for wall angles of 15° and 30°. The expansion wave is propagated to the left and has already passed over the back end of the wedge. The flow up the rear face separates in a bubble at the rear corner, in the same way as has been found in expansion diffraction tests, and remains attached there. However, even before this happens, a complex layered boundary layer is developed. At these early stages, no shock waves are evident, although these develop at a later time as shown. What is particularly interesting is the way this turbulent boundary layer curves as it approaches the corner. There may even be a circulating region at the corner itself but this has not been identified yet. However, there is evidence of the flow separating at the corner. Furthermore, this does indicate that the shock wave will be initiated by a compression fan arising from this curved flow.

Similar effects occur in the study of an expansion wave propagating into a cavity. These are interesting cases because of the very low pressures and temperatures that can result due to wave focusing. The first image in Fig. 12 shows the wave entering the high-pressure driver section before the leading edge has reached the apex of the cavity. The shock waves from either side propagate up the side walls into the very low-pressure region left behind after wave reflection, and cross over each other forming reflected waves. They subsequently merge and propagate back up the tube. Initial temperature is 300 K and a channel pressure is 83 kPa. With a starting diaphragm pressure ratio of 7, this results in a minimum temperature at focus of 80 K, and pressure of 6.8 kPa.

Similar results occur for a curved wall. Figure 13 shows typical results for a cylindrical cavity. As the head of the expansion engages with the curved surface, flow is induced out from the cavity which then experiences a concave surface and generates compression waves which merge into a shock that propagates up into the cavity.

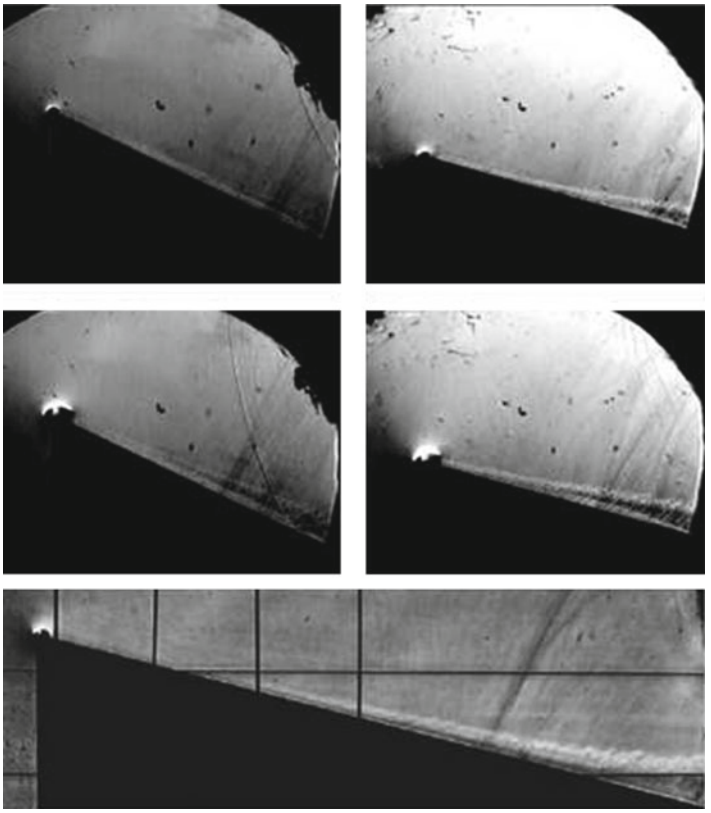

Fig. 11 Experimental images of expansion diffraction up a wedge

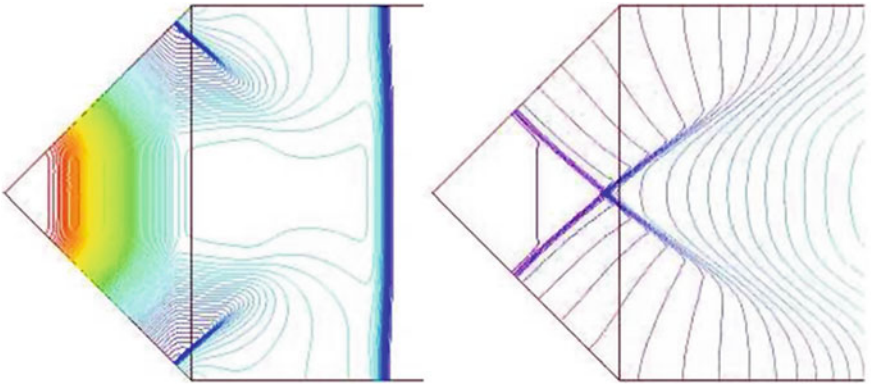

Fig. 12 Expansion wave propagation into a two-dimensional triangular cavity

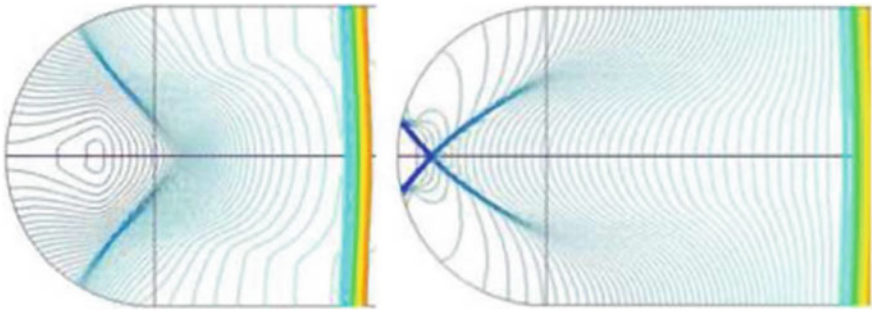

Fig. 13 Expansion wave propagation into a two-dimensional cylindrical cavity

This occurs on either sides of the symmetry plane, and the two shocks then reflect off each other as shown and subsequently interact with the cavity walls and eventually reflect out of the cavity. In this case, minimum pressures and temperatures are 33 kPa and 125 K.

4 Conclusions

It is demonstrated that a plane expansion wave encountering a change in surface slope in two dimensions can generate embedded shocks. These can result from either the development of compression waves which consolidate into a shock or because of local areas of transonic or supersonic flow being generated. Initial experimental studies show a number of features evident in the simulations but for both the concave and convex walls show complex turbulent flow features as the expansion wave propagates. Experimental visualisation of expansive flows presents many challenges so normally only the shocks become evident.

Acknowledgements The results of projects from a number of undergraduate and postgraduate students, which have been included, are gratefully acknowledged. The support from the National Research Foundation in supporting these projects, either in the form of bursaries or for project costs is much appreciated.

References

1. Mahomed, I., Skews, B.W.: Expansion wave diffraction over a 90 degree corner. J. Fluid Mech. **757**, 649–664 (2014)

Hypersonic Shock Wave Boundary Layer Interaction Studies on a Flat Plate at Elevated Surface Temperature

Alexander Wagner, Jan Martinez Schramm, Klaus Hannemann, Ryan Whitside and Jean-Pierre Hickey

Abstract Experimental shock wave boundary layer interactions (SBLI) at a compression corner of a flat plate model with deflectable flap and variable surface temperature were studied in the High Enthalpy Shock Tunnel Göttingen (HEG) of the German Aerospace Center (DLR) at Mach 7.4 and 6.65×10^6 m^{-1} unit Reynolds number. The present paper focuses on the effect of the leading edge bluntness and surface temperature. The effects are discussed based on surface heat flux and surface pressure measurements as well as schlieren visualizations. The study confirms that the state of the incoming boundary layer is crucial for the interaction. A small change of the leading edge bluntness was found to affect the boundary layer stability and thus the SBLI. In contrast, surface heating was found to destabilize the boundary layer. Tests at different flap deflection angles and transitional incoming boundary layers revealed that the transition process was completed in the separated shear layer, leading to a fully turbulent reattachment on the flap. The experimental effort is complemented by Reynolds-Averaged Navier–Stokes (RANS) computations providing insights into fundamental trends. The 2D simulations underpredict the size of the separation bubble in the compression corner but qualitatively mirrored the experimental trends. The wall heating resulted in an increased boundary layer thickness, reduced the extent of the separation bubble and elevated the peak boundary layer temperature on the flap.

A. Wagner (✉) · J. M. Schramm · K. Hannemann
Spacecraft Department, German Aerospace Center (DLR), Institute of Aerodynamics and Flow Technology, Göttingen, Germany
e-mail: alexander.wagner@dlr.de

J. M. Schramm
e-mail: jan.martinez@dlr.de

K. Hannemann
e-mail: klaus.hannemann@dlr.de

R. Whitside · J.-P. Hickey
Mechanical and Mechatronics Engineering, University of Waterloo, Waterloo, ON, Canada
e-mail: rwwhitsi@uwaterloo.ca

J.-P. Hickey
e-mail: j6hickey@uwaterloo.ca

K. Kontis (ed.), *Shock Wave Interactions*,
https://doi.org/10.1007/978-3-319-73180-3_19

1 Introduction

A shock/boundary-layer interaction (SBLI) occurring within a flow can be a crucial factor in the design of a hypersonic vehicle or a propulsion system. SBLIs occur on external or internal surfaces causing intense adverse pressure gradients in the boundary layer imposed by the shock. If the shock is sufficiently strong, the boundary layer separates which can lead to dramatic changes in the entire flow field structure including intense vortices or complex shock patterns. In addition, shock-induced separation may cause large-scale unsteadiness leading to, e.g. air intake disturbances and unsteady aerodynamic loads. Consequently, uncontrolled SBLIs are likely to limit the performance of a vehicle and could even cause structural damage [1].

During the last decades, the understanding of SBLI and the ability to predict these flows have advanced significantly [3]. However, most of the experimental and numerical work concentrated on cases with nearly adiabatic wall, i.e. where the wall temperature T_w is close to the recovery temperature T_r of the incoming boundary layer, e.g. [9, 13, 18, 19]. Considering the realistic design of hypersonic vehicles using cooling strategies this is problematic, since a cooled wall affects, e.g. the speed of sound close to the wall, the boundary layer thickness and its stability which largely affects SBLIs, e.g. leading to a change of the wall shear stress distribution and its gradients.

Only a limited number of experimental studies at cooled wall conditions are available. These studies are typically conducted in shock tunnels taking advantage of the high total temperatures while the model basically rests at ambient temperature over the test time, e.g. [7, 8, 18]. In these facilities, the variation of the ratio T_w/T_r is usually realized by choosing test conditions with different total temperatures. This in turn causes large variations in the free-stream conditions preventing a direct study of the wall temperature effects on SBLIs. To isolate the effect, it is desirable to keep the free-stream test conditions constant while changing the model wall temperature only. This can be realized by, e.g. using liquid nitrogen to cool the wind tunnel model as reported in [14] or by heating the wind tunnel model as reported in [2, 15, 21]. Since heating and cooling techniques involve an enormous increase of the complexity of experimental setup, the available experimental database for CFD validation is very limited.

The aim of the present study is to experimentally investigate shock/boundary-layer interactions on a flat plate model with compression corner and variable surface temperature in the High Enthalpy Shock Tunnel Göttingen (HEG). The experimental effort is supported by Reynolds-Averaged Navier–Stokes (RANS) computations aiming to explore the parameter space of the present experiments and to prepare future LES computation on this setup.

2 Experimental Setup

All tests were conducted in the HEG which is a free-piston driven reflected shock tunnel. Originally, the facility was designed to investigate the influence of high-temperature effects such as chemical and thermal relaxation on the aerothermodynamics of entry or reentry space vehicles. In this operating range, total specific enthalpies of up to 23 MJ/kg and nozzle stagnation pressures of up to 150 MPa can be reached. Since its commission in 1991, the range of operating conditions has been extended to allow the investigation of hypersonic flight configurations from low altitude Mach 6 up to Mach 10 at approximately 33 km altitude [6]. This new operating range was recently used in studies on shock wave boundary layer interactions on flat plate/shock generator configurations at Mach 6 investigating the effect of shock impingement on the boundary layer transition process. Furthermore at Mach 8 conditions, studies on supersonic combustion [11], hypersonic boundary layer transition and passive transition control [12, 23, 24], were conducted.

The wind tunnel model used in the scope of the present study is shown in Fig. 1. It consists of a heatable flat plate section, an unheated flap, deflectable at 0°, 15° and 30°, and an exchangeable leading edge. The latter is passively heated through the contact surface toward the heated model section. At the hinge line, a gap of 0.2 mm was created between the flap and flat plate to account for a more realistic setup with respect to a flight vehicle. Figure 2 provides the basic dimensions of the model. An electrical heating element was implemented below the surface of the flat

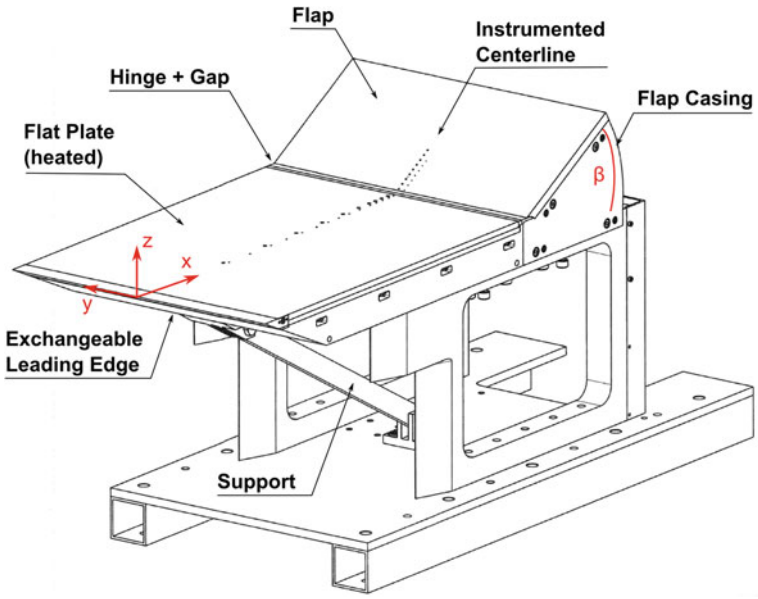

Fig. 1 Perspective drawing of the wind tunnel model

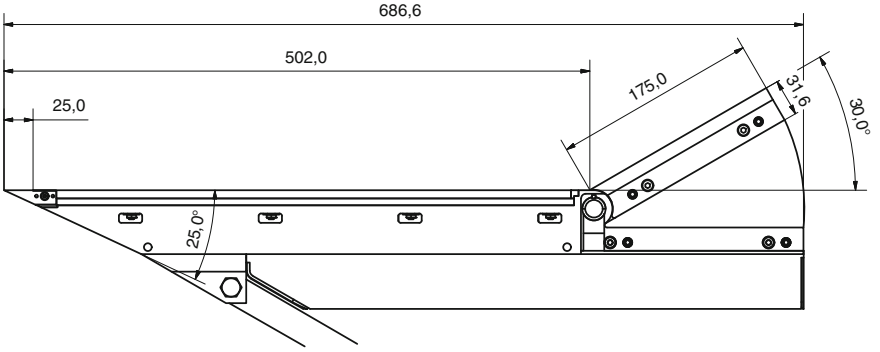

Fig. 2 Model side view with basic model dimensions. The model width is 360 mm. All dimensions are provided in millimeters

plate section allowing to increase the model surface temperature up to 800 K. The model flap was not heated and thus remained at room temperature. This allows the use of standard instrumentation which is less expensive and can be mounted with smaller spacing to increase the spatial resolution of the measurements on the flap. The authors expect that the SBLI in the compression corner is dominated by the upstream flow conditions. Therefore, it is assumed that the effect of the unheated flap on the SBLI can be neglected.

The surface temperature and its distribution are measured using an infrared camera of the type IRCam Equus 327k M which was calibrated for use in a temperature range of 470–1070 K. Figure 3a depicts the model prepared for infrared imaging by coating the heated flat plate section and the flaps with a high-temperature-resistant black paint. Figure 3b provides the surface temperature distribution of the heated surface revealing temperatures of up to 800 K. The center line of the model remained uncoated to protect the installed instrumentation. As shown in Fig. 3, the model was designed such that the model flap remained near ambient temperature while the flat plate section was heated. This allowed the use of densely spaced standard surface pressure and surface temperature transducers in the flap while using high-temperature-resistant transducers with inevitable larger spacing in the heated section. The surface-based measurements were supported by schlieren visualizations using a Phantom v1210 high-speed camera with a sampling frequency of 25 kHz in combination with a noncoherent laser to freeze the fluid motion.

Table 1 summarizes the averaged reservoir conditions with the corresponding standard deviation, σ. The free-stream test conditions were computed using the DLR TAU code [5, 10, 17, 20]. Based on the averaged test conditions and the model surface temperature range, the wall temperature to total temperature ratio was varied between 0.11 and 0.30.

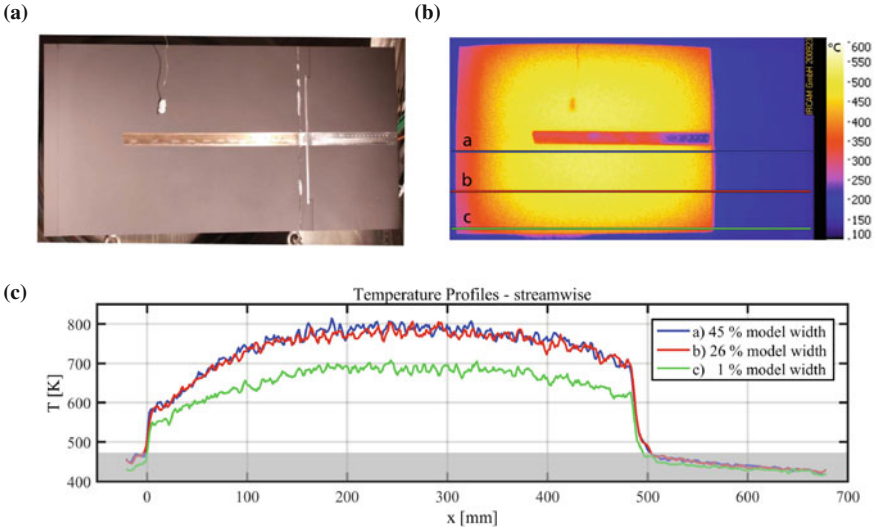

Fig. 3 Top view of the wind tunnel model prepared for infrared measurements (**a**) and surface temperature distribution by means of thermography (**b**). Extracted temperature profiles in streamwise direction (**c**). Note that surface temperatures below 470 K cannot be measured using the high-temperature configuration of the camera

Table 1 Mean free-stream conditions computed using the DLR TAU code and the standard deviation of the nozzle reservoir conditions based on 21 runs

	Mean	σ (%)
p_0 (MPa)	31.54	1.73
T_0 (K)	2687	0.65
h_0 (MJ/kg)	3.18	0.78
M (–)	7.4	
p_∞ (Pa)	3442	
T_∞ (K)	261	
ρ_∞ (g/m^3)	45.7	
u_∞ (m/s)	2400	
Re_m (10^6 m^{-1})	6.65	

3 Experimental Results

In the experimental study, a number of parameters such as leading edge radius, surface temperature, flap deflection angle, and the gap size at the hinge line of the flap were varied. However, the present section focuses on the effect of the following parameters only: the effect of leading edge bluntness and surface temperature.

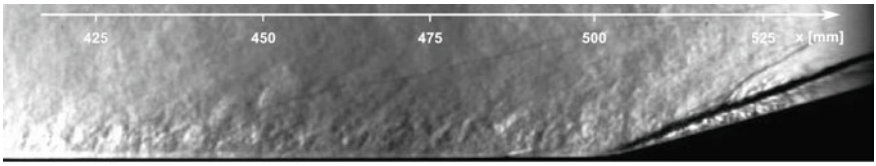

(a) Sharp leading edge

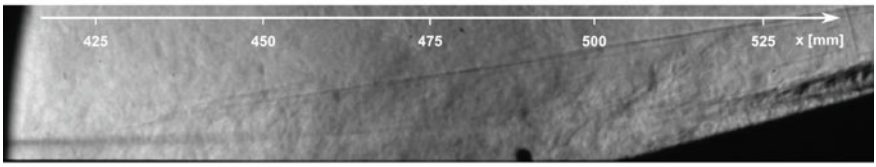

(b) Blunted leading edge, $R_{le} = 0.1$ mm

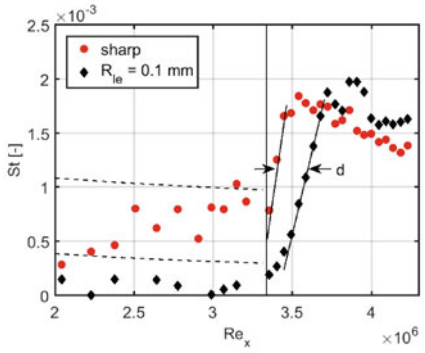

(c) Heat flux coefficient

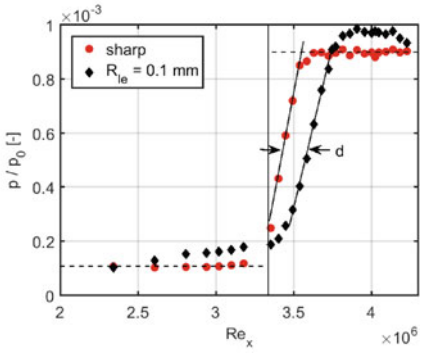

(d) Normalized surface pressure

Fig. 4 Schlieren visualization of the compression corner with 15° flap deflection and sharp leading edge in (**a**) and blunted leading edge in (**b**). Stanton number and surface pressure distribution for both cases (**c**, **d**). The hinge position is marked with a vertical line. The dashed lines in (**c**) depict the laminar and turbulent Stanton number level for the flat plate section according to [4] being normalized using the corresponding wall enthalpy of the model. The dashed lines in (**d**) mark the expected surface pressure levels according to oblique shock theory

Leading edge bluntness was found to strongly affect the boundary layer state immediately ahead of the SBLI. Tests with sharp leading edge resulted in a transitional or fully turbulent boundary layer ahead of the SBLI as depicted by the schlieren visualization in Fig. 4a. As shown in Fig. 4c, the heat flux coefficient significantly increases in the downstream direction indicating the transition process of the boundary layer. The surface heat flux coefficient increases between $Re_x = 2 \times 10^6$ and $Re_x = 3.3 \times 10^6$ almost reaching the fully turbulent level upstream of the compression corner. For the present case, flow separation is not observed based on the surface pressure readings and the schlieren visualization. The reattachment occurs directly downstream of the hinge line. The surface pressure and the surface heat flux increase immediately. The viscous nature of the SBLI causes the streamwise

lag until which the full pressure and heat flux on the flap is reached. In contrast, a small increase in the bluntness, i.e. a leading edge radius of 0.1 mm, stabilized the boundary layer sufficiently to observe a predominantly laminar boundary layer upstream the compression corner as depicted in the schlieren visualization in Fig. 4b. The impact of the boundary layer is striking. A massive flow separation at the compression corner is visible in the schlieren visualization. The reattachment on the flap is delayed in downstream direction, leading to a delayed rise of the surface heat flux and the surface pressure on the flap as indicated by d in Fig. 4c. Note that the Stanton number after reattachment is slightly higher in the case of a laminar incoming boundary layer. According to Sandham et al. [18], this suggests that the incoming boundary layer was already at an early transitional state causing higher surface heat flux compared to the interaction of a boundary layer at a late transitional stage.

The surface pressure measurements, depicted in Fig. 4d, provide information on the size of the separation zone. The region with increased pressure upstream the hinge line, observed for the blunted leading edge case, is an indicator of the separation zone. Its most upstream extent can be estimated, limited by the transducer spacing, to approximately $Re_x = 2.6 \times 10^6$ which corresponds to an upstream extent of about 105 mm measured from the hinge line. This is in good agreement with the schlieren visualization in Fig. 4b.

The effect of surface temperature is depicted in Fig. 5 providing two test cases with different surface temperatures. All other parameters were kept constant between the tests. The blunted leading edge was used for both test cases. The schlieren visualizations provided in Fig. 5a, b reveal that surface heating destabilizes the boundary layer resulting in an earlier transition. Hence, a fully developed turbulent boundary layer is observed at the compression corner. This is supported by the increase of the boundary layer thickness and the turbulent structures visible in Fig. 5b. The Stanton number distributions provided in Fig. 5c further support the observation showing a turbulent Stanton number at the hinge line for both heated cases. It should be noted that a good run to run repeatability of the free transition process was obtained. The Stanton number distribution of the unheated model indicates a transitional boundary layer at the compression corner as well, although with a lower intermittency.

The effect of the surface temperature on the SBLI and thus on the Stanton number distribution on the flap is small. However, a small shift of the surface heat flux peak on the flap in downstream direction is noted for the heated cases indicating a delay of the reattachment, Fig. 5c. The effect might be caused by the larger boundary layer thickness due to the increased surface temperature. A similar observation is made regarding the surface pressure distribution on the flap, Fig. 5d. For the heated cases, the maximum pressure on the flap is reached further downstream. Although the differences are small, the schlieren visualizations provided in Fig. 5a, b support the above assessment.

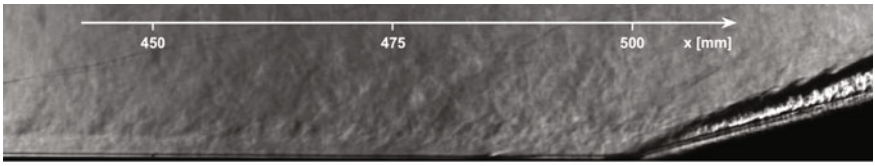

(a) $T_w = 295$ K

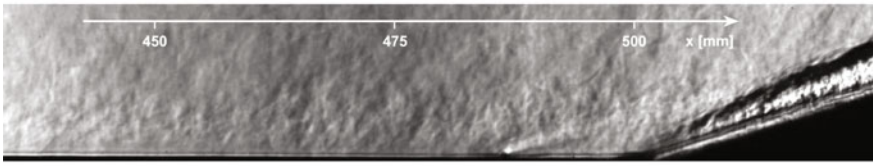

(b) $T_w = 800$ K

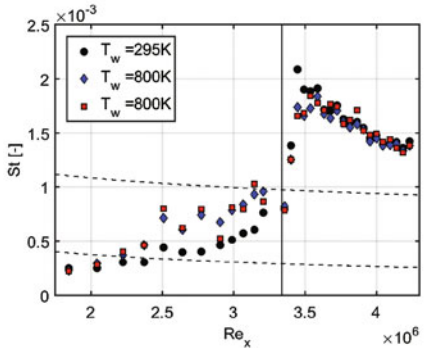

(c) Heat flux coefficient

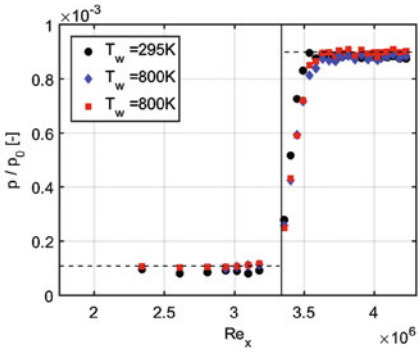

(d) Normalized surface pressure

Fig. 5 Schlieren visualization of the compression corner with 15° flap deflection, blunted leading edge and 295 K wall temperature in (**a**) and 800 K wall temperature in (**b**). Stanton number and surface pressure distribution for different wall temperatures (**c**, **d**). The hinge position is marked with a vertical line. The dashed lines in (**c**) show the laminar and turbulent Stanton number level for the flat plate section according to [4] being normalized using the corresponding wall enthalpy of the model. The dashed lines in (**d**) mark the expected surface pressure levels according to oblique shock theory

4 Numerical Results

A numerical study was undertaken to complement the experimental efforts. The simulations were conducted with the objective of further exploring the parameter space of the experiment and as a first step toward a high-fidelity, wall-modeled Large-Eddy Simulation of the most relevant setups. In this work, the computational tractability was the most important parameter, therefore a Reynolds-Averaged Navier–Stokes (RANS) approach was used. The simulations were conducted using the compressible RANS solver: SU2 (Stanford University Unstructured) [16]. In the present setup, the nonequilibrium thermodynamic effects are localized near the sharp leading edge,

thus permitting the use of a nonreacting, equilibrium solver to study the region of interest near the hinge. A second-order spatial integration with a slope limiter [22] was used for the convective terms; an explicit Runge–Kutta scheme advanced the pseudo-time toward a steady-state solution. The turbulence was accounted for with the SST k-omega turbulence model. The setup, including the sharp leading edge, was meshed using a fully structured block grid with smooth stretching, thus limiting numerical errors in the flux calculations. Detailed grid independence studies were undertaken, but grid convergence was only reached for two-dimensional cases. Therefore, the 2D cases will be reported herein, with the acknowledgment that the separation bubble physics is highly three-dimensional. The grid count for the medium mesh is 1.2 million control volumes with the first grid point located at 2.0×10^{-6} m, which corresponds to $y^+ \approx 0.5$ at $x = 0.5$ m. A domain size sensitivity analysis revealed the importance of a well captured leading edge shock (as opposed to a domain size reduction through oblique shock calculations). The domain size analysis permitted a domain size reduction, thus computational savings, while capturing the relevant physics of the problem. The simulations were conducted on the GPC cluster on SciNet at the University of Toronto.

The experiments highlighted the importance of the transition location on the SBLI physics. To numerically predict the exact transition location with varying bluntness or wall temperature within the context of Reynolds-averaged equations remains far too challenging for classical transitional models. Therefore, the transition location was defined a priori by forcing the turbulent viscosity to zero upstream of the predefined transition location.

The heating of the flat plate resulted in a noticeable growth of the boundary layer thickness as can be seen in the velocity profiles in Fig. 6. This growth is expected given the reduced near-wall density associated with the higher temperature. The heating of the flat plate increases the momentum thickness immediately upstream of the SBLI by 23% (26% for the displacement thickness) when the transition is

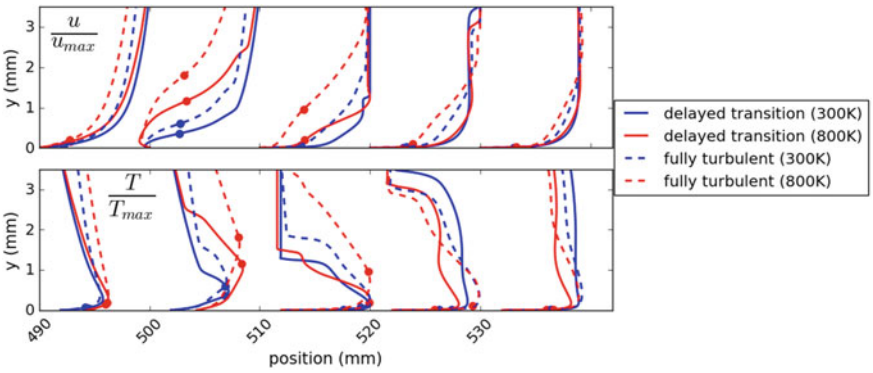

Fig. 6 Wall normal velocity and temperature profiles at various streamwise locations near the wedge for delayed transition ($Re_x = 1.33 \times 10^6$) and fully turbulent flat plate conditions. The symbols indicate the sonic line

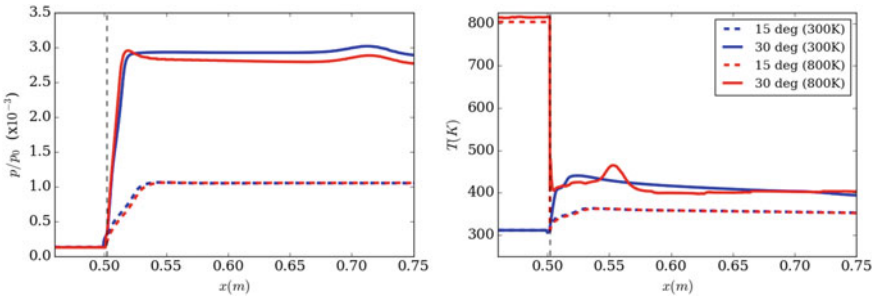

Fig. 7 Pressure (left) and temperature (right) profiles along the flat plate and the flap for the 15° (dashed line) and 30° (full line) cases. The blue and red lines correspond respectively to the cold ($T_w = 300$ K) and hot ($T_w = 800$ K) wall setups

set at $Re_x = 1.33 \times 10^6$. For the fully turbulent case, the variation is even greater (26% momentum and 32% displacement thickness). As observed in the experimental results in Fig. 5c, the wall heating slightly delays the reattachment on the flap which is evidenced by the velocity profiles for the cases at $x = 510$ and 520 mm in Fig. 6. As a direct consequence, we observe a delayed heat flux peak (estimated

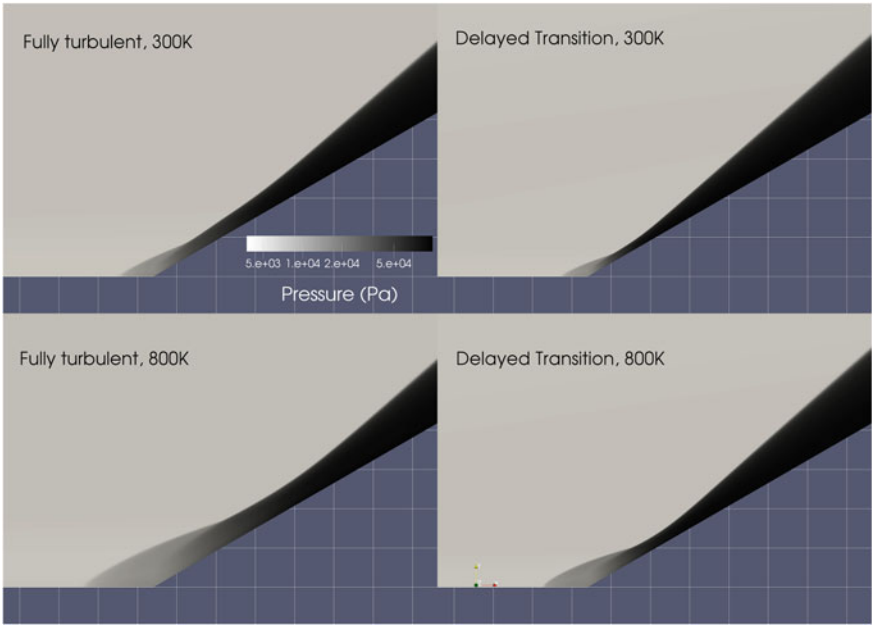

Fig. 8 Effect of heating and transition location on the pressure distribution near the hinge. The delayed case assumes that transition occurs at $Re_x = 1.33 \times 10^6$. The grid spacing on the figure corresponds to 20 mm

based on the temperature gradients at the wall) on the flap for the heated cases which support the experimental claim. The delayed heat flux peak for the heated flat plate is also noted in the temperature profile along the flap in Fig. 7.

The wall heating has a complex effect on the separation bubble as observed by the pressure distribution in Fig. 8. For a fixed transition location, the wall heating results in an earlier boundary layer separation as the reduced near-wall velocity gradient is more sensitive to the streamwise pressure gradient near the SBLI. This results in a thicker separation bubble. But the total streamwise extent of the separation region is not greatly influenced by the wall heating. The wall heating had a modest effect on the pressure distribution on the flap. A very slight pressure drop on the flap was noted due to wall heating for the 30° inclination case; no differences were observed for the 15° inclined flap, see Fig. 7.

5 Conclusion

SBLI at a compression corner of a flat plate model with deflectable flap and variable surface temperature were studied by means of experiments in the HEG and complementary RANS computations. The wind tunnel model was designed to facilitate surface temperatures of up to 800 K and thus to investigate the effect of surface temperature on SBLI. The experimental study confirmed the strong dependence of the interaction on the state of the incoming boundary layer which was found to be very sensitive to small changes of the leading edge bluntness and to the change of surface temperature. Increasing bluntness was found to stabilize the boundary layer while heating the model surface was found to be destabilizing. For all cases with flap deflection, a predominantly laminar boundary layer upstream the interaction zone resulted in a large separation bubble. In contrast, for predominantly turbulent incoming boundary layers, the separation bubble was found to be present but very limited in its extent. Apart from the change of the boundary layer state, no additional effects of wall heating were resolvable in the present experiments. The latter observation might be due to the moderate change of the ratio wall temperature to total temperature which ranges from 0.1 at cold conditions and to 0.3 for the heated case. The present study was conducted to allow SBLI studies with transitional boundary layers. However, the results indicate the need of a transition control strategy to limit the number of free parameters in a test case, e.g. to avoid a change of boundary layer state due to a change of surface temperature.

The grid-converged 2D RANS simulations conducted to complement the experimental efforts were used to further explore the parameter space of the experiments. Due to the three-dimensional nature of the separation, a perfect match with the experimental data cannot be expected. This is reflected by the underpredicted size of the separation region. However, the computations mirrored the experimental trends. Wall heating acted to increase the boundary layer thickness but had a modest effect on the integral parameters of the flow. To isolate the influence of the transitional boundary layer state on the compression corner, comparative simulations were conducted

by fixing the transition location on the flat plate. For a thicker boundary layer (due to wall heating or earlier transition), the separation moved upstream and the thickness of the separation bubble increased but the streamwise extend remained roughly unchanged. Wall heating also confirmed the delayed peak temperature gradient on the flap.

Acknowledgements This work was performed within the Aero-Thermodynamic Loads on Lightweight Advanced Structures II project investigating high-speed transport. ATLLAS II, coordinated by ESA-ESTEC, is supported by the EU within the 7th Framework Programme Theme 7 Transport, Contract no.: ACP0-GA-2010-263913. Further info on ATLLAS II can be found on http://www.esa.int/techresources/atllas_II. Computations were performed on the GPC supercomputer at the SciNet HPC Consortium through Compute Canada's Resource Allocation Competition (RAC).

References

1. Babinsky, H., Harvey, J.K. (eds.): Shock Wave-Boundary-Layer Interactions. Cambridge University Press (2011)
2. Bleilebens, M., Olivier, H.: On the influence of elevated surface temperatures on hypersonic shock wave/boundary layer interaction at a heated ramp model. Shock Waves (Springer) **15**, 301–312 (2006)
3. Dolling, D.S.: Fifty years of shock-wave/boundary-layer interaction research: what next? AIAA J. **39**(8), 1517–1531 (2001)
4. van Driest, E.R.: The problem of aerodynamic heating. In: Aeronautical Engineering Review, pp. 26–41 (1956)
5. Gerhold, T.: Overview of the Hybrid RANS Code TAU MEGAFLOW—Numerical Flow Simulation for Aircraft Design in Notes on Numerical Fluid Mechanics and Multidisciplinary Design, vol. 89. Springer (2005)
6. Hannemann, K., Schramm, J.M., Karl, S.: Recent extensions to the high enthalpy shock tunnel Göttingen (heg). In: 2nd International ARA Days (2008)
7. Holden, M.S.: Shock wave-turbulent boundary layer interaction in hypersonic flow. In: AIAA 10th Aerospace Sciences Meeting (1972)
8. Holden, M.S.: A study of flow separation in regions of shock wave-boundary layer interaction in hypersonic flow. In: AIAA 11th Fluid and Plasma Dynamics Conference (1978)
9. Horstman, C.C.: Hypersonic shock-wave/turbulent-boundary-layer interaction flows. AIAA J. **30**(6), 1480–1481 (1992)
10. Karl, S.: Numerical investigation of a generic scramjet configuration. Ph.D. thesis, University of Technology Dresden (2011)
11. Laurence, S., Lieber, D., Schramm, J.M., Hannemann, K., Larsson, J.: Incipient thermal choking and stable shock-train formation in the heat-release region of a scramjet combustor. Part I: Shock-tunnel experiments. Combust. Flame **162**(4) (2014)
12. Laurence, S., Wagner, A., Hannemann, K.: Schlieren-based techniques for investigating instability development and transition in a hypersonic boundary layer. Exp. Fluids **55**(8) (2014)
13. Law, C.H.: Supersonic shock wave turbulent boundary-layer interactions. AIAA J. **14**(4), 730–734 (1976)
14. Lewis, J.E., Kubota, T., Lees, L.: Experimental investigation of supersonic laminar two-dimensional boundary layer separation in a compression corner with and with cooling. In: AIAA 5th Aerospace Science Meeting (1967)
15. Neuenhahn, T.: Investigation of the shock wave/boundary layer interaction of scramjet intake flows. Ph.D. thesis, Rheinisch-Westflischen Technischen Hochschule Aachen Fakultät für Maschinenwesen (2010)

16. Palacios, F., Alonso, J., Duraisamy, K., Colonno, M., Hicken, J., Aranake, A., Campos, A., Copeland, S., Economon, T., Lonkar, A., Lukaczyk, T., Taylor, T.: Stanford university unstructured: an open-source integrated computational environment for multi-physics simulation and design. In: Aerospace Sciences Meetings. AIAA (2013). https://doi.org/10.2514/6.2013-287
17. Reimann, B., Johnston, I., Hannemann, V.: DLR τ-code for high enthalpy flows. In: Breitsamter, C., Laschka, B., Heinemann, H.J., Hilbig, R. (eds.) New Results in Numerical and Experimental Fluid Mechanics IV: Contributions to the 13th STAB/DGLR Symposium Munich, Germany 2002, pp. 99–106. Springer, Berlin, Heidelberg (2004)
18. Sandham, N.D., Schülein, E., Wagner, A., Willems, S., Steelant, J.: Transitional shock-wave/boundary-layer interactions in hypersonic flow. J. Fluid Mech. **752**, 349–382 (2014). https://doi.org/10.1017/jfm.2014.333
19. Schülein, E.: Effects of laminar-turbulent transition on the shock-wave/boundary-layer interaction. In: 44th AIAA Fluid Dynamics Conference (2014)
20. Schwamborn, D., Gerhold, T., Heinrich, R.: The DLR tau-code: recent applications in research and industry. In: European Conference on Computational Fluid Dynamics ECCOMAS CFD (2006)
21. Scortecci, F., Paganucci, F., d'Agostino, L.: Experimental investigation of shock wave/boundary layer interactions over an artificially heated model in hypersonic flow. AIAA (1998)
22. Venkatakrishnan, V.: Convergence to steady state solutions of the Euler equations on unstructured grids with limiters. J. Comput. Phys. **118**(1), 120–130 (1995)
23. Wagner, A., Hannemann, K., Kuhn, M.: Ultrasonic absorption characteristics of porous carbon-carbon ceramics with random microstructure for passive hypersonic boundary layer transition control. Exp. Fluids **55**(6) (2014)
24. Wagner, A., Kuhn, M., Martinez Schramm, J., Hannemann, K.: Experiments on passive hypersonic boundary layer control using ultrasonically absorptive carbon-carbon material with random microstructure. Exp. Fluids **54**(10) (2013)

Extinguishing Detonation in Pipelines—Optimization of the Process

Z. A. Walenta and A. M. Słowicka

1 Introduction

The necessity of extinguishing detonation, which may occur in pipelines transporting gaseous fuels, creates nowadays a very important technological problem. The standard devices used for this purpose consist of matrices of very narrow channels. Cooling the gas by cold walls of such channels may extinguish the flame and stop detonation. Detonation may also be extinguished if the cross section of the channel transporting gas increases abruptly at some place. The desired effect is achieved if the generated rarefaction waves decrease sufficiently the temperature of the flame [2, 3, 6, 7]. It might be expected that simultaneous use of both methods—using narrow channels with variable cross section—should give even better results. Additional profit might come from the fact that the flow in narrow channels is usually laminar; the abrupt increase of the cross section would introduce some turbulence which, in turn would enhance cooling by the walls. However, if the cross section of the channel increases and decreases, the unwanted heating of the gas may occur. To estimate the net result, which is not obvious, it is necessary to perform suitable simulations and experiments. The present paper is devoted to numerical simulation of the phenomenon.

2 Method of Simulation

The simulations presented in this paper were performed with the standard Direct Simulation Monte-Carlo (DSMC) technique [1] and the selection of molecules for collisions was performed with the ballot-box scheme, as proposed by Yanitskiy [9].

Z. A. Walenta (✉) · A. M. Słowicka
Institute of Fundamental Technological Research, Polish Academy of Sciences, Warsaw, Poland
e-mail: zwalenta@ippt.gov.pl

K. Kontis (ed.), *Shock Wave Interactions*,
https://doi.org/10.1007/978-3-319-73180-3_20

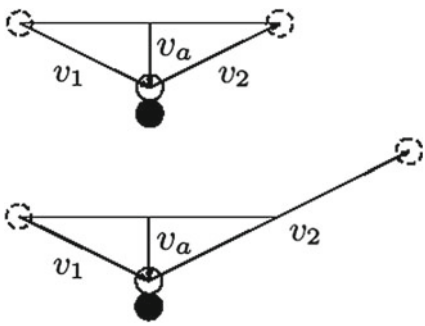

Fig. 1 Collision of two molecules in reference frame connected with one of them: top—elastic, bottom—with energy release; v_1—relative velocity of the molecules before collision, v_2—relative velocity after collision, v_a—"velocity of approach" of the molecules

The DSMC technique makes it possible to simulate flows in various geometrical configurations and, apart from that, it offers a possibility of taking into account the relaxation phenomena and chemical reactions [1, 4]. This, unfortunately, increases complexity of the computer programs and the necessary computing times. However, in the considered case, considerable simplifications can be made because in a detonation wave, the medium is far from thermodynamic equilibrium, combustion proceeds very fast and the relaxation processes at the molecular level may therefore be disregarded. The factor of prime importance, which remains, is the produced thermal energy.

2.1 Model of a Detonating Medium

As always in the Direct Monte-Carlo simulations, the medium is treated as an ensemble of molecules, colliding with each other and with walls and moving along straight lines with constant speed between collisions. Since in the present work, only the influence of the shape of the channel upon the process of extinguishing detonation is investigated, a very simple model of the detonating medium [7, 8] may be used. It is assumed, that all molecules of this medium are identical, hard spheres. Part of them, uniformly distributed in space, carry certain amount of "internal" energy (of unspecified character). The remaining molecules are "inert"—they can carry no "internal" energy and cannot accept it in any way. The "internal" energy of the molecule may be transformed into kinetic energy during collision with an "inert" molecule, provided that the two colliding molecules approach each other with sufficiently high velocity (see Fig. 1 for definition of the "velocity of approach"). The relative velocity of the molecules after collision is then increased suitably. The "internal" energy may be released either in the first collision of this kind (no delay), or during some later collisions (delayed energy release). A molecule which had lost its "internal" energy may regain it in collision with an "inert" molecule if their "velocity of approach" is higher than velocity corresponding to this "internal" energy (the "inverse reaction"). The relative velocity of the molecules after collision is then decreased suitably.

2.2 Interactions with Solid Walls

To simulate the interactions of the molecules with solid walls, the very simple model introduced by J. C. Maxwell [5] has been employed: molecules reflect from the walls either specularly (without exchange of tangential momentum and energy) or diffusely (molecules are adsorbed by the wall and re-emitted in directions selected at random with energies corresponding to temperature of the reflecting wall). The ratio of the number of molecules reflected diffusely to the total number of the reflected molecules (called "accommodation coefficient", α) may vary from the value 0 to 1. The value $\alpha = 0$ (purely specular reflections) corresponds to no exchange of tangential momentum and energy, the value $\alpha = 1$ corresponds to maximum possible exchange (maximum friction and cooling). For the majority of the so-called "technological surfaces", the accommodation coefficient is close to unity.

2.3 Details of Calculations

Here, we present the results of simulations of the behavior of a detonation wave in four channels of different geometries, in the medium containing different percentages of the molecules "carrying energy". The energy, carried by a single molecule and released in a collision, increased the relative velocity of the colliding molecules by the value equal to 10 times the most probable molecular speed. The "threshold velocity" of approach of the colliding molecules, necessary to release the "internal energy", was equal to about 5.48 times the most probable molecular speed.

Channel 1 (Fig. 2) was of standard geometry (straight, rectangular cross-section of constant area); its length was equal to 1200 units and its cross-section was 70×70 units, where the unit of length was equal to 1 mean free path of the molecular motion in front of the detonation wave. The interior of the channel was divided into cubic cells of dimension equal to 1 unit of length. Each cell contained, in average, about 5 molecules.

The remaining channels are also shown schematically in Fig. 2. The width of each channel was constant and equal to 70 units. All other dimensions are given in the figure.

The interior of each channel was divided into cubic cells of dimension equal to 1 unit—similar to channel 1. Each cell contained, as before, about 5 molecules.

The wave was initiated by instant removal of a "diaphragm", placed at $x = 100$ units. The temperature of the driver gas (behind the diaphragm) was 10 times higher than that of the driven gas. The pressure was such that after the diaphragm removal the shock wave of Mach number $Ms = 2$ was produced.

At both ends of each channel, i.e., for $x < 400$ units and $x > 1000$ units in channels 1 and 2 and for $x < 500$ units and $x > 1100$ units in channels 3 and 4, the molecules were reflected from the walls specularly, i.e., without exchange of tangential momentum and energy. Such region of flow without losses at the beginning

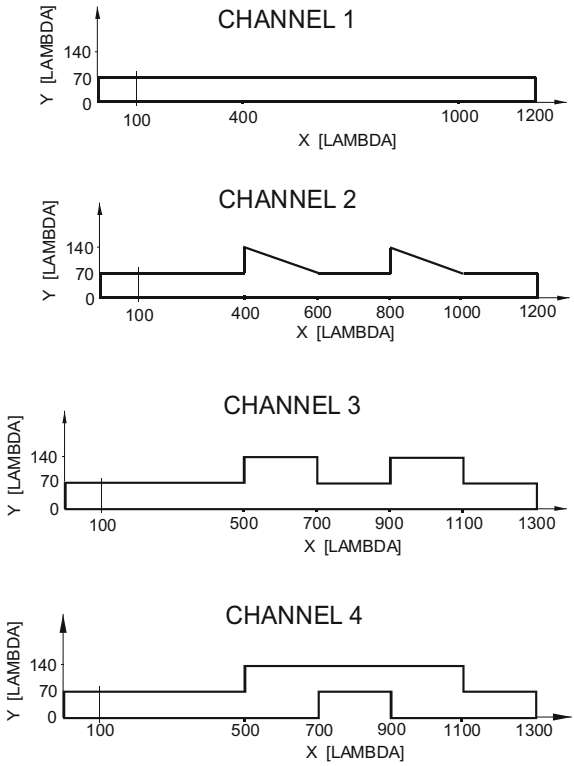

Fig. 2 Shapes of the considered channels. Lambda—mean free path in front of the wave

of the channel was necessary for the detonation to develop. The flow without losses at the end of the channel was assumed to check whether the extinguished detonation would not reappear.

The simulations were performed for a number of different percentages of the "energetic" molecules in the medium in front of the diaphragm. Table 1 presents these percentages for all channels considered in this investigation.

Table 1 Percentages of molecules carrying "internal" energy in the considered channels

Number of channel	Percentage of molecules carrying "internal" energy (%)
1	20, 21, 22
2	23, 24, 25
3	25, 26, 27
4	26, 27, 28

3 Results

The results of the performed simulations are presented in the following figures. Each of them contains a number of diagrams of temperature and percentage of "energetic" molecules (averaged over the local cross-section) along the channel, for a number of time intervals (evenly spaced) from removing the diaphragm, superimposed upon one another. The diagrams of temperature have been selected, because distribution of this parameter is very characteristic for the detonation wave and makes it easy to recognize its presence. The percentage of "energetic" molecules supplies the additional information on the position of the flame—whether it moves forward together with the wave, or lags behind it. The first three figures show the results for channel 1 (Figs. 3, 4 and 5), the next—for channels 2 (Figs. 6, 7, and 8) and 3 (Figs. 9, 10 and 11), the last—for channel 4 (Figs. 12, 13, and 14).

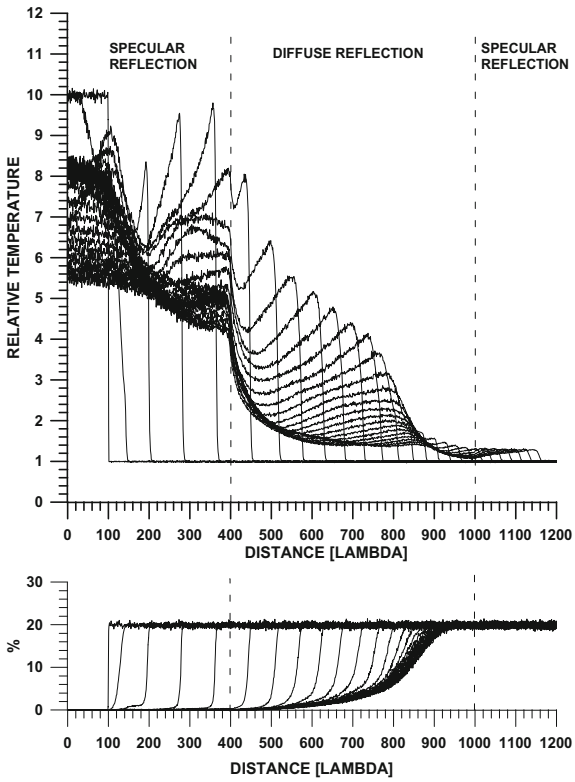

Fig. 3 Detonation in channel 1, in the medium containing 20% of "energetic" molecules. Temperature distributions along the channel (top), percentages of "energetic" molecules (bottom). Lambda—mean free path in front of the wave

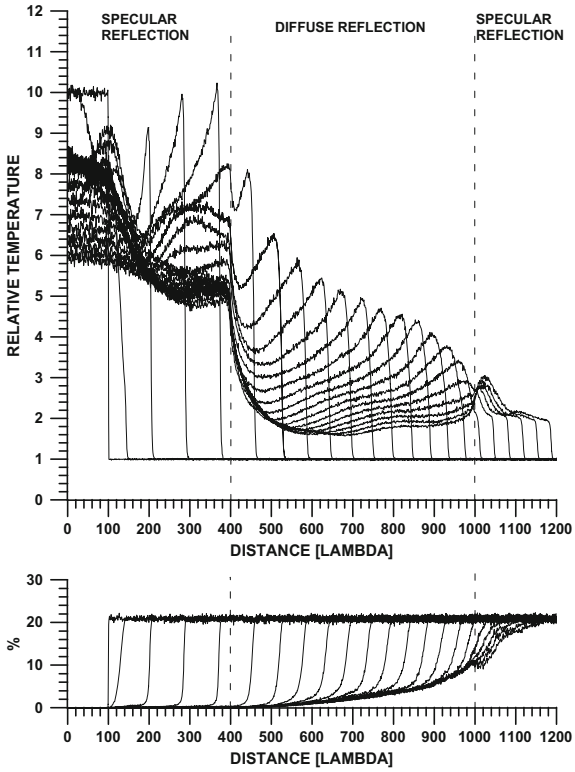

Fig. 4 Detonation in channel 1, in the medium containing 21% of "energetic" molecules. See Fig. 3 for explanation

3.1 Channel 1

In Fig. 3 (top), the diagrams of temperature inside the channel 1 for the medium containing 20% of "energetic" molecules are presented. After the diaphragm removal, the detonation wave is formed. It then speeds up, increases its intensity, and subsequently enters into the area where molecules reflect from the channel walls diffusely, the "burning" gas is cooled down and the flame disappears. The detonation wave is transformed into shock, which is weak and seems to decay gradually.

In Fig. 3 (bottom), the corresponding distributions of percentage of the "energetic" molecules are shown. Close to the diaphragm, practically all "energetic" molecules lose their "internal" energy when passing through the detonation wave. In the central part of the channel, where cooling by the walls takes place, only part of those molecules lose the energy and finally, at the end of the channel, where the temperature behind the wave is low, practically all of them keep the energy.

Figure 4 shows similar diagrams for the medium containing 21% of "energetic" molecules. The general picture is very close to that shown in Fig. 3, however the shock emerging at the end of the channel is stronger and it is not certain whether farther downstream it would not transform back into detonation wave.

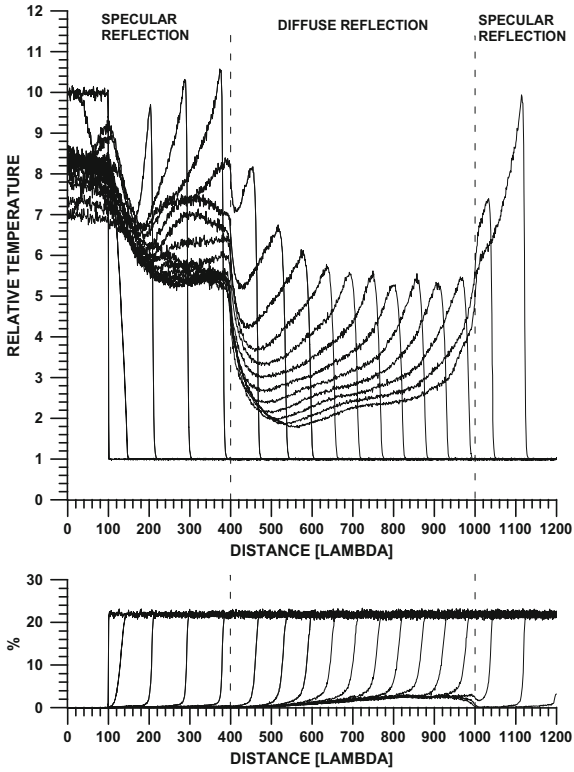

Fig. 5 Detonation in channel 1, in the medium containing 22% of "energetic" molecules. See Fig. 3 for explanation

Figure 5 shows finally the situation for the medium containing 22% of "energetic" molecules. In the central part of the channel, where friction and heat exchange at the walls are present, the detonation wave only becomes weaker, but retains its character. After entering the area of no friction and cooling it returns back to its former intensity and speed. This is clearly visible on both, the temperature distributions (Fig. 5, top) and the diagrams of percentage distributions of "energetic" molecules (Fig. 5, bottom). The last picture shows that in the part of the channel, where cooling takes place, only part of the "energetic" molecules lose their energy. Farther downstream, where there is no cooling, the situation is the same as at the beginning of the channel.

From the above results, the conclusion may be drawn that 21% is the limiting amount of "energetic" molecules (as defined above) in the "detonating medium", below which the detonation may be extinguished in channel 1.

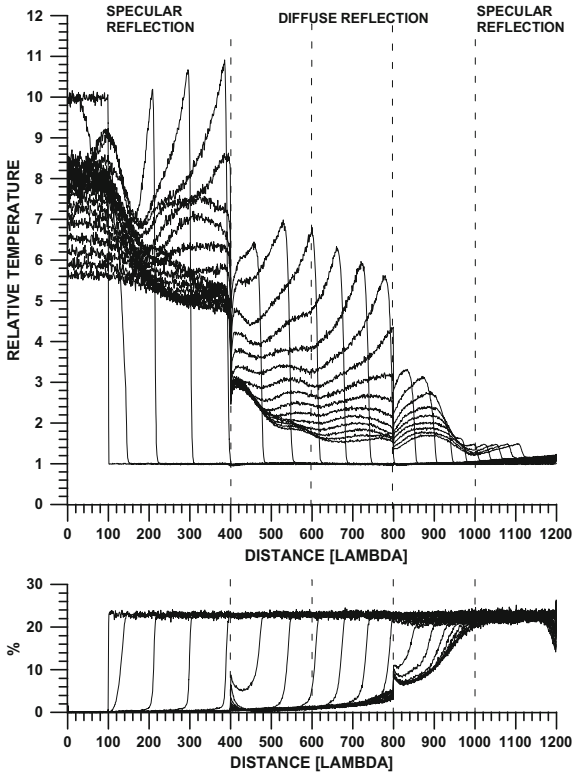

Fig. 6 Detonation in channel 2, in the medium containing 23% of "energetic" molecules. See Fig. 3 for explanation

3.2 Channel 2

In Fig. 6, the diagrams for the medium containing 23% of "energetic" molecules inside the channel 2 are presented. Formation of the detonation is here similar to that in the previous case, only the speed and intensity of the wave are higher. The passage to the area of increased cross-section and diffuse reflection of molecules from walls causes appreciable decrease of temperature. The detonation wave, however, quickly regains its character, only its speed and intensity are lower than before. Farther downstream, it smoothly passes to the part of channel of constant cross section, where its intensity decreases under the influence of friction and cooling at the walls. The passage to the second area of increased cross-section causes next, sharp decrease of temperature. Farther downstream, the heat exchange and friction at the walls extinguish the flame and damp the detonation, so that only very weak shock passes to the last part of the channel.

Figure 7, for the medium containing 24% of "energetic" molecules, is similar to the previous one, up to the second increase of cross section. The detonation wave is here only slightly stronger and faster than before. However, behind the second

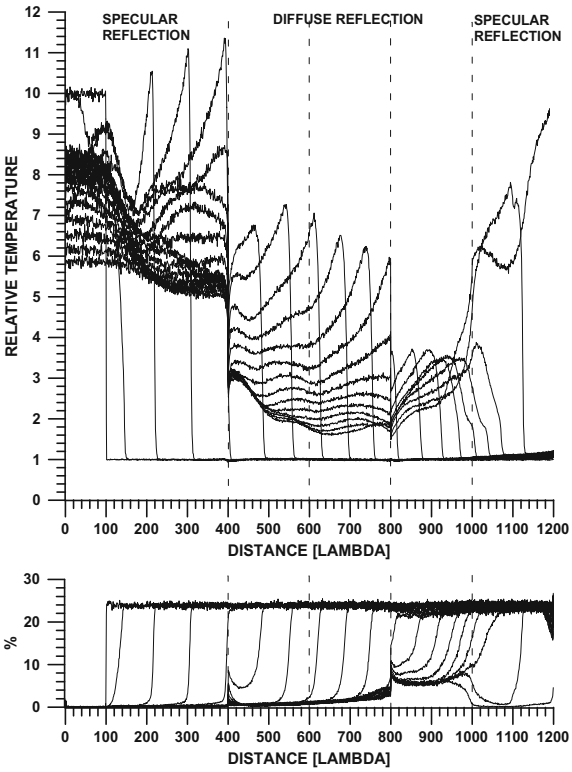

Fig. 7 Detonation in channel 2, in the medium containing 24% of "energetic" molecules. See Fig. 3 for explanation

increase of cross section, it remains sufficiently strong to regain its initial intensity in the last part of the channel, in the absence of friction and cooling .

Figure 8 shows the case of the medium containing 25% of "energetic" molecules. Here the detonation wave, slightly stronger than that shown in Fig. 7, retains its character all the time and in the last part of the channel (without friction and heat exchange at the walls), it quickly regains its initial intensity.

From the results presented above, it may be concluded that channel 2 is capable of extinguishing detonation in the medium containing no more than 23% of "energetic" molecules.

3.3 Channel 3

In Fig. 9, the diagrams for the medium containing 25% of "energetic" molecules inside the channel 3 are presented. Formation of the detonation is here similar to that in the previous case, only the speed and intensity of the wave are higher. The passage to the area of increased cross section and diffuse reflection of molecules

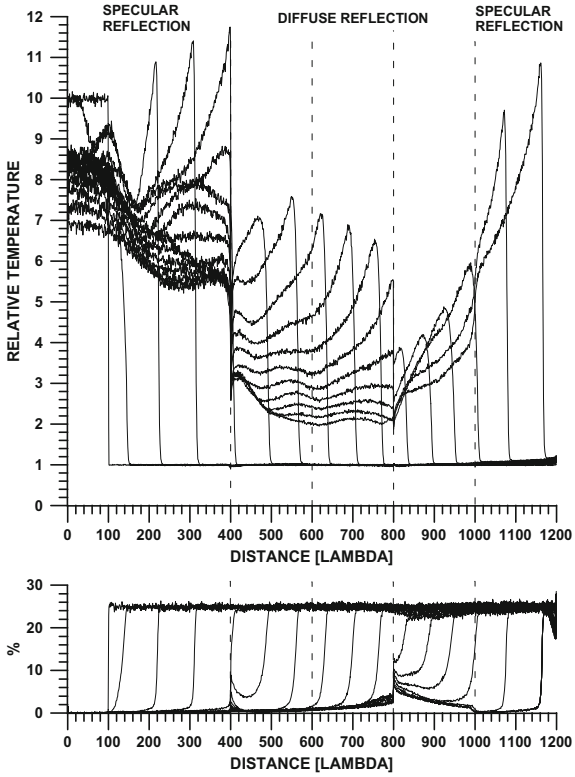

Fig. 8 Detonation in channel 2, in the medium containing 25% of "energetic" molecules. See Fig. 3 for explanation

from walls causes appreciable decrease of temperature. The detonation then quickly regains its character, only its speed and intensity are lower than before. The passage into the next, narrower part of the channel causes slight but distinct decrease of the intensity of the detonation wave, as well as the temperature of the gas behind it, which is rather unexpected.

The passage to the second area of increased cross section causes next decrease of temperature which, together with heat exchange and friction at the walls, leads to extinguishing the flame and damping the detonation, so that only very weak shock passes to the last, narrow part of the channel.

Figure 10, for the medium containing 26% of "energetic" molecules, is similar to the previous one. All waves are only slightly stronger and faster. It applies, in particular, to the shock emerging at the end of the channel—it is not certain if later it would not transform back into the detonation wave.

Figure 11 shows the case of the medium containing 27% of "energetic" molecules. Here the detonation wave, stronger than that, shown in Fig. 10, retains its character all the time and in the last part of the channel (without friction and heat exchange at the walls), it quickly regains its initial intensity.

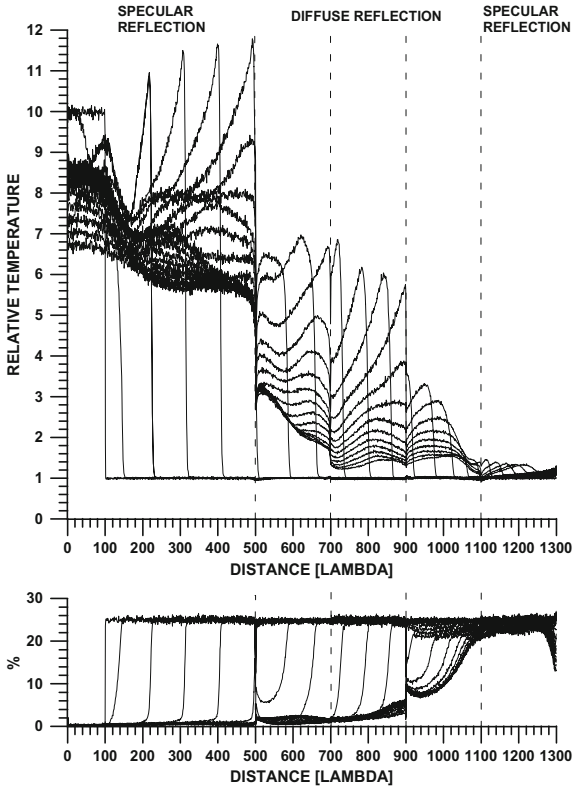

Fig. 9 Detonation in channel 3, in the medium containing 25% of "energetic" molecules. See Fig. 3 for explanation

From the results presented above, it may be concluded that channel 3 is capable of extinguishing detonation in the medium containing no more than 26% of "energetic" molecules.

3.4 Channel 4

The behavior of detonation wave in channel 4 (see Figs. 12, 13 and 14) seems to be very close to the described above for channel 3. They differ only slightly in efficiency: channel 4 is capable of extinguishing detonation in the medium containing no more than 27% of "energetic" molecules (instead of 26% for channel 3). This may be due to the fact that the flow in channel 4, apart from expansions and contractions, makes several turns, which may additionally increase the level of turbulence of the flow and enhance the heat exchange with the walls.

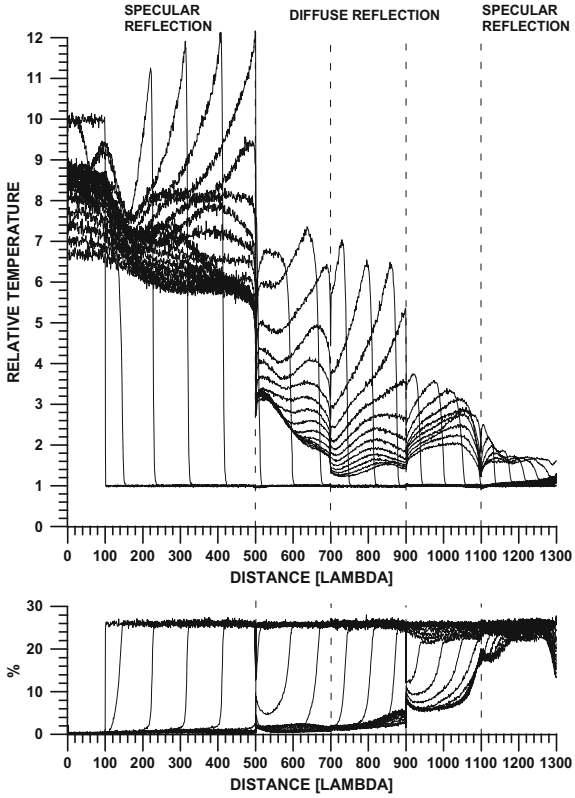

Fig. 10 Detonation in channel 3, in the medium containing 26% of "energetic" molecules. See Fig. 3 for explanation

4 Structure of the Flow

To explain why, unexpectedly, sharp contractions of the channel have positive influence upon the efficiency of extinguishing detonation, the structures of the flow in the three channels with expansion and contraction are presented in the Fig. 15. As can be seen from this figure, behind the sharp contraction, a region of lower temperature connected with flow around the corner appears. Its presence is, most probably, the reason of improving the capability of extinguishing the flame.

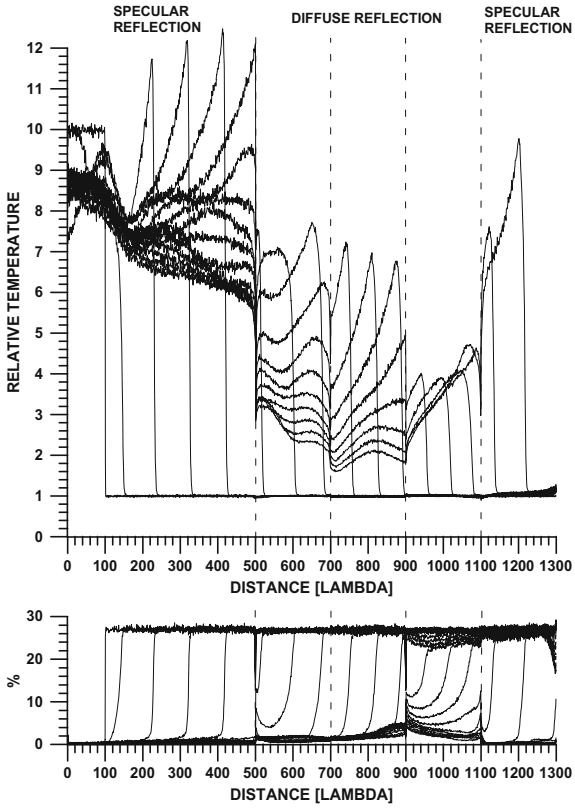

Fig. 11 Detonation in channel 3, in the medium containing 27% of "energetic" molecules. See Fig. 3 for explanation

5 Discussion and Conclusions

The presented simulation results look very promising, as far as increasing efficiency of devices for extinguishing detonation in pipelines is concerned. It may be concluded that:

- presence of sharp increases of the channel cross section significantly improves efficiency of the extinguishing detonation device.
- sharp decreases of cross section seem to have also some positive influence.
- out of considered shapes of channels, the most efficient was channel 4, with increases of cross section, contractions, and sharp turns.

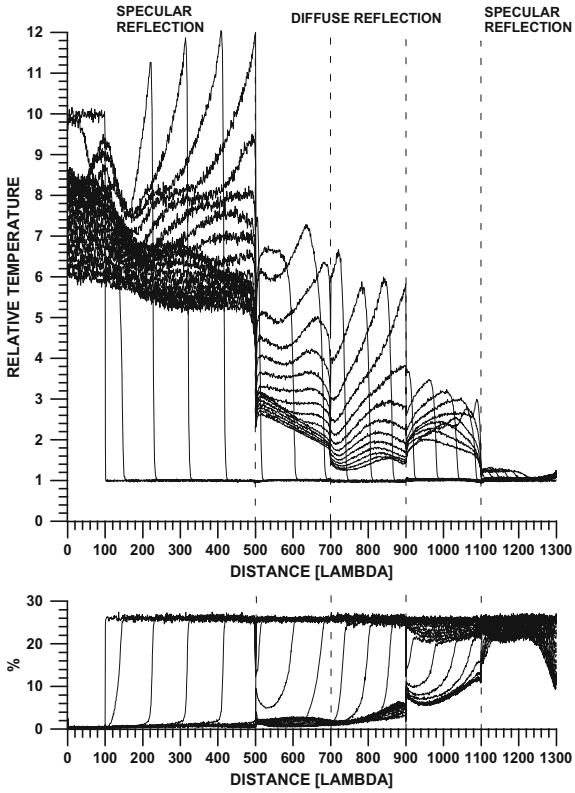

Fig. 12 Detonation in channel 4, in the medium containing 26% of "energetic" molecules. See Fig. 3 for explanation

However, it must be kept in mind that:

- the simulations were performed for a strongly simplified model of the detonating medium.
- the dimensions of the considered channels were very small, which was connected with limited capacity of the available computers. It is not obvious that at larger scale, the results will be equally good.

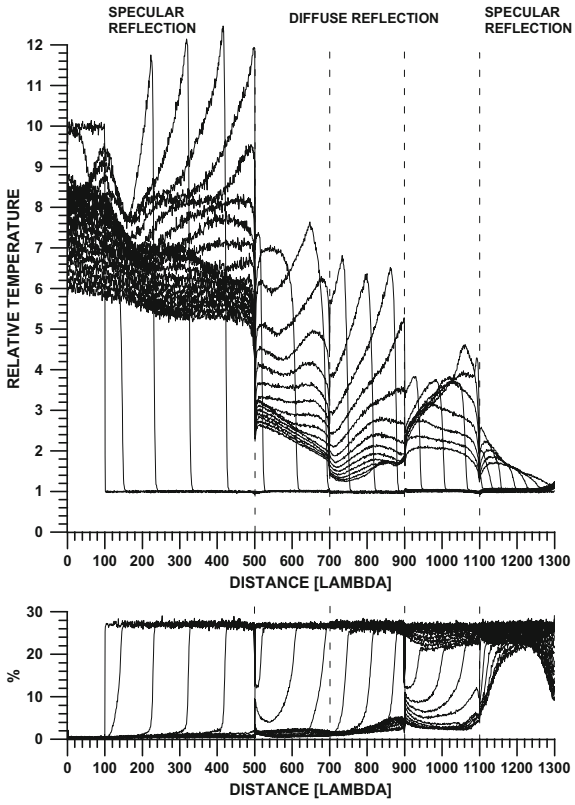

Fig. 13 Detonation in channel 4, in the medium containing 27% of "energetic" molecules. See Fig. 3 for explanation

- the channels of the suggested shapes may create big resistance to the flow. To overcome that, it may be necessary to increase their cross-sections, which would decrease the efficiency of the device so that the net result may not be worthwhile.

At the present stage, it seems necessary to make experiments validating the performed simulations. The work is still in progress and we hope to be able to present the results in the future.

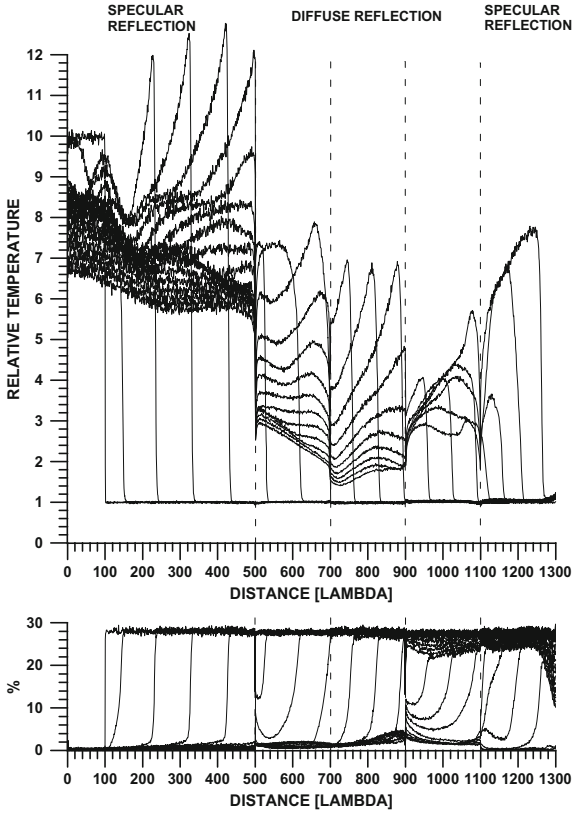

Fig. 14 Detonation in channel 4, in the medium containing 28% of "energetic" molecules. See Fig. 3 for explanation

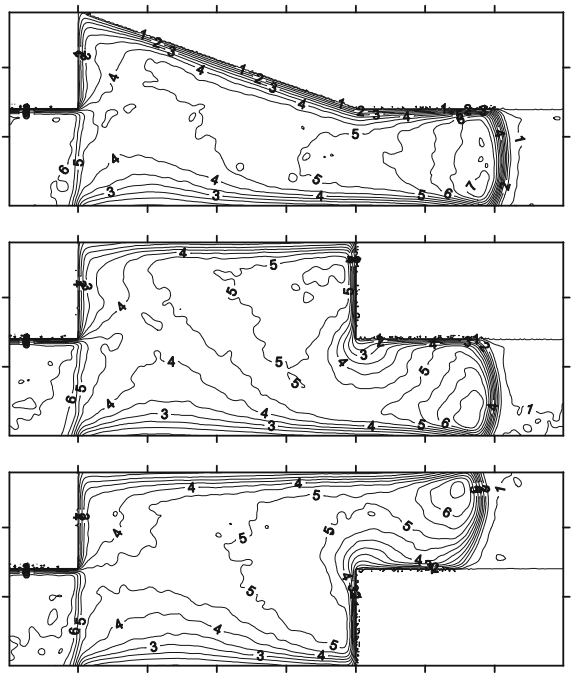

Fig. 15 Maps of temperature distributions behind the detonation wave in expansion and contraction of the channel. Medium contains 25% of "energetic" molecules. Top—channel 2, middle—channel 3, bottom—channel 4. The numbers indicate local values of temperature, related to temperature in front of the detonation wave

References

1. Bird, G.A.: Molecular gas dynamics and the direct simulation of gas flows. Clarendon Press, Oxford (1994)
2. Cai, P., Hoshi, S., Obara, T., Ohyagi, S., Yoshihashi, T.: Diffraction and re-initiation of detonations behind a backward-facing step. Shock Waves **12**, 221–226 (2002)
3. Dremin A.N.: Toward detonation theory. Springer (1999)
4. Larsen P.S., Borgnakke C.: Becker, M., Fiebig, M. (eds.) Rarefied Gas Dynamics, 1, Paper A7. DFVLR Press, Porz–Wahn, Germany (1974)
5. Maxwell J.C.: Niven, W.D. (ed.) The scientific papers of James Clerk Maxwell, vol. 2, p. 706. New York, Dover (1952)
6. Teodorczyk, A., Lee, J.H.S., Knystautas, R.: Propagation mechanism of quasi-detonations. Proc. Combust. Inst. **22**, 1723–1731 (1988)
7. Walenta, Z.A., Teodorczyk, A., Dabkowski, A., Witkowski, W.: Direct Monte-Carlo simulation of a detonation wave in a narrow channel, containing flammable gas. Central Eur. J. Energ. Mat. **1**(1), 49–59 (2004)
8. Walenta, Z.A., Lener, K.: Direct Monte-Carlo simulation of developing detonation in gas. Shock Waves **18**, 71–75 (2008)
9. Yanitskiy, V.E., Belotserkovskiy, O.M.: The statistical method of particles in cells for the solution of problems of the dynamics of a rarefied gas. Part I, Zh. Vychisl. Mat. Mat. Fiz. **15**, 1195–1208; Part II. Zh. Vychisl. Mat. Mat. Fiz. **15**, 1553–1567 (1975)

Triple-Shock Configurations, Vortices, and Instabilities Resulting from the Interaction of Energy Release with a Shock Layer in Gaseous Media

O. A. Azarova and L. G. Gvozdeva

Abstract Triple-shock configurations and vortex structures are researched in problems of control of a high-speed flow past an aerodynamic body "plate-cylinder" at freestream Mach number $M = 4$. The effect of an energy source dislocated in the incoming flow ahead of a bow shock is evaluated for the gaseous media of different physical–chemical properties in a range of the ratio of specific heats γ from 1.1 to 1.4. The energy source is modeled as a heated rarefied channel. Changing the angles in triple-shock configuration and the effect of the stagnation pressure decreasing together with the front drag force reduction is studied depending on γ and rarefaction factor in the energy source. Generation of the Richtmyer–Meshkov instability accompanied the forming of the triple configuration is modeled for $M = 8$. Complex conservative difference schemes are used in the simulations.

1 Introduction

Triple-shock configurations together with vortex structures constitute the basic elements of supersonic aerodynamics both the external and internal ones. These configurations define the distribution of the dynamics and heat stresses on flight vehicles, thrust and efficiency of rocket engines. Investigations of such types of structures appear as a fundamental problem in supersonic aerodynamics. In aerospace high-velocity engineering, it is necessary to consider physical–chemical reactions which are taken place behind the shock waves fronts and lead to the decreasing of the ratio of the specific heats γ there.

O. A. Azarova
A. A. Dorodnicyn Computing Centre of Federal Research Center "Computer Sciences, and Control" RAS, Vavilova Str. 40, 119333 Moscow, Russia

L. G. Gvozdeva (✉)
Joint Institute for High Temperatures RAS, Izhorskaya Str. 13/2, 125412 Moscow, Russia
e-mail: gvozdevalg@mail.ru

K. Kontis (ed.), *Shock Wave Interactions*,
https://doi.org/10.1007/978-3-319-73180-3_21

The effect of γ on triple configurations in the processes of unsteady reflection has been studied in Bazhenova et al. [1]. Theoretical investigations of the specific heats ratio γ effect on the particular features of shock waves reflection were conducted in Arutyunyan et al. [2]. In Gvozdeva et al. [3], it has been shown that the factor γ effects essentially not only on the dislocation of the shock waves in a triple configuration but on the share layers generating in the unsteady triple configurations. Essential effect of the specific heats ratio γ on triple-shock wave structures in a steady flow has been shown in Gvozdeva and Gavrenkov [4].

The triple configurations accompanied by the vortices generation have been obtained in problems of flow control via external energy supply (e.g., see Georgievsky and Levin [5], Azarova [6], Azarova et al. [7]). Supersonic flows with the Mach number of the incoming flow M in the range 1.89–3 and $\gamma = 1.4$ have been considered. Extensive reviews on the problems of flow control via external energy supply are presented in Knight [8, 9] and Russell et al. [10].

The research of the effect of physical–chemical transformations in a wide range of the values of γ on the dynamics of unsteady triple-shock configurations and vortex structures arising in the problems of supersonic streamlining with external energy sources in gaseous media is the objective of this chapter. The approach has been suggested in Azarova and Gvozdeva [11] where together with the angles of triple configurations the stagnation pressure and frontal drag force were studied for different γ.

In this chapter, the connection of the dynamics of triple-shock configurations with the defining flow parameters has been considered for $M = 4$, γ from 1.1 to 1.4 and different energy source characteristics. For $M = 8$ and $\gamma = 1.3$, the generation of the Richtmyer–Meshkov instability has been modeled. The obtained results may be useful for the developing the techniques of supersonic flow control via microwave and laser energy deposition.

2 Statement of Problem and Methodology

The modeling is based on the Euler equations for an ideal gas with the constant ratio of specific heats γ in the range from 1.1 to 1.4:

$$\frac{\partial \mathrm{U}}{\partial t} + \frac{\partial \mathrm{F}}{\partial x} + \frac{\partial \mathrm{G}}{\partial y} = \mathrm{H}, \tag{1}$$

$$\mathrm{U} = \begin{pmatrix} \rho \\ \rho u \\ \rho v \\ E \end{pmatrix}, \ \mathrm{F} = \begin{pmatrix} \rho u \\ p + \rho u^2 \\ \rho uv \\ u(E+p) \end{pmatrix}, \ \mathrm{G} = \begin{pmatrix} \rho v \\ \rho uv \\ p + \rho v^2 \\ v(E+p) \end{pmatrix}, \ \mathrm{H} = \begin{pmatrix} 0 \\ 0 \\ 0 \\ 0 \end{pmatrix}.$$

Here ρ, p—density and pressure of the gas, u and v are x- and y- components of the gas velocity, $\varepsilon = p/\rho(\gamma\text{-}1)$, $E_S = \rho(\varepsilon + 0.5(u^2 + v^2))$ is the total energy per unit

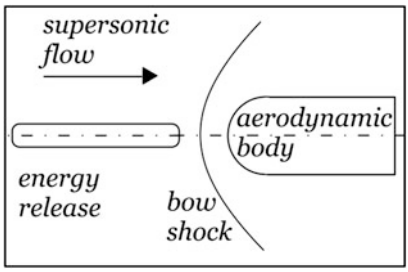

Fig. 1 Flow configuration (schematic)

volume, ε is the specific internal energy. The schematic of the statement of the problem of supersonic flow control using an external energy source is presented in Fig. 1. Initial condition for the problem is a converged supersonic steady flow streamlining an aerodynamic body "a plate blunted by a cylinder". Nondimensional freestream parameters are $\rho_\infty = 1$, $p_\infty = 0.2$, $u_\infty = \mathrm{M}c_\infty$, $v_\infty = 0$ (c_∞ is the undisturbed sound speed). For normalizing parameters for density 1.293 kg/m^3 and pressure 5.06625×10^5 Pa, the dimensional freestream values of density and pressure correspond to those of air under the normal conditions. In Sects. 3.1–3.4 the freestream Mach number M is equal to 4, and in Sect. 3.5 M = 8.

The energy release is supposed to arise instantly ahead of the bow shock wave at a time moment t_i. The energy source is modeled as a heated rarefied homogeneous channel (layer). This model of the energy release was suggested in Artem'ev et al. [12]. Density in this channel is set as $\rho_i = \alpha_\rho \rho_\infty$, i.e., $\alpha_\rho = \rho_i/\rho_\infty$ is a rarefaction factor of the gas in the energy source. Other parameters inside the energy release area are set equal to the parameters of the oncoming flow.

Complex conservative difference schemes of the second approximation order are used in the simulations (see Azarova [13]). The schemes are a subset of the minimum stencil schemes (see Grudnitsky and Prohorchuk [14] and Belotserkovsky et al. [15]) with enlarged conservation properties which are based on the divergence forms for the systems of differential consequences for space derivatives (see Azarova [19]). The staggered Cartesian difference grids with the equal space steps, $h_x = h_y$, and 1000 nodes per the body's diameter are used.

3 Results

3.1 Generation of a Triple Configuration

It has been stated that the triple configuration accompanied by the vortex structure was generated at the beginning stage of the process of the energy release—shock layer interaction (Fig. 2). The very beginning of the generation of the triple configuration is shown in Fig. 3. It can be seen that in the process of forming triple configuration the second triple point is originating on the bow shock (Fig. 3a). This

situation resembles the arising of the second triple point on the Mach wave in a problem of unsteady reflection of a shock wave of the wedge surface. The appearance of this point was obtained experimentally in Semenov et al. [16] and explained physically in Bazhenova et al. [17]. Numerically the effect of arising the second triple point on the Mach wave was found in Gvozdeva et al. [18].

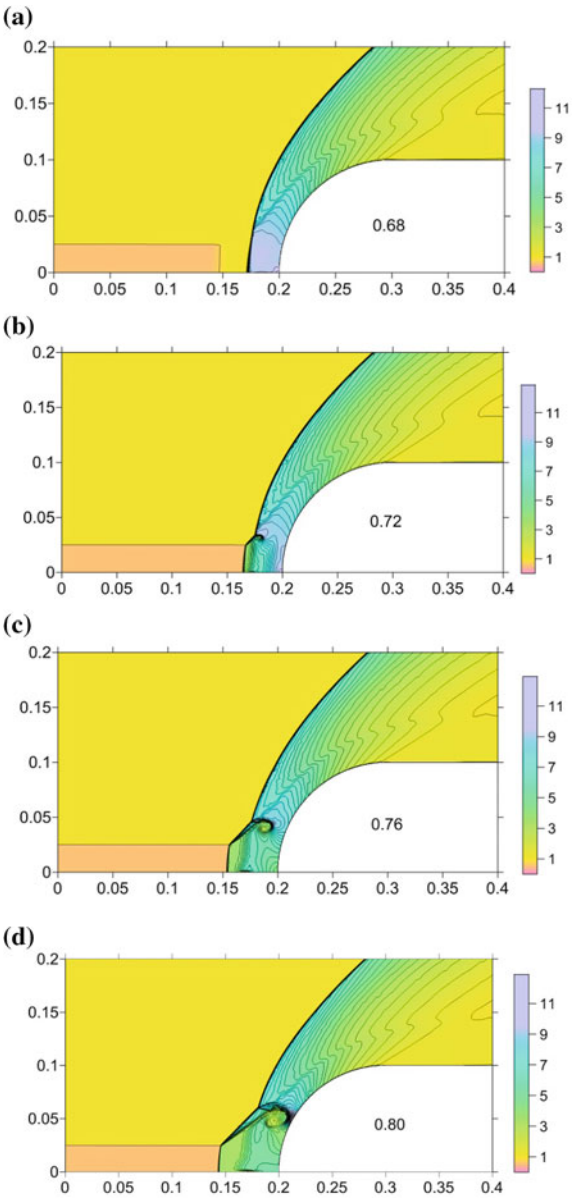

Fig. 2 Dynamics of the triple-shock configuration initiated by energy release—shock layer interaction, fields of density: M = 4, $\gamma = 1.1$, $\alpha_\rho = 0.5$, $t_i = 0.601$; **a** nondimensional time $t = 0.68$, **b** $t = 0.72$, **c** $t = 0.76$, **d** $t = 0.8$

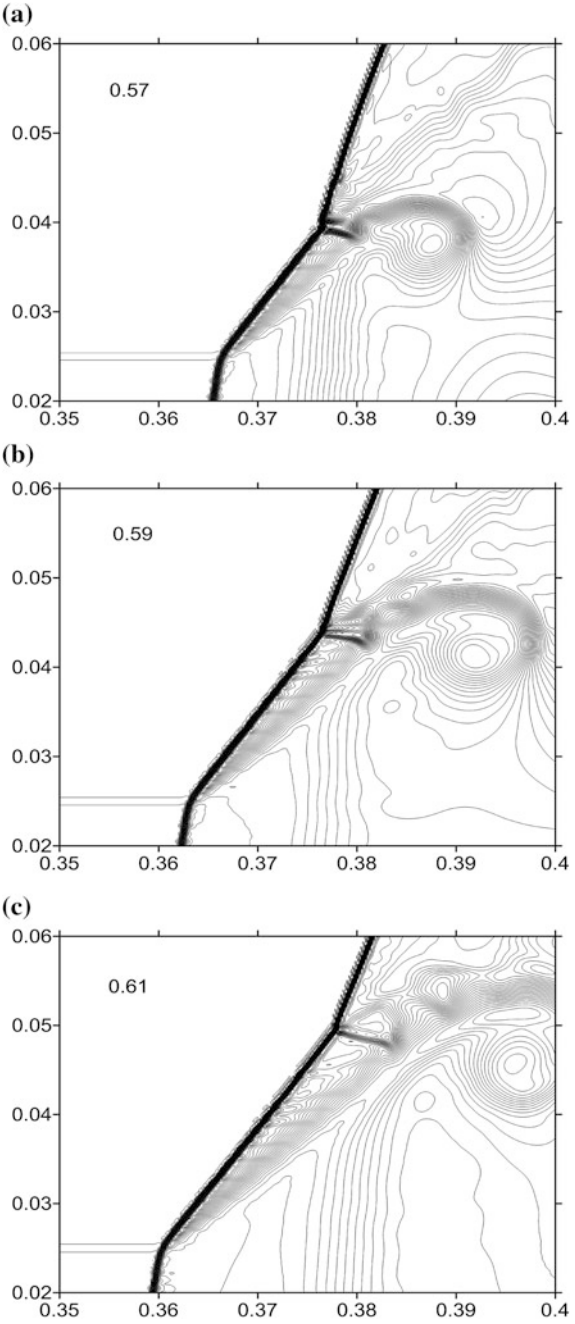

Fig. 3 Dynamics of the very beginning of generation of a triple configuration, fields of density: M = 4, $\gamma = 1.1$, $\alpha_\rho = 0.65$, $t_i = 0.501$; **a** nondimensional time $t = 0.57$, **b** $t = 0.59$, **c** $t = 0.61$

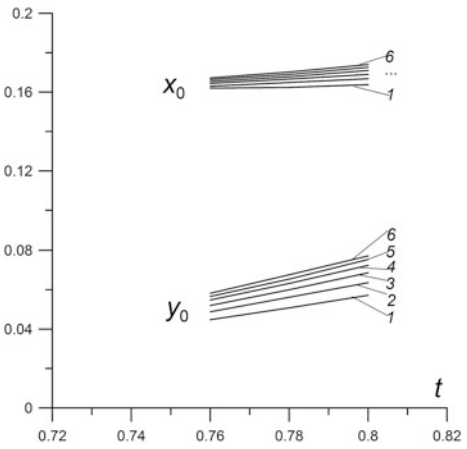

Fig. 4 Dynamics of the coordinates of the centers of triple configurations, M = 4, $\gamma = 1.2$: *curve 1*—$\alpha_\rho = 0.59$, *curve 2*—$\alpha_\rho = 0.50$, *curve 3*—$\alpha_\rho = 0.41$, *curve 4*—$\alpha_\rho = 0.33$, *curve 5*—$\alpha_\rho = 0.25$, *curve 6*—$\alpha_\rho = 0.18$

From some time moment the type of the developing of the triple configuration is close to a self-similar one, i.e., the angles in it are changing negligibly (Fig. 2c, d). Actually, in Fig. 4 the dynamics of the coordinates of centers of triple configurations are presented for different α_ρ which are seen to be the straight lines. Thus, Fig. 4 confirms the self-similar character of the considered processes. It allows us to study the angles forming the triple configuration using the three shock theory.

3.2 *Analysis of Triple Configurations for Different γ*

The scheme of the flow in the area of the triple configuration applying to the three shock theory and the researched angles can be seen in Fig. 5. The triple configurations for different γ are presented in Fig. 6.

Let us study the angles with the direction of the oncoming flow of the elements of the triple configuration: ω_1—the angle of the incident shock wave (1), ω_2—the angle of the reflected shock wave (2), ω_3—the angle of the Mach wave (3) and ω_4—the angle of the contact discontinuity (shear layer) (4) (see Fig. 5). Indeed, the angle ω_4 is the angle of the flow deflection by the Mach shock in the stationary system of coordinates connected with the center of the triple configuration (defined as θ_3 in Gvozdeva and Gavrenkov [4]).

Dependences of these angles on γ for $\alpha_\rho = 0.5$ have been obtained earlier in Azarova, Gvozdeva [11] (Fig. 7). The angles were estimated via the coordinates on the shock fronts. These fronts are not precisely straight lines, so the coordinates have been chosen in the areas in which the fronts were the closest to the linear ones.

One can see that the angle formed by the reflected shock ω_2 is changing significantly with γ decreasing from 1.4 to 1.1 (by 51.8%), the angle of the Mach wave ω_3 is changing not so strongly (by 11.5%) and the angles ω_1 and ω_4 are practically

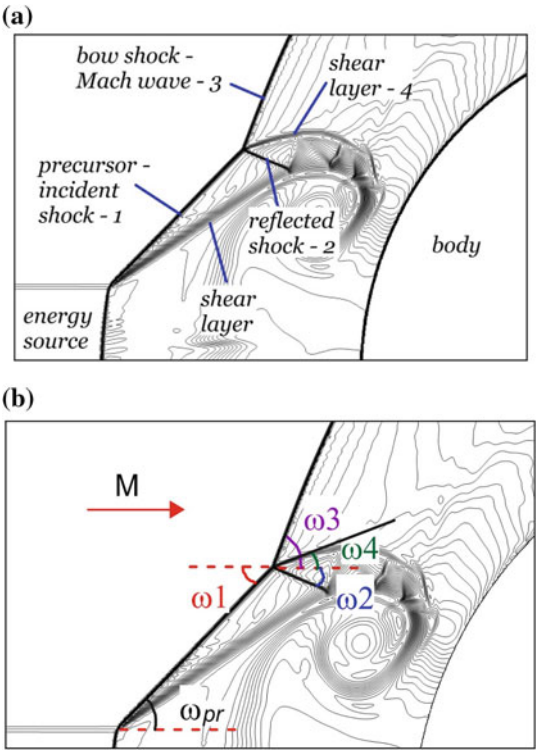

Fig. 5 Scheme of the triple-shock configuration (**a**); considered angles (**b**)

independent of γ. In Table 1, the values of these angles are collected for γ decreasing from 1.4 to 1.1.

It is established that the angle ω_1 is quite well approximated (about 3% for moderate α_ρ) by the relation:

$$\sin^2 \omega_{pr} = \alpha_\rho \tag{2}$$

which was obtained in Artem'ev et al. [12] for the precursor angle ω_{pr} (Fig. 8). So ω_1 increases against α_ρ. In its turn, the calculations have shown that the precursor angle is excellently described by (2) for γ from 1.4 to 1.1 (with the deviation about 0.3–0.4% for moderate α_ρ) and is independent of γ.

The behavior of the other considered angles for α_ρ changing in the interval (0.11; 0.66) for different γ is presented in Figs. 9 and 10. It is obtained that for all γ the angle of the reflected shock ω_2 has the local minimum in the interval $0.11 < \alpha_\rho < 0.66$, the angle of the Mach shock ω_3 decreases slightly against α_ρ and the angle of the contact discontinuity ω_4 increases against α_ρ. At the same time ω_2 decreases with decreasing γ, ω_3 slightly increases with decreasing γ and the dependence on γ is not shown in the behavior of ω_4.

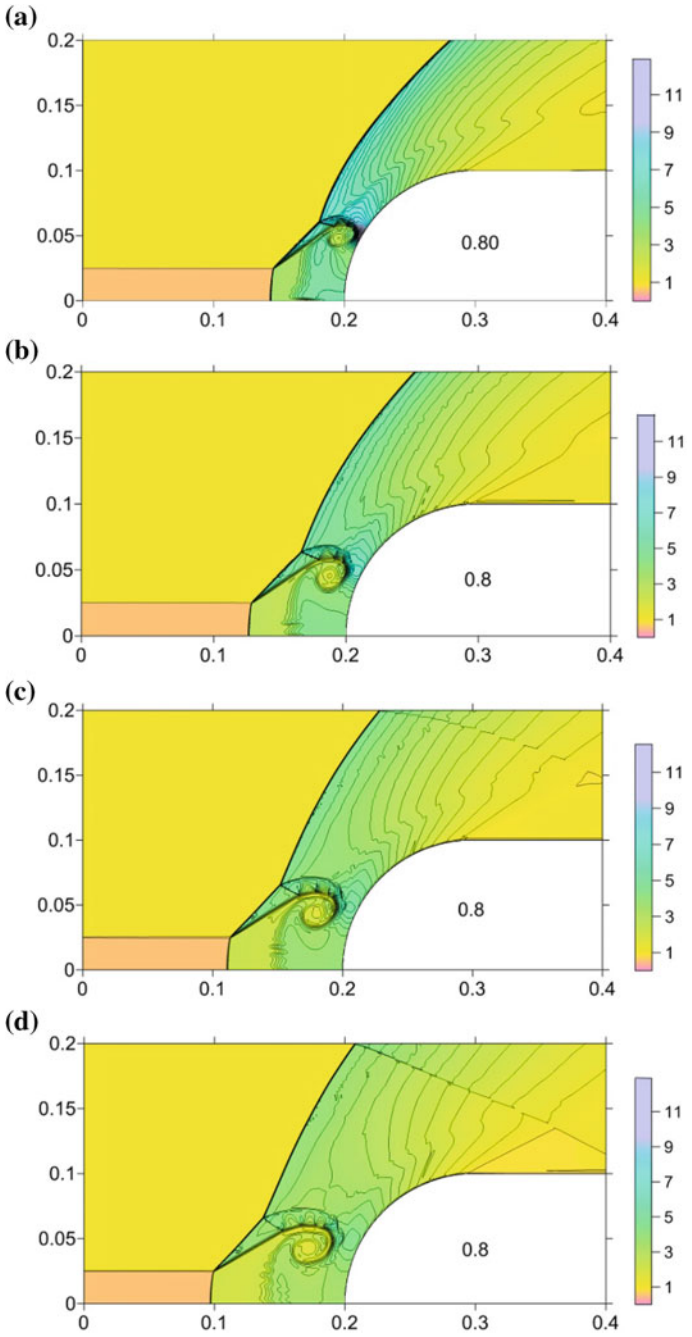

Fig. 6 Triple-shock configurations for different γ, fields of density, M = 4, t = 0.8, $\alpha_\rho = 0.5$, $t_i = 0.601$: **a** γ = 1.1, **b** γ = 1.2 (Azarova and Gvozdeva [11]), **c** γ = 1.3, **d** γ = 1.4

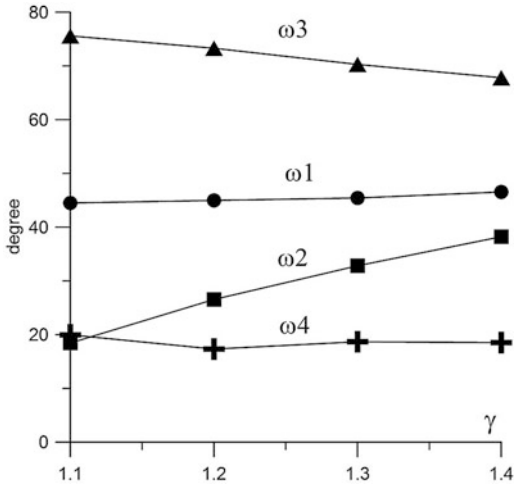

Fig. 7 Dependences of the angles in triple configurations on γ, M = 4, $\alpha_\rho = 0.5$ from Azarova and Gvozdeva [11]

Table 1 Analysis of changing the angles in the triple-shock configurations for γ decreasing from 1.4 to 1.1

Angle	Related changing: abs[(ω(1.4)- $\omega_{min}(\gamma)$)/ω(1.4)] (%)	Character of changing with decreasing γ
ω_1	4.5	practically independent of γ
ω_2	51.8	decreases
ω_3	11.5	increases
ω_4	6.8	practically independent of γ

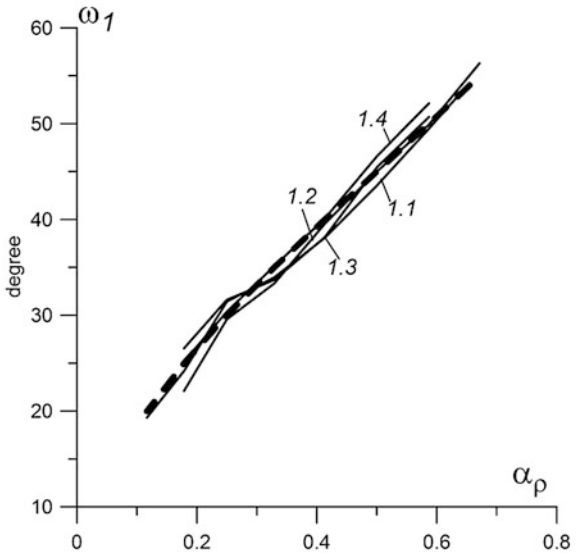

Fig. 8 Dependence of the angle ω_1 (solid lines) and ω_{pr} (dashed line) on α_ρ for different γ, M = 4

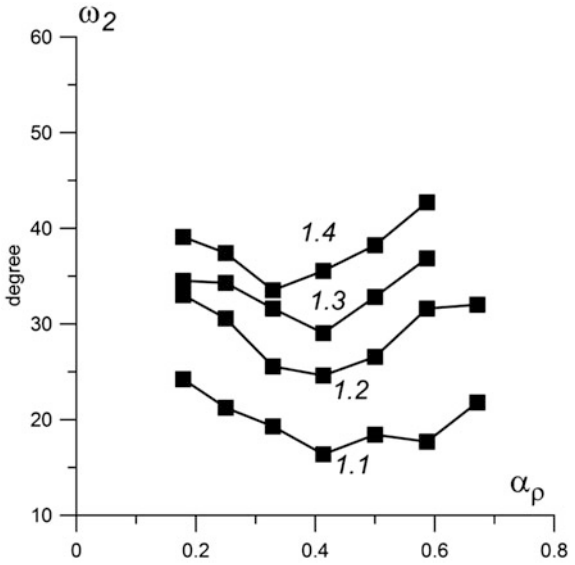

Fig. 9 Dependence of the angle ω_2 on α_ρ for different γ, M = 4

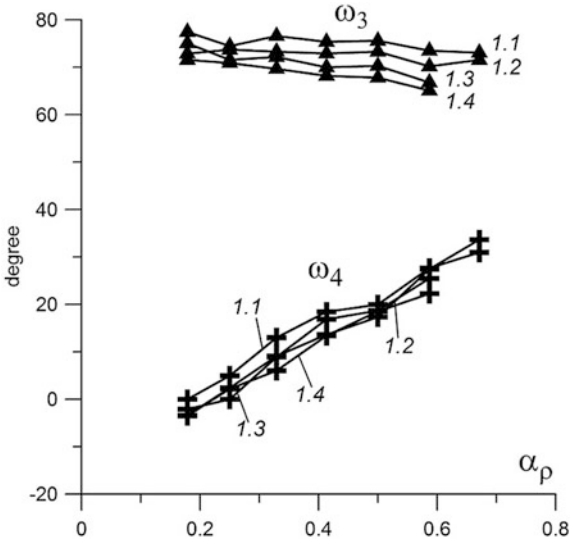

Fig. 10 Dependences of the angles ω_3 and ω_4 on α_ρ for different γ, M = 4

3.3 Accuracy of the Angles Calculations

The scheme accuracy of the shock fronts in the calculations constitutes tenth parts of a percent. Basically, a total accuracy of a triple configuration angles evaluation for the flow mode close to the self-similar one is connected with the accuracy of the angles calculations using flow images. We have used the enlarged flow images and

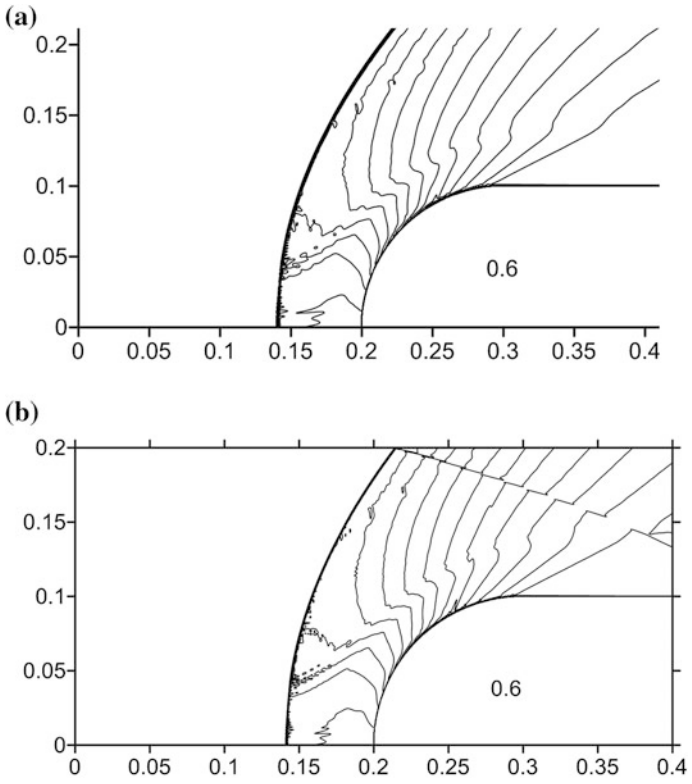

Fig. 11 Steady flow mode for simulations on different calculation areas, M = 4, $\gamma = 1.4$: **a** $0 \le x \le 0.5$, $0 \le y \le 0.5$, $h_x = h_y = 0.0002$ (framed); **b** $0 \le x \le 0.2$, $0 \le y \le 0.4$, $h_x = h_y = 0.0001$

have calculated the angles throw the coordinates of the centers of the triple configurations and the points on the shock fronts in the neighborhood of the center (via the facilities of a graphical editor). The precision is 1–2° for moderate α_ρ and 3–4° for small α_ρ.

It should be noted that the boundary conditions can affect the details of forming a triple configuration (see Kemm [20]). To evaluate this influence the additional simulations have been made on the enlarged calculation area: $0 \le x \le 0.5$, $0 \le y \le 0.5$ (Fig. 11). It can be seen that the fields of the parameters are quite the same for these two calculations. Besides, it was obtained that the maximal difference in the values of the angles is 3–4° (the difference is maximal for the reflected shocks). For example, for $\alpha_\rho = 0.5$ and $\gamma = 1.4$ the difference in the calculations of the angles was 0.9° for ω_1, 3.4° for ω_2, 1° for ω_3 and 2.7° for ω_4.

3.4 Analysis of Stagnation Pressure and Front Drag Force for Different γ

The dynamics of the stagnation pressure p_t and the front drag force F have been studied in this section (see Fig. 12, subscript "0" is referred to the values of the parameters in the absence of the energy source). The first minimum in the curves is caused by a rarefaction wave reflection which is generated at the very beginning of the interaction process (see Georgievsky and Levin [21]). In Azarova and Knight [22] it has been shown that the next fall down is connected with the action of the vortex structure on the body's boundary. The drag reduction initiated by a vortex has been obtained numerically in Kolesnichenko et al. [23].

It is seen that the pressure fall down (together with the drag force) at the first stage is greater for smaller γ, but the stagnation pressure fall down has no effect on the decreasing of the drag force. On the contrary, the vortex action at the next stage is significantly large for smaller γ and caused the essential drag force reduction. That is, in the case of smaller γ a new qualitative behavior of the drag force is taken place. Analysis of the stagnation pressure and frontal drag force for γ varying from 1.4 to 1.1 is presented in Table 2.

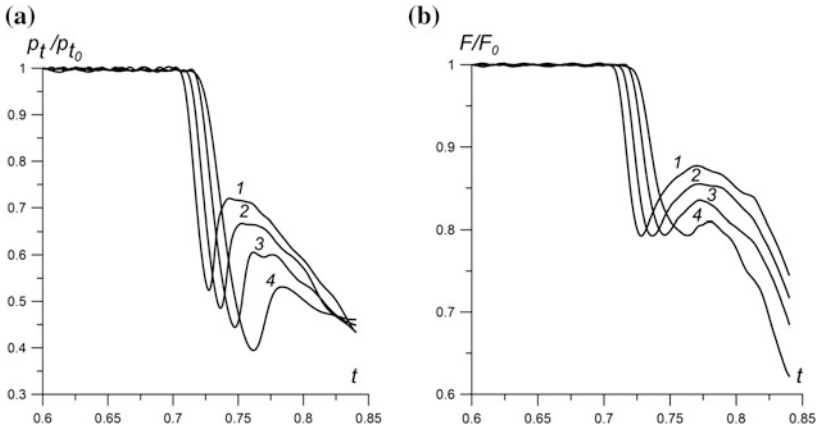

Fig. 12 Dynamics of the related stagnation pressure (left) and front drag force (right) for different γ, M = 4, $\alpha_\rho = 0.5$: *curve 1*—γ = 1.4, *curve 2*—γ = 1.3, *curve 3*—γ = 1.2, *curve 4*—γ = 1.1 (Azarova and Gvozdeva [11])

Table 2 Analysis of change of stagnation pressure and frontal drag force with decreasing γ from 1.4 to 1.1

f (γ)	Related change of f: $[f\ (1.4) - f\ (1.1)]/f\ (1.4)$ (%)	Character of changing f (γ) with decreasing γ
min (p_t/p_{t0})	24.7	decreases
min (F/F_0)	16.5	decreases

3.5 Generation of the Richtmyer–Meshkov Instability in the Case of M = 8

Earlier in Azarova [24], it has been shown that the interaction of a heated channel with a bow shock can give a rise to the Richtmyer–Meshkov instability. Another mechanism of this instability generation is described in this section. Generation of the considered triple-shock configuration is accompanied by forming the vortex structure which includes two contact discontinuities (shear layers) (Fig. 5a). For $M = 8$ and $\gamma = 1.3$ between these contact discontinuities, there arises a flow structure consisting of the rarefaction waves which reflect as the compression waves. This flow structure is similar to that which generates in the shock–shock interaction of "Edney IV" type (see Edney [25]), where the bow shock interacts with the impinging oblique shock. The schematic of the Edney IV shock–shock interaction and a wide review of this subject is presented in Adelgren et al. [26].

The vortex-contact structure obtained here differs from that described earlier by the fact that it is forming as the result of the interaction of the bow shock with two contact discontinuities, which are the boundaries of the heated channel. In the arising vortex-contact structure, the compression waves between shear layers become stronger with increasing freestream Mach number and decreasing γ.

At some time moment, an intersection of the characteristics is taken place causing the "overturn" of the pressure profile in a compression wave and generation of a secondary shock wave. This shock wave interacts with the contact discontinuity which is dislocated under an angle to the shock front being a reason for the Richtmyer–Meshkov instability generation (see Hawley and Zabusky [27]).

This situation has been modeled in the problem of the plane shock wave interacting with the boundary of the heated channel with $\alpha_\rho = 0.5$ (Fig. 13). One can see the primary vortex generated by the Richtmyer–Meshkov instability (the upper vortex initiated by this instability is suppressed by the high-speed flow) and accompanied by the secondary vortices originated due to the Kelvin–Helmholtz instabilities. Thus, it can be concluded that the generation of the Richtmyer–Meshkov instabilities is typical in such type of problems.

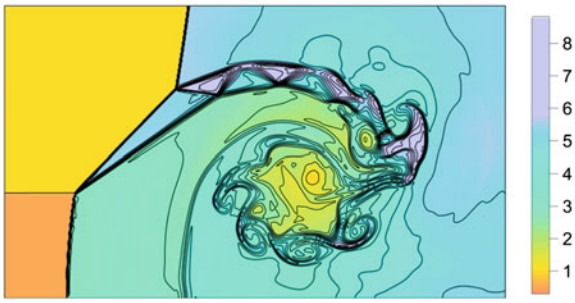

Fig. 13 Generation of Richtmyer–Meshkov instability, density, $M = 8$, $\gamma = 1.3$, $\alpha_\rho = 0.5$

4 Conclusions

Unsteady Mach triple-shock configurations have been studied at the first stage of the process of interaction of an energy source with a shock layer in the flow mode close to the self-similar one. For freestream Mach number 4, the dependences of the angles of the triple configurations on the ratio of the specific heats γ changing from 1.4 to 1.1 have been studied.

It has been established that with decreasing γ from 1.4 to 1.1 the angle between the reflected shock and the flow direction decreases (by 51.8% for $\alpha_\rho = 0.5$), the angle of the Mach shock increases (by 11.5% for $\alpha_\rho = 0.5$), and the angles of the incident shock and of the contact discontinuity are practically independent of γ.

The dependences of the angles of the triple configurations on the rarefaction factor in the energy source α_ρ, $0.11 < \alpha_\rho < 0.66$, for γ from 1.4 to 1.1 have been obtained. It has been shown that for all considered γ, the angles of the incident shock and of the contact discontinuity increase against α_ρ, the angles of the reflected shock have local minima in the interval $0.11 < \alpha_\rho < 0.66$ and the angles of the Mach shock decrease slightly against α_ρ.

It has been shown also that with decreasing γ the stagnation pressure fall down caused by the effect of the energy release in the external flow increases by 24.7% and the frontal drag force reduction increases by 16.5% (for $\alpha_\rho = 0.5$), the latter effect is due to the vortex structure action.

Generation of the Richtmyer–Meshkov instability accompanying the triple-shock configuration has been modeled in the case of $M = 8$. It has been shown that the generation of the Richtmyer–Meshkov instabilities is expected in such types of problems.

Acknowledgements The research is partially supported by RFBR under the Project No. 16-08-01228.

References

1. Bazhenova, T.V., Gvozdeva, L.G., Nettleton, M.A.: Unsteady interactions of shock waves. Prog. Aerosp. Sci. **21**, 249–331 (1984)
2. Arutyunyan, G.M., Belokon, V.A., Karchevsky, L.V.: On adiabatic index effect on reflection of shock waves. J. Appl. Mech. Tech. Phys. (1), 62–66 (1970) (in Russian)
3. Gvozdeva, L.G., Gavrenkov, S.A., Nesterov, A.A.: Study of slipstreams in triple-shock wave configuration. Shock Waves **25**(3), 283–291 (2015)
4. Gvozdeva, L.G., Gavrenkov, S.A.: New configuration of irregular reflection of shock waves. In: Knight, D., Lipatov, I., Reijasse, Ph. (eds.) Progress in Flight Physics, vol. 7, pp. 437–452. Torus Press (2015)
5. Georgievsky, P.Y., Levin, V.A.: Front separation flows for blunt and streamlined bodies supported by localized upstream energy deposition. In: 2nd European Conferences of Aerospace Sciences (EUCASS, July 1–6, Brussels), pp. 1–8 (2007)
6. Azarova, O.A.: Simulation of stochastic pulsating flows with instabilities using minimum-stencil difference schemes. J. Comp. Math. Math. Phys. **49**(8), 1397–1414 (2009)

7. Azarova, O.A., Knight, D.D., Kolesnichenko, Y.F.: Pulsating stochastic flows accompanying microwave filament/ supersonic shock layer interaction. Shock Waves **21**(5), 439–450 (2011)
8. Knight, D.: Survey of aerodynamic drag reduction at high speed by energy deposition. J. Propul. Power **24**, 1153–1167 (2008)
9. Knight D.: A short review of microwave and laser discharges for supersonic flow control. J. AerospaceLab (10), 1–12 (2015)
10. Russell, A., Zare-Behtash, H., Kontis, K.: Joule heating flow control methods for high-speed flows. J. Electrost. (4), 1–90 (2016)
11. Azarova, O.A., Gvozdeva, L.G.: Unsteady triple configurations and vortex-contact structures initiated by interaction of an energy source with a shock layer in gases. Tech. Phys. Lett. **42** (8), 799–803 (2016)
12. Artem'ev, V.I., Bergel'son, V.I., Nemchinov, I.V., Orlova, T.I., Smirnov, V.A., Hazins, V. M.: Changing the regime of supersonic streamlining obstacle via arising the thin channel of low density. Fluid Dyn. (5), 146–151 (1989) (in Russian)
13. Azarova, O.A.: Complex conservative difference schemes for computing supersonic flows past simple aerodynamic forms. J. Comp. Math. Math. Phys. **55**(12), 2025–2049 (2015)
14. Grudnitsky, V.G., Prohorchuk, Y.A.: An approach of construction of difference schemes with arbitrary order of approximation of differential equations in partial derivatives. Reports of RAS **234**(6), 1249–1252 (1977) (in Russian)
15. Belotserkovsky, O.M., Grudnitsky, V.G., Prohorchuk, Y.A.: Difference scheme of the second order accuracy on a minimal stencil for hyperbolic equations. J. Comp. Math. Math. Phys. **23** (1), 119–126 (1983) (in Russian)
16. Semenov, A.N., Syschikova, M.P., Berezkina, M.K.: Experimental study of the specific features of the Mach reflection in a shock tube. J. Tech. Phys. **15**(5), 795–803 (1970) (in Russian)
17. Bazhenova, T.V., Gvozdeva, L.G., Lagutov, Y.P., Lyakhov, V.N., Poresov, Y.M., Fokeev, V. P.: Unstedy Interaction of Shock and Detonation Waves in Gases, 208 p. Nauka, Moscow (1986) (in Russian)
18. Gvozdeva, L.G., Borsch V.L., Gavrenkov, S.A.: Analytical and numerical study of three shock configurations with negative reflection angle. In: Kontis, K. (ed) 28th International Symposium on Shock Waves, vol. 2, pp. 587–592. Springer (2012)
19. Azarova, O.A.: Complex conservative difference schemes in modeling of instabilities and contact structures. In: Kontis, K. (ed) 28th International Symposium on Shock Waves, vol. 2, pp. 683–689. Springer (2012)
20. Kemm, F.: On the proper setup of the double mach reflection as a test case for the resolution of gas dynamics codes. Comput. Fluids (4), 1–7 (2014)
21. Georgievsky, P.Y., Levin, V.A.: Unsteady interaction of a sphere with atmospheric temperature inhomogeneity at supersonic speed. Fluid Dyn. **28**(4), 568–574 (1993)
22. Azarova, O.A., Knight, D.D.: Interaction of microwave and laser discharge resulting "heat spots" with supersonic combined cylinder bodies. Aerosp. Sci. Technol. (43), 343–349 (2015)
23. Kolesnichenko, Y.F., Brovkin, V.G., Azarova, O.A., Grudnitsky, V.G., Lashkov, V.A., Mashek, I.C.: Microwave energy release regimes for drag reduction in supersonic flows. Paper AIAA-2002-0353, 1–12 (2002)
24. Azarova, O.A.: Generation of Richtmyer-Meshkov and secondary instabilities during the interaction of an energy release with a cylinder shock layer. Aerosp. Sci. Technol. (42), 376–383 (2015)
25. Edney, B.: Anomalous heat transfer and pressure distributions on blunt bodies at hypersonic speeds in the presence of an impinging shock. Aeronautical Research Institutes of Sweden, FAA Rept. 115, Stockholm (1968)
26. Adelgren, R.G., Yan, H., Elliott, G.S., Knight, D.D., Beutner, T.J., Zheltovodov, A.A.: Control of Edney IV interaction by pulsed laser energy deposition. AIAA J. **43**(2), 256–269 (2005)
27. Hawley, J.P., Zabusky, N.J.: Vortex paradigm for shock-accelerated density-stratified interfaces. Phys. Rev. Lett. No. **63**, 1241–1244 (1989)

Analysis of Planar and Spherical Shock-Wave Mitigation by Wet Aqueous Foams

C. Breda, S. Kerampran, M.-O. Sturtzer, M. Arrigoni and J.-F. Legendre

1 Introduction

In a context where more and more Improvised Explosive Devices (IED) are found on national territories or theaters of external operations, the fight against IEDs has intensified since 2008, aiming, in particular, at designing reliable blast mitigation systems. Aqueous foams were identified in the 1970s as an efficient protective medium against blast and sound effects. They have been widely used because of their ease of application, but the quantification of the physical phenomena leading to mitigation remains unclear. This study proposes to analyze the interaction with foam and either a spherical shock wave (pyrotechnic tests) or a planar shock wave (shock tube experiments), varying both the foam and the wave properties.

Winfield and Hill [1] performed experiments with 0.9 kg TNT charges located in a 3 m^3 volume of dry foam with a density 10 kg m^{-3}. They reached the conclusion that the blast peak overpressure and the positive impulse are reduced, respectively, by 95% and 75%. Similar experiments were performed by Hartman et al. [2] with C4 charges (TNT equivalent ranging from 0.25 to 25 kg) and Domergue et al. [3] with plastrite charges, yielding comparable results. McCallen [4], Hartman [2], and Del Prete [5] established empirical relations for overpressures, impulses, and times of arrival for foam densities ranging from 2 to 40 kg m^{-3} and for scaled distances from the charge from 0.7 to 2 kg $m^{-\frac{1}{3}}$.

Some attempts have been made to propose a theoretical model of blast wave attenuation by diphasic media, and in particular by aqueous foams. For instance, assuming the foam can be considered as an equivalent gas with modified thermodynamical

C. Breda · S. Kerampran (✉) · M. Arrigoni
IRDL, ENSTA Bretagne, Brest, France
e-mail: steven.kerampran@ensta-bretagne.fr

C. Breda · M.-O. Sturtzer · J.-F. Legendre
Institut Franco-allemand de Saint Louis, St. Louis, France

K. Kontis (ed.), *Shock Wave Interactions*,
https://doi.org/10.1007/978-3-319-73180-3_22

properties, and denoting ϵ the liquid fraction, Gelfand [6] expressed the ratio between overpressures P^* in the foam and P in air as a function of heat capacity and density

$$\frac{P^*}{P} = (1 + \gamma\mu\delta)^{-0.5}$$

with

$\delta = \frac{c_{p,l}}{c_{p,g}}$ the ratio of the heat capacity of the phases
$\mu = \frac{\epsilon\rho_l}{(1-\epsilon)\rho_g}$ the mass loading factor.

Studies have not been limited to evaluating the attenuation of the wave. The influence of some parameters has also been taken into consideration, in order to better design the foam confinement. Authors seem to agree on the fact that wet foams ($5\% < \epsilon < 30\%$) are more efficient than dry foams. The importance of the foam density has been experimentally evidenced: it is more efficient to increase the foam density than the foam thickness [7–9]. The available experimental data make it possible to roughly design a confinement. McCallen [4] established some empirical rules (using 100 kg charges in a foam volume of 2500 m^3 with a density of about 40 kg m^{-3}), stating for example that if the aqueous foam is heavier than the explosive charge by a factor ten, the resulting overpressure is divided by two.

Attention has also been paid to the structure of a shock or blast wave propagating in wet aqueous foams. Concerning blast waves, Borisov [10] differentiates two cases, depending on the ratio of the transmitted wave velocity in the foam (D) to the sound velocity of the gas contained in the foam bubbles (a):

- if $D < a$: the transmitted shock in the foam is divided in two successive compression waves:
  - a precursor wave, responsible for the foam liquid films rupture in droplets.
  - a main compression wave, which accounts for most of the overpressure and progressively accelerates the droplets until they reach an equilibrium state defined by a stationary pressure. This wave propagates at a lower velocity than the precursor.
- if $D > a$: the transmitted wave in the foam exhibits a single front, with no precursor.

Britan [8] and Del Prete [5] performed shock tube experiments to analyze the shock structure in a wet aqueous foam and concluded that it is similar to the one observed with blast waves. A double structure is observed, with a bell-shaped overpressure profile linked to a compression zone (from t_p to t_c), preceded by a precursor wave characterized by a sharp rise (from t_a to t_p), as depicted in Fig. 1. This precursor is the signature of the foam fragmentation in smaller droplets and the compression then accelerates droplets into an equilibrium between the gaseous and liquid phases. Britan [11] visualized the atomization phenomena in shock tubes and identified two cases depending on the density of the foam. When the impedance mismatch at the

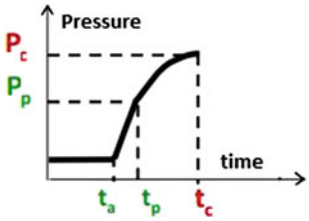

Fig. 1 Characteristic overpressure profile in an aqueous foam

air–foam boundary is close to unity, the precursor pressure (P_p) is close to transmitted pressure in the foam (P_c). But when the impedance mismatch is larger than one, the precursor pressure is noticeably lower than the transmitted pressure.

Because of its peculiar structure, aqueous foam is able to mitigate shock waves through the dissipation of kinetic energy. Indeed, such a medium is characterized by the following properties:

- a high compressibility of the gaseous phase in the bubbles
- a high heat capacity of the liquid phase, which can behave as a thermal sink
- a low sound velocity, relatively to the sound velocity in the gaseous and liquid phases
- a visco-elastic mechanical behavior [12].

During the shock–foam interaction, several physical phenomena can account for the overpressure mitigation:

- dissipation (heat, viscous, acoustic) [13–17]
- dispersion due to the wave reflection on the bubbles [13, 15–19]
- thickening of the shock front [15, 20, 21]
- partial transmission of shock at the foam–air interface [9, 14, 22]
- drainage, which increases the non-homogeneity of the foam in the direction perpendicular to the shock propagation and causes transverse effects leading to an increase of the shock obliquity [11, 22]
- pulsation and resonance of the bubbles [16, 17]
- fragmentation of foam into smaller droplets which absorb energy in the form of heat [5, 10, 12, 15].

The quantification of the relative effects of these phenomena is still unclear. Several authors differentiate two cases as a function of a nondimensional thickness X defined as [7, 8, 23, 24]:

$$X = d\left(\frac{\rho_m}{m_{ch}}\right)^{\frac{1}{3}}$$

with

ρ_m the foam density
m_{ch} the explosive mass TNT equivalent
$d = \frac{(lwh)^{\frac{1}{3}}}{2}$

l, w, h the dimensions of foam confinement.

Close to the charge ($X < 2.5$), the foam is completely destroyed. The liquid fraction and the foam density play dominant roles. The acceleration and heating of the resulting droplets are the consequence of the interaction between the foam and the blast. The single-phase model or the Effective Gas Flow model (EGF) can represent this case. The foam is considered as a gas with an effective adiabatic index that allows to take into account the real water content of the foam [10, 12, 17]. Far from the charge ($X > 2.5$), the foam can sustain the impact. Shattering of the shock wave at the bubbles, viscous dissipation at solid boundaries, bubble pulsation, and thermal conduction are the dominant mechanisms of the foam–blast interaction. It seems intuitively that as the foam becomes drier, the role of the pulsation increases and the viscous dissipation enhances the wave mitigation.

As can be seen, the topic of shock mitigation by aqueous foams has drawn some attention over the past decades. Nonetheless, this phenomenon is still only partially understood and despite some reliable experimental studies, the influence of some of the foam properties is still unclear. This can in part be attributed to insufficient characterization of the foam in the aforementioned studies and to the fact that large-scale studies make it difficult to accurately analyze the phenomenon. The present work has two main goals. We first aim at complementing the existing experimental results, both for blast and shock waves. We also study the so far mostly overlooked influence of the bubble size on the shock mitigation. In this respect, we performed experiments using both explosive charges and shock tubes, focusing on the control and accurate evaluation of the aqueous foam properties.

2 Foam Generation and Characterization

Wet aqueous foams (i.e., with densities larger than 50 kg m^{-3}) were chosen for this study, on the basis of the available experimental results. A bibliographical review indeed showed that previous works were mostly concerned with dry foams, which present a more regular structure than wet foams and can more easily be produced in a reproducible way. Yet, it appears that acoustic waves are better attenuated in wet foams. Besides, wet foams seem to be able to slow down the fragments generated by the detonation of an explosive device more efficiently (the interaction between supersonic projectiles and aqueous foams will be presented in a forthcoming paper).

Several requirements have to be fulfilled by the foam in order to ensure the quality of the results:

- foam production needs to be reproducible enough, i.e., the foam density must not vary by more than 20% from one test to the other,
- the foam must be monodisperse, which implies a polydispersity coefficient lesser than 0.5. This is particularly important since the bubble size is taken as a parameter.

- the foam must be stable in time, with a density that does not vary by more than 10% of its initial value after 30 min.

To generate foam, one needs a foaming liquid (obtained by mixing water and a foaming agent), a gas supply (air in the present case) and a generating device. The bubble size is highly dependent on the generating device. Since we intend to evidence the influence of the bubble diameter on the shock mitigation, we need to use different devices, in order to produce foams with significantly different mean bubble diameters. The foaming agent was selected among a panel of industrial agents designed for fire safety. These products are far from the academic foaming agents usually used, but have better properties with respect to stability. Eight preselected foaming agents were submitted to the Bikermann test, which consists in generating a foam with a sintered diffuser plunged into the foaming liquid and measuring the foam height in a column (indicative of an equilibrium state where foam formation by bubbling compensates the foam collapse). The influence of the dilution with demineralized water was also taken into account. A foaming liquid constituted with Ecopol from Bio-ex diluted with 60% of water was eventually chosen for its ability to produce a wet foam dense and stable enough, as illustrated in Fig. 2, which shows the temporal evolution of foam density for several Ecopol dilutions. The rheological behavior of the chosen foaming liquid was fully characterized. In particular, its apparent viscosity was measured at 100 ± 30 mPa s.

In the scope of this work, a given aqueous foam can be characterized by considering its density, mean bubble diameter, and sound velocity. These parameters were controlled before each test. Density can be evaluated either by weighting a foam sample or by measuring the foam conductivity. Both methods were used. For the

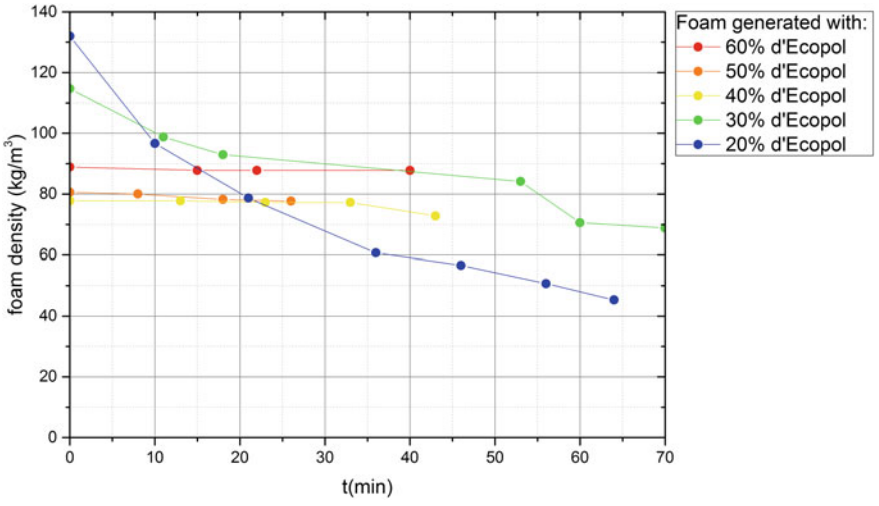

Fig. 2 Temporal evolution of the density of foams generated with different concentrations of foaming liquid

first one, 9.5 L foam samples were weighted with a Kern EMB balance, yielding a maximal incertitude of 20%. An empiric relation links the liquid fraction and the foam electrical resistance [25]. A setup constituted by a conductivity cell (two 8 cm^2 aluminum plates separated by a 4 cm gap) and a RLC Fluke PM6304 bridge (with 0.1% accuracy) was used to access the foam density. Foams are unstable. Three phenomena of foam aging are involved: drainage (under the gravity, the liquid in the foam flows along the skeleton composed by the gaseous bubbles), coarsening (the pressure in the small bubbles is higher than in their larger neighbors and they tend to empty the latter), and coalescence (the liquid film dividing two bubbles breaks). The foam stability can be measured by successive weightings of a drilled container that enables the drained liquid to be evacuated, or by conductimetry, which is more convenient. An average density can therefore be determined by conductimetry with this method and the designed cell.

Bubble diameters can be determined by taking a picture of a layer of bubbles dropped on a microscope slide. An example of such a picture is presented in Fig. 3. Pictures are then analyzed with the ImageJ image processing software which, assuming the bubbles are spherical (a sensible assumption for wet foams), yields the diameter distribution. The polydispersity coefficient p can then be calculated to evaluate the foam quality [25].

$$p = \frac{< R^3 >^{\frac{2}{3}}}{< R^2 >} - 1$$

with

R the bubble radius (m)
$< R >$ the average bubble radius of the foam sample (m)

Sound velocity in aqueous foams is a difficult topic, which is still debated. It is a common approach to evaluate it with the Wood model [26]. Recent works by Pierre et al. [27] highlighted the fact that the sound velocity in a foam varies widely as a function of several parameters, including the liquid fraction ϵ, the wave frequency, and the bubble mean diameter. Using the results provided in this paper, we could evaluate the sound velocity of the different foams used in our experiments. They vary between 25 m s^{-1} for the smallest bubbles (mean diameter 0.2 mm) and 275 m s^{-1} for

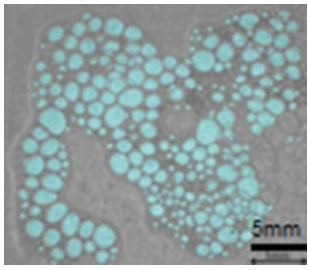

Fig. 3 Example of taken foam bubbles picture by camera and processed by ImageJ

Table 1 Main properties of the foams used in the blast and shock tube experiments

Device	Flow-focusing	Venturi
Uses	Shock tube tests	Pyrotechnic tests
Foaming liquid concentration	0 – 100%	6%
Foam density (kg.m^{-3})	40 – 60	15 – 50
Average bubble radius (mm)	0.2 – 1.4	0.2 – 0.4
Polydispersity coefficient	0.3	0.2

the largest ones (mean diameter 1.4 mm). The inverse of the pressure rising time in the shock wave was considered as the wave frequency.

Three systems were used to generate the foam according to the requirements specified in the beginning of this part. Large-scale experiments (blast experiments involving explosive charges, in the frame of the present study) require large volumes of foam. In this case, we resorted to a commercial system used by firemen and were able to obtain flow rates higher than 500 L/min. This system is based on the Venturi method and allows the generation of foams with a density between 15 and 50 kg m^{-3} while keeping a constant mean bubble radius of 0.3 mm. For small-scale experiments (shock tube tests), we designed two systems based on the classical flow-focusing method [5, 25], which consists in mixing air and foaming liquid through a Y connector. After this constriction, single bubbles are produced. To obtain large bubble foams, we resorted to a rake of Y connectors. To obtain smaller bubbles, a single generator was fitted with an array of 2 mm spheres positioned at the exit of the Y connector. With these systems, bubble diameter could be varied between 0.2 and 1.4 mm and density between 40 and 60 kg m^{-3}. The properties of the foams produced are summed up in Table 1, along with their respective average polydispersity coefficients, which are quite satisfying.

3 Spherical Shock–Foam Interaction

This part of our work studies the tridimensional propagation of the shock wave generated by a reference explosive charge in a wet foam volume with a density between 40 and 60 kg m^{-3}. Pressure gauges are placed in the foam at different distances from the charge. A stated previously, our aim is both to add to the existing experimental results and to establish a reference case for the study of the mitigation of the effects generated by the blast and fragments produced by an explosive device. Experiments were performed with C4 cylindrical charges placed at 10 cm from the ground in the center of a metallic enclosure shown in Fig. 4. The inner volume of the container is 6 m^3. C4 was chosen because it is easy to handle and to mold. Three pencil-type baseline 137A22 pressure gauges from PCB Piezoelectronics were located in the foam

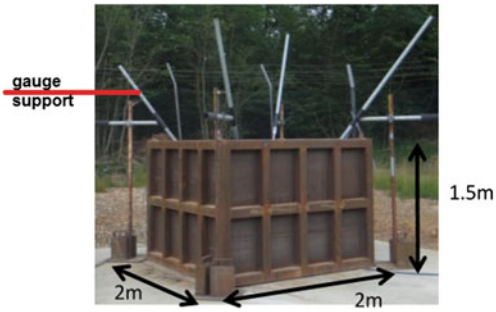

Fig. 4 Blast experimental setup

at respective distances of 0.8, 1.1, and 1.4 m of the center of the charge. Charges of 300 and 700 g were detonated to vary the blast overpressure.

Three tests were performed with a 300 g charge and without foam in order to assess the experimental reproducibility and to provide a reference case, since the partially confined configuration is not standard. The pressure profiles obtained from the three gauges are shown in Fig. 5, with each color corresponding to one test. The first part of the profiles is straightforward to analyze: a first peak corresponding to the

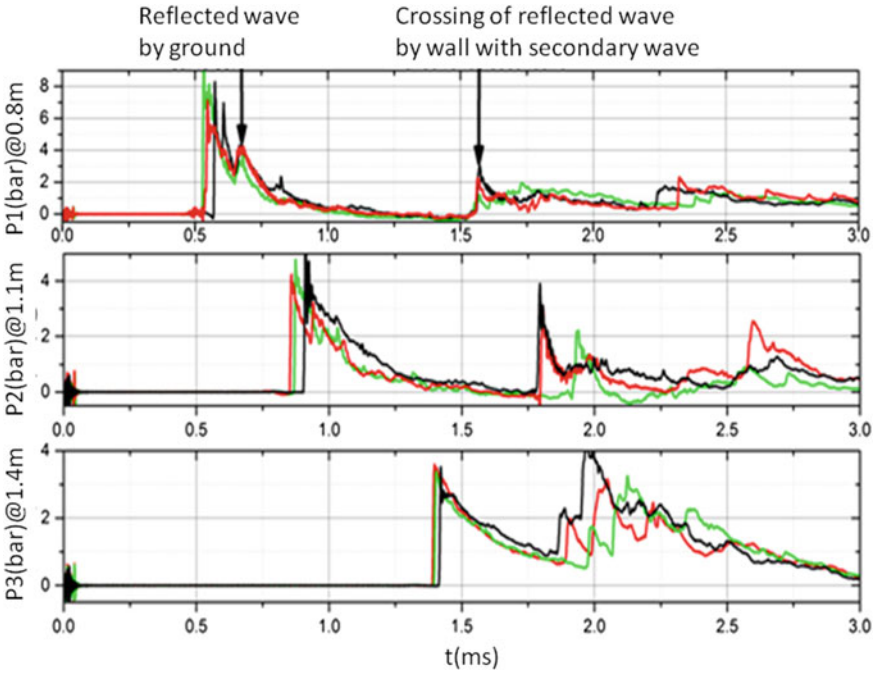

Fig. 5 Temporal evolution of the overpressure for gauges 0.8, 1.1, and 1.4 m from a bare 300 g C4 cylindrical charge for three different tests

incident blast wave is followed by a second one corresponding to the wave reflected on the walls of the confinement. The following parts of the signals are indicative of the multiple-wave reflections in the enclosure. The incident overpressure was compared with reference data from Kinney and Graham [28] and computational results (obtained with ANSYS Autodyn) with good agreement. As can be seen from these results, the reproducibility is satisfying, with variations in overpressures and times of arrival below 20%.

Given the scale of the setup and the generating device used, measuring the bubble size did not make sense. As stated in Table 1, the generating device was tested before the experimental campaign, showing that the average bubble size did not significantly vary and was about 0.3 mm. Therefore, only the average density was controlled before each shot. The overpressures measured with foam for both charges are shown in Fig. 6. Contrary to the case of the bare charge, no significant reflected wave can be seen on these signals, which highlights the damping capacity of the foam. Furthermore, the incident overpressure exhibits the usual double structure (cf. Fig. 1). Although the overpressures recorded for the 700 g C4 charge remains sharper for a longer time, both signal eventually take the bell profile associated with the main compression phase in the fragmented foam. The profiles were post-processed, in order to determine the time of arrival of the incident wave t_a, the duration $t_p - t_a$ and overpressure P_p of the precursor wave and the duration $t_c - t_p$ and overpressure P_c of the compression wave. Wave diagrams were plotted (not shown here, but t_a, t_p, t_c, P_p and P_c are indicated in Fig. 6). The evolution of the recorded overpressure P_c as a function of scaled distance Z was compared with the recently published experimental results of Del Prete et al. [5] and with the aforementioned empirical formulas by Hartman and Larsen [2, 29] (cf. Fig. 7). Overall, the maximal overpressure P_c is decreased by 90% for the shortest scale distances considered in this study, and up to

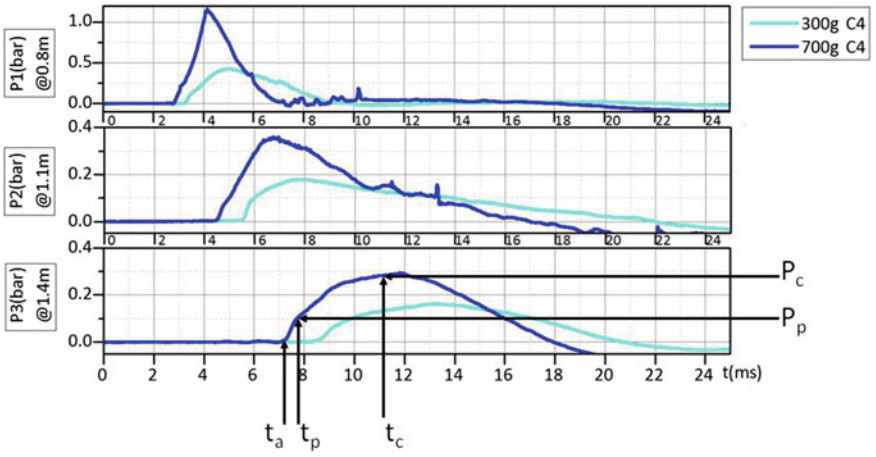

Fig. 6 Temporal evolution of the overpressure for gauges 0.8, 1.1, and 1.4 m from 300 and 700 g C4 cylindrical charges in aqueous foam

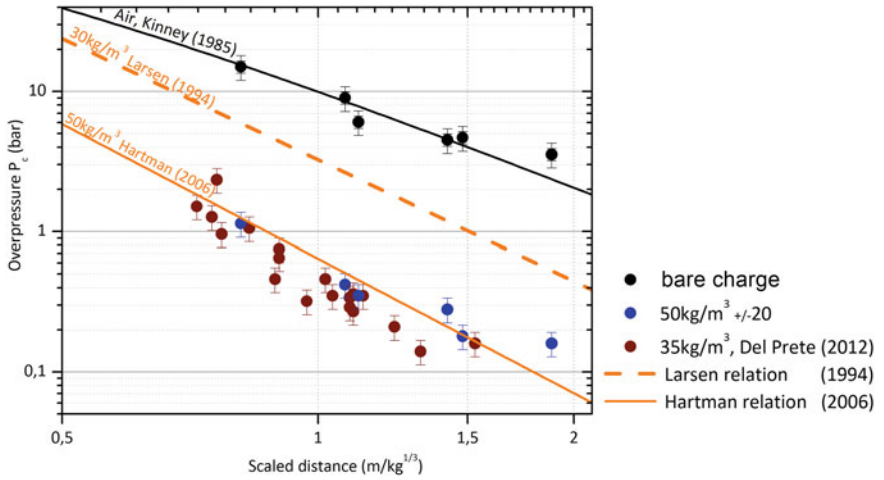

Fig. 7 Maximal overpressure P_c as a function of scaled distance for different aqueous foams and different charges

95% for the largest ones. Comparing our data with those of Del Prete et al. [5] does not permit to draw any conclusive result regarding the influence of the foam density on the blast mitigation. Besides, other factors (such as the mean bubble diameter) must also be taken into account.

Figure 8 shows the evolution of the precursor wave overpressure as a function of the scale distance. Here again, our results follow the same trend as those from

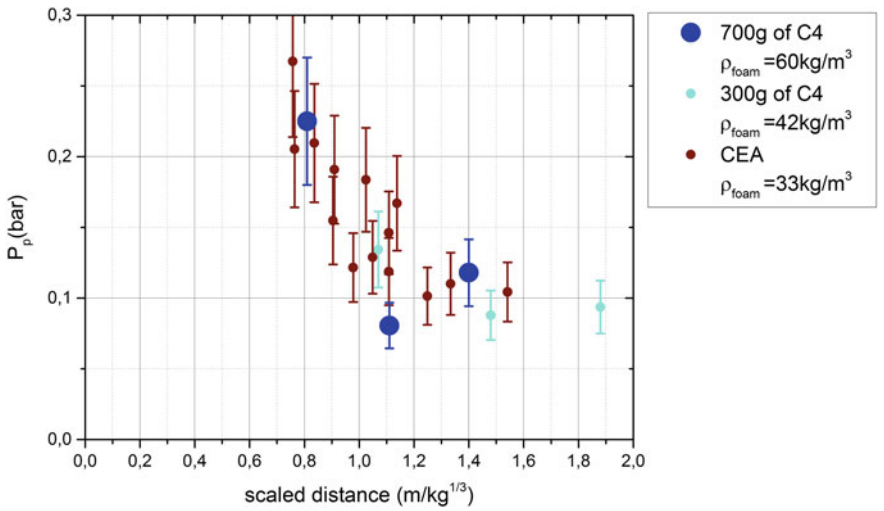

Fig. 8 Maximal overpressure of the precursor wave P_p generated by an explosive charge in a liquid foam as a function of the scaled distance Z for our experiments and those of the CEA [5]

Del Prete et al. [5]. The precursor overpressure varies between 0.1 and 0.3 bar. It decreases with the scale distance, which can be attributed both to the blast attenuation and to the spherical wave propagation. It is not possible to discriminate the influence of either effect. The precursor velocity was post-processed from the pressure signals, and satisfactorily compared with a simple empirical relation provided by Gelfand [6]. The fragmentation duration $t_p - t_a$ varies between 400 and 1400 µs. It is slightly larger than the duration observed by Del Prete, which seems coherent, since our foam has a larger density. This duration increases with distance, which could be explained by the diminution of the precursor overpressure with distance.

4 Planar Shock–Foam Interaction and Study of the Bubble Size Influence

For this part of our study, we used a shock tube with a length of 3.94 m and an inner square section of $80 \times 80\,\text{mm}^2$. The high-pressure section is 0.8 m long and separated from the low-pressure section by a Mylar diaphragm (100 to 225 µm thick). The tube was fitted with six PCB 113B21 piezoelectric pressure gauges as shown in Fig. 10. The end section was filled with about 3 L of foam, leaving two pressure gauges (P1 and P2) outside the foam. Two shock wave Mach numbers were studied: 1.4 and 1.6. Bubble size (depending on the foam generating system used, cf. Sect. 2) and foam density were systematically controlled before each shot. As in the previous case, reproducibility was thoroughly tested, both with and without foam. In the case of an incident shock Mach number of 1.6, the pressure profiles obtained with each gauge are shown for the small bubble foam (SB) and large bubble foam (LB) in Fig. 11. Two equivalent tests are considered for each configuration. It appears that reproducibility is very good in the initial stages of the phenomenon. Discrepancies then appear, which can easily be attributed to the differences in the foam density from one test to the other, and, in some extent, to some nonuniformity in the foam volume. This is particularly true for the large bubble foam, which is arduous to produce. Figure 11 highlights one shortcoming of our experiments. When comparing the profiles obtained for each foam, they seem to exhibit a different structure, with a peak beginning at t = 2 ms observed only with the large bubbles. This is classically observed in shock tube experiments, and is due to the shock wave R_m reflected at the extremity of the test section (see Fig. 9). This reflected shock wave is then attenuated by the rarefaction propagating from the driver section. In the case of the small bubbles, the velocity of the incident shock wave decreases more than with large bubbles. It takes therefore more time for the reflected wave to reach the pressure sensors, and the interaction with the rarefaction wave occurs almost simultaneously. Therefore, only the very beginning of the pressure rise caused by the reflected shock wave can be recorded. This implies that the phenomena occurring in each foam are not fundamentally different, contrary to what the pressure recordings would suggest.

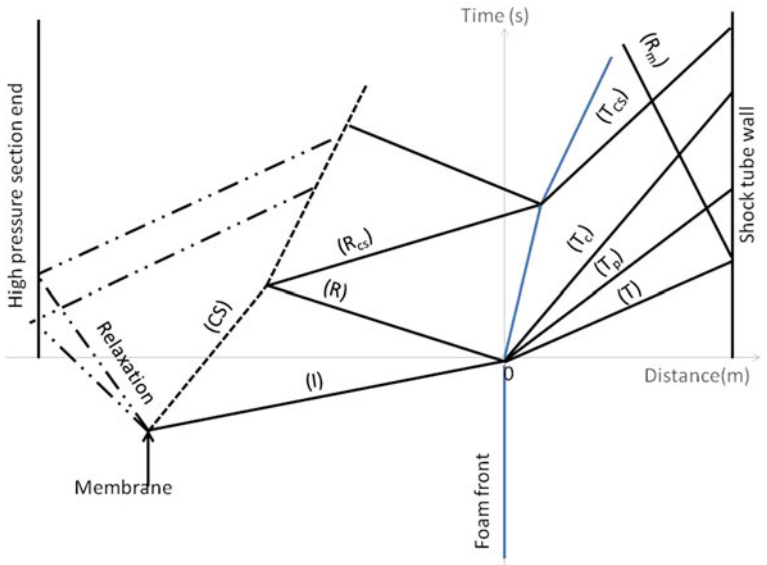

Fig. 9 Theoretical wave diagram for a shock tube partly filled with aqueous foam

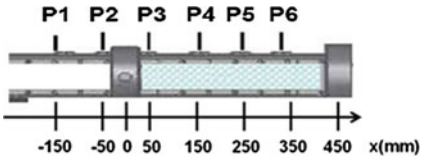

Fig. 10 Positions of the pressure gauges in the shock tube test section

Sensors P1 and P2, which are outside the foam, show similar signals and evidence P_r, the maximal reflected pressure at the air–foam interface (associated with wave R in Fig. 9). When the incident shock wave I meets the air–foam interface, a shock wave is reflected and propagates toward the driver section. This is due to the impedance mismatch at the interface. The sound velocity in the small bubbles is much lower than in the large bubbles (cf. Sect. 2). The acoustic impedances follow the same trend, which accounts for the difference in the transmitted overpressures. The overpressure of wave T transmitted in the foam is close to the one of the reflected shock wave. In the foam, the double structure of the wave front is again recorded for this experimental configuration.

The velocity of the transmitted shock wave V_{ta} was determined from the pressure profiles (Fig. 12), highlighting the fact that the wave is more decelerated in the small bubbles. This can intuitively be attributed to the fact that, in this case, the wave needs to cross more liquid films per unit volume, and is consistent with Britan's conclusions [8]. It can be seen that for small bubbles, the wave velocity seems to reach a constant value (around 100 m s^{-1}) independent of the Mach number of the incident wave. This velocity is also significantly different from the estimated sound

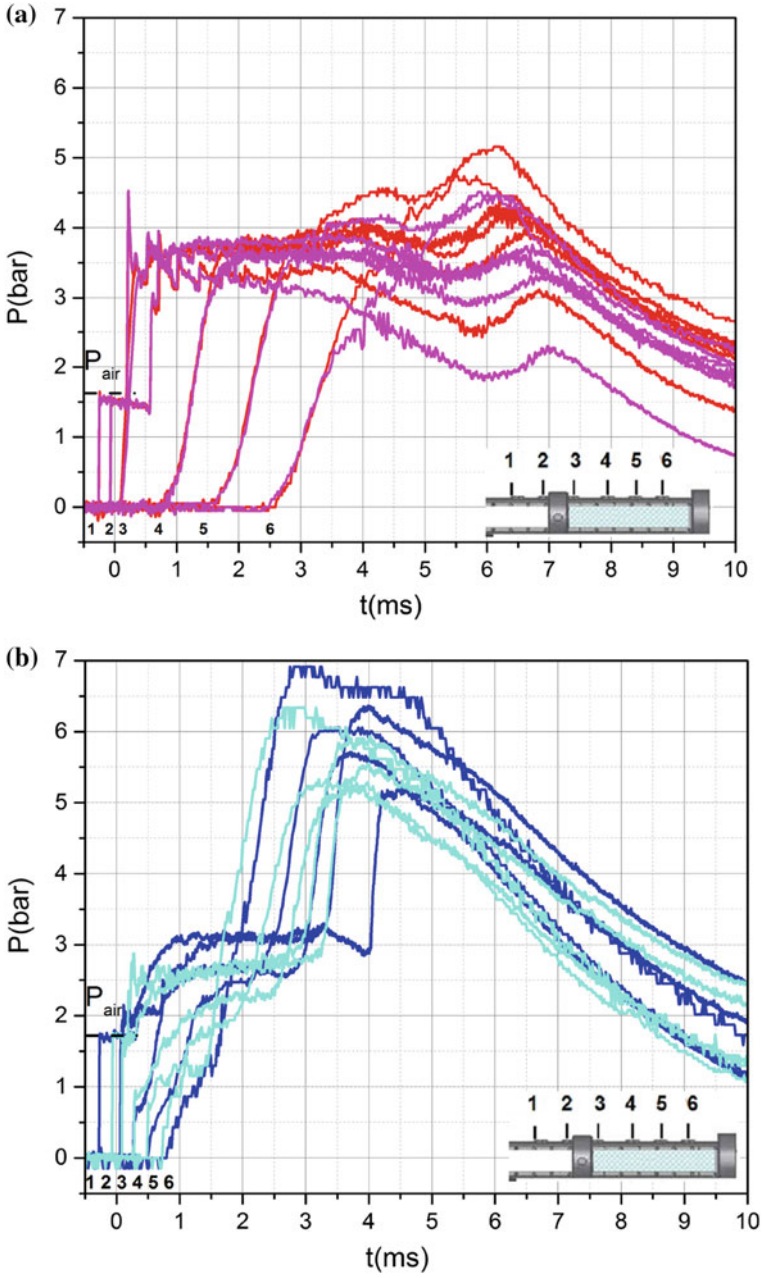

Fig. 11 Temporal evolution of the overpressure for the interaction between a M = 1.6 shock wave and an aqueous foam—**a** Small bubbles—**b** Large bubbles

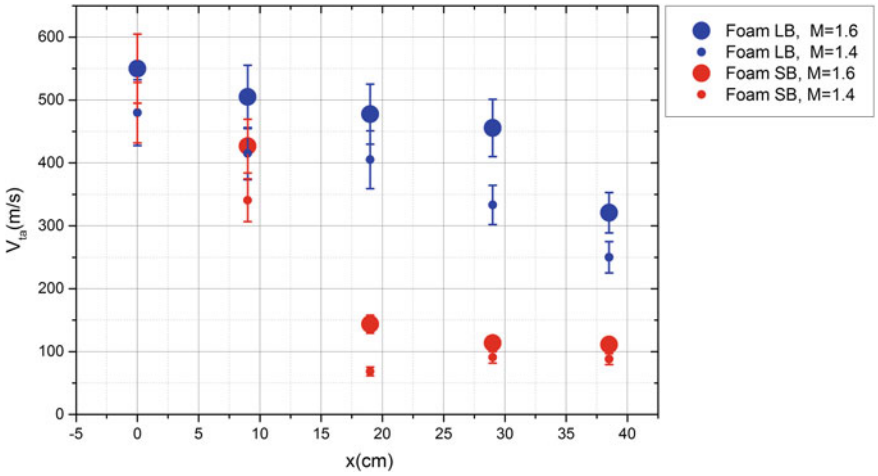

Fig. 12 Spatial evolution of the wave velocity in an aqueous foam as a function of wave Mach number and bubble size

velocity in the small bubble foam (25 m s^{-1}). It seems that the same behavior is not observed for large bubbles. It can also be noted that the concavities of both $V_{ta}(x)$ curves are not the same, although we so far have no explanation for this.

The evolution of the precursor in the large bubbles is also worth noticing. As shown in Fig. 13, it exhibits a large amplitude (initially larger than 1.5 bar, instead of the few kPa usually recorded), which is usually observed with dry foams. It is also

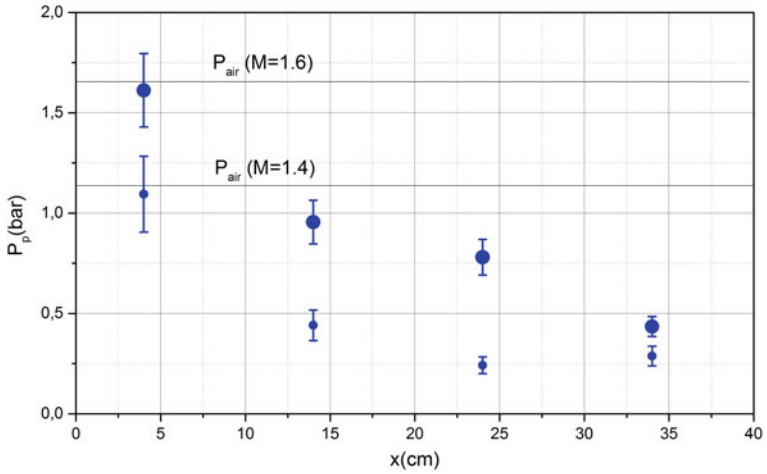

Fig. 13 Spatial evolution of the overpressure of the precursor wave as a function of Mach number for a large bubble foam

strongly attenuated as it propagates, which is not observed for more usual bubble radii (up to 0.5 mm). Further analysis of this peculiar behavior requires a local study of the wave front focused on the dynamic interaction of a shock wave and a series of aqueous films. To our knowledge, such a study is not available in the open literature.

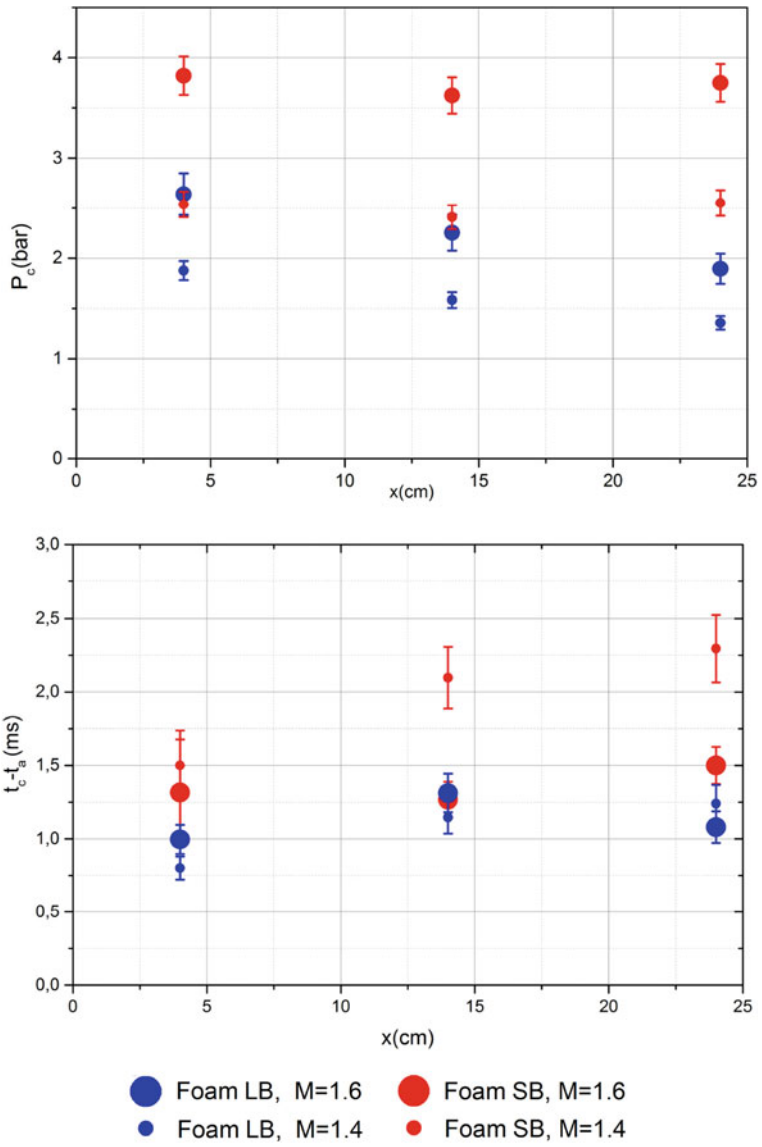

Fig. 14 Spatial evolution of the overpressure and duration of the compression wave as a function of Mach number and bubble size

The progressive rise from the precursor pressure P_p up to the equilibrium pressure P_c corresponds to a relaxation zone in which momentum and energy are transferred between the liquid and gas phases [8]. The evolution of the compression pressure P_c as a function of distance is plotted in Fig. 14 for the two Mach numbers and the two kinds of foam considered. For the small bubbles, this equilibrium pressure seems to tend toward the reflected pressure at the air–foam interface. Pressure P_c is lower in the large bubbles, and seems to keep decreasing as the wave propagates, showing that an equilibrium state has not been reached in this case. Pressure P_c seems to be less sensitive to Mach number in this case. Some differences can also be noticed as regards the duration of the compression phase. For the small bubbles, it keeps increasing and is very sensitive to the incident wave Mach number. This behavior is consistent with the previously published observations. On the contrary, in the case of the propagation in the large bubble foam, the overpressure duration reaches a limit value (around 1.25 ms) and seems almost insensitive to Mach number (over the considered range).

The pressure profiles recorded in both foams, along with the reference case in air, are plotted in Fig. 15 for M = 1.6. Owing to the impedance adaptation at the air–foam interface, an equilibrium overpressure higher than double the incident pressure is reached in the small bubble foam. This pressure is constant until the arrival of either of the waves reflected at the tube extremities. In this case, the mitigation can

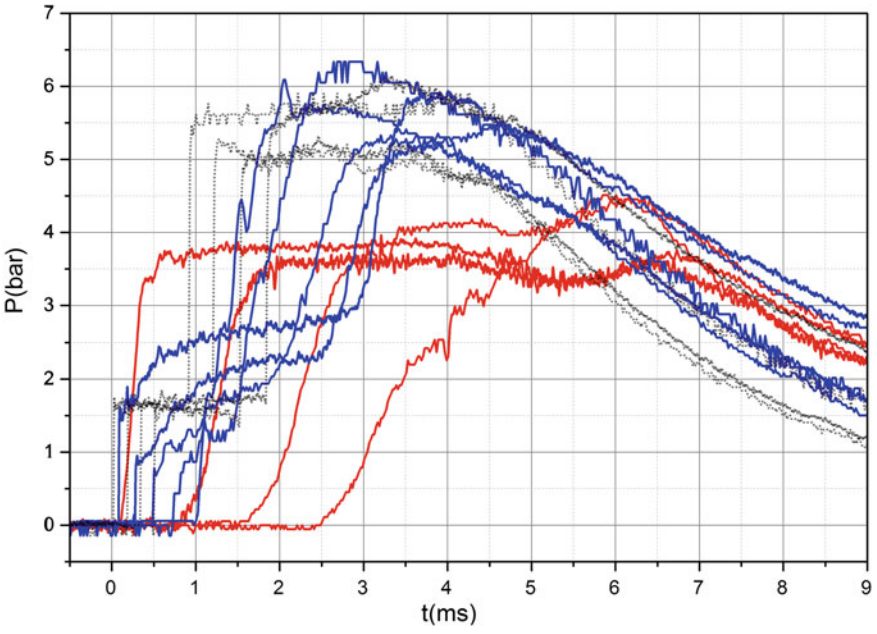

Fig. 15 Comparison of the overpressure profiles for a M = 1.6 shock wave in air (gray) and small bubble (red) and large bubble (blue) foams

be obtained because of the progressive attenuation of the pressure gradient as the wave travels in the foam. For the large bubbles, the overpressure increases by about 50% when the incident shock wave enters the foam. No precursor can initially be seen (i.e., the wave remains sharp). As the wave propagates in the foam, the double structure is recovered, with a precursor wave decreasing strongly. In this case, no equilibrium pressure can be reached. The wave also propagates much faster than in the small bubbles. Mitigation can nonetheless be obtained because the amplitude of the transmitted wave eventually decreases below the one of the incident wave and because the attenuation of the precursor generates a smoother wave front.

5 Conclusions

In this work, we have studied two reference configurations concerning the mitigation of shock waves by wet aqueous foams: spherical (blast wave) and planar (normal shock wave) propagation. Great care has been taken to accurately control the experimental conditions, in particular regarding the aqueous foam. A comparative study was conducted to select an appropriate foaming liquid and foam generation devices were designed in order to vary the mean bubble size. The foam properties (density and mean bubble diameter) were systematically measured before each test. In the case of blast wave attenuation, the results obtained are in good agreement with those already available in the literature. As regards the planar shock wave–foam interaction, two significantly different bubble sizes were considered (0.2 and 1.4 mm). It is to be noted that the 1.4 mm is a very unusual bubble diameter in the case of aqueous foams. The tested foams exhibited very different behaviors. For small bubbles, an equilibrium overpressure in the foam could always be reached, albeit at a noticeably larger value than the amplitude of the incident wave. The evolution of the wave in the large bubbles seems more complex. No equilibrium state seems to be reached, but the transmitted overpressure eventually decreases to a value close to the initial amplitude. As regards the evolution of the pressure gradient in the foam, it is strongly mitigated for small bubbles. Mitigation is longer to achieve for larger bubbles, and the wave initially remains very sharp. Although the wave propagates faster in the large bubble foam, it seems that, in the frame of this work's experimental conditions, it is at least as efficient to attenuate a planar shock wave. This macroscopic study raises quite a number of questions, which can only be answered by considering a more local experimental approach. The small-scale study of the interaction of a shock wave and a mock foam constituted by a series of interconnected aqueous films seems to be the logical continuation of this work.

References

1. Winfield, F.H., Hill, D.A.: Preliminary results on the physical properties of aqueous foams and their blast attenuating characteristics. Suffield Technical Notes, Defense Research Establishment, Suffield, Ralston, Alberta (1977)
2. Hartman, W., Boughton, B., Larsen, M.: Blast mitigation capabilities of aqueous foam, Technical report SAND2006-0533, Sandia National Laboratories (2006)
3. Domergue, L., Nicolas, R., Marle, J.-C., Mathey, L., Daloisio, M., Buche, L., Hubert, C.: Shock wave attenuation in aqueous foam. In: 3rd International Conference on Safety and Security Engineering, Inbook Series: WIT Transactions on the Built Environment,Safety and Security Engineering III, Rome, Italy, vol. 108, pp. 83–92 (2009)
4. McCallen, R.C. et al.: SERDP Munition Disposal source characterization pilot study, UCRL-CR-121838, Lawrence Livermore National Laboratory (1995)
5. Del Prete, E., Chinnayya, A., Domergue, L., Hadjadj, A., Haas, J.-F.: Blast wave mitigation by dry aqueous foams. Shock waves **23**(1), 39–53 (2012)
6. Gelfand, B.: Blast Effects Caused by Explosions (2004)
7. Raspet, R., Griffiths, S.K.: The reduction of blast noise with aqueous foam. J. Acoust. Soc. Am. **74**(6), 1757–1763 (1983)
8. Britan, A., et al.: Macromechanical modeling of blast-wave mitigation in foams. Part I: review of available experiments and models. Shock Waves **23**, 5–23 (2013)
9. Ball, G.J., East, R.A.: Shock and blast attenuation by aqueous foam barriers: influence of barrier geometry. Shock waves **9**(1), 37–47 (1999)
10. Borisov, A.A., Gelfand, G.E., Kudinov, V.M., Palamarchuk, B.I., Stepanov, V.V., Timofeev, E.I., Khomik, S.V.: Shock waves in water foams. Acta Astronautica **5**, 1027–1033 (1978)
11. Britan, B., Ben-Dor, G., Shapiro, H., Liverts, M., Shreiber, I.: Drainage effects on shock wave propagating through aqueous foams. Colloids Surf. Physicochem.Eng. Asp. **309**, 137–150 (2007)
12. Kudinov, V.M., Palamarchuk, B.I., Vakhnenko, V.A.: Attenuation of a strong shock wave in a two-phase medium. Sov. Phys. Dokl. **28**(10), 842–842 (1983)
13. Goldfarb, I.I., Shreiber, I.R., Vafina, F.I.: Heat transfer effect on sound propagation in foam. J. Acoust. Soc. Am. **92**, 2756 (1992)
14. Ranjan, D., Oakley, J., Bonnazza, R.: Shock-Bubble interactions. Ann. Rev. Fluid Mech. **43**, 117–140 (2010)
15. de Krasinski, J.S.: Some aspects of the fluid dynamics of liquid-air foams of high dryness fraction. Prog. Aerosp. Sci. **29**, 125–163 (1993)
16. Mallock, A.B.: The damping of sound by frothy liquids. Proc. Roy. Soc. Ser. A **84**, 391–395 (1910)
17. Surov, V.S.: Comparative analysis of two foam models. Combustion, Explosion and Shock Waves, vol. 31, n 31 (1995)
18. de Krasinski, J.S., Khosla, A.: Shock wave propagation and attenuation in foams. In: Fifth Australian Conference, University of Canterbury (1974)
19. Weaver, P.M., Pratt, N.H.: Experiment study of shock structure in aqueous foams and the unsteady shock emergence at a foam/air boundary. AIP Conf. Proc. **208**, 819 (1990)
20. Igra, O., Shreiber, I.: Formation of shock waves in gas-liquid foams. shock Waves **5**, 189–192 (1995)
21. Miura, H.: Weak Shock Waves in a liquid containing gas bubbles. J. Phys. Soc. Jpn. **32**(3) (1972)
22. Weaver, P.M., Pratt, N.H.: An experimental Investigation of the mechanisms of shock wave aqueous foam interactions. In: Proceedings of the International Symposium on Shock Tubes and Waves. VCH, Aachen, Germany (1988)
23. Zhdan, C.A.: Numerical modeling of the explosion of a high explosive charge (HE) in foam. Combust. Explos. Shock Waves **26**(2), 221–227 (1990)
24. Panczak, T.D., Krier, H.: Shock propagation and blast attenuation through aqueous foams. J. Hazard. Mat. **14**, 321–336 (1987)

25. Cantat, I., et al.: Les Mousses: Structure et Dynamique. Belin, Paris (2010)
26. Wood, A.B.: A Textbook of Sound. Bell, London (1944)
27. Pierre, J., Dollet, B., Leroy, V.: Resonant acoustic propagation and negative density in liquid foams. Phys. Rev. Lett. **112**, 148307 (2014)
28. Kinney, G.F., Graham, K.J.: Explosive Shocks in Air, 2nd edn. Springer, New York (1985)
29. Larsen, M.: Nest calculator, Technical report SAND94-2030, SANDIA National Laboratory (1994)

The Effect of Increasing Rarefaction on the Edney Type IV Shock Interaction Problem

Craig White and Konstantinos Kontis

Abstract Two-dimensional direct simulation Monte Carlo simulations of the Edney Type IV shock interaction problem, where an oblique shock wave generated by a wedge encounters the bow shock from a cylinder, are carried out for three different Knudsen numbers using the *dsmcFoam+* code. The numerical results for surface and flow properties are in good agreement with experiment for a Knudsen number of 0.0067. When the degree of rarefaction is increased, the oblique and normal shock waves become more diffuse and the bow shock standoff distance increases. The supersonic jet that forms in the interaction region becomes weaker as the Knudsen number increases and the point at where it impinges on the cylinder surface moves in a clockwise direction due to the jet being turned upward. The location of the peak heat transfer coefficient, peak pressure coefficient, and zero skin friction coefficient on the cylinder surface follow the supersonic jet impingement in a clockwise direction around the cylinder. The peak heat transfer and pressure coefficients decrease with increasing Knudsen number.

1 Introduction

The Edney type IV shock interaction [1] is the result of an oblique shock wave from one part of a hypersonic vehicle's body impinging on the bow shock from another part of the body. A supersonic jet region forms and reaches far inside the subsonic layer of the bow shock, as shown in the pseudo-schlieren (gradients of density from a numerical simulation) plot in Fig. 1; the resulting surface pressure and heat loads are greatly increased compared to that for a bow shock with no interaction. Such a shock–shock interaction was identified as the failure scenario for the X-15-2 flight test, where a dummy ramjet engine became detached after its pylon was damaged by the local increase in heat flux [2]. Accurate prediction of these regions of increased aerothermodynamic loads is important so that a hypersonic vehicle can either have

C. White (✉) · K. Kontis
Aerospace Sciences Division, School of Engineering, University of Glasgow, Glasgow G12 8QQ, UK
e-mail: Craig.White.2@glasgow.ac.uk

K. Kontis (ed.), *Shock Wave Interactions*,
https://doi.org/10.1007/978-3-319-73180-3_23

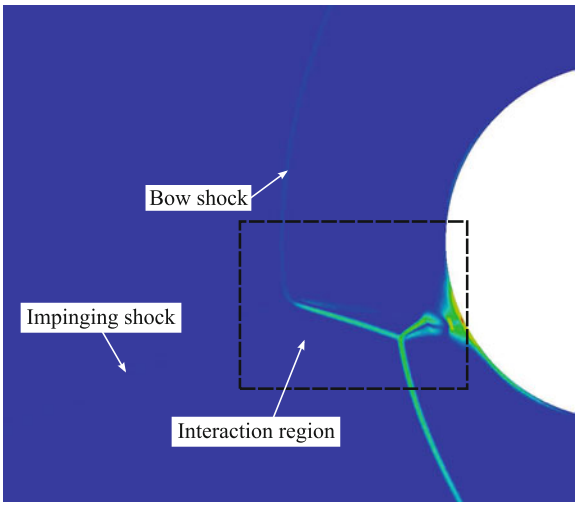

Fig. 1 Pseudo-schlieren of the Edney type IV shock interaction

its design altered to remove the shock–shock interactions, or have sufficient thermal protection installed in the relevant areas.

In addition to operating at high velocities, future hypersonic vehicles are likely to operate at high altitudes, where the air becomes rarefied. The nondimensional Knudsen number,

$$Kn = \lambda / L, \tag{1}$$

is used to define the rarefaction of a gas, where λ is the mean free path (average distance a gas molecule travels between successive collisions) of the gas and L is a characteristic length scale of the problem. When $Kn > 0.01$, nonequilibrium effects begin to dominate the flow behaviour. A gas can become non-continuum and nonequilibrium in various applications, such as low-density hypersonic flows [3], and very low speed flows at the micro and nanoscale [4]. In order to obtain a reliable numerical solution, the Boltzmann equation, rather than the Navier–Stokes–Fourier equations, must be solved. One of the most successful methods for finding a solution to the Boltzmann equation is direct simulation Monte Carlo (DSMC) [5], which is a stochastic particle based method.

2 Numerical Technique

DSMC has been developed for over 50 years and is now one of the dominant numerical techniques for simulating rarefied and nonequilibrium gas flows [5]. It is a stochastic particle based method that aims to emulate the physics of a real gas to recover a solution to the Boltzmann equation.

The basic premise is to track a statistically representative set of particles in time and space as they interact with each other and the boundaries of the simulation domain. In order to reduce computational expense, a single DSMC particle represents a large number of real gas atoms/molecules. Particle movements and collisions are uncoupled: movements are performed in a deterministic manner according to the particles' velocity vectors and the local time step, with any interactions with simulation boundaries being calculated during this movement phase. In order to uncouple the movements and collisions, the time step must remain smaller than the local mean collision time of the real atoms/molecules.

Interparticle collisions are handled in a stochastic manner, on a cell-by-cell basis, after all movements are complete. Various methods for ensuring the correct number of intermolecular collisions take place are available, such as the majorant frequency scheme [6], the no-time counter (NTC) [5], and simplified Bernoulli trials [7]. The NTC method is used in the current work and it requires that there are a minimum of 10–20 DSMC particles in a single cell to recover accurate collision frequency statistics.

In order to ensure that only particles in close proximity to one another are allowed to collide, the mesh cells must be remain smaller than the local mean free path. This allows for a realistic transfer of mass, momentum, and energy to take place. Many DSMC codes restrict the collisions further to virtual "sub-cells", meaning that collisions are restricted to a fraction of a single cell, which helps to promote nearest neighbour collisions. Each cell is split in to eight such virtual sub-cells during the collision process throughout the current work.

The cells are also used to recover macroscopic properties in the domain, so must be small enough to capture gradients of these properties. Particle positions, momentums, velocities, and energies collected in each cell are recorded and used to calculate properties such as density, temperature, and pressure. In order to reduce statistical scatter in the results, the particle properties must be averaged over time [8].

A free and open source DSMC solver, called *dsmcFoam+* [9, 10, 16], is used to perform all of the simulations in this work. A greatly extended version of the solver is implemented within the framework of OpenFOAM [11] version 2.4.0 and released publicly through a Git repository.[1]

3 Problem Description

In the present work, *dsmcFoam+* is used to investigate an Edney type IV shock interaction geometry that has previously been studied experimentally [12] and simulated using DSMC [13, 17]. The experiment consisted of a 20° wedge and a cylinder with a diameter D located a distance L_3 downstream and a height H from the leading edge of the wedge, as shown in Fig. 2. The experiments were performed in the French Office National d'Etudes et de Recherches Aérospatiales (ONERA) R5Ch

[1] https://github.com/MicroNanoFlows/OpenFOAM-2.4.0-MNF.

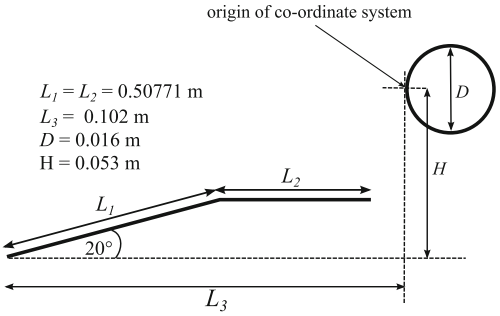

Fig. 2 Schematic of the experimental and numerical set up

Table 1 Knudsen numbers, freestream densities, and time steps for the different simulations

Kn	Re	ρ_∞ (kg/m^3)	τ (s)
0.0067	1820	3.916×10^{-4}	5×10^{-9}
0.0133	910	1.958×10^{-4}	2.6×10^{-8}
0.0267	455	9.790×10^{-5}	2.6×10^{-8}

low-density wind tunnel, with a model width-to-cylinder diameter ratio of 6.25. It is assumed that this was wide enough that a 2D flow assumption can be made at the centre of the model, and so 2D DSMC simulations are performed throughout this work.

In order to investigate how these shock–shock interactions change with increasing altitude, the same geometry is tested at increasing Knudsen number, while the freestream Mach number remains constant. Table 1 contains the Knudsen numbers Kn, freestream densities ρ_∞, and time steps τ for the different simulations. The Knudsen number is based on the freestream mean free path, calculated using the variable hard sphere (VHS) formulation [14], and the cylinder diameter D : $Kn = \frac{\lambda_\infty}{D}$. The Reynolds number, $Re = \frac{\rho_\infty U_\infty D}{\mu_\infty}$, is also given for each case, where μ_∞ is the freestream viscosity, taken to be 4.99×10^{-6} kg m^{-1} s^{-1}, based on the VHS power law. It should be noted that the Mach, Reynolds, and Knudsen numbers are connected through the relation $Kn \propto \frac{Ma}{Re}$. In all cases, the freestream velocity U_∞ and temperature T_∞ are 1450 m/s and 52.5 K, respectively, giving a freestream Mach number Ma_∞ of 10. The gas is considered to be an air mixture of 79% nitrogen and 21% oxygen. A smaller time step is used in the smallest Knudsen number case to account for the higher collision rates present in the interaction region. For $Kn = 0.0067$, it is known that the flow is steady from a time accurate Navier–Stokes simulation [15] and it is assumed in this work that the flow is steady for the higher Knudsen numbers.

Table 2 contains the details for VHS viscosity exponent ω, the reference diameter d_{ref}, molecular mass m, characteristic vibrational temperature Θ_{vib}, and the rotational Z_{rot} and vibrational Z_{vib} collision numbers for each species. All interactions with

Table 2 Nitrogen and oxygen species parameters

	N_2	O_2
ω	0.74	0.77
d_{ref} (m)	4.07×10^{-10}	3.96×10^{-10}
m (kg)	46.5×10^{-27}	53.12×10^{-27}
Z_{rot}	5	5
Z_{vib}	50	50
Θ_{vib} (K)	3371	2256

the solid surfaces of the cylinder and wedge are treated as fully diffuse Maxwellian reflections with a constant surface temperature of 300 K.

4 Results and Discussion

Figures 3 and 4 compare the surface heat transfer coefficient and surface pressure coefficient, respectively, from *dsmcFoam+* to that obtained from the ONERA R5Ch experiment, along with DSMC results from Xiao et al. [17] and Moss et al. [13]. The heat transfer coefficient, C_H is calculated as

$$C_H = \frac{q}{\frac{1}{2}\rho_\infty U_\infty^3}, \tag{2}$$

and the pressure coefficient C_P is given by

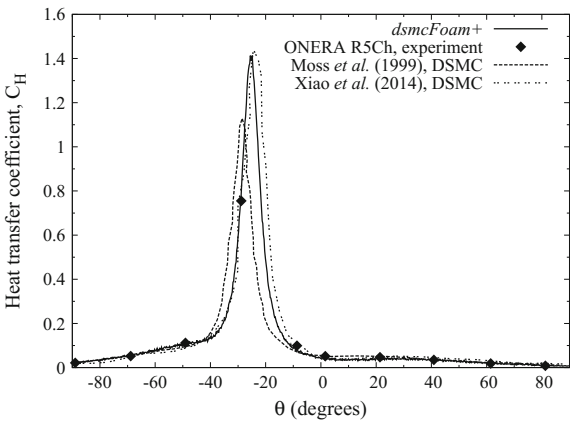

Fig. 3 Heat transfer coefficient on cylinder surface, for $Kn = 0.0067$. Comparison of DSMC and experimental results from [12]

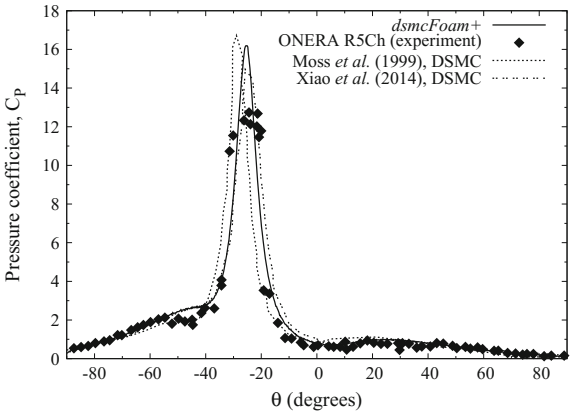

Fig. 4 Pressure coefficient on cylinder surface, for $Kn = 0.0067$. Comparison of DSMC and experimental results from [12]

$$C_P = \frac{P - P_\infty}{\frac{1}{2}\rho_\infty U_\infty^2}, \tag{3}$$

where q is the local heat flux, P is the local pressure, and P_∞ is the freestream pressure. The zero degree location is at the origin of the coordinate system, as shown in Fig. 2. There were only ten locations for heat flux measurement on the experimental model and with this low resolution it is not possible to determine the exact location of the peak heat flux from the experimental results. The *dsmcFoam+* results match with the experimental data well, with the peak heat transfer coefficient predicted as 1.4 at a location of around -25°. The *dsmcFoam+* results are in closer agreement to the results of Xiao et al. [17] than those from Moss et al. [13]. It is not stated which DSMC code the former used, and the latter used a 2D version of Bird's DSMC code. Both Xiao et al. and Moss et al. state that a mesh with 97,060 cells was used to obtain their results; the *dsmcFoam+* results were obtained on a mesh with 619,218 cells, which was built with local refinement regions to ensure that the cells remained small in comparison to the local mean free path throughout.

The pressure coefficient results from *dsmcFoam+* are in reasonable agreement with the experimental data, predicting a peak pressure coefficient of about three nondimensional units higher than the experiment. The *dsmcFoam+* results match those from Xiao et al. better than from Moss et al. again. The experimental measurements were made at the centre of the cylinder's width, but these differences may be due to the fact that 2D simulations have been used to replicate an experiment that had a finite width-to-diameter ratio.

Experimentally, the rotational temperature and density were obtained using a DL-CARS measurement technique. These measurements are compared to the *dsmcFoam+* results at a vertical location 1 mm below the point where the supersonic jet impinges on the cylinder surface in Fig. 5; for the experiment, this is stated to be 4 mm below the origin of the coordinate system and it is 3.7 mm below it in the *dsmcFoam+* results. The experimental and numerical results are in reasonable

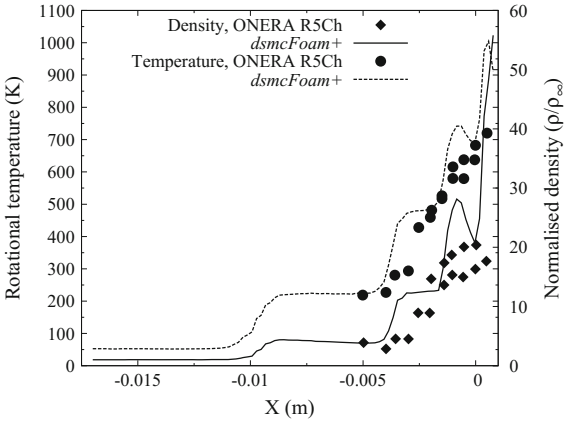

Fig. 5 Horizontal profiles of rotational temperature and density at a location 1 mm below the jet impingement ($y \approx -4$ mm). Comparison of *dsmcFoam+* and experimental results from [12]

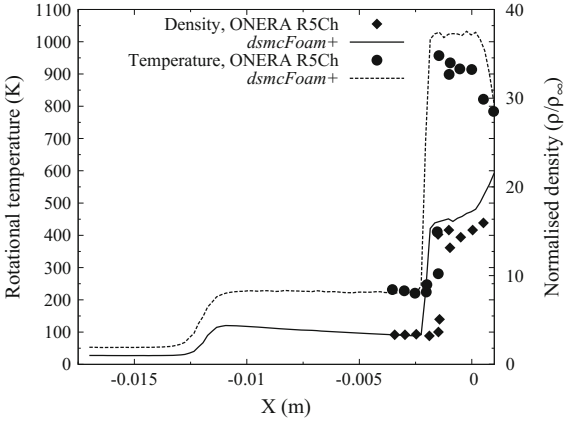

Fig. 6 Horizontal profiles of rotational temperature and density at a location just below the lower triple point ($y \approx -5$ mm). Comparison of *dsmcFoam+* and experimental results from [12]

agreement, with the DSMC results consistently predicting increases in temperature and density earlier than the experimental results, which again may be due to a 2D simulation being used to replicate an experiment that has a finite width. The effect of the oblique shock wave can be seen at around −0.01 m, with three further increases in temperature and density in the complex supersonic jet inside the supersonic region further downstream.

The same properties are compared at a vertical location of −5 mm, which is just below the second triple point, in Fig. 6. The effect of the oblique shock wave can be seen at around −0.014 m, and then there is a second increase in temperature and density as the flow passes through the bow shock from the lower surface of the cylinder. The agreement is reasonably good, but the numerical results predict a slightly higher post-shock rotational temperature and a larger standoff distance.

Figure 7 shows the contours of Mach number in the interaction region at $Kn = 0.0067$, as calculated by *dsmcFoam+*. The location of the bow shock, impinging

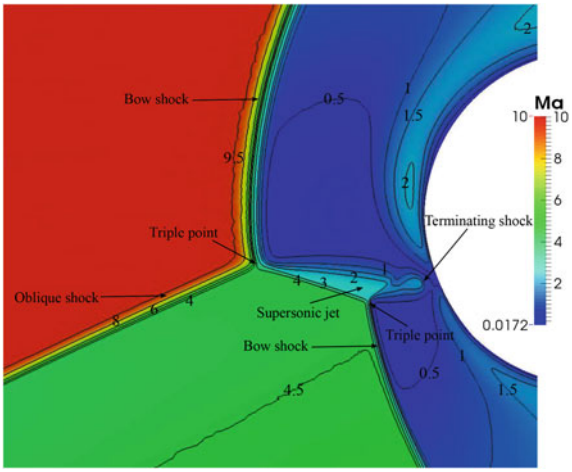

Fig. 7 Mach number contours in the interaction region, for $Kn = 0.0067$

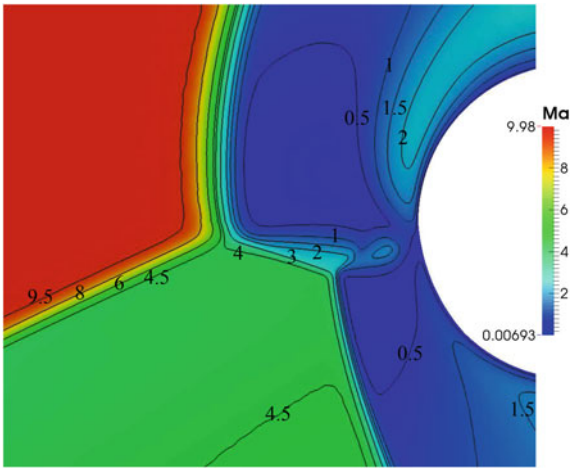

Fig. 8 Mach number contours in the interaction region, for $Kn = 0.0133$

oblique shock, and terminating shock are indicated, along with the supersonic jet that reaches inside the bow shock.

Figure 8 shows the contours of Mach number in the interaction region, for $Kn = 0.0133$. Qualitatively, compared to $Kn = 0.0067$, it is clear that the bow and oblique shocks become more diffuse, and that the bow shock standoff distance increases. The supersonic jet does not impinge as far behind the bow shock and is turned up toward the zero degree location on the cylinder surface.

Figure 9 shows the contours of Mach number in the interaction region, for $Kn = 0.0267$. The bow shock and oblique shock have become more diffuse again. At this Knudsen number, there is a very weak supersonic jet that extends over the top of the cylinder. There is no terminating shock because this supersonic jet is not terminated by the cylinder surface.

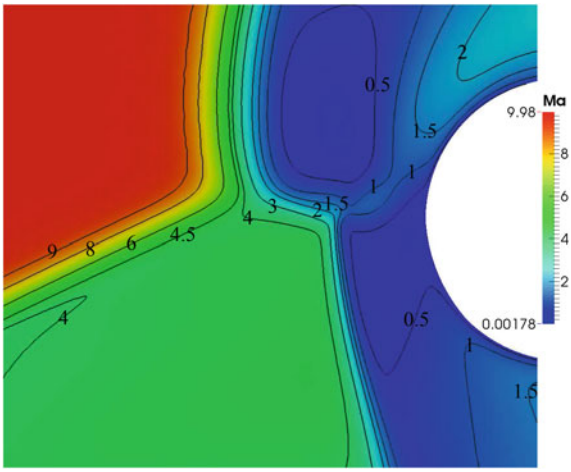

Fig. 9 Mach number contours in the interaction region, for $Kn = 0.0267$

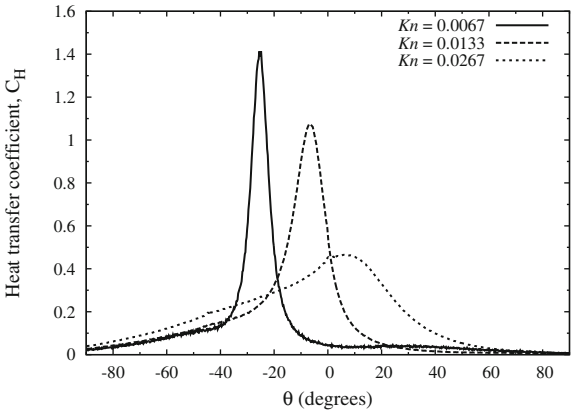

Fig. 10 *dsmcFoam+* results of heat transfer coefficient on the cylinder surface, for the three different Knudsen numbers

The effect of increasing rarefaction on the surface heat transfer coefficient is shown in Fig. 10. The peak value of heat transfer coefficient decreases as the Knudsen number is increased. The position of the peak heat transfer coefficient also moves in a clockwise direction around the cylinder surface as the Knudsen number increases. This is due to the supersonic jet being forced upward as the Knudsen number increases, as shown in Figs. 7 and 8. In addition, the terminating shock becomes weaker as the Knudsen number increases, which reduces the peak heat transfer coefficient. At the highest Knudsen number considered in the present study, there is a very weak supersonic jet and no terminating shock as shown in Fig. 9. There is a larger decrease in the peak heat transfer coefficient when the Knudsen number is increased to 0.0267 from 0.0133, than when it is increased to 0.0133 from 0.0067.

Although the peak heat transfer and pressure coefficients reduce as the Knudsen increases, the surface area over which these properties are enhanced increases, as can

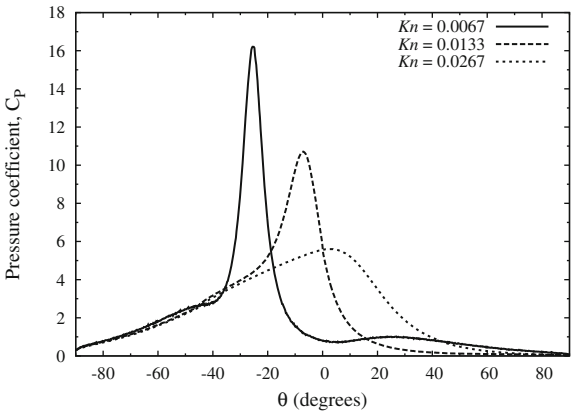

Fig. 11 *dsmcFoam+* results of pressure coefficient on the cylinder surface, for the three different Knudsen numbers

be seen in the wider profiles for $Kn = 0.0267$ in Figs. 10 and 11. Although the peak heat flux is reduced, the region of enhanced peak flux becomes larger with increasing rarefaction.

When the Knudsen number is increased, the pressure coefficient changes in a very similar manner to the heat transfer coefficient, as shown in Fig. 11. The peak pressure coefficient is reduced and the location of the peak moves toward clockwise around the cylinder diameter.

The skin friction coefficient C_F is calculated as

$$C_F = \frac{\tau}{\frac{1}{2}\rho_\infty U_\infty^2}, \tag{4}$$

where τ is the local shear force on the surface. Figure 12 shows a plot of C_F over the cylinder surface for the three different Knudsen numbers. For all Knudsen numbers, there are two distinct peaks of skin friction coefficient, between which the value falls to zero. The position of this zero location is plotted in Fig. 13 and moves in a clockwise direction around the cylinder surface with increasing Knudsen number and is located at the same position as the peak heat transfer and pressure coefficients. The rate of change of the zero stress location decreases with increasing Knudsen number for the range in this present study.

The second peak in skin friction coefficient becomes relatively larger than the first with increasing Knudsen number and the distance between the peaks increases. The location of these peaks corresponds to where the flow is accelerating over the surface below and above the stagnation point behind the terminating shock. At $Kn = 0.0067$, there is significant acceleration both below and above the stagnation point, but the acceleration below the stagnation point becomes relatively weaker than that above as the degree of rarefaction increases, hence the smaller peak before zero degrees for the higher Knudsen numbers in Fig. 12.

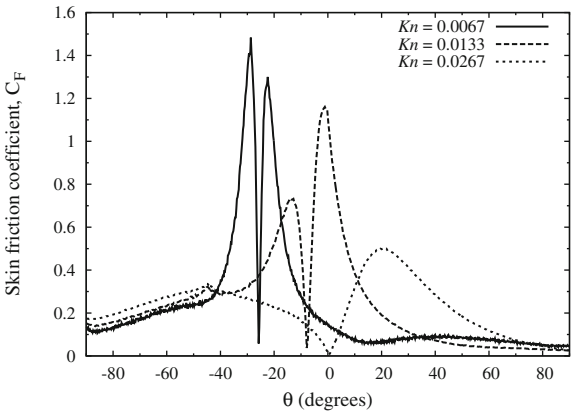

Fig. 12 *dsmcFoam+* results of skin friction coefficient on the cylinder surface, for the three different Knudsen numbers

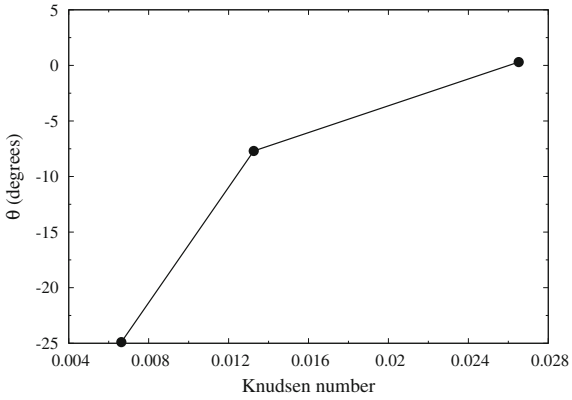

Fig. 13 *dsmcFoam+* results for the location of $C_F = 0$ as a function of Knudsen number

5 Conclusions and Future Work

The comparison of experimental and numerical results for $Kn = 0.0067$ is in reasonable agreement and the observed disagreements in peak pressure coefficient could be down to 2D simulations being used to replicate an experiment with a width-to-diameter ratio of 6.25. Using a full 3D DSMC simulation would be prohibitively computationally expensive for the current simulations. This experimental comparison shows that *dsmcFoam+* can be used to predict macroscopic properties in the gas and on the cylinder surface. There was significant disagreement in the two previous DSMC calculations for this problem; a much finer mesh has been used for the current *dsmcFoam+* simulation and the results are in good agreement with the results of Xiao et al. [17].

When the degree of rarefaction is increased by decreasing the gas density, the oblique shock wave generated by the wedge, and the cylinder's bow shock both become more diffuse. The standoff distance of the bow shock also increases. The

supersonic jet turns upward and the terminating shock becomes weaker, leading to decreasing peak heat transfer coefficient and pressure coefficients that move in a clockwise direction around the cylinder surface. If a future hypersonic aircraft is expected to climb to altitudes where rarefaction is important, the fact that the location of the peak heat transfer coefficient will move should be taken into account during the design stage.

At the highest Knudsen number studied here, there is no terminating shock as the weak supersonic jet is turned so far up that it does not encounter the cylinder surface. This works assumes that all of the flows are steady; the small time steps required for DSMC simulations, and the need to time average results, have prevented this assumption from being tested by using ensemble averaging.

Future work on Edney type IV shock/shock interactions using *dsmcFoam+* could add more Knudsen numbers to give more resolution on how the stagnation point moves around the cylinder surface, could include the effect of different gas–surface interaction models, and different gas compositions to model, for example, Martian applications.

References

1. Edney, B.: Anomalous heat transfer and pressure distributions on blunt bodies at hypersonic speeds in the presence of an impinging shock. Technical report 115, Aeronautical Research Institute of Sweden (1968)
2. Watts, J.: Flight experience with shock impingement and interference heating on the X-15-2 research airplane. Technical report TM X-1669, NASA (1968)
3. Padilla, J.F., Boyd, I.D.: Assessment of gas-surface interaction models for computation of rarefied hypersonic flow. J. Thermophys Heat Transf. **23**(1), 96–105 (2009)
4. GadelHak, M.: The fluid mechanics of microdevices—the freeman scholar lecture. J. Fluids Eng. **121**(1), 5–33 (1999)
5. Bird, G.A.: Molecular Gas Dynamics and the Direct Simulation of Gas Flows. Oxford Science Publications, Oxford University Press Inc, New York (1994)
6. Ivanov, M.S., Markelov, G.N., Gimelshein S.F.: Statistical simulation of reactive rarefied flows—numerical approach and applications. In: 7th AIAA/ASME Joint Thermophysics and Heat Transfer Conference (1998)
7. Stefanov, S.K.: On DSMC calculations of rarefied gas flows with small number of particles in cells. SIAM J. Sci. Comput. **33**(2), 677–702 (2011)
8. Hadjiconstantinou, N.G., Garcia, A.L., Bazant, M.Z., He, G.: Statistical error in particle simulations of hydrodynamic phenomena. J. Comput. Phys. **187**(1), 274–297 (2003)
9. Scanlon, T.J., Roohi, E., White, C., Darbandi, M., Reese, J.M.: An open source, parallel DSMC code for rarefied gas flows in arbitrary geometries. Comput. Fluids **39**(10), 2078–2089 (2010)
10. White, C., Borg, M.K., Scanlon, T.J., Reese, J.M.: A DSMC investigation of gas flows in microchannels with bends. Comput. Fluids **71**, 261–271 (2013)
11. OpenFOAM Foundation (2016). http://www.openfoam.org
12. Pot, T., Chanet, B., Lefebvre, M., Bouchardy, P.: Fundamental study of shock/shock interference in low density flow: flowfield measurements by DL-CARS. In: 21st Rarefied Gas Dynamics Symposium, pp. 545–552 (1998)
13. Moss, J.N., Pot, T., Chanetz, B., Lefebvre, M.: DSMC simulation of shock/shock interactions: emphasis on type IV interaction. In: Proceedings of the 22nd International Symposium on Shock Waves, vol. 3570, pp. 1337–1342. Imperial College, London, UK (1999)

14. Bird, G.A.: Definition of mean free path for real gases. Phys. Fluids **26**(11), 3222–3223 (1983)
15. Glass, C.E.: Numerical simulation of low density shock-wave interactions. NASA/TM-1999-209358 (1999)
16. White, C., Borg, M.K., Scanlon, T.J., Longshaw, S.M., John, B., Emerson, D.R., Reese, J.M.: dsmcFoam+: An OpenFOAM based direct simulation Monte Carlo solver. In press, Computer Physics Communications (2017)
17. Xiao, H., Shang, Y., Wu, D.: DSMC simulation and experimental validation of shock interaction in hypersonic low density flow. Sci. World J. **2014**, 732765 (2014)

Laser Ignition for Pulse Detonation Engines

Pavel Bulat and Konstantin Volkov

Abstract The high pressures and resultant momentum flux out of the chamber generate thrust. The ignition system of PDE has always posed problems in commercial applications. Microwave and laser-induced detonation in the mixture of hydrogen with flake aluminum particles is simulated based on Eulerian approach. Minimum pulse energy of detonation is calculated for different parameters of laser pulse, mass fractions of particles, and compositions of gas mixture. The threshold intensity of optical breakdown on individual metal particle, and its dependence on contributing factors (particle radius, location of particle, total energy and time of laser pulse, radius of laser spot) are studied.

1 Introduction

A pulse detonation engine (PDE) is an unsteady propulsive device in which the combustion chamber is periodically filled with a reactive gas mixture, a detonation is initiated, the detonation wave propagates through the chamber, and the combustion products are exhausted. The high pressures and resultant momentum flux out of the chamber generate thrust. It suffers, however, from the lack of an appropriate ignition system designed especially for this propulsion technique. The ignition system of PDE has always posed problems in commercial applications. Many experimental, theoretical, and numerical studies have been performed for the past years, and various ignition systems (e.g., electric discharge and laser radiation) have been tested. Use of laser pulse allows to create desired temporal and spatial distributions of ignition centers and to perform a homogeneous ignition within the sub-microsecond interval [5]. Use of spark plugs for ignition is convenient for small-scale testing at low frequencies. Preliminary studies demonstrated a great potential of microwave radiation [2].

P. Bulat (✉)
ITMO University, St. Petersburg, Russia
e-mail: pavelbulat@mail.ru

K. Volkov
Kingston University, London, UK
e-mail: k.volkov@kingston.ac.uk

K. Kontis (ed.), *Shock Wave Interactions*,
https://doi.org/10.1007/978-3-319-73180-3_24

Practical systems require frequencies of the order of 100 Hz for long durations. The study discusses the possibility of use of microwave radiation to initiate detonation.

In the propagation of a detonation wave in a curvilinear channel (for example, in a toroidal channel), reflection of detonation wave from the channel walls can be regular or Mach with the formation of triple points. A rapid combustion, as shown by previous experience, takes place behind the Mach stem.

The reactive metal particles are used to enhance blast performance. Although the total energy released by the metal combustion is significant and comparable to the total energy released by the explosive itself, the timescale of this energy release (timescale of particle reaction) for typical particle sizes is too long to contribute directly to the detonation front itself. The metal particles react with gas or detonation products behind the blast wave. It has been shown that the metal particle reaction significantly increases the strength of the blast and the total impulse delivered to nearby objects or structures [7].

The injection of metal particles with low evaporation temperature and low ionization potential (e.g., aluminum) leads to drop of detonation minimum pulse energy (MPE) due to optical breakdown on individual particles. Many experimental, theoretical, and numerical studies have been performed for the past years [5, 11]. Processes that control transport and combustion of particles remain unresolved, and introduce significant uncertainties into modeling and simulation. They include qualitative and quantitative description of processes around individual particle, knowledge in particle microphysics and optical properties of particles, sub-models of heating and evaporation, transport of aggregates of complex morphology, threshold values of optical breakdown, and dependence of MPE on the contributing factors (laser pulse, composition of gas mixture, shape of particles).

Vapor aureole around metal particle is a source of free electrons, and optical breakdown in the gas–particle mixture comes for lower intensity of laser pulse than in pure gas [3, 10]. Vapor aureole around metal particle is a source of free electrons, and optical breakdown in the gas–particle mixture comes for lower energy of laser pulse than in pure gas. Compared to metal particles, heating and evaporation of liquid droplets are delayed due to transparency of a droplet and weak absorption of laser radiation. Formation of plasma arising during the interaction of laser radiation with solids and metal particles is discussed in [17]. Concentration of free electrons in a vapor aureole is insufficient for development of an electron avalanche.

There are similarities between the laser-induced acoustic shock waveforms and those associated with blast waves and sonic booms. The acoustic pulses associated with laser-induced sparks could be used in the laboratory to simulate blast sounds from explosions or sonic booms and to investigate the associated propagation effects. Laser-generated acoustic shocks can be used for laboratory-based research into nonlinear acoustics [13]. The sound energy of the laser-induced acoustic shocks lies between 3 and 150 kHz with a peak at 20 kHz.

Simulation of the interaction of a laser pulse with hydrogen–air mixture containing aluminum particles is carried out in [5]. The injection of metal particles leads to a drop of MPE. The mathematical models of various stages of the optical breakdown on individual particle and numerical methodology for computer modeling

of the laser-induced detonation in particle-laden systems are developed. The threshold intensity of optical breakdown on individual metal particle and its dependence on location of particle, total energy, and time of laser pulse are studied [16].

The detonation wave structure and detonation stability in mixtures of reactive gases and solid particles were studied in [11] for one-dimensional and two-dimensional flows. Increasing the particle volume fraction results in a rapid drop of the detonation wave speed, and smaller particle diameters resulted in slightly lower detonation velocities. A detonation suppression in a stoichiometric hydrogen–oxygen mixture with chemically inert particles was simulated in [6].

Initiation of detonation of clouds of aluminum particles in unconfined and confined domains was discussed in [8, 15, 18]. It was found that detonation was only achieved for flaked aluminum particles equivalent to spherical particles of diameter less than 1 μm. The detonation wave was typical of spinning detonation regime, and a relatively strong initiation source was required when compared with gaseous DDT.

Ignition and reaction of metal particles in a high explosive environment were studied in [14]. The ignition delay time observed in experiments and computational analysis was a result of convective heating of the particle to a critical temperature for chemical reaction.

The model proposed in [9] neglected the volume occupied by the particles and, therefore, is valid for flows of dilute mixtures. It involves a two-step induction mechanism to model the chemical reactions in a dilute, stoichiometric hydrogen–oxygen system. The influence of inert particles on the propagation of detonation waves was studied in [12]. The numerical simulation showed that the momentum and energy transfers from the gas to the particles tend to suppress the instabilities of the front but result in lower detonation velocities and longer reaction zones. Further, as the shock wave propagates through the two-phase mixture, a particle compaction zone was formed in the wake of the detonation. Due to the absence of mass transfer between two phases, the length of the compaction zone increases with time.

One of the most important parameters for laser ignition applications is the MPE and its dependence on the pressure. It is of critical importance to determine the laser conditions at which a spark is produced. Knowledge of these conditions is important not only for fundamental understanding of the ignition process but also for the selection of lasers, optical windows, and beam delivery system for the design of a practical laser ignition system. Processes that control transport and combustion of droplets remain unresolved and introduce significant uncertainties into modeling and simulation. Two of the most important parameters for practical applications are MPE required to induce ignition and detonation of the mixture, and the threshold intensity of laser pulse required for optical breakdown on individual particle or droplet.

The study exploits experimental and computational techniques. The test rig has been designed and used to investigate a feasibility of the use of microwave radiation to induce detonation in PDEs (attached and streamer discharges are used). In the numerical method, the Navier–Stokes equations are used for the simulation of propagation of detonation waves. Physical and mathematical models of optical breakdown on individual metal particle, and numerical methodology for computer modeling are developed. Laser-induced detonation in gas–particle mixtures is

studied. The in-house computer code has been developed, and contribution of parameters of laser pulse and composition of the mixture are reported. Comparison of some numerical results with experimental data is made.

2 Breakdown Mechanism

When a high-power laser pulse ($I \sim 10^{11}$ W/cm^2) is focused at a point and interacts with a gas, the gas is heated to temperatures of thousands of degrees within several microseconds, breaking down and becoming highly ionized. This process is always accompanied by a light flash and generation of sound (acoustic shock wave). LIB generates vapor bubbles within the droplet. The development of electron cascade requires the existence of initial free electrons in a gas.

A chain of processes leading to explosion and optical breakdown of individual metal particle is developed (Fig. 1). These processes depend on optical properties of particle, its shape, and ratio of particle size to radius of laser spot.

The particle is heated up to high temperature, melting and evaporation start (Fig. 1a). Evaporation of a particle leads to the formation of a vapor aureole around the particle. Free electrons are generated in the vapor aureole as a result of thermal emission from particle surface (if $T < T_b$) and isothermal ionization in vapor aureole (if $T > T_b$). This leads to collisions of electrons with ions and atoms, and electron–electron collisions. Ionization of vapor aureole due to reverse drag effect leads to the development of electron avalanche and formation of micro-plasma spots around the particle (Fig. 1b). The cascade ionization process is significant at high pressure and longer laser pulse because under these conditions, electron–atom or electron–ion collisions have sufficient time to occur during the laser pulse. Then, micro-plasma spots are expanded due to thermal diffusion of electrons and ionization of molecules and atoms of surrounding gas. Micro-plasma spots are merged, and plasma fireplace is formed around the ensemble of particles (Fig. 1c). The plasma fireplace absorbs laser radiation, and contributes to development and propagation of self-sustaining shock wave in the gas–particle mixture (Fig. 1d). This shock wave leads to initiation of detonation in surrounding mixture.

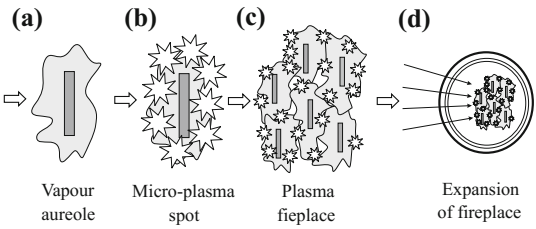

Fig. 1 Optical breakdown on metal particle

3 Mathematical Model

The mathematical formulation of the problem is divided into low-level and high-level models. Low-level models correspond to the processes in the volume occupied by an individual particle. The high-level models correspond to the processes in the volume occupied by multiphase mixture.

Low-level models describe melting, heating, evaporation, and formation of vapor aureole, appearance of free electrons due to thermal ionization on front of shock wave, and development of electron avalanche due to reverse drag effect. The particles are considered to have a uniform temperature distribution, and heterogeneous surface reactions are neglected. When the temperature of the particle reaches the melting point, the particle temperature is kept constant until an amount of heat equal to the latent heat of fusion is transferred to the particle.

The equations describing electron avalanche in the vapor aureole include the equation of heating of vapor aureole due to electron–atom collisions, the equation of warming up of electrons, the ionization kinetic equation of vapor as a result of electron impact and the equation of particle mass. The plasma in vapor aureole is considered as an ideal gas. The Euler equations are used for the simulation of gas dynamical processes in vapor aureole. A simple model of one-step chemical reaction is used in order to reproduce explosion of individual particle. Threshold value of optical breakdown on an individual particle is computed as a result of the solution of low-level models.

The fluid and the solid particles are treated as two separated continua with mass, momentum and energy conservation equations for each phase, continuity equations for species, and conservation equations for solid particle numbers. The interactions between the two continua are described using the source terms for the rate of mass, momentum, and energy transfer. The data obtained from solution of low-level problems are used to calculate source terms in the governing equations describing high-level problem. It is assumed that particles are uniformly distributed in the domain.

Some volume of the mixture depending on particle volume fraction is associated with each particle (individual reactor of a particle). The model of unsteady well-stirred reactor is used to calculate physical quantities in this volume. The fuel–oxidizer mixture is considered as one specie (reactant) and all the products are treated as single specie (products).

The governing equations include conservative equations for mass, momentum, total energy, and species densities with source terms due to the chemistry and to the coupling with the solid phase. The conservation equations for the gaseous phase are

$$\frac{\partial \rho_g}{\partial t} + \nabla \cdot \left(\rho_g \mathbf{v}_g\right) = J;$$

$$\frac{\partial \rho_g \mathbf{v}_g}{\partial t} + \nabla \cdot \left(\rho_g \mathbf{v}_g \mathbf{v}_g\right) + \nabla p = \mathbf{F} + J(\mathbf{v}_* - \mathbf{v}_g);$$

$$\frac{\partial \rho_g e_g}{\partial t} + \nabla \cdot \left[\left(\rho_g e_g + p\right) \mathbf{v}_g\right] = \mathbf{F} \cdot (\mathbf{v}_g - \mathbf{v}_s) + Z - J(\mathbf{v}_* - \mathbf{v}_s)^2;$$

$$\frac{\partial \rho_g Y}{\partial t} + \nabla \cdot \left(\rho_g Y \mathbf{v}_g\right) = W.$$

The conservation equations for the solid phase are

$$\frac{\partial \rho_s}{\partial t} + \nabla \cdot \left(\rho_s \mathbf{v}_s\right) = -J;$$
$$\frac{\partial \rho_s \mathbf{v}_s}{\partial t} + \nabla \cdot \left(\rho_s \mathbf{v}_s \mathbf{v}_p\right) + \nabla p = -\mathbf{F} - J(\mathbf{v}_* - \mathbf{v}_s);$$
$$\frac{\partial \rho_s e_s}{\partial t} + \nabla \cdot \left(\rho_s e_s \mathbf{v}_g\right) = -\mathbf{F} \cdot \mathbf{v}_s - Q.$$

Here, ρ, $\mathbf{v}$, p, e, and Y are the density, velocity, pressure, specific total energy, and reactant mass fraction for the gaseous phase. The velocity $\mathbf{v}_*$ is the velocity of the mass experiencing transition from the gas phase to the particulate phase. The subscripts g and s refer to the gas mixture and particles, respectively. The reactant mass fraction equals unity when the gaseous phase consists of the reactive substance A, and it equals zero when the gaseous phase consists of the inert substance B.

The specific total energy of gaseous phase is given by

$$e_g = \frac{p_g}{(\gamma - 1)\rho_g} + \frac{1}{2}\left|\mathbf{v}_g\right|^2 + qY,$$

where γ is the ratio of specific heat capacities (it is assumed common for both A and B), and q is the heat release from the reaction. The equation of state of ideal gas is $p = \rho_g R T_g$, where R is the gas constant.

The volume fraction of particles is assumed small enough ($\chi_s \to 0$), and the partial density and partial pressure of the gaseous phase are equal to those in a pure gas mixture ($\chi_g \to 1$). The particle volume fraction, χ_s, and the particle number density, n_s, are connected with the relation $\chi_s = (\pi d_s^3/6) n_s$, where d_s is the particle diameter. The partial density of particles is $\rho_s = \chi_s \rho_s^o$, where ρ_s^o is the pure density of particle material. The specific total energy of the solid phase is given by

$$e_s = c_s T_s + \frac{1}{2}\left|\mathbf{v}_s\right|^2,$$

where c_s is the specific heat capacity of the solid species.

The source term W is the one-step Arrhenius kinetics law that describes the progress of the reaction

$$W = -a\rho_g Y \exp\left(-\frac{E}{RT_g}\right),$$

where a and E are the reaction's pre-exponential factor and activation energy, respectively.

The source term $\mathbf{F}$ describes the momentum exchange between two phases, and it is modeled as the drag on a spherical particle of the equivalent volume

$$\mathbf{F} = 3\pi C_D \mu d_s \left(\mathbf{v}_s - \mathbf{v}_g\right) n_s,$$

where C_D is the drag coefficient, and μ is the dynamic viscosity of the gas. The calculation of drag coefficient is based on empirical relationship depending on particle Reynolds number $\mathrm{Re}_s = \rho_g \left|\mathbf{v}_g - \mathbf{v}_s\right| d_s/\mu$. The dynamic viscosity is a function of temperature

$$\frac{\mu}{\mu_0} = \left(\frac{T_g}{T_0}\right)^n \quad (n = 0.75),$$

where T_0 is the temperature of the quiescent mixture, and μ_0 is the viscosity at the temperature T_0.

The source term Z describes the heat transfer between two phases, and it is modeled as conduction heat transfer between the particles and the gas

$$Z = \pi \lambda \mathrm{Nu}_s d_s \left(T_g - T_s\right) n_s,$$

where Nu_s is the Nusselt number. The calculation of Nusselt number is based on empirical relationship depending on particle Reynolds number and Prandtl number.

4 Computational Procedure

Equations describing heating and evaporation of particle, and development of electron avalanche are solved numerically to obtain the threshold irradiance required to produce breakdown for a given pulse duration, using a Runge–Kutta fourth-order technique with adaptive time step. Optical breakdown is assumed to occur when the free electron density obtained during the laser pulse exceeds the given critical value (10^{19}–$10^{20}\,\mathrm{cm}^{-3}$).

Accurate simulation of detonations and explosions presents challenges for numerical methods. The finite volume code, solving transient and fully compressible Euler equations, has been developed for numerical simulation [16]. The detonation solver uses the total variation diminishing (TVD) numerical schemes which are suitable for shock capturing. Implementing an adequate chemical reaction mechanism has been challenging. A one-step reaction mechanism has been developed following first principles.

Nonlinear CFD solver works in an explicit time-marching fashion, based on a three-step Runge–Kutta stepping procedure and piecewise parabolic method. The governing equations are solved with Chakravarthy–Osher scheme for inviscid fluxes. Convergence to a steady state is accelerated by the use of multigrid techniques, and by the application of block-Jacobi preconditioning for high-speed flows, with a separate low-Mach number preconditioning method for use with low-speed flows. The numerical simulations are performed in a rectangular computational domain using a uniform Cartesian mesh with about 10 cells to resolve the structure of the reaction zone. The length of the reaction zone is the smallest characteristic length of the

problem (it is shorter than the length of dynamic and thermal relaxation times of particles). Proper resolution of the reaction zone ensures that all other characteristic lengths have been properly resolved.

5 Laser Pulse

The intensity of laser pulse is represented as a product of the maximal intensity, the function describing the time distribution of the intensity, the function taking into account the spatial distribution of the intensity, and the function describing absorption of radiation in the medium. The time distribution of the intensity is represented by a continuous piecewise-linear function. In a plane normal to the direction of laser pulse, the spatial distribution of the intensity is described by the normal distribution.

The theoretical peak intensity of laser pulse at any radial point is calculated for given power and degree of focus. The laser does not reach its peak operating power at the moment when it is turned on. It requires a short time to ramp up to its peak output. For a laser pulse which lasts 8 μs, the laser output reaches its peak intensity in about one fourth of a pulse duration and will have dropped to roughly three-fourth of its peak value when the laser is shut off. The laser model includes a ramp time parameter during which time the laser's output increases linearly to a maximum (Fig. 2).

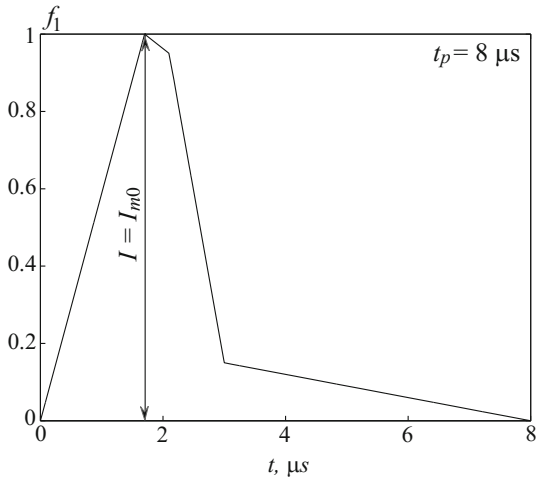

Fig. 2 Intensity of laser pulse as a function of time

6 Results and Discussion

The source of laser radiation is provided by a pulsed chemical HF laser with the following characteristics: time of laser pulse is 2.6 μs, wavelength is 4.2 μm, radius of laser spot is 5 mm, and integral temporal characteristics is 1.5 μs. Particle location relative to the centerline of the laser beam, total energy, time, and shape of laser pulse vary in the calculations. In all simulations, a Gaussian intensity profile in time is assumed.

Figure 3 shows heating of metal particle up to the boiling temperature. The particle temperature depends on total energy of laser pulse and distance from particle to centerline of laser beam. The first plateau at 923 K corresponds to the melting of the particle. The second plateau at 2792 K corresponds to the boiling point. Larger particles take a longer time to heat up to the melting point and the boiling point.

The results computed show that the energy required to heat particle up to evaporation temperature depends on particle size and particle material [10]. The particle reaches the temperature of phase transition for short time (about 1 μs). Development of electron avalanche takes about 0.1% from the time of breakdown formation.

Laser pulse with intensity of 10^{11} W/cm^2 leads to gas breakdown. In a laser-induced plasma, inverse bremsstrahlung absorption leads to an increase in electron energy. Electrons are able to ionize the surrounding gas and form an exponentially growing electron cascade. Development of an electron avalanche in the form of its dependence on the degree of ionization of the vapor aureole with time is shown in Fig. 4. The particle is located on the centerline of the laser beam. The electron avalanche is developed in 0.68 μs from the laser pulse started, and ionization takes place within a short time interval (about 0.04 μs). The electron density starts to grow after a period of 0.5 μs with an electron density not exceeding 10 cm^{-3}. Beyond this time, line suffers a sudden increase reaching a value of 1020 cm^{-3} at a time of

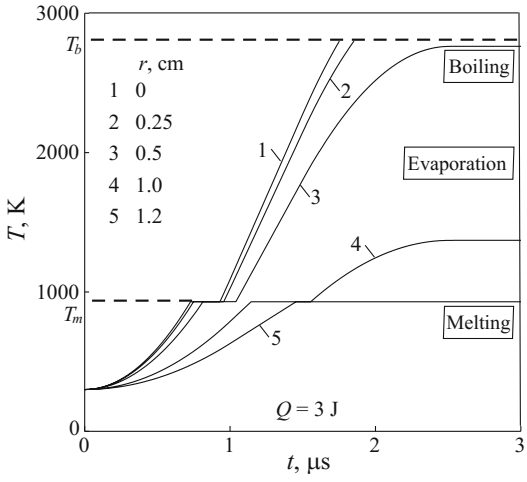

Fig. 3 Temperature of metal particle

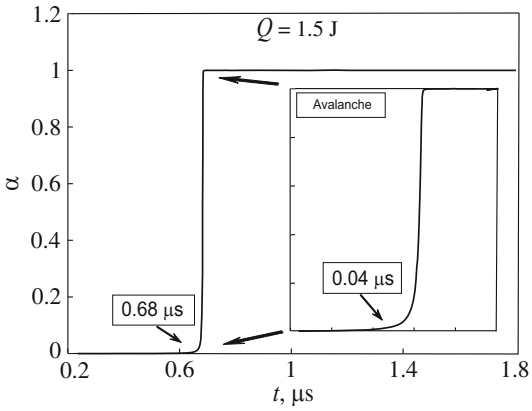

Fig. 4 Development of electron avalanche

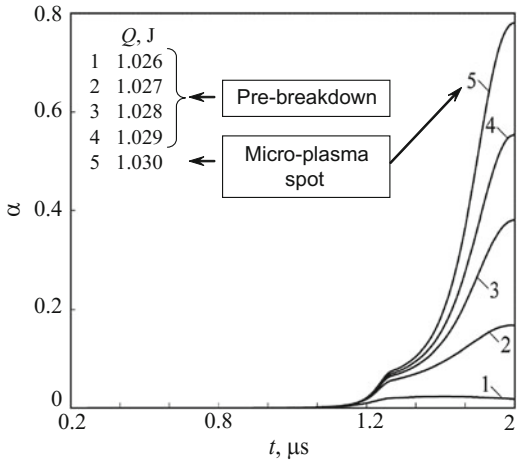

Fig. 5 Degree of ionization of vapor aureole

0.68 μs. At that intensity, the rate of cascade ionization is so high that the breakdown proceeds almost instantaneously to the critical electron density (10^{20} cm^{-3}).

The degree of ionization as function of time and total energy of the laser pulse is shown in Fig. 5. Micro-plasma spots around the particle are formed at an energy of 1.03 J. Pre-breakdown conditions are sensitive to a small change of energy of the laser pulse. The threshold of plasma formation is defined as a proportion of the laser energy used up to the beginning of breakdown.

The particle temperature depends on the energy of laser pulse. The heating of a particle to the boiling temperature with subsequent evaporation depends significantly on the particle position. The particles which are peripheral with respect to the beam centerline do not reach the mode of developed vaporization and fail to develop conditions for the beginning of the plasma generating process. Because the radiation intensity varies as a function of the distance from the beam centerline by the

Gaussian law, the breakdown occurs at different times. No conditions of breakdown are observed for the particle that is the most remote from the centerline.

Interaction of laser pulse with individual metal particle is related to one of the following stages.

1. Pre-threshold energy of laser pulse ($Q < 1$ J). Energy of laser pulse is not enough to ionize vapor aureole around particle. Evaporation of particle exists but degree of ionization is small, and vapor aureole is transparent for laser radiation.
2. Near-threshold energy of laser pulse ($Q = 1$–2 J). Degree of ionization changes from some percents to 100%.
3. Post-threshold energy of laser pulse ($Q > 2$ J). The process proceeds at completely ionized vapor aureole around particle. Ionization has an avalanche character within short time interval. Threshold intensity of LIB on metal particle corresponds to that observed in experimental study6 (qualitative comparison is complicated by various temporal profiles of laser pulse).

For modeling purposes, the reaction of particle material is considered to occur as soon as the metal reaches the gas phase. It is assumed that this happens at a critical particle temperature. For metals such as magnesium, this temperature is usually taken as the metal boiling point, whereas for aluminum, the oxide melting point is usually used. A comparison of the peak temperature reached by the particle and the ignition temperature reveals whether or not the particle was successfully ignited. The time at which the particle reaches the ignition temperature (if it ever does) is the reaction delay. The delay time for chemical reaction increases with increasing particle size. This is consistent with the view that particles should be heated up to a high enough temperature before chemical reaction occurs. Larger particles certainly take longer to heat up than smaller ones, explaining the longer delay time.

Threshold intensity of LIB on metal particle corresponds to that observed in experimental study [10] (qualitative comparison is complicated by various temporal profiles of laser pulse).

The computational results are presented in Fig. 6 in comparison with the experimental data [1] for flake aluminum particles in the hydrogen–oxygen–nitrogen mixture. Volume fraction of hydrogen is 15%. Volume fraction of oxygen changes from 15 to 35%. Mass fraction of particles is 1 g/m^3. At $Q = 150$ J, combustion of hydrogen takes place in small region adjacent to shock wave front. At $Q = 200$ J, the temperature and pressure in shock wave front increase, and volume fraction of hydrogen decreases on 20–30% for time of laser pulse. Further energy supply to mixture leads to considerable increase in temperature and pressure in the mixture, and development of unsteady gas dynamics processes in vapor aureole. At $Q = 300$ J, about 60% of hydrogen is used, and at $Q = 300$ J, about 95% of hydrogen burns beyond the shock wave front. The energy of laser pulse 350–400 J is the MPE of detonation.

Figure 7 shows the depth of penetration of laser beam into multiphase mixture and locations of melting front (line 1), evaporation front (line 2), and plasma formation front (line 3) as functions of mass fraction of particles. The melting, evaporation, and plasma formation take place under the corresponding lines (half of computational

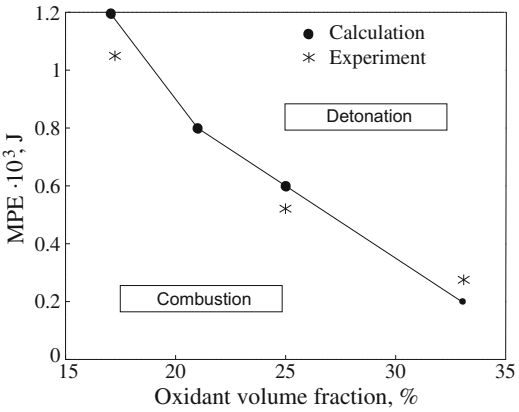

Fig. 6 MPE as a function of oxidizer volume fraction

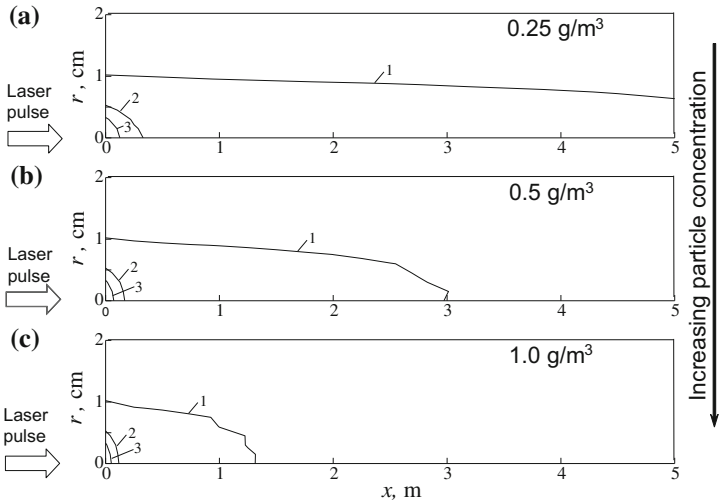

Fig. 7 Location of specific fronts at the end of laser pulse

domain is shown in the figures). When the mass fraction of particles increases, the regions of melting, evaporation, and plasma formation become smaller.

The state of the multiphase mixture is described by the accumulative operating characteristics which is the intensity that passed through the computational domain [4]

$$B(t,x,y,z) = \int_0^t I(\tau,x,y,z)d\tau.$$

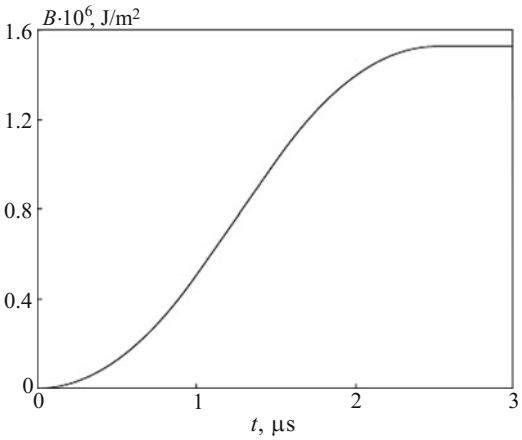

Fig. 8 Accumulative operating characteristic as a function of time

Table 1 Specific values of accumulative operating characteristics, J/cm^2

B_{sv}	$B_{vi} - B_{sv}$	$B_e - B_{vi}$
5.6×10^5	5.4×10^5	7.2×10^5

The specific values of the accumulative operating characteristics are the intensity of laser pulse that passed through domain from the time evaporation, ionization and optical breakdown started. Dependence of the accumulative operating characteristics on time from which laser pulse started is presented in Fig. 8.

The specific values are shown in Table 1, where B_{sv}, B_{vi} and B_e are the values of the accumulative operating characteristics corresponding to the start of evaporation, start of ionization, and start of optical breakdown. These values are only applicable to the mixture of the given composition and properties of the laser pulse. In new variables, dependencies describing interaction of laser pulse with particle (mass of particle, temperature of electronic component, and degree of ionization) have universal form.

For a given material of the solid phase, the momentum and energy exchange between the two phases depends on the particle volume fraction of the quiescent mixture ahead of the shock, and the particle size. The structure of the detonation wave is determined by the values of these two parameters. Higher initial particle volume fractions result in higher momentum and energy transfer rates, and the detonation wave speed is expected to drop as particle volume fraction increases. Lower particle diameters, under constant particle volume fraction, result in larger surface area of particles and, therefore, higher momentum and energy transfer from the gas to the particles. It is expected that smaller particle diameters produce larger drops in the detonation wave speed. The effect of particle size is weaker with comparison of the effect of particle volume fraction.

7 Conclusion

Experimental and computational studies have indicated the possibility of initiation of detonation using subcritical pulsed microwave discharges of various types. Detonation wave propagation in the combustion chamber is studied experimentally and numerically.

The mathematical formulation of the problem was divided into low-level models and high-level models. The low-level models correspond to the processes in the volume occupied by an individual particle. The high-level models correspond to the processes in the volume occupied by the multiphase mixture. The data obtained from solution of low-level problems are used to calculate source terms in the governing equations describing high-level model. The solution of high-level model provides volume fraction of particles and volume occupied by an individual particle.

Sub-models of optical breakdown on metal particle include heating of particle to boiling temperature, evaporation, and formation of vapor aureole around the particle, ionization of vapor aureole around particle and development of electron avalanche, appearance of micro-plasma spots and their expansion, and propagation of shock wave in the volume occupied by the particle. The threshold intensity of optical breakdown on individual metal particle, and its dependence on contributing factors (location of particle, total energy and time of laser pulse, radius of laser spot) are studied.

Laser-induced detonation in the mixture of hydrogen with flake aluminum particles is simulated based on Eulerian approach, and MPE of detonation is calculated. The results obtained agree well with the experimental data.

Acknowledgements This work was financially supported by the Ministry of Education and Science of Russian Federation (agreement No 14.578.21.0203, unique identifier of applied scientific research RFMEFI57816X0203).

References

1. Aleksandrov, B.S., Klimuk, E.A., Kutumov, K.A., Lacour, B.M., Puech, V., Troshchinenko, G.A.: A repetitively pulsed HF laser with a large discharge gap operating on the F_2-H_2 mixture. Quantum Electron. **35**, 805–808 (2005)
2. Bityurin, V.A., Brovkin, V.G., Vedenin, P.V.: Investigation of the electromagnetic wave scattering dynamics during microwave streamer evolution. J. Tech. Phys. **57**, 95–105 (2012)
3. Chang, R.K., Eickmans, J.H., Hsieh, W.-F., Wood, C.F., Zhang, J.-Z., Zheng, J.: Laser-induced break-down in large transparent water droplets. Appl. Opti. **27**, 2377–2385 (1988)
4. Emelyanov, V.N., Volkov, K.N.: Prediction of the characteristics of the process of interaction of pulsed laser radiation with gas-dispersed systems. J. Eng. Phys. Thermophys. **78**, 440–448 (2005)
5. Emelyanov, V.N., Volkov, K.N.: Numerical simulation of laser-induced detonation in mixture of hydrogen with suspended metal particles. Int. J. Hydrog. Energy **39**, 6222–6232 (2014)
6. Fomin, P.A., Chen, J.-R.: Effect of chemically inert particles on parameters and suppression of detonation in gases, Combustion. Explos. Shock Waves **45**, 303–313 (2009)
7. Frost, D.L., Zhang, F.: Non-ideal blast waves from heterogeneous explosives. Mater. Sci. Forum **465–466**, 421–426 (2004)

8. Ingignoli, W., Veyssiere, B., Khasainov, B.A.: Study of detonation initiation in unconfined aluminium dust clouds. In: Gaseous and Heterogeneous Detonations, pp. 337–350. Moscow (1999)
9. Loth, E., Sivier, S., Baum, J.: Dusty detonation simulations with adaptive unstructured finite-elements. AIAA J. **35**, 1018–1024 (1997)
10. Negin, A.E., Osipov, V.P., Pakhomov, A.V.: Optical breakdown in aerosols under the influence of pulsed CO_2 laser radiation. Quantum Electron. **16**, 1458–1463 (1986)
11. Papalexandris, M.V.: Numerical simulation of detonations in mixtures of gases and solid particles. J. Fluid Mechan. **507**, 95–142 (2004)
12. Papalexandris, M.V.: The multidimensional structure of detonation waves in heterogeneous mixtures containing inert solid particles. In: Proceedings of the European Combustion Meeting. Louvain-la-Neuve (2005)
13. Qin, Q., Attenborough, K.: Characteristics and application of laser-generated acoustic shock waves in air. Appl. Acoust. **65**, 325–340 (2004)
14. Tanguay, V., Goroshin, S., Higgins, A.J., Zhang, F.: Aluminum particle combustion in high-speed detonation products. Combust. Sci. Technol. **181**, 670–693 (2009)
15. Tulis, A.J., Selman, J.R.: Detonation tube studies of aluminum particles dispersed in air. Proc. Combust. Inst. **19**, 655–663 (1982)
16. Volkov, K.: Laser-induced breakdown and detonation in gas-particle and gas-droplet mixtures. Horiz. World Phys. **284**, 127–178 (2015)
17. Vorobiev, V.S.: Plasma arising during the interaction of laser radiation with solids. Adv. Phys. Sci. **36**, 1129–1157 (1993)
18. Zhang, F., Grőnig, H., Van De Ven, A.: DDT and detonation waves in dust-air mixtures. Shock Waves **11**, 53–71 (2001)

Numerical Simulation of Reactive Gas Mixes Flows in the Detonation Engine

S. N. Martyushov

1 Introduction

Mathematical modeling of gas flows with chemical reaction, with deflagration and detonation reactions, namely flows in detonation engines, demands taking into account a large number of physical factors: viscosity (laminar or turbulent), heat conductivity, multicomponents diffusion, changing of energy from chemical reactions, and so on. Example of such complex mathematical model can be found in [1]. On the other hand, new constructions of detonation engines have complicated geometry of internal flows and using of non-ordinary boundary and initial conditions, for example [2–4].

In these conditions, numerical algorithm construction can be provided in two ways: first one—construction of algorithm from blocks for separate physical process (gas dynamics, kinetics, turbulence models) (this has place, in particular, inside of commercial complex of codes); second one—construction of algorithms consequently as a whole one with connection to demands of approximation, convergence, and conservativeness. In this paper, the attempt of the second way of an algorithm realization was made.

2 Mathematical Model

Mathematical model based on the full system of gas dynamics equations accompanied with the system of kinetic equations in the integral form was used for numerical simulation of flows of reactive gas mixes. The state equations for each component of

S. N. Martyushov (✉)
The Moscow Aviation Institute - National Research University,
Volokolamskoe 4, Moscow 125993, Russia
e-mail: martyush@mail.ru

K. Kontis (ed.), *Shock Wave Interactions*,
https://doi.org/10.1007/978-3-319-73180-3_25

gas are set in tabular form, thus the enthalpy of formation and heat conductivity are considered as tabular functions of temperature of gas mix (one temperature model). The gas mix was assumed to be nonviscous.

The system of the equations of ideal gas and the kinetic equations in the integral form for axial symmetric flows can be presented as follows:

$$\frac{d}{dt}\oint_V \overrightarrow{U}dV + \oint_S \vec{n}\hat{F}dS + \Phi = 0, \tag{1}$$

where conservative unknowns vector will be:$\overrightarrow{Q} = (\rho, \overrightarrow{m}, \rho e, \rho)c_i, i = 1, ..., n$, of length $i + 4$, $\rho, c_i = \rho_i/\rho$—component density and concentration per unit mass, consequently, $\Phi = (0, 0, 0, 0, \rho f_i)$—source term, vector of fluxes normal to boundary of control volume can be written in the form

$$\vec{F}_n = \vec{n}\hat{F} = (\vec{m}, \vec{m}/\rho + P\vec{I}, \vec{m}(e + P) / \rho, \vec{m}c_i),$$

where pressure $P = \rho R_B T \sum c_i/\mu_i$—equation of state,

$$e = R_B T \sum c_i/\mu_i/(\gamma - 1) + V^2/2 + \sum c_i h_i$$

full energy of finite volume, $\sum c_i h_i$—internal energy of chemical reactions.

Equations of chemical reactions can be presented as follows:

$$\sum_{i=1}^{N} \alpha_{ij} A_i = \sum_{i=1}^{N} \beta_{ij} B_i \, j = 1, ..., M,$$

where M, N—number of reactions and components of the mix, α_{ij}, β_{ij}—stoichiometric coefficients of direct and inverse reactions. Arrhenius hypothesis is predicted for calculating the speeds of changing of mix components concentration (Eq. 1, source term)

$$f_i = \frac{dc_i}{dt} = \sum_{i=1}^{M} (\beta_{ij} - \alpha_{ij}) W_j(\vec{c}, T), \tag{2}$$

where

$$W_j(\vec{c}, T) = k_f \prod_{i=1}^{N} c_i^{\alpha_{ij}} - k_b \prod_{i=1}^{N} c_i^{\beta_{ij}}$$

$$k_{f,b} = A_{f,k} T^{l_{f,b}} exp(-E_{f,b}/RT).$$

Scheme with 9 hydrogen–air reactions, similar to the one used in [2] was used.

$$H_{(2)} + O_{(2)} = 2OH; H + O_{(2)} = OH + O;$$

$$OH + H_{(2)} = H_{(2)}O; OH + M = H_{(2)}O_{(2)} + M;$$

$$H + H_{(2)}O_{(2)} = H_{(2)} + HO_{(2)}; H + O_{(2)} + M$$

$$H_{(2)} + O = OH + H; 2H + M = H_{(2)} + M;$$

$$2HO_{(2)} = 2HO + O_{(2)}$$

3 Numerical Algorithm

For application of modern TVD or ENO algorithms, transition to characteristic variables of full system of the equations for any number of components of gas mixes is carried out. This procedure should be made because of convergence of arbitrary TVD-algorithm vas proved in [7] only for one equation. Decomposition on eigenvectors was made for real tabular equations of state. Transition was performed by Roe–Pike method, for which we need not explicit definition of left eigenvectors matrix. For this procedure sufficient to found intensity of characteristic waves. Let us define difference of fluxes

$$\Delta F = F_R - F_L = \sum_{k=1}^{N} \Delta_{i+1/2} W_k \lambda_k \vec{r}_k,$$

here $\Delta_{i+1/2} W_k$—intensity of k-characteristic wave. For calculation of flow throw the bound of control volume we use the next relations:

$$F_L + \sum_{\lambda_k > 0}^{N} \Delta_{i+1/2} W_k \lambda_k \vec{r}_i = F_R + \sum_{\lambda_k < 0}^{N} \Delta_{i+1/2} W_k \lambda_k \vec{r}_i$$

$$F_{i+1/2} = \frac{1}{2}(F_L + F_R) - \frac{1}{2} \sum_{i=1}^{N} \Delta_{i+1/2} W_k |\lambda_k| r_k, \tag{3}$$

where $\vec{r}_i, \vec{L}_i$—right and left eigenvectors of Jacobian matrix $A(\vec{Q}) = \partial \vec{F}_n / \partial \vec{Q}$, $\Delta \vec{W} = \vec{L} \Delta \vec{Q}$.

For finding $\Delta \vec{W}$, one can use equality $\Delta \vec{W} \vec{R} = \Delta \vec{Q}$, where

$$\Delta \vec{Q} = (\Delta\rho, \Delta(\rho U), \Delta(\rho V), \Delta E, \Delta(\rho c_1), ..., \Delta(\rho c_n))^T.$$

System of the right eigenvectors $\vec{r}_i$ for $A(\vec{Q}) = \partial\vec{F}_n/\partial\vec{Q}$ can be taken in the form:

$\vec{r_1} = (0, 0, 1, V, 0, ..., 0)^T$
$\vec{r_2} = (0, 0, 1, V, 0, ..., 0)^T,$
$\vec{r_3} = (1, U + a, V, H + Ua, c_1, ..., c_n)^T,$
$\vec{r_4} = (1, U - a, V, H - Ua, c_1, ..., c_n)^T,$
$\vec{r_5} = (0, 0, 0, h_1, 1, ..., 0)^T,$
$\vec{r_6} = (0, 0, 0, h_2, 0, 1, ..., 0)^T,$
$\vec{r_n} = (0, 0, 0, h_n, 0, ..., 1)^T,$
$\vec{\lambda} = (U, U, U + a, U - a, U, ..., U),$

where $U = \vec{V}\vec{n}$, $V = \vec{V}\vec{\tau}$—normal and tangential to bound of control volume components of gas velocity. Denoting $\Delta W = (\alpha_1, \alpha_2..., \alpha_n)$, we can solve system of linear equations for finding components $\alpha_1, \alpha_2..., \alpha_n$:

$$\alpha_2 + \alpha_3 + \alpha_4 = \Delta\rho \tag{4}$$

$U\alpha_2 + (U + a)\alpha_3 + (U - a)\alpha_4 = \Delta(\rho U)$
$\alpha_1 + V\alpha_2 + V\alpha_3 + V\alpha_4 = \Delta(\rho v)$
$V\alpha_1 + \omega\alpha_2 + (H + Ua)\alpha_3$
$+(H - Ua)\alpha_4 + \Sigma_{i=1}^{n}\alpha_i h_i = \Delta(E)$
$c_i(\alpha_3 + \alpha_4) + \alpha_i = \Delta(\rho c_i)$

System (4) has the simple decision for arbitrary number of gas mix components:

$$\alpha_2 = \Delta\rho(H - U^2 - \Sigma_{i=1}^{n} c_i h_i) \tag{5}$$

$+\Delta(\rho U)U + \Sigma_{i=1}^{n} h_i\Delta(\rho c_i) - \tilde{E})/\omega$
$\alpha_4 = ((U + a)\Delta\rho - \Delta(\rho U) - a\alpha_2)/2a;$
$\alpha_3 = (-(U - a)\Delta\rho + \Delta(\rho U) - a\alpha_2)/2a;$
$\alpha_1 = \Delta(\rho V) - V\Delta\rho$
$\alpha_{i+4} = \Delta(\rho c_i) - c_i(\Delta\rho U - \alpha_2), i = 1, ..., n$
$\tilde{E} = \Delta E - V(\Delta(\rho V) - V\Delta\rho).$

Analogous formulae can be written for three-dimensional case. For state equations of real gases, mathematical model (1)–(5) was modified in the next way. Adiabatic quotient γ was calculated in connection with classic formulae for value of γ for one, two, and three atomic gases:

$$\gamma = \Sigma_{i1}5c_i/7 + \Sigma_{i2}5c_i/3 + \Sigma_{i3}4c_i/7$$

where $i1, i2, i3$—number of one, two, and three atomic components of gas mixes. Calculation of temperature on every time step was provided with respect to dependence of enthalpy formation from temperature by iterative algorithm:

$$P = (\gamma - 1)(\rho e - \rho \vec{V}^2/2 + \Sigma_i \rho_i h_i(T_n), \tag{6}$$

$$T_{n+1} = P/\rho R_B \sum \frac{c_i}{\mu_i}$$

In connection with [3] for real state equations, parameter ω for the calculation of α_2 was calculated by the formulae

$$\omega = H - \rho U^2/(\partial P/\partial i),$$

where i—internal energy of gas mix (for ideal gases $\omega = a^2/(\gamma - 1)$.

The second aspect of numerical algorithm, which should be provided for all equations and processes simultaneously, is normalizing of all physical unknowns. Because of high meanings of chemical reaction constants and of temperature value during detonation process, normalizing of gas dynamics parameters and constants of Arrhenius formulae where providing, namely: pressure was normalized by $\rho_0 q$, temperature—by q/R, where q, R—enthalpy of formation of mass unit for water (gas) and gas constant for dry air. Time was normalized by $l/\sqrt{q}$, gas velocity and sound speed was normalized by $\sqrt{q}$. Energy of activation of mass unit $E_{f,b}$ and pre-exponential factor in (2) were normalized by q and $\sqrt{q}$, consequently (as usual for gas dynamics equation constant of normalizing is speed of sound of resting gas).

The third aspect of numerical algorithm, which should be provided for all equations and processes simultaneously, is one scale of time step. System of equations of kinetics are stuff systems of ODE's, which can be solved separately by numerical multistep methods for ODE (Gir algorithm for stuff systems, for example). Multistep method for gas dynamics system (Runge–Kutta as usual) has its own time step. In this situation, it seems natural to use one time approximation for all processes (in this work Runge–Kutta was used). Spatial discretization was made on the basis of TVD schemes of Harten and Chakravarthy–Osher.

The last element of algorithm, which should be discussed, is non-usual boundary condition. Some constructions of detonation engines are [2–4] based on the effect of periodic (in time or space) closing of the ring nozzle. Nonstationary boundary condition in this case can be formulated in the following form. Meanings of pressure P', P'' for supersonic and subsonic regimes of flows for Laval nozzle (with quotient $S/S_* = \lambda$ and meanings of gas dynamics values in reactor ρ_m, P_m) can be found as roots of nonlinear equation:

$$(P/P_m)^{1/\gamma}(1 - (P/P_m)^{(\gamma-1)/\gamma})^{1/2} = (2/(\gamma + 1))^{1/(\gamma-1)}((\gamma - 1)/(\gamma + 1))^{1/2}/\lambda \tag{7}$$

In these conditions, gas dynamics values on Laval nozzle exit can be found as follows:

$u = 0$ when $P_m < P_p$;

$P = P_p$ when $P' < P_p < P_m$;

$$P = P', u = u_{max}\sqrt{1 - (P/P_m)^{(\gamma-1)/\gamma}} \tag{8}$$

$\rho = \rho_*(P/P_*)^{1/\gamma}$

when $P'' < P_p < PP^m$

$\rho u S = \rho_* u_* S_*$, $\gamma P/(\gamma - 1)\rho + u^2/2 = u_{max}^2/2$

when $P_p < P''$.

4 Numerical Simulations of Test Problem: Detonation Appearing on the Front of Plane Strong Shock Wave

Plane shock wave is situated in two-dimensional channel between two cylinders, filled with hydrogen–oxygen mix moving with the speed of shock wave(shock wave initially stable). From some value of intensity of shock (Mach of shock wave is near to 4.2) at some time from the beginning of calculation process spot of detonation on the front of shock wave appears. This detonation structure grows faster in size and begins to interfere with borders of the channel. This Mach interference lead to accelerating of wave front, wave became a detonation one, and line of it front became characteristic "tulpe" form, Fig. 1. Chemical reactions on the front are proved by level lines of concentration of hydrogen, Fig. 2.

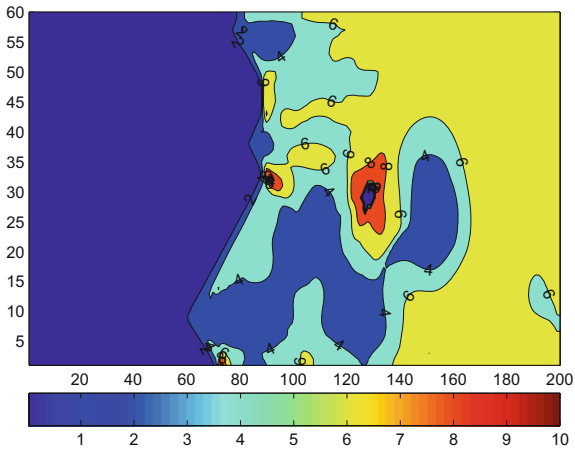

Fig. 1 Isopicts of detonation spot on the shock wave

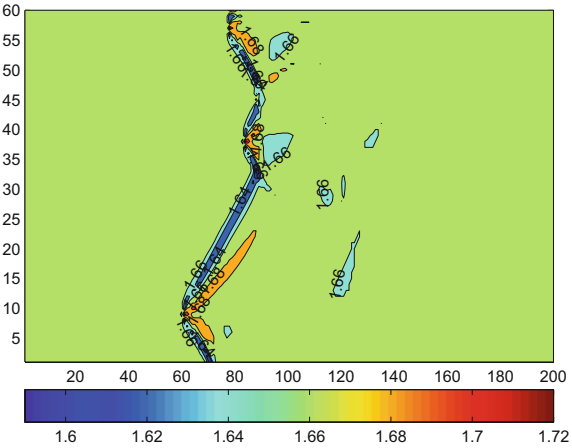

Fig. 2 Level lines of hydrogen concentration for the same time moment

5 Numerical Simulations of Flow in Levin–Tarasov Detonation Engine

Different designs of detonation engine have been proposed and investigated during the past decades. The advantages of type of detonation engine, introduced in [2] are: the absence of moving parts in its design; continuity injection of fuel into resonator; and very high frequencies of cycles. This engine comprises a reactor, where fuel–oxidizer mixture is prepared for detonation and a resonator chamber of semisphere form, Fig. 1.

By the idea of authors, the detonation cycle consists of the next steps:

(1) jet from ring nozzle focus near the center of the resonator and reject as spherical shock wave;
(2) shock rich the bounds of resonator, reject from it, and again focus near center, which provide detonation wave;
(3) spherical detonation wave moves to the bound of the resonator, when it rich it ring nozzle is closed;
(4) Intensive jet of products of detonation moves from the resonator, pressure in the resonator fall down, ring nozzle become open and new cycle of engine periodic work begin.

Flow in Levin–Tarasov detonation engine was investigated numerically by number of authors (one of the best investigations was made by [6]). As a result, the detonation appears not only at every cycle of pulsation in resonator but also at other cycles which consist of fast deflagration. This phenomena cannot be explained in scheme of flow in resonator, which was declared by authors of construction [4] (Fig. 3).

Aim of our investigation was testing the structure of flow in resonator during working cycle and in particular at the moment of detonation appearing. Numerical

simulations were provided on the basis of mathematical model explained in previous section. By the results of calculation (Figs. 4 and 5), zone of high pressure and temperature establishes near bound of resonator. In this region, large amount of gas mix is collected. Without connection to rejection of ring jet from the center of the resonator, this amount enlarges and at one moment begins to move to the exit from resonator. During this movement, high-speed rotor near ring nozzle appears and close it. query Kindly check the phrase 'and close it' for clarity.

Moment of detonation appearing in pulsing detonation engine of Levin–Tarasov can be defined by the rising of pressure in resonator and, closing of ring nozzle (numerically defined by boundary condition (8)). Detonation appears in ring rotor flow near nozzle Fig. 4. After closing of resonator chamber, strong jet of products of detonation propagates outside the resonator Fig. 5. As a result, it can be pointed work of this detonation engine based on fast deflagration appearing as the result of heating walls of resonator and that detonation appears ones for some circles in dependence of resonator size.

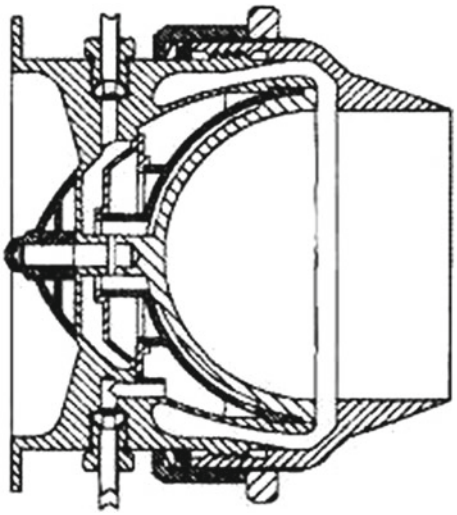

Fig. 3 Scheme of resonator of PDE with ring nozzle

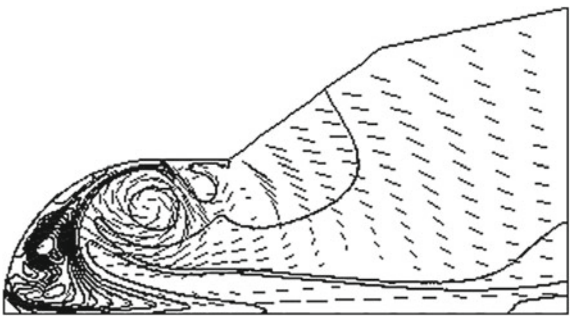

Fig. 4 Isopicts and velocity vectors in resonator when ring nozzle closing

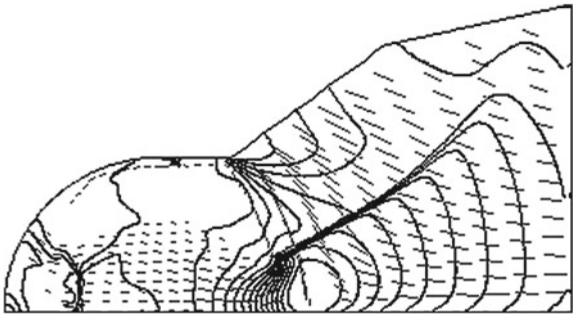

Fig. 5 Isopicts and velocity vectors in resonator; jet expansion

6 Conclusions

Nonlinear difference TVD method for the calculation of problems of reactive gas mixes flows (with arbitrary number of components and real equations of state for them), especially for detonation wave appearance for curvilinear grids for nonviscous case was constructed.

Test problem of detonation appearing on plane shock wave of sufficient intensity was calculated for the verification of numerical method.

Flow in resonator chamber of well-known Levin–Tarasov PDD was numerically simulated and mechanism of nonperiodic detonation appearance was discussed.

References

1. Liberman, M.A., Ivanov, M.F., Valyev, D.M.: Sci. Tech. **178**, 1613 (2006)
2. Levin, V.A., Nechaev, Y.N., Tarasov, A.I.: Control of detonation processes. In: Roy, G. (ed.), pp. 197–201. Moscow, Elex-KM Publishers (2000)
3. Jdan, S.A., Bykovsky, F.A., Vedernikov, E.F.: Continuous spin and pulse detonation of hydrogen-air mixtures in supersonic flow generated by a detonation wave. In: Proceediings of 22 ICDERS. Minsk, Belarus (2009)
4. Voitsehovsky, B.V.: Stationery Detonation. Dokl. Akad. Sci. USSR. **129**(6), 1254–1256 (1959)
5. Yee, H.C., Warming, R.P., Harten, A.: Application of TVD-scheme for the Euler equations of gas dynamics. Lect. Ap. Math. **22**(2), 357–377 (1985)
6. Fujivara, T.: Investigation of pulsing detonation engines in Japan. In: Frolov, C.M. (ed.), pp. 493–517. Moscow, Torus Press (2006)
7. Glaister, P.J.: An approximation linearised riemann solver for the three-dimensional euler equations for real gas using operator splitting. J. Comp. Phys. **77**, 361–383 (1988)

On the Propagation of Planar Blast Waves Through Nonuniform Channels

J. T. Peace and F. K. Lu

Nomenculture

a	Sound speed, m/s
A	Channel cross-sectional area, m^2
M	Mach number
p	Pressure, N/m^2
Q	$\partial p/\partial t + \rho a \partial u/\partial t$, kg/m-$s^3$
t	Time coordinate, s
u	Velocity, m/s
W	Shock wave velocity, m/s
x	Axial coordinate, m
α	Coefficient function
β	Coefficient function
γ	Ratio of specific heats
ρ	Density, kg/m^3

Subscripts

0	Initial or undisturbed gas state
s	Property on the shock

J. T. Peace (✉) · F. K. Lu
Mechanical and Aerospace Engineering Department, Aerodynamics Research Center, University of Texas at Arlington, Arlington, TX 76019, USA
e-mail: james.peace@mavs.uta.edu

F. K. Lu
e-mail: franklu@uta.edu

K. Kontis (ed.), *Shock Wave Interactions*,
https://doi.org/10.1007/978-3-319-73180-3_26

1 Introduction

The propagation of shock waves through nonuniform channels with slowly varying cross sections has been studied analytically from the 1950s. Notably, the work of [1] was one of the first analytical treatments of shock wave dynamics in a channel. Chester provided a linearized solution to the problem of a transmitted shock wave in a channel of nonuniform cross-sectional area, namely, channels that feature monotonically increasing or decreasing cross-sectional area. The solution allowed for an approximate determination of the change in shock strength over a finite length of channel of arbitrary shape. A significant result was that the shock strength averaged at any time over the flow cross-sectional area is proportional to the change in area of the channel. A similar theoretical treatment by Chisnell [2] yielded a closed-form approximate expression for the change in shock strength as a function of channel area by using a steady-state analysis. This was achieved by neglecting the reflected disturbances generated by the shock. The final major theoretical treatment was that of [3]. Whitham's theory allowed for the computation of the shock motion without directly determining the flow field following the shock. The shock motion was determined by integrating the Rankine–Hugoniot shock jump conditions on the forward propagating characteristic, which yielded an explicit relationship for the channel area and the local Mach number. The shock strength and channel area relation obtained is exact to that of Chester and Chisnell. This approximate theory has been used in analyzing the motion of shock waves in various geometries with accurate results. Collectively, the theory is known as the CCW theory in recognition of the three authors. It can also be noted that the CCW theory is the basis for formulating the theory of geometrical shock dynamics [4].

In the case of blast waves, or shock motion with a nonuniform flow field following the shock, the application of the CCW theory is not entirely appropriate. This is due to the CCW theory neglecting gradients in the flow field just behind a shock wave, which strictly prohibits its application to initially uniformly propagating shocks. In regards to this aspect, [5] provided a theoretical framework for the generalization of the CCW theory. The motion of a shock through a channel of slowly varying cross section was reconsidered and described by an infinite sequence of ordinary differential equations. Truncation was used to show the varying degree of approximation between the original CCW theory and the generalized CCW theory with the inclusion of higher order terms for cylindrical and spherical shock motion. In this manner, a nonuniform flow field following the shock can be taken into account. Best applied the generalized theory successfully to the propagation of underwater blast waves. The theory was shown to have excellent agreement with the approximate Kirkwood–Bethe [6] method.

The focus of the current work is to understand the propagation of planar blast waves through nonuniform channels using the generalized theory of Best. It is desired to analyze the case of an arbitrary strength shock that is being overtaken by a rarefaction wave. For this particular wave process, the overtaking rarefaction creates a nonuniformity in the flow behind the shock that can largely influence the

shock wave propagation dynamics as it traverses through a channel area change. The original CCW theory is unable to account for this nonuniformity that is present in decaying shock and blast wave profiles. For the case of a decaying shock wave, the shock profile has been analytically described by Sharma et al. [7] and will be used in conjunction with the generalized CCW theory. Similarly, the classical [8–10] (S–vN–T) blast wave will be analyzed with the generalized theory. The present analysis will enable the description of blast wave dynamics for both an arbitrary strength shock and in the case of a strong shock limit assumption. The dynamics of such planar waves in nonuniform channels have yet to be discussed in the literature when accounting for the nonuniform flow behind the wave. Lastly, the results will be compared with the results of planar shock waves to demonstrate the difference in shock and blast propagation through nonuniform channels.

2 Governing Equations

2.1 Area–Mach Relation

The area–Mach (A–M) relation is a classical result obtained by [1–3] from linearization of the governing equations of inviscid, quasi-one-dimensional flow with no heat transfer or mass addition. Substituting the Rankine–Hugoniot shock jump conditions on the forward propagating C_+ characteristic yields the ordinary differential equation

$$\frac{dM}{dx} = -\frac{1}{g(M)}\frac{A'(x)}{A(x)} \tag{1}$$

where the prime denotes the derivative in $A(x)$, and where the function $g(M)$ is given by

$$g(M) = \frac{M}{M^2-1}\left(1+\frac{2}{\gamma+1}\frac{1-\mu^2}{\mu}\right) \times \left(1+2\mu+\frac{1}{M^2}\right) \tag{2}$$

and

$$\mu^2 = \frac{(\gamma-1)M^2+2}{2\gamma M^2-(\gamma-1)} \tag{3}$$

It is noted that through linearization, the accuracy of the above result is dependent upon the condition that

$$a_0 M\frac{\rho a^2 u}{a+u}\left|\frac{A'(x)}{A(x)}\right| \gg \left|\frac{a_0 M}{a+u}-1\right|\left|\frac{\partial p}{\partial t}+\rho a\frac{\partial u}{\partial t}\right|$$

([5]). The term $\left|a_0 M/(a+u)-1\right|$ is a measure of the coincidence of the C_+ characteristic and the shock wave; it becomes zero as $M \to 1$, and approaches 0.215 as $M \to \infty$ for $\gamma = 7/5$. Similarly, the term $|\partial p/\partial t + \rho a \partial u/\partial t|$ is a measure of the nonuniformity of the flow behind the shock and is exactly zero for uniform planar shock motion, but is generally very small for planar shock waves [11]. These conditions are what justify the assumptions of (1) and make the A–M relation a good approximation for describing the dynamics and strength of a shock wave as it traverses through a nonuniform area change.

2.2 Higher Order Equations

For the cases of decaying shock and blast wave propagation, such that the wave is continuously being overtaken by a rarefaction wave, the term $|\partial p/\partial t + \rho a \partial u/\partial t|$ can be very large, thereby violating the inequality relation that permits use of the A–M relation. This is especially true if the transient and spatial decay rates of such waves are rapid. The theory of shock dynamics must therefore be extended to take into account the nonuniformity of the flow following the shock wave. This generalization was carried out by Best [5]. Best reconsidered the propagation of a shock wave down a channel of slowly varying cross section and determined that the motion of the shock wave is governed by an infinite sequence of ordinary differential equations given by

$$\frac{dM}{dx} = -\left[\frac{1}{g(M)}\frac{A'(x)}{A(x)} + f(M)\,Q_1\right], \tag{4}$$

where

$$\begin{aligned}\frac{dQ_n}{dx} = -\Bigg[&\frac{\partial^n}{\partial t}\left(\frac{\rho a^2 u}{a+u}\right)\frac{A'(x)}{A(x)} \\ &+ \sum_{i=1}^{n}\left\{\binom{n}{i}\frac{\partial^i}{\partial t}\left(\frac{1}{a+u}\right)Q_{n+1-i}\right\} \\ &+ \frac{\partial^{n-1}}{\partial t}\left(\frac{\partial(\rho a)}{\partial t}\frac{\partial u}{\partial x} - \frac{\partial(\rho a)}{\partial x}\frac{\partial u}{\partial t}\right) \\ &+ \left(\frac{1}{a+u} - \frac{1}{a_0 M}\right)Q_{n+1}\Bigg]\end{aligned} \tag{5}$$

for $n = 1, 2, 3, \ldots$, where the variables Q_n are defined by $Q_n = \partial_t^{n-1}(\partial p/\partial t + \rho a \partial u/\partial t)$,

$$\begin{aligned}f(M) = (\gamma+1)\Big((\gamma-1)M^2+2\Big)\Big((\gamma-1)M^2 \\ -(\gamma+1)\nu M+2\Big)\Big\{2a_0^3 M\rho_0\Big(2M^2\end{aligned}$$

$$+(\gamma+1)\nu M-2\Big)\Big((\gamma+1)\nu \tag{6}$$
$$+2(\gamma-1)M^3+(\gamma+1)\nu M^2+4M\Big)\Big\}^{-1}$$

and

$$\nu^2=\frac{\Big((\gamma-1)M^2+2\Big)\Big(2\gamma M^2-(\gamma-1)\Big)}{(\gamma+1)^2M^2} \tag{7}$$

These equations have been recast from that reported by Best for convenience to include ordinary derivatives of the spatial coordinate x as opposed to time t. By using the general Leibniz rule combined with the characteristic form of the governing equations, Best obtained explicit formulas for the nth-order time and space partial derivatives of p, u, ρ, and a. These formulas are not repeated here; however, it is noted that the expressions were reduced in terms of the Rankine–Hugoniot shock jump conditions and channel area profile.

It is obvious that truncation is required in order to obtain a closed set of ordinary differential equations in terms of the Mach number M and variables Q_n. As a first-order approximation for $n=0$, (5) becomes null and therefore truncating Q_1 in (4) yields the classical CCW A–M relation. Moreover, for higher order approximations, the term Q_{n+1} is truncated to yield a closed set of $n+1$ coupled ordinary differential equations in the variables M and Q_n such that each equation is coupled to its successor. This is the same closure scheme of [5], where details regarding the convergence of such a closure scheme were discussed.

For the purposes of this work, only a second-order approximation is considered and the resulting equation set is used to describe the motion of decaying shock waves and blast waves in nonuniform channels. Therefore, with $n=1$, the resulting equation set takes the form

$$\frac{dM}{dx}=-\left[\frac{1}{g(M)}\frac{A'(x)}{A(x)}+f(M)Q\right] \tag{8a}$$

$$\frac{dQ}{dx}=-\left[\frac{\partial}{\partial t}\left(\frac{\rho a^2u}{a+u}\right)\frac{A'(x)}{A(x)}+\frac{\partial}{\partial t}(\rho a)\frac{\partial u}{\partial x}\right.$$
$$\left.-\frac{\partial}{\partial x}(\rho a)\frac{\partial u}{\partial t}+\frac{\partial}{\partial t}\left(\frac{1}{a+u}\right)Q\right] \tag{8b}$$

In the above equations, Q_1 has been replaced with Q, where $Q=\partial p/\partial t+\rho a\partial u/\partial t$. The nonuniformity of the flow following the shock is accounted for in this second-order approximation. In essence, this second-order approximation allows for an analytical description of waves in nonuniform channels where the initial value of Q is nonzero. In the event the initial condition $Q_0=0$, namely the gradients in the flow field following the shock are exactly zero, the shock motion is simply that of a uniformly propagating shock. However, in the case where $Q_0<0$, the shock motion is

representative of a shock that is being overtaken by a rarefaction wave resulting in the propagation of a decaying shock. It is also worth noting that for decaying shock and blast waves, the rarefaction following the wave is continuously overtaking the wave causing a decrease in the strength and speed of the wave as it propagates. Similarly, when the wave is subjected to a nonuniform area change, the effects of the changing area alter the wave dynamics. This process is a coupling between the effects of the following rarefaction and the change in channel cross-sectional area. The current work does not exactly treat this coupling in closed form. However, the effects of the overtaking rarefaction enter the analysis through the initial condition imposed on Q. This aspect will be further discussed in the following sections.

As previously mentioned, it is desired to use the second-order approximation of (8) in the context of the strong shock limit to analyze the behavior of the S–vN–T blast wave in nonuniform channels. In the development of the S–vN–T blast wave theory, the pressure ahead of the wave is assumed to be negligible compared to the pressure behind the wave. As a result, the Mach number becomes a meaningless quantity and focus must be redirected to the shock wave speed $W = a_0 M$. Applying this consideration and the strong shock limit to (8), the equations can be recast into the form

$$\frac{dW}{dx} = -\left[\frac{1}{r(W)}\frac{A'(x)}{A(x)} + s(W)\,Q\right] \tag{9a}$$

$$\frac{dQ}{dx} = -\left[\frac{\partial}{\partial t}\left(\frac{\rho a^2 u}{a+u}\right)\frac{A'(x)}{A(x)} + \frac{\partial}{\partial t}(\rho a)\frac{\partial u}{\partial x} - \frac{\partial}{\partial x}(\rho a)\frac{\partial u}{\partial t} + \frac{\partial}{\partial t}\left(\frac{1}{a+u}\right)Q\right], \tag{9b}$$

where the functions

$$r(W) = \frac{\left(2+\lambda\right)\left(\lambda + 2(\gamma-1)\right)}{\lambda^2 W} \tag{10}$$

and

$$s(W) = \frac{(\gamma-1)(\gamma+1)(\lambda-\gamma+1)}{2\rho_0 W^2(\lambda+2)(\lambda+2(\gamma-1))} \tag{11}$$

with

$$\lambda^2 = 2\gamma(\gamma-1) \tag{12}$$

Hence, in the strong shock limit for blast waves, two coupled ordinary differential equations are obtained in the shock speed W and variable Q.

A final remark is given regarding the nature of the second equation in (8) and (9). Substitution of the first-order partial time and space derivatives is required to show

the complete structure of these equations. By using the formulas obtained by [5], the Rankine–Hugoniot shock jump conditions for (8b), and the strong shock limit jump conditions for (9b), the following equations are obtained:

$$\begin{aligned}\frac{dQ}{dx} &= \alpha_1(M)\frac{A'(x)}{A(x)}Q + \alpha_2(M)\frac{dM}{dx}Q \\ &+ \alpha_3(M)\left(\frac{dM}{dx}\right)^2 + \alpha_4(M)\frac{A'(x)}{A(x)}\frac{dM}{dx} \\ &+ \alpha_5(M)\left(\frac{A'(x)}{A(x)}\right)^2\end{aligned} \tag{13}$$

$$\begin{aligned}\frac{dQ}{dx} &= \beta_1(W)\frac{A'(x)}{A(x)}Q + \beta_2(W)\frac{dW}{dx}Q \\ &+ \beta_3(W)\left(\frac{dW}{dx}\right)^2 + \beta_4(W)\frac{A'(x)}{A(x)}\frac{dW}{dx} \\ &+ \beta_5(W)\left(\frac{A'(x)}{A(x)}\right)^2\end{aligned} \tag{14}$$

In this form, α_i has functional dependence $\alpha_i = \alpha_i\left[p, u, \rho, a, dp/dM, du/dM, d\rho/dM\right]$ where β_i in the strong shock limit has functional dependence $\beta_i = \beta_i\left[p, u, a, dp/dW\right]$. Explicit formulas were obtained within a Mathematica environment for α_i and β_i; for brevity, these relations are not reported here. It is evident that the shock wave motion for a second-order approximation is governed by two first-order coupled nonlinear ordinary differential equations. A Mathematica environment was used to numerically compute solutions to these governing equations given a channel cross-sectional area profile $A(x)$ and initial conditions M_0 or W_0, and Q_0.

3 Shock and Blast Wave Propagation

3.1 Decaying Planar Shock Wave

For application of the current work to planar decaying shock waves, it is required to know the behavior of these waves in constant cross-sectional area channels. Sharma et al. [7] provided an analytical solution for the case of a shock wave that is being overtaken by a rarefaction wave. The solution satisfies the governing equations and most of the boundary conditions but only approximately satisfies the entropy and particle velocity jump boundary conditions. Despite this aspect, the resulting error was determined to be very small even for strong shock waves. The nature of the solution is self-similar with respect to the variable $z = t/h$ where h is the Lagrangian

mass coordinate and has the relationship, $\partial x/\partial h = 1/\rho$. Moreover, the solution is obtained by considering a piston in a confined channel that begins to move forward with a prescribed velocity into an undisturbed gas that is initially at rest. The instantaneous piston motion at $t = -t_p$ from a distance $x = -x_p$ creates a uniform shock wave with Mach number M_s that begins to traverse the length of the channel. At a later instant, the piston suddenly stops at $t = 0$ and distance $x = 0$, propagating an unsteady rarefaction into the disturbed uniform gas behind the shock wave. At a time defined by t_0 and distance x_0, the leading characteristic of the unsteady rarefaction catches the shock wave and begins to overtake the shock. The analytical solution is dependent upon the change in entropy state behind the shock at the initial and final conditions of the decay.

Sharma et al. [7] detailed the behavior of the decay from the initial shock strength to an eventual acoustic wave using a derived shock propagation law. This solution is shown for an initial shock Mach number of 3.0 for various values of γ in Figs. 1 and 2. Although, not shown in these figures, the far-field behavior as $x/x_0 \to \infty$ approaches

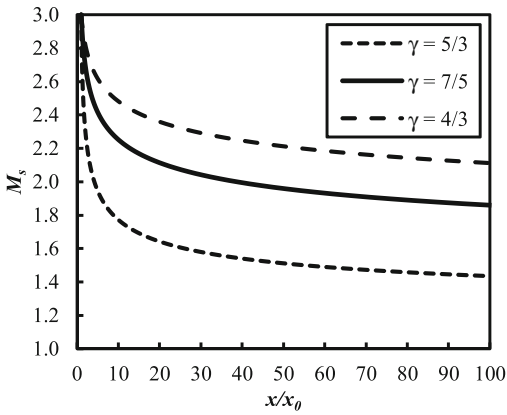

Fig. 1 Planar shock wave Mach number decay versus x/x_0

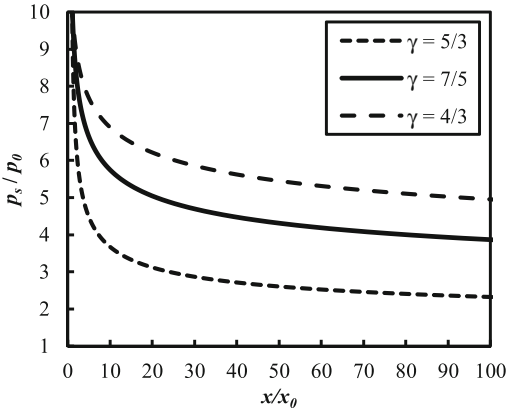

Fig. 2 Planar shock wave pressure ratio decay versus x/x_0

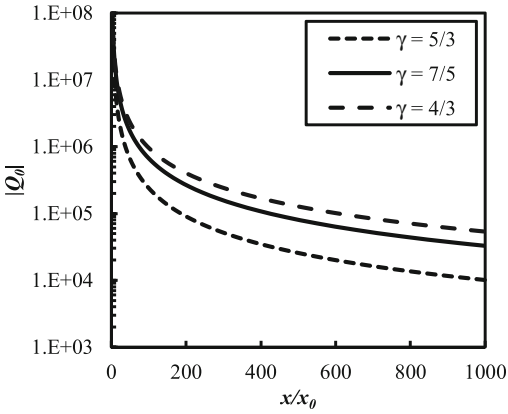

Fig. 3 $|Q| = |\partial p/\partial t + ua\partial u/\partial t|$ evaluated on the decaying shock versus x/x_0 in units of kg/m-s^3

that of an acoustic wave of $M = 1$ and $p_s/p_0 = 1$ as a result of the Riemann invariant. Despite not showing the far-field solution, it can be noted that at a distance of $x/x_0 = 10$, the quantity $|\nabla p_s/\nabla p_{s,0}|$ evaluated on the shock has approached 0.004, 0.028, and 0.052 for $\gamma = 5/3$, $7/5$, and $4/3$, respectively. This is an indication that the spatial decay rate is very rapid in the immediate near-field region of the decaying shock solution.

Although the spatial decay rate is shown to only be rapid in the near field, the defined quantity Q is the main parameter of interest for the current work. Evaluation of $Q = \partial p/\partial t + ua\partial u/\partial t$ on the shock is shown in Fig. 3. It is evident that despite having a more gradual decay beyond $x/x_0 = 100$, the magnitude of $|Q_0|$, where the subscript indicates the initial condition for the Q equation, is relatively high even at a distance $x/x_0 = 1.0 \times 10^3$ for all values of γ. This is a consequence of the nonuniformity of the flow causing the decay in strength and speed of the shock wave. This result also demonstrates the invalidity of the A–M relation for describing the dynamics of a planar decaying shock wave that is subject to a given cross-sectional area change. The magnitude of $|Q|$ in this particular case would likely render the inequality condition that permits the use of the A–M relation untrue.

3.2 Sedov–von Neumann–Taylor Planar Blast Wave

Similar to the previous section, it is required to know the dynamics of the S–vN–T planar blast wave in a constant cross-sectional area channel for application of the current work. The classical planar blast wave solution was achieved by similarity arguments upon which a self-similar shock motion was derived as the result of an intense explosion subject to the strong shock limit. The solution is readily obtained by introducing an initial charge energy E_0 at the origin of the channel and applying the derived similarity relations.

It is important to note in the far field where the pressure ahead of the shock is no longer negligible, the strong shock limiting assumption begins to break down, making the blast solution invalid. More important, similarity break down once p_0 is introduced into the defining variables of the physical problem. It is for this reason that the solution of [7] is used in this study to analyze both arbitrary strength decaying shocks and shocks in the strong shock limit. For $t > 0$, the subsequent blast motion was obtained in closed form by Sedov [8] for a constant initial gas density; however, for the purposes of this work, the solution procedure outlined by Kamm [12] has been used. For an initial charge energy of 1.0 MJ and constant undisturbed gas density of $\rho_0 = 1.0\ \mathrm{kg/m^3}$, the blast motion and strength are shown in Figs. 4 and 5 for various values of γ, respectively. Physical variables are shown in order to differentiate between the different values of γ as a consequence of the self-similarity solution. In this representation, x_0 is defined as the distance traveled by the blast following a time of $t_0 = 1.0$ ms in order to negate the singularity at the origin. Similar to the decaying shock wave, the S–vN–T blast wave has a very rapid decay behavior in the near-field solution. In the case of planar blast waves at a distance of $x/x_0 = 10$, the quantity $|\nabla p_s/\nabla p_{s,0}|$ evaluated on the shock has approached 0.01 for all values of γ. This is again an indication that the spatial decay rate is very rapid in the immediate near-field region of the blast wave solution. However, as mentioned previously, the defined quantity Q is the main parameter of interest for the current work. Therefore, Q is once again evaluated on the shock for the S–vN–T blast solution and the results are shown in Fig. 6. It is evident that despite having a more gradual decay beyond $x/x_0 = 50$, the magnitude of $|Q_0|$ is very high even at a distance $x/x_0 = 1.0 \times 10^3$ for all values of γ. This is attributed to the nonuniformity of the flow causing the rapid decay in strength and speed of the blast wave. This result also demonstrates the invalidity of the A–M relation for describing the dynamics of a planar blast wave when traversing a cross-sectional area change.

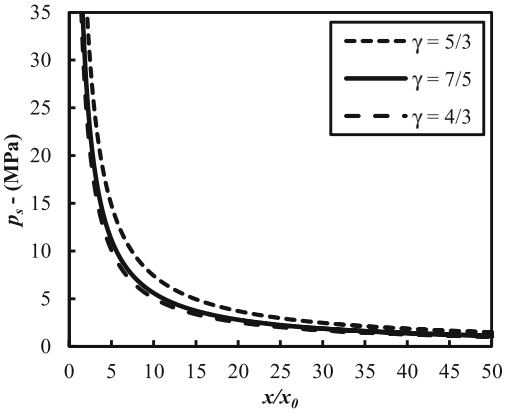

Fig. 4 Planar S–vN–T blast wave velocity decay versus x/x_0

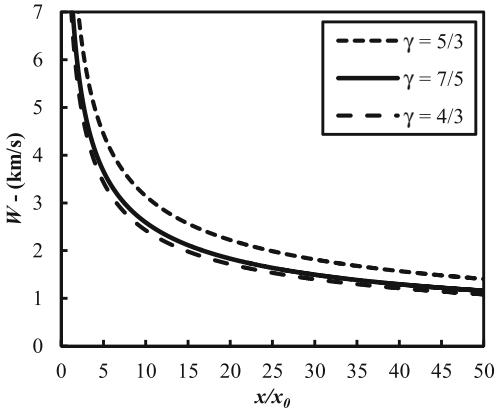

Fig. 5 Planar S–vN–T blast wave pressure decay versus x/x_0

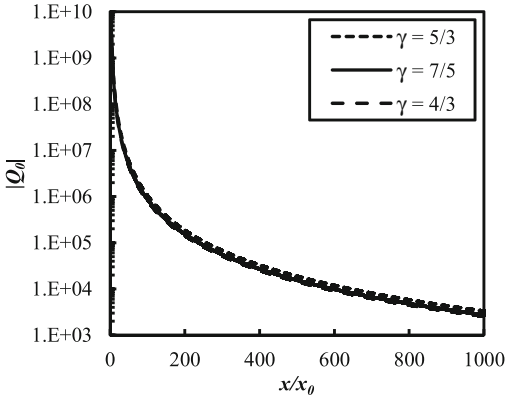

Fig. 6 $|Q| = |\partial p/\partial t + ua\partial u/\partial t|$ evaluated on the decaying blast versus x/x_0 in units of kg/m-s^3

4 Results and Discussion

It is desired to analyze and discuss the nature of the solutions to (8) and (9) for converging and diverging channels for arbitrary strength shocks and shocks in the strong shock limit. For the remainder of this paper, the channel under consideration consists of an initial cross-sectional area of 1.0 m^2 with a concave or convex angle of 1.0° for converging or diverging channels, respectively. It is also noted that the cross-sectional area must always be monotonically increasing or decreasing for the A–M relation and the current work to be applied. The ratio of specific heats for the gas is taken as $\gamma = 7/5$. For an initially planar shock wave, it follows that $Q_0 \equiv 0$ and a direct comparison can be made between the A–M relation and the current second-order approximation. In essence, both orders of approximation experience the same coincidence between the C_+ characteristic and the shock trajectory. Therefore, making $Q_0 = 0$ allows for isolating the effects of Q on the solution behavior.

Figure 7 shows the behavior of planar shock waves with initial Mach numbers of 2.0 and 4.0 for both converging and diverging channels. It is clear that for

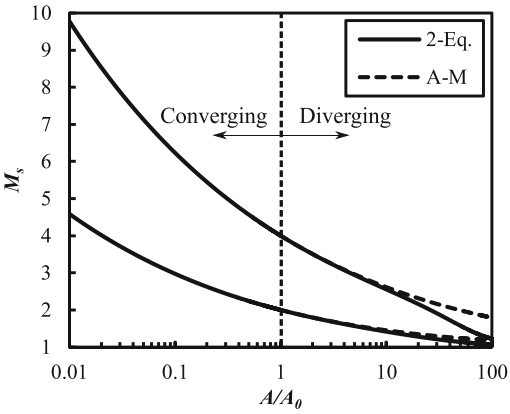

Fig. 7 Comparison of A–M relation and second-order approximation for initial shock Mach numbers of 2.0 and 4.0 in converging and diverging channels

converging channels that the A–M relation and second-order approximation have very good agreement. This indicates that the converging channel area is the primary source that influences the strength of the shock. Additionally, in the case of $Q_0 = 0$, the contribution of $|Q|$ in the converging geometry is negligible. However, for the diverging channels, the two solutions begin to diverge. This is caused by the initial increase in $|Q|$ as the shock traverses the diverging channel. Figure 8 better demonstrates the disagreement for diverging channels. It is evident that the second-order approximation approaches an acoustic wave much faster for both initial shock Mach numbers. However, the deviation is more pronounced for the initial shock Mach number of 4.0. The large deviation is caused by the introduction of Q into the second-order approximation. Although the initial condition $Q_0 = 0$ is being imposed, once the wave begins to propagate into the diverging channel, the value of $|Q|$ momentarily becomes very large on the shock as a result of the initially uniform shock wave starting to decay. It should be noted that the effects of re-reflected disturbances are not accounted for in this study. Moreover, the degree to which these disturbances influence the shock trajectory in counter to the changing area and $|Q|$ may become more significant at large distances from the start of the area change. Further analysis would be required to formally assess this aspect of shock waves propagating in diverging channels.

Figure 9 compares the A–M relation and the second-order approximation in the strong shock limit for $Q_0 = 0$ with initial shock wave velocities of 5 and 10 km/s. This figure clearly shows that for converging channels, the A–M relation and second-order approximation have very good agreement. Once again, this is an indication that the influence of Q in converging channels is negligible compared to the effects of the converging channel area. The same is not true for the case of diverging channel areas. In the strong shock limit, the second-order approximation yields a nonphysical zero shock velocity at A/A_0 of approximately 37.5. Similar results were obtained by [5] for spherical and cylindrical diverging geometries in the strong shock limit. This is mostly caused by the introduction of Q into the second-order approximation, but is also influenced by the divergence in coincidence between the C_+ characteristic and

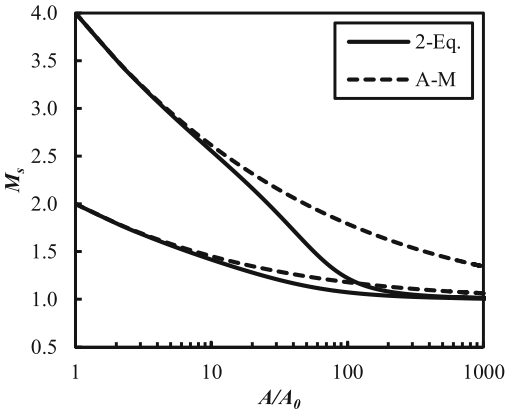

Fig. 8 Comparison of A–M relation and second-order approximation for initial shock Mach numbers of 2.0 and 4.0 in diverging channels

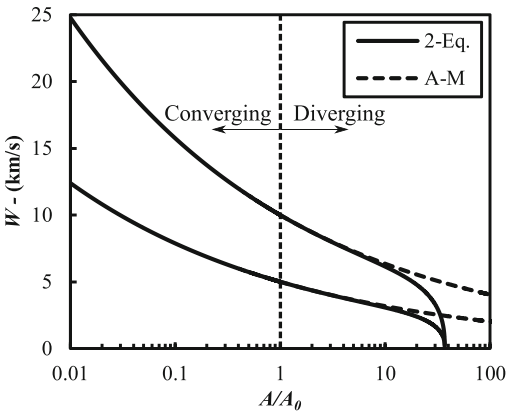

Fig. 9 Comparison of A–M relation and second-order approximation for initial shock velocities of 5 and 10 km/s in the strong shock limit for converging and diverging channels

the shock wave trajectory. A singularity in Q is approached in (14) for diverging channel area geometry. For the case of weaker shocks, this is likely avoided as the strong shock limit assumption is removed and the fact that the C_+ characteristic and shock trajectory become more coincident.

It is also desired to consider the influence of Q_0 on the behavior of the solutions in both converging and diverging channel geometries. In the strong shock limit, only the converging geometries are considered. For an initial shock Mach number of 2.0, the solution of (8) is shown in Fig. 10 for values of Q_0 ranging from 0, -1.0×10^5, -1.0×10^6, and -1.0×10^7 kg/m-s^3. For the case of a converging channel, it is evident that the planar shock dynamics become independent of the initial nonuniformity of the flow Q_0. As a result, all the solutions of the second-order approximation collapse on the A–M relation. A similar result was obtained by [5] for the case of converging cylindrical and spherical shocks in the strong shock limit. This result has yet to be reported for an arbitrary strength shock in converging planar geometry. Furthermore, it should be noted that a deviation in the converging channel solution was achieved for values of Q_0 that were orders of magnitude above those

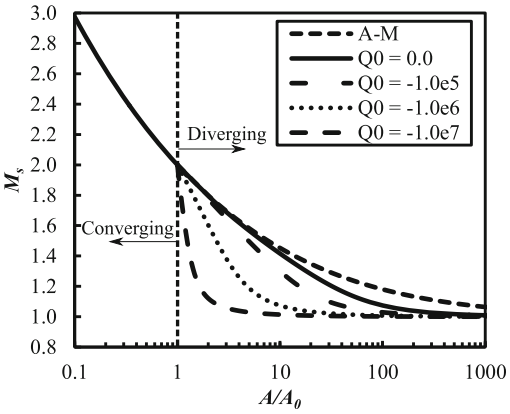

Fig. 10 Comparison of A–M relation and second-order approximation for an initial shock Mach number of 2 for converging and diverging channels at various Q_0

obtained from the solution of [7] for a decaying shock wave with an initial Mach number of 3.0. Given the physical considerations of the decay process, the values were deemed nonphysical and disregarded from the analysis. For the diverging channel geometry, the initial value of Q_0 significantly influences the rate at which the decaying shock wave approaches an acoustic wave. For these cases, it intuitively follows that the larger the initial value of $|Q_0|$, the more rapid the physical decay of the wave that is taking place. However, the solutions reported in Fig. 10 must be taken with caution as the influence of re-reflected disturbances has not been taken into account. It is likely that the solutions are more accurate for smaller channel expansion area ratios although this suggestion would require further analysis and possibly experimental data to confirm.

For the strong shock solutions of (9), the same behavior was obtained for the arbitrary decaying shocks in converging geometries. The second-order approximation solutions are independent of the initial nonuniformity of the flow Q_0 and all the subsequent solutions collapsed on that obtained with the A–M relation. As a result, for an initial shock velocity of 10 km/s, the solutions are exact to the converging channel geometry shown in Fig. 9. It should be noted that deviations in the solutions for converging geometries were obtained for very large initial values of Q_0; however, these values were orders of magnitude above those obtained from the S–vN–T blast solution and were once again deemed nonphysical. Lastly, the influence of Q_0 for the case of diverging channel area was not analyzed due to the nonphysical behavior of the solution in the strong shock limit.

A final remark of analysis is taken to demonstrate the capability of the current second-order approximation for the case of an arbitrary strength decaying shock wave in both a converging and diverging channel. The solution of [7] is used where the description of the wave process has previously been discussed. In short, a piston is set in motion and moments later suddenly stopped such that a uniform planar shock wave with a Mach number of 3.0 is created. At $t = t_0$ and $x = x_0$, the leading characteristic of the rarefaction wave catches and begins to overtake the traveling shock. At $x/x_0 = 50$, the planar shock wave has decayed to a Mach number of $M_0 = 1.96$

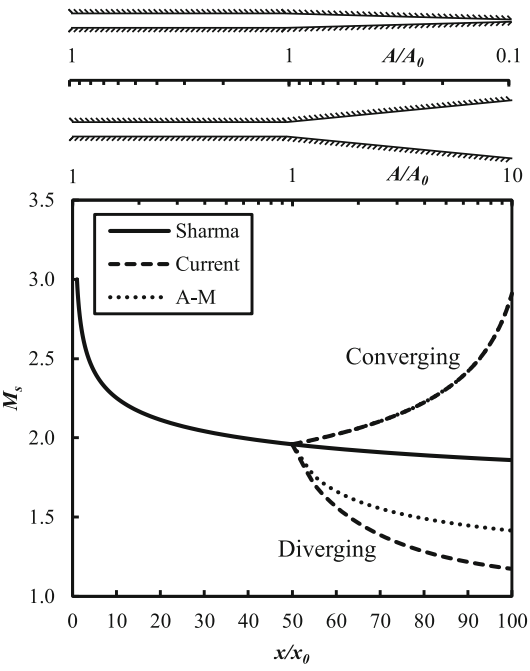

Fig. 11 Comparison of A–M relation and second-order approximation for a decaying shock wave in a nonuniform channel

with nonuniformity value of $Q_0 = -1.696 \times 10^7$ kg/m-s^3. These two parameters are then the initial conditions for the second-order approximation of (8). Similarly, at a location of $50 \leq x/x_0 \leq 100$, the channel features either a converging or diverging section with total area ratios of 0.1 and 10, respectively. The solution to this particular geometry is shown in Fig. 11. It is noted that the solid line indicates the solution of Sharma et al. and is assumed to continuously decay in a uniform channel for $x/x_0 > 50$. As expected, the converging channel case in Fig. 11 is independent of the nonuniformity of the flow behind the decaying shock wave as it approaches the origin of the converging channel. Alternatively, for the diverging channel case a more relaxed solution is obtained from that of the A–M relation as a result of Q_0 being nonzero and negative. The second-order solution is believed to be more accurate as a result of accounting for the nonuniformity of the flow Q behind the shock. However, no justification can be made in the current study as to the complete accuracy of the predicted solution. This would require additional analysis that extends beyond the scope of the current work.

5 Conclusions

The current work has demonstrated two possible shock wave cases where the classical A–M relation is potentially invalid due to the nonuniformity of the flow following the shock. These cases include the propagation of an arbitrary strength decaying planar shock wave and the propagation of planar blast waves. In regard to this aspect, a second-order approximate equation set was proposed to take into account the nonuniformity of the flow following the shock wave. It was shown that the A–M relation and second-order approximation have very good agreement for the case of converging channels. More importantly, it was determined that the second-order approximate solution becomes independent of the nonuniformity of the flow following the shock, such that the dynamics of the shock are solely governed by the changing area in the converging channel. In the case of diverging channels, the second-order approximation showed to be strongly dependent on the nonuniformity of the flow following the shock. Even for the case of a uniformly propagating shock with $Q_0 = 0$, the second-order solution slightly deviates from the A–M relation. It was shown that the deviation becomes more pronounced for higher values of Q_0. It is believed that the second-order approximation is more accurate for weaker shocks in diverging channels within a limiting channel length. However, a formal consideration of the re-reflected disturbances behind the wave would be required to assess the complete accuracy of the solution.

References

1. Chester, W.: The quasi-cylindrical shock tube. Phil. Mag. **45**, 1293–1301 (1954)
2. Chisnell, R.F.: The motion of a shock wave in a channel, with applications to cylindrical and spherical shock waves. J. Fluid Mech. **2**, 286–298 (1957)
3. Whitham, G.B.: On the propagation of shock waves through regions of non-uniform area or flow. J. Fluid Mech. **4**, 337–360 (1958)
4. Whitham, G.B.: A new approach to problems of shock dynamics Pt. I Two dimensional problems. J. Fluid Mech. **2**, 145–171 (1957)
5. Best, J.P.: A generalization of the theory of geometrical shock dynamics. Shock Waves **4**, 251–273 (1991)
6. Kirkwood J.G., Bethe H.A., Progress report on the pressure wave produced by an underwater explosion I. OSRD Rept. 588 (1942)
7. Sharma, V.D., Ram, R., Sachdev, P.L.: Uniformly valid analytical solution to the problem of a decaying shock wave. J. Fluid Mech. **185**, 153–170 (1987)
8. Sedov, L.I.: Similarity and Dimensional Methods in Mechanics. Academic Press, New York, NY (1959)
9. Bethe, H.A., Fuchs, K., Hirschfelder, J.O., Magee, J.L., Peierls, R.E., von Neumann, J.: Blast Waves. Los Alamos Scientific Laboratory Report, LA–2000 (1947)
10. Taylor, G.I.: The formation of a blast wave by a very intense explosion. In: Proceedings of Royal Society of London, A–201, pp. 159–174 (1950)
11. Han, Z., Yin, X.: Shock Dynamics. Kluwer Academic Publisher, Beijing, China (1993)
12. Kamm, J.R.: Evaluation of the Sedov-von Newman-Taylor Blast Wave Solution. Los Alamos Scientific Laboratory Report, LA–UR–00–6055 (2000)

Shock Reflection in Axisymmetric Internal Flows

B. Shoesmith, S. Mölder, H. Ogawa and E. Timofeev

Abstract The flow downstream of an axisymmetric conical shock wave, with a downstream pointing apex, can be predicted by solving the Taylor-Maccoll equations. Previous research, however, has suggested that these theoretical flowfields are not fully realisable in practice, and that a Mach reflection forms towards the centreline of the flow. This phenomenon is investigated for the case where the freestream Mach number is 3.0 and the shock angle is 150°. A range of complementary prediction techniques that include the solution to the Taylor-Maccoll equations, the method of characteristics, curved shock theory and CFD, are used to gain insight into this flow. The case where a cylindrical centrebody is placed along the axis of symmetry is studied for several values of centrebody radius that are expected to produce regular reflection at the centrebody surface. An analysis of pressure gradients suggests that the flowfield downstream of the reflected shock does not contribute to the process of transition from regular to Mach reflection at these conditions.

B. Shoesmith (✉) · E. Timofeev
Department of Mechanical Engineering, McGill University,
817 Sherbrooke Street West, Montreal, QC H3A 0C3, Canada
e-mail: ben.shoesmith@mail.mcgill.ca

E. Timofeev
e-mail: evgeny.timofeev@mcgill.ca

S. Mölder
Department of Aerospace Engineering, Ryerson University, 350 Victoria Street,
Toronto, ON M5B 2K3, Canada
e-mail: smolder@ryerson.ca

H. Ogawa
School of Engineering, RMIT University, GPO Box 2476,
Melbourne, VIC 3001, Australia
e-mail: hideaki.ogawa@rmit.edu.au

K. Kontis (ed.), *Shock Wave Interactions*,
https://doi.org/10.1007/978-3-319-73180-3_27

1 Introduction

Previous theoretical analyses have shown that converging, conical, incident shocks cannot occur at a centreline of symmetry [1–5], and that Mach reflection of the converging shocks should occur instead. This theoretical result is supported by numerical and physical experiments [6, 7] that have shown that a conical incident shock and its regular shock reflection, near the axis of symmetry and, in particular, at the apex point, do not exist. In approaching the axis, the incident, conical, shock becomes stronger, its angle increases and a Mach reflection results; even for flows with weak incident shocks. Similar behaviour has also been shown for non-conical shocks [3, 4, 7]. It thus appears that the transition to, and the appearance of, Mach reflection is caused by the effects of shock and flow convergence near the centreline. This raises the intriguing question: How far off the centreline does the regular reflection have to be so as not to suffer the effects that force Mach reflection?

In studying shocks that converge towards the centreline, it is useful to work with shocks that maintain a constant strength (shock angle) as they approach the axis. Such conical shocks and flows can be produced from the solutions of the Taylor-Maccoll (TM) equations. Integration of the TM equations produces a streamtube, which may be viewed as a solid surface supporting the conical shock. The trailing edge of such a streamtube ends at a conical singularity. The flow between the conical shock, the singularity and the streamtube is called 'M-flow' [8] and is one of the four possible cases of supersonic, conically symmetric, flowfields that are bounded by a uniform flow [2]. Grozdovskii [2] identified a 'limiting characteristic' in the M-flow, upstream of which the flow is controlled by the surface and is conical. The downstream flow is therefore not controlled by the M-flow surface, which raises a question about the nature of the flow further towards the axis. Rylov [5] showed that centreline Mach reflection must occur since the portion of the shock downstream of the limiting characteristic must steepen continuously as it approaches the axis. Furthermore, it was shown that even a sharp expansion corner at the downstream end of the M-flow surface, producing a local Prandtl–Meyer fan (ordinarily expected to weaken the shock), cannot prevent the shock from strengthening near the centreline. The conclusion therefore is that the flow in this region cannot be conically symmetric and that centreline Mach reflection is unavoidable.

A number of M-flow features render its investigation challenging. Steepening of the incident shock occurs, primarily, close to the axis of symmetry, as compared to the entry radius of the M-flow surface. As a result, the size of the Mach disk at the axis of symmetry may be small, especially for initially weak shocks (a spectacular example of smallness is provided in [6]). The angle between the bounding rays of the theoretical M-flow (*i.e.*, between the shock and the singularity) is relatively small, requiring high-resolution calculations to describe the incident shock angle and curvature with good accuracy.

The aim of the present study is to provide detailed quantitative analysis of an M-flow with a freestream Mach number of 3.0 and a shock angle of 150°, referred to as M3/150. To add further insight into the issue of centreline shock reflection,

the case where a cylindrical centrebody is placed along the flowfield axis is studied for several different values of centrebody radius. Results are then used to look for mechanisms that may contribute to the transition to Mach reflection. In view of the above-mentioned flow features and associated difficulties, several complementary techniques are used, which include: (1) the solution of the TM equations, (2) curved shock theory (CST) [9], (3) the method of characteristics (MOC) and (4) an adaptive unstructured inviscid time-marching finite-volume CFD code `Masterix` [10]. Another potentially useful tool to be considered elsewhere is a space-marching CFD code, such as the one described in [11].

2 Approaches

2.1 Theoretical Conical Flow

The TM equations are integrated by a Runge–Kutta scheme starting from the oblique shock conditions downstream of the conical incident shock. The solution yields the radial and circumferential components of Mach number in the flowfield [8]. A streamline and a C^- characteristic are also traced as part of the calculation. The fact that the downstream extent of M-flow is terminated by a singularity in the TM equations means that it can never be exactly reached by numerical integration. The singularity exists where the Mach number normal to the ray is equal to -1, and therefore the integration process is stopped within a tolerance of 10^{-5} of this value. Then, due to the self-similarity of conical flows, the C^- characteristic can be scaled such that it begins at the downstream end of the M-flow surface. This defines the limiting C^- characteristic, as originally shown by Grozdovskii [2]. These features are shown in Fig. 1. For M3/150, it is found that the limiting characteristic intersects the shock at $y/y_1 = 0.384$ (where y_1 is the leading edge radius), and therefore the shock is expected to be of constant strength from the leading edge to this point and then to strengthen towards the axis. Only the straight portion of the shock is shown in Fig. 1 as a solid red line.

2.2 Method of Characteristics

Calculations are conducted for the flow downstream of the limiting characteristic, where the flow must be assumed to be non-conical. The characteristics method is based on that described in [12] and is suitable for the analysis of axisymmetric rotational flows. Boundary condition data is provided by the limiting C^- characteristic at the M-flow surface trailing edge, where the surface takes on infinite curvature [5], indicating a corner, so that the local flow can be modelled as a Prandtl–Meyer expansion. The M-flow shock angle of 150° is applied at the point where the shock

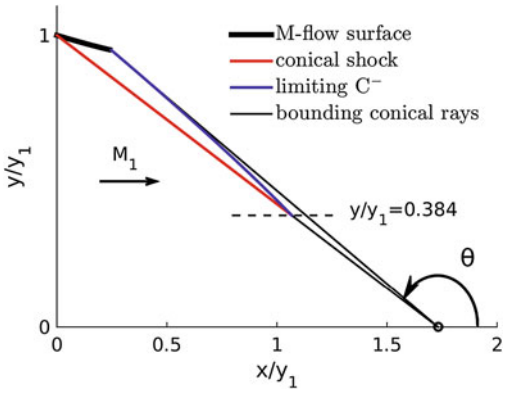

Fig. 1 Schematic for M3/150 M-flow configuration

meets the limiting C^- characteristic. Only 4.5° of flow turning at the expansion corner (out of ∼9° flow turning required to realign the local flow with the freestream direction) is modelled. This is sufficient to take the shock close enough to the axis and generate a large enough field for cases where the shock reflects from a centrebody. The spacing between characteristics is defined to be 0.01° at the expansion corner and $\Delta/y_1 = 0.001$ along the shock. These particularly fine spacings are chosen to accurately capture gradients for CST analysis, although a convergence study has shown that the basic shock geometry is captured using much coarser spacings. Calculations are physically limited to $y/y_1 = 0.02$ (where the incident shock angle $\theta_i = 134.55°$) to avoid convergence problems associated with the flow approaching sonic conditions behind the shock.

For cases that include a cylindrical centrebody, MOC analysis of the shock reflection is possible when the reflection is of regular type with supersonic flow downstream from the reflected shock. Flow calculations behind the reflected shock are driven by the centrebody geometry and the incident field. In theory, MOC can be used to analyse the reflected field for $\theta_i > 140.66°$, which corresponds to the sonic limit of shock reflection, and occurs at a centrebody radius of $y/y_1 = 0.0387$. In practice however, the downstream Mach number M_3 must be slightly above sonic and a value of $y/y_1 = 0.04$ ($M_3 = 1.047$) is found to be the practical minimum centrebody radius at which MOC solutions could be obtained. Characteristics are distributed along the reflected shock with a spacing of $\Delta/y_1 = 0.001$.

2.3 Curved Shock Theory

CST relates gradients of pressure, flow inclination and vorticity immediately upstream and downstream of a shock to the curvature of the shock itself. This includes shocks with curvatures in both the flow and flow-normal planes, such as those discussed here. The main quantities of interest are: the normalised pressure

gradient $P = (\partial p/\partial s)/\rho V^2$; the streamline curvature $D = \partial\delta/\partial s$; and shock curvatures in the flow plane $S_a = \partial\theta/\partial\sigma$, and in the flow-normal plane, $S_b = -\cos\theta/y$, where s is measured along the streamline; σ is measured along the shock; δ is the flow inclination to the x-axis; y is the distance from the symmetry axis; θ is the angle of shock inclination to the incoming velocity vector; V is the flow velocity along the streamline; ρ is the density; p is the pressure. In general, two unknown quantities can be determined given all other values. Further details can be found in [9, 13].

This work applies CST in several ways. First to the incident shock, where downstream gradients of pressure, P_2, and flow inclination, D_2, are determined having input the incident shock geometry (θ_i, $S_{a,\mathrm{i}}$, $S_{b,\mathrm{i}}$) and the freestream conditions. Second, to the point of shock reflection from a centrebody to determine the downstream pressure gradient, P_3, and the reflected shock curvature, $S_{a,\mathrm{r}}$. In this case, CST is used to determine gradients downstream of the incident shock and then again to determine values downstream of the reflected shock, which allows P_3 and $S_{a,\mathrm{r}}$ to be found given $D_3 = 0$ at the cylinder surface. The third application is off-surface data for the reflected shock, where downstream gradients (P_3 and D_3) are found given the reflected shock geometry and the gradients in the incident field.

Where the incident shock is conical ($S_{a,\mathrm{i}} = 0$), P_2 and D_2 can be determined based on the known shock geometry. Where the flow plane curvature of the incident shock is finite, or in cases where a reflected shock is predicted, the method for obtaining shock angles and curvatures becomes more involved. These values are provided by MOC, which predicts a discrete set of coordinates with associated shock properties as part of the solution process and requires minimal post-processing to derive the required data; extracting similar data from a CFD solution, for example, would not have been possible with the same accuracy.

2.4 CFD

The numerical CFD modelling results presented below are obtained with the Euler (inviscid, non-heat-conducting) flow model. The gas (air) is assumed to be ideal with constant specific heats (the specific heat ratio $\gamma = 1.4$). An adaptive unstructured finite-volume flow solver [10] is used. The solver employs a node-centred, second order in space and time (for smooth solutions and uniform grids), MUSCL-Hancock TVD finite-volume scheme, see [14] for more details. The grid is locally adapted to solution peculiarities (e.g. shock fronts, slipstreams etc.) via an h-refinement procedure governed by a sensor based on the normalised second derivative of density. Additional uniform refinement is applied in the regions deemed essential for computational accuracy.

The geometry of the solid surface begins at the M-flow leading edge. At the M-flow trailing edge, the surface becomes parallel to the freestream direction, generating a sharp corner. The inflow boundary runs from the leading edge of the M-flow surface along the conical shock and then becomes vertical and comes to the axis (see Fig. 2). This is done to avoid accuracy issues arising from the interaction of

numerically smeared shock profile with the M-flow surface. Such inaccuracies can be, in principle, reduced by grid refinement along the shock. However, very fine meshes, resulting in very small time steps, render the flow solver computationally inefficient.

Freestream conditions are used to initialise the entire computational domain for each computational run, which corresponds to instant placement of the M-flow surface into the freestream. Each computation proceeds until a steady state is reached. The mesh size for the current case includes $\sim 1.62 \times 10^5$ grid nodes. A region of refinement is specified to begin upstream of the incident shock and end downstream of the conical singularity. Another region of refinement is specified towards the centreline to capture the region around the Mach reflection. The minimum cell width (normalised by the leading edge radius y_1) in both of these regions is $\sim 1.3 \times 10^{-3}$. The minimum allowable cell width within the entire computational domain is $\sim 6.25 \times 10^{-4}$.

3 Results

Figure 2 shows the CFD prediction of the Mach number field, with results from TM and MOC overlaid for comparison. The CFD prediction shows that incident shock steepening occurs downstream from the limiting C^- characteristic. Mach reflection has occurred, with a Mach stem that appears to be approximately perpendicular to the freestream flow with a height of $y/y_1 = 0.027$. The subsonic streamtube (bound by the slip-surface) downstream of the Mach stem contracts as the flow re-accelerates towards sonic conditions. The end point of the TM-predicted limiting C^- characteristic is located almost exactly on the CFD-predicted shock, which appears to be straight upstream of that point, in agreement with the TM theory. The MOC prediction of the shock begins to deviate slightly from the CFD prediction as it approaches the axis, although the level of agreement is generally good, with a maximum discrepancy of $x/y_1 = 0.003$ found at the triple point and visible only on the enlarged Fig. 2c. The disagreement may be attributed to coarser CFD grids (as compared to MOC spacings) downstream from the incident shock in the flow regions which affect the shock shape. Further grid convergence studies are required.

The MOC-predicted Mach number field as well as associated shock angle and flow plane shock curvature are shown in Figs. 3 and 4. The shock wave clearly becomes steeper with reducing y, whilst the rate at which it steepens is also found to increase as it approaches the axis. It is to be noted that the CFD/MOC-calculated incident shock, that is close to the axis, may be strong enough not to reflect regularly off an axisymmetric cylinder. Then a Mach reflection would ensue for this as well as for all smaller cylinders. As an example: the MOC calculation reached its limit at $y/y_1 = 0.020$ whereas CFD predicted Mach reflection with a stem radius of $y/y_1 = 0.027$, so that the Mach stem radius is greater than the MOC limit.

The effects of shock curvature on the pressure gradient P_2 and streamline curvature D_2 are shown in Fig. 5. In the region between the M-flow surface and the limiting C^- characteristic, the flow is conical and the trends are explained by considering

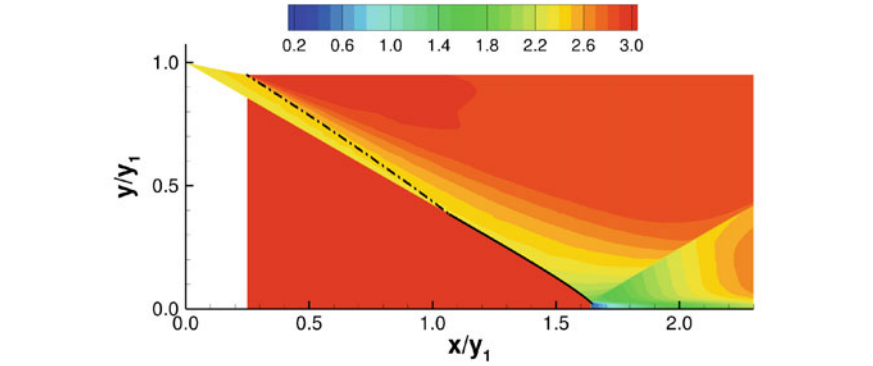

(a) Overall Mach number field

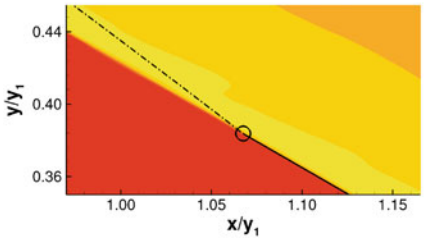

(b) Limiting C^- at shock

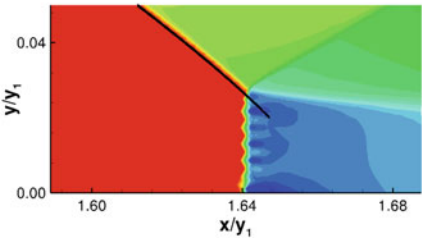

(c) Triple-point vicinity

Fig. 2 CFD prediction of M3/150 (without centrebody cylinder) Mach number field with TM prediction of limiting C^- characteristic (dash-dotted black line) and MOC prediction of shock position (solid black line)

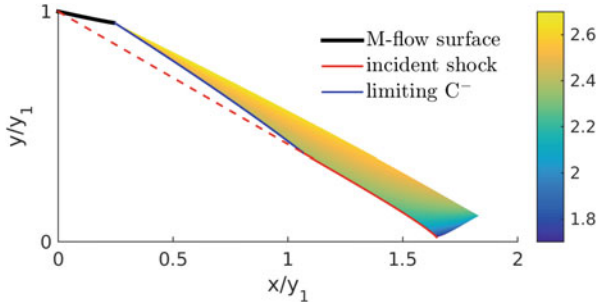

Fig. 3 MOC prediction of Mach number field downstream from the incident shock and limiting C^- characteristic

that in the direction of streamlines, conical rays become closer to one another when moving towards the axis; if the conical shock were continued towards the axis both P_2 and D_2 would approach infinity. Discontinuities in the gradient of P_2 and D_2 are found where the limiting C^- characteristic meets the shock, which is where the

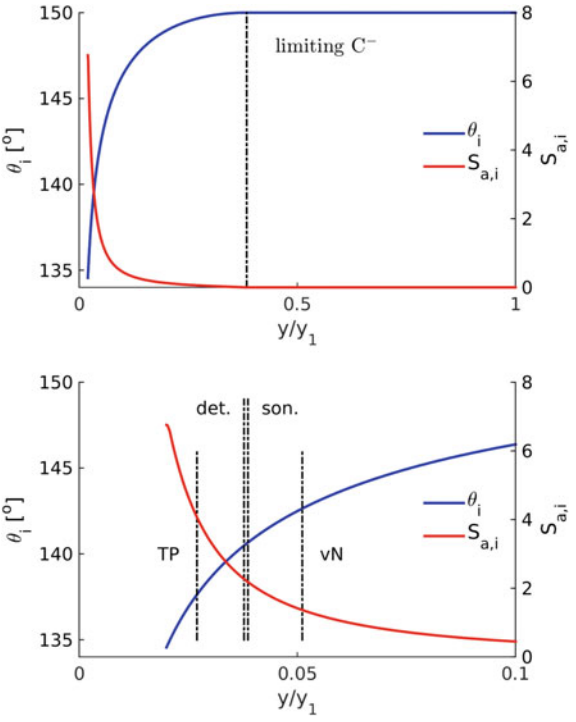

Fig. 4 MOC-predicted shock angle θ_i and curvature $S_{a,i}$ along the incident shock. Top: complete predicted shock. Bottom: focus on shock in the centreline region. TP indicates the location of CFD-predicted triple point for shock reflection from the axis of symmetry; 'det.', 'son.'and 'vN' indicate the positions of the detachment, sonic and von-Neumann points, respectively, for shock reflection from a straight cylindrical centrebody

incident shock curvature $S_{a,i}$ departs from zero (see Fig. 4). The pressure gradient P_2 passes through zero at $y/y_1 = 0.173$, which separates regions of accelerating and decelerating flow downstream of the shock. This point is known as the Thomas point [9].

MOC predictions for cases with a centrebody cylinder are plotted in Fig. 6 and 7. Reflected shock angles are consistent with the two-shock theory of shock reflection, which is applied as part of the MOC solution. Figure 7 shows that the incident shock (in the non-conical region) is concave towards the incident flow whereas the reflected shock is convex, *i.e.*, $S_{a,i} > 0$ and $S_{a,r} < 0$. This is in agreement with CST [9]. Mach number distributions downstream of the reflected shock show that pressure gradients in the positive x and y directions are negative. This observation is highlighted by the results in Fig. 8, where the black line shows surface pressure gradient, immediately downstream of the reflected shock, for the possible range of centrebody radius, *i.e.*, $y_{cb}/y_1 = 0.0387 \rightarrow 1.0$. It shows that negative pressure gradients exist in this region for any chosen centrebody radius. Other, coloured, lines are for specific centrebody radii and include off-surface data, which confirms that negative pressure gradients continue along the reflected shock. A similar picture is found by plotting values along the centrebody surface itself, see Fig. 9. Again, the black line shows surface pressure gradient, immediately downstream of the reflected shock, for the possible range of centrebody radius. Other, coloured, lines are obtained by applying a finite

difference method to surface MOC data obtained for specific cylinder radii. These curves indicate that gradients decrease significantly downstream of the shock, and although asymptotic values are difficult to determine, it seems reasonable to suggest that the gradients approach zero far from the point of shock impingement.

The reason of our particular attention to Mach number and pressure gradients behind the reflected shock is related to recent conjectures [9, 15, 16] that regular-to-Mach-reflection transition might occur not only due to reflected shock detachment by excessive flow turning, but also due to reflected shock detachment due to *local flow choking*. In [9], the post-shock pressure gradient is identified as the underlying cause

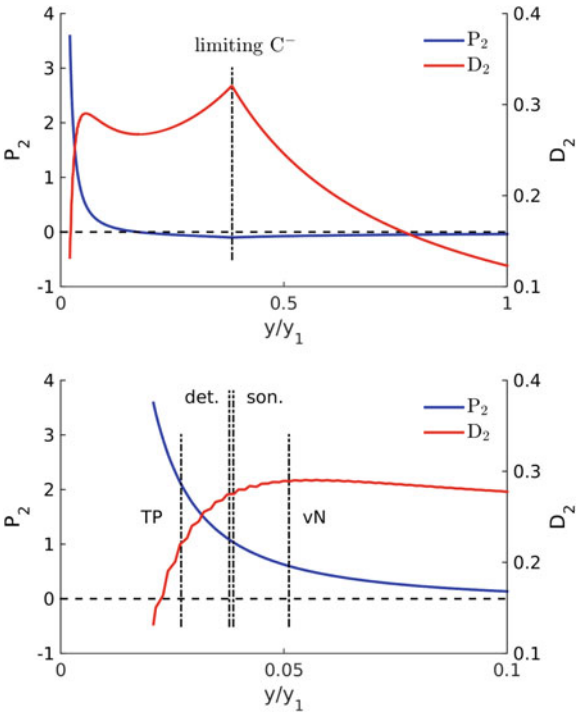

Fig. 5 MOC-predicted pressure gradient P_2 and streamline curvature D_2 downstream of the M3/150 incident shock. Top: complete predicted shock. Bottom: focus on shock in the centreline region. TP indicates location of CFD-predicted triple point; 'det.', 'son.'and 'vN' indicate the position of the detachment, sonic and von-Neumann points, respectively, for shock reflection from a straight cylindrical centrebody

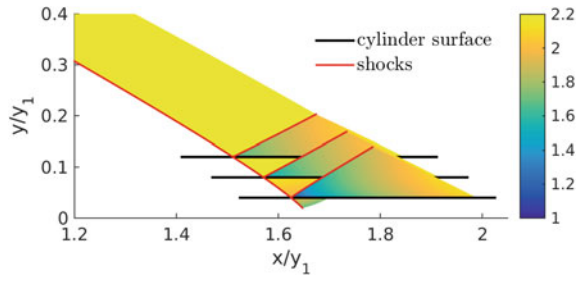

Fig. 6 MOC-calculated Mach number field for flow behind the reflected shocks on cylinders with $y_{cb}/y_1 = 0.04, 0.08, 0.12$ (from bottom to top)

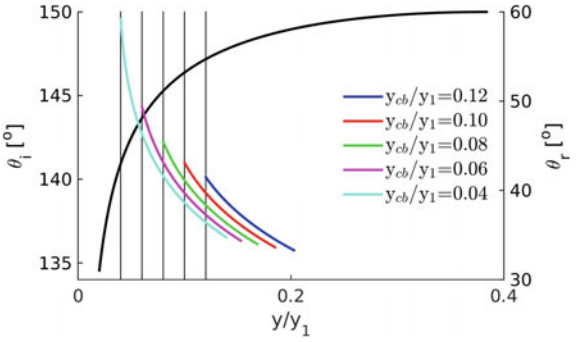

Fig. 7 MOC-calculated incident, θ_i, and reflected, θ_r, shock angles. The common incident shock is shown in black. Various reflected shocks corresponding to various cylinder radii (indicated by thin black lines) are shown in colour

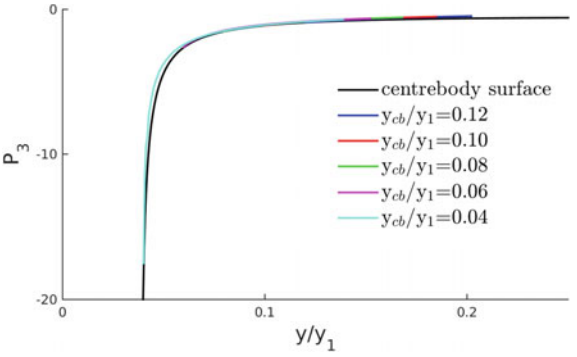

Fig. 8 Pressure gradient P_3 downstream of the reflected shock. Surface values at the reflection point for all potential values of centrebody radius are shown in black. Off-surface values for specific centrebody radii are shown in colour

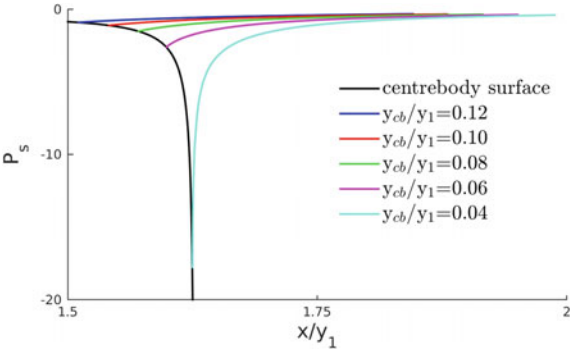

Fig. 9 Surface pressure gradient P_s downstream of shock impingement. Values immediately downstream of reflected shock, at the reflection point, for all potential values of centrebody radius are shown in black. Downstream surface values for specific centrebody radii are shown in colour

of local choking. The above results show that the supersonic flow downstream of the reflected shock is expanding, and therefore, in the cases considered, the situation is not conducive to local choking.

4 Conclusions

An exploratory, analytical study is presented of the flow associated with an initially conical shock (M-flow) as the shock approaches the axis of symmetry and as it impinges on, and reflects off, coaxial cylinders of various radii. The analysis uses direct solutions of the Taylor-Maccoll equations, the method of characteristics, curved shock theory and CFD. Agreement between CFD and MOC is generally very good, with some minor discrepancies in the prediction of the shock geometry. MOC has proved to be a useful tool in terms of providing detailed shock wave data at discrete points along the shock, facilitating analysis by CST. Nonetheless, it has the obvious restriction of only being able to provide prediction in flows with regular reflections.

The pressure gradient behind the reflected shock is examined to see if it could lead to local flow choking and detachment of the reflected shock. For the Mach 3.0, 150° incident M-flow shock the pressure gradient is found to be negative and not conducive to local choking and termination of regular reflection. Further exploration of stronger incident shocks is warranted for situations where the Mach number behind the reflected shock is subsonic and the pressure gradient is negative so that the flow would tend towards choking.

Acknowledgements The present research of B.S. and E.T. is supported by the Fonds de recherche du Quèbec - Nature et technologies (FRQNT) via the Team Research Project program and the National Science and Engineering Research Council (NSERC) via the Discovery Grant program. B.S. gratefully acknowledges the McGill Engineering Doctoral Award (MEDA) funded in part by the Faculty of Engineering, McGill University. Rabi Tahir's support regarding `Masterix` code is greatly appreciated.

References

1. Courant, R., Friedrichs, K.O.: Supersonic flow and shock waves. Interscience (1948)
2. Grozdovskii, G.L.: Supersonic axisymmetric conical flows with conical shocks adjacent to uniform parallel flows. Prikl Mat. Mekh. **23**(2), 379–383 (1959)
3. Isakova, N.P., Kraiko, A.N., P'yankov, K.S., Tillyayeva, N.I.: The amplification of weak shock waves in axisymmetric supersonic flow and their reflection from an axis of symmetry. J. Appl. Math. Mech. **76**, 451–465 (2012)
4. Kraiko, A.N., Tillyayeva, N.I.: Axisymmetric-conical and locally conical flows without swirling. J. Appl. Mech. Tech. Phy. **55**(2), 282–298 (2014)
5. Rylov, A.I.: On the impossibility of regular reflection of a steady-state shock wave from the axis of symmetry. Appl. Math. Mech. **54**(2), 245–249 (1990)
6. Mölder, S., Gulamhussein, A., Timofeev, E., Voinovich, P.A.: Focusing of conical shocks at the centerline of symmetry. In: Proceedings of the 21th ISSW, Vol. 2, pp. 875–880, Panther Publishing (1997)
7. Timofeev, E., Mölder, S., Voinovich, P., Hosseini, S.H.R., Takayama, K.: Shock wave reflections in axisymmetric flow. In: Lu, F. (ed) Shock Waves, CD-ROM Proc of the 23th International Symp on Shock Waves, Fort Worth, USA, 22–27 July, 2001, University of Texas at Arlington, pp. 1486–1493 (2001)

8. Mölder, S.: Internal axisymmetric conical flow. AIAA J. **5**(7), 1252–1255 (1967)
9. Mölder, S.: Curved aerodynamic shock waves. PhD Thesis, McGill University (2012)
10. Masterix, ver. 3.40, RBT Consultants, Toronto, Ontario, Canada (2003–2015)
11. Savchuk, A., Timofeev, E.: On further development of an unstructured space-marching technique. AIAA Paper 2011–3690 (2011)
12. Délery, J.: Handbook of compressible aerodynamics. Wiley (2010)
13. Mölder, S.: Curved shock theory. Shock Waves **26**(4), 337–353 (2015)
14. Saito, T., Voinovich, P., Timofeev, E., Takayama, K.: Development and application of high-resolution adaptive numerical techniques in Shock Wave Research Center. In: Toro, E.F. (ed) Godunov Methods: Theory and Applications, pp. 763–784. Kluwer Academic/Plenum Publishers, New York, USA (2001)
15. Mölder, S., Timofeev, E., Emanuel, G.: Shock detachment from curved surfaces. In: Kontis, K. (ed) Proc of the 28th International Symposium on Shock Waves, Manchester, UK, 17-22 July, 2011, Springer, Vol. 2, pp. 593–598 (2011)
16. Mölder, S., Timofeev, E.: Regular-to-Mach reflection transition on curved surfaces. In: Book of Papers, XXIV ICTAM, 21–26 August 2016, Montreal, Canada (2016)

On Unsteady Shock Wave Reflection from a Concave Cylindrical Surface

E. Timofeev, F. Alzamora Previtali and H. Kleine

Abstract The paper is devoted to a combined—analytical, numerical, and experimental—study of initially planar shock reflection from a full concave cylindrical surface with the emphasis on the transition from inverse Mach reflection to transitioned regular reflection. The numerically predicted and experimentally observed transition angles for a range of incident shock Mach numbers are found to be in good agreement with each other and at the same time significantly different from previous experimental observations in the literature. It is shown that among existing analytical predictions of the transition point location, the theory by Itoh et al. (JFM 108:383–400) provides the best agreement with new experimental and numerical data, even though this theory is in significant error with respect to the triple-point trajectory and Mach stem intensity. By tracking the corner signal, it is shown that it remains attached to the Mach stem during the entire course of flow development and, hence, effectively propagates with the Mach stem velocity. This finding is used for the initial development of another analytical treatment to predict the location of the transition point.

1 Introduction

The paper presents work aiming at the reexamination of the current state of knowledge regarding initially planar shock reflection from a concave cylindrical surface schematically illustrated in Fig. 1. No other surface geometry except a cylindrical

E. Timofeev (✉) · F. Alzamora Previtali
Department of Mechanical Engineering, McGill University, 817 Sherbrooke Street West, Montreal, QC H3A 0C3, Canada
e-mail: evgeny.timofeev@mcgill.ca

F. Alzamora Previtali
e-mail: federico.alzamoraprevitali@mail.mcgill.ca

H. Kleine
School of Engineering and Information Technology, University of New South Wales, Northcott Drive, Canberra, NSW ACT 2600, Australia
e-mail: H.Kleine@adfa.edu.au

K. Kontis (ed.), *Shock Wave Interactions*,
https://doi.org/10.1007/978-3-319-73180-3_28

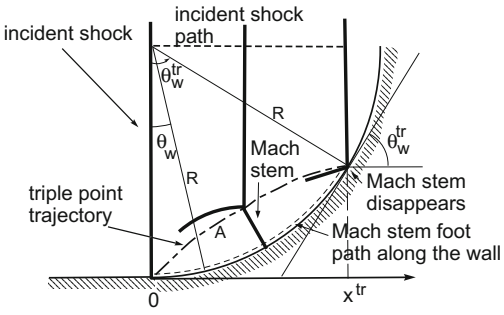

Fig. 1 Schematical drawing of InMR–TRR transition on a concave cylindrical surface

arc is considered. In all cases, the initial wall angle is assumed to be zero, i.e., the influence of the initial wall angle is outside the scope of the present study. The transition from a Mach reflection (InMR—inverse Mach reflection) to transitioned regular reflection (TRR) is of primary interest. Combined—analytical, numerical, and experimental—studies are undertaken.

In Sect. 2, some results of numerical simulations are provided. These results and their implications served, in fact, as the driving force motivating the analytical and experimental studies presented in Sects. 3 and 4. The concluding remarks in Sect. 5 briefly summarize the newly achieved state of knowledge and outline the most immediate subsequent research steps.

2 Numerical Modeling

2.1 CFD Tools

The flow is considered to be inviscid and non-heat-conducting, and the gas (air) is assumed to be ideal with constant specific heats ($\gamma = 1.4$). Numerical simulations are carried out with an adaptive unstructured finite-volume Euler code [1]. This node-centered MUSCL-Hancock TVD flow solver [2] is of second-order accuracy in space and time on smooth solutions and uniform grids.

We also use the numerical signal tracking technique proposed by Hakkaki-Fard and Timofeev [3, 4] to observe the propagation of weak (acoustic) disturbances in unsteady flowfields. In the context of the present work, it allows to obtain detailed information on the velocity and front geometry of the corner signal propagating from the leading edge of the cylindrical surface and, therefore, its propagation path. It is envisioned that such information would provide further insight into the gasdynamics of the reflection process and, hopefully, will assist in the development and improvement of theories predicting the InMR–TRR transition angle. It is assumed that an infinitesimally weak disturbance, once having been introduced, is propagating in all directions with the local speed of sound and at the same time being carried along with the flow as dictated by the value and direction of flow velocity as shown in Fig. 2,

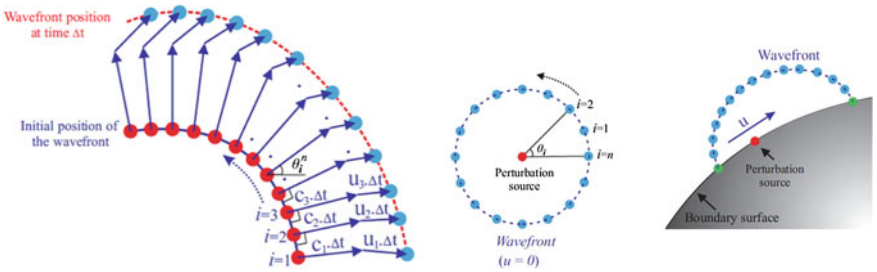

Fig. 2 Schematics illustrating the technique for tracking acoustic disturbances. Reproduced from [3]

left schematic. The corner signal front is represented as a set of discrete points (Fig. 2, central and right schematics), typically from a few tens to a few hundreds, and the locations of these points are updated at each time step of the flow solver according to the principle mentioned above.

2.2 *Results*

A number of computational experiments were run to determine the transition point for various incident shock Mach numbers M_s. According to [5] and our numerical modeling, the triple-point trajectory is tangential to the reflecting surface prior to transition. This results in very small Mach stems over a rather wide range of wall angles and poses significant challenges for obtaining a grid-independent value for the transition angle. This fact is illustrated in Fig. 3 showing an instant when the

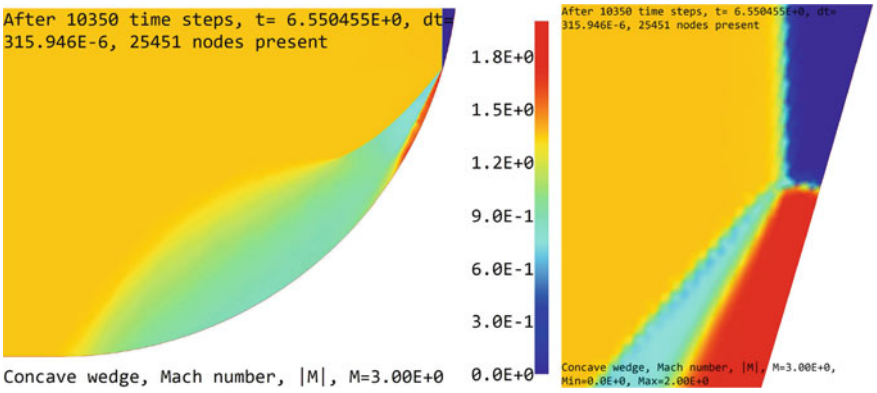

Fig. 3 CFD result for shock Mach number $M_s = 3.0$ ($\gamma = 1.4$) and an instant close to InMR–TRR transition. The Mach number distribution is shown. Left: entire flowfield, the reflection seems to be regular; right: magnified image near the reflecting surface revealing true nature of the reflection

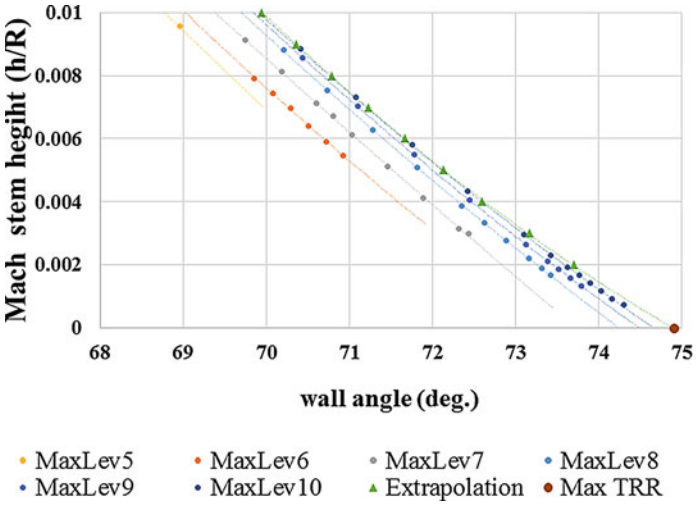

Fig. 4 Influence of grid refinement on the InMR–TRR transition angle for the incident shock Mach number 3.0. Small colored full circles correspond to simulations with different numbers of grid refinement levels. Green triangles (labeled as 'Extrapolation' in the legend) correspond to the extrapolation to zero grid step at a fixed Mach stem height. Large brown circle (labeled as 'MaxTRR' in the legend) corresponds to the subsequent extrapolation of these values to zero Mach stem height using a quadratic fit

Mach stem height is $\sim 0.0016\,R$, where R is the radius of curvature of the reflecting surface.

Our current numerical results for the transition angle are shown in Fig. 5 as full black triangles and labeled as 'present CFD'. The parametric study was conducted using the background mesh with average grid spacing of $\sim 0.05\,R$ and 7 grid refinements levels. Each refinement level reduces the minimum grid spacing in 2 times, i.e., with 7 levels, the minimum grid spacing at discontinuities is $\sim 0.00039\,R$.

To investigate the influence of grid refinement on the InMR–TRR transition angle, a grid convergence study was conducted for the case of incident shock Mach number $M_s = 3.0$. The results are shown in Fig. 4. The number of grid refinement levels varies from 5 to 10. As expected, finer meshes allow to resolve smaller Mach stems. Extrapolation to zero Mach stem height using quadratic fits at each refinement level leads to estimates of the transition angle for given grid resolutions. The black triangles plotted in Fig. 5 corresponds to such extrapolated values for the refinement level 7 (for example, for $M_s = 3.0$ and 7 levels of grid refinement, the extrapolated transition angle is $\sim 74.07°$). Furthermore, it is clearly seen in Fig. 4 that for a given Mach stem height, grid convergence takes place when the minimum grid spacing is reduced, and by extrapolation to zero grid step it is possible to obtain the grid-independent wall angle at which the Mach stem is of a given height; the results of such extrapolations are shown in Fig. 4 with green triangles. These extrapolated-to-zero-grid-step values can be in their turn extrapolated using a quadratic fit to zero

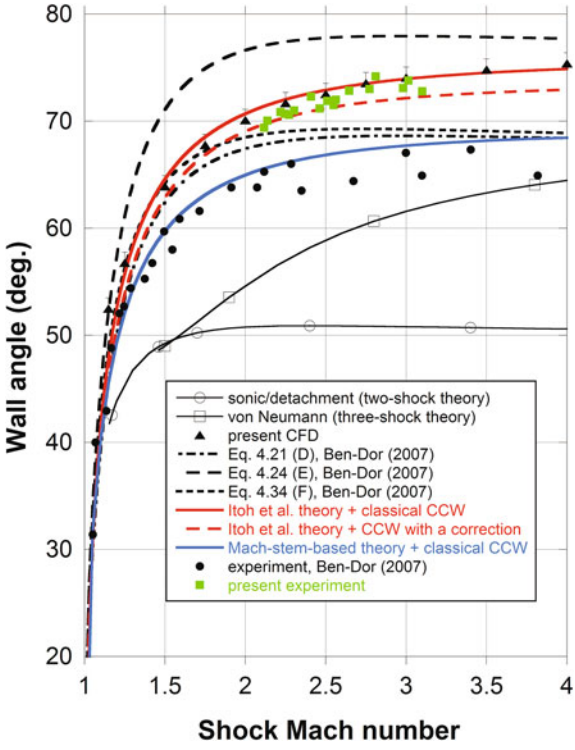

Fig. 5 Analytical, experimental, and numerical predictions of InMR–TRR transition on the concave cylindrical surface. A more detailed explanation of the legend is given in the text

Mach stem height, thus resulting in the grid-independent estimate of the transition angle for $M_s = 3.0$ being close to 75°. Thus, based on these grid convergence studies, it can be concluded that with 7 levels of grid refinement, the error in the transition angle does not exceed 1°. The respective error bar is plotted in Fig. 5.

It is immediately seen in Fig. 5 that the InMR–TRR transition is numerically predicted to happen at appreciably higher wall angles as compared to the experimental results from [6] (taken from [5]) and [7], which are shown as full black circles in Fig. 5. Furthermore, comparison with the three analytical theories from [5], shown as black dashed and dash-dotted curves in Fig. 5 and labeled according to the respective equation in [5], reveals that neither of those theories agrees with the numerical data for Mach numbers exceeding ~1.7.

It is the significant mismatch between our numerical data and available experimental and analytical data that motivated the present study. Since the theories by Ben-Dor and Takayama [8] and Takayama and Ben-Dor [9], summarized in [5], rely heavily on the notion of corner signal propagation and the communication of information (via the corner signal) to the reflection point, we performed numerical simulations with explicit corner signal tracking. Typical results are shown in Fig. 6.

In the simulation illustrated in Fig. 6, the corner signal, induced when the incident shock wave arrives at the leading edge of the reflecting surface (where the wall angle

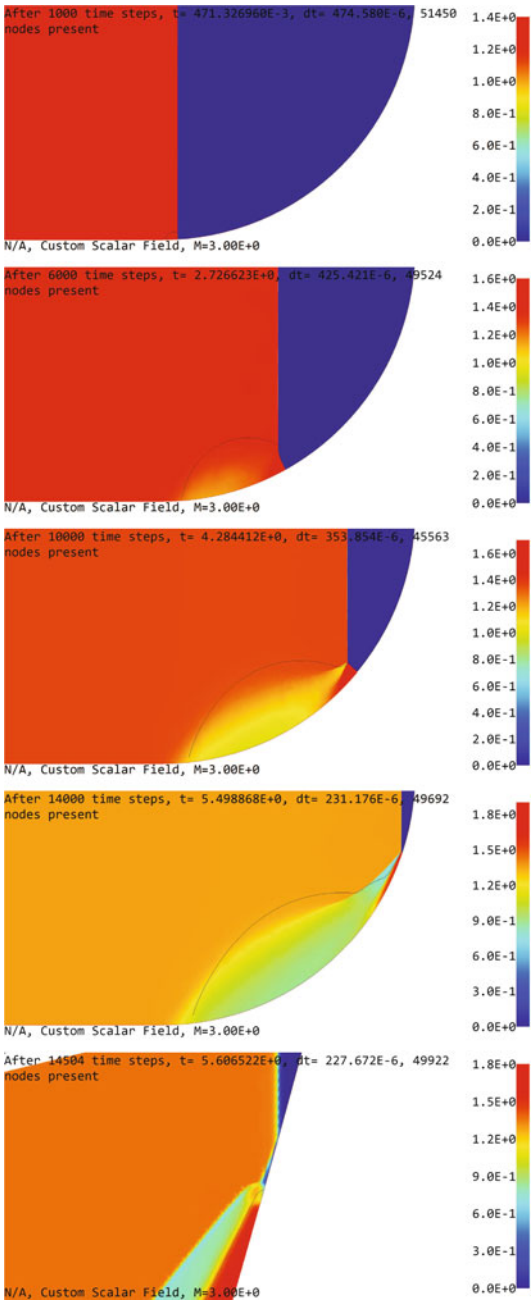

Fig. 6 Inviscid CFD simulation of shock wave ($M_s = 3.0$) reflection from a concave cylindrical wedge with corner signal tracking. The corner signal front is represented by a thin solid line. The top four images show the entire flow field while the bottom one is a magnified view near the wall right after the transition. It is seen that at all times, from the initial moment to the moment of transition, the Mach stem and the respective portion of the corner signal front coincide. At the bottom image, corresponding to a time moment shortly after the transition, it is clearly seen that the corner signal front has detached from the reflection point

is zero), is tracked. It can be stated with confidence that the corner signal front stays attached to the Mach stem at all times till the transition point and never detaches. That is consistent with the fact that the flow behind the Mach stem is subsonic with respect to the Mach stem itself. When the Mach stem vanishes (see the bottom image in Fig. 6), the corner signal immediately falls behind the reflection point because the wall angles at this moment are significantly greater than the sonic angle for the incident shock Mach number.

3 Analytical Treatments

Prior to the discussion of various ways to predict the InMR–TRR transition angle, an important statement should be made regarding the criterion according to which all theories are to be judged. One common feature of all theories existing so far and discussed below is that they are based on the assumption of inviscid, non-heat-conducting flow, that is, viscous effects are not taken into account. Therefore, it would be correct, from a methodological point of view and also taking into account the absence of an exact analytical solution of the Euler equations for the problem under consideration, to compare the results of all theories with *grid-convergent, inviscid* numerical results. The best approximate theory should be capable of reproducing them as closely as possible. Comparison of theoretical inviscid results with experimental data, as it is done in [5], does not appear to be particularly instructive in view of a number of factors affecting experimental results (as discussed further in Sect. 4).

The theoretical treatments by Ben-Dor and Takayama [8] and Takayama and Ben-Dor [9], described also in [5], are based on two main assumptions: (1) the InMR–TRR transition takes place when the corner signal generated at the leading edge of the reflecting surface is no longer capable of catching up with the reflection point; (2) the corner signal velocity is evaluated using the flow parameters behind the incident shock, assuming that the reflected shock is weak, i.e., the velocity is $V_1 + c_1$, where V_1 and c_1 are the flow velocity and the speed of sound behind the incident shock wave, respectively. The three modifications of the theory shown in Fig. 5 differ in the additional assumption regarding the path which the corner signal follows, which is illustrated in Fig. 7. The modification labeled as 'Eq. 4.21 (D)' in Figs. 5 and 7 corresponds to the assumption of the propagation path being along the reflecting surface. The version labeled as 'Eq. 4.24 (E)' assumes that the propagation path is a straight line connecting the leading edge of the reflecting surface and the triple point. Finally, the theory modification labeled as 'Eq. 4.34 (F)' makes an assumption that the corner signal is, first, being convected with the flow velocity V_1 along a straight path to another point on the reflecting surface and, then, propagates with the speed of sound c_1 straight to the triple point (the reflection point at transition).

As it is already mentioned above, none of the three theories can provide satisfactory agreement with the numerical findings for the entire range of Mach numbers.

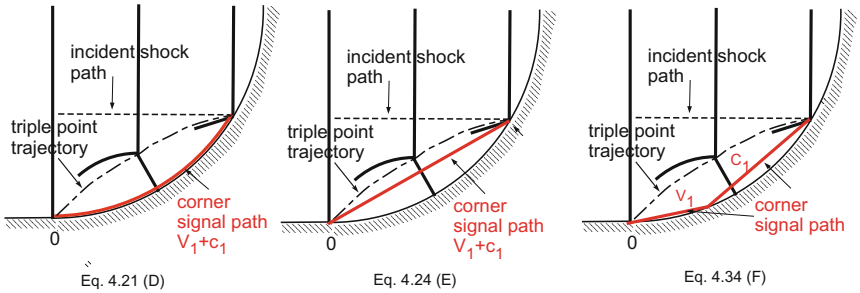

Fig. 7 Schematic illustrations of the assumptions regarding the corner signal propagation paths in the theories by Ben-Dor and Takayama [8] and Takayama and Ben-Dor [9]. The labels correspond to the equation numbers and curve labels in [5]. The same labels are used in Fig. 5

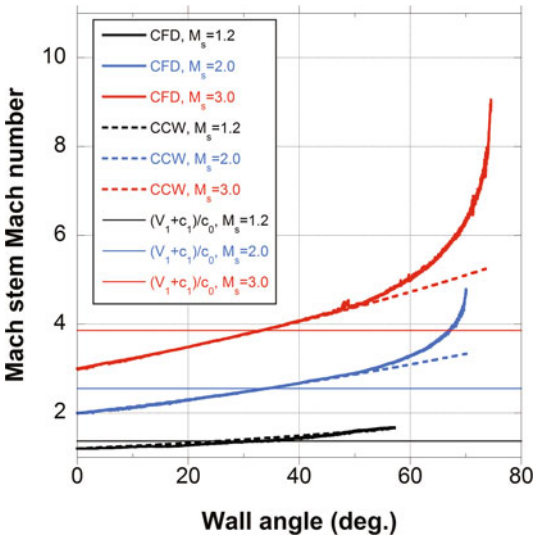

Fig. 8 Variation of the Mach number of the Mach stem foot along the reflecting surface from the leading edge to the transition point: thick solid lines—CFD results; dashed lines—results from the CCW theory; thin solid horizontal lines—values of nondimensional velocity $V + c$ behind the incident shock wave, which are assumed to be the corner signal speeds in the theories of Ben-Dor and Takayama

Furthermore, for high Mach numbers (above ~1.7), all three theories are in significant disagreement. The examination of corner signal tracking allows to identify possible reasons of the observed discrepancies. As it is clear from the above illustrations, the corner signal always stays attached to the Mach stem along its whole length and, therefore, it is problematic to unambiguously define its propagation path. However, it can be stated with confidence that the corner signal propagates with the speed of the Mach stem, and not with its own speed behind the Mach stem which is always greater. The Mach stem velocity and Mach number vary along the reflecting surface. This is illustrated in Fig. 8 by the thick solid lines. The variation is much more pronounced for higher Mach numbers and especially prominent close to the transition angle.

Let us now develop an analytical treatment taking into account that, according to numerical simulations, the transition is decided not by the speed of the corner signal but by the velocity of the Mach stem propagating along the wall. As shown in Fig. 1, the transition takes place at the time moment t^{tr} when the Mach stem vanishes at $x = x^{\mathrm{tr}}$. The incident shock moves with a constant velocity V_{s} so that $t^{\mathrm{tr}} = x^{\mathrm{tr}}/V_{\mathrm{s}}$. The foot of the Mach stem moves with a velocity $V_{\mathrm{w}}^{\mathrm{st}}$ which is changing in time during the course of wave propagation. Therefore, the time t^{tr} can be also determined via an integration along the reflecting surface. This then leads to the following general relation for the determination of the transition point:

$$\frac{x^{\mathrm{tr}}}{V_{\mathrm{s}}} = \int_0^{s^{\mathrm{tr}}} \frac{\mathrm{d}s}{V_{\mathrm{w}}^{\mathrm{st}}}\,, \tag{1}$$

where the curvilinear coordinate s is along the circular arc of radius R and its origin is at the leading edge of the concave surface. It is more convenient to operate with the respective Mach numbers M_{s} and $M_{\mathrm{w}}^{\mathrm{st}}$ which can be obtained by dividing the velocities by the speed of sound of the gas at rest in front of the incident shock. Furthermore, it is clear in Fig. 1 that $x^{\mathrm{tr}} = R\sin\theta_{\mathrm{w}}^{\mathrm{tr}}$ and $\mathrm{d}s = R\mathrm{d}\theta_{\mathrm{w}}$. Taking into account all the above and dividing Eq. (1) by the arc radius R, one obtains:

$$\frac{\sin\theta_{\mathrm{w}}^{\mathrm{tr}}}{M_{\mathrm{s}}} = \int_0^{\theta_{\mathrm{w}}^{\mathrm{tr}}} \frac{\mathrm{d}\theta_{\mathrm{w}}}{M_{\mathrm{w}}^{\mathrm{st}}(\theta_{\mathrm{w}})}\,. \tag{2}$$

For interpretation purposes, it is instructive to divide both sides of Eq. (2) by $\theta_{\mathrm{w}}^{\mathrm{tr}}$ which yields:

$$\frac{\sin\theta_{\mathrm{w}}^{\mathrm{tr}}}{\theta_{\mathrm{w}}^{\mathrm{tr}}} = M_{\mathrm{s}} \times \left[\frac{1}{\theta_{\mathrm{w}}^{\mathrm{tr}}}\int_0^{\theta_{\mathrm{w}}^{\mathrm{tr}}} \frac{\mathrm{d}\theta_{\mathrm{w}}}{M_{\mathrm{w}}^{\mathrm{st}}(\theta_{\mathrm{w}})}\right]. \tag{3}$$

The expression in the square brackets can be interpreted as an averaged value of the inverse Mach number of the Mach stem foot and can be denoted as $\langle\frac{1}{M_{\mathrm{w}}^{\mathrm{st}}}\rangle$. This results in

$$\frac{\sin\theta_{\mathrm{w}}^{\mathrm{tr}}}{\theta_{\mathrm{w}}^{\mathrm{tr}}} = M_{\mathrm{s}} \times \left\langle\frac{1}{M_{\mathrm{w}}^{\mathrm{st}}}\right\rangle. \tag{4}$$

It is to be noted that if we assume that

$$M_{\mathrm{w}}^{\mathrm{st}} = \frac{V_1 + c_1}{c_0} \tag{5}$$

and substitute this value in Eq. (3), we immediately recover Eq. 4.21 from [5] and the transition angles will be represented by the respective curve in Fig. 5. That shows the relation between the present approach and the one by Ben-Dor and Takayama. However, in fact, the Mach number along the wall varies as shown in Fig. 8 and its averaged value is higher than the one from Eq. (5).

A very important observation to make is that if we take the function $M_w^{st}(\theta_w)$ from the CFD data in Fig. 8 and use it in Eq. (3), the resulting transition angles would perfectly (with an uncertainty less than 0.5°) match those obtained from numerical simulations (see triangles in Fig. 5). Certainly, this does not constitute a new stand-alone theory since numerical data are used. However, it proves that an accurate prediction of transition angles would automatically result if it were possible to predict the Mach stem velocity along the wall.

Thin solid lines in Fig. 8 represent constant values of the nondimensional signal velocity $V_1 + c_1/c_0$ behind the incident shock used in Ben-Dor and Takayama's theories. It is seen that at lower wall angles, these constant values are above the Mach stem Mach number while at higher wall angles, close to transition when the reflected shock is strong, they are significantly below it. From the graph it is visually clear that, for higher Mach numbers, these constant values are lower than the averaged values of the Mach number variations obtained from CFD. This explains why the theories of Ben-Dor and Takayama based on the velocity $V_1 + c_1$ predict lower transition angles as compared to the numerical ones (see Fig. 5). In the numerical model, the Mach stem propagates faster and hence is able to reach higher wall angles.

As to the prediction of the Mach stem Mach number along the wall, one obvious option is to use the CCW theory, without or with a correction accounting for the presence of the reflected shock and the slipstream, to obtain $M_w^{st}(\theta_w)$ and then substitute it into Eq. (3) for subsequent prediction of transition angles. The result is shown in Fig. 5 as the solid blue line. As seen in the figure, this approach results in rather low transition angles. Figure 8, where $M_w^{st}(\theta_w)$ distributions from the CCW theory are shown, immediately explains why: the CCW theory leads to rather low Mach stem Mach numbers prior to transition when the wall angles become high and the Mach stem is therefore strong. The introduction of the correction by Itoh et al. [7] does not improve the situation: the Mach stem Mach number becomes even slightly lower (these results are not shown in Figures). Therefore, a more accurate prediction of the Mach stem Mach number along the wall remains a challenge. It is to be pointed out that, as may be observed in Fig. 5, the proposed Mach-stem-based theory results in the transition wall angle curve (the blue solid curve in Fig. 5) being qualitatively similar to the numerical results (black triangles): the results could be brought close to each other by using a constant scaling factor. At the same time, the curves corresponding to the theories by Ben-Dor and Takayama are qualitatively different: the transition wall angle becomes nearly constant for high Mach numbers.

At the end of the present section, another theory for predicting the transition angles on cylindrical concave walls should be mentioned. Historically, it precedes the theories by Ben-Dor and Takayama. Itoh et al. [7] suggest to follow the definition of the InMR–TRR transition as the point of intersection of the triple-point trajectory with the wall surface and to use geometrical shock dynamics (GSD) to obtain the triple-point trajectory. GSD leads to an ordinary differential equation for the Mach stem height as a function of wall angle. To integrate, it is necessary to use either the area-Mach number relation from the classical CCW theory or to introduce a correction to account for the presence of the reflected shock and the slipstream. Itoh et al. [7] generalize the correction by Milton [10] for the case of a shock wave of arbitrary

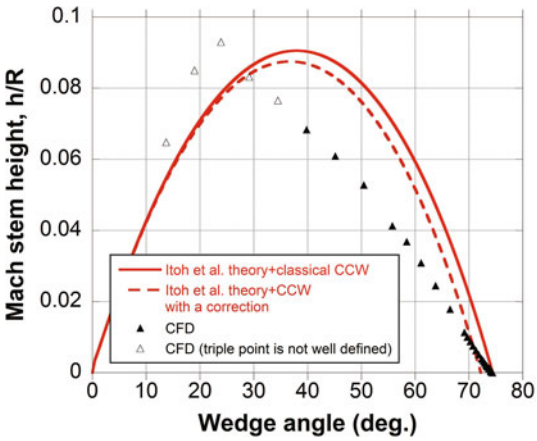

Fig. 9 Mach stem height versus wall angle for Itoh et al. theory and numerical simulations; $M_s = 3.0$

strength. The results are shown in Fig. 5 as a red solid line (classical CCW) and a red dashed line (CCW with correction). Interestingly enough, even though the CCW theory (with or without correction) grossly underpredicts the Mach stem Mach number close to transition (see Fig. 8), the resulting transition angles are the closest match to the current CFD values, i.e., the theory by Itoh et al. [7] should be judged as the best available at the moment.

It is also of interest to compare the Mach stem height predicted by the theory of Itoh et al. and the results obtained from numerical experiments. Such a comparison is shown in Fig. 9. It should be noted that solid symbols in this figure correspond to the numerical results at angles when the triple point is clearly identifiable. At the early stages of reflection, the incident shock is smoothly curved and the triple point does not exist as such. In these cases, the highest point on the incident shock which is reached by the corner signal at that moment is chosen as the triple point. Open symbols are used to distinguish these results. It is seen in Fig. 9 that the theory of Itoh et al. significantly overpredicts the height of the Mach stem. And yet, the respective triple-point trajectory intersects the wall almost at the same point as the numerically simulated trajectory—possibly serendipitously. This explains the very good correspondence with the numerical results in terms of the transition angle, as seen in Fig. 5.

4 Experimental Observations

There are at least two major reasons why the experimental results from the literature in Fig. 5 differ so significantly from the present numerical predictions. First of all, viscous effects manifesting themselves in the finite shock wave thickness and effective modification of local wall angles due to boundary layer displacement may play their role. Second, small Mach stems at later stages, prior to transition, when the

triple-point trajectory approaches the reflecting surface at shallow angles, typically pose a significant challenge for optical flow visualization.

Therefore, to clarify the issue, in the present work, new experimental observations are undertaken with a cylindrical concave model of larger radius, which would reduce the influence of viscous effects (due to a higher Reynolds number) and somewhat mitigate the challenges related to optical resolution (since Mach stem height scales with the radius). Optical resolution issues are also alleviated by using up-to-date high-resolution imaging with variable magnification. More details are provided in the next subsections.

4.1 Experimental Setup

The experimental setup used in this work is similar to that described in [11–13]. The experiments were conducted in a conventional diaphragm-operated shock tube with rectangular 150 mm × 75 mm cross section. The test section windows of 215 mm in diameter allow for optical access. Mounting of the test model is illustrated in Fig. 10. The model features a cylindrical reflecting surface of 140 mm radius with wall angles ranging from 0° to 90°.

The test gas is air. The tests were conducted at ambient temperature, which is in the range from 290 K to 293 K. The initial pressure in the test section was always between 5 and 7 kPa. The diaphragm thickness and material was kept constant throughout the tests, and therefore the burst pressure in the driver section was largely constant. Different shock Mach numbers from 2.1 to 3.1 were obtained by

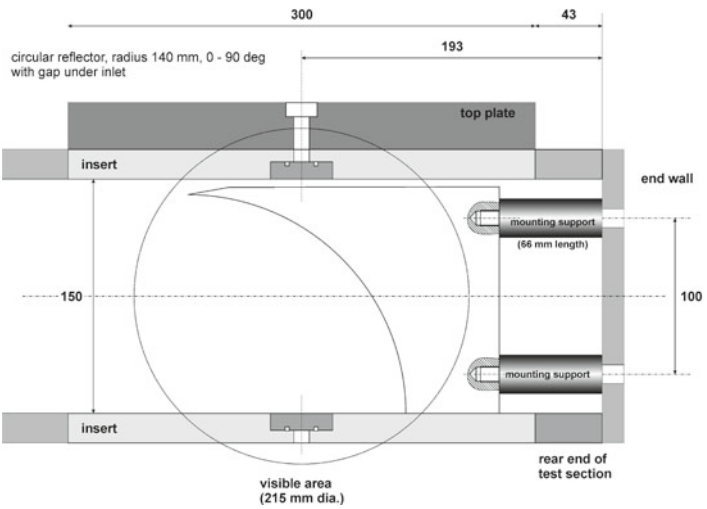

Fig. 10 Schematic sketch of the test section with the test model mounted in it

changing the driver gas (from pure helium to a helium–air mixture with different mixture ratios). The Reynolds number per meter (calculated for the initial test gas properties) was reasonably constant: 2.94×10^6 1/m to 3.9×10^6 1/m. The shock Mach number is determined from time-of-arrival data obtained by means of two KISTLER pressure transducers mounted flush with the shock tube wall ahead of the test section. The third transducer located inside the test section was mainly used to trigger the visualization system.

The uncertainty of each Mach number measurement was determined in two different ways. As the Mach number is the result of combining a time and a temperature measurement (all other properties are assumed constant), the individual measurement uncertainties were combined to give both the highest and the lowest Mach number value. In addition, the uncertainty for the Mach number was determined with the help of standard uncertainty analysis [14]. Both approaches show that each measured Mach number has an uncertainty of about ± 0.008 (which is smaller than the chosen symbol size in the plot of transition wall angle vs. Mach number).

The primary measurement output was a time-resolved sequence of density-sensitive visualization images obtained at frame rate of 5,000,000 fps. The sequences were recorded with a Shimadzu HPV-X2 high-speed camera (resolution 400×250 pixels, 128 frames per test, exposure time 55 ns). Front lighting was used. One test without front lighting was conducted to verify that the front lighting itself did not lead to spurious effects on the visualization records.

The first three initial tests visualized a large field of view (0°–75° and 43°–90° on the reflector, image magnification ~0.1). The next three showed a magnified view of the region in which the InMR-to-TRR transition occurred (13.5° angular range, 66°–79.5°, on the reflector, image magnification 0.254). Nine additional tests were conducted with a further increased image magnification (0.42, 8° angular range (68°–76°, 64°–72° and 65°–73°) on the reflector). All these tests provided omnidirectional schlieren visualizations. A final set of 11 tests was conducted with the highest magnification possible in the current setup (1.07, angular range 5°, 67.5°–72.5° and 69.5°–74.5°, on the reflector). For these tests, the camera was tilted by about 90° (later measurements showed that the angle was 89.7°). As the schlieren technique is too light-inefficient at such a magnification, these tests were run with the shadowgraph method. A summary of the imaging scales and resulting image properties of the visualized shocks is given in Fig. 11.

The imaging sequences (such as the one shown in Fig. 12) were evaluated in order to find the angle on the reflector at which the Mach stem vanishes. The frame on which the last remnant of the Mach stem can still be made out was used to identify this angle. The associated uncertainty in determining the transition angle on the selected frame is estimated as $\pm 0.1°$ for the highest image magnification and $\pm 0.2°$ for the second highest image magnification. Through independent measurements (by determining the height of a scale marker above the shock tube floor), the angular scale on the front face of the reflector was found to be accurate within $\pm 0.05°$ (meaning that, for example, the angle 70° seen on the front-lit scale is in reality between 69.95° and 70.05°). The rather generous uncertainty estimates for the transition angle include this possible inaccuracy of the applied scale.

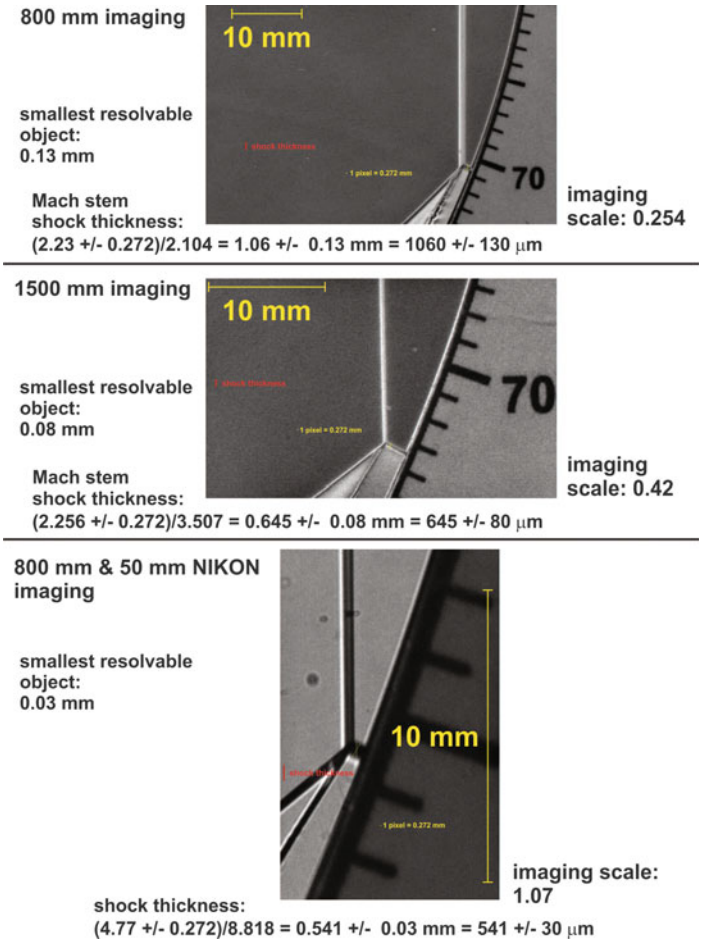

Fig. 11 Illustration of three magnifications used in the present experiments

4.2 Experimental Results

New experimental results on the InMR-to-RR transition angle are included in Fig. 5 and shown as a magnified view in Fig. 13 as full green squares. The error bars do not exceed the size of symbols and therefore are not visible. It is clearly seen that for the tested range of Mach numbers the transition angle is changing from about 70° to 74°. This is in strong contrast to the data published in [5, 6], where this angle is around 65° for the same range of Mach numbers, see Fig. 13. The model used in the experiments [6] was about one-third the size of the one used in the present work (50 mm vs. 140 mm). The size of flow features such as the Mach stem scales with model size, which explains why a small Mach stem cannot as easily be seen

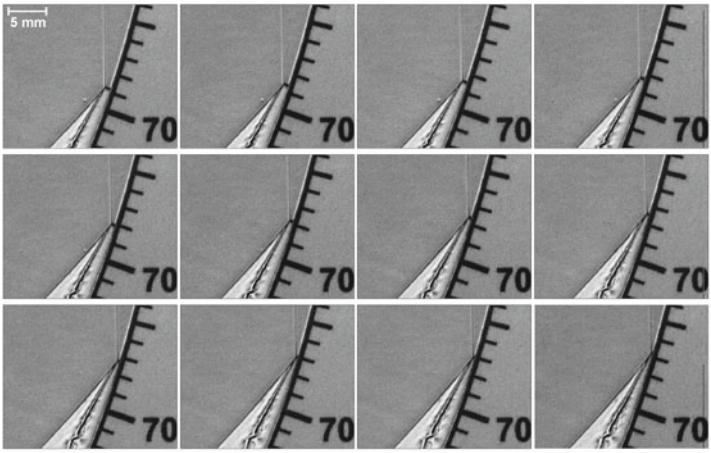

Fig. 12 The sequence of movie frames for $M_s = 2.99 \pm 0.01$. The time interval between the frames is 0.2 μs

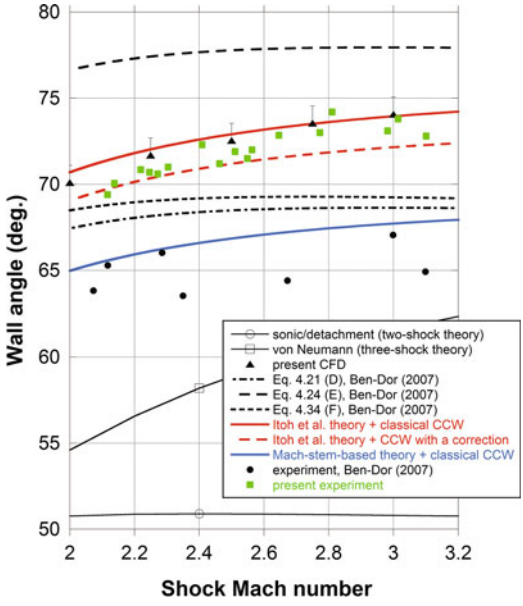

Fig. 13 Analytical, experimental, and numerical predictions of InMR–TRR transition on the concave cylindrical surface for shock Mach numbers ranging from 2.0 to 3.2

on a small model as on a larger one. The importance of the size of the model is demonstrated in the present work indirectly via comparing the results for the same Mach number (nominal Mach number 3.0) and different image magnifications: the successive increase in magnification changes the transition angle from ~70.5° to ~71.8° and finally to ~73°. Furthermore, the streak schlieren technique used in [6], while quite novel and ingenious in principle, appears to be very sensitive to minute

misalignments, in particular if the test object is small. These factors may explain the difference between the two experimental series.

It is also seen in Fig. 13 that the present experimental results lie slightly lower (by 1–2°) than the numerical values (full black trangles). It is likely that the main reason is in the still insufficient optical resolution just prior to transition. Viscous effects may also play a role but in view of relatively high Reynolds numbers (∼400, 000 based on the model radius), they do not seem to be the dominant factor. Further investigation is certainly warranted.

5 Conclusions

The new experimental and numerical data on the InMR-to-TRR transition angle are very close to each other. The slight difference between them may be attributed to still insufficient optical resolution (more likely) and viscous effects (less likely in view of high Reynolds numbers). However, the new results are significantly different from the experimental results available in the literature [6]. It may be conjectured that the model size and the resolution and sensitivity of the streak photograph technique used in [6] are the most important factors contributing to this discrepancy. The respective demonstrative analysis is in progress now. Viscous effects may also have some effect for the smaller model so that numerical modeling using the Navier–Stokes equations would be very useful in evaluating the magnitude of viscous effects in all cases.

It appears that there is still no fully satisfactory analytical model of the reflection process on concave cylindrical surfaces. A markedly better agreement between the theory by Itoh et al. with the new numerical and experimental predictions as compared to other theories appears to be a serendipitous coincidence rather than based on a solid physical ground. The ideas of the present paper based on the corner signal propagation analysis to consider the intensity of the Mach stem on the wall are certainly worth further exploration.

Acknowledgements The present research is supported by the Fonds de recherche du Quèbec - Nature et technologies (FRQNT) via the Team Research Project program and the National Science and Engineering Research Council (NSERC) via the Discovery Grant program. F.A.P. gratefully acknowledges the McGill Engineering Undergraduate Student Masters Award (MEUSMA) funded in part by the Faculty of Engineering, McGill University. Rabi Tahir's support regarding `Masterix` code is greatly appreciated.

References

1. Masterix, version 3.40, RBT Consultants, Toronto, Ontario (2003–2015)
2. Saito, T., Voinovich, P., Timofeev, E., Takayama, K.: Development and application of high-resolution adaptive numerical techniques in Shock Wave Research Center. In: Toro, E.F. (ed.) Godunov methods: theory and applications, pp. 763–784. Kluwer Academic/Plenum Publishers, New York, USA (2001)

3. Hakkaki-Fard, A.: Study on the Sonic Point in Unsteady Shock Reflections via Numerical Flowfield Analysis. PhD Thesis, McGill University (2012). http://digitool.Library.McGill.CA:80/R/-?func=dbin-jump-fullŹobject_id=106502Źsilo_library=GEN01
4. Hakkaki-Fard, A., Timofeev, E.: On numerical techniques for determination of the sonic point in unsteady inviscid shock reflections. Int. J. Aerospace Innovat. **4**, 41–52 (2012)
5. Ben-Dor, G.: Shock Wave Reflection Phenomena. Springer, 2nd ed (2007)
6. Ben-Dor, G., Takayama, K., Kawauchi, T.: The transition from regular to Mach reflexion and from Mach to regular reflexion in truly non-stationary flows. J. Fluid Mech. **100**, 147–160 (1980)
7. Itoh, S., Okazaki, N., Itaya, M.: On the transition between regular and Mach reflection in truly non-stationary flows. J. Fluid Mech. **108**, 383–400 (1981)
8. Ben-Dor, G., Takayama, K.: Analytical prediction of the transition from Mach to regular reflection over cylindrical concave wedges. J. Fluid Mech. **158**, 365–380 (1985)
9. Takayama, K., Ben-Dor, G.: A reconsideration of the transition criterion from Mach to regular reflection over cylindrical concave surface. Korean Soc. Mech. Eng. **3**, 6–9 (1989)
10. Milton, B.E.: Mach reflection using ray-shock theory. AIAA J. **13**(11), 1531–1533 (1975)
11. Alzamora Previtali, F., Timofeev, E., Kleine, H.: On unsteady shock wave reflections from wedges with straight and concave tips. AIAA Paper 2015–2642, https://doi.org/10.2514/6 2015–2642 (2015)
12. Kleine, H., Timofeev, E., Hakkaki-Fard, A., Skews, B.: The influence of Reynolds number on the triple point trajectories at shock reflection off cylindrical surfaces. J. Fluid Mech. **740**, 47–60 (2014)
13. Timofeev, E., Alzamora Previtali, F., Kleine, H.: New findings on the shock reflection from wedges with small concave tips. In: Present ISIS22 Proceedings (2016)
14. Squires, G.L. Practical Physics. Cambridge University Press, 3rd ed (1985)

New Findings on the Shock Reflection from Wedges with Small Concave Tips

F. Alzamora Previtali, H. Kleine and E. Timofeev

Abstract Planar shock reflection from straight wedges and wedges with small concave tips is considered. It is demonstrated that, in shock tube experiments for a certain wedge angle and incident shock Mach number, the resulting reflection is of irregular type in the presence of a small concave tip with an arc radius as small as 4 mm while a straight wedge with the same wedge angle produces a regular reflection. In the numerical experiments, corner signal tracking is used to demonstrate that in the case of a concave tip wedge the corner signal is always merged with the Mach stem and never detaches. It is concluded that for the prediction of the Mach-to-regular reflection transition angle for wedges with concave tips, it is essential to predict as accurately as possible the strength of the Mach stem. An initial development of an analytical method to predict the transition angle is then provided.

1 Introduction

The present paper continues previous studies on unsteady shock wave reflections from wedges with straight and concave tips [1, 2]. Lau-Chapdelaine and Radulescu [2] numerically demonstrated that the resulting reflection pattern (regular or Mach reflection) established far away from the wedge tip may differ depending on whether the reflecting wedge has a straight or concave tip. Parametric studies by Alzamora Previtali et al. [1] showed that the effect is observed for shock Mach numbers corresponding to the dual solution domain (where both Mach and regular reflection are

F. Alzamora Previtali (✉) · E. Timofeev
Department of Mechanical Engineering, McGill University, 817 Sherbrooke Street West, Montreal, QC H3A 0C3, Canada
e-mail: federico.alzamoraprevitali@mail.mcgill.ca

E. Timofeev
e-mail: evgeny.timofeev@mcgill.ca

H. Kleine
School of Engineering and Information Technology, University of New South Wales, Northcott Drive, ACT, Canberra, NSW 2600, Australia
e-mail: H.Kleine@adfa.edu.au

K. Kontis (ed.), *Shock Wave Interactions*,
https://doi.org/10.1007/978-3-319-73180-3_29

physically admissible) and wedge angles ranging from the transition angle predicted by the sonic criterion to a value slightly lower than predicted by von Neumann's criterion, i.e., within the most part of the dual solution domain. The first experimental demonstration of the effect for a concave tip wedge with the radius of curvature $R = 12$ mm and a straight wedge with the same angle (52°) is also provided in [1].

It is obviously of interest to investigate whether or not even smaller, minute, radii of curvature would also alter the resulting reflection pattern as compared to the one observed with a straight wedge of the same angle. As a step in this direction, Sect. 2 of the present paper presents experimental results obtained with the radius of curvature R as small as 4 mm.

The subsequent Sect. 3 contains some preliminary developments aiming at an analytical treatment to predict the Mach-to-regular reflection transition angle for wedges with concave tips. The final section of this paper summarizes the current findings and outlines the directions of future studies.

2 Experimental Studies

The experimental shock tube setup and diagnostics used in the present paper are similar to the ones described in [1, 3]. As shown in Fig. 1, the experiments are conducted in a conventional diaphragm-operated shock tube with rectangular 150 mm × 75 mm

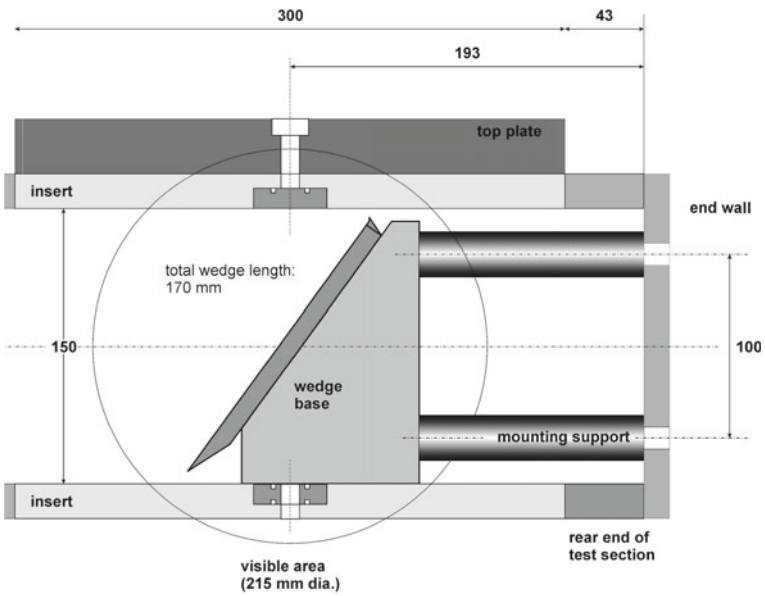

Fig. 1 Schematic sketch of the experimental model in the test section

cross section. The test section windows of 215 mm in diameter allow for optical access. The wedge plate of 170 mm in length attached to the wedge base has two tips: straight and concave. Therefore, by simply turning the plate by 180°, the desired tip is facing the incoming shock wave.

The test gas is air. Different initial pressures in the test section, ranging from 3.7 to 16 kPa, are used to obtain the desirable shock Mach numbers for given driver gas pressure and diaphragm thickness. The tests are conducted at ambient temperature, which is in the range of 290–293 K. The driver gas is helium. The shock Mach number is determined from time-of-arrival data obtained by means of three KISTLER pressure transducers mounted flush with the shock tube wall ahead of and within the test section. Each Mach number obtained from such a measurement has an uncertainty of ± 0.006.

High-speed video cameras (Shimadzu HPV-1 and HPV-X) are used for time-resolved shadowgraph or schlieren visualization at frame rates of 10^6 (HPV-1) and 10^7 (HPV-X) frames per second with an exposure time of 250 ns (HPV-1) and 55 ns (HPV-X). The spatial resolution of the cameras is 312×260 pixels for the HPV-1 and 400×250 pixels for the HPV-X. The pixels of the HPV-X are about half the size of those of the HPV-1, which leads to an improved spatial resolution. Both cameras have an in-situ image storage sensor (ISIS) and record 100 (HPV-1) and 128 (HPV-X) frames, respectively.

2.1 Results

The experimental results for a nominal incident shock Mach number 3, a wedge angle of 52°, and a wedge tip radius of 4 mm are shown in Figs. 2 and 3.

With the goal of improving resolution, different portions of the test model were visualized in different experiments with correspondingly increased image magnification. The first three images in Fig. 2a–c are from a single test giving a magnified view near the rounded tip of the wedge while the fourth image, Fig. 2d, shows the area near the wedge's trailing edge in a second test (the Mach numbers for the two experiments are essentially identical within measurement uncertainty: 3.017 ± 0.006 and 3.020 ± 0.006). Figure 3 corresponds to an experiment (shock Mach number 2.986 ± 0.006) with an even higher magnification near the concave tip. It is clear from these images that even with such a small concave tip the resulting reflection (Fig. 2) is and remains of irregular type.

The characteristic shape of the reflected wave corresponding to a DMR (double Mach reflection) is not only clearly visible near the trailing edge of the wedge but can also be traced back to very early moments, such as the right image of Fig. 3.

As shown in Fig. 4, a straight wedge of the same angle, for a close shock Mach number of 2.872 ± 0.006, produces a regular reflection. As is typical for a

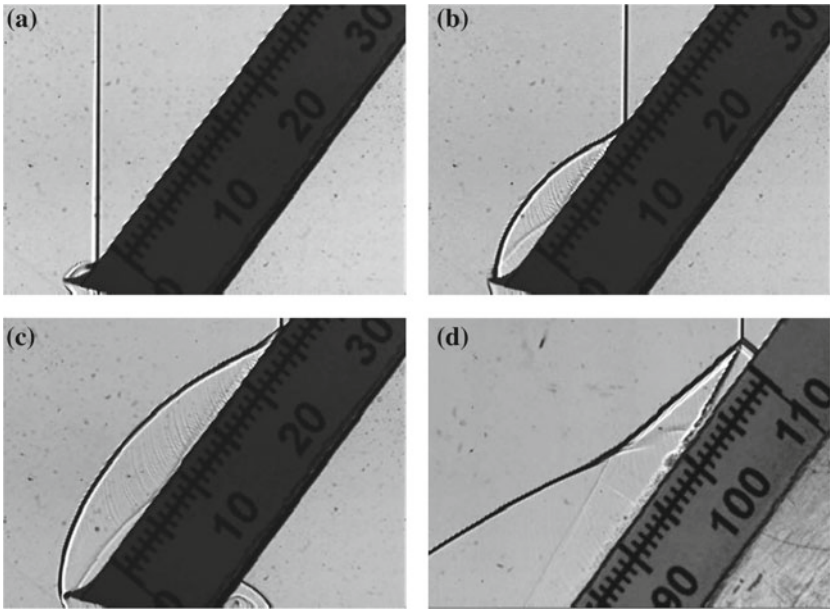

Fig. 2 Shadowgraph movie frames for the wedge angle $\theta_w = 52°$ and the concave tip radius $R = 4$ mm: **a**–**c** the shock Mach number $M_s = 3.017$; **d** $M_s = 3.020$. The scale on the wedge indicates length in millimeters

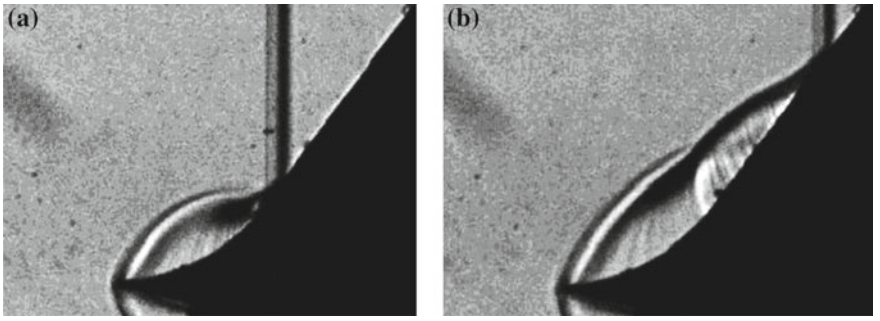

Fig. 3 Shadowgraph movie frames for the wedge angle $\theta_w = 52°$, the concave tip radius $R = 4$ mm, and the shock Mach number $M_s = 2.986$. The scale on the wedge is not visible due to the absence of front lighting; however, the scale can be judged from the radius of wall curvature equal to 4 mm. The experiment corresponds to the highest magnification possible with the present setup

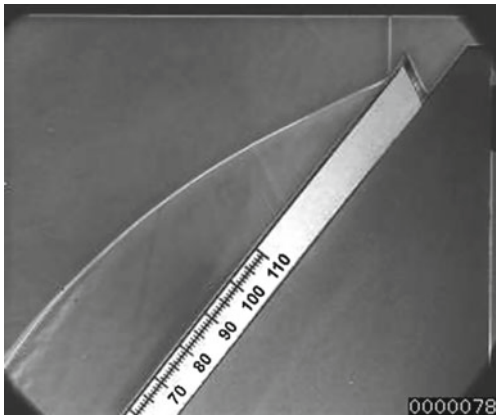

Fig. 4 Schlieren movie frame for the *straight* wedge with the angle of $\theta_w = 52°$, and the shock Mach number $M_s = 2.872$. The scale on the wedge indicates length in millimeters

regular reflection off a wedge with an angle exceeding the angle corresponding to the sonic transition criterion, the reflected shock is initially straight and begins to bend smoothly only when affected by the corner signal.

3 Preliminary Theoretical Analysis

The theoretical analysis suggested below is partly based on the findings from numerical modeling. Therefore, in the next subsection, a brief summary of the CFD tools used in the present study is given.

3.1 CFD Tools

The numerical results presented below are obtained with the Euler (inviscid, non-heat-conducting) flow model. The gas is assumed to be ideal with constant specific heats ($\gamma = 1.4$). An adaptive unstructured finite-volume flow solver [4] is used. The solver employs a node-centered, second order in space and time (for smooth solutions and uniform grids), MUSCL-Hancock TVD finite-volume scheme [5].

To shed some light on the disturbance propagation in the flow under consideration, the signal tracking technique proposed in [6] is used to study the propagation of the corner signal front. In this technique, signals are considered as infinitesimally weak sound waves propagating with the local speed of sound relative to the flow and being carried by the flow itself as well. The tracking is done at the end of each time step as a post-processing procedure. Since no actual disturbance is introduced

to the flow, the technique is as accurate as the numerical flowfield itself. Information about the velocity of the corner signal and its path can therefore be obtained from numerical experiments.

3.2 Analytical Considerations

There are at least three ways to be followed if one desires to develop an analytical treatment to predict the Mach-to-regular reflection transition angle for wedges with concave tips. It is to be emphasized that the transition considered here is between the *resulting* Mach or regular reflection established asymptotically, far away from the concave tip. In other words, for wedges with concave tips, the initial reflection is always of irregular type which eventually (when the incident shock has covered a distance considerably exceeding the tip radius of curvature) either remains a Mach reflection or, if the wedge angle exceeds a certain critical angle called "transition angle," turns into a regular reflection. It is the transition angle between these two final outcomes that are of interest.

The first possible approach is to generalize the treatment suggested by Itoh et al. [7] for the transition on a fully concave (cylindrical) surface. Their idea is to consider the trajectory of the triple point and find its intersection with the wall surface, which is, by definition, the transition point. Since this task appears to be intractable using the full conservation laws (the Euler equations) without any simplifying assumptions, Itoh et al. [7] use the geometrical shock dynamics approach based on the CCW (Chester–Chisnell–Whitham) theory. Along the lines proposed by Milton [8], they derive a correction accounting for the presence of the reflected shock wave and the tangential discontinuity for an incident shock of arbitrary strength.

The second way is to follow the ideas of Ben-Dor and Takayama [9, 10], see also a summary in [11], for the transition on concave cylindrical surfaces. Their approach is based on the length-scale concept and involves the consideration of corner signal propagation behind the incident shock and the induced Mach stem. According to this concept, the moment just before transition represents the last time the corner-generated signal can catch up with the triple point.

Finally, another approach is advocated for concave cylindrical surfaces in the companion paper of these Proceedings [12]. It is based on the examination of the propagation of weak disturbances ("corner signals") in the flow. Such an examination, carried out via numerical modeling, reveals that the speed of corner signals (generated by the leading edge of the reflecting surface as well as by all subsequent wall segments) always exceeds that of the foot of the Mach stem, and, therefore, the signal fronts stay merged with the Mach stem at all times. From this point of view, the speed of corner signals does not appear to be the deciding factor in transition. In [12], it is shown that the prediction of the Mach stem velocity along the reflecting surface is a key for accurate prediction of transition.

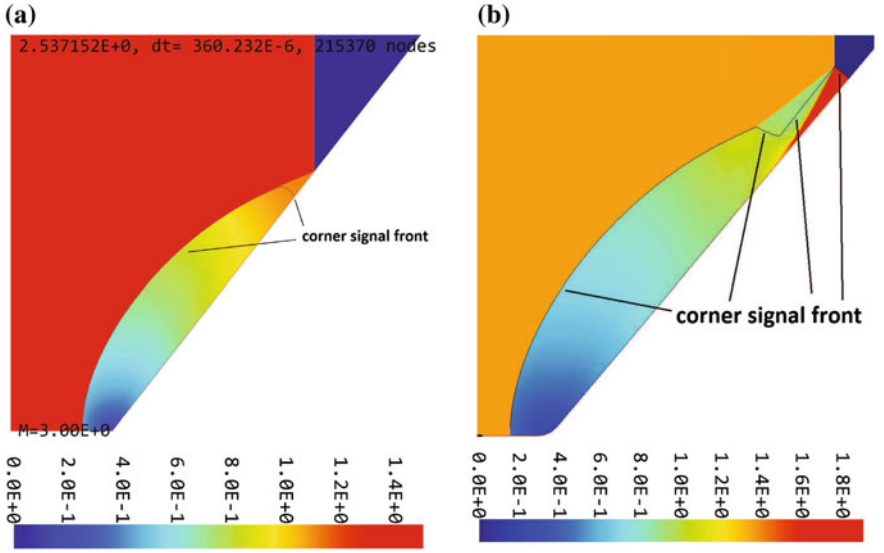

Fig. 5 Inviscid CFD simulations of shock wave ($M_s = 3.0$) reflection from wedges with corner signal tracking. The corner signal front at the displayed time moment is shown with a thin solid line. The wedge angle is $\theta_w = 52°$ in both cases shown: **a** the case of a straight wedge; the corner signal front runs along the reflected shock and then comes to the surface well behind the reflected point, i.e., the signal is not catching up with the reflection point. This corresponds to the regular nature of the observed shock reflection; **b** the case of a concave tip wedge; it is seen that the Mach stem and the respective portion of the corner signal front coincide

In the present paper, a similar examination of corner signal propagation is conducted for wedges with concave tips. Figure 5a shows an instant Mach number flowfield (the Mach number is given in the laboratory frame of reference) generated when a planar shock wave with shock Mach number 3.0 reflects from a *straight* wedge of 52° (the same angle as in the experiments shown in the previous section). This simulation tracks the corner signal, which is induced when the incident shock has just reached the wedge leading edge. The instant corner signal front is shown in Fig. 5a as a thin black line. As expected for a wedge angle exceeding the sonic angle (50.81°), the corner signal is clearly behind the reflection point. There is a straight portion of the reflected shock, not affected by the corner signal. Figure 5b shows the instant corner signal front for a concave tip wedge with the wedge angle of 52°. It is seen that the portion of the front propagating along the wedge coincides with the Mach stem, from the wedge wall to the triple point. The analysis of the reflection process as a whole confirms that the corner signal is always merged with the Mach stem and never detaches. This should be expected because the flow downstream from the Mach steam is always subsonic relatively to the Mach stem and, therefore, the corner signal velocity $V + c$ behind the Mach stem in the laboratory frame of reference is greater than the velocity of the Mach stem in the same reference frame (V is the local flow velocity, and c is the local speed of sound). Hence, the corner signal catches up

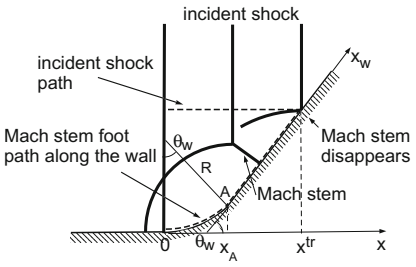

Fig. 6 Schematics of InMR–TRR (inverse Mach reflection–transitioned regular reflection) transition on a wedge with a concave tip, illustrating the analytical treatment of the present paper

with the Mach stem at the same instant as it is generated and stays merged with it (obviously, it cannot go ahead of the Mach stem).

From this point of view, as already mentioned above, similarly to the case of a fully concave reflecting surface, the corner signal speed does not appear to be the deciding factor in transition: the speed of the foot of the Mach stem will determine when (and if) the Mach stem vanishes.

The subsequent derivations are assisted by the schematics shown in Fig. 6. The transition takes place at the time moment t^{tr} when the Mach stem vanishes at $x = x^{\mathrm{tr}}$ or $x_{\mathrm{w}} = x_{\mathrm{w}}^{\mathrm{tr}}$. In Fig. 6, the coordinate x is along the horizontal x-axis while the curvilinear coordinate x_{w} is along the reflecting surface; the origin of both coordinates is at the leading edge of the wedge. The incident shock moves with a constant velocity V_{s} so that $t^{\mathrm{tr}} = x^{\mathrm{tr}}/V_{\mathrm{s}}$. The foot of the Mach stem moves with a velocity $V_{\mathrm{w}}^{\mathrm{st}}$ which is changing in time during the course of wave propagation. Therefore, the time t^{tr} can be also determined via integration along the reflecting surface. This would then lead to the following general relation for the determination of the transition point:

$$\frac{x^{\mathrm{tr}}}{V_{\mathrm{s}}} = \int_0^{x_{\mathrm{w}}^{\mathrm{tr}}} \frac{\mathrm{d}x_{\mathrm{w}}}{V_{\mathrm{w}}^{\mathrm{st}}} \tag{1}$$

The integral can be split into two parts corresponding to the circular arc of the concave tip and the straight portion of the wedge:

$$\frac{x^{\mathrm{tr}}}{V_{\mathrm{s}}} = \int_0^{x_{\mathrm{w}}^{A}} \frac{\mathrm{d}x_{\mathrm{w}}}{V_{\mathrm{w}}^{\mathrm{st}}} + \int_{x_{\mathrm{w}}^{A}}^{x_{\mathrm{w}}^{\mathrm{tr}}} \frac{\mathrm{d}x_{\mathrm{w}}}{V_{\mathrm{w}}^{\mathrm{st}}}, \tag{2}$$

where x_{w}^{A} (or x^{A}) is the coordinate of the point where the circular and straight segments of the wedge meet.

It would be more convenient to operate with the wall angle θ_{w} (which is also the polar angle of the arc, see Fig. 6) and the respective transition angle $\theta_{\mathrm{w}}^{\mathrm{tr}}$. Furthermore, let us express the distance between point A and the transition point as λR where λ is a nondimensional factor and R is the radius of the concave cylindrical portion of the

wedge. This leads to the following relation:

$$\frac{R\sin\theta_{\mathrm{w}}^{\mathrm{tr}}+\lambda R\cos\theta_{\mathrm{w}}^{\mathrm{tr}}}{V_{\mathrm{s}}}=\int_{0}^{\theta_{\mathrm{w}}^{\mathrm{tr}}}\frac{R\mathrm{d}\theta_{\mathrm{w}}}{V_{\mathrm{w}}^{\mathrm{st}}}+\int_{x_{\mathrm{w}}^{A}}^{x_{\mathrm{w}}^{A}+\lambda R}\frac{\mathrm{d}x_{\mathrm{w}}}{V_{\mathrm{w}}^{\mathrm{st}}}. \tag{3}$$

After dividing both sides by R and making a simple variable transformation, $\tilde{x}_{\mathrm{w}}=(x_{\mathrm{w}}-x_{\mathrm{w}}^{A})/R$, in the second integral, we arrive at

$$\frac{\sin\theta_{\mathrm{w}}^{\mathrm{tr}}+\lambda\cos\theta_{\mathrm{w}}^{\mathrm{tr}}}{V_{\mathrm{s}}}=\int_{0}^{\theta_{\mathrm{w}}^{\mathrm{tr}}}\frac{\mathrm{d}\theta_{w}}{V_{\mathrm{w}}^{\mathrm{st}}}+\int_{0}^{\lambda}\frac{\mathrm{d}\tilde{x}_{\mathrm{w}}}{V_{\mathrm{w}}^{\mathrm{st}}}. \tag{4}$$

It is to be noted that assuming $\lambda=0$, i.e., considering a fully concave cylindrical surface, without a straight wedge, Eq. (4) reduces to the relation obtained in [12] for the concave cylindrical surface:

$$\frac{\sin\theta_{\mathrm{w}}^{\mathrm{tr}}}{\theta_{\mathrm{w}}^{\mathrm{tr}}}=V_{\mathrm{s}}\times\frac{1}{\theta_{\mathrm{w}}^{\mathrm{tr}}}\int_{0}^{\theta_{\mathrm{w}}^{\mathrm{tr}}}\frac{\mathrm{d}\theta_{w}}{V_{\mathrm{w}}^{\mathrm{st}}}. \tag{5}$$

Numerical experiments show, see the data presented in [1], that the asymptotic angle χ between the triple point trajectory and the wedge surface approaches zero at transition, and therefore, it can be safely assumed that $\lambda\gg 1$, which means that the transition takes place far away from the wedge tip—it may be conjectured that this happens "at infinity." This is also consistent with the goal of obtaining the transition angle between the resulting, asymptotic ($x_{\mathrm{w}}\to\infty$) reflection patterns. By considering that $\lambda\gg 1$, Eq. (4) can therefore be simplified to

$$\frac{\cos\theta_{\mathrm{w}}^{\mathrm{tr}}}{V_{\mathrm{s}}}=\frac{1}{\lambda}\int_{0}^{\lambda}\frac{\mathrm{d}\tilde{x}_{\mathrm{w}}}{V_{\mathrm{w}}^{\mathrm{st}}}=\left\langle\frac{1}{V_{\mathrm{w}}^{\mathrm{st}}}\right\rangle \tag{6}$$

or

$$\cos\theta_{\mathrm{w}}^{\mathrm{tr}}=V_{\mathrm{s}}\times\left\langle\frac{1}{V_{\mathrm{w}}^{\mathrm{st}}}\right\rangle \tag{7}$$

where $\langle\frac{1}{V_{\mathrm{w}}^{\mathrm{st}}}\rangle$ denotes an averaged value of the inverse velocity of the Mach stem foot along the straight portion of the wedge.

Numerical experiments indicate that the strength of the Mach stem does not vary significantly when it propagates along the wedge away from the tip, see Fig. 7. Then, the Mach stem velocity $V_{\mathrm{w}}^{\mathrm{st}}$ can be assumed to have a constant value of $\langle V_{\mathrm{w}}^{\mathrm{st}}\rangle$, resulting in

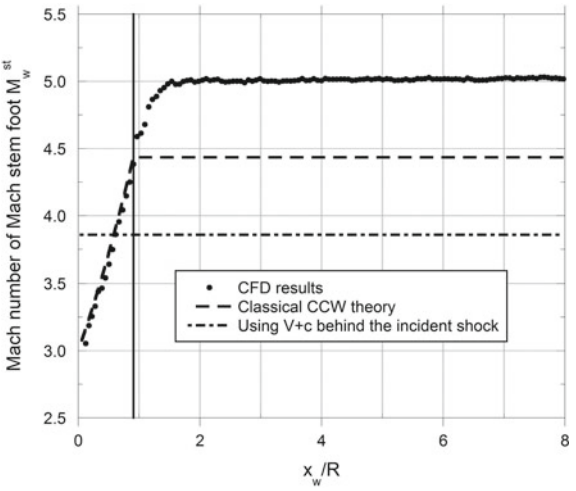

Fig. 7 Mach number history of the Mach stem on the reflecting surface of a wedge with a concave tip ($M_s = 3.0$ and $\theta_w = 52°$). The vertical solid line corresponds to the point where the concave tip and the straight portion of the wedge meet

$$\cos\theta_w^{tr} = \frac{V_s}{\langle V_w^{st}\rangle}\,. \tag{8}$$

The relation can be also rewritten in terms of Mach numbers as follows:

$$\cos\theta_w^{tr} = \frac{M_s}{\langle M_w^{st}\rangle}\,. \tag{9}$$

Thus, to predict the transition angle, it is necessary to predict the Mach stem strength when it propagates along the wedge. The correctness of this principle can be verified via numerical experiments. For example, for the incident shock Mach number $M_s = 3.0$ and the wedge angle $\theta_w = 59.5°$ (the value is chosen to be close to the transition angle), numerical experiments give the value of 5.852 for $\langle M_w^{st}\rangle$ at the end of the wedge. Then, Eq. (9) results in $\theta_w^{tr} = 59.2°$, which is very close to the transition angle value of 59.79° for $M_s = 3.0$ determined via numerical experiments in [1]. Thus, it is to be concluded that if one succeeded in predicting the Mach stem strength along the wedge, this would automatically lead to a correct prediction of transition.

As demonstrated in Fig. 7, the CCW theory results in a significantly lower value of the Mach stem Mach number as compared to the numerical prediction. It is also seen that the use of $V + c$ value behind the incident shock as the velocity of the Mach stem, as in [9, 10], is completely unacceptable. The issue remains open for investigation.

4 Conclusions

In the shock tube experiments of the present paper, it is demonstrated that, for a certain wedge angle and incident shock Mach number, the resulting reflection is of irregular type in the presence of a small concave tip with the arc radius as small as 4 mm while a straight wedge with the same wedge angle produces a regular reflection. The result is of obvious practical significance: it clearly points to the possibility, under certain conditions, of having an unexpected reflection pattern (and pressure and temperature values associated with it) due to corner roundings which might be erroneously perceived as insignificant.

The present paper provides a basis for the subsequent development of an analytical method to predict the MR–RR transition angle for wedges with concave tips. It is shown that it is essential to predict as accurately as possible the strength of the Mach stem. Further developments aiming at such predictions are presently under way.

Numerical simulations using the Navier–Stokes equations are also to be carried out. The study of the influence of viscous effects is essential because in most shock tube experiments, high Mach numbers (>2) can only be achieved at low pressures in the test section. As a result, the Reynolds number based on the tip radius R can be as low as 15,000 for $R = 4$ mm, and, therefore, viscous effects may significantly shift the transition boundaries.

Acknowledgements The present research is supported by the Fonds de recherche du Québec—Nature et technologies (FRQNT) via the Team Research Project program and the National Science and Engineering Research Council (NSERC) via the Discovery Grant program. F.A.P. gratefully acknowledges the McGill Engineering Undergraduate Student Masters Award (MEUSMA) funded in part by the Faculty of Engineering, McGill University. Rabi Tahir's support regarding `Masterix` code is greatly appreciated.

References

1. Alzamora Previtali, F., Timofeev, E., Kleine, H.: On unsteady shock wave reflections from wedges with straight and concave tips. AIAA Paper 2015–2642 (2015). https://doi.org/10.2514/6.2015-2642
2. Lau-Chapdelaine, S.S., Radulescu, M.I.: Non-uniqueness of solutions in asymptotically self-similar shock reflections. Shock Waves **23**(6), 595–602 (2013)
3. Kleine, H., Timofeev, E., Hakkaki-Fard, A., Skews, B.: The influence of Reynolds number on the triple point trajectories at shock reflection off cylindrical surfaces. J. Fluid Mech. **740**, 47–60 (2014)
4. `Masterix`: Ver. 3.40, RBT Consultants, Toronto, Ontario (2003–2015)
5. Saito, T., Voinovich, P., Timofeev, E., Takayama, K.: Development and application of high-resolution adaptive numerical techniques in shock wave research center. In: Toro, E.F. (ed.) Godunov Methods: Theory and Applications, pp. 763–784. Kluwer Academic/Plenum Publishers, New York, USA (2001)
6. Hakkaki-Fard, A., Timofeev, E.: On numerical techniques for determination of the sonic point in unsteady inviscid shock reflections. Int. J. Aerosp. Innovations **4**, 41–52 (2012)
7. Itoh, S., Okazaki, N., Itaya, M.: On the transition between regular and Mach reflection in truly non-stationary flows. J. Fluid Mech. **108**, 383–400 (1981)

8. Milton, B.E.: Mach reflection using ray-shock theory. AIAA J. **13**(11), 1531–1533 (1975)
9. Ben-Dor, G., Takayama, K.: Analytical prediction of the transition from Mach to regular reflection over cylindrical concave wedges. J. Fluid Mech. **158**, 365–380 (1985)
10. Takayama, K., Ben-Dor, G.: A reconsideration of the transition criterion from Mach to regular reflection over cylindrical concave surface. Korean Soc. Mech. Eng. **3**, 6–9 (1989)
11. Ben-Dor, G.: Shock Wave Reflection Phenomena, 2nd edn. Springer (2007)
12. Timofeev, E., Alzamora Previtali, F., Kleine, H.: On unsteady shock wave reflection from a concave cylindrical surface. In: Proceedings of Present ISIS22 (2016)

Normal Shock Wave Diffraction Over a Three-Dimensional Corner

Randall T. Paton, Beric W. Skews and Cheryl M. Cattanach

Abstract The diffraction over a corner normal to the direction of travel of a shock wave has been well documented. This has also been extended to the diffraction of a shock wave over edges with discontinuous profiles in the flow direction. However, these studies have only considered the diffraction of a shock wave travelling over a single, plane surface initially. The current study extends this to consider the dynamics of a plane shock wave travelling simultaneously over two orthogonal surfaces, analogous to a shock wave travelling over the roof and wall of a rectangular building. The flow field bears similarity to the diffraction of a shock wave over a convex diffraction edge whereby there is thickening of the vortex tube formed at the axis defined by the common edge of the two surfaces with outboard thinning. However, as the Mach number of the incident shock wave increases, the vortex tubes shed from the two diffraction edges no longer merge into a single tube but rather each terminates in the downstream face. This also results in curvature of these vortex tubes away from the face rather than remaining approximately parallel to the downstream face as seen in most cases. These results were derived experimentally and computationally for a Mach number in the range M1.3–M1.6.

1 Introduction

Since the original description of the behaviour of a plane shock wave diffracting over corners of various two-dimensional geometries by Skews [1], the effect on the canonical flow field of different three-dimensional geometries has been explored. Skews established that the features of the post-diffraction flow field, such as the

R. T. Paton (✉) · B. W. Skews · C. M. Cattanach
Flow Research Unit, School of Mechanical, Industrial, and Aeronautical Engineering, University of the Witwatersrand, PO WITS 2050, Johannesburg, South Africa
e-mail: Randall.Paton@wits.ac.za

B. W. Skews
e-mail: Beric.Skews@wits.ac.za

C. M. Cattanach
e-mail: Cheryl.Cattanach@students.wits.ac.za

K. Kontis (ed.), *Shock Wave Interactions*,
https://doi.org/10.1007/978-3-319-73180-3_30

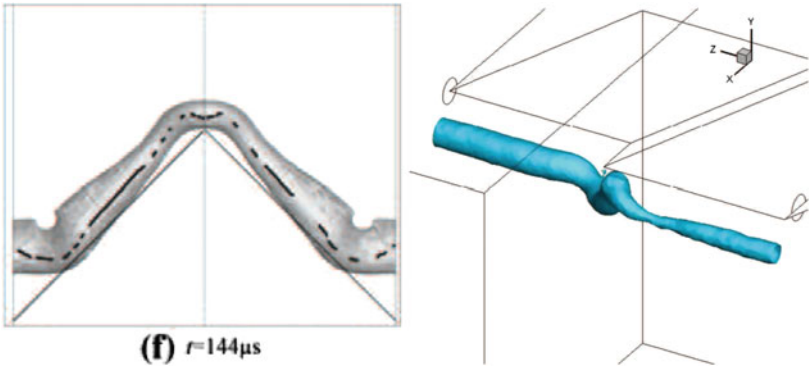

Fig. 1 Vortex profiles sometime after diffraction of a normal shock wave over a discontinuous (*left*) convex edge [3] and (*right*) aligned edge [4]

contact surface, vortex and expansion wave, depend on the angle of diffraction and the incident shock wave number. However, the geometry and behaviour of these features, especially the vortex, can change significantly in the presence of a singular corner in the diffracting edge. Jiang et al. [2] explored a plane shock wave diffracting at the normal exit of a square cross-section shock tube and showed that the vortex that is shed at the exit edge conforms approximately to the profile of the exit edge at early times and has a fairly consistent cross-section size. However, as the vortex propagates, it undergoes axis swapping and changes in cross-section size and vortex loop planarity arise because of variations in vortex strength between the corners and mid-side vortex segments.

Reeves and Skews [3] studied shock waves diffracting over normal parabolic and square corners and, as in Fig. 1, this results in a thickening and bending of the vortex core along the symmetry plane followed by a contraction outboard of that. Further study of diffraction over discontinuous edges by Cooppan and Skews [4] showed that the portion of the vortex along the aligned diffraction edge deforms out of the plane defined by the vortex lines.

The current study considers a plane shock wave diffracting over a three-dimensional corner where the incident shock wave is parallel to the diffraction surface and perpendicular to the mutually orthogonal edges leading to the corner. Unlike the case studied by Jiang et al., the diffracted shock wave will interact with itself following diffraction since this is diffraction over edges forming an acute rather than an obtuse angle. This is analogous to a shock wave travelling down the side and roof of a building and diffracting over the downstream face of the building.

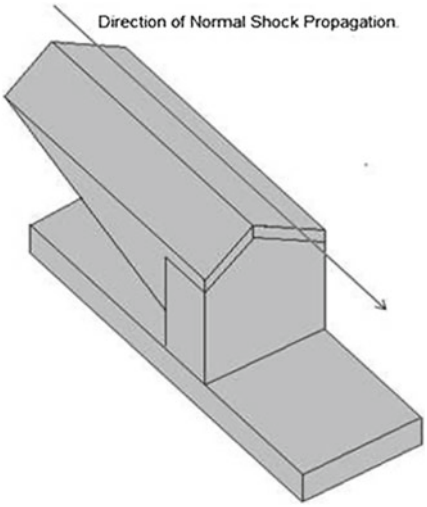

Fig. 2 Current study test piece

2 Apparatus

The diffraction behaviour was tested experimentally in a conventional shock tube expanding into ambient conditions at incident Mach numbers of approximately 1.3, 1.45 and 1.6. and visualised using high-speed z-type shadowgraph with both horizontal and vertical sensitivities in separate tests. The high-speed schlieren was captured using a Photron SA5-77K-C1 at a speed of 75 kfps and a resolution of 320×264 px resulting in a spatial resolution of approximately 0.25 mm per pixel. A schematic of the apparatus installed flush between the walls of the shock tube is shown in Fig. 2. The image acquisition was triggered by upstream PCB M114A21 pressure transducers.

A computational study was also undertaken using ANSYS Fluent 15 to facilitate interpretation of the experimental results. The model employed an AUSM flux formulation and third-order MUSCL scheme for flow discretisation. The model comprised 1.05 million cells and was executed with a time step of 1 μs. The model has been run initially inviscid to determine the pressure-driven effects.

3 Results

3.1 Experimental Results

The experimental results have been presented as time series where the results for the horizontally and vertically sensitive shadowgraph systems (hereafter referred to h-shadowgraph or v-shadowgraph, respectively) have been placed alongside each

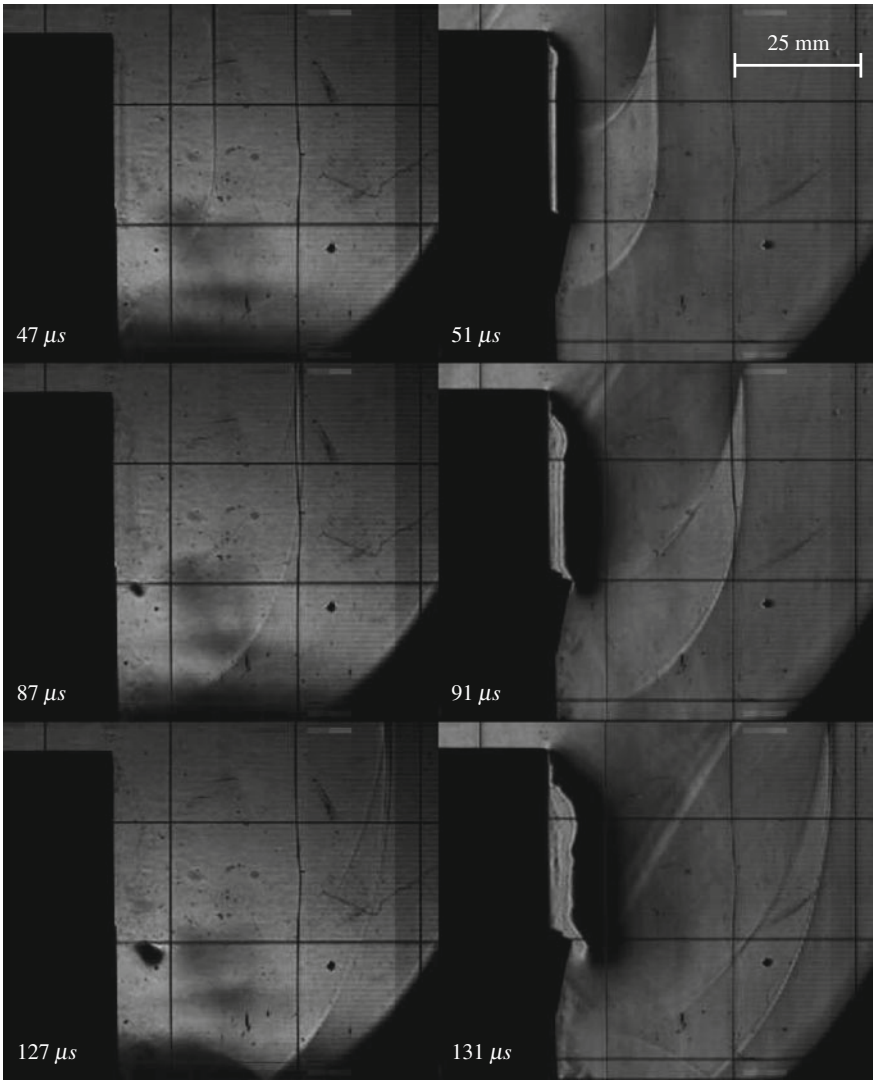

Fig. 3 Experimental shadowgraphs with vertical (*left*) and horizontal (*right*) sensitivity for an incident shock wave strength of M1.3

other for ease of comparison. The results have been annotated with the approximate time since the arrival of the incident shock wave at the diffraction edge. Since the two sets of results for each Mach number were acquired in separate tests, the comparison images may not be exactly synchronised but the mis-synchronisation is no greater than 4 μs.

The results for the lowest incident wave strength, Mach 1.3 in Fig. 3, will be discussed in detail and then comparisons drawn for the other sets of results. It should be noted at this stage that the images for the v-shadowgraphs shown a dark shape protruding from the diffraction face. This is a piece of the tape used to seal the models against the test section windows that slipped for these tests and, due to time constraints, these tests could not be repeated. This thin tape (approximately 0.2 mm thickness) was not deemed to have a significant effect on the results given the width of the shock tube (75 mm).

At the earliest time, in the top row, the shock wave has fully diffracted along the entire edge. As a result of this, there appear to be two wave diffractions visible in the h-shadowgraph: the upper is the apex of the diffracted shock wave surface along the centreline of the model, while the lower diffraction is the edges of the diffraction at the windows of the test section. It is assumed that the reflection of these two waves is regular at this time. In the v-shadowgraph, the edge of the vortex can only be faintly seen but the thickening near the apex of the model, seen in the h-shadowgraph, is also visible here. This thickening is similar to that seen near the apex and outboard thinning of the vortex tube seen in [3].

In the second v-shadowgraph, the core of the vortex where it terminates against the test section is clearly visible. The vortex is also detaching from the diffraction surface and convecting downstream. In the h-shadowgraph, it is clear that the bend in the vortex has curved significantly by the way that it is quite far away from the apex of the diffraction edge and the very significant thickening of the vortex.

In the final frames, the vortex is now quite separated from the diffraction surface though the upper portion still remains close, as evident in the third h-shadowgraph. The reflected shock wave from the floor of the test section can be seen and thus no further results can be presented.

The initial diffraction for the Mach 1.45 wave, shown in Fig. 4, is very similar to that for Mach 1.3. The most significant difference is that the edge of the vortex is quite clear in the v-shadowgraph as is the vortex core where it meets the test section window. These both suggest that, despite the fairly small increase in incident Mach number, the vortex shed is much stronger. This is also borne out by the greater extent by which the corner of the vortex has thickened and curved even at this early stage of the flow.

Something to note in the h-shadowgraphs of this series is the disturbance of the flow field below the diffracted shock wave. This is as a result of some leakage of flow past the model on one side of the model. While this certainly affected the vortex where it meets the boundary layer on the test section window, this effect seems to be minimal.

In the second set of images, it is clear that the portion of the vortex towards the bottom of the frame is separating from the diffraction face much more than that near the top. In the v-shadowgraph, the vortex edge has a backward-S shape which is also clear in the vortex centreline (the boundary between the black and light regions of the vortex) in the h-shadowgraph. Rather than being as a result of a difference in vortex strength, which should be consistent along the entire diffraction edge due to

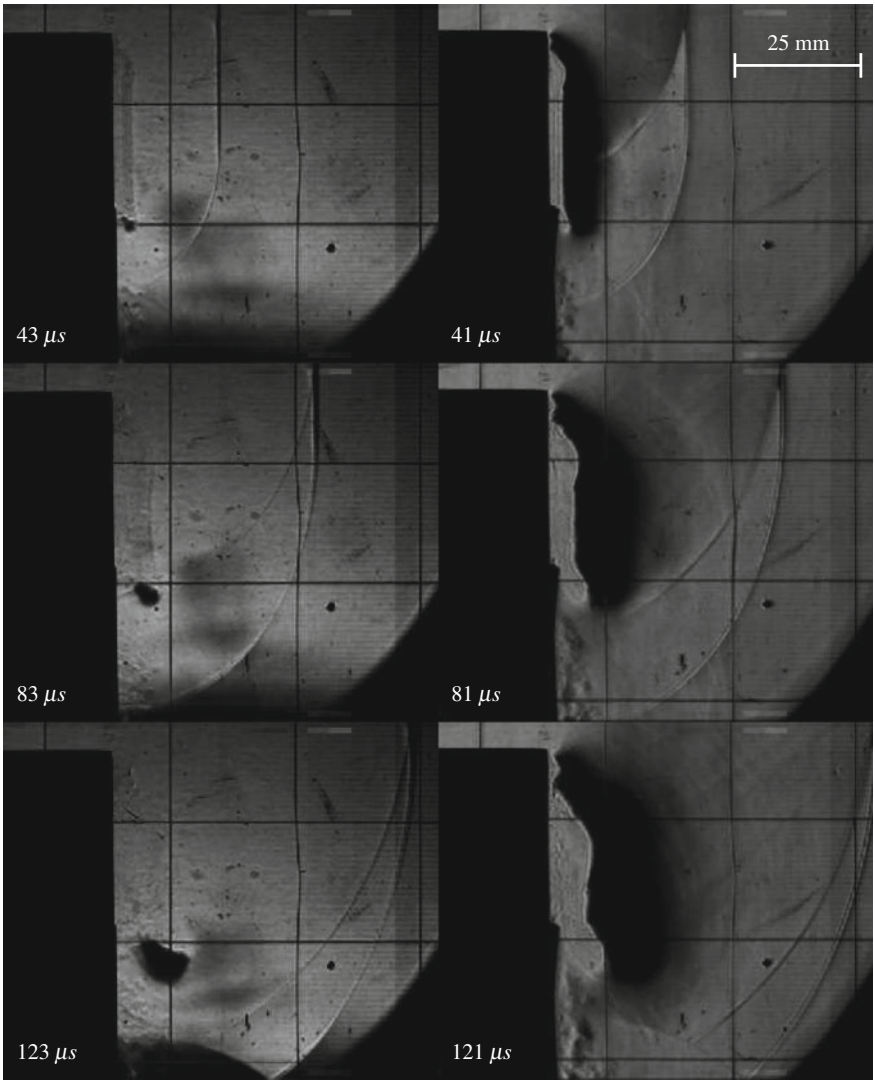

Fig. 4 Experimental shadowgraphs with vertical (*left*) and horizontal (*right*) sensitivity for an incident shock wave strength of M1.45

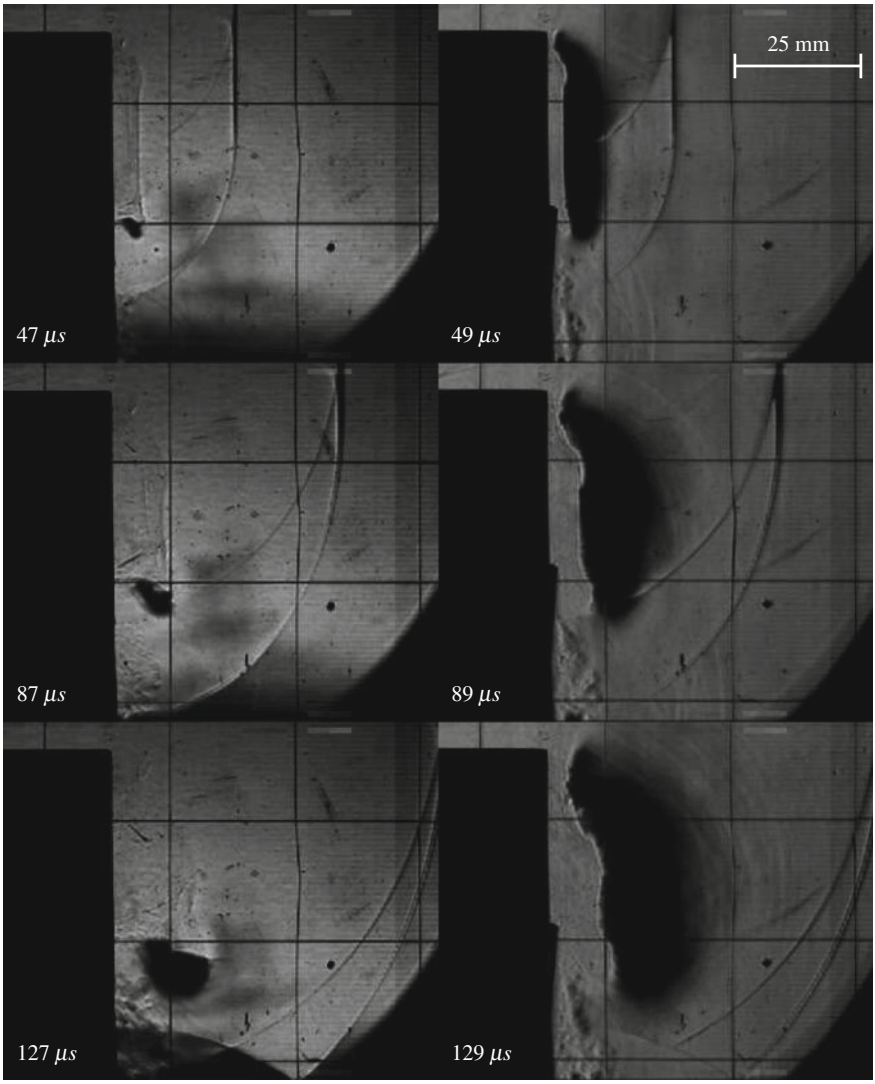

Fig. 5 Experimental shadowgraphs with vertical (*left*) and horizontal (*right*) sensitivity for an incident shock wave strength of M1.6

simultaneous diffraction, it is thought that this is due to curvature of the vortex that happens so that it terminates normal to the test section window.

The curvature of the vortex near the window is clear here and in the final images for this series, by the thickening of the vortex as well, which was clearly described in [3]. By directly comparing the final v-shadowgraphs for the Mach 1.3 and Mach 1.45 results, the greater strength of the vortex is also clear by the much larger core at the window.

In the results for Mach 1.6, it is clear that the vortex here is significantly stronger still. This seems to have further strange effects on the vortex behaviour. While the first h-shadowgraph in Fig. 5 seems very similar to the previous results (with some leakage here as well), in the second frame, the distortion of the vortex near the corner has a rather different aspect. It appears here as though the thickened portion of the vortex has curved it such that the centre lies almost halfway down the height of the vortex but there is still evidence of a vortex above this. Unfortunately, a more detailed interpretation is not possible from these results.

3.2 Computational Results

The results presented here have been selected to match, as closely as possible, the times since the arrival of the incident shock wave at the diffraction edge of the frames discussed for the experimental results. In all cases, isopycnics (surfaces of constant density) of 0.75, 0.825 and 0.9 kg m^{-3} were plotted to visualise the vortex formed by the diffraction of the shock wave. In these images, the 0.9 kg m^{-3} isopycnic is the outermost and is considered the boundary of the vortex. The other two surfaces are included to give a sense of the change of density within the vortex, where the density falls to approximately 0.5 kg m^{-3} in all cases, but these can only be seen in the side visualisations as the isopycnic surfaces are presented as opaque.

Considering first the results for the incident shock wave strength of M1.3 shown in Fig. 6, the vortex tube appears incomplete in the first frame. Although the vortex lines appear near the apex of the diffraction edge, the weaker portion outboard of this presents as an incomplete vortex. This is because the vortex formed is insufficiently strong to drop the density as low as 0.9 kg m^{-3}. The remainder of the vortex appears quite uniform in diameter except where it thins to bend to meet the test section windows normally. Altogether, the weakness of the vortex here explains the faint presentation in the v-shadowgraphs in Fig. 3.

An aspect of the flow field to bear in mind is that the shock wave diffraction is normal to the upstream surfaces and so there is a significant induced flow towards the longitudinal centreline of the domain. The reflection of the diffracted shock waves on this centreline will also complicate this field. This is expected to have a marked effect on the vortex development.

As the flow field develops, the portion of the vortex immediately outboard of the centre remains thinner than the remainder of the vortex. This is likely a result of the spanwise outboard flow that must arise as a result of the diffracted shock fronts

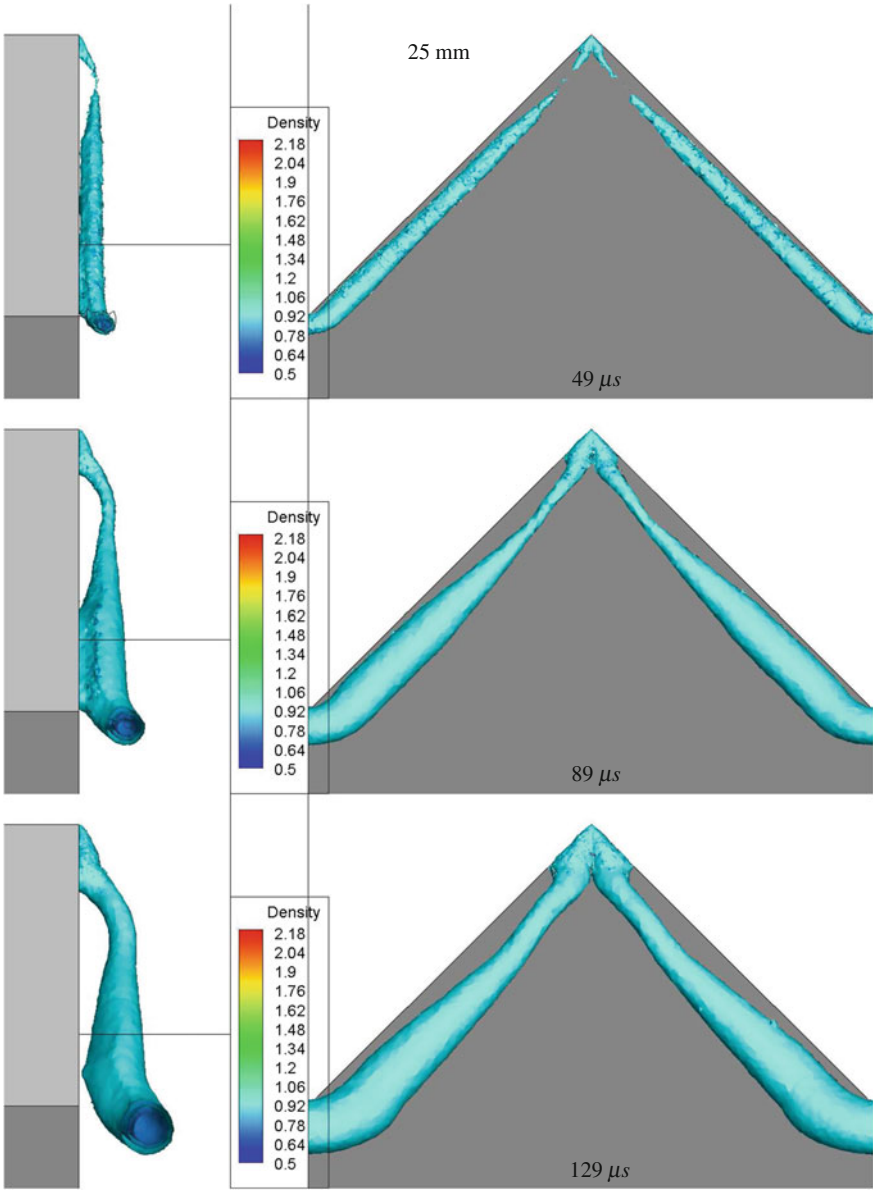

Fig. 6 Computational isopycnics in side elevation (*left*) and the longitudinal direction (*right*) for an incident shock wave strength of M1.3

interacting along the symmetry plane. Such outboard flow would suggest that the vortex tube be conical away from the centreline, which is the appearance apart from the kink formed near the test section walls.

By far the most interesting feature of these vortices is that they seem to terminate near the centreline in the diffraction surface rather than forming a continuous vortex tube. In the side elevation for the final frame of this time series, the vortices seem almost normal to the diffraction surface while the remainder of the vortex is separating from the diffraction face and convecting downstream. This suggests that, in the absence of the test section walls, the two vortex tubes might terminate in the diffraction face while the outboard sections convect downstream and towards the centreline.

Examining the results for an incident shock strength of M1.45 in Fig. 7, similar behaviour can be seen though the vortices show no break at early times. It seems that the portion of the vortex midway between the centreline and the domain edge has ongoing interaction with the diffraction face, evident in the second and third side elevations. The curvature in the longitudinal direction of the vortex centrelines as seen experimentally is clear here and could be explained by the proposed mechanism of the detachment of the vortices from the diffraction face while one end terminates in the same face near the centreline.

The time series for the incident Mach number of 1.6 (Fig. 8) shows the most interesting behaviour. The top end of the vortices is clearly terminating normal to the diffraction face near the centreline, and there is noticeable curvature of the vortex centreline in the longitudinal direction from the first frame. The vortex-induced flow around the end of the vortex terminating in the diffraction face would explain the tapered region from the knee of the vortex tube near towards the apex of the diffraction edge. This also explains the strange shape noted in the experimental images.

The centrelines of the vortices are steeply curved in the longitudinal direction in this series and, although the affected region appears smaller than in the lower shock strength cases, part of the vortex still has a significant interaction with the diffraction face. This suggests that rather than the vortex tubes washing entirely downstream while one end terminates in the diffraction face, there is a portion of the vortex outboard of the apex of the diffraction edge which will deform in the longitudinal direction while the rest (for a significantly long diffraction edge) will remain attached to the corner.

Another feature of interest arises in the case of a Mach 1.6 incident shock wave: there appears to be a secondary vortex tube forming on top of the primary one seen for the lower shock strength cases. The exact cause of such a flow is not immediately apparent. One possibility is that the very strong vortex induces a counter-rotating vortex between its own boundary and the flow off of the upstream surface.

To better visualise the development of these vortices as a function of time, isometric elevations of the isopycnics are presented in Fig. 9. From these images, it is clear that there is a region of the vortices shed off of each of the diffraction edges that curves in the downstream longitudinal direction and that the extent of this region seems to increase with incident shock wave strength. In the case of the flow for the

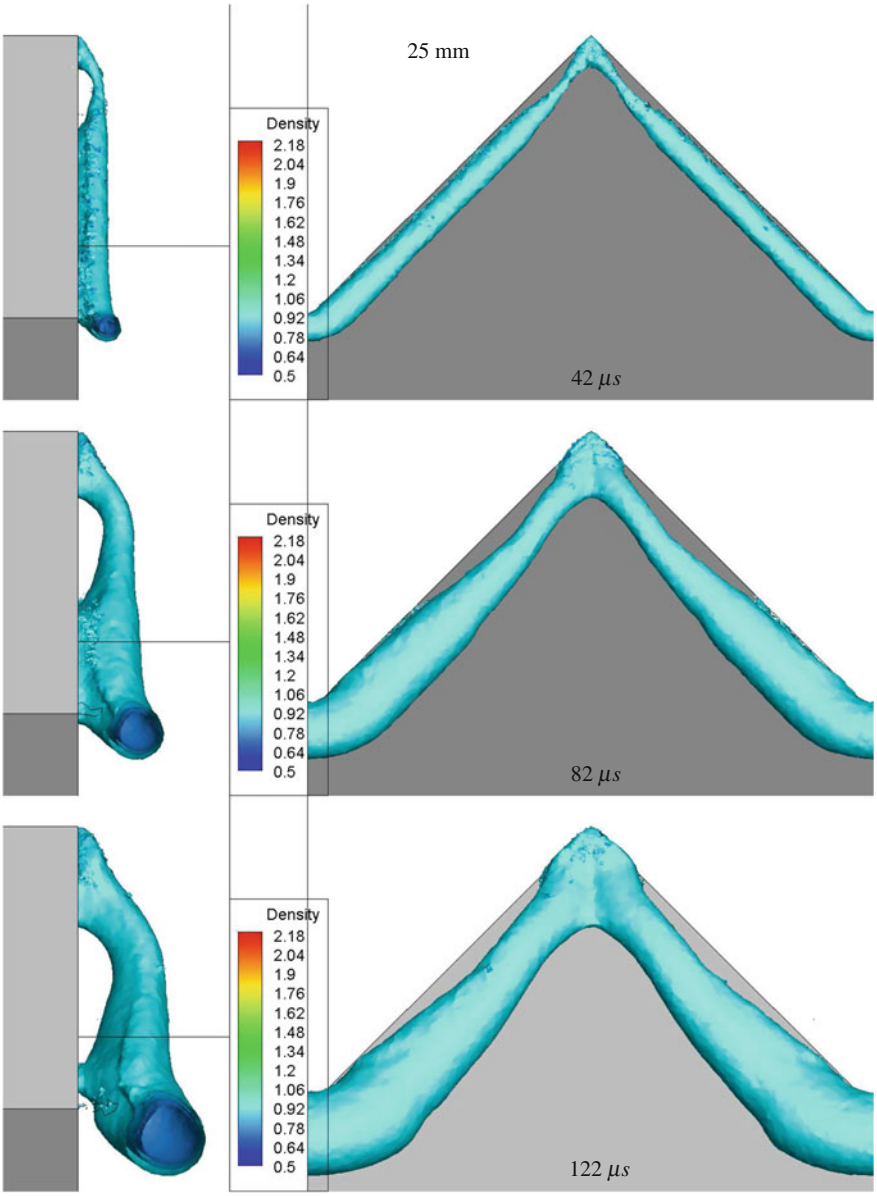

Fig. 7 Computational isopycnics in side elevation (*left*) and the longitudinal direction (*right*) for an incident shock wave strength of M1.45

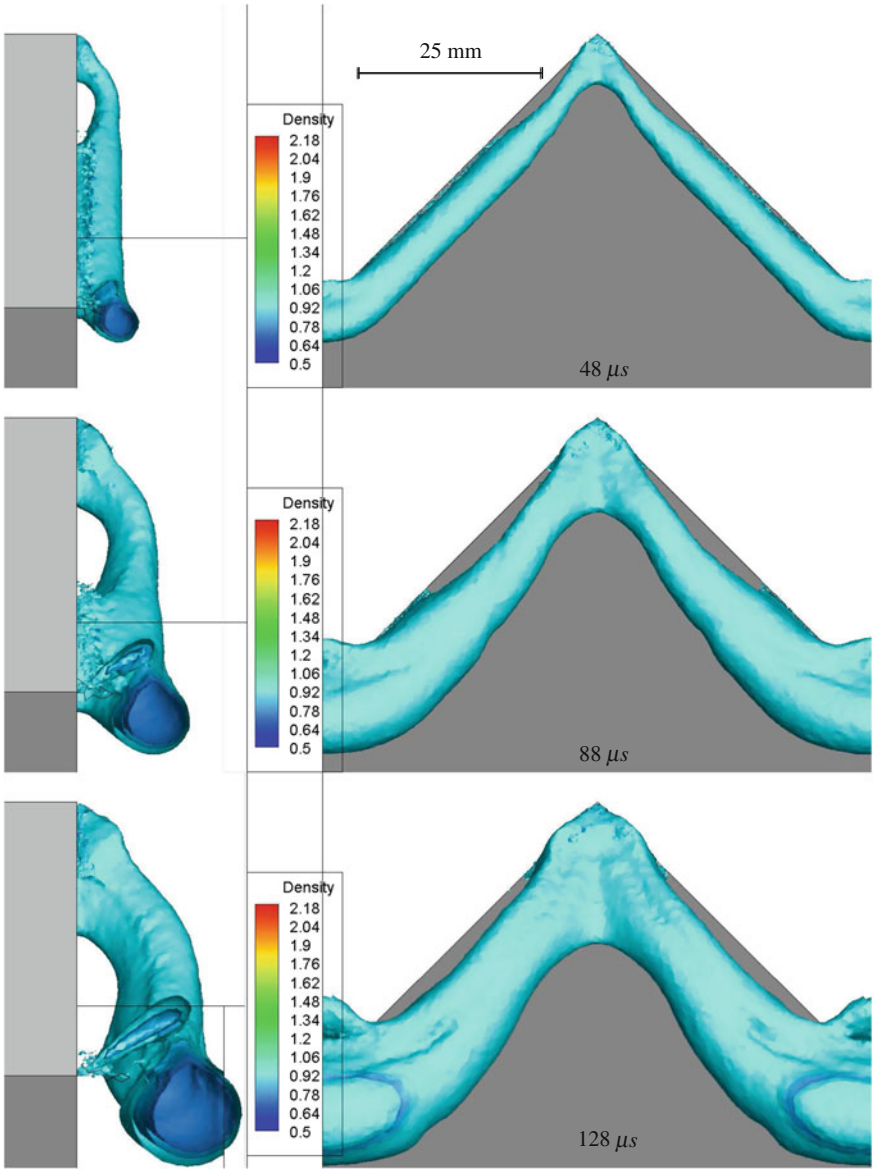

Fig. 8 Computational isopycnics in side elevation (*left*) and the longitudinal direction (*right*) for an incident shock wave strength of M1.6

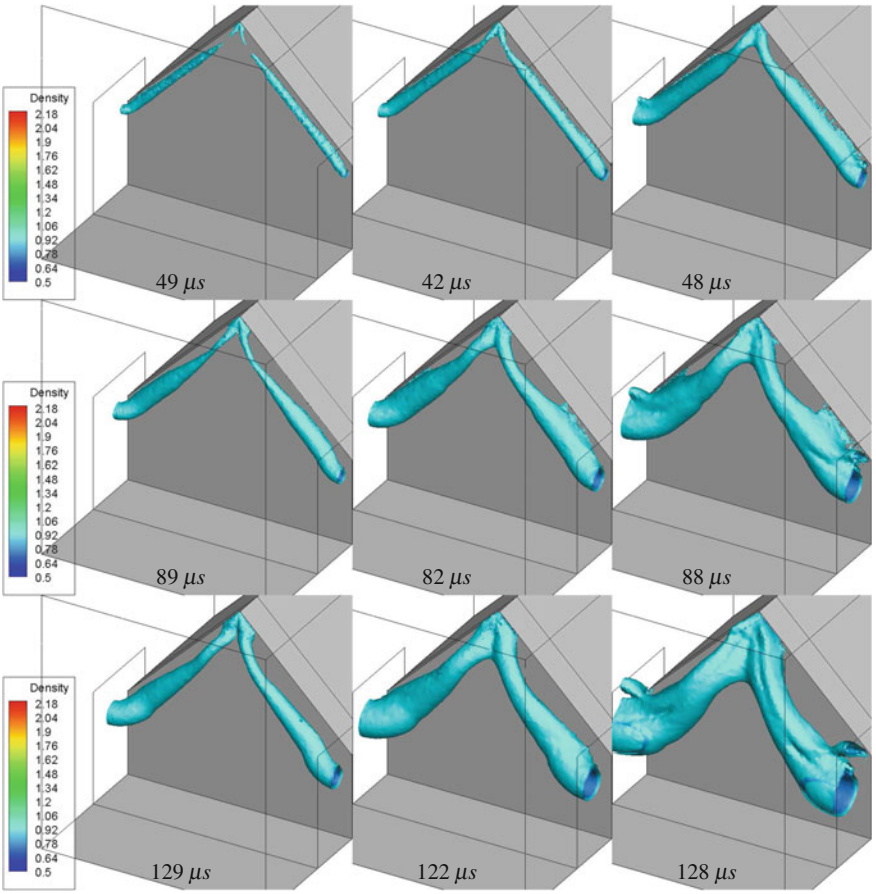

Fig. 9 Computational isopycnics in isometric elevation for incident shock wave strengths of M1.3 (*left*), M1.45 (*centre*) and M1.6 (*right*)

Mach 1.6 incident shock, this region seems to be almost the entire semi-span of the test section.

It is also evident from the images for the Mach 1.6 incident shock wave that the secondary vortex structure seems to develop closer to the centreline of the test section before spreading outwards. This suggests that it may be independent of the geometry of the test section but has been constrained by it to the form evident in the final frame. That would also suggest that there is an inherent length scale to the feature despite a corner having no implicit length scale. The feature size does seem to depend on the size of the region curving away from the diffraction face and so the length scale of importance here may be related to the vorticity length scale. Unfortunately, none of these details can be tested here as all results are particular to the model and shock tube used.

4 Conclusion

The vortices shed at the diffraction edge of a corner normal to the direction of shock wave travel exhibit similar behaviour to that for the diffraction of a shock wave over an edge shaped in the direction of flow. However, there is the significant difference that the vortex lines shed here seem to terminate on the diffraction face instead of forming into a single vortex tube as in the latter case. The portion of the vortex outboard of this then curves, more strongly with increasing incident shock wave strength, in the longitudinal direction while the remainder of the vortex seems to remain attached to the diffraction face. At high incident shock wave strengths, a secondary structure develops on top of the primary vortex tube. Further details of these dynamics cannot be determined as the facility used resulted in a reflected shock wave interacting with the vortex lines at that time. There were also issues of leakage of flow past the model which may have affected the results of some visualisations.

5 Recommendations

The experimental work should be repeated with a model with a greater separation from the floor of the shock tube test section and better sealing. This will increase the time in which the vortex can develop before the reflected wave returns. If possible the experimentation should be undertaken in a wider test section or the model be modified to employ symmetry.

Computationally, the model domain should be extended to much greater span. This will remove the length scale of the test section width and allow confirmation of the spanwise changes in the vortex strength and shape without the influence of the boundary layer on the test section walls. The model should also be run employing a viscous solver.

References

1. Skews, B.W.: The shape of a diffracting shock wave. J. Fluid Mech. **29**(02), 297–305 (1967)
2. Jiang, Z., Onodera, O., Takayama, K.: Evolution of shock waves and the primary vortex loop discharged from a square cross-sectional tube. Shock Waves **9**(1), 1–10 (1999)
3. Reeves, J.O., Skews, B.W.: Unsteady three-dimensional compressible vortex flows. Shock Waves **22**, 161–172 (2012)
4. Cooppan S., Skews B.W.: Vortex shedding over a discontinuous edge. In: Bonazza R., Ranjan D. (eds.), Proceedings of the 29th International Symposium on Shock Waves, pp. 1573–1578. Madison, USA (2015)